INFORMATION TO USERS

This manuscript has been reproduced from the microfilm master. UMI films the text directly from the original or copy submitted. Thus, some thesis and dissertation copies are in typewriter face, while others may be from any type of computer printer.

The quality of this reproduction is dependent upon the quality of the copy submitted. Broken or indistinct print, colored or poor quality illustrations and photographs, print bleedthrough, substandard margins, and improper alignment can adversely affect reproduction.

In the unlikely event that the author did not send UMI a complete manuscript and there are missing pages, these will be noted. Also, if unauthorized copyright material had to be removed, a note will indicate the deletion.

Oversize materials (e.g., maps, drawings, charts) are reproduced by sectioning the original, beginning at the upper left-hand corner and continuing from left to right in equal sections with small overlaps.

Photographs included in the original manuscript have been reproduced xerographically in this copy. Higher quality 6" x 9" black and white photographic prints are available for any photographs or illustrations appearing in this copy for an additional charge. Contact UMI directly to order.

ProQuest Information and Learning
300 North Zeeb Road, Ann Arbor, MI 48106-1346 USA
800-521-0600

Magnetic Reconnection in the MST Reversed Field Pinch

by

Neal Acker Crocker II

A dissertation submitted in partial fulfillment of
the requirements for the degree of

Doctor of Philosophy
(Physics)

at the

UNIVERSITY OF WISCONSIN – MADISON

2001

UMI Number: 3012544

UMI Microform 3012544
Copyright 2001 by Bell & Howell Information and Learning Company.
All rights reserved. This microform edition is protected against unauthorized copying under Title 17, United States Code.

Bell & Howell Information and Learning Company
300 North Zeeb Road
P.O. Box 1346
Ann Arbor, MI 48106-1346

Readers' Page. This page is not to be hand-written except for the signatures

Readers' Page. This page is not to be hand-written except for the signatures

A dissertation entitled

Magnetic Reconnection in
the MST Reversed Field Pinch

submitted to the Graduate School of the
University of Wisconsin-Madison
in partial fulfillment of the requirements for the
degree of Doctor of Philosophy

by

Neal A. Crocker II

Date of Final Oral Examination: May 7, 2001

Month & Year Degree to be awarded: **December** **May** 2001 **August**

* * *

Approval Signatures of Dissertation Readers:

James D Callen

Signature, Dean of Graduate School

Virginia S. Hinshaw/EH

Magnetic Reconnection in the MST Reversed Field Pinch

Under the supervision of Professor Stewart C. Prager (Physics) at the
University of Wisconsin – Madison

ABSTRACT

Magnetic field line reconnection is a process whereby magnetic field lines which are otherwise topologically preserved by, and frozen into, a plasma can break and reconnect to form field lines with different topologies. It plays a significant role in a wide variety of plasmas, including stellar, space and laboratory plasmas. The focus of this dissertation is the underlying dynamics of reconnection in one particular kind of laboratory plasma: the Reversed FIeld Pinch (RFP). Specifically, this dissertation reports measurements, made using a pair of insertable diagnostics in conjunction with arrays of magnetic sensing coils positioned near the plasma surface, of the spatial structure of the magnetic and parallel current density fluctuations associated with reconnection in the edge of MST.

At least four significant results are obtained from such measurements:

First, we observe direct evidence of reconnection, which takes the form of tearing modes in an RFP. Specifically, we measure a (radial) magnetic field fluctuation that causes reconnection at the so-called *reversal surface*, or $q = 0$ surface, in the edge of MST. Notably, this evidence of reconnection at the reversal surface is the first of its kind in an RFP.

Second, we measure the radial width of the associated *current sheet*, or fluctuation in the component of the current density parallel to the equilibrium magnetic field. Such current sheets are a characteristic feature of the reconnection process, but their radial widths are sensitive to the specific effects that allow reconnection to occur, sometimes called *non-ideal* effects because

reconnection is forbidden by ideal MHD. We compare the observed width to those expected from models of reconnection that incorporate different non-ideal effects in Ohm's law. In particular, we see that the observed width is significantly larger than those expected from resistivity in the context of linearly unstable tearing modes, and electron inertia. It is a factor of a few larger than the width expected from the electron pressure gradient effect. It is significantly smaller than the width expected from ion inertia, but this width is not expected to be relevant to a strongly magnetized plasma such as an RFP. Notably, it is comparable to the width of the magnetic island produced by the associated tearing mode. This is consistent with expectation for *saturated*, or fully developed, resistive tearing modes, such as MST is believed to exhibit. It is also consistent with the broadening of a smaller width current sheet through current transport due to parallel streaming of charge carriers (along the field lines of the associated island).

Third, we obtain estimates of the radial charge transport, or radial current density, due to streaming of charge carriers along magnetic field lines that results from reconnection in the edge of MST. This charge transport due to *parallel streaming* is given by $\Gamma_q = \left\langle \tilde{j}_{\parallel} \tilde{b}_r \right\rangle_{F.S.} / B_0$, where $\left\langle \tilde{j}_{\parallel} \tilde{b}_r \right\rangle_{F.S.}$ is the flux surface average product of fluctuations in the radial magnetic field, $\tilde{b}_r$, and the magnetic field aligned, or *parallel*, component of the current density, $\tilde{j}_{\parallel}$. We find that, in contradiction with the theoretical expectation for isolated tearing modes, it is non-vanishing, and, in fact, large enough to imply both the existence of another charge transport mechanism to maintain charge neutrality, and a significant difference in the radial ion and electron particle fluxes due to parallel streaming of particles.

Fourth, we interpret the flux surface average of $\tilde{j}_{\parallel}$ and $\tilde{b}_r$ as a $\bar{J} \times \bar{B}$ force density on the plasma. We observe, in agreement with theory and observation for interacting tearing modes in an RFP, that the radial structure of the force density during sawtooth crashes is such as to flatten the equilibrium radial gradient in toroidal velocity. We observe, also, that it is sufficiently large as to imply the existence of other force densities on the plasma.

Acknowledgements

At long last, I'm finishing my Ph. D.. There are many people who helped me reach this point and I like to take this opportunity to thank them. Unfortunately, there are so many that I'm bound to miss some, but here it goes... First, I'd like to thank my advisor, Prof. Stewart C. Prager, who gave my research direction and who helped me to understand what it means within the larger context of plasma research. I'd like to thank Gennady Fiksel, who acted as a hands-on instructor and general problem solver when I did the experiments discussed here. I'd like to thank Darren Craig and Abdulgader Almagri, who designed and built the probes I used (and taught me how to fix them when I broke them). I'd like to thank John Sarff who allowed himself to be roped into an active role in the research presented here, even going so far at to coauthor a journal articles based on it. I'd also like to thank a number of other scientists who contributed material directly to this dissertation (in no particular order): John Wright, Nicholas Lanier, James Chapman, Paul Fontana and the soon-to-be-doctor Jay Anderson.

I'd like to thank Chris Hegna, who got me started on the topic of magnetic reconnection with a course he taught on the subject, and who, unlike many instructors, had to put up with followup questions for several years after the course ended, since reconnection eventually became the topic of my dissertation.

I'd like to thank the MST research group, including its engineers, technicians and computer systems administrators such as John Lauffenberg, Steve Oliva, Mark Thomas, Tom Lovell, Mikhail Reyfman, Paul Wilhite and Larry Smith, for its support in a variety of forms including, among other things, assistance in late night and marathon experimental sessions, technical support, a pervasive atmosphere of creativity, and a free exchange of ideas.

I'd like to thank Roch Kendrick, who taught me most of what I know about probe building, maintenance and repair.

Finally, I'd like to thank my family, for encouraging me when I decided to go for a doctorate, rather than telling me it was impractical.

Table of Contents

Abstract i

Acknowledgements iii

Table of Contents iv

Chapter 1 - Introduction 1

1.1 - Magnetized Plasmas and The Frozen Flux Condition 1

1.2 - Magnetic Reconnection 2

1.3 - Reversed Field Pinches and Magnetic Reconnection 4

1.4 - Observation of Magnetic Reconnection in The Madison Symmetric Torus 6

1.5 - The Role of Reconnection in Charge, Particle and Momentum Transport 7

1.6 - Overview of this Dissertation 8

References 9

Chapter 2 - Review of Magnetic Field Line Reconnection and its Role in Reversed Field Pinches 10

2.1 - Introduction 10

2.2 - Ideal MHD and The Frozen Flux Condition 11

2.3 - Non-Ideal MHD, Magnetic Reconnection and Current Sheets 13

2.4 - Tearing Modes: Magnetic Reconnection in the Reversed Field Pinch 20

2.5 - Magnetic Islands and the Reconnected Flux 22

2.6 - Classes of Tearing Modes: Reversal Surface Resonant (m = 0) and Core Resonant (m = 1) 23

2.7 - Parallel Current Density and Radial Magnetic Field Fluctuations 25

2.8 - Parallel Streaming of Particles and Charge Transport 25

2.9 - Interaction of Tearing Modes: $\bar{J} \times \bar{B}$ Force 26

2.10 - Summary 28

References 30

Chapter 3 - Experimental Technique **31**

3.1 - Introduction 31

3.2 - MST Plasmas and Probe Use 34

3.3 - Measuring Magnetic and Current Density Fluctuations: Magnetic Sensing Coils and Rogowskii Coils 35

3.4 - Rogowskii Probes 39

3.5 - Processing Coil Signals: Sources of Error and Noise 40

3.6 - Interaction of Rogowskii Probes with Plasma Fluctuations 44

3.7 - Toroidal Coil Arrays 48

3.8 - Analyzing Fluctuations: Crossspectral Analysis 49

3.9 - Approximating Flux Surface Averages of Fluctuation Products 51

3.10 - Principles of Pseudospectral Analysis 54

3.11 - Pseudospectral Analysis in MST 56

3.12 - Two-point Spectral Analysis 59

3.13 - Ensemble Averaging - Approximating Expected Averages 62

3.14 - Determining Statistical Uncertainties of Spectral Measurements 63

3.15 - Summary 64

References 66

Chapter 4 - Reconnection in MST **67**

4.1 - Introduction 67

4.2 - Pseudospectra of Poloidal Current Density and Magnetic Field Fluctuations in MST Edge 70

4.3 - Two-Point Toroidal Spectra of Poloidal Current Density and Magnetic Field Fluctuations in MST Edge 81

4.4 - Two-Point Poloidal Spectra of Poloidal Current Density and Magnetic Field Fluctuations in MST Edge 86

4.5 - Comparison of Tearing Mode Structure in MST Edge with Observations

in DEBS 89

4.6 - Reconnection at the Reversal Surface in MST 104

4.7 - The Reversal Surface Reconnection Current Sheet 107

4.8 - Conclusions 111

References 114

Chapter 5 - Charge, Particle and Momentum Transport 115

5.1 - Introduction 115

5.2 - Measurement of $\left\langle \tilde{j}_{\parallel}\tilde{b}_{r}\right\rangle_{F.S.}$ 117

5.3 - Coherence and Phase Relationship of $\tilde{j}_{\parallel}$ and $\tilde{b}_{r}$ 121

5.4 - Decomposition of $\left\langle \tilde{j}_{\parallel}\tilde{b}_{r}\right\rangle_{F.S.}$ in Terms of Toroidal Modes 123

5.5 - Charge and Particle Transport due to Parallel Streaming of Particles 128

5.6 - $\left\langle \tilde{j}_{\parallel}\tilde{b}_{r}\right\rangle_{F.S.}$ as a $\bar{J}\times\bar{B}$ Force 133

5.7 - Conclusions 136

References 138

Chapter 6 - Conclusions and Future Work 139

6.1 - Conclusions 139

6.2 - Future Work 142

Appendix A - Supplemental Figures and Description of Data Sets for Chapter 4 144

A.1 - Introduction 144

A.2 - Pseudospectra of Poloidal Current Density and Magnetic Field Fluctuations in MST Edge 144

A.3 - Two-Point Toroidal Spectra of Poloidal Current Density and Magnetic Field Fluctuations in MST Edge 146

A.4 - Two-Point Poloidal Spectra of Poloidal Current Density and Magnetic Field

Fluctuations in MST Edge 147

A.5 - Comparison of Tearing Mode Structure in MST Edge with Observations in DEBS 148

Figures 149

Appendix B - Supplemental Figures and Description of Data Sets for Chapter 5 **221**

B.1 - Introduction 221

B.2 - Measurements of $\left\langle \tilde{j}_{\parallel}\tilde{b}_r \right\rangle_{F.S.}$ and $\left\langle \left|\tilde{j}_{\parallel}\right|^2 \right\rangle_{F.S.}^{1/2} \left\langle \left|\tilde{b}_r\right|^2 \right\rangle_{F.S.}^{1/2}$ 222

B.3 - Crossspectral Coherence and Phase and Amplitude of $\tilde{j}_{\parallel}$ and $\tilde{b}_r$ 222

B.4 - Pseudospectral Decomposition of $\left\langle \tilde{j}_{\parallel}\tilde{b}_r \right\rangle_{F.S.}$ 222

B.5 - Magnetic Fluctuation Driven Charge and Particle Transport 223

Figures 224

Chapter 1 - Introduction

1.1 - Magnetized Plasmas and The Frozen Flux Condition

Plasmas, which are composed of charged particles in a disordered, gas-like or fluid-like state, exhibit a wide variety of interesting phenomena across a broad range of temporal and spatial scales. They are subject to all the complex dynamics of neutral fluids. In addition, since they are capable of carrying currents and electric charges, they can also interact strongly with electric and magnetic fields. Magnetized plasmas, in particular, are subject to a rich set of dynamics.

Magnetized plasmas are characterized by magnetic energy densities that are significant compared to their thermal energy densities. Such plasmas may frequently be described by fluid-like equations that represent the dynamics governing the evolution of their particle, momentum and energy densities. However, these equations typically incorporate physical effects that do not affect neutral fluids since the fluid's momentum and energy densities interact with the charge density and currents carried by the plasma. Thus descriptions of such plasmas must also include equations that describe the evolution of their charge density and current, as well as Maxwell's equations.

One theory that has proven very successful in describing many types of magnetized plasmas, ranging from laboratory plasmas to space plasmas, over a broad range of temporal and spatial scales, is ideal magnetohydrodynamics (ideal MHD). Ideal MHD is a variant of a broad class of plasma theories, collectively referred to as MHD, that treat plasmas as conducting fluids whose evolution is influenced by their interaction with electric and magnetic fields. Different variants of MHD are distinguished by the physical effects that are incorporated in Ohm's Law, which describes the relationship between the electric field ($\bar{E}$), the magnetic field ($\bar{B}$) and various properties of the MHD fluid, such as it's fluid velocity field ($\bar{V}$). Ideal MHD is characterized by the approximation that the plasma fluid is infinitely or *ideally* conducting. Thus, while Ohm's Law for a conducting material, or fluid, with finite conductivity might take

the form

$$\vec{E} + (\text{other terms}) = \eta \vec{J}, \tag{1.1.1}$$

where η is the material's resistivity (which is inversely proportional to its conductivity) and $\vec{J}$ is the current density conducted by the material, ideal Ohm's Law has no contribution from $\eta \vec{J}$. In fact, Ohm's Law for ideal MHD is:

$$\vec{E} + \vec{V} \times \vec{B} = 0 \tag{1.1.2}$$

One of the consequences of the ideal Ohm's Law for plasmas is the *frozen flux* theorem. In physical terms, this theorem states that magnetic flux is frozen into the plasma. More precisely, the magnetic flux through any closed loop is constant if the loop moves (and deforms) with the plasma fluid. This, in turn, has an important consequence for the evolution of magnetic field lines in the plasma fluid. It implies that magnetic field line topology is conserved in an ideal MHD fluid. In other words, magnetic field lines are advected by the plasma fluid without breaking (or crossing other lines).

1.2 - Magnetic Reconnection

In spite of the success of ideal MHD in describing magnetized plasmas under a broad range of conditions, a large collection of experimental observations has been amassed of magnetized plasmas that are expected to be well described by ideal MHD that evolve in ways that change the topology of their embedded magnetic fields. Examples include solar flares, magnetic substorms and sawtooth collapse in tokamak plasmas. (Each of these examples is reviewed by, for instance, Battacharjee, et al..[1])

Historically, attempts to explain such experimental observations invoke a theoretically predicted phenomenon referred to as *magnetic field line reconnection.* Magnetic field line reconnection is a process in which magnetic field line topology alters as a result of spatially localized violations of the frozen flux condition (*i.e.*, ideal Ohm's becomes locally invalid). In other words, magnetic reconnection occurs when magnetic field lines momentarily break at

particular locations and reconnect with a different topology.

Magnetic field line reconnection which, in general, is permitted in the context of MHD theories as a result of effects in Ohm's law that are neglected in ideal MHD, commonly referred to as *non-ideal effects*, can have a significant impact on the global evolution of a plasma. By permitting localized violations of the frozen flux condition, magnetic field line reconnection, or magnetic reconnection, relaxes a strong constraint on plasma motion, allowing the conversion of various forms of stored energy into plasma kinetic energy. The details of this conversion process, such as the rate of conversion, or rate of reconnection, and the spatial scale of the region of reconnection, where the frozen flux condition breaks down, depend on which non-ideal effects are significant in that region.

Despite the possibility that the process of magnetic reconnection might help explain many phenomena, such as those mentioned above, that cannot be explained by ideal MHD, the question of which non-ideal effects govern the process remains open for a broad range of plasma conditions. Early theoretical work[2,3,4] focused on models of reconnection that incorporated resistivity as the only non-ideal effect. However, such theoretical models predicted reconnection rates that were much slower than that observed in many types of plasmas. Later theoretical work considered models of reconnection that incorporated other non-ideal effects, such as electron inertia,[5,6,7] electron pressure,[8,9] ion inertia[10] and streaming of charge carrying particles along magnetic field lines. Such models are commonly termed *collisionless* reconnection models, to distinguish them from the earlier *collisional* models which incorporated only resistivity, a collisional effect, as a non-ideal effect in Ohm's Law.

Both collisional and collisionless models of reconnection have met some success in accurately describing experimental observations of magnetic reconnection under a variety of plasma conditions. For instance, collisional models of reconnection have been used to explain measurements in MRX[11] which produces plasmas that are cold enough and dense enough that collisionality can be significant. Collisionless models of reconnection, on the other hand, have

been applied with some success to explaining the sawtooth collapse[1] in the hot core of the tokamak, where collisionality is a very weak effect.

1.3 - Reversed Field Pinches and Magnetic Reconnection

One class of plasmas whose evolution is believed, on the basis of theoretical work and experimental observation, to be strongly influenced by magnetic reconnection is the Reversed Field Pinch (RFP) configuration. Reversed Field Pinch plasmas exhibit a variety of phenomena, such as strong magnetic fluctuations, which are not expected from ideal MHD. In addition, tearing mode theory, which is intrinsically a model for magnetic reconnection in the RFP, makes a strong prediction that tearing modes are unstable in an RFP.[2]

An RFP is an axisymmetric toroidal magnetic plasma confinement device. As with many other axisymmetric toroidal plasma configurations, the dynamics governing magnetic reconnection in an RFP are intimately connected to the structure of the equilibrium magnetic field. (The equilibrium magnetic field can be loosely defined as the average magnetic field for a set of many plasmas created under similar conditions). The equilibrium magnetic field of an RFP can be described as a set of nested toroidal *magnetic flux surfaces*, or *flux surfaces* (surfaces in which magnetic field lines are confined as they wander through plasma). At the center of these nested surfaces is the *magnetic axis*. The magnetic field within each surface has a particular *helicity*, sometimes referred to as the surface's q, or *safety factor*. This helicity is defined by the number of transits that a field line in the surface will make around the axis of the torus (*e.g.*, the number of *toroidal transits*) in the course of one transit about the magnetic axis (*e.g.*, one *poloidal transit*). This helicity varies monotonically from some small number (typically of order 0.1) at the magnetic axis to a much smaller negative number at the outermost flux surface in the plasma. It passes through zero at what is termed the *reversal surface*, which is near the edge of the plasma. The reversal surface is so named because beyond it the toroidal magnetic field reverses direction. The toroidal magnetic field is the component of the magnetic

field in the *toroidal direction*, which is the angular direction around the toroidal axis. This structure creates regions within the plasma, in the vicinity of what are known as *rational surfaces*, where the frozen flux condition may potentially breakdown. Rational surfaces are those surfaces with a helicity which is a rational number. In other words, rational surfaces are those surfaces in which the field lines close on themselves after a finite number of transits about the magnetic axis. As with many other axisymmetric plasma configurations exhibiting rational surfaces, RFP plasmas are susceptible to a category of plasma perturbations commonly referred to as *tearing modes*, which can develop only because magnetic field reconnection, or *tearing*, can occur at rational surfaces.

Tearing modes in an RFP cause simultaneous, approximately helical perturbations to a broad variety of plasma quantities, including, in particular, the magnetic field and the parallel current density (the component of current density parallel to the equilibrium magnetic field), as they develop. This approximately helical structure arises because the equilibrium magnetic field in an RFP is symmetric in the toroidal direction and approximately symmetric in the *poloidal* direction, which is the angular direction around the magnetic axis.

Tearing modes in an RFP will exhibit any of several possible approximate periodicities in the poloidal direction and any of a broad range of possible exact periodicities in the toroidal direction. In particular, they will exhibit approximate *helical periodicities* (specific combinations of toroidal and poloidal periodicity) that are determined by the helicities of the rational surfaces in the plasma. Only tearing modes with a ratio of poloidal to toroidal periodicities equal to the helicity of some rational surface in the plasma may develop. As a tearing mode develops, reconnection occurs at the rational surface whose helicity matches its helical periodicity in this way. The tearing mode is said to be *resonant* at that rational surface.

The tearing modes that are most active in an RFP plasma can be divided into two categories, as a consequence of the types of rational surfaces exhibited by the RFP's equilibrium magnetic field: those with a poloidal periodicity of 1 (*i.e.*, with poloidal mode number $m = 1$)

and those which are poloidally symmetric (*i.e.*, with poloidal mode number m = 0). For the m = 0 tearing modes, the region of reconnection is in the plasma edge, at the reversal surface, whose helicity is zero. Thus, this category of tearing modes is sometimes referred to in the following chapters as *edge tearing modes*, or *reversal surface resonant tearing modes*. The m = 1 tearing modes, on the other hand, can be resonant at rational surfaces throughout the plasma (except the reversal surface). The m = 1 tearing whose resonant surfaces are closest to the core of the plasma tend to be the most active (*i.e.*, they typically have the largest amplitude), so the the m = 1 tearing modes are sometimes referred to in the following chapters as *core tearing modes*.

1.4 - Observation of Magnetic Reconnection in The Madison Symmetric Torus

The Madison Symmetric Torus[12] (MST) is an RFP capable of generating plasmas whose edge region is particularly suited to the use of relatively deeply penetrating probes, both in terms of the effect of plasma conditions on probe survival, and in terms of the perturbing effects of probes on the plasmas that they diagnose. Consequently, the edge, or m = 0, category of tearing modes is accessible to detailed experimental study in MST. Both magnetic and current density fluctuations can be measured by suitable arrangements of magnetic sensing coils mounted on a probe. Thus, the structure of the magnetic and current density perturbations associated with magnetic reconnection can be studied in the plasma edge. More importantly, these fluctuations can be measured directly in the region around a resonant surface, where magnetic reconnection occurs.

Such measurements have been made in MST and are discussed in this dissertation. These measurements have, in particular, yielded estimates of the poloidal and toroidal mode number spectra of the magnetic field and parallel current density fluctuations in the edge of MST, as well as other details of their spatial structure. Analysis of these measurements provides verification that magnetic reconnection is indeed active in the edge of MST, as expected theoretically and

from prior experimental observation in MST. For instance, the magnetic perturbation which constitutes the actual reconnected magnetic flux for the m = 0 tearing modes has been observed. Also, the poloidal and toroidal spectra of the current density fluctuations clearly show existence of the current sheet associated with magnetic reconnection at the reversal surface. The measured radial width of this current sheet provides a sensitive test of the various models of reconnection that might be invoked to describe reconnection in the edge of MST.

1.5 - The Role of Reconnection in Charge, Particle and Momentum Transport

There are two ways, in particular, in which tearing modes significantly affect the behavior of RFP plasmas, that may be studied in MST. First, tearing mode theory predicts that tearing modes resonant at different magnetic surfaces in an RFP plasma may interact with each other or a nearby conducting wall in a way that causes the associated radial magnetic field and parallel current density perturbations to exert $\bar{J} \times \bar{B}$ forces on the plasma. Evidence of such an interaction has, in fact, already been observed in MST.[13] Second, magnetic field line reconnection may alter magnetic field line topology in an RFP plasma in such a way as to permit electric charge to be redistributed across the flux surfaces of the equilibrium magnetic field by streaming of charge carriers along magnetic field lines. Since an RFP plasma will, to a very high degree, maintain electrical neutrality, such a charge transport would in turn have an impact on particle transport. Both of these phenomena, the exertion of a $\bar{J} \times \bar{B}$ force, and charge transport due to parallel streaming, have in common that they depend on the character of both the radial magnetic field and parallel current density perturbations produced by tearing modes in a plasma.

In this dissertation we report measurements of both the radial magnetic field and parallel current density perturbations in the edge of MST. Analysis of these measurements indicate both that there is a $\bar{J} \times \bar{B}$ exerted on the edge plasma in MST as expected from the theory for interacting tearing modes and that there is a substantial charge transport in the edge region of the MST plasmas due to streaming of charge carriers along reconnected magnetic field lines.

1.6 - Overview of this Dissertation

The material in this dissertation is organized into several parts. This chapter, Chapter 1, has introduced the subject of this dissertation. Chapter 2 provides a review of the theory behind magnetic field line reconnection, focusing, in particular, on how it is expected to be manifested in MST. Chapter 3 discusses how the measurements described in this dissertation have been made, both in terms of the devices used to make those measurements and the techniques used to analyze the data acquired. Chapter 4 discusses observations of tearing mode structure in the edge of MST, including the direct observation of magnetic pertubation that causes reconnection at the reversal suface and the implications of the width of the related current sheet as to the nature of the process governing reconnection in the edge of MST. Chapter 5 discusses the charge transport and $\bar{J} \times \bar{B}$ forces in the edge MST plasmas implied by the radial magnetic field and parallel current density perturbations observed there. Finally, Chapter 6 summarizes the results presented in this dissertation and outlines the major conclusions.

References

[1] A. Battacharjee, et al., J. of Geophys. Res. **104,** 14543 (1999).

[2] H. P. Furth, J. Killeen, and M. N. Rosenbluth, Phys. Fluids **6,** 459 (1963).

[3] E. N. Parker, J. of Geophys. Res. **62,** 509 (1957).

[4] P. A. Sweet, *International Astronomical Union Symposium No. 6: Electromagnetic Phenomena in Cosmical Physics,* (Ed. by B. Lehnert), (Cambridge at the University Press; Cambridge, England; 1958). p. 123.

[5] D. Biskamp, E. Schwarz, and, J. F. Drake, Phys. Plasmas **4,** 1002 (1997).

[6] J. F. Drake and R. G. Kleva, Phys. Rev. Lett. **66,** 1458 (1991).

[7] D. Biskamp, E. Schwarz, and, J. F. Drake, Phys. Rev. Lett **75,** 3850 (1995).

[8] B. Rogers and L. Zakharov, Phys. Plasmas **3,** 2411 (1996).

[9] R. G. Kleva, J. F. Drake, and F. L. Waelbroeck, Phys. Plasmas **2,** 23 (1995).

[10] M. A. Shay, J. F. Drake, R. E. Denton, and D. Biskamp, J. of Geophys. Res. **103,** 9165 (1998).

[11] H. Ji, et al., Phys. Rev. Lett. **80,** 3256 (1998).

[12] S. C. Prager, et al., Phys. Fluids B **2,** 1367 (1990).

[13] A. K. Hansen, et al., Phys. Rev. Lett. **85,** 3408 (2000).

Chapter 2 - Review of Magnetic Field Line Reconnection and its Role in Reversed Field Pinches

2.1 - Introduction

Magnetized plasmas are constrained in their fluid motion, under a broad range of conditions, to preserve the topology of their embedded magnetic field lines. At the same time, under these conditions, the magnetic fields in these plasmas evolve as if composed of magnetic field lines that are advected by the fluid. However, this constraint, called the *frozen flux condition*, may sometimes be violated by a spatially localized process called *magnetic field line reconnection* in plasmas that are otherwise subject to it. During the course of magnetic field line reconnection, field lines are advected by plasma motion into a region where the frozen flux condition fails. In this region, they effectively break and reconnect in a way which changes their topologies. One class of plasmas whose evolution is believed, both from theory and from experimental observation, to be strongly influenced by the process of magnetic reconnection is the class of plasmas produced in the Reversed Field Pinch (RFP) configuration. In this chapter, we briefly review some aspects of the theory underlying magnetic reconnection and some ways it specifically applies to RFP plasmas. In particular, we discuss the roles it is expected to play in charge, particle and momentum transport in RFP plasmas.

In Sections 2.2 and 2.3 of this chapter, we discuss the frozen flux condition and magnetic reconnection, respectively, both of which may be understood in the context of a plasma theory called magnetohydrodynamics (MHD). We discuss various effects that break the frozen flux condition and permit magnetic reconnection. Additionally, we discuss a characteristic feature of magnetic reconnection which we also address experimentally in Ch. 4 of this dissertation. Specifically, magnetic reconnection characteristically produces a significant increase in the magnetic field aligned, or *parallel,* component of current density, which is sometimes called a *current sheet,* in the region where it occurs.

In Sections 2.4 – 2.6, we discuss the form magnetic reconnection is expected to take in

RFP plasmas. Specifically, magnetic reconnection in RFP plasmas is associated with a class of plasma perturbations called tearing modes, and may produce magnetic islands. Tearing modes can have any of a variety of possible spatial structures, each of which is associated with magnetic reconnection that is localized to a particular rational surface in the plasma. This association between tearing modes and rational surfaces allows us to introduce a system of classification for tearing modes that we make use of in Ch. 4 and 5 in the discussion of our experimental results. Specifically, we are able to divide tearing modes into two classes: those which exhibit approximate poloidal symmetry (the $m = 0$ tearing modes) and those which exhibit an approximate poloidal periodicity of 1 (the $m = 1$ tearing modes). The $m = 0$ tearing modes are associated with magnetic reconnection at the reversal surface. The $m = 1$ tearing modes, on the other hand, are associated with reconnection at other rational surfaces throughout the plasma, although the most active of these tearing modes are associated with reconnection at surfaces in the core of the plasma.

In Sections 2.7 – 2.9, we discuss the roles that magnetic reconnection potentially plays in the charge, particle and momentum balances of RFPs. Specifically, we discuss the joint role that the parallel current density, $\tilde{j}_{\parallel}$, and radial magnetic field perturbations, $\tilde{b}_r$, associated with tearing modes may play in these balances through their flux surface average product $\left\langle \tilde{j}_{\parallel}\tilde{b}_r \right\rangle_{F.S.}$. If $\left\langle \tilde{j}_{\parallel}\tilde{b}_r \right\rangle_{F.S.}$ is non-vanishing, it represents both a $\bar{J} \times \bar{B}$ force on the plasma and a charge transport across the flux surfaces of the equilibrium magnetic field due to parallel streaming of charge carriers. Such a charge transport, in turn, has implications for particle transport.

In Section 2.10, we summarize the major points of this chapter.

2.2 - Ideal MHD and The Frozen Flux Condition

The dynamics that govern many magnetized plasmas are well described over a broad range of temporal and spatial scales by the equations of MHD, which treat such plasmas as conducting fluids whose evolution is influenced by their interaction with electric and magnetic

fields. An important part of the MHD description of plasma is Ohm's Law, which describes the relationship between the electric field, $\bar{E}$, the magnetic field, $\bar{B}$, the fluid velocity field, $\bar{V}$, and various other properties of the MHD fluid:

$$\bar{E} + \bar{V} \times \bar{B} = \bar{R}, \tag{2.2.1}$$

where $\bar{R}$ represents the combined contributions from other plasma properties. MHD theory has many variants that are distinguished by the physical effects they incorporate in the term $\bar{R}$ on the right hand side of Eq. 2.2.1.

One widely applicable variant of MHD is known as ideal MHD. Ohm's law for ideal MHD is:

$$\bar{E} + \bar{V} \times \bar{B} = 0 \tag{2.2.2}$$

Ideal MHD derives its name from a particular approximation it makes in neglecting one the plasma effects that contribute to the term $\bar{R}$ on the right hand side of Eq. 2.2.1. Specifically, it treats plasma fluids as infinitely or *ideally* conducting by neglecting the plasma resistivity term, $\eta\bar{J}$, where η is the plasmas' resistivity and $\bar{J}$ is its current density.

One of the consequences of the ideal Ohm's Law for plasmas is the frozen flux theorem: the magnetic flux through any area bounded by a closed loop is constant if the loop is advected by (*i.e.,* moves and deforms with) the plasma fluid. The magnetic flux, Ψ, through an area, A, that is bounded by a loop, L, and is advected by the plasma at velocity, $\bar{V}$, varies in time according to:

$$d\Psi/dt = \tfrac{d}{dt}\int_A \bar{B}\cdot d\bar{a} = \int_A \left(\partial\bar{B}/\partial t\right)\cdot d\bar{a} + \oint_L \bar{B}\cdot\left(\bar{V}\times d\bar{l}\right). \tag{2.2.3}$$

Since

$$\oint_L \bar{B}\cdot\left(\bar{V}\times d\bar{l}\right) = -\oint_L d\bar{l}\cdot\left(\bar{V}\times\bar{B}\right) = -\int_A \bar{\nabla}\times\left(\bar{V}\times\bar{B}\right)\cdot d\bar{a}, \tag{2.2.4}$$

and since Eq. 2.2.2 can be recast, using Faraday's law, into the form

$$\partial\bar{B}/\partial t = \bar{\nabla}\times\left(\bar{V}\times\bar{B}\right), \tag{2.2.5}$$

it can be seen that, in ideal MHD plasmas,

$$d\Psi/dt = \int_A \left(\partial\vec{B}/\partial t - \bar{\nabla}\times\left(\vec{V}\times\vec{B}\right)\right)\cdot d\vec{a} = 0. \qquad (2.2.6)$$

In physical terms, the frozen flux theorem states that magnetic flux is frozen into the plasma fluid. This, in turn, has an important consequence for the evolution of magnetic field lines in a plasma fluid. It implies that magnetic field lines in an ideal MHD fluid can be described as being advected by the plasma fluid in such a way that their topology is conserved. Consequently, magnetic field lines in an ideal MHD fluid are advected by the plasma fluid without breaking (or crossing other lines).

2.3 - Non-Ideal MHD, Magnetic Reconnection and Current Sheets

Ideal MHD, and consequently the frozen flux condition, may break down when physical effects neglected in ideal Ohm's Law, or *non-ideal effects*, which are represented by the term $\vec{R}$ on the right hand side of Eq. 2.2.1, become significant in the evolution of the plasma's magnetic field. Variants of MHD that incorporate such effects are collectively referred to as *non-ideal MHD*. In order for frozen flux condition to break down in some region of the plasma, Eq. 2.2.6 must cease to be even approximately valid there. Thus, the combined non-ideal effects represented by $\vec{R}$ must satisfy the condition

$$\left|\bar{\nabla}\times\vec{R}\right| \gtrsim \left|\bar{\nabla}\times\left(\vec{V}\times\vec{B}\right)\right|, \qquad (2.3.1)$$

in some region of the plasma.

There are some important processes in the dynamics of magnetized plasmas that can only be described by non-ideal MHD. One such non-ideal process is magnetic reconnection. Magnetic reconnection is a process in which magnetic field line topology changes as a result of spatially localized violations of the frozen flux condition. Specifically, magnetic reconnection occurs when magnetic field lines momentarily break at particular locations and reconnect to form new field lines with different topologies.

Reconnection potentially occurs in an approximately ideal MHD fluid whenever opposing flows compress a region of sheared magnetic field (Fig. 1). If the ideal MHD

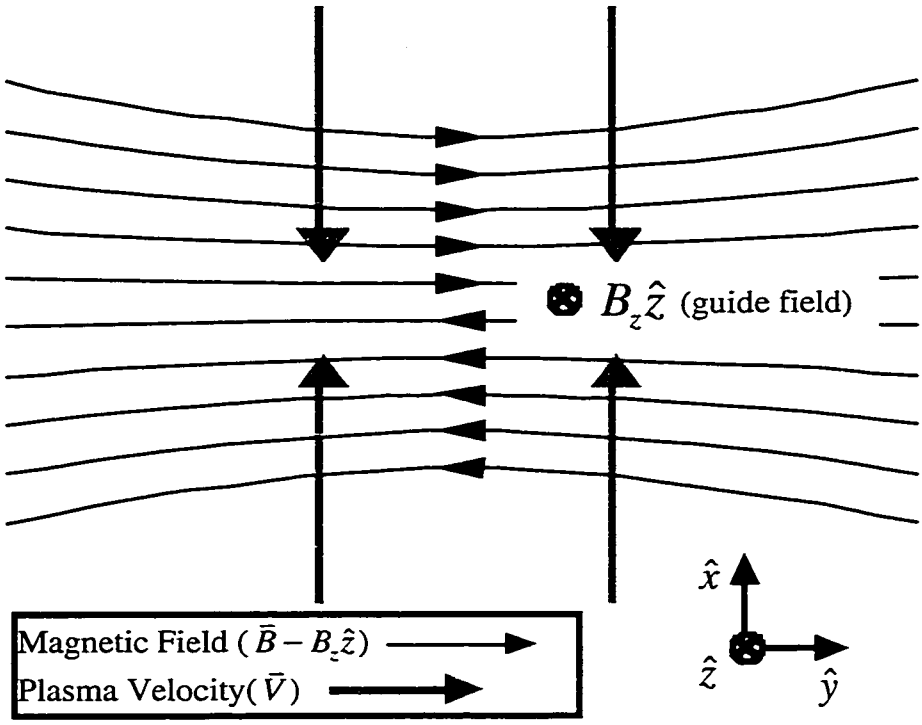

Figure 1: Schematic of opposing plasma flows that compress sheared magnetic. Magnetic reconnection potentially occurs in region of compression.

approximation were to remain valid in the region of compression where the opposing flows, sometimes called the *inflow*, meet, the frozen flux condition would remain in effect. In this situation, magnetic field shear would simply increase in this region. However, there are a number of non-ideal effects that are sensitive to gradients in plasma quantities, including, for instance, the magnetic field. These effects may become significant in the compression region because, just as magnetic shear increases in this region, gradients in other plasma quantities may increase, as well. Additionally, some non-ideal effects in Ohm's law are sensitive to the time scale of the compression and may become significant if the compression is sufficiently rapid. Various non-ideal effects of both these types have been treated theoretically, including, among other things, resistivity,[1,2,3] electron inertia,[4,5,6] electron pressure[7,8] and ion inertia.[9] With all of these non-ideal effects incorporated, Ohm's Law can be expressed as

$$\bar{E} + \bar{V} \times \bar{B} = \eta \bar{J} + \left(\varepsilon_0 \omega_{pe}^2\right)^{-1} d\bar{J}/dt + \left(\bar{J} \times \bar{B} - \bar{\nabla} p_e\right)/(en), \tag{2.3.2}$$

where $\omega_{pe} = \left(e^2 n/m_e \varepsilon_0\right)^{1/2}$, m_e is electron mass).

Another non-ideal effect that has been treated theoretically is the transport of current density by streaming of charge carriers along magnetic field lines.[10, 11, 12, 13] Since the increased magnetic shear in the compression region implies a peaking of current density there, current transport processes potentially may play a significant role in reconnection.

When the combined non-ideal effects in Ohm's law become significant in the compression region (by satisfying the condition in Eq. 2.3.1), then magnetic reconnection occurs. Magnetic flux associated with the sheared component of the magnetic field is destroyed, or dissipated, in the compression region, and an equivalent amount of new magnetic flux oriented along the axis of the opposing plasma inflow is created (Fig. 2). This new magnetic flux, or *reconnected flux*, is carried out of the dissipation region by a diverging plasma outflow. The process of the destruction of incoming flux can be viewed, in some sense, as the severing of incoming magnetic field lines. The process of the creation of new flux can, in turn, be viewed as the joining, or reconnection, of the ends of these severed field lines to produce new field lines with different topologies. The new field lines are then carried out of the dissipation region by the plasma outflow.

There are many different theoretical models of the reconnection process that occurs in the compression region. Different models are characterized by, among other things, the different combinations of non-ideal effects the incorporate in Ohm's law. Each non-ideal effect in Ohm's law adds a spatial scale to model the which incorporates it. Typically, such models show non-ideal plasma behavior in the compression region at the largest scale corresponding to a significant non-ideal effect in Ohm's law. Additionally, such models typically show a peaked current density at this scale in the direction perpendicular to the plane of reconnection (the $\hat{z}$ direction in Fig. 2) which is associated with the increase in magnetic shear. This peaked current density is often called a *current sheet* or *current layer.*

One effect that has been studied extensively, perhaps the first non-ideal effect to be

studied in the context of reconnection, is resistivity[2, 3] (the $\eta\bar{J}$ term in Eq. 2.3.2). The incorporation of resistivity in Ohm's Law in a theoretical model of reconnection introduces the resistive MHD scale, $\delta_{MHD} = L/S^{\alpha}$, as a spatial scale, where $\alpha \sim 1/2$. The width L is the width of the non-ideal region along the axis of plasma outflow (see Fig. 2) and S is the Lundquist number.

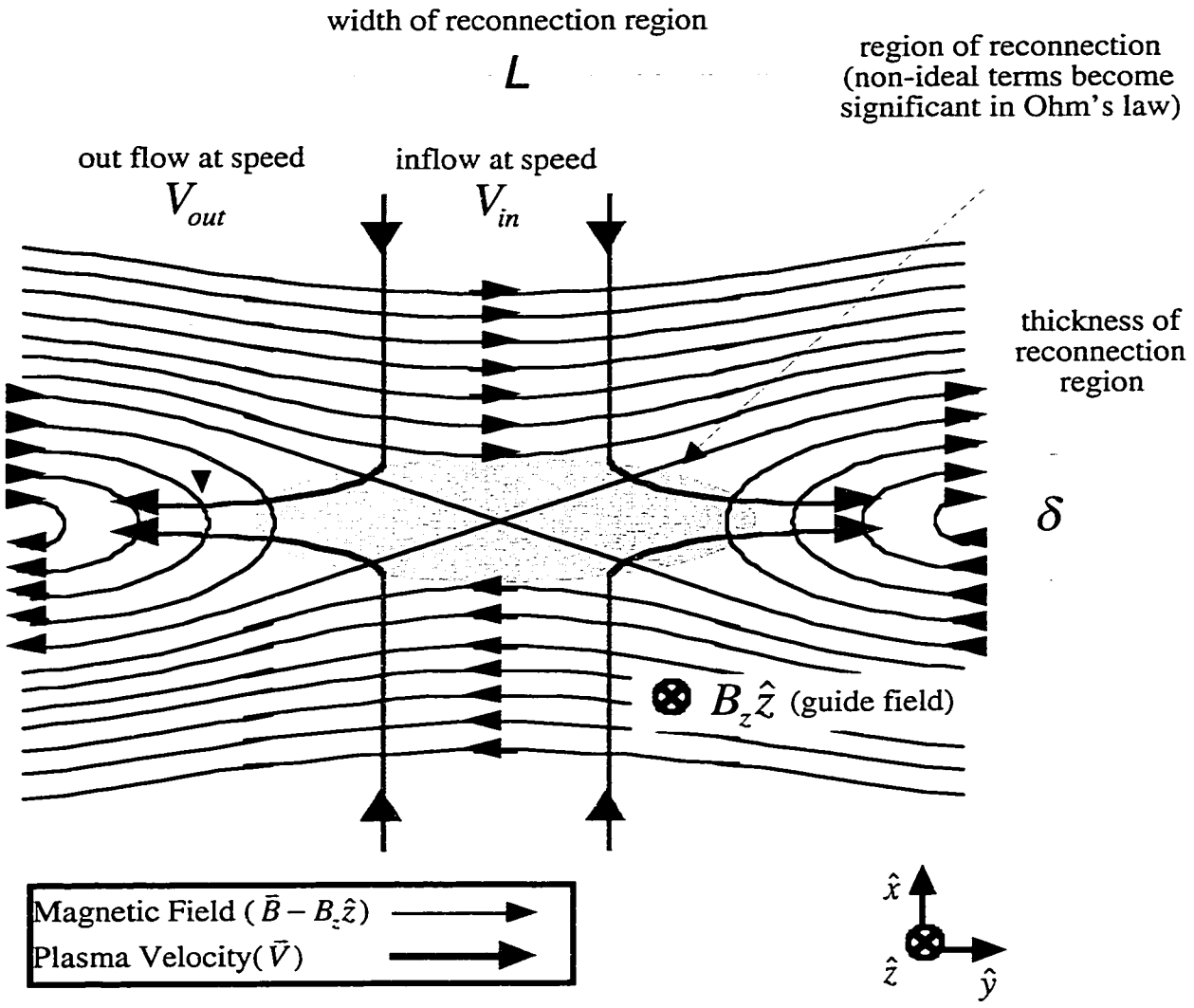

Figure 2: Schematic of reeonnection process: Opposing flows oriented along x-axis compress sheared magnetice field (B_y). Inside region of compression, non-ideal terms in Ohm's law become significant, forming region where magnetic reconnection occurs. Incoming y-oriented magnetic flux is destroyed, severing magnetic field lines. Equivalent amount of x-oriented magnetic flux (B_x) is created, joining "ends" of severed incoming field lines to create new field lines with different topology. New field lines are carried out of region of reconnection by outflow.

The Lundquist number is given by $S = \tau_{Resistive} V_{Alfvén}/L = \left(L^2\mu_0/\eta\right)\left(B/\left(\mu_0 m_i n_i\right)^{1/2}\right)/L$, where m_i is the ion mass, n_i is the ion density and B is the strength of the reconnecting component of the incoming magnetic field at the boundary of the non-ideal region. The exact value that α takes depends slightly on the details of the model. For tearing modes in RFP plasmas, $\alpha = 2/5$.[1]

The form shown for δ_{MHD} above, $\delta_{MHD} = L/S^{\alpha}$, comes about because the $\eta\bar{J}$ term becomes significant when $B_{y_{in}} V_{in} \sim \eta J_z$, where $B_{y_{in}}$ (called B in the definition of S, above) is the magnitude of the reconnecting component of the incoming magnetic field at the boundary of the reconnection region (see Fig. 2). When the $\eta\bar{J}$ term is the dominant non-ideal term, the reconnection region has a thickness of δ_{MHD} and $\mu_0 J_z \sim B_{y_{in}}/\delta_{MHD}$, so $\delta_{MHD} \sim \eta/\left(\mu_0 V_{in}\right) = \left(L/S\right)\left(V_{in}/V_{Alfvén}\right)^{-1}$. Also, theoretical models indicate resistive reconnection is slow enough that the plasma fluid is effectively incompressible ($\bar{\nabla}\cdot\bar{V} = 0$), so $LV_{in} \sim \delta_{MHD} V_{out}$ and $\delta_{MHD} \sim \left(L/S^{-1/2}\right)\left(V_{out}/V_{Alfvén}\right)^{-1/2}$. Finally, although the exact value of V_{out} in any particular resistive reconnection model is sensitive to the details of the model, it is frequently comparable to $V_{Alfvén}$. This is because typically the energy density associated with $B_{y_{in}}$ is converted to kinetic energy density in the outflow. Using $V_{Alfvén}$ for V_{out} gives $\delta_{MHD} \sim L/S^{-1/2}$.

An important feature of non-steady-state resistive reconnection models is that the current sheet associated with reconnection can broaden beyond the δ_{MHD} scale. When this happens, the dynamics of the reconnection process in such models changes. As discussed in Sec. 2.5 below, reconnection in an RFP is often associated with the formation of a *magnetic island.* When a magnetic island does form, the current sheet associated with reconnection fills the island.[14]

Another non-ideal effect that has been studied extensively in the context of magnetic reconnection is the electron inertia effect[4, 5, 6] (the $d\bar{J}/dt$ term in Eq. 2.3.2). The electron inertia effect is so named because, under a broad range of conditions, $d\bar{J}/dt \approx en_e\, d\bar{v}_e/dt$. (Despite the origin of this naming convention, typically no such approximation is used in reconnection models that incorporate the electron inertia effect). The incorporation of the electron inertia effect into Ohm's law in a theoretical model of reconnection introduces the electron skin depth,

δ_e, as a spatial scale. The electron skin depth is given by c/ω_{pe}. The electron skin depth is introduced as a scale length because $\gamma B_{y_{in}} \sim \gamma\delta^{-1}\delta_e^2\mu_0 J_z$ when the term $\left(\varepsilon_0\omega_{pe}^2\right)^{-1} d\bar{J}/dt$ $(= \delta_e^2\mu_0\, d\bar{J}/dt)$ becomes significant in Ohm's law, where γ is the larger of τ^{-1} or $\delta^{-1}V_{in}$ and τ and δ are the reconnection time scale and non-ideal layer thickness. Additionally, $\mu_0 J_z \sim B_{y_{in}}/\delta$ in the non-ideal region. This gives $\delta \sim \delta_e$.

Another effect that has been studied extensively in the context of magnetic reconnection is the ion inertia effect[9] (the Hall term, or $\bar{J}\times\bar{B}$ term, in Eq. 2.3.2), often in conjunction with the electron inertia effect . The Hall term is called the ion inertia effect because $\bar{J}\times\bar{B}$ can be expressed in terms of $m_i d\bar{V}/dt$ using the MHD momentum equation.

$$\rho d\bar{V}/dt = \bar{J}\times\bar{B} - \bar{\nabla}p. \tag{2.3.3}$$

The plasma mass density, ρ, is approximately given by $m_i n_i$. The incorporation of the ion inertia effect in Ohm's Law in a theoretical model of reconnection adds as a spatial scale the ion skin depth, c/ω_{pi}, where $\omega_{pi} = \left(e^2 n_i/m_i\varepsilon_0\right)^{1/2}$. Neglecting the $\bar{\nabla}p$ term in Eq. 2.3.3, and using $n_i \approx n$, $\bar{J}\times\bar{B}/(en) \approx \delta_i^2\mu_0 en\, d\bar{V}/dt \approx \delta_i^2\mu_0\, d\bar{J}_i/dt$, where $\bar{J}_i$ is the current density due to ion motion. The ion inertia effect is expected to become significant only in high β, or weakly magnetized, plasmas (*i.e.*, when the energy density of the full magnetic field is small compared to the plasma pressure).

Another effect that has been studied is the electron pressure gradient effect[7, 8] (the $\bar{\nabla}p_e$ term in Eq. 2.3.2), often in conjunction with the electron and ion inertia effects. The incorporation of the electron pressure gradient effect in Ohm's law in a theoretical model of reconnection adds as the spatial scale of the ion acoustic gyroradius. The ion acoustic gyroradius is given by $\rho_s = \left(T_e m_i\right)^{1/2}/eB_o$, where m_i is mass of the plasma's ion species and T_e is the electron temperature. The ion acoustic gyroradius spatial scale arises in models that incorporate it from the process which creates the electron pressure gradient in Ohm's law in such models. These models typically assume that there is a strong *guiding* magnetic field, B_0, perpendicular to the plane in which flux reconnects (the $\hat{z}$ direction in Fig. 2). When a strong guiding field exists, the

plasma fluid moves at the $\vec{E}\times\vec{B}$ velocity, which is given by

$$\vec{v}_{\vec{E}\times\vec{B}} = \vec{E}\times\vec{B}/B^2 \approx \vec{E}\times\vec{B}_0/B_0^2 . \tag{2.3.4}$$

The electric field, $\vec{E}$, which produces this velocity may be time varying if the reconnection is non-steady-state. Either way, it will exhibit strong spatial variation in the region of reconnection. Both of these characteristics will produce a polarization flow in the ions given by

$$\vec{v}_p \approx \omega_{ci}^{-1}\tfrac{d}{dt}\vec{E}_\perp/B_0 . \tag{2.3.5}$$

which has a non-vanishing divergence, where $\omega_{ci} = eB_0/m_i$ is the ion cyclotron frequency and $\frac{d}{dt}$ is the full convective time derivative. This, in turn, produces an ion density perturbation n_i that is described by the ion density continuity equation:

$$\tfrac{d}{dt}n_i \approx -n\vec{\nabla}\cdot\vec{v}_p \approx -n\vec{\nabla}\cdot\left(\omega_{ci}^{-1}\tfrac{d}{dt}\vec{E}_\perp/B_0\right), \tag{2.3.6}$$

where n is the equilibrium, or background, density. In models that include this effect, this expression for n_i is solved to give

$$n_i \approx -n\vec{\nabla}\cdot\left(\omega_{ci}^{-1}\vec{E}_\perp/B_0\right). \tag{2.3.7}$$

Preservation of quasi-neutrality dictates that $n_i \approx n_e$, so the ion density perturbation leads to an electron density perturbation and an electron pressure gradient. Thus, the $\vec{\nabla}p_e/(en)$ term in Ohm's law (Eq. 2.3.2) takes the form

$$\vec{\nabla}p_e/(en) \approx \rho_s^2\vec{\nabla}\left(\vec{\nabla}\cdot\vec{E}_\perp\right). \tag{2.3.8}$$

It is interesting to note that non-ideal effects are often categorized as *collisional* or *collisionless* effects, depending on whether they result from particle collisions. Of all the non-ideal effects included in the version of Ohm's law presented here (Eq. 2.3.2) only the resistivity effect is collisional. Another example of a collisional non-ideal effect would be electron viscosity. This effect is typically weak compared to resistivity and is neglected in Eq. 2.3.2. The distinction between collisional and collisionless non-ideal effects is important, particularly from a historical perspective, since collisionality can be very weak in hot plasmas, including, for instance, some kinds of astrophysical plasmas. Early attempts to understand reconnection, which were often motivated by observations of such hot plasmas, unsuccessfully hypothesized that

resistivity could explain such reconnection. Later attempts to explain reconnection are more successful by making use of collisionless non-ideal effects. The electron inertia effect is one of first collisionless non-ideal effects to be studied in the context of reconnection.

2.4 - Tearing Modes: Magnetic Reconnection in the Reversed Field Pinch

Magnetic reconnection in an RFP is believed to result from a general class of non-ideal MHD plasma perturbations commonly referred to as tearing modes.[1] Tearing modes derive their name from the magnetic field line reconnection, or field line tearing, which is a common feature of their evolution. Reconnection associated with tearing mode activity occurs frequently, and at a large variety of locations throughout an RFP plasma.

The locations where magnetic reconnection occurs in an RFP plasma are determined by the RFP's characteristic equilibrium magnetic field, shown in Fig. 3. The poloidal component of

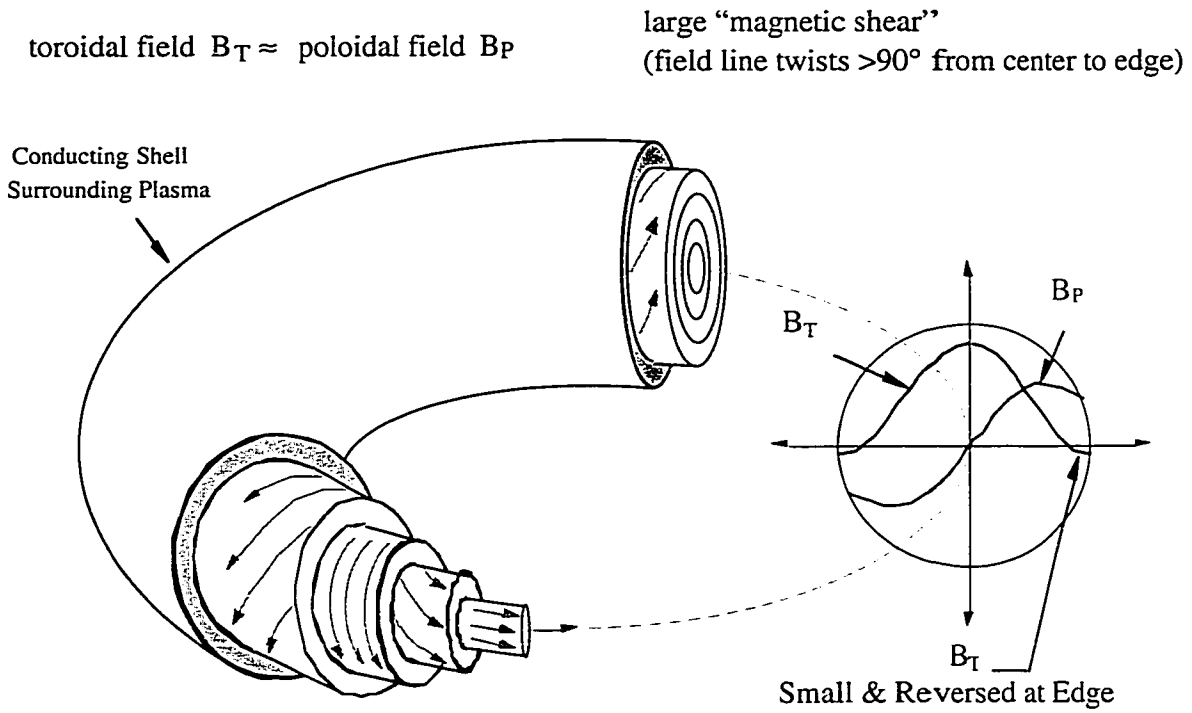

Figure 3: Schematic of magnetic field structure in MST (picture courtesy of Nicholas Lanier, John Sarff).

this field, or *poloidal magnetic field*, varies monotonically with minor radius from zero at the magnetic axis to it's full value at the plasma edge. The toroidal component, or *toroidal magnetic field*, varies monotonically with minor radius from its full, positive value at the magnetic axis to zero near the plasma edge and then to a relatively small negative value at the plasma edge. This means that the toroidal magnetic field *reverses direction* at the plasma edge (which motivates the name Reversed Field Pinch). The peak values of the poloidal and toroidal magnetic fields are of comparable magnitude.

As with many other plasma confinement configurations, such as tokamaks and stellarators, the RFP's equilibrium magnetic field possesses well defined, nested toroidal magnetic surfaces within which magnetic field lines are confined. Such surfaces fall into two categories depending on the helicity, q (sometimes called safety factor), of their embedded field lines. A surface's helicity, or safety factor, can be either irrational or rational. The helicity of a surface represents the number of *toroidal transits*, or transits about the axis of the torus in the toroidal direction, made by its confined field lines during the course of one *poloidal transit*, or transit about the magnetic axis (the field line at the center of the nesting of surfaces) in the poloidal direction. In the limit where the *inverse aspect ratio, a/R*, where R is the plasma major radius and a is the plasma minor radius, goes to zero, the nested flux surfaces of an RFP are concentric cylinders (*i.e.*, surfaces of constant minor radius), and the helicity is given by $q = rB_\phi / RB_\theta$. Irrational surfaces, as a consequence of their irrational helicity, each contain a single, unclosed magnetic field line which, in the course of repeated toroidal transits, fills the entire surface. Rational surfaces, on the other hand, contain sets of parallel, closed field lines. Each field line makes an integral number, m, of toroidal transits in the course of an integral number, n, of poloidal transits, before closing on itself. For such a surface, $q = m/n$ (independent of inverse aspect ratio).

The RFP's equilibrium magnetic field is susceptible to magnetic reconnection at rational surfaces. Specifically, if a helical radial magnetic field perturbation, $\tilde{b}_r$, becomes non-vanishing

at a particular rational surface within the plasma, the topology of the field lines in the vicinity of that rational surface will be changed. This special rational surface is the surface where the $\tilde{b}_r$ is *resonant*. At this surface, $\tilde{b}_r$ will satisfy $\vec{k} \cdot \vec{B}_0 = 0$, where $\vec{k}$ is the *helical wave vector* given by $\vec{k} = (m/r)\hat{\theta} - (n/R)\hat{\phi}$, and n and m are toroidal and poloidal periodicities of $\tilde{b}_r$.

A radial magnetic field perturbation, $\tilde{b}_r$, can only grow at its rational surface if non-ideal effects become significant in Ohm's law. When non-ideal effects become significant in Ohm's law (Eq. 2.2.1), the evolution equation for $\vec{B}$ becomes

$$\partial \vec{B}/\partial t = \bar{\nabla} \times \left(\vec{V} \times \vec{B} \right) - \bar{\nabla} \times \vec{R}, \tag{2.4.1}$$

where $\vec{R}$ represents the combined non-ideal effects. Assuming $\bar{\nabla} \cdot \vec{V} = 0$ and $\vec{V}_0 = 0$, and neglecting products of perturbations, Eq. 2.4.1 gives the linear evolution equation for $\tilde{b}_r$,

$$\partial \tilde{b}_r/\partial t = \vec{B}_0 \cdot \bar{\nabla} \tilde{v}_r - \hat{r} \cdot \bar{\nabla} \times \tilde{\vec{R}} = \vec{B}_0 \cdot \vec{k} \tilde{v}_r - \hat{r} \cdot \bar{\nabla} \times \tilde{\vec{R}}, \tag{2.4.2}$$

where $\tilde{v}_r$ and $\tilde{\vec{R}}$ are the associated perturbations in V_r and $\vec{R}$. Thus, at the resonant rational surface for $\tilde{b}_r$, it can only change if $\hat{r} \cdot \bar{\nabla} \times \tilde{\vec{R}} \neq 0$.

The susceptibility of the RFP equilibrium magnetic field to reconnection is what allows tearing modes, which can be either forced to grow (externally, or by interaction with other tearing modes), or driven by a plasma instability, to develop. When a tearing mode grows, it produces simultaneous helically periodic, toroidally rotating perturbations in multiple plasma quantities, including, for instance, $\vec{B}$ and $\vec{V}$, which are resonant with the equilibrium magnetic field at some rational magnetic surface in the plasma. In particular, a tearing mode produces a $\tilde{b}_r$ that is non-vanishing at its resonant rational surface, thus causing the reconnection associated with its development. Except in a radially localized region around its rational surface where non-ideal effects become significant, a tearing mode's evolution is generally well described by ideal MHD everywhere in an RFP plasma.

2.5 - Magnetic Islands and the Reconnected Flux

Under certain circumstances, a tearing mode in an RFP can cause the formation of a

magnetic island, a set of nested magnetic surfaces centered around a field line in a rational surface, at its associated resonant rational surfaces. Specifically, when the magnetic field in region around a rational surface is well ordered (*i.e.*, consists of a single set of nested magnetic surfaces that includes the rational surface), the $\tilde{b}_r$ associated with a tearing mode resonant at that rational surface causes a magnetic island to form. In fact, the reconnection process can be thought of as a transfer of flux to such an island from the surrounding plasma. Interestingly, this $\tilde{b}_r$ provides a measure of the amount of the amount of flux that was reconnected to create the magnetic island. The surface integral of this component of $\tilde{b}_r$ over a particular portion of the tearing mode's resonant surface gives the amount of *reconnected flux*. The portion of the surface over which integral is performed is bounded on one edge by the field line at the center of island's nested surfaces (the so-called *o-point* line). It is bounded on the other edge by first field line in the surface that is not part of the island (the so-called *x-point* line).

2.6 - Classes of Tearing Modes: Reversal Surface Resonant ($m = 0$) and Core Resonant ($m = 1$)

As a consequence of the magnetic field structure of the RFP configuration, the tearing modes that are active in an RFP plasma can be divided into two categories (Fig. 4): those with a poloidal periodicity of 1 (*i.e.*, with poloidal mode number $m = 1$) and those that are poloidally symmetric (*i.e.*, with poloidal mode number $m = 0$). The $m = 1$ tearing modes are resonant at those rational surfaces whose magnetic fields have nonzero toroidal components. Consequently, tearing modes of this class can have any of a broad range of toroidal periodicities (given by the toroidal mode number, n). The toroidal mode number range of the $m = 1$ modes which are most active in an RFP are determined by two factors. First, the minimum n is determined by the asymptotic behavior of the equilibrium magnetic field line pitch near the magnetic axis (where the poloidal field vanishes). In an RFP, the minimum n is approximately twice its *aspect ratio*, $2R/a$ (≈ 6 in MST). Second, energetic considerations indicate that modes with larger n should be

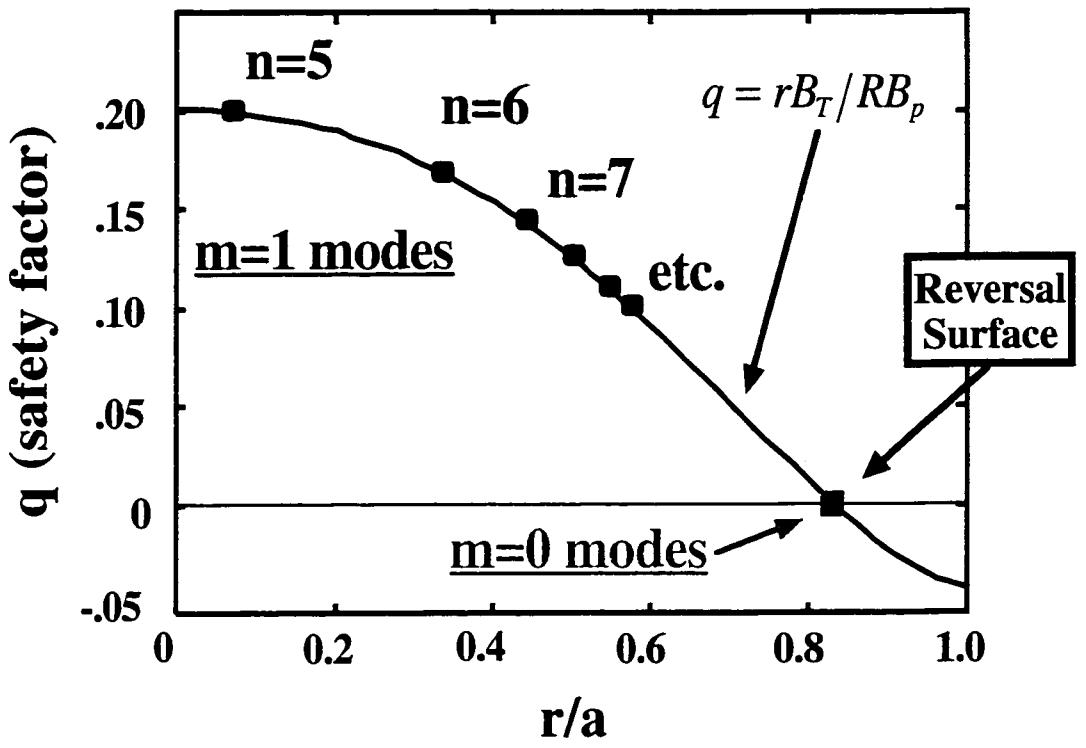

Figure 4: Typical MST q profile. Two categories of resonant surfaces indicated: $m = 0$ and $m = 1$.

less active. Tearing modes with higher values of n require more magnetic field line bending energy to grow. Thus, the $m = 1$ modes resonant nearest the core are the most active. For this reason, these modes are often referred to in this dissertation as the core resonant tearing modes, although, in fact, the rational surfaces where modes of this class are resonant occur throughout the plasma. In MST, toroidal spectra of magnetic fluctuations measured at the wall (using array of coils discussed in Sec. 3.7 of Ch. 3) indicate that the $m = 1$ modes are dominated by toroidal mode numbers in the range $n \approx 5 - 10$.

The $m = 0$ modes are resonant at the reversal surface, where the magnetic field is purely poloidal, and can have any toroidal mode number. As with the core resonant tearing modes, lower toroidal toroidal mode numbers are more active for energetic reasons. These modes are sometimes referred to as the reversal surface resonant modes. In MST, toroidal spectra of magnetic fluctuations measured at the wall indicate that the $m = 0$ modes are dominated by toroidal mode numbers in the range $n \approx -3 - -1$.

2.7 - Parallel Current Density and Radial Magnetic Field Fluctuations

Tearing mode theory for an isolated tearing mode in an RFP (with infinite aspect ratio) predicts that the associated radial magnetic field perturbation, $\tilde{b}_r$, will be spatially out of phase with the component of the associated current density fluctuation, $\tilde{j}_\parallel$, which is parallel to the equilibrium magnetic field.[1] More precisely, $\tilde{j}_\parallel$ and $\tilde{b}_r$, which have helically periodic structures, are expected to have spatial phases that differ by $\pi/2$. One consequence of this is that the average product of the radial magnetic field and parallel current density fluctuations, $\left\langle \tilde{j}_\parallel \tilde{b}_r \right\rangle_{F.S.}$, over a flux surface of the equilibrium magnetic field, is expected to be zero. On the other hand, the theory for interacting tearing modes predicts just the opposite.

There are at least two ways in which interaction of tearing modes can lead to a non-vanishing $\left\langle \tilde{j}_\parallel \tilde{b}_r \right\rangle_{F.S.}$. First, tearing modes create magnetic islands which, in and of themselves, consist of magnetic field lines that cross the surfaces of the equilibrium magnetic field, and which can potentially overlap, resulting in stochastic magnetic field lines in the region of overlap. Either of these effects can, in turn, lead to a charge transport (Γ_q), or current density, in the direction across the equilibrium magnetic field due to the streaming of charge carriers along magnetic field lines. This current density due to *parallel streaming* of charge carriers can be expressed identically as $\Gamma_q = \left\langle \tilde{j}_\parallel \tilde{b}_r \right\rangle_{F.S.} / B_0$. Second, tearing modes can interact with other tearing modes in ways which alter the relative phase between their associated $\tilde{j}_\parallel$ and $\tilde{b}_r$. Such interactions result in $\bar{J} \times \bar{B}$ force densities on the plasma of the form $\left\langle \tilde{j}_\parallel \tilde{b}_r \right\rangle_{F.S.} \hat{b}_0 \times \hat{r}$.

2.8 - Parallel Streaming of Particles and Charge Transport

Magnetic reconnection in an RFP alters the topology of the magnetic field lines in the plasma, causing them to cross equilibrium magnetic surfaces. Consequently, charged particles streaming along such field lines may cross the magnetic surfaces of the equilibrium. Such parallel streaming of charge potentially results in a net cross-surface, or radial, charge flux. This may be seen by examining the contribution of parallel streaming charged particles to the

(equilibrium) flux surface averaged total radial charge flux which is given by $\left\langle \left(\bar{J}\cdot\hat{b}\right)\hat{b}\cdot\hat{r}\right\rangle_{F.S.}$. It can be seen from the relation

$$\left(\bar{J}\cdot\hat{b}\right)\hat{b}\cdot\hat{r}=\left(\bar{J}\cdot\hat{b}\right)\tilde{b}_r/B\approx\left(J_{\|0}+\tilde{j}_{\|}\right)\tilde{b}_r/B_0, \tag{2.8.1}$$

where B_0 is the magnitude of the equilibrium magnetic field, $J_{\|0}=\left\langle \bar{J}\cdot\hat{b}\right\rangle_{F.S.}$ and $\tilde{j}_{\|}=\bar{J}\cdot\hat{b}-J_{\|0}$, using the subscript $\|$ to denote "parallel to the magnetic field", that

$$\left\langle \left(\bar{J}\cdot\hat{b}\right)\hat{b}\cdot\hat{r}\right\rangle_{F.S.}\approx\left\langle \tilde{j}_{\|}\tilde{b}_r\right\rangle_{F.S.}/B_0. \tag{2.8.2}$$

2.9 - Interaction of Tearing Modes: $\bar{J}\times\bar{B}$ Force

The magnetic perturbations associated with tearing modes in RFPs typically grow to sufficient amplitudes for their interaction with either each other or a close conducting wall bounding the plasma to lead to a significant $\bar{J}\times\bar{B}$ force density on the plasma.[15] The $\bar{J}\times\bar{B}$ force density resulting from these interactions comes about through the alteration of the relative phase between the associated $\tilde{j}_{\|}$ and $\tilde{b}_r$.

One means by which tearing modes may interact with each other requires that a triplet of tearing modes have the right combination of helical wave vectors to satisfy the *three wave condition*. Specifically, a pair of tearing modes with helical wave vectors $\bar{k}'$ and $\bar{k}''$ may interact with a third tearing mode whose helical wave vector $\bar{k}$ satisfies one of the relations

$$\bar{k}=\bar{k}'\pm\bar{k}'' \tag{2.9.1}$$

to produce a so-called *nonlinear* contribution to its parallel current density, $\tilde{j}_{\bar{k},\|}$, of the form

$$\tilde{j}_{\bar{k},\|N.L.}=\tilde{\tilde{b}}_{\bar{k}'}\cdot\tilde{c}_{\bar{k},\bar{k}',\pm\bar{k}''}\cdot\tilde{\tilde{b}}_{\bar{k}''}, \tag{2.9.2}$$

where $\tilde{c}_{\bar{k},\bar{k}',\pm\bar{k}''}$ is a matrix of *coupling coefficients* that depend on the plasma equilibrium. The subscript $\|$ denotes "parallel to the equilibrium magnetic field." This nonlinear contribution to the parallel current density perturbation of a tearing mode alters its phase relative to the mode's radial magnetic field perturbation, $\tilde{b}_{\bar{k},r}$, to produce a $\bar{J}\times\bar{B}$ force density on the plasma. When this occurs, $\left\langle \tilde{j}_{\bar{k},\|N.L.}\tilde{b}_{\bar{k},r}\right\rangle_{F.S.}\neq 0$. Such force densities produced by interaction between interacting

tearing modes are reciprocal in the sense that any three tearing modes interact to produce a zero total force on the plasma (*i.e.*, plasma momentum is conserved). In other words, such interactions between tearing modes result in a transfer of momentum from one part of the plasma to another, rather than a global force on the plasma.

In addition to exhibiting interaction between triplets of tearing modes, an RFP with a finite aspect ratio may exhibit interactions between pairs of tearing modes with the same toroidal mode number whose poloidal mode numbers differ by 1. This interaction results from the lack of exact poloidal symmetry inherent in toroidal plasma configurations of finite aspect ratio. Such *toroidicity* induced interactions between tearing modes may be considered, in some sense, interactions of triplets of tearing of tearing modes, where the each triplet consists of a pair of actual tearing modes and a virtual tearing mode with mode numbers $m = 1$ and $n = 0$.

Evidence of triplet interactions between tearing modes has been observed on MST.[16] In particular, evidence has been observed indicating that, during sawtooth crashes, interactions of this type between core and reversal surface resonant tearing modes result in a momentum transfer between the plasma core and plasma edge that flatten the equilibrium radial profile of the toroidal velocity. The evidence for this takes the form of measured flux surface averages of triple products of magnetic perturbation amplitudes whose mode numbers satisfy the three wave condition (Eq. 2.9.1). These measurements were made using a toroidal array of magnetic sensing coils (described in Sec. 3.7 of Ch. 3) to measure magnetic perturbation amplitudes. Despite this evidence for tearing mode interactions, an overall uncertainty remains as to the magnitude of the resulting force densities, because the coupling coefficients $\tilde{c}_{\tilde{k},\tilde{k}',\pm\tilde{k}''}$ are unknown.

A third way in which tearing modes may produce a $\tilde{J} \times \tilde{B}$ force density on the plasma is through interaction with a nearby resistive conducting wall. Specifically, the $\tilde{b}_r$ associated with a tearing mode penetrates the resistive wall, which produces image currents in the wall that perturb it. Because of the non-vanishing resistivity of the wall, there is phase lag between $\tilde{b}_r$ and

image currents induced. This phase lag plays a role in establishing the phase relation between $\tilde{j}_{\parallel}$ and $\tilde{b}_r$ in the tearing mode's non-ideal layer, which, as a result, is not $\pi/2$, as it would be for an isolated tearing mode.

2.10 - Summary

In summary, magnetic field line reconnection is a process permitted by non-ideal MHD which breaks a very powerful constraint imposed on plasmas by ideal MHD: the frozen flux condition. During the process of magnetic reconnection, magnetic field lines, whose topologies are conserved under the frozen flux condition, break and reconnect to form field lines with new topologies. Such a process potentially occurs in plasmas that are approximately described by ideal MHD in locations where plasma flows compress regions of sheared magnetic field. The compression of the magnetic field and other plasma quantities in this region may cause otherwise negligible terms in Ohm's law which are sensitive to such gradients to become significant. This, in turn, would break the frozen flux condition.

There are several effects that can become significant in the region of compression which have been studied theoretically and computationally in various combinations. Each of these effects has an associated characteristic scale length that may determine the thickness of the reconnection region. This scale length also potentially determines the thickness of a parallel current density current layer that is typically produced by reconnection. These effects include resistivity, electron inertia, ion inertia and the electron pressure gradient effect The associated scale lengths are: $L/S^{1/2}$, or possibly, in the case of reconnection in an RFP, the associated magnetic island width, the electron skin depth, the ion skin depth, the ion acoustic gyroradius. Another effect that has been studied is transport of current density by parallel streaming of charge carriers.

Magnetic reconnection in an RFP takes the form of tearing mode activity. Tearing modes are toroidally rotating, helical perturbations that simultaneously affect multiple plasma

quantities, including, in particular, the radial magnetic field. It is the perturbation in the radial magnetic field that causes reconnection. This perturbation, which can only occur when non-ideal effects become significant in the vicinity of the rational surface, forms a magnetic island if the magnetic surfaces around the rational surface are concentrically nested with it. Tearing modes in an RFP can divided into two categories based on their poloidal structure: the reversal surface $m = 0$ category, which consists of approximately poloidally symmetric modes and the core resonant $m = 1$ category, which consists of modes with a poloidal periodicity of 1. The $m = 0$ category of modes is dominated in MST by modes with toroidal mode numbers approximately in the range $n = -3 - -1$. The $m = 1$ category of modes, on the other hand, is dominated in MST by modes with toroidal mode numbers approximately in the range $n = 5 - 10$.

Magnetic reconnection in an RFP potentially play a role in its charge, particle and momentum balances. In particular, the parallel current density, $\tilde{j}_{\parallel}$, and radial magnetic field perturbations, $\tilde{b}_r$, associated with tearing modes play roles in these balances through their flux surface average product $\left\langle \tilde{j}_{\parallel}\tilde{b}_r \right\rangle_{F.S.}$. If $\left\langle \tilde{j}_{\parallel}\tilde{b}_r \right\rangle_{F.S.}$ is non-vanishing, it represents both a $\bar{J} \times \bar{B}$ force on the plasma and a charge transport across the flux surfaces of the equilibrium magnetic field due to parallel streaming of charge carriers. Such a charge transport, in turn, has implications for particle transport.

References

[1] H. P. Furth, J. Killeen, and M. N. Rosenbluth, Phys. Fluids **6,** 459 (1963).

[2] E. N. Parker, J. of Geophys. Res. **62,** 509 (1957).

[3] P. A. Sweet, *International Astronomical Union Symposium No. 6: Electromagnetic Phenomena in Cosmical Physics,* (Ed. by B. Lehnert), (Cambridge at the University Press; Cambridge, England; 1958), p. 123.

[4] D. Biskamp and E. Schwarz and J. F. Drake, Phys. Plasmas **4,** 1002 (1997).

[5] J. F. Drake and R. G. Kleva, Phys. Rev. Lett. **66,** 1458 (1991).

[6] D. Biskamp, E. Schwarz and J. F. Drake, Phys. Rev. Lett **75,** 3850 (1995).

[7] B. Rogers and L. Zakharov, Phys. Plasmas **3,** 2411 (1996).

[8] R. G. Kleva, J. F. Drake and F. L. Waelbroeck, Phys. Plasmas **2,** 23 (1995).

[9] M. A. Shay, J. F. Drake, R. E. Denton, and D. Biskamp, J. of Geophys. Res. **103,** 9165 (1998).

[10] J. F. Drake and Y. C. Lee, Phys. Rev. Lett. **39,** 453 (1977).

[11] I. Katanuma and T. Kamimura, Phys. Fluids **23,** 2500 (1980).

[12] K. Swartz and R. D. Hazeltine, Phys. Fluids **27,** 2043 (1984).

[13] J. F. Drake and Y. C. Lee, Phys. Fluids **20,** 1341 (1977).

[14] D. Biskamp, *Nonlinear Magnetohydrodynamics*, (Cambridge University Press; Cambridge, England; 1993), p. 107.

[15] A. K. Hansen, *Kinematics of Nonlinearly Interacting MHD Instabilities in a Plasma*, (Ph. D. dissertation, University of Wisconsin – Madison, 2000), p. 10

[16] A. K. Hansen, et al., Phys. Rev. Lett. **85,** 3408 (2000).

Chapter 3 - Experimental Technique

3.1 - Introduction

MST[1] is capable of making RFP plasmas into which probes can be inserted relatively deeply without significant perturbation to the plasma, or, for that matter, the probes. In an effort to study magnetic reconnection in an RFP, the measurements described in Ch. 4 – 5 take advantage of this capability. These measurements make use of two similar insertable plasma diagnostics, each of which possesses current sensing Rogowskii coils that can be used to measure the magnetic field aligned, or parallel, component of the current density, as well as a variety of magnetic sensing coils. These *Rogowskii probes* are used in conjunction with toroidally distributed arrays of magnetic sensing coils mounted near the plasma on the wall of MST.

The measurements made with these diagnostic devices are used, in turn, to obtain estimates of the poloidal and toroidal mode number spectra of magnetic and current density fluctuations in the plasma edge, in the vicinity of magnetic reconnection, as well as other details of the spatial structure of these perturbations. Two different analysis techniques, with complementary strengths and weaknesses, are used to make estimates of the toroidal mode number spectra: *pseudospectral analysis* and *two-point spectral analysis*. The latter technique is also used to make estimates of poloidal mode number spectra.

Pseudospectral analysis makes use of measured *crossspectra* between the magnetic and current fluctuations inside the plasma, as measured by the insertable probes, and magnetic toroidal mode amplitudes at the plasma edge, as measured by the toroidal arrays of magnetic sensing coils. Crossspectra are the product of a form of statistical analysis called crossspectral analysis. They provide a particular measure of the information shared between time-dependent signals produce by two different sources.

The second spectral estimate technique, two-point spectral analysis, makes use of simultaneous measurements of the magnetic and current fluctuations inside the plasma obtained

from the pair of probes to generate two-point toroidal or poloidal mode spectra. The type of two-point spectra generated, toroidal or poloidal, depends on whether the probes are displaced toroidally of poloidally.

One of the probes has, among its complement of magnetic sensing coils, a radially aligned magnetic sensing coil. Measurements from this coil, in conjunction with measurements of the parallel current density fluctuations from the probe's current sensing Rogowskii coil, can be used to obtain an estimate of the flux surface averaged product of the radial magnetic field and parallel current density fluctuations. As discussed in Sec. 2.7 of Ch. 2, this product plays a significant role in the charge, particle and momentum balances of MST.

The structure of this chapter is as follows:

In Section 3.2, we briefly describe the plasmas MST is capable of producing, with particular attention to the conditions in edge region of such plasmas, which is where probes are inserted. Additionally, we discuss the particular plasma conditions that were used for the measurements discussed in Chs. 4 – 5 of this dissertation, and the effect on such plasmas of the insertion of Rogowskii probes. We conclude that the plasmas in which the measurements discussed in Chs. 4 – 5 were made were not significantly perturbed by the insertion of the probes.

In Section 3.3, we discuss the basic principles of magnetic sensing coils and current sensing Rogowskii coils, which are used to make the measurements of magnetic and current density fluctuations that are discussed in Chs. 4 – 5.

In Section 3.4 we describe the two Rogowskii probes that house the magnetic sensing coils and current sensing Rogowskii coils and allow us to use them within the edge of MST plasmas.

In Section 3.5, we discuss practical considerations in the processing of Rogowskii coil and magnetic sensing coil signals. In particular, we discuss several possible sources of error in these signals, including, for instance, digitizer bit-noise and integrator drift.

In Section 3.6, we consider a very basic issue in the use of probes to measure plasma fluctuations. We consider the degree to which the Rogowskii probes we use interfere with the parallel current density and magnetic field fluctuations whose measurements we present in Chs. 4 – 5. We ultimately conclude that there is no significant interference.

In Section 3.7, we describe the toroidal coil arrays that we use in conjunction with the Rogowskii probes to make the pseudospectral measurements presented in Chs. 4 – 5 of this dissertation.

In Section 3.8, we discuss crossspectral analysis, a basic technique for statistically analyzing fluctuations. Crossspectral analysis plays a significant role in estimating flux surface averaged products of fluctuations and in pseudospectral analysis.

In Section 3.9, we discuss a technique for estimating flux surface averages of fluctuation products. This techniques makes use of pairs of point measurements of fluctuations and crossspectral analysis. Measurements of the flux surface average of the product of parallel current density and radial magnetic field fluctuations estimated using this technique are presented in Ch. 5.

In Section 3.10, we discuss the principles of pseudospectral analysis. Pseudospectral analysis is a statistical technique for estimating spatial spectra of fluctuating quantities in a cylindrical plasma from a limited set of measurements. In particular, it makes use of point measurements of the fluctuations whose spectrum is desired in conjunction with a poloidally and toroidally distributed, two-dimensional array of measurements of a reference fluctuating quantity. We also discuss the limitations of pseudospectral analysis.

In Section 3.11, we discuss the practical application of the pseudospectral analysis technique in MST. We note that, while MST lacks poloidally and toroidally distributed, two-dimensional arrays of measurements for use as reference fluctuating quantities, it does have toroidally distributed, one-dimensional arrays of measurements: the toroidal arrays of magnetic sensing coils mounted on the wall of MST. We discuss an approximation permitted by the

character of the dominant fluctuations in MST that allows us to use pseudospectral analysis with these one-dimensional arrays.

In Section, 3.12, we discuss two-point spectral analysis, a statistical technique for estimating spatial spectra using pairs of closely space measurement. We also discuss a potential limitation in using the technique in MST that arises from the character of the dominant fluctuations in MST.

In Section 3.13, we describe some basic procedures common to performing the statistical analyses inherent in crossspectral, pseudospectral and two-point spectral analysis. Specifically, we discuss the construction of the two kinds of statistical ensembles we use for the measurements presented in this dissertation: sawtooth crash ensembles and between-crash ensembles. We also discuss some ways in which we condition the signals obtained from the Rogowskii coil and magnetic sensing coils in order to isolated their fluctuating components.

In Section 3.14, we discuss some basic issues regarding the determination of the statistical uncertainties for the various spectral measurements we present in Chs. 4 – 5 of this dissertation. In particular, we describe certain statistical assumptions we make regarding the fluctuations we measure.

In Section 3.15, we summarize the major points of this chapter.

3.2 - MST Plasmas and Probe Use

MST produces hydrogen plasmas with chord averaged densities in the range 0.5×10^{19} m^{-3} – 2×10^{19} m^{-3}, core electron temperatures in the range 200 eV – 500 eV (with core ion temperatures approximately half as large), and plasma currents in the range 100 kAmps – 500 kAmps. More importantly, with respect to inserting probes into the plasma edge, its edge plasmas have densities in the range 0.01×10^{19} m^{-3} – 0.5×10^{19} m^{-3} and electron temperatures in the range 10 eV – 100 eV (with edge ion temperatures approximately the same). MST plasmas last approximately 30 to 60 msec and are typically produced every 2 to 5 min, with

approximately a few hundred (or less) plasmas produced during the course of a typical day. The particular plasmas used for the measurements described in Chs. 4 – 5 of this dissertation had plasma currents of 160 kAmps and chord average densities of 5×10^{12} cm^{-3}. They lasted ~ 50 msec each and were generated once every ~ 3 min. Also, they had edge densities and temperatures of ~ 1×10^{12} cm^{-3} and 50 eV, respectively.

Plasmas with temperatures in the lower end of the available range can have probes made of refractory materials such as boron nitride and molybdenum inserted as deep as ~ 10 cm ($r/a \sim 0.8$) without significantly disturbing the plasma or destroying the probe. In particular, such refractory materials are typically capable of accepting the instantaneous and long term average heat loads delivered by repeated exposure to such a plasma at sufficiently shallow depths without ablating significant material into the plasma. Also, as discussed in Sec. 3.4 below, the probes used for the measurements described in this dissertation are very small compared to the plasma and its equilibrium scale length. The plasma occupies a toroidal volume with a major radius of 1.5 m and a minor radius of 0.52 m. Its equilibrium has radial gradients with a scale length given by its minor radius. The probes are much smaller in every dimension. The effects of inserting the Rogowskii probes used for measurements described in this dissertation are illustrated by, for example, Figures 1a – 1h, which compare key plasma parameters (plasma current, chord average electron density, loop voltage and field reversal parameter) for a case with such a probe inserted to those for a case with no probe inserted.

3.3 - Measuring Magnetic and Current Density Fluctuations: Magnetic Sensing Coils and Rogowskii Coils

As discussed in Sec. 3.2, above, MST is capable of generating RFP plasmas whose edge region is suited to the use of probes. Both magnetic and current density fluctuations can be measured by suitable arrangements of magnetic sensing coils mounted on a probe. Thus, the structure of the magnetic and current density perturbations associated with magnetic

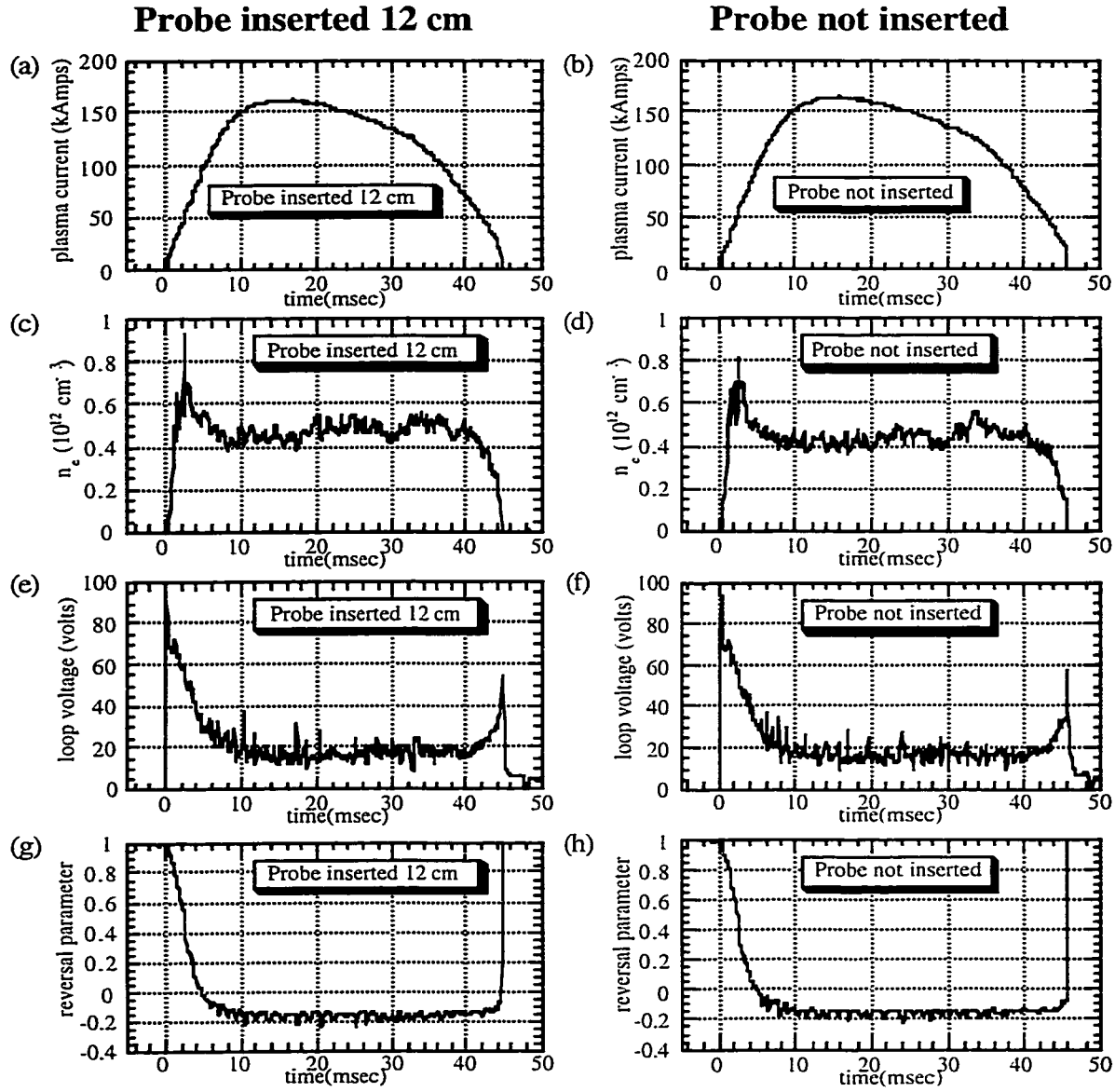

Figure 1: Figures (a) thru (h) compare four important plasma parameters for two typical shots: one with a probe inserted to a depth of 12 cm (r/a = 0.77) at 105 °P, 180 °T and one with no probe inserted at all. The figures on the left, (a), (c), (e) and (g) show plasma parameters for the shot with a probe inserted. The figures on the right, (b), (d), (f) and (h) show plasma parameters for the shot with no probe inserted. In descending order: figures (a) and (b) show plasma current, figures (c) and (d) show chord averaged electron density, figures (e) and (f) show loop voltage, and figures (g) and (h) show field reversal parameter (the ratio of the toroidal magnetic field at the plasma edge to the average toroidal magnetic field). Note that the shot with a probe inserted is not significantly different from the shot without.

reconnection can be studied in the edge of MST. More importantly, since the $m = 0$ class of tearing modes (discussed Sec. 2.6 of Ch. 2) is resonant in the edge of MST, the associated perturbations can be measured directly in the region where magnetic reconnection occurs. The measurements described in this dissertation make extensive use use of magnetic sensing coils and current sensing Rogowskii coils. Both magnetic sensing coils and current sensing Rogowskii coils function according to similar principles.

A magnetic sensing coil is a coil of conducting wire shaped to sense variations in the ambient magnetic field at the location of the coil by taking advantage of Faraday's law (Fig. 2) The loops of the magnetic coil approximately bound an area (normal to the axis of the coil) such that Faraday's law relates the time derivative of the magnetic flux through the area to the voltage difference between the two ends of the wire forming the coil. In other words,

$$-A_{coil}\dot{\bar{B}} \approx -\int_{\text{coil area}} \dot{\bar{B}} \cdot d\bar{a} = \oint_{\text{coil loop}} \bar{E} \cdot d\bar{l} \approx V_{\text{coil}} N^{-1}_{\text{coil loops}}, \tag{3.3.1}$$

where V_{coil} is the voltage difference between the two ends of the wire forming coil, $N_{\text{coil loops}}$ is the number of loops in the coil, and A_{coil} is the area bounded by the a single loop of the coil (*i.e.*, the coil's cross-sectional area). The area integral of the magnetic field is over the coil's cross-sectional area and the path integral of the electric field is over the circumference of the coil. The trailing leads of a magnetic sensing coil are twisted together to insure that they bound as little area as possible through which magnetic flux can pass.

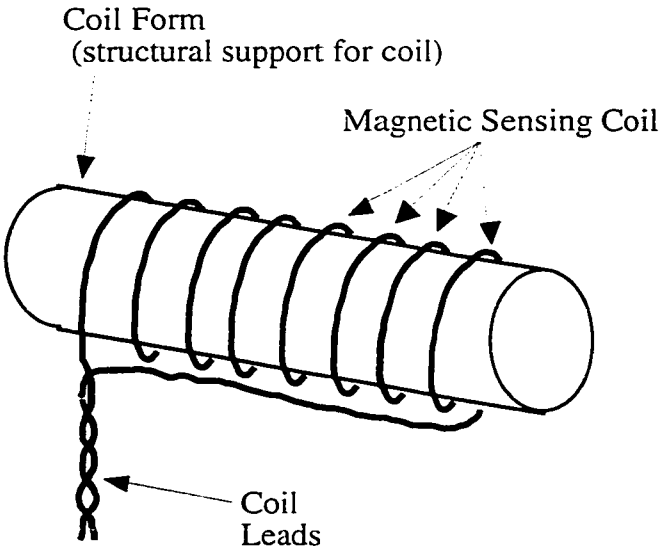

Figure 2: Schematic of magnetic sensing coil.

A current sensing Rogowskii is fundamentally a magnetic sensing coil that has been

modified to take advantage of Ampere's law in order to measure some component of the ambient current density. As shown in Figure 3, a Rogowskii coil is formed from a magnetic sensing coil whose axial extent is much larger than it's diameter. The coil's axis is bent so that the coil's two end faces are brought together, causing the coil's axis to form a loop. A magnetic sensing coil whose axial length is much longer than it's diameter can be described as a helix (of wire) that maps out the surface of a cylinder. A Rogowskii coil, on the other hand, can be considered as a helix that bounds the surface of a torus. Current passing through hole of the torus formed by a Rogowskii coil generates a magnetic field along the Rogowskii coil's coil axis. Acting as a magnetic sensing coil, therefore, a Rogowskii coil senses variations in the current passing through hole of the torus that it forms by sensing variations in the magnetic flux generated in the Rogowskii coil by that current. In other words, $V_{rog} = C_{rog}\dot{I}_{hole}$, where V_{rog} is the voltage difference between the two ends wire forming the Rogowskii coil, $\dot{I}_{hole}$ is the time derivative of the total current passing through the hole of the torus formed by the coil and C_{rog} is the sensitivity of the Rogowskii coil.

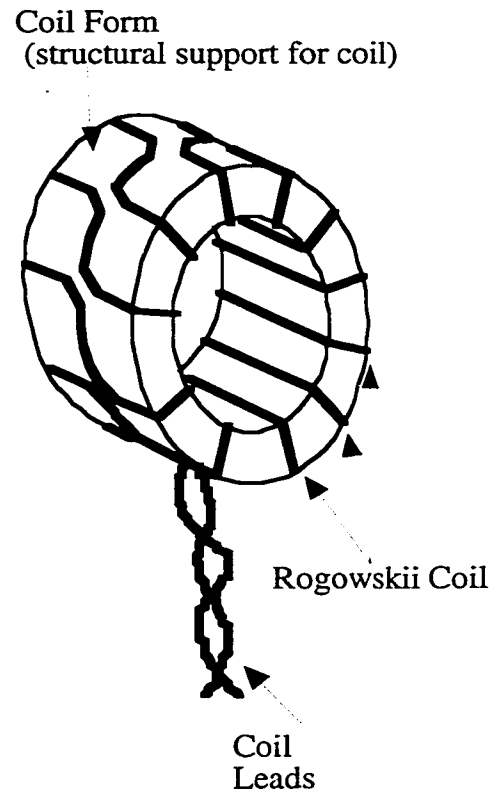

Figure 3: Schematic of Rogowskii coil. (Picture courtesy of Darren. J. G. Craig.)

The sensitivity of a Rogowskii depends on many factors, such as the the number of loops in the Rogowskii coil, the geometry of each loop and the major radius of the torus formed by the Rogowskii coil. In practice, this sensitivity is measured using a test current.

As indicated, magnetic sensing coils and Rogowskii coils measure time derivatives of magnetic field strength and current, respectively. Sometimes, as is the case for the measurements presented in Chs. 4 – 5 of this dissertation, it is not these time derivatives that are

desired, but, rather, measurements of the quantities themselves. Under such circumstances, magnetic sensing coil and Rogowskii coil signals will be integrated. In the case of the measurements presented in Chs. 4 – 5, analog integrator circuits were used with 0.1 msec time constants. The analog integrator circuits also applied amplification to the coil signals (*i.e.*, $V_{integ} = G/\tau \int V_{coil} dt$, where τ and G are the time constant and gain, respectively). Specifically, the Rogowskii coil signals in Chs. 4 – 5 were amplified with a gain of 50. The signals for the poloidally, toroidally and radially aligned magnetic sensing coils were amplified with gains of 10, 50 and 100, respectively. All gains, as well as the integrator time constant, were, of course, accounted for in converting coils signals into physical units.

3.4 - Rogowskii Probes

Each of the two insertable probes, or Rogowskii probes,[2] used for the measurements discussed in Chs. 4 – 5 of this dissertation contains a Rogowskii coil that is used to measure the parallel current density and two magnetic-sensing coils, one of which senses the poloidal component of the magnetic field, and the other of which senses the toroidal component of the magnetic field. One of the probes has, in addition, has a coil aligned to sense the (minor) radial component of the magnetic field. The latter probe, commonly referred to as Rogowskii #8 (for historical reasons), has the following coil sensitivities: $C_{rog}^{-1} = 2.486 \times 10^{7}$ Amps/(V sec), $A_\theta = 5.805 \times 10^{-4}$ m^2, $A_\phi = 1.576 \times 10^{-4}$ m^2 and $A_r = 1.476 \times 10^{-4}$ m^2. The former probe, commonly referred to as Rogowskii #7 (also for historical reasons), has the following coil sensitivities: $C_{rog}^{-1} = 2.387 \times 10^{7}$ Amps/(V sec), $A_\theta = 5.782 \times 10^{-4}$ m^2 and $A_\phi = 1.593 \times 10^{-4}$ m^2. The notation A_x indicates the effective area of the coil aligned in the x direction. Each effective coil area incorporates both the coil's cross-sectional area, as well as its number of windings. The Rogowskii and magnetic sensing coils in each of the probes are encased as a unit in a shell of ceramic (hot-pressed boron nitride) capable of withstanding the high temperatures of the plasmas into which the probes are inserted (Fig. 4). The ceramic encasement, or shroud, of each probe is

an approximately 2 cm x 3 cm x 4 cm block at the end of a ~ 1 cm diameter shaft. The shroud of each probe has a cylindrical hole of circular cross-section through which plasma can pass. This cylindrical hole, which is ~ 2 cm in axial length and ~ 2 cm in diameter for each probe, is concentric with, and axially aligned with, the toroidal axis of the Rogowskii coil in each probe, so that the Rogowskii coil can sense the component of the plasma current density that passes through it. When the probe is inserted into the plasma, this cylindrical hole, and, thus, the Rogowskii coil's axis, is typically aligned in the direction of the equilibrium magnetic field at the position of measurement, allowing for the measurement of the component of the current density that is parallel to the magnetic field. The actual cross-sectional area of the cylindrical hole of Rogowskii #7 is 2.32 cm^2, while the actual cross-sectional area of the cylindrical hole of Rogowskii #8 is 2.6 cm^2.

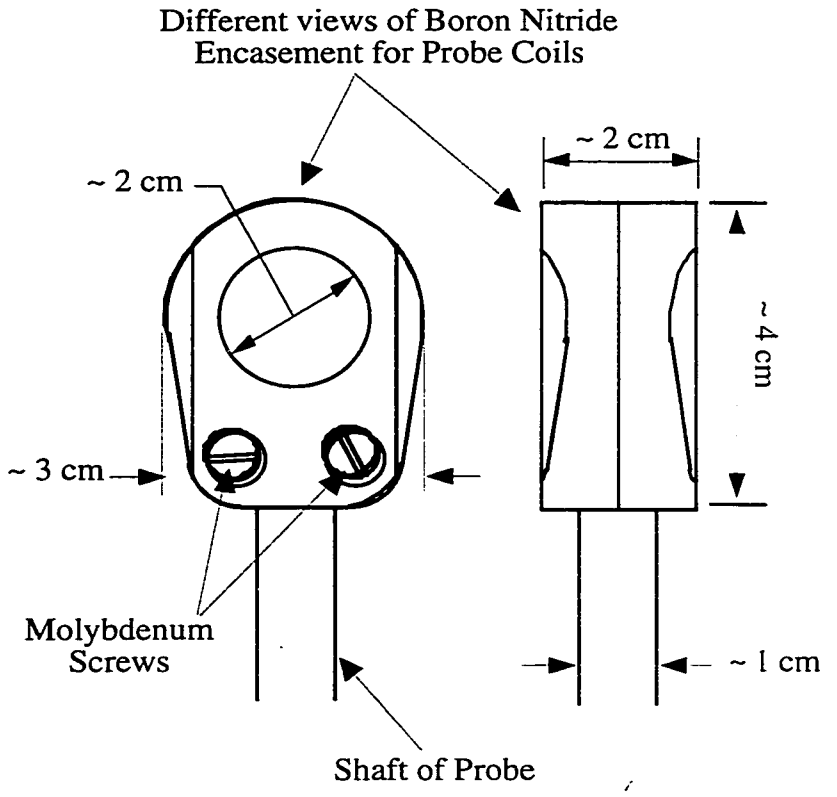

Figure 4: Schematic of Rogowskii Probe encasement, or shroud, for protecting coils from plasma. Made of hot-pressed boron nitride ceramic. Different views are shown. (Picture courtesy of Paul. W. Fontana.)

3.5 - Processing Coil Signals: Sources of Error and Noise

Rogowskii and magnetic coils allow for measurements that are very simple in concept. However, there are a number of practical considerations attendant in processing and interpreting

the signals they produce. In particular, there are several sources of noise or error inherent in the process of acquiring coils signals.

Coils signals, integrated or otherwise filtered, are typically acquired through a digitization process. This process introduces a form of broadband random noise commonly referred to as *bit-noise*. Bit-noise is the product of the numerical rounding-off process imposed on a signal by the digitizer. This error introduced in the rounding-off process is non-linearly related to the signal to which it is applied and behaves effectively as random noise. In particular, it adds equal amounts of random error to the signal at all frequencies from D. C. to the Nyquist frequency (the maximum frequency to which the digitizer is sensitive, given by half the digitization rate). For the measurements described in Chs. 4 – 5 of this dissertation, the digitizers have a 5 mV bit-size (*i.e.*, resolution). These measurements are frequency filtered to eliminate frequencies outside the range 1 – 25 kHz, which filters out some of the noise. The remaining bit-noise added to a signal is ~ 1.5 mV. The measurements discussed in Chs. 4 – 5 represent signals with amplitudes typically in the range ~ 0.03 – ~ 0.3 V. Thus, bit-noise is small and we neglect it for the measurements discussed in Chs. 4 – 5.

As discussed in Sec 3.3, above, Rogowskii and magnetic coil signals represent the time derivatives of measured current densities and magnetic fields, respectively. Sometimes, the measurement of interest is not these time derivatives, but, rather the quantities themselves. When this is the case, as it is with the measurements described in Chs. 4 – 5 of this dissertation, it is accomplished by using an electronic circuit to integrate the coil signals prior to digital acquisition. Such an *integrator* circuit introduces an error into the signal known as *integrator drift*. Integrator drift amounts to a small, slowly varying, spurious offset in the integrated signal. This drift rate depends on the degree to which the integrator amplifies its signal and for the integrators used in the measurements discussed in Chs. 4 – 5, it is typically in the range 0.1 – 0.5 V/sec. The measurements discussed in Chs. 4 – 5 of this dissertation represent integrated coil signals with amplitudes typically in the range ~ 0.03 – ~ 0.3 V, measured over

~ 0.5 msec intervals. The cumulative integrator drift over such an interval is < ~ 0.25 mV, and, therefore, is negligible.

Another potential source of noise in process of acquiring coils signals is *aliasing*. The digitizer samples signals at a certain rate and Fourier components in the signal at frequencies higher than half this rate (the Nyquist frequency) actually appear in the digitized signal as lower frequency components. For example, when digitized, a sine wave signal at a frequency $f = f_N+\delta f$ (where the Nyquist frequency f_N = (digitizer rate)/2), will appear to have a Fourier component at frequency δf. This potential source of error in the signal can be minimized very simply by significantly attenuating Fourier components in the signal at frequencies higher than the Nyquist frequency prior to digitization. For the measurements described in this dissertation, the magnetic and Rogowskii coil signals are digitized at 200 kHz. In practice, no attenuation of these signals prior to digitization has proved necessary because they are dominated by Fourier components in the frequency range 1 – 25 kHz, and have very little contribution from Fourier components at higher frequencies.

Another source of error in the process of making the measurements described in this dissertation result from a particular problem to which the Rogowskii probes described in Sec. 3.4 above are susceptible. Both probes, when subject to a sufficient heat load, either instantaneous or accumulated over repeated plasma shots, show a spurious, time varying offset in their integrated Rogowskii coil signals which is evident because these signals are non-vanishing even after the plasma has died away. This *heating effect* error is believed to result from a heating induced opening of nominally closed seams in the boron nitride shroud that encases the coils in each probe. This opening of seams directly, but weakly, exposes the Rogowskii coil in each probe to the plasma. The direct interaction of the Rogowskii coil with the plasma affects the integrator that processes its signal in a way which produces the spurious offset of the integrated signal.

The heating effect error has been studied by inserting a Rogowskii probe that has been

plugged to prevent the measurement of any actual current density into a plasma and observing the integrated Rogowskii coil signal. It appears to slowly vary in time during each plasma shot, much like an integrator drift. Its rate of variation changes randomly in amplitude and sign from one shot to the next, and can as large as 2 V/sec in magnitude. For the measurements discussed in Chs. 4 – 5 of this dissertation, the heating effect is compensated by applying a simple linear offset to the integrated Rogowskii coil signal acquired during each plasma shot. This correction is calculated from the accumulated offset that is apparent in the signal after the plasma shot has ended. Even were it not compensated by this technique, however, it would still be small. The measurements discussed in Chs. 4 – 5 represent integrated coil signals with amplitudes typically in the range ~ 0.03 – ~ 0.3 V, measured over ~ 0.5 msec intervals. The cumulative heating error over such an interval is < ~ 1 mV.

Another source of error in Rogowskii coils signals results from asymmetric winding of the Rogowskii coil during the construction process. For instance, if the loops of Rogowskii coil are more densely packed on one side of the coil than the other, the extra loops effectively act as a magnetic sensing coil whose signal adds to the signal induced by current passing through the Rogowskii coil's hole. Careful design and construction can minimize this problem, but it is typically not completely eliminated. The remaining sensitivity of the Rogowskii coil to the magnetic field is largely compensated by using the nearby magnetic sensing coils that are built into the probe.

The sensitivities of a Rogowskii coil to the components of the magnetic field aligned with and perpendicular (but non-radial) to its axis are measured by inserting the Rogowskii probe that contains the coil into the MST vacuum vessel while the toroidal magnetic field is pulsed. By rotating the probe around the axis of its shaft, the Rogowskii coil can be aligned perpendicular to the vacuum magnetic field or parallel to it, permitting determination of the parallel and perpendicular sensitivities. These sensitivities can be expressed as effective coil areas. For Rogowskii #8 they are $A_{rog_{\parallel}} = 0.4 \times 10^{-4}$ m^2 and $A_{rog_{\perp}} = 0.5 \times 10^{-4}$ m^2. For Rogowskii #7 they are

$A_{rog_{\parallel}} = 0.4 \times 10^{-4}$ m^2 and $A_{rog_{\perp}} = 0.1 \times 10^{-4}$ m^2 . The notation A_{rog_x} indicates the effective area of the Rogowskii coil as a magnetic sensing coil the x direction.

The sensitivity of the Rogowskii coil in Rogowskii #7 is typically ignored, since the radial magnetic field in MST is typically much weaker than the toroidal or poloidal magnetic field. However, Rogowskii #8 is used for the measurements of the average product of the radial magnetic field and current density fluctuations that are discussed in Ch. 5 of this dissertation. Any sensitivity of the Rogowskii coil in Rogowskii #8 will potentially introduce a bias into these measurements and, thus, must be compensated. The sensitivity of Rogowskii #8 to the radial magnetic field is determined by plugging Rogowskii #8 to prevent the measurement of any actual current density and inserting it into a plasma. The Rogowskii coil's sensitivity to the radial magnetic field is calculated by comparing the Rogowskii coil's signal to the radial magnetic field fluctuations measured by the radially aligned magnetic sensing coil. This sensitivity is $A_{rog_r} = 0.1 \times 10^{-4}$ m^2.

3.6 - Interaction of Rogowskii Probes with Plasma Fluctuations

In any attempt to make a measurement in a plasma with a probe, some consideration must be given to whether the interaction of the probe with the plasma alters the very plasma properties whose measurement is desired. Such would make it difficult to interpret the measurement. For the measurements reported in Chs. 4 – 5 of this dissertation, the quantities of interest are the magnetic and parallel current density fluctuations associated with reconnection. There are reasons to believe that these fluctuations at the scales of interest are not significantly susceptible to interference from the Rogowskii probes. Additionally, there is some observational evidence supporting this belief.

The magnetic fluctuations associated with reconnection should not be significantly susceptible to direct interference by the Rogowskii probe because the magnetic field in the vicinity of the probe is dominantly produced by current density distributed throughout the

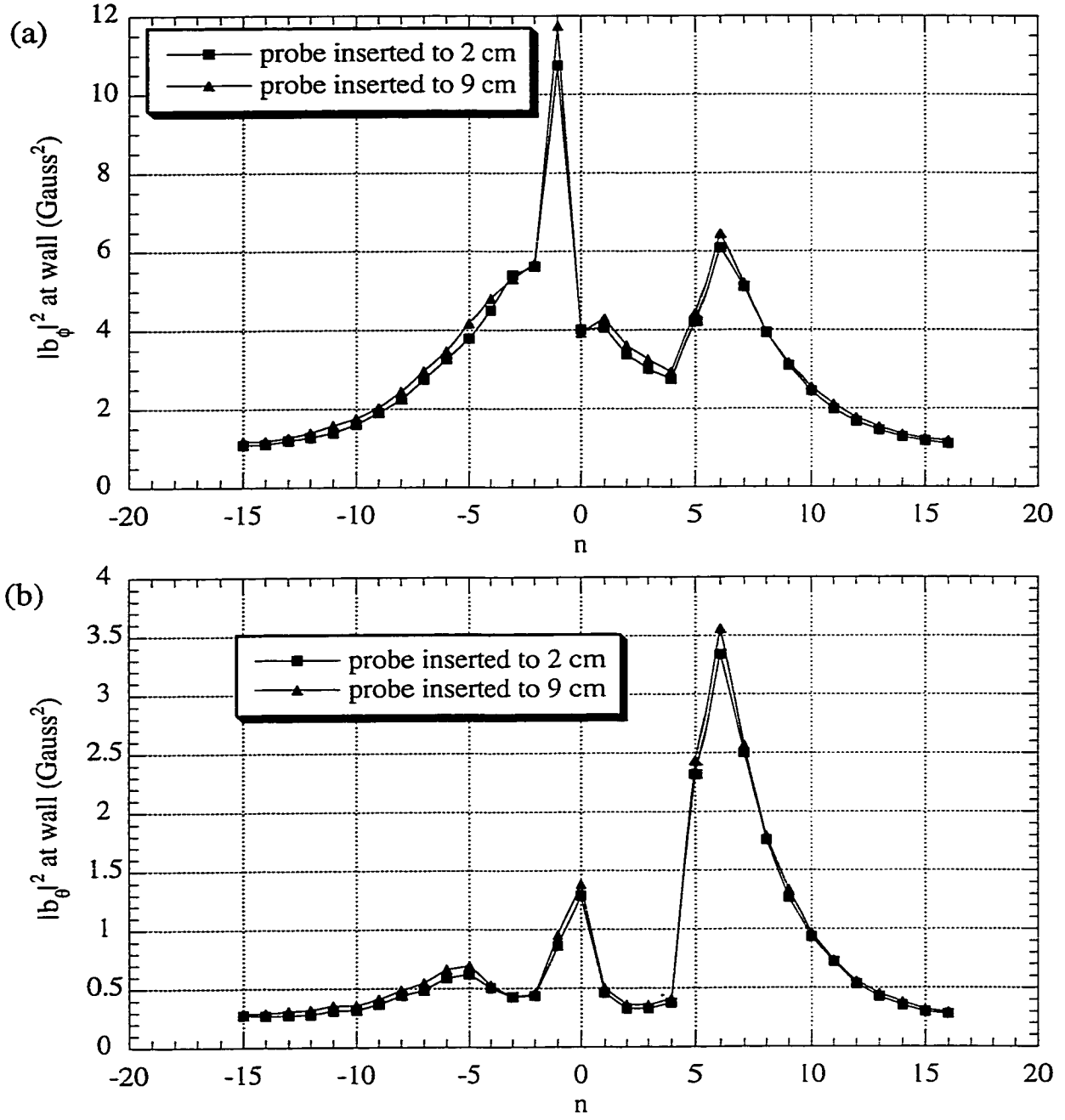

Figure 5: Comparison of magnetic fluctuations measured at wall with Rogowskii probe shallowly inserted (to 2 cm) to magnetic fluctuations measured at wall with Rogowskii probe deeply inserted (to 2 cm). Figure (a) shows toroidal spectra of toroidal magnetic field fluctuations at wall with toroidal array during sawtooth crashes for both cases. Figure (b) shows toroidal spectra of poloidal magnetic field fluctuations at wall with toroidal array during sawtooth crashes for both cases. Note that magnetic field fluctuations at wall do not significantly differ between shallow insertion case and deep insertion case.

plasma, most of which is far away from the probe. There is also observational evidence suggesting that insertion of the Rogowskii probe does not interfere with such magnetic fluctuations. Figures 5a and 5b compare the toroidal spectrum of toroidal and poloidal magnetic field fluctuations at the wall measured for plasmas that have a probe shallowly inserted (to 2 cm) to those measured for plasmas that have a probe deeply inserted (to 9 cm). It can be seen from these measurements that the spectrum is unchanged by deep insertion of a Rogowskii probe.

On the other hand, the parallel current density, and therefore its fluctuations, are potentially significantly susceptible to direct interference from the Rogowskii probes through an effect called *shadowing*. The region of measurement includes the reversal surface, where the magnetic field is purely poloidal. When a single probe is inserted to the reversal surface, as it is for some of the pseudospectral measurements discussed in Ch. 4 – 5, field lines in the vicinity of the reversal surface that intersect the probe can intersect it a second time after only a single poloidal transit. This means that when the Rogowskii is in the vicinity of the reversal surface, it is effectively a very short distance downstream from itself with regard to the charge carriers whose motion comprises the current density in that region. In such a circumstance, the Rogowskii probe potentially obstructs the current density it measures. This is called *self-shadowing*. In practice, there is no indication that self-shadowing affects the current density that the Rogowskii probe measures. This self-shadowing effect would be apparent in, for instance, a measured radial profile of the equilibrium parallel current density as a reduction of current density in the region of the reversal surface. As illustrated by Figure 6, however, such a reduction is not apparent.

While it is unlikely that a single Rogowskii inserted into the plasma edge will disturb the parallel current density it measures through self-shadowing, two closely spaced, poloidally separated probes inserted into the plasma edge have the potential to shadow each other. This possibility is of interest because Ch. 4 of this dissertation presents two-point poloidal spectra of parallel current density fluctuations that are obtained using a pair of Rogowskii probes in just

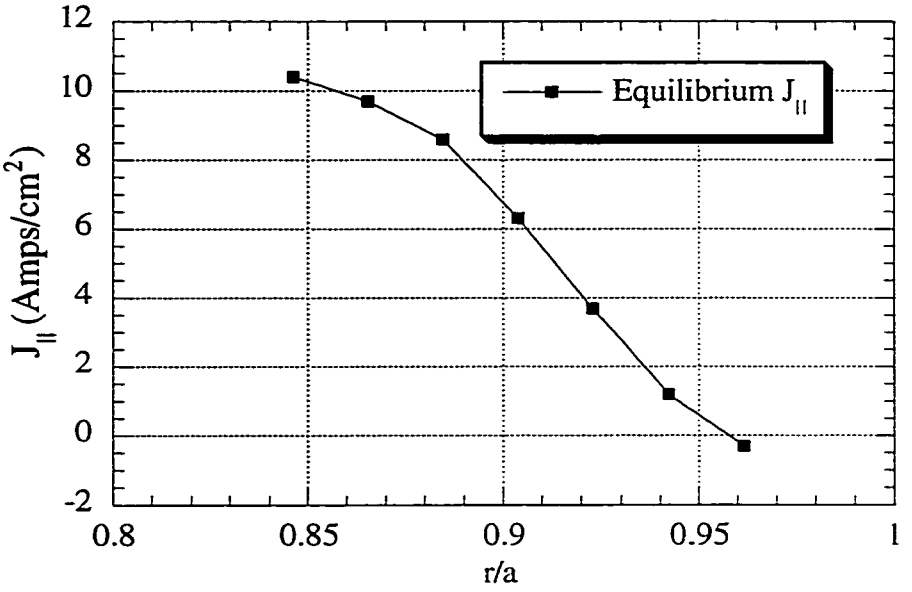

Figure 6: Equilibrium parallel current in edge of MST measured by inserted Rogowskii probe. Note that there is no reduction of current density near reversal surface (r/a = 0.86) as would be expected if Rogowskii probe shadows itself. The statistical uncertainties for these measurements are the size of the plot symbols or smaller.

such an arrangement. Such shadowing is, in fact, evident in the equilibrium parallel current density measurements obtained from this pair of probes. One of the probes typically measures an equilibrium parallel current density on the order of 10% smaller with both probes inserted to the same flux surface than it does when the other probe was not inserted. However, despite the fact that shadowing does, in face, occur, it is not clear that a poloidal two-point spectrum will be significantly affected. As discussed in Sec. 3.12, below, a two-point spectrum is calculated from the relative phases measured between fluctuations at two-points. While shadowing certainly affects the amplitude of the fluctuations at the probe that is shadowed, it is not certain that it affects the relative phase between the fluctuations at both probes. It worth noting that when two poloidally separated probes are positioned close to each other on the reversal surface, as they are for the two-point spectral measurements presented in Ch. 4, the shadowing effect is minimized because much of the plasma passing through one probe is able to pass unimpeded through the other.

There is also another argument suggesting that Rogowskii probes do not significantly

interfere with the magnetic and parallel current density fluctuations at the spatial scales of interest. The toroidal wavelengths of the plasma perturbations associated with reconnection are of the order of 1 m or larger. Specifically, they have toroidal mode numbers of $|n| = 1 - 10$ and poloidal mode numbers $m = 0 - 1$. Also, they have radial scales ranging from ~ 10 cm (for current density fluctuations) to ~ 1 m (for magnetic fluctuations). The Rogowskii probes, on the other hand, are of order 1 cm in all dimensions, and are significantly smaller in scale than these plasma fluctuations. Thus, the Rogowskii would tend to introduce fluctuations with perpendicular scale lengths (toroidal and radial) of 1 cm, which are smaller than those of interest. Also, when two probes are simultaneously inserted for two-point spectral measurements, they are typically much more closely spaced than the wavelength associated with reconnection.

3.7 - Toroidal Coil Arrays

In addition to the Rogowskii probes, the measurements related in Ch. 4 – 5 make use of a toroidally distributed array of pairs of magnetic sensing coils. This array, mounted on MST's wall near the plasma surface, consists of 64 pairs of poloidally and toroidally aligned magnetic sensing coils with approximately 1.5 cm^2 area each. The magnetic fluctuation power at the toroidal mode numbers of $|n| \geq 16$ are small enough that typically only 32 of the coils for each magnetic field component are used. The 64 pairs are all located at poloidal location 241° P, where "° P" denotes "poloidal angle in degrees." The poloidal angle coordinate on MST starts with 0° P on the outboard side of MST (the side at greatest major radius) at the horizontal midplane and increases in the (poloidal) angular direction that goes over the top of MST. In other words, the poloidal position of the top of MST is 90° P. Thus, the toroidal arrays are located below the horizontal midplane, on the inboard side .

Except for the two pairs of coils that bracket the poloidal gap in MST's close conducting shell (at 0° T, where "° T" denotes "toroidal angle in degrees") the coil pairs are evenly spaced at the toroidal locations $(i+1/2)(360/64)°$ T, $\forall i \in \{1,2,...,62\}$. The two pairs that bracket the gap

are at toroidal 3 1/8° T and 356 7/8° T. These two locations are very near the toroidal locations of (1/2)(360/64)° T and (63+1/2)(360/64)° T that the pairs would occupy if all 64 pairs were evenly distributed over the full 360° of toroidal angle and positioned to evenly bracket the poloidal gap. As noted above, the toroidal angle coordinate system on MST starts at the poloidal gap at 0° T. Looking down on MST from above, the toroidal angle coordinate increases counter-clockwise from the poloidal gap.

The toroidal coil arrays on MST are a well understood diagnostic, and are described in greater detail by, for instance, the discussion by S. Assadi.[3]

3.8 - Analyzing Fluctuations: Crossspectral Analysis

A particularly useful statistical tool in analyzing fluctuations in MST is *crossspectral analysis*. In general, crossspectral analysis may serve many different purposes. In particular, however, it serves three specific purposes for the measurements described in Chs. 4 – 5 of this dissertation. The first use of crossspectral analysis, discussed in Sec. 3.9 below, is to explore the dynamics underlying $\tilde{j}_{\parallel}$ and $\tilde{b}_r$, both of which contribute to the $\bar{J} \times \bar{B}$ force on MST plasmas, and to the charge balance in MST plasmas through their flux surface averaged product, or flux surface variance. The second use of crossspectral analysis is to obtain a measure of the shared information between $\tilde{j}_{\parallel}$ and $\tilde{b}_r$ through one of its products, the crossspectral *coherence* and a measure of the relative phase between $\tilde{j}_{\parallel}$ and $\tilde{b}_r$ through another of it products, the crossspectral *phase*. The third use of crossspectral analysis lies in the fundamental role it plays in pseudospectral analysis, which is discussed in more detail in Sec. 3.10 below.

The theory of crossspectral analysis is very sophisticated and well-developed. (See, for instance, Bendat and Piersol.[4]) However, for the purposes of analyzing fluctuations in MST, it can be described in very simple and narrow terms. Specifically, given repeated measurements of a pair of fluctuating quantities $\tilde{x}$ and $\tilde{y}$ (*i.e.*, quantities expected, on average, to be zero), crossspectral analysis decomposes their expected average product, or expected covariance,

$E[\tilde{x}\tilde{y}]$, into contributions from their Fourier components. (The notation $E[a]$ means the expected average of a over infinite measurements.) For example, suppose $\tilde{x}$ and $\tilde{y}$ are time-dependent fluctuating quantities with temporal Fourier components at frequencies greater in magnitude than ω_0. Then for any particular measurement of $\tilde{x}$, it will have the form

$$\tilde{x}(t) = \sum_{\forall \omega : |\omega| \geq \omega_0} \hat{\tilde{x}}_\omega e^{i\omega t} \tag{3.8.1}$$

and $\tilde{y}$ will have a similar form. In principle, $\hat{\tilde{x}}_\omega$ and $\hat{\tilde{y}}_\omega$ will vary randomly from one measurement to the next of $\tilde{x}$ and $\tilde{y}$. The crossspectral decomposition $E[\tilde{x}\tilde{y}]$, or *crossspectrum* $\tilde{x}$ and $\tilde{y}$, is given by the relation

$$E[\tilde{x}\tilde{y}] = \sum_{\forall \omega : |\omega| \geq \omega_0} E\left[\hat{\tilde{x}}_\omega \hat{\tilde{y}}_\omega^*\right]. \tag{3.8.2}$$

The quantity $E\left[\hat{\tilde{x}}_\omega \hat{\tilde{y}}_\omega^*\right]$ is the contribution of Fourier components of $\tilde{x}$ and $\tilde{y}$ at frequency ω to the expected variance of $\tilde{x}$ and $\tilde{y}$, $E[\tilde{x}\tilde{y}]$.

Other useful quantities produced by crossspectral analysis are the crossspectral phase and coherence and the *autospectrum*. The quantity $E\left[\hat{\tilde{x}}_\omega \hat{\tilde{y}}_\omega^*\right]$, called the crossspectral *amplitude* of $\tilde{x}$ and $\tilde{y}$ at frequency ω, has a complex phase, called the crossspectral phase between $\tilde{x}$ and $\tilde{y}$ at frequency ω, that represents the phase between $\tilde{x}$ and $\tilde{y}$ at that frequency. Additionally, the magnitude of the crossspectral *amplitude* of $\tilde{x}$ and $\tilde{y}$ at frequency ω depends on the information shared statistically between $\tilde{x}$ and $\tilde{y}$ at frequency ω. The crossspectral coherence of $\tilde{x}$ and $\tilde{y}$ at frequency ω, $E\left[\hat{\tilde{x}}_\omega \hat{\tilde{y}}_\omega^*\right] \Big/ \left(E\left[\left|\hat{\tilde{x}}_\omega\right|^2\right] E\left[\left|\hat{\tilde{y}}_\omega\right|^2\right]\right)^{1/2}$, provides a measure of this information, by normalizing the crossspectral amplitude of $\tilde{x}$ and $\tilde{y}$ at frequency ω using the autospectra of $\tilde{x}$ and $\tilde{y}$. An can be seen, the autospectrum $E\left[\left|\hat{\tilde{x}}_\omega\right|^2\right]$ of a quantity, $\tilde{x}$, is just the special case of a crossspectrum of a fluctuating quantity with itself.

The concepts of crossspectral phase, coherence and amplitude can be generalized to provide an overall characterization of the statistical relationship between $\tilde{x}$ and $\tilde{y}$, as opposed to a characterization of the relationship between their temporal Fourier components. The overall

crossspectral amplitude $\tilde{x}$ and $\tilde{y}$ is just the sum of crossspectral amplitudes for specific frequencies over an appropriate range of frequencies ($\omega_{low} - \omega_{hi}$):

$$\text{amplitude of } \tilde{x} \text{ and } \tilde{y} \equiv \sum_{\omega\in[\omega_{low},\omega_{hi}]} \mathrm{E}\left[\hat{\tilde{x}}_\omega \hat{\tilde{y}}_\omega^*\right]. \tag{3.8.3}$$

A particularly useful choice for a frequency range is the positive frequencies. Since $\tilde{x}$ and $\tilde{y}$ are real quantities (as opposed to complex), the crossspectral amplitude of $\tilde{x}$ and $\tilde{y}$ at any frequency ω is the complex conjugate of that at frequency $-\omega$. Thus, a sum over positive and negative frequencies would result in a cancelation of contributions from the imaginary parts of the crossspectral amplitudes at positive frequencies with those at negative frequencies. The overall crossspectral phase and coherence of $\tilde{x}$ and $\tilde{y}$ are similarly given by

$$\text{phase of } \tilde{x} \text{ and } \tilde{y} \equiv \text{phase}\left(\sum_{\omega\in[\omega_{low},\omega_{hi}]} \mathrm{E}\left[\hat{\tilde{x}}_\omega \hat{\tilde{y}}_\omega^*\right]\right) \tag{3.8.4}$$

and

$$\text{coherence of } \tilde{x} \text{ and } \tilde{y} \equiv \sum_{\omega\in[\omega_{low},\omega_{hi}]} \mathrm{E}\left[\hat{\tilde{x}}_\omega \hat{\tilde{y}}_\omega^*\right] \Bigg/ \left(\sum_{\omega\in[\omega_{low},\omega_{hi}]} \mathrm{E}\left[\left|\hat{\tilde{x}}_\omega\right|^2\right] \sum_{:\omega\in[\omega_{low},\omega_{hi}]} \mathrm{E}\left[\left|\hat{\tilde{y}}_\omega\right|^2\right]\right)^{1/2}. \tag{3.8.5}$$

3.9 - Approximating Flux Surface Averages of Fluctuation Products

Much like a crossspectrum, the average product, or variance, $\langle\tilde{x}\tilde{y}\rangle_{F.S.}$, of a pair of spatially dependent fluctuations $\tilde{x}$ and $\tilde{y}$ over a flux surface of the equilibrium magnetic field, can be decomposed into contributions from their spatial Fourier components. For example, suppose $\tilde{x}$ and $\tilde{y}$ are fluctuating quantities, where $\tilde{x}$ has the form

$$\tilde{x}(r,\phi,\theta,t) = \sum_{\forall(n,m)\neq(0,0)} \hat{\tilde{x}}_{n,m}(r,t) e^{i(-n\phi+m\theta)} \tag{3.9.1}$$

and $\tilde{y}$ has a similar form. In a plasma where an equilibrium flux surface is a surface of constant minor radius (which is a good approximation in MST, and which will be used throughout the

following discussion), $\langle \tilde{x}\tilde{y} \rangle_{F.S.}$ is given by

$$\langle \tilde{x}\tilde{y} \rangle_{F.S.} \approx (2\pi)^{-2} \iint_{\forall \phi,\theta} \tilde{x}\tilde{y} d\phi d\theta = \sum_{\forall (n,m) \neq (0,0)} \tilde{x}_{n,m} \tilde{y}^{*}_{n,m} . \tag{3.9.2}$$

The fluctuating quantities, $\tilde{j}_{\parallel}$ and $\tilde{b}_r$, have spatial Fourier components at many different wave numbers. Furthermore, their flux surface variance, $\langle \tilde{j}_{\parallel} \tilde{b}_r \rangle_{F.S.}$, is potentially composed of contributions from every spatial Fourier mode. Since the flux surface variance of $\tilde{j}_{\parallel}$ and $\tilde{b}_r$ can have a significant impact on the evolution of plasmas in MST, the question arises as to which spatial Fourier components significantly contribute to it. The different Fourier components of the fluctuating quantities have different physical origins (*i.e.*, different resonant surfaces for the modes that produce them), so the answer to this question provides insight into the dynamics that govern the equilibrium. Unfortunately, the flux surface variance of $\tilde{j}_{\parallel}$ and $\tilde{b}_r$ is difficult to measure in MST. In practice, however, its expected value (*i.e.*, its expected average over infinite measurements) may be estimated using the expected variance of point-measurements of $\tilde{j}_{\parallel}$ and $\tilde{b}_r$.

Because of the character of the fluctuations in MST, the expected value, $\mathrm{E}\left[\langle \tilde{x}\tilde{y} \rangle_{F.S.}\right]$, of the flux surface variance of a pair of fluctuating quantities, $\tilde{x}$ and $\tilde{y}$, may be estimated using, $\mathrm{E}[\tilde{x}\tilde{y}]$, the expected variance of point-measurements of those quantities. As discussed in Sec. 2.4 of Ch. 2, fluctuations in many plasmas quantities in MST are dominated by slowly varying, toroidally rotating, helical perturbations. These perturbations have the characteristic that perturbations with different helicities and phase velocities are approximately statistically independent (ignoring *toroidicity effects*, which are discussed later in this section). Since these perturbations rotate, a probe making repeated point-measurements samples them at all spatial phases, effectively sampling their variation over the entire flux surface on which the probe is positioned. In other words, in MST, any fluctuating quantity $\tilde{x}$ will approximately take the form

$$\tilde{x}(r,\phi,\theta,t) = \sum_{\substack{\forall \omega,n,m \\ (\omega,n,m) \neq (0,0,0)}} \hat{\tilde{x}}_{\omega,n,m}(r) e^{i(-n\phi + m\theta - \omega t)}, \tag{3.9.3}$$

where the values of $\hat{\tilde{x}}_{\omega,n,m}(r)$ vary from one measurement to the next according to some

statistical distribution. The statistical independence of perturbations with different helicities and phase velocities is expressed by the relations,

$$\mathrm{E}\left[\hat{\tilde{x}}_{\omega,n,m}(r)\hat{\tilde{x}}^{*}_{\omega',n',m'}(r)\right] \approx \mathrm{E}\left[\hat{\tilde{x}}_{\omega,n,m}(r)\hat{\tilde{x}}^{*}_{\omega,n,m}(r)\right]\delta_{\omega\omega'}\delta_{nn'}\delta_{mm'}, \tag{3.9.4}$$

and

$$\mathrm{E}\left[\hat{\tilde{x}}_{\omega,n,m}(r)\hat{\tilde{y}}^{*}_{\omega',n',m'}(r)\right] \approx \mathrm{E}\left[\hat{\tilde{x}}_{\omega,n,m}(r)\hat{\tilde{y}}^{*}_{\omega,n,m}(r)\right]\delta_{\omega\omega'}\delta_{nn'}\delta_{mm'}, \tag{3.9.5}$$

where $\tilde{y}$ is some other fluctuating quantity.

From this form for a pair of quantities $\tilde{x}$ and $\tilde{y}$, using Eq. 3.9.2, comes the relation,

$$\mathrm{E}[\tilde{x}\tilde{y}] \approx \sum_{\substack{\forall\omega,n,m \\ (\omega,n,m)\neq(0,0,0)}} \mathrm{E}\left[\hat{\tilde{x}}_{\omega,n,m}(r)\hat{\tilde{y}}^{*}_{\omega,n,m}(r)\right] \approx \mathrm{E}\left[(2\pi)^{-2}\iint_{\forall\phi,\theta}\tilde{x}\tilde{y}\,d\phi\,d\theta\right] = \mathrm{E}\left[\langle\tilde{x}\tilde{y}\rangle_{F.S.}\right], \tag{3.9.6}$$

where $\mathrm{E}[\tilde{x}\tilde{y}]$ and $\mathrm{E}\left[\langle\tilde{x}\tilde{y}\rangle_{F.S.}\right]$ implicitly depend on r.

Since MST's equilibrium is toroidal, rather than cylindrical, fluctuations in MST typically exhibit toroidicity effects. In other words, fluctuations in MST are actually composed of coherent perturbations that have toroidal periodicity, but only approximate poloidal periodicity. While Eqs. 3.9.4 and 3.9.5 are good approximations in many circumstances, sometimes toroidicity effects may not be negligible. In such cases, typically, helical perturbations whose poloidal mode numbers, m, differ by 1 exhibit weak, but non-negligible, statistical dependence. When toroidicity effects become important, an expected variance, $\mathrm{E}[\tilde{x}\tilde{y}]$, of point-measurements of quantities $\tilde{x}$ and $\tilde{y}$, may be more accurately considered a toroidal average. In other words

$$\mathrm{E}[\tilde{x}\tilde{y}] \approx \sum_{\substack{\forall\omega,n,m \\ (\omega,n,m)\neq(0,0,0)}} \sum_{\substack{\delta m\in[-1,1] \\ m+\delta m\neq 0}} \mathrm{E}\left[\hat{\tilde{x}}_{\omega,n,m}(r)\hat{\tilde{y}}^{*}_{\omega,n,m+\delta m}(r)\right] \approx \mathrm{E}\left[(2\pi)^{-1}\int_{\forall\phi}\tilde{x}\tilde{y}\,d\phi\right] \tag{3.9.7}$$

where $\mathrm{E}[\tilde{x}\tilde{y}]$ implicitly depends on r and θ. In such cases, however, it is expected that, in plasmas such as MST where $a \ll R$, the terms where $\delta m = \pm 1$ will be small compared to the terms where $\delta m = 0$, and therefore, that the poloidal dependence of $\mathrm{E}[\tilde{x}\tilde{y}]$ will be weak.

3.10 - Principles of Pseudospectral Analysis

Pseudospectral analysis is a tool that makes use of crossspectral analysis in estimating the frequency and mode number spectra of fluctuations in a plasma. It assumes that the fluctuations in a cylindrical (or high-aspect ratio toroidal) plasma equilibrium may be approximately described as a superposition of statistically independent, propagating global helical perturbations. It also assumes that these helical perturbations affect multiple plasma quantities in some sense coherently. In other words, it assumes that fluctuations in the plasma approximately take the form, in repeated measurements, of

$$\tilde{x}(r,\phi,\theta,t) = \sum_{\substack{\forall \omega,n,m \\ (\omega,n,m)\neq(0,0,0)}} \hat{\tilde{x}}_{\omega,n,m}(r) e^{i(-n\phi+m\theta-\omega t)}, \tag{3.10.1}$$

where the values of $\hat{\tilde{x}}_{\omega,n,m}(r)$ vary from one measurement to the next and are statistically independent of each other (*i.e.*, $\mathrm{E}\left[\hat{\tilde{x}}_{\omega,n,m}(r)\hat{\tilde{x}}^{*}_{\omega',n',m'}(r')\right] \propto \delta_{\omega\omega'}\delta_{nn'}\delta_{mm'}$). The assumption of coherence between pairs of plasma $\tilde{x}$ and $\tilde{y}$ quantities is expressed by the relation

$$\mathrm{E}\left[\hat{\tilde{x}}_{\omega,n,m}(r)\hat{\tilde{y}}^{*}_{\omega',n',m'}(r')\right] \approx \delta_{\omega\omega'}\delta_{nn'}\delta_{mm'}\left(\mathrm{E}\left[\left|\hat{\tilde{x}}_{\omega,n,m}(r)\right|^2\right]\mathrm{E}\left[\left|\hat{\tilde{y}}_{\omega,n,m}(r')\right|^2\right]\right)^{1/2} e^{i\left(\varphi_{x\omega,n,m}(r)-\varphi_{y\omega,n,m}(r')\right)}. \tag{3.10.2}$$

The phase $\varphi_{x\omega,n,m}(r)-\varphi_{y\omega,n,m}(r')$ represents, in a sense, the expected phase between the Fourier components of $\tilde{x}$ and $\tilde{y}$ for the propagating helical perturbation with frequency ω and mode numbers n and m. Pseudospectral analysis makes no assumptions about this phase other than it is invariant. It is expected that values of $\varphi_{x\omega,n,m}(r)$ and $\varphi_{y\omega,n,m}(r')$ are determined by the dynamics underlying the helical perturbations in the plasma.

The pseudospectrum of a fluctuating quantity takes advantage of the relations expressed by Eqs. 3.10.1 and 3.10.2 to estimate the spatio-temporal spectrum of a fluctuating quantity using a point measurement of it and a reference fluctuating quantity obtained from an appropriately configured spatial array of diagnostics. It also provides a measure of the spatial phases of each of spatio-temporal components of the point-measured fluctuation. The pseudospectrum of a point-measured fluctuating quantity, $\tilde{x}$, measured at toroidal angle, ϕ_0, and

poloidal angle, θ_0, is defined in terms of a reference fluctuating quantity, $\tilde{y}$, by the relation

$$\hat{\tilde{x}}_{y_{\omega,(n),(m)}}(r) \equiv e^{-i(-n\phi_0+m\theta_0)}\,\mathrm{E}\Big[\hat{\tilde{x}}_{\omega}(r,\phi_0,\theta_0)\hat{\tilde{y}}^{*}_{\omega,n,m}(r')\Big]\Big/\mathrm{E}\Big[\Big|\hat{\tilde{y}}_{\omega,n,m}(r')\Big|^2\Big]^{1/2}, \tag{3.10.3}$$

where the subscripts ω, m and n denote, as usual, temporal and spatial Fourier components. In this definition, the subscripts *(n)* and *(m)* denote pseudospectral components, as opposed to actual spatial Fourier components. The subscript y of $\hat{\tilde{x}}_{y_{\omega,(n),(m)}}(r)$ simply denotes that $\hat{\tilde{x}}_{y_{\omega,(n),(m)}}(r)$ is a pseudospectral amplitude determined from reference quantity $\tilde{y}$. Note that the elements of a pseudospectrum are all nominally measurable using a single point diagnostic for $\tilde{x}$ and a toroidally and poloidally distributed array of diagnostics for $\tilde{y}$. Although, as discussed in Sec. 3.11 below, no such two dimensional arrays of diagnostics are available in MST, a simplifying assumption can be made that permits the use of measurements from a one dimensional, toroidally distributed array of diagnostics for a reference fluctuation.

Using the assumptions expressed in Eqs. 3.10.1 and 3.10.2, it can seen that the pseudospectrum of a fluctuation $\tilde{x}$, as defined in Eq. 3.10.3, provides an estimate of the spatio-temporal spectrum of $\tilde{x}$. From Eqs. 3.10.1 and 3.10.2 it can seen that

$$\begin{aligned}\mathrm{E}\Big[\hat{\tilde{x}}_{\omega}(r,\phi_0,\theta_0)\hat{\tilde{y}}^{*}_{\omega,n,m}(r')\Big] &= \sum_{\substack{\forall n',m' \\ (n',m')\neq(0,0)}} \mathrm{E}\Big[\hat{\tilde{x}}_{\omega,n',m'}(r)\hat{\tilde{y}}^{*}_{\omega,n,m}(r')\Big]e^{i(-n'\phi_0+m'\theta_0)} \\ &\approx \Big(\mathrm{E}\Big[\Big|\hat{\tilde{x}}_{\omega,n,m}(r)\Big|^2\Big]\mathrm{E}\Big[\Big|\hat{\tilde{y}}_{\omega,n,m}(r')\Big|^2\Big]\Big)^{1/2} e^{i\left(\varphi_{x_{\omega,n,m}}(r)-\varphi_{y_{\omega,n,m}}(r')-n\phi_0+m\theta_0\right)}\end{aligned} \tag{3.10.4}$$

So, from the definition of a pseudospectrum in Eq. 3.10.3 and Eq. 3.10.4, it follows that

$$\Big|\hat{\tilde{x}}_{y_{\omega,(n),(m)}}(r)\Big|^2 \approx \mathrm{E}\Big[\Big|\hat{\tilde{x}}_{\omega,n,m}(r)\Big|^2\Big]. \tag{3.10.5}$$

It can also be seen that the pseudospectra for a pair of fluctuating quantities $\tilde{x}$ and $\tilde{z}$ satisfy the rather useful relation

$$\hat{\tilde{x}}_{y_{\omega,(n),(m)}}(r)\hat{\tilde{z}}^{*}_{y_{\omega,(n),(m)}}(r) \approx \Big(\mathrm{E}\Big[\Big|\hat{\tilde{x}}_{\omega,n,m}(r)\Big|^2\Big]\mathrm{E}\Big[\Big|\hat{\tilde{z}}_{\omega,n,m}(r)\Big|^2\Big]\Big)^{1/2} e^{i\left(\varphi_{x_{\omega,n,m}}(r)-\varphi_{z_{\omega,n,m}}(r)\right)} \approx \mathrm{E}\Big[\hat{\tilde{x}}_{\omega,n,m}(r)\hat{\tilde{z}}^{*}_{\omega,n,m}(r)\Big]. \tag{3.10.6}$$

Recall from Eq. 3.9.6 that the flux surface averaged product of $\tilde{x}$ and $\tilde{z}$, $\mathrm{E}[\tilde{x}(r)\tilde{z}(r)]$, can be

decomposed into the contributions, $\mathrm{E}\left[\hat{\tilde{x}}_{\omega,n,m}(r)\hat{\tilde{z}}^{*}_{\omega,n,m}(r)\right]$, from different Fourier modes.

An important consideration in the interpretation of pseudospectral measurements is an inherent bias that affects such measurements. If the plasma fluctuations are not completely composed of globally coherent helical perturbations then the pseudospectrum of a fluctuation may underestimate the spatio-temporal spectrum. In other words, when

$$\left|\mathrm{E}\left[\hat{\tilde{x}}_{\omega,n,m}(r)\hat{\tilde{y}}^{*}_{\omega,n,m}(r')\right]\right| < \left(\mathrm{E}\left[\left|\hat{\tilde{x}}_{\omega,n,m}(r)\right|^{2}\right]\mathrm{E}\left[\left|\hat{\tilde{y}}_{\omega,n,m}(r')\right|^{2}\right]\right)^{1/2} \tag{3.10.7}$$

for a fluctuation $\tilde{x}$ and a reference fluctuation $\tilde{y}$, then

$$\left|\hat{\tilde{x}}_{y_{\omega,(n),(m)}}(r)\right|^{2} < \mathrm{E}\left[\left|\hat{\tilde{x}}_{\omega,n,m}(r)\right|^{2}\right]. \tag{3.10.8}$$

3.11 - Pseudospectral Analysis in MST

It is impossible to measure a pseudospectrum in MST using the definition provided in Sec. 3.10 because MST lacks two-dimensional, poloidally and toroidally distributed arrays of diagnostics. However, MST does have one-dimensional, toroidally distributed arrays of diagnostics in the form of wall mounted toroidally distributed arrays of poloidal and toroidal magnetic sensing coils. Fortunately, the character of the dominant fluctuations in MST justifies an approximation that permits the use of such one-dimensional arrays to obtain pseudospectra.

As discussed in Secs. 2.4 and 2.6 of Ch. 2, the dominant fluctuations in MST result from tearing modes and consist approximately of a set of poloidally and toroidally propagating, helically periodic global perturbations with the useful property that there is one dominant poloidal periodicity for all tearing modes with the same toroidal periodicity. In particular, the dominant poloidal mode number, m_n, for a tearing mode with toroidal mode number n is given by $m_n \equiv nq_{res}$, where q_{res} is the safety factor of the equilibrium magnetic field at the tearing mode's resonant surface. The possible values for m_n are 0 and 1. As a consequence, in any given measurement over an appropriate time period, such as, for example, 0.5 msec in MST, the dominant fluctuations in the plasma approximately take the form

$$\tilde{x}(r,\phi,\theta,t) \approx \sum_{\substack{\forall \omega,n \\ (\omega,n)\neq(0,0)}} \hat{\tilde{x}}_{\omega,n}(r) e^{i(-n\phi+m_n\theta-\omega t)}, \tag{3.11.1}$$

for any plasma fluctuation $\tilde{x}$, where the values of $\hat{\tilde{x}}_{\omega,n}(r)$ vary from one measurement to the next according to some statistical distribution and are independent of poloidal angle, θ. From this approximation comes the relation for the toroidal and temporal Fourier amplitude $\hat{\tilde{x}}_{\omega,n}(r,\theta)$ of any fluctuating quantity $\tilde{x}$,

$$\hat{\tilde{x}}_{\omega,n}(r,\theta) \equiv \tfrac{1}{2\pi T}\oint \int_{t}^{t+T} \tilde{x}(r,\phi,\theta,t') e^{i(\omega t+n\phi)} d\phi dt' \approx \hat{\tilde{x}}_{\omega,n}(r) e^{im_n\theta}. \tag{3.11.2}$$

where the quantity $\hat{\tilde{x}}_{\omega,n}(r)$ was introduced in Eq. 3.11.1 and T is the time over which $\hat{\tilde{x}}_{\omega,n}(r,\theta)$ is measured.

MST has toroidally distributed arrays of measurements (*i.e.*, toroidal and poloidal magnetic fluctuations measured at the wall), but not poloidally and toroidally distributed arrays. Consequently, there is no possible reference fluctuating quantity, $\tilde{y}$, whose full poloidal, toroidal and temporal Fourier modes, $\hat{\tilde{y}}_{\omega,n,m}(r)$, can be measured. However, there are possible reference fluctuating quantities, $\tilde{y}$, whose toroidal and temporal Fourier modes, $\hat{\tilde{y}}_{\omega,n}(r,\theta_y)$, can be measured. (For the toroidal magnetic sensing coil arrays mounted on the wall, θ_y = 241° P.) Thus, using the general definition of the pseudospectral amplitude $\hat{\tilde{x}}_{y_{\omega,(n),(m)}}(r)$ given in Eq. 3.10.3, and the relation in Eq. 3.11.2, it follows that

$$\hat{\tilde{x}}_{y_{\omega,(n),(m)}}(r) \approx \delta_{mm_n} e^{-i\left(-n\phi_0+m_n(\theta_0-\theta_y)\right)} \mathrm{E}\left[\hat{\tilde{x}}_{\omega}(r,\phi_0,\theta_0)\hat{\tilde{y}}^{*}_{\omega,n}(r',\theta_y)\right] \Big/ \mathrm{E}\left[\left|\hat{\tilde{y}}_{\omega,n}(r',\theta_y)\right|^2\right]^{1/2}. \tag{3.11.3}$$

It is important to note that, in practice, there are a broad range of toroidal mode numbers ($n \geq 5$), for which fluctuations in MST may be dominated by core resonant $m = 1$, and yet consist, to a small but non-negligible degree, of reversal surface resonant $m = 0$ modes in the vicinity of the reversal surface. For such modes, a better approximation than that described by Eq. 3.11.1 might be

$$\tilde{x}(r,\phi,\theta,t) \approx \sum_{\substack{\forall \omega,n \\ (\omega,n)\neq(0,0)}} \left(\hat{\tilde{x}}_{\omega,n,0}(r) e^{i(-n\phi-\omega t)} + \hat{\tilde{x}}_{\omega,n,1}(r) e^{i(-n\phi+\theta-\omega t)}\right) \tag{3.11.4}$$

where $\left|\hat{\tilde{x}}_{\omega,n,0}(r)\right|^2 << \left|\hat{\tilde{x}}_{\omega,n,1}(r)\right|^2$ for $n \geq 5$ and minor radii, r, in the vicinity of the reversal surface, and where $\hat{\tilde{x}}_{\omega,n,0}(r)$and $\hat{\tilde{x}}_{\omega,n,1}(r)$ are statistically independent (*i.e.*, $\mathrm{E}\left[\hat{\tilde{x}}_{\omega,n,0}(r)\hat{\tilde{x}}_{\omega,n,1}(r)\right]=0$). For $n < 5$, of course, $\hat{\tilde{x}}_{\omega,n,1}(r)=0$. This distinction can be important in interpreting pseudospectral measurements. The approximate relation described in Eq. 3.11.3, which permits the determination of pseudospectral amplitudes using the toroidal and temporal Fourier amplitudes of the reference quantity $\hat{\tilde{y}}_{\omega,n}\left(r,\theta_y\right)$, breaks down. Pseudospectral amplitudes, $\hat{\tilde{x}}_{y_{\omega,(n),(m)}}(r)$, are implicitly independent of the poloidal angles θ_0 and θ_y, at which $\tilde{x}$ and $\tilde{y}$ are measured. If Eq. 3.11.1 was accurate, then the quantity $e^{-i\left(-n\phi_0+m_n\left(\theta_0-\theta_y\right)\right)}\mathrm{E}\left[\hat{\tilde{x}}_{\omega}\left(r,\phi_0,\theta_0\right)\hat{\tilde{y}}^{*}_{\omega,n}\left(r',\theta_y\right)\right]$, where $m_n=1$ in this case, would be independent of the relative poloidal position at which $\tilde{x}$ is measured, $\theta_0-\theta_y$. Using the approximation described in Eq. 3.11.4, it is actually weakly dependent on $\theta_0-\theta_y$. Its dependence on $\theta_0-\theta_y$ becomes smaller as the ratio $\left|\hat{\tilde{x}}_{\omega,n,0}(r)\right|^2 \Big/ \left|\hat{\tilde{x}}_{\omega,n,1}(r)\right|^2$ becomes smaller.

It should be noted that a similar analysis technique, sometimes called pseudospectral analysis by those who use it, has been extensively employed for other experiments on MST. (See, for instance, Chapman[5] and Fontana.[6]) This technique is similar to the one described here in that it uses toroidal modes measured with the toroidal array at the wall as a reference fluctuation to decompose point-measured (or, in some cases, chord-averaged) fluctuations in terms of contributions from toroidal modes. The principal difference lies in what, exactly, is used as the reference fluctuation. While the technique described here makes use of fully complex toroidal mode amplitudes, $\hat{\tilde{y}}_{\omega,n}\left(r,\theta_y\right)$, the other technique discards part of this information. Specifically, it uses only real part of $\hat{\tilde{y}}_{\omega,n}\left(r,\theta_y\right)$, on the assumption that the imaginary part is perfectly coherent with the real part, and, therefore, contains no useful information. This assumption only holds, however, in cases where the helical perturbations comprising the fluctuations in MST have very slowly varying amplitudes. This assumption may, therefore, break down during sawtooth crashes.

3.12 - Two-point Spectral Analysis

Two-point spectral analysis is a commonly used technique for estimating the frequency and mode number spectra of fluctuating quantities.[7, 8, 9] It makes use of the simultaneous measurements of a fluctuating quantity at pairs of nearby points. For instance, for some time-and-toroidal-angle-dependent fluctuating quantity, $\tilde{x}(\phi,t)$, which takes the form over repeated measurements of

$$\tilde{x}(\phi,t) = \sum_{\substack{\forall \omega,n \\ (\omega,n)\neq(0,0)}} \hat{\tilde{x}}_{\omega,n} e^{i(-n\phi-\omega t)}, \tag{3.12.1}$$

the two-point frequency and toroidal mode number spectrum may be obtained from measurements at two different toroidal angles ϕ_0 and $\phi_0+d\phi$. Specifically, the two-point spectrum is given by

$$\left|\hat{\tilde{x}}_{\omega,(n)}\right|^2 \equiv \left|\mathrm{E}\left[\mathrm{P}\left(\hat{\tilde{x}}_\omega(\phi_0),\hat{\tilde{x}}_\omega(\phi_0+d\phi_0)\right)\mathrm{W}\left(\hat{\tilde{x}}_\omega(\phi_0)\hat{\tilde{x}}^*_\omega(\phi_0+d\phi_0),n,d\phi_0\right)\right]\right|, \tag{3.12.2}$$

where, for some complex quantity a with a complex phase in the range $[-\pi/2,\pi/2)$,

$$\mathrm{W}(a,n,d\phi_0) = \begin{cases} 1, \text{ phase}(a) \in \left[(n-1/2)d\phi_0,(n+1/2)d\phi_0\right) \\ 0, \text{ phase}(a) \notin \left[(n-1/2)d\phi_0,(n+1/2)d\phi_0\right) \end{cases}, \quad \forall n \in \left[-\frac{\pi}{d\phi_0},\frac{\pi}{d\phi_0}\right). \tag{3.12.3}$$

(The notation $[c,d)$ indicates the range of numbers b such that $c \le b < d$.) Here, $\mathrm{P}\left(\hat{\tilde{x}}_\omega(\phi_0,),\hat{\tilde{x}}_\omega(\phi_0+d\phi_0)\right)$ represents a measure of the fluctuation power in $\tilde{x}$ at frequency ω in a given measurement of $\tilde{x}$. Two possible forms for P are

$$\mathrm{P}\left(\hat{\tilde{x}}_\omega(\phi_0),\hat{\tilde{x}}_\omega(\phi_0+d\phi_0)\right) = \hat{\tilde{x}}_\omega(\phi_0)\hat{\tilde{x}}^*_\omega(\phi_0+d\phi_0) \tag{3.12.4}$$

and

$$\mathrm{P}\left(\hat{\tilde{x}}_\omega(\phi_0),\hat{\tilde{x}}_\omega(\phi_0+d\phi_0)\right) = \tfrac{1}{2}\left(\left|\hat{\tilde{x}}_\omega(\phi_0)\right|^2 + \left|\hat{\tilde{x}}_\omega(\phi_0+d\phi_0)\right|^2\right). \tag{3.12.5}$$

The latter form is used for the experiments described Chs. 4 – 5 of this dissertation.

A two-point frequency and poloidal mode number spectrum of a fluctuating quantity $\tilde{x}(\theta,t)$ measured at toroidal angles θ_0 and $\theta_0+d\theta$ is similarly obtained, by substituting the

poloidal angle θ for the toroidal angle ϕ, and the poloidal mode number m for the toroidal mode number n.

There is an important consideration attendant to interpreting two-point spectra. As discussed in Sec. 2.6 of Ch. 2, fluctuations in MST are dominated by helical modes that fall into two categories: reversal surface resonant $m = 0$ modes with toroidal mode numbers roughly in the range $n = -3 - -1$ and core resonant $m = 1$ modes with toroidal mode number roughly in the range $n = 5 - 10$. The degree to which the two categories of modes contribute to fluctuations in any given plasma quantity depends on the quantity in question and varies with minor radius. For instance, as discussed in Sec. 4.3 of Ch. 4, the spectrum of the toroidal magnetic field fluctuations at the wall between sawtooth crashes shows comparable amounts of fluctuations power in both bands of modes. When a fluctuation is thus composed of toroidal modes (with the same frequency) that fall into two distinct narrow bands of toroidal mode numbers, the toroidal modes in both bands will interfere with each other in a such a way that the resulting two-point spectrum shows both bands smeared together into one wide band of toroidal mode numbers. This effect is illustrated by two-point spectra obtained from data generated from simulated spectra. Figure 7a compares a simulated spectrum with fluctuation power roughly in the bands $n = -3 - -1$ and $n = 5 - 10$ to the smeared two-point spectrum that results from it. Figures 7b and 7c show comparisons of single-banded simulated spectra and the two-point spectra that result from them, which are fairly similar. The first figure, Figure 7b, shows a case where the fluctuations are roughly in the band $n = -3 - -1$, while the second figure, Figure 7c, shows a case where the fluctuations are roughly in the band $n = 5 - 10$. This effect, of course, depends on the extent to which the two distinct bands overlap in frequency. The two bands in the simulated spectrum shown in Figure 7a overlap in frequency completely. As discussed in Sec. 4.3 of Ch. 4, this smearing effect appears to affect the toroidal two-point spectra of both parallel current density fluctuations and, to a lesser extent, the toroidal magnetic field fluctuations measured in the edge of MST.

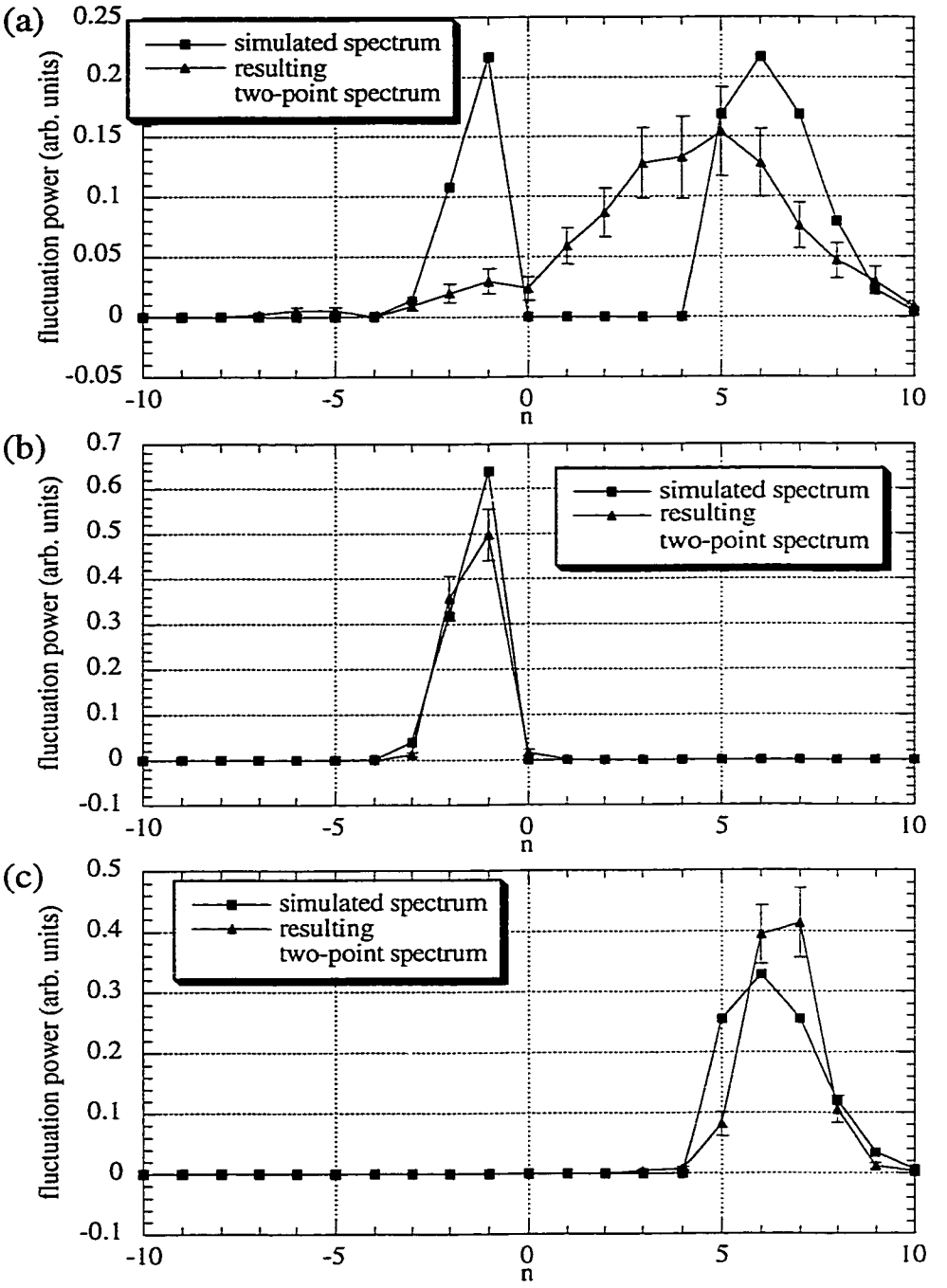

Figure 7: Comparisons of simulated spectra with two-point spectra generated from them for three cases: (a) fluctuation power roughly in the bands n = -3 – -1 and n = 5 – 10, (b) fluctuation power roughly in the band n = -3 – -1 and (c) fluctuation power roughly in the band n = 5 – 10. Note that the two-point spectrum generated from the double-banded simulated spectrum in case (a) shows a single broader band of fluctuation power. Effectively the two bands in the simulated spectrum are smeared together. Note that the two-point spectra generated from the single banded simulated spectra in cases (b) and (c) are fairly similar to the simulated spectra from which they are generated.

3.13 - Ensemble Averaging - Approximating Expected Averages

In practice, measuring expected averages requires infinite measurements, and is impossible. Instead, for the measurements discussed in this dissertation, expected averages are approximated by averages over an ensemble of time records, or realizations, and over time within each realization. Each ensemble is selected from from a collection of similar MST plasmas and consists of roughly two or three hundred realizations.

Because MST exhibits a semi-periodic sawtooth cycle, and and because the character of fluctuations changes between and during the crash phase of this cycle, the time records composing ensembles are chosen using two different methods. One method is to select time records that are centered around sawtooth crashes. This produces a *crash ensemble* of time record. The other method is to choose time records that fall between sawtooth crashes. This produces a *between-crash ensemble* of time records. In order to maximize the similarity between realizations, all time records in both types of ensemble are chosen from the so-called *flattop* period within each shot where plasma current, reversal parameter, loop voltage, line averaged electron density and other plasma parameters are relatively constant. This period typically lasts from 15 msec to 35 msec after the beginning of each plasma shot for the measurements discussed in this dissertation.

The exact timing of each realization in a crash ensemble is determined using the *field reversal parameter*, or reversal parameter, which is the ratio of the toroidal magnetic field at the edge of the plasma to the average toroidal magnetic field. Crashes typically lasts about 100 μsec and are accompanied by an increase in the magnitude of the reversal parameter. Each crash ends with a peaking in the magnitude of the reversal parameter. These peaks are used to identify the crashes and for each crash, a time record is chosen which extends form -0.21 msec before the peak to 0.11 msec after it. Since the Rogowskii coil and magnetic coils signals are digitized at a rate of 200 kHz for the measurements discussed in this dissertation, this gives 64 time points for each time record in a crash ensemble.

The timing of realizations in a between-crash ensemble is also determined using the reversal parameter. All peaks in the field reversal parameter are identified within the flattop period of each shot to identify the sawtooth crashes within that period. The entire flattop period is then parceled into 0.64 msec intervals such that no time interval, from beginning to end, is within ±0.5 msec of a peak in the field reversal parameter. Since the Rogowskii coil and magnetic coils signals are digitized at a rate of 200 kHz, this gives 128 time points for each time record in a between-crash ensemble.

Once an ensemble is chosen, the measurements within it are conditioned prior to their use in obtaining the crossspectra, pseudospectra or two-point spectra discussed in Chs. 4 – 5 of this dissertation. The Rogowskii coil and magnetic coil signals are conditioned by removing the linear trend from each signal in each time record in the ensemble. This is done to remove the slowly varying equilibrium component from each coil signal in each record.

An extra conditioning step is applied to not just the the Rogowskii coil and magnetic coil signals, but to the toroidal array coil signals, as well. For each time dependent quantity $\tilde{x}(t)$, the average time dependence of $\tilde{x}(t)$ over the ensemble, $\bar{\tilde{x}}(t)$, is subtracted from each record. In other words, an ensemble of measurements, $\tilde{x}(t)$, is conditioned by transforming it into and ensemble of measurements, $\tilde{x}'(t)$, where $\tilde{x}'(t)$ is given by

$$\tilde{x}'(t) = \tilde{x}(t) - \bar{\tilde{x}}(t). \tag{3.13.1}$$

This is done to remove the statistical equilibrium from each signal.

3.14 - Determining Statistical Uncertainties of Spectral Measurements

All two-point spectral measurement, relative phase measurements and pseudospectral measurements presented in Chs. 4 – 5 of this dissertation are shown with statistical uncertainties. All of these uncertainties are obtained through standard error analysis and propagation of errors using certain basic assumptions.[10] Fluctuating quantities such as parallel current density and the three components of the magnetic field are assumed to exhibit certain statistical closure relations.

First, the temporal Fourier components $\hat{\tilde{x}}_\omega$ and $\hat{\tilde{y}}_\omega$ of any pair of fluctuating quantities $\tilde{x}$ and $\tilde{y}$, are assumed to satisfy the relation

$$\mathrm{E}\left[\hat{\tilde{x}}_\omega \hat{\tilde{y}}_\omega\right] = 0. \tag{3.14.1}$$

Second, quartets of fluctuating quantities $\tilde{a}$, $\tilde{b}$, $\tilde{c}$ and $\tilde{d}$ are assumed to satisfy the closure relation

$$\mathrm{E}\left[\tilde{a}\tilde{b}\tilde{c}\tilde{d}\right] = \mathrm{E}\left[\tilde{a}\tilde{b}\right]\mathrm{E}\left[\tilde{c}\tilde{d}\right] + \mathrm{E}\left[\tilde{a}\tilde{c}\right]\mathrm{E}\left[\tilde{b}\tilde{d}\right] + \mathrm{E}\left[\tilde{a}\tilde{d}\right]\mathrm{E}\left[\tilde{b}\tilde{c}\right]. \tag{3.14.2}$$

As an example to illustrate how the assumptions in Eqs. 3.14.1 and 3.14.2 can be used to calculate uncertainties, we calculate the statistical uncertainty in a quantity such as $\left|\hat{\tilde{x}}_\omega \hat{\tilde{y}}^*_\omega\right|$. The uncertainty in a quantity is given square root of its expected variance. In other words,

$$\mathrm{Uncertainty}\left[\left|\hat{\tilde{x}}_\omega \hat{\tilde{y}}^*_\omega\right|\right] = \left(\mathrm{E}\left[\left|\hat{\tilde{x}}_\omega \hat{\tilde{y}}^*_\omega\right|^2\right] - \left|\mathrm{E}\left[\hat{\tilde{x}}_\omega \hat{\tilde{y}}^*_\omega\right]\right|^2\right)^{1/2}. \tag{3.14.3}$$

From Eq. 3.14.2, we can see that

$$\mathrm{E}\left[\left|\hat{\tilde{x}}_\omega \hat{\tilde{y}}^*_\omega\right|^2\right] = \left|\mathrm{E}\left[\hat{\tilde{x}}_\omega \hat{\tilde{y}}^*_\omega\right]\right|^2 + \mathrm{E}\left[\left|\hat{\tilde{x}}_\omega\right|^2\right]\mathrm{E}\left[\left|\hat{\tilde{y}}_\omega\right|^2\right] + \mathrm{E}\left[\hat{\tilde{x}}_\omega \hat{\tilde{y}}_\omega\right]\mathrm{E}\left[\hat{\tilde{x}}^*_\omega \hat{\tilde{y}}^*_\omega\right]. \tag{3.14.4}$$

From Eq. 3.14.1, we can see that

$$\mathrm{E}\left[\hat{\tilde{x}}_\omega \hat{\tilde{y}}_\omega\right]\mathrm{E}\left[\hat{\tilde{x}}^*_\omega \hat{\tilde{y}}^*_\omega\right] = 0. \tag{3.14.5}$$

So, from Eqs. 3.14.3 – 3.14.5,

$$\mathrm{Uncertainty}\left[\left|\hat{\tilde{x}}_\omega \hat{\tilde{y}}^*_\omega\right|\right] = \left(\mathrm{E}\left[\left|\hat{\tilde{x}}_\omega\right|^2\right]\mathrm{E}\left[\left|\hat{\tilde{y}}_\omega\right|^2\right]\right)^{1/2}. \tag{3.14.6}$$

A final step used in translating calculated uncertainties that depend on expected averages, such as that shown in Eq. 3.14.6, into numbers is to approximate expected averages with averages over finite ensembles of measurements.

3.15 - Summary

In summary, the measurements presented in the dissertation make use of parallel current

density and magnetic field fluctuations measured in the edge of MST with insertable Rogowskii probes and wall mounted, toroidally distributed arrays of magnetic sensing coils. It is noted that the insertion of these probes into the edge of MST does not significantly perturb the plasma equilibrium, nor does it significantly perturb the fluctuations that probes are intended to measure. Each Rogowskii probes contain Rogowskii coils, which are used to measure the parallel current density fluctuations, and magnetic sensing coils, which are used to measure the magnetic field fluctuations. There are a number of practical issues in processing the signals from these coils that have been considered for the measurements presented in this dissertation.

The magnetic field and parallel current density fluctuation measurements obtained from the Rogowskii probes are subject to statistical analyses in the forms of crossspectral, pseudospectral and two-point spectral analysis. Crossspectral analysis plays a role in estimating the (equilibrium) flux surface averaged product of radial magnetic field and parallel current density fluctuations, measurements of which are presented in Ch. 5. It also plays a role in pseudospectral analysis, which is used to estimate the toroidal spectra of the magnetic and parallel current density fluctuations in the edge of MST. Measurements of pseudospectra are presented in Ch. 4, and the technique is also made use of in Ch. 5. Two-point spectral analysis provides an alternative method for estimating toroidal spectra of the magnetic and parallel current density fluctuations in the edge of MST, although it has limitations given the character of these fluctuations. It also provides a method for estimating poloidal spectra of the magnetic and parallel current density fluctuations in the edge of MST. Measurements of two-point spectra are presented in Ch. 4. In performing these statistical analyses of magnetic and parallel current density fluctuations, certain basic procedures are performed, such as the construction of ensembles of measurements and the conditioning of the coil signals comprising these measurements to eliminate equilibrium components. Also, in calculating statistical uncertainties for the results of these analyses, certain basic assumptions are made regarding the character of the fluctuations and standard error analysis with propagation of errors is used.

References

[1] S. C. Prager, et al., Phys. Fluids B **2,** 1367 (1990).

[2] D. J. G. Craig, *Controlled Fluctuations and Transport in the Reversed Field Pinch with Edge Current Drive and Plasma Biasing*, (Ph. D. dissertation, University of Wisconsin – Madison, 1998), p. 69.

[3] S. Assadi, *Measurement of Magnetic Turbulence Structure and Nonlinear Mode Coupling of Tearing Fluctuations in the Madison Symmetric Torus Revered Field Pinch,* (Ph. D. dissertation, University of Wisconsin – Madison, 1992), p. 39.

[4] J. S. Bendat and A. G. Piersol, *Random Data Analysis and Measurement Procedures, Second Edition (Revised and Expanded),* (Wiley-Interscience, New York, 1986), p. 120.

[5] J. T. Chapman, *Spectroscopic Measurement of the MHD Dynamo in the MST Reversed Field Pinch*, (Ph. D. dissertation, University of Wisconsin – Madison, 1998), p. 138.

[6] P. W. Fontana, *Ion Dynamic and the Dynamo in the Edge of the Reversed Field Pinch*, (Ph. D. dissertation, University of Wisconsin – Madison, 1999), p. 30.

[7] S. Assadi, *Measurement of Magnetic Turbulence Structure and Nonlinear Mode Coupling of Tearing Fluctuations in the Madison Symmetric Torus Reversed Field Pinch,* (Ph. D. dissertation, University of Wisconsin – Madison, 1992), p. 58.

[8] W. Shen, *Measurement of Current Density Fluctuations and Ambipolar Particle Flux Due to Magnetic Fluctuations in MST*, (Ph. D. dissertation, University of Wisconsin – Madison, 1992) p. 108.

[9] J. M. Beall, et al., J. of Appl. Phys., **53,** 3933 (1982).

[10] J. S. Bendat and A. G. Piersol, *Random Data Analysis and Measurement Procedures, Second Edition (Revised and Expanded),* (Wiley-Interscience, New York, 1986), p. 252.

Chapter 4 - Reconnection in MST

4.1 - Introduction

Using insertable probes and arrays of magnetic sensing coils (as described in Secs. 3.4 and 3.7 of Ch. 3), fluctuations in the poloidal current density and magnetic field associated with tearing mode activity have been measured in the edge of MST. The spatial structure of these fluctuations has been probed making use of two different spectral analysis techniques (see Secs. 3.11 and 3.12 of Ch. 3). The results of these measurements are presented in this chapter and compared with measurements of tearing mode structure obtained from DEBS, a resistive MHD simulation of RFP plasmas. It is observed that the edge radial structures of both core and reversal surface resonant tearing mode perturbations are qualitatively similar to those observed for such perturbations in plasmas simulated by DEBS. In addition to comparing measurements in MST and DEBS, the radial structures of the poloidal current density and magnetic field perturbations associated with reversal surface resonant tearing modes are considered in detail. First, examination of the radial structure of the reversal surface resonant radial magnetic field perturbation provides direct evidence that reconnection occurs at the reversal surface. Such direct evidence of reconnection is the first of its kind in an RFP. Second, the radial structure of the reversal surface resonant perturbation is compared with predictions from various models of reconnection that are distinguished, in part, by the physical effects they incorporate into Ohm's law.

In Section 4.2, we present the toroidal pseudospectra for fluctuations in the poloidal current density and all three components of the magnetic field at several depths for $r/a > 0.8$. We also present measurements, for each toroidal mode, of the poloidal phases of these fluctuations relative to toroidal magnetic fluctuations at the wall. These measurements of toroidal mode spectra and relative phase are obtained at several radial positions in the plasma edge and at two different, widely separated poloidal and toroidal positions: -15° P, 330° T and 75° P, 120° T, where, as noted in Sec. 3.7 of Ch. 3, "° P" denotes "degrees poloidal" and "° T" denotes "degrees

toroidal." Furthermore, for each position within the plasma, pseudospectra are measured both between and during the crash phase of the sawtooth cycle. A principal result of these measurements is that magnetic fluctuations in the edge of MST are dominantly composed of toroidal modes with mode numbers in the range $n = 5 - 10$ while poloidal current density fluctuations are composed of toroidal modes with mode numbers in the range $n = -1 - -3$. Furthermore, comparison of the relative poloidal phase measurements obtained at -15° P with those obtained at 75° P indicates that the $n = 5 - 10$ toroidal modes of the magnetic fluctuations are dominantly, but not purely, composed of the $m = 1$ poloidal mode, while the $n = -1 - -3$ toroidal modes of the poloidal current density fluctuations are dominantly composed of the $m = 0$ poloidal mode. Thus, the magnetic fluctuations in the region of measurement are dominated by global magnetic perturbations, while the poloidal current density fluctuations in this region are dominated by a locally resonant current perturbation, or current sheet, associated with reconnection.

In Sections 4.3, we present the toroidal two-point spectra of fluctuations in the poloidal current density and the poloidal and toroidal components of the magnetic field. The toroidal two-point spectra are measured at several depths within the plasma edge using a pair of probes at -15° P, 320° T and -15° P, 330° T. They are measured simultaneously with the set of toroidal pseudospectra at -15° P, 330° T discussed in Section 4.2. As with the pseudospectra, the two-point spectra are measured both between and during the crash phase of the sawtooth cycle. A principal result of the toroidal two-point spectral measurements is to verify that, as indicated by the pseudospectral measurements discussed in Section 4.2, the magnetic fluctuations in the edge of MST are dominantly composed of toroidal modes with mode numbers in the range $n = 5 - 10$. Aside from this area of agreement, the two-point spectral measurements differ in many ways from the pseudospectral measurement. Possible causes of these differences are considered and arguments are presented supporting the validity of the toroidal pseudospectral measurements where they differ from the toroidal two-point spectral measurements.

In Sections 4.4, we present the poloidal two-point spectra of fluctuations in the poloidal current density and the poloidal and toroidal components of the magnetic field. The poloidal two-point spectra are measured with a pair of probes at 75° P, 120° T and 105° P, 120° T inserted to the reversal surface. These two-point spectra are measured both between and during the crash phase of the sawtooth cycle. A principal result of these measurements is that the magnetic fluctuations are dominantly composed of the $m = 1$ poloidal mode, while the poloidal current density fluctuations are dominantly composed of the $m = 0$ poloidal mode. This provides independent verification of the conclusions reached from the pseudospectral measurements regarding the poloidal mode content of the dominant magnetic and poloidal current density fluctuation.

In Section 4.5, we compare the radial structure of selected core resonant and reversal surface resonant tearing modes in the edge of MST with the structure of these modes as observed in DEBS, and we see qualitative similarity. The simulations also qualitatively reproduce other features of the measured fluctuations. For instance, MST and DEBS tearing modes exhibit certain similarities in the relative ordering of magnetic field perturbation amplitudes in the vicinity of the reversal surface. Additionally, they exhibit similarities in relative magnitudes for the poloidal current density and magnetic field fluctuations compared to the equilibrium poloidal current density and magnetic field. Perhaps most notably, they both exhibit a current sheet associated with reconnection at the reversal surface, although the processes that control the radial scale of this current sheet potentially differ in significant respects.

In Section 4.6, we examine the measured radial structure of the dominant reversal surface resonant radial magnetic field fluctuation ($m = 0$, $n = -1$). It is observed to be non-vanishing at the reversal surface, providing direct evidence of reconnection at the reversal surface. This observation of the reconnecting magnetic perturbation associated with reversal surface resonant tearing modes is notable in the study of tearing modes and magnetic reconnection in the RFP configuration. Historically, theoretical predictions for tearing mode activity in RFPs have made

a compelling, but none-the-less circumstantial, case that reconnection occurs at the reversal surface. This observation of the reconnecting magnetic perturbation for the reversal surface is the first direct experimental evidence of reconnection at the reversal surface obtained in the RFP configuration.

In Section 4.7, we examine, the radial structure of the poloidal current density perturbation, or current sheet, associated with reconnection at the reversal surface. The radial width of this current sheet is compared to the widths that are theoretically and computationally expected from models of reconnection which include a variety of different non-ideal physical effects in Ohm's law. It is determined that incorporation of resistivity and electron inertial effects in Ohm's law would, by themselves, produce current sheets much narrower than that observed. Incorporation of the electron pressure gradient effect in Ohm's law, however, might produce a current sheet of the observed width. Another non-ideal effect that may explain the observed width of the current sheet, which is comparable to the width of the island produced at the reversal surface by reconnection, is current transport by streaming of charge carriers along magnetic field lines. Such current transport would tend to distribute any current sheet produced by some reconnection mechanism with a radial width smaller than the island over the associated magnetic island. Other possible explanations for the radial width of the reversal surface resonant current perturbations are considered, as well.

Finally, in Section 4.8 summarize the major conclusions of this chapter.

4.2 - Pseudospectra of Poloidal Current Density and Magnetic Field Fluctuations in MST Edge

Using the pseudospectral analysis technique discussed in Sec. 3.11 of Ch. 3, we obtain estimates of toroidal mode number spectra for fluctuations in the poloidal current density and all three components of the magnetic field in the edge of MST. These pseudospectra, which include fluctuations in the range of frequencies $1 - 25$ kHz, are obtained for four cases: during or

between sawtooth crashes, at either of two toroidal and poloidal positions, -15° P, 330° T or 75° P, 120°. For each case, pseudospectra are obtained at several different minor radii. All of these pseudospectral measurements were made using toroidal magnetic field fluctuations at the wall of MST (measured with the toroidal array at 241° P) as the reference fluctuation. Additionally, for each of the four cases, we obtain measurements of the relative poloidal phase between the toroidal magnetic field fluctuations at 241 °P and each of the four fluctuating quantities: the poloidal current density and the three components of the magnetic field. An exhaustive set of figures showing this rather large collection of measurements is presented, for reference purposes, in Appendix A of this dissertation. However, certain key observations regarding the spatial structure of the poloidal current density and magnetic field fluctuations in the edge of MST are presented here. In particular, we note the toroidal modes that dominantly contribute to these fluctuations and we consider the implications of their poloidal phases (as measured at different poloidal positions) for their poloidal mode content. Ultimately, we conclude that the magnetic fluctuations in the region of measurement are dominated by helical modes with toroidal mode numbers $n = 5 - 10$ and poloidal mode number $m = 1$ that are resonant in the core and have broad, or global, radial structures. The poloidal current density fluctuations, on the other hand, are dominated by helical modes with toroidal mode numbers $n = -3 - -1$ and poloidal mode number $m = 0$ that are resonant at the reversal surface, which is within the region of measurement. We note that, as discussed in Sec. 2.6 of Ch. 2, the $m = 0$ component of the poloidal current density fluctuations may be identified as the current sheet associated with reconnection at the reversal surface. This observed current sheet is discussed in the context of the theory of magnetic reconnection in Sec. 4.7 of this chapter.

One observation is that both during and between sawtooth crashes, the fluctuations in all three components of the magnetic field are dominated throughout the edge of the plasma by toroidal modes with mode numbers approximately in the range $n = 5 - 10$, although at the shallowest depths, fluctuations in the toroidal component of the magnetic field have a strong

$n = -1$ component. This is illustrated by, for example, the pseudospectra of fluctuations in the toroidal (Fig. 1), poloidal (Fig. 2) and radial (Fig. 3) components of the magnetic field at 75° P, 120° T during sawtooth crashes. Each figure shows pseudospectra at several different minor radii.

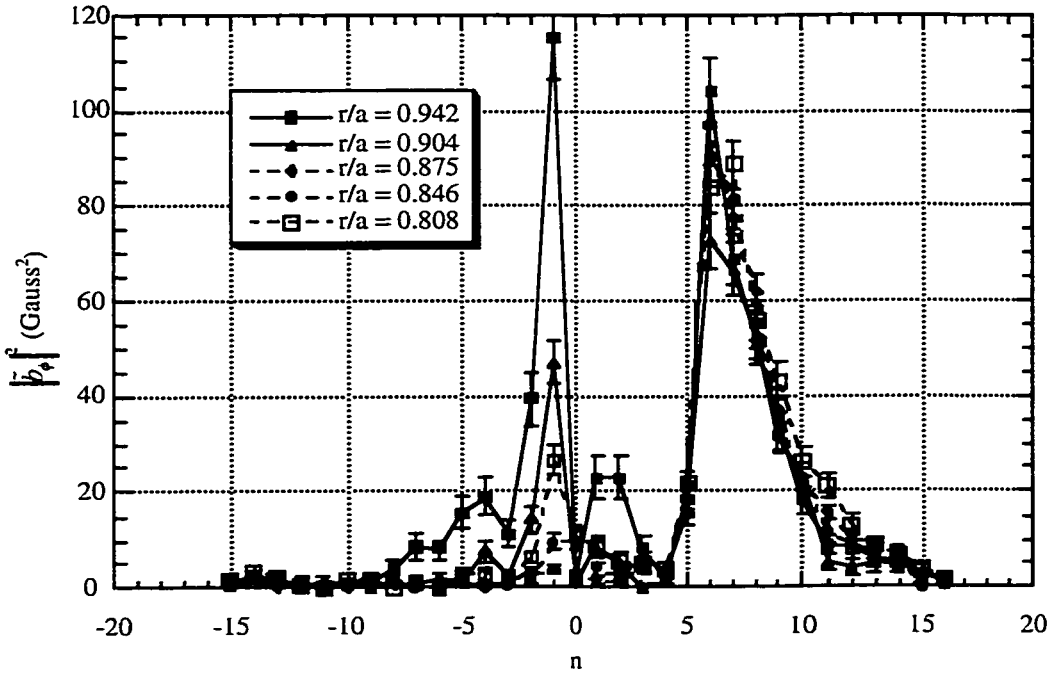

Figure 1: Toroidal pseudospectrum of toroidal magnetic field fluctuations during sawtooth crashes at 75° P, 120° T. Measured with reference to toroidal magnetic field fluctuations at the wall.

It is interesting that during crashes, while the toroidal spectrum of the toroidal magnetic field fluctuations, $\tilde{b}_\phi$, within the edge of the plasma is dominated by the $n = 5 - 10$ modes, it is instead dominated by the $n = -1$ mode at the wall (Fig. 4). Traditionally, tearing modes are expected to have large radial scale lengths (comparable to the minor radius of the plasma). It is apparent from the pseudospectra shown at several different minor radii in Figure 1 and the spectrum at the wall shown in Figure 4 that, during crashes, the $n = -1$ mode of the toroidal magnetic field has a short radial scale length, < 10 cm. In contrast, the poloidal magnetic field fluctuations, $\tilde{b}_\theta$, between and during sawtooth crashes and the toroidal magnetic field fluctuations between sawtooth crashes are dominated by the $n = 5 - 10$ modes within the edge

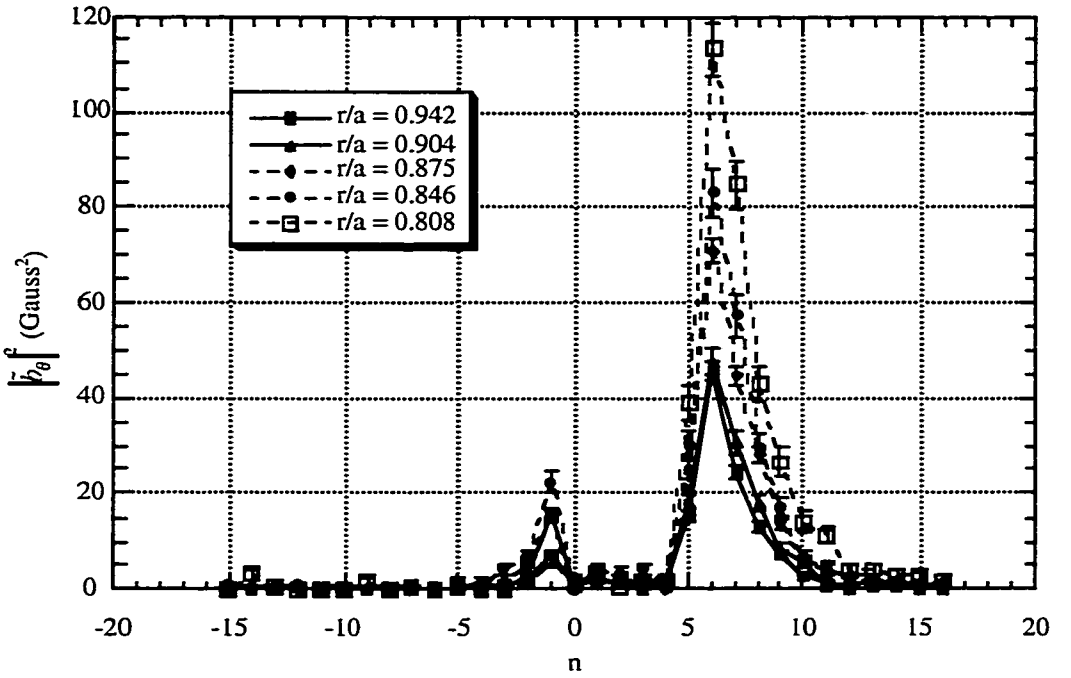

Figure 2: Toroidal pseudospectrum of poloidal magnetic field fluctuations during sawtooth crashes at 75° P, 120° T. Measured with reference to toroidal magnetic field fluctuations at the wall.

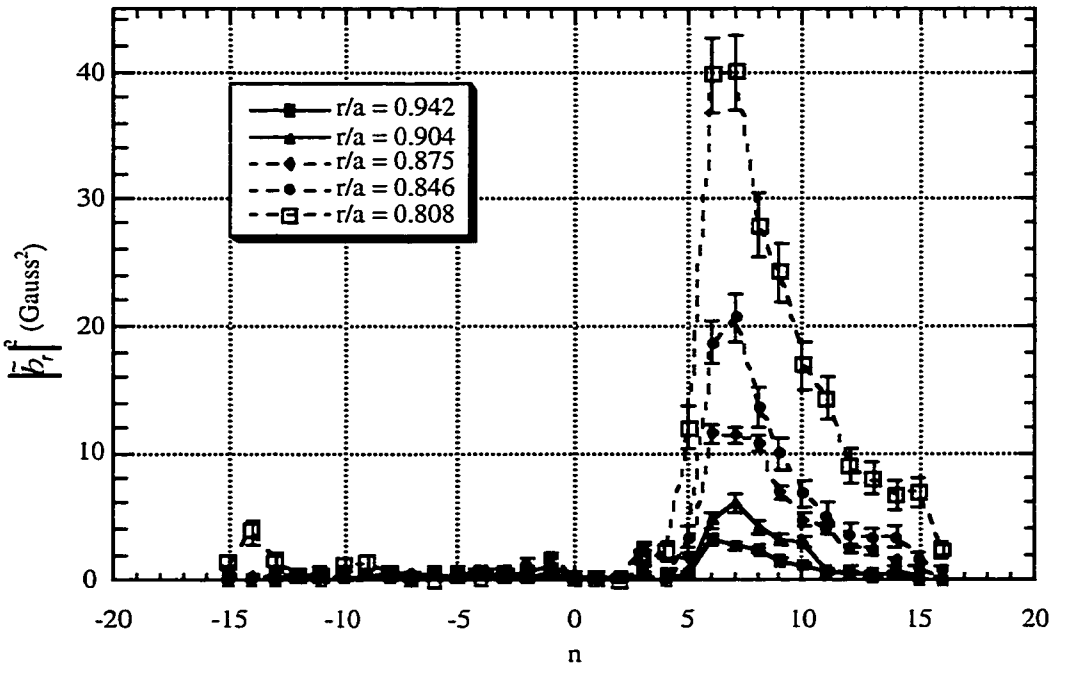

Figure 3: Toroidal pseudospectrum of radial magnetic field fluctuations during sawtooth crashes at 75° P, 120° T. Measured with reference to toroidal magnetic field fluctuations at the wall.

plasma and at the wall, as expected. The toroidal spectra of $\tilde{b}_\phi$ and $\tilde{b}_\theta$ between crashes at the wall are shown in Figure 5, while the toroidal spectra of the poloidal magnetic field fluctuations during crashes at the wall is shown in Figure 4.

Another observation permitted by the pseudospectral measurements reported here is that the toroidal spectrum of the poloidal current density fluctuations, $\tilde{j}_\theta$, is very different in the edge of MST from those of the magnetic fluctuations. For the most part, $\tilde{j}_\theta$ is dominated by toroidal modes with mode numbers approximately in the range $n = -3 - -1$. This is illustrated by, for example, the pseudospectra of $\tilde{j}_\theta$ at 75° P, 120° during sawtooth crashes shown in Figure 6. Figure 6 shows pseudospectra at several different minor radii. However, the $\tilde{j}_\theta$ pseudospectra measured at the deepest insertions (r/a = 0.808 for measurements at 75° P and r/a = 0.827 for measurements at -15° P) show significant fluctuation power in the $n = 5 - 10$ modes (Fig. 6). In particular, the pseudospectra measured at r/a = 0.827 and -15° P during crashes are dominated by the $n = 5 - 10$ modes (Fig. 7).

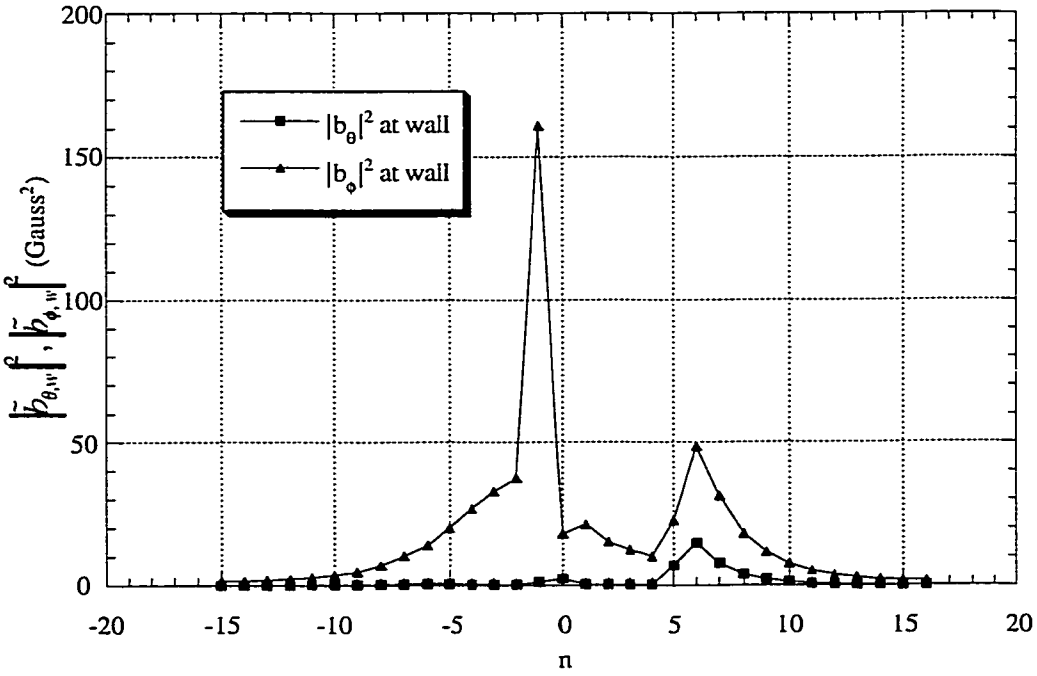

Figure 4: Toroidal spectra of toroidal and poloidal magnetic field fluctuations during sawtooth crashes. Measured with toroidal arrays at wall 241° P and renormalized to estimate spectra at wall at 75° P. Renormalization assumes fluctuation amplitudes vary inversely with major radius and adjusts for difference in major radius of wall at 75° P and 241° P.

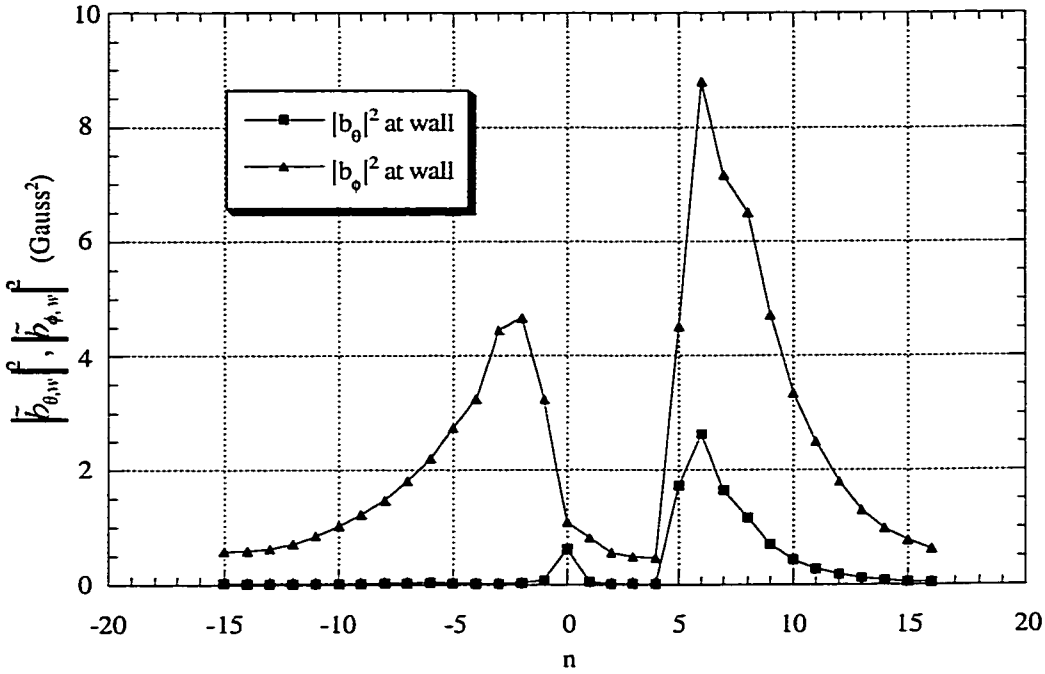

Figure 5: Toroidal spectra of toroidal and poloidal magnetic field fluctuations between sawtooth crashes. Measured with toroidal arrays at wall 241° P and renormalized to estimate spectra at wall at 75° P. Renormalization assumes fluctuation amplitudes vary inversely with major radius and adjusts for difference in major radius of wall at 75° P and 241° P.

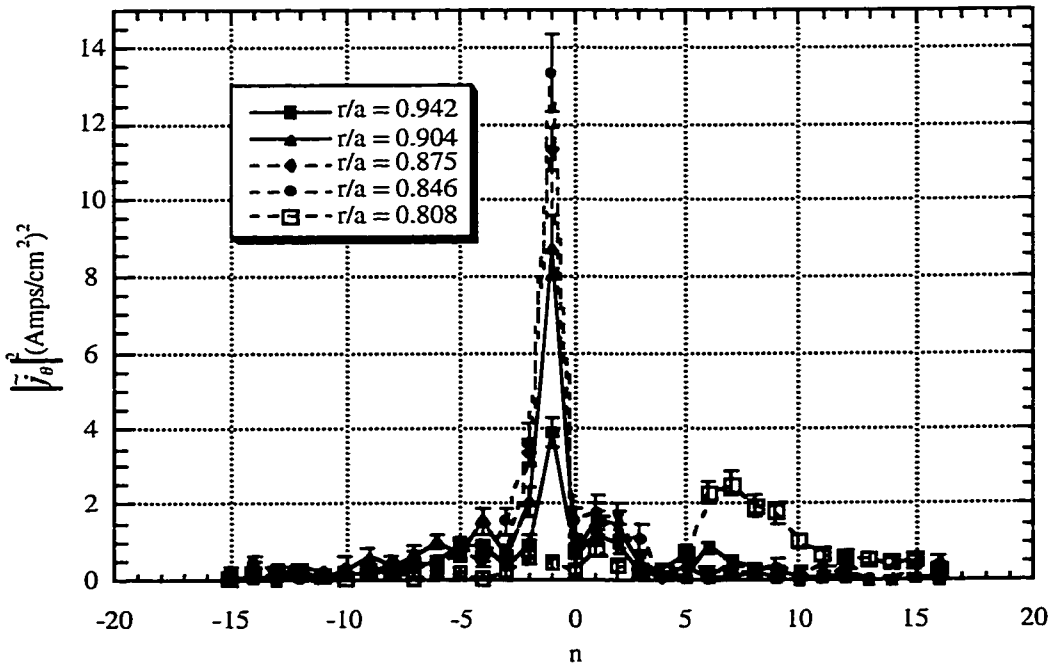

Figure 6: Toroidal pseudospectrum of poloidal current density fluctuations during sawtooth crashes at 75° P, 120° T. Measured with reference to toroidal magnetic field fluctuations at the wall.

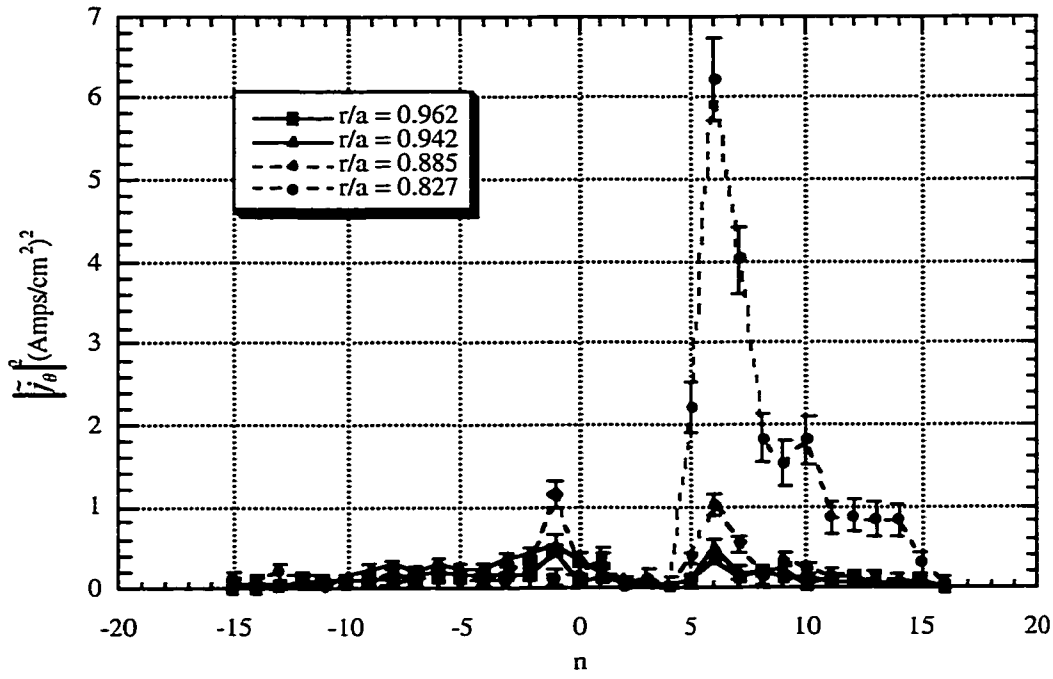

Figure 7: Toroidal pseudospectrum of poloidal current density fluctuations during sawtooth crashes at -15° P, 330° T. Measured with reference to toroidal magnetic field fluctuations at the wall.

The relative poloidal phases between $\tilde{j}_\theta$ and the toroidal magnetic field fluctuations at the wall at 241° P, $\tilde{b}_{\phi_w}$, for the dominant $n = -3 - -1$ toroidal modes are consistent, both between and during sawtooth crashes, with the expectation (discussed in Sec. 2.6 of Ch. 2) that these toroidal modes are dominantly $m = 0$ in character (*i.e.*, reversal surface resonant). Specifically, this relative poloidal phase, phase$\left(\tilde{j}_\theta, \tilde{b}_{\phi_w}\right)$, is roughly independent of the poloidal position at which $\tilde{j}_\theta$ is measured. This is illustrated by, for example, comparing phase$\left(\tilde{j}_\theta, \tilde{b}_{\phi_w}\right)$ for $\tilde{j}_\theta$ measured at -15° P during crashes (Fig. 8) with that for $\tilde{j}_\theta$ measured at 75° P during crashes (Fig. 9). Similarly, phase$\left(\tilde{b}_\phi, \tilde{b}_{\phi_w}\right)$ for the $n = -3 - -1$ toroidal modes, both between and during sawtooth crashes, is consistent with the expectation that these toroidal modes are dominantly $m = 0$ in character. Specifically, phase$\left(\tilde{b}_\phi, \tilde{b}_{\phi_w}\right)$ appears to have a radial structure that is similar for $\tilde{b}_\phi$ measured at -15° P and 75° P. This is illustrated by, for example, comparing phase$\left(\tilde{b}_\phi, \tilde{b}_{\phi_w}\right)$ for $\tilde{b}_\phi$ measured at -15° P during crashes (Fig. 10) with that for $\tilde{b}_\phi$ measured at 75° P during crashes (Fig. 11).

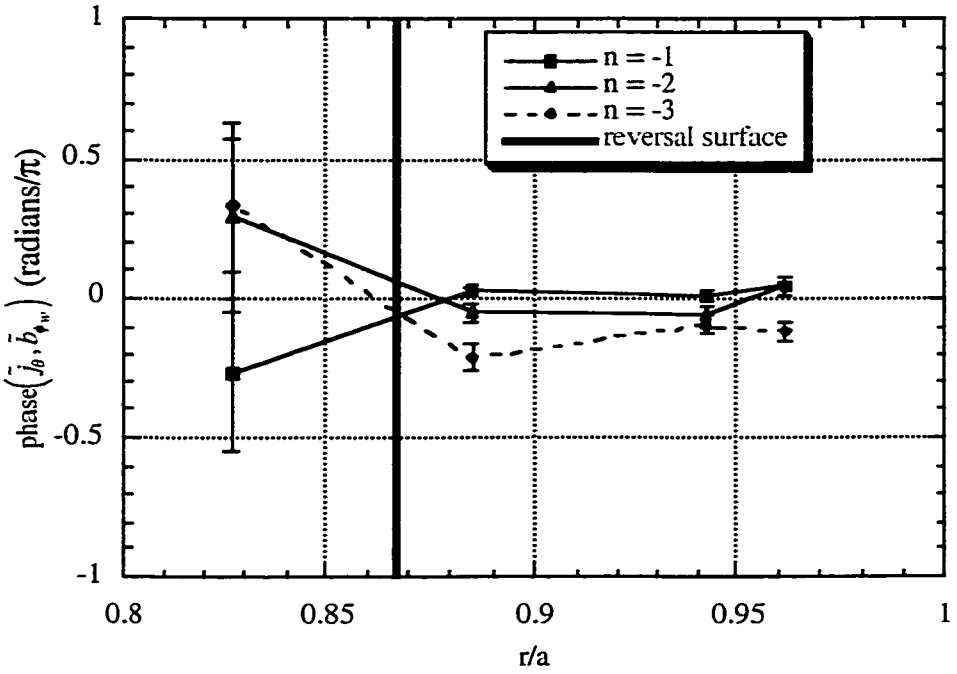

Figure 8: Relative phase between poloidal current density fluctuation at -15° P and toroidal magnetic field fluctuation at wall at 241° P for reversal surface resonant toroidal modes measured during sawtooth crashes.

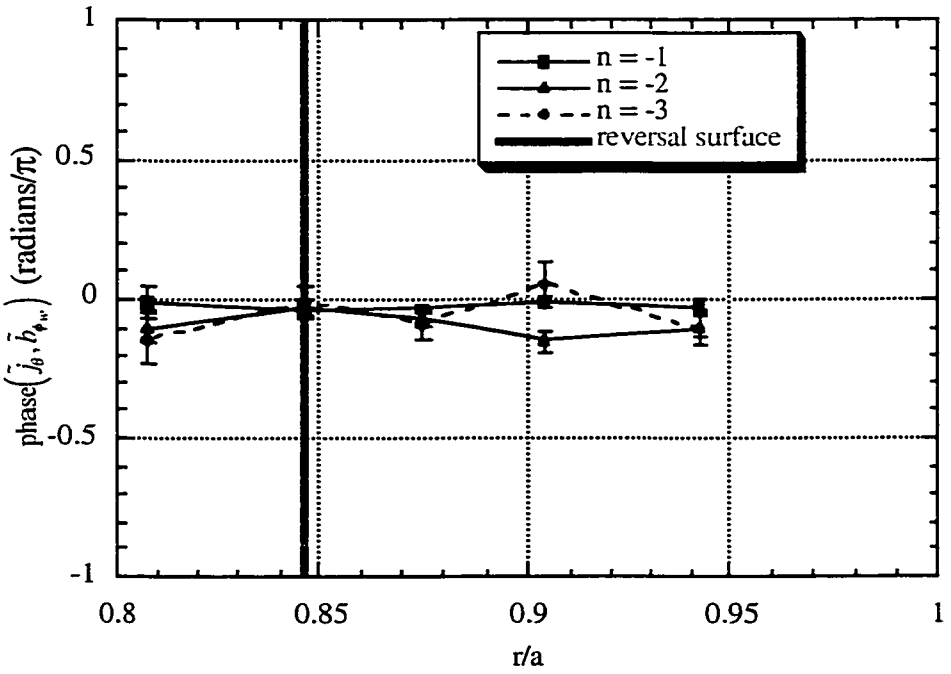

Figure 9: Relative phase between poloidal current density fluctuation at 75° P and toroidal magnetic field fluctuation at wall at 241° P for reversal surface resonant toroidal modes measured during sawtooth crashes.

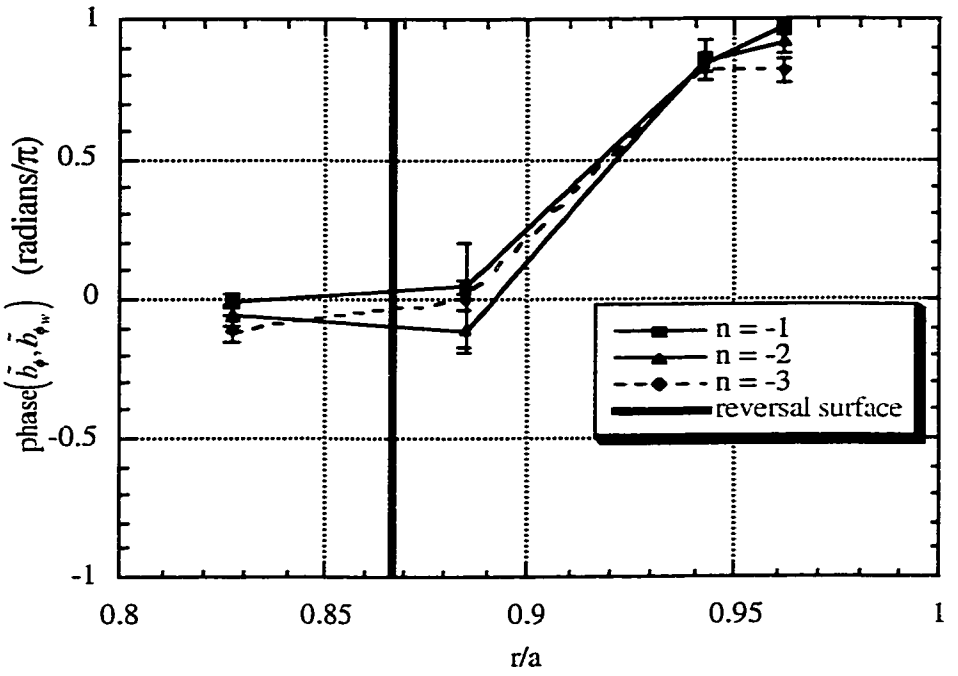

Figure 10: Relative phase between toroidal magnetic field fluctuation at -15° P and toroidal magnetic field fluctuation at wall at 241° P for reversal surface resonant toroidal modes measured during sawtooth crashes.

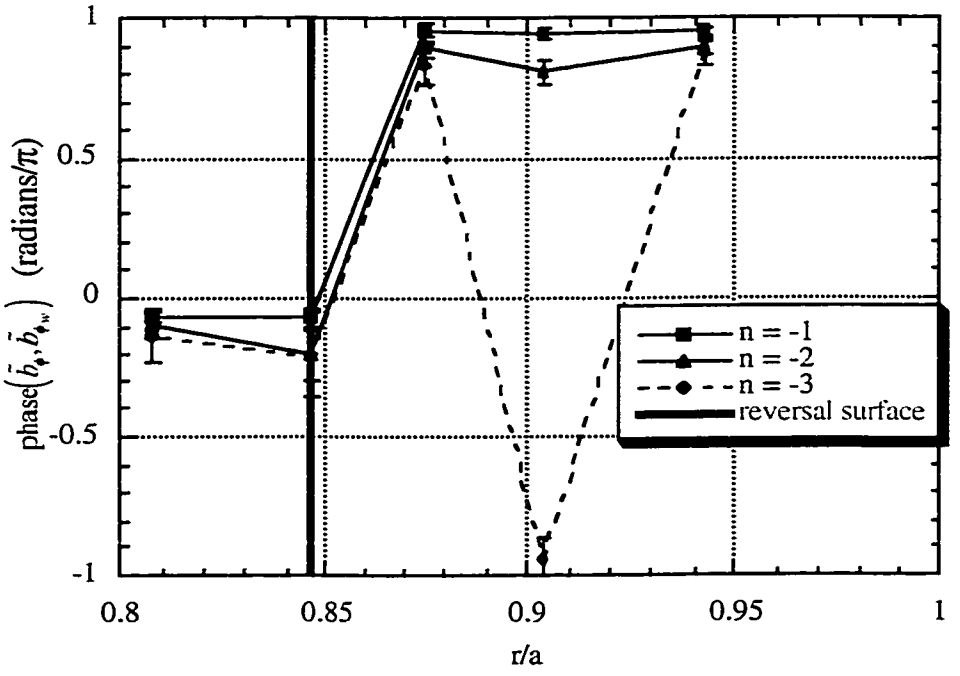

Figure 11: Relative phase between toroidal magnetic field fluctuation at 75° P and toroidal magnetic field fluctuation at wall at 241° P for reversal surface resonant toroidal modes measured during sawtooth crashes.

The apparent $m = 0$ character of the $n = -3 - -1$ toroidal modes of $\tilde{j}_\theta$ is expected from Ampere's law given the $m = 0$ character of those toroidal modes of $\tilde{b}_\phi$. The $n = -3 - -1$ toroidal modes $\tilde{b}_\phi$ exhibit radial scale lengths of < 10 cm (Fig. 1). For toroidal modes with such radial scales, which are much smaller than the relevant toroidal scales ($2\pi R/n \sim 3$ m – 10 m), $\tilde{b}_\phi$ is approximately proportional to the radial gradient of $\tilde{j}_\theta$. Specifically, under such conditions, $\partial \tilde{b}_{\phi n,m} / \partial r \approx \mu_0 \tilde{j}_{\theta n,m}$ [in an (r, ϕ, θ) coordinate system] where $\tilde{b}_{\phi n,m}$ and $\tilde{j}_{\theta n,m}$ are the helical Fourier components of the toroidal magnetic fluctuation and poloidal current density fluctuation, respectively, for poloidal and toroidal mode numbers m and n.

The relative poloidal phases between the toroidal magnetic field fluctuations at the wall at 241° P and each of the three components of the magnetic field for the $n = 5 - 10$ toroidal modes are consistent, both between and during sawtooth crashes, with the expectation (discussed in Sec. 2.6 of Ch. 2) that these toroidal modes are dominantly $m = 1$ in character (e. g. core resonant). For instance, phase$\left(\tilde{b}_\phi, \tilde{b}_{\phi_w}\right)$ for $\tilde{b}_\phi$ measured during crashes at -15° P (Fig. 12) and

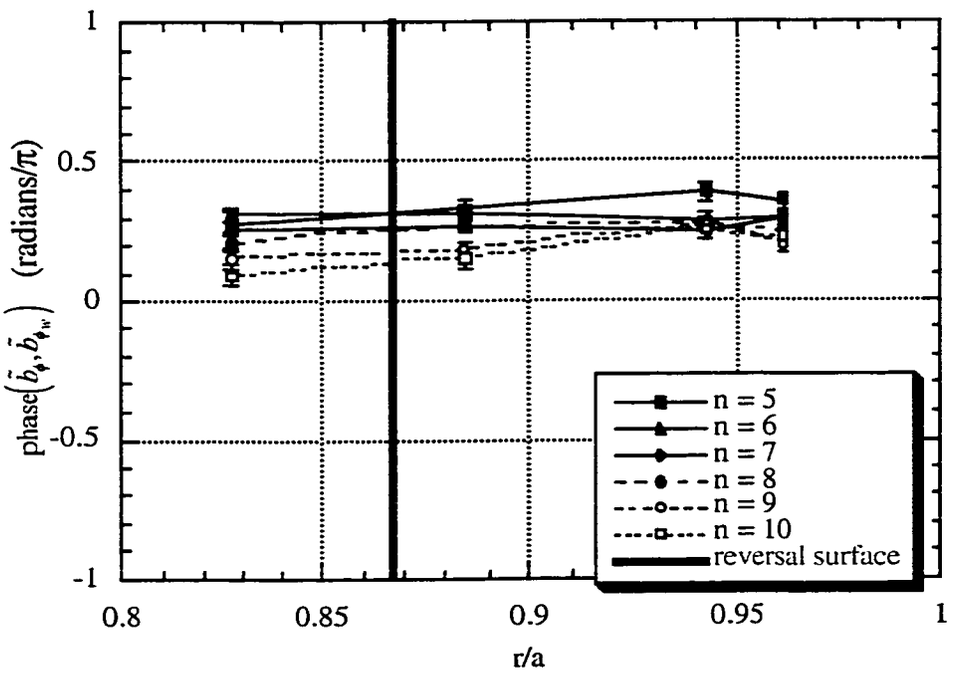

Figure 12: Relative phase between toroidal magnetic field fluctuation at -15° P and toroidal magnetic field fluctuation at wall at 241° P for core resonant toroidal modes measured during sawtooth crashes.

75° P (Fig. 13) differs by roughly $\pi/2$ radians for the $n = 5 - 10$ modes. This difference would be expected for $m = 1$ modes since the two poloidal positions, -15° P and 75° P, differ by 90°, or $\pi/2$ radians. The variation in phase$\left(\tilde{b}_\phi, \tilde{b}_{\phi_w}\right)$ for $\tilde{b}_\phi$ measured between crashes at -15° P and 75° P is similarly ~ $\pi/2$. Also, phase$\left(\tilde{b}_\theta, \tilde{b}_{\phi_w}\right)$ and phase$\left(\tilde{b}_r, \tilde{b}_{\phi_w}\right)$ for the $n = 5 - 10$ modes differ by roughly $\pi/2$ radians each for $\tilde{b}_\theta$ and $\tilde{b}_r$ measured at -15° P and 75° P both between and during sawtooth crashes. It interesting that, while these differences in relative poloidal phase between measurements at -15° P and 75° P are approximately $\pi/2$, they are not, to within statistical uncertainty, exactly $\pi/2$. In fact, the difference in relative poloidal phase can sometimes be as low as ~ 0.3π. This indicates that the $n = 5 - 10$ toroidal modes for the three components of the magnetic field are partly $m = 0$ in character.

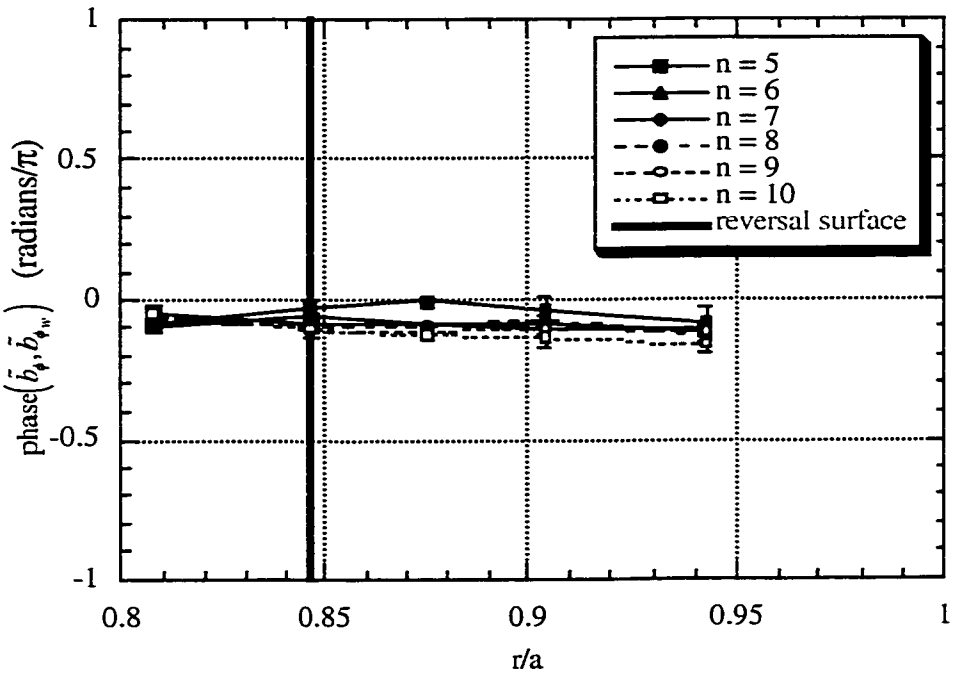

Figure 13: Relative phase between toroidal magnetic field fluctuation at 75° P and toroidal magnetic field fluctuation at wall at 241° P for core resonant toroidal modes measured during sawtooth crashes.

4.3 - Two-Point Toroidal Spectra of Poloidal Current Density and Magnetic Field Fluctuations in MST Edge

Using the two-point spectral analysis technique discussed in Sec. 3.12 of Ch. 3, we obtain estimates of toroidal mode number spectra for fluctuations in the poloidal current density and poloidal and toroidal components of the magnetic field in the edge of MST. These spectra, which include fluctuations in the range of frequencies $1 - 25$ kHz, are measured with probes at -15° P , 320° T and -15° P, 330° T, both between and during crash phase of the sawtooth cycle. A set of figures showing this collection of measurements, organized for ease of reference, is presented in Appendix A of this dissertation. Here, we present a discussion of how these measurements agree with and differ from their pseudospectral counterparts. We note, in particular, two important areas of agreement. First, two-point spectra and pseudospectra agree as to which toroidal modes dominantly contribute to $\tilde{b}_\phi$ and $\tilde{b}_\theta$. Second, in some cases, they roughly agree as to which toroidal modes dominantly contribute to $\tilde{j}_\theta$. In cases where the two-point spectra and their counterpart pseudospectra differ, we discuss the relative validity of the

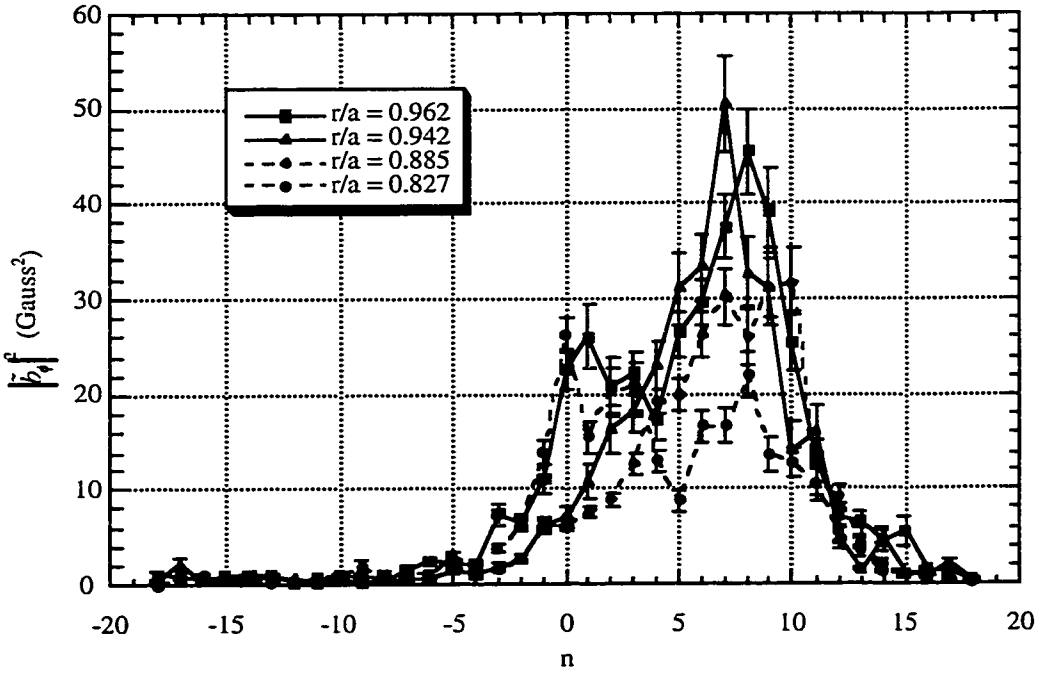

Figure 14: Two-point toroidal spectrum of toroidal magnetic field fluctuations measured during sawtooth crashes with probes at -15° P, 320° T and -15° P, 330° T.

two types of spectral estimates. In particular, we conclude that, while pseudospectra less accurately reflect the total fluctuation power of the spectra they estimate, they more accurately reproduce its shape.

The toroidal two-point spectra of $\tilde{b}_\theta$ and $\tilde{b}_\phi$ reported here qualitatively, and to some extent quantitatively, reproduce many of the features observed in the analogous pseudospectra discussed in Section 4.2. Between and during sawtooth crashes, $\tilde{b}_\theta$ and $\tilde{b}_\phi$ are dominated by toroidal modes with mode numbers in the range $n = 5 - 10$. For example, Figure 14 shows the two-point spectra of $\tilde{b}_\phi$ during sawtooth crashes at several minor radii. This may be compared to Figure 15, which shows the simultaneously measured, analogous pseudospectra. In contrast with the magnetic fluctuations, the two-point spectra of $\tilde{j}_\theta$ are very different from the analogous pseudospectra. For instance, compare the two-point spectra of $\tilde{j}_\theta$ during sawtooth crashes (Fig. 16) with the simultaneously measured, analogous pseudospectra (Fig. 7). In spite of these differences, there are some similarities between the two-point spectra and pseudospectra of $\tilde{j}_\theta$, particularly at the shallower measurement depths, $r/a \geq 0.885$. Both types of spectra, between

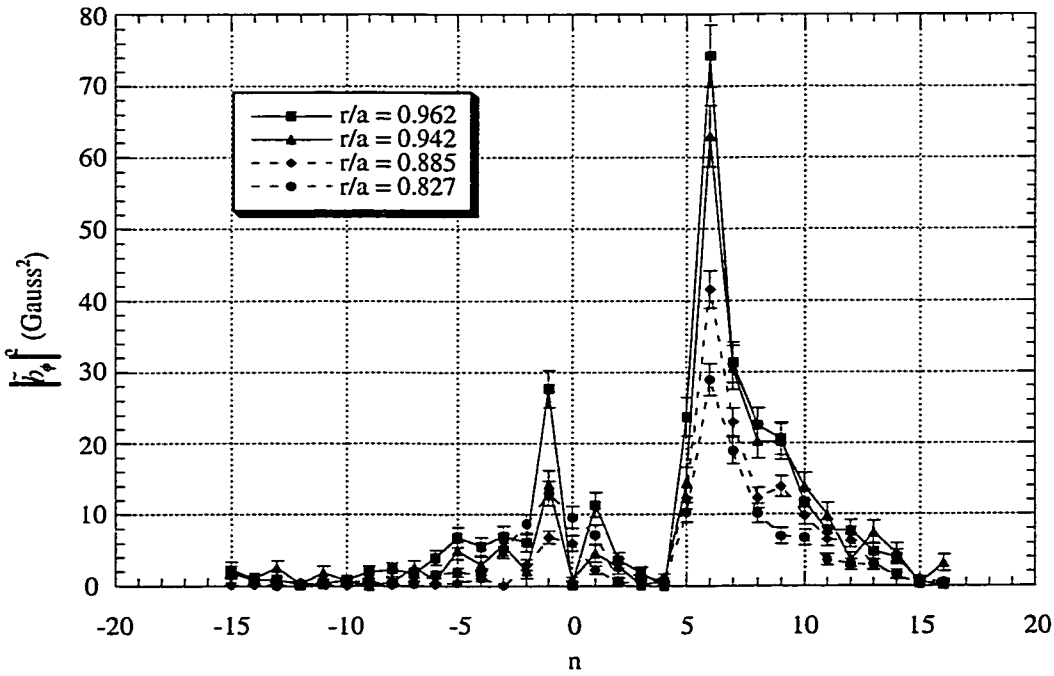

Figure 15: Toroidal pseudospectrum of toroidal magnetic field fluctuations during sawtooth crashes at -15° P, 330° T. Measured with reference to toroidal magnetic field fluctuations at the wall.

and during sawtooth crashes, show a peak in fluctuation power at approximately $n = -1$ at $r/a \geq 0.885$. Also, the two-point spectra at $r/a = 0.827$ show greater fluctuation power at positive mode numbers than at negative mode numbers, while the pseudospectra at the same minor radius show a peak in the $n = 5 - 10$ range of mode numbers.

In addition to these similarities, there are a number of significant differences between the two-point spectra of the magnetic and poloidal current density fluctuations and their pseudospectral counterparts. In many cases, the two-point spectra show significantly more total fluctuation power than do the analogous pseudospectra. Also, in many cases, the two-point spectra have distinctly different shapes from the analogous pseudospectra. These differences may result from a combination of factors. As discussed in Sec. 3.10 of Ch. 3, the pseudospectral technique has an inherent bias that causes it to underestimate, to some degree, the fluctuation power in any given mode. On the other hand, as discussed in Section 3.12 of Ch. 3, the two-point spectral technique will properly measure the total fluctuation power (summed over all modes), but may improperly decompose that fluctuation power into contributions from different

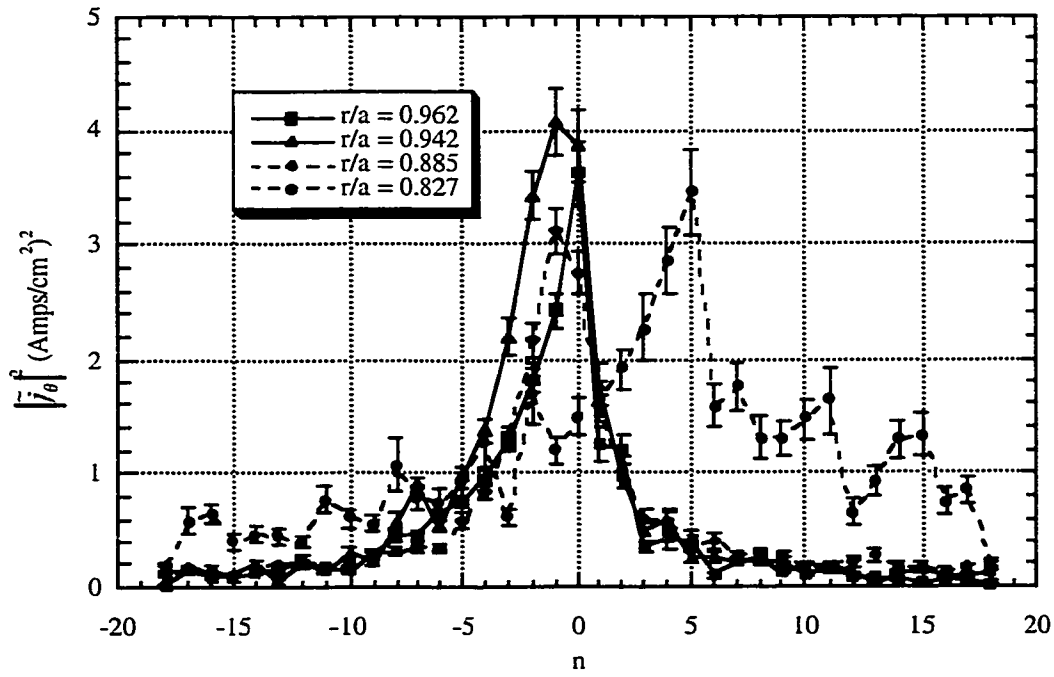

Figure 16: Two-point toroidal spectrum of poloidal current density fluctuations measured during sawtooth crashes with probes at -15° P, 320° T and -15° P, 330° T.

modes. In particular, when it is used to estimate spectra that contain fluctuation power in multiple distinct bands, it may produce an estimated spectrum in which the distinct bands are smeared together, possibly appearing only as a single broader band.

Comparison of the two-point spectra and pseudospectra of $\tilde{b}_\phi$ and $\tilde{j}_\theta$, both during and between sawtooth crashes, shows indications of both effects. See, for example, the two-point spectra and the simultaneously measured pseudospectra of $\tilde{b}_\phi$ during sawtooth crashes shown in Figures 14 and 15, respectively. Also, see the two-point spectra and the simultaneously measured pseudospectra of $\tilde{j}_\theta$ during sawtooth crashes shown in Figures 16 and 7, respectively. In all cases, the two-point spectra of $\tilde{b}_\phi$ and $\tilde{j}_\theta$ show significantly more total fluctuation power than is shown by the analogous pseudospectra. Furthermore, these two-point spectra show fluctuation power distributed (*i.e.*, smeared) over a broader range of toroidal mode numbers than do the analogous pseudospectra. Such smearing is to be expected if, as indicated by the pseudospectral measurements, $\tilde{b}_\phi$ and $\tilde{j}_\theta$ have significant fluctuation power in two distinct bands, $n = 5 - 10$ and $n = -1 - -3$.

There is also another indicator, more subtle yet perhaps more distinctive, that many of the two-point spectra reported are affected by smearing. In some cases, the pseudospectra of $\tilde{b}_\theta$ or $\tilde{b}_\phi$, either between or during sawtooth crashes, show distinct, relatively low amplitude peaks in the $n = -1 - -3$ range of mode numbers that are not apparent in the analogous two-point spectra. In such cases, while the two-point spectra show power in the $n = -1 - -3$ range of mode numbers, it appears as part of the tail of a peak that appears in the $n = 5 - 10$ range of mode numbers. Compare, for example, the pseudospectra of $\tilde{b}_\theta$ during sawtooth crashes (Fig. 17) with the analogous two-point spectra (Fig. 18).

Given the significant differences in the two-point spectra and pseudospectra reported in this chapter, some consideration must be given as to what may be learned of the actual spectra which they both purport to estimate. While it is very likely that the pseudospectra reported here, unlike the two-point spectra, underestimate the total fluctuation power of the actual spectra, it is

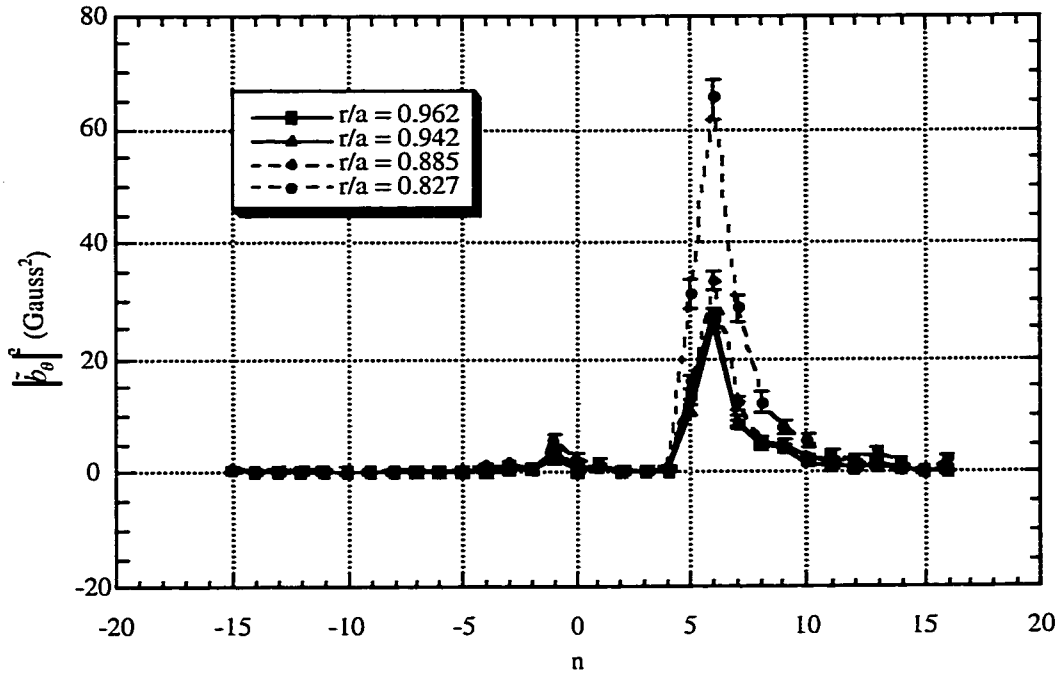

Figure 17: Toroidal pseudospectrum of poloidal magnetic field fluctuations during sawtooth crashes at -15° P, 330° T. Measured with reference to toroidal magnetic field fluctuations at the wall.

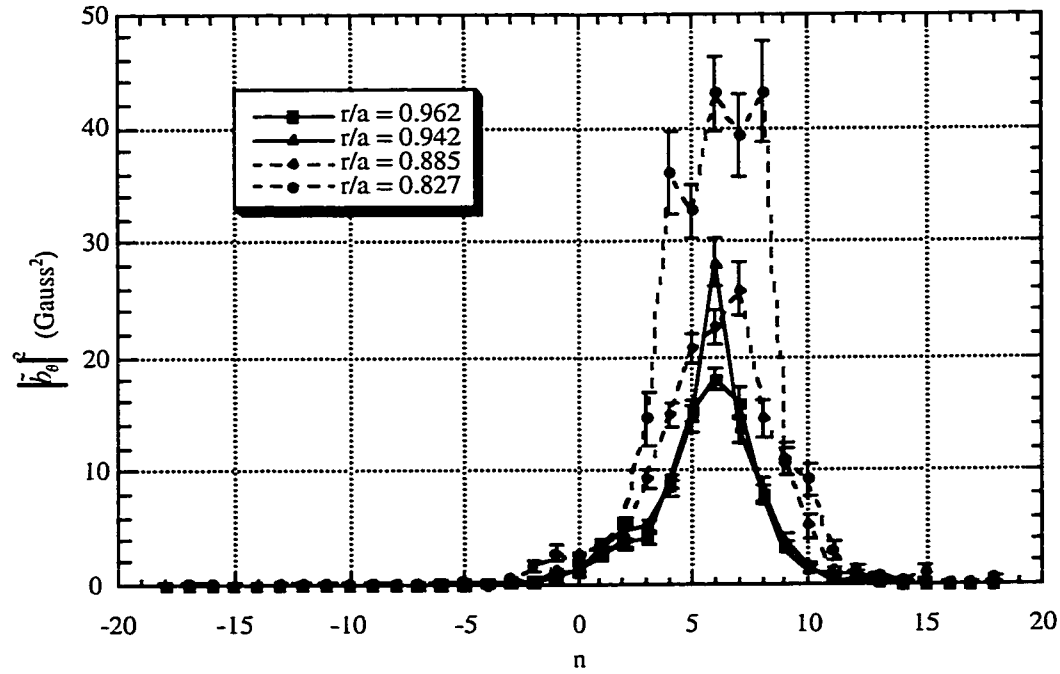

Figure 18: Two-point toroidal spectrum of poloidal magnetic field fluctuations measured during sawtooth crashes with probes at -15° P, 320° T and -15° P, 330° T.

also very likely these pseudospectra more accurately reflect the shape of the actual spectra. Measurements of the actual toroidal spectra of $\tilde{b}_\theta$ and $\tilde{b}_\phi$ at the wall show that they are dominated by toroidal modes in two distinct bands of mode numbers, $n \approx -3 - -1$ and $n \approx 5 - 10$. Even discounting the pseudospectral measurements reported in Sec. 4.2 above, this, by itself, would mandate a certain degree of caution in interpreting the two-point toroidal spectra measured in reported here. However, this double-banded spectral structure is consistent with the toroidal pseudospectra of $\tilde{b}_\theta$ and $\tilde{b}_\phi$ measured in the edge. In contrast, the two-point spectra do not show mode numbers in the range $n \approx -3 - -1$ as a distinct band. Furthermore, the pseudospectra for $\tilde{j}_\theta$, unlike the analogous two-point spectra, suggest that, in most cases, $\tilde{j}_\theta$ is dominantly composed of toroidal modes with mode numbers in the same two distinct bands. This is the structure for the toroidal spectra of $\tilde{j}_\theta$ that would be expect from Ampere's law given the structure of the toroidal spectra of $\tilde{b}_\phi$, yet the two-point spectra don't show such distinct bands.

4.4 - Two-Point Poloidal Spectra of Poloidal Current Density and Magnetic Field Fluctuations in MST Edge

Using the two-point spectral analysis technique discussed in Sec. 3.12 of Ch. 3, we obtain estimates of poloidal mode number spectra for fluctuations in the poloidal current density and poloidal and toroidal components of the magnetic field in the edge of MST. These spectra, which include fluctuations in the range of frequencies $1 - 25$ kHz, are measured at the reversal surface with probes at 75° P, 120° T and 105° P, 120° T, both between and during the crash phase of the sawtooth cycle. A set of figures showing this collection of measurements, organized for ease of reference, is presented in Appendix A of this dissertation. Here, we briefly discuss the principal implications of the measurements.

The two-point poloidal spectra reported here indicate that $\tilde{b}_\theta$ and $\tilde{b}_\phi$ are dominated by the $m = 1$ poloidal mode at the reversal surface. This is illustrated by, for example, the poloidal two-

point spectra of $\tilde{b}_\theta$ (Fig. 19) and $\tilde{b}_\phi$ (Fig. 20) during sawtooth crashes. On the other hand, $\tilde{j}_\theta$ is dominated by the $m = 0$ poloidal mode there. This is illustrated by, for example, the poloidal two-point spectra of $\tilde{j}_\theta$ during sawtooth crashes (Fig. 21). Unlike the toroidal two-point spectra, these poloidal two-point spectral have no counterpart in the form of poloidal pseudospectra to which they may be directly compared. However, they are qualitatively consistent with the measurements of phase$\left(\tilde{b}_\phi, \tilde{b}_{\phi_w}\right)$, phase$\left(\tilde{b}_\theta, \tilde{b}_{\phi_w}\right)$ and phase$\left(\tilde{j}_\theta, \tilde{b}_{\phi_w}\right)$ discussed in Section 4.2. In particular, they independently verify the conclusions that, both between and during sawtooth crashes, the dominant magnetic fluctuations in the region of measurement (the $n = 5 - 10$ toroidal modes) are $m = 1$ in character, while the dominant poloidal current density fluctuations in this region (the $n = -3 - -1$ toroidal modes) are $m = 0$ in character.

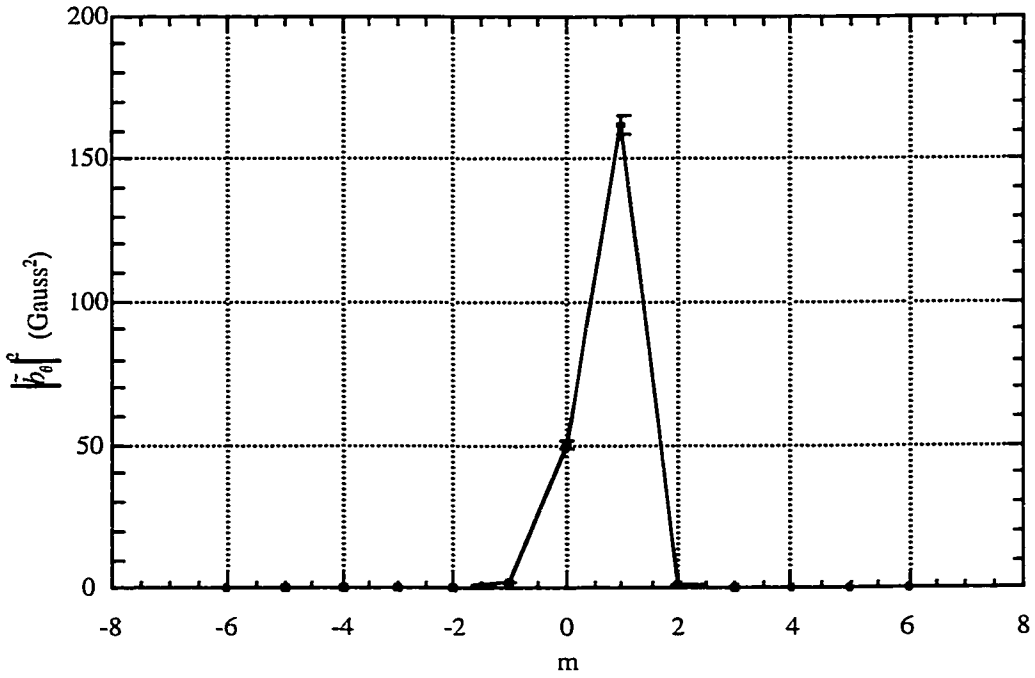

Figure 19: Two-point poloidal spectrum of poloidal magnetic field fluctuations measured during sawtooth crashes at reversal surface. Probes are at 75° P, 120° T and 105° P, 120° T.

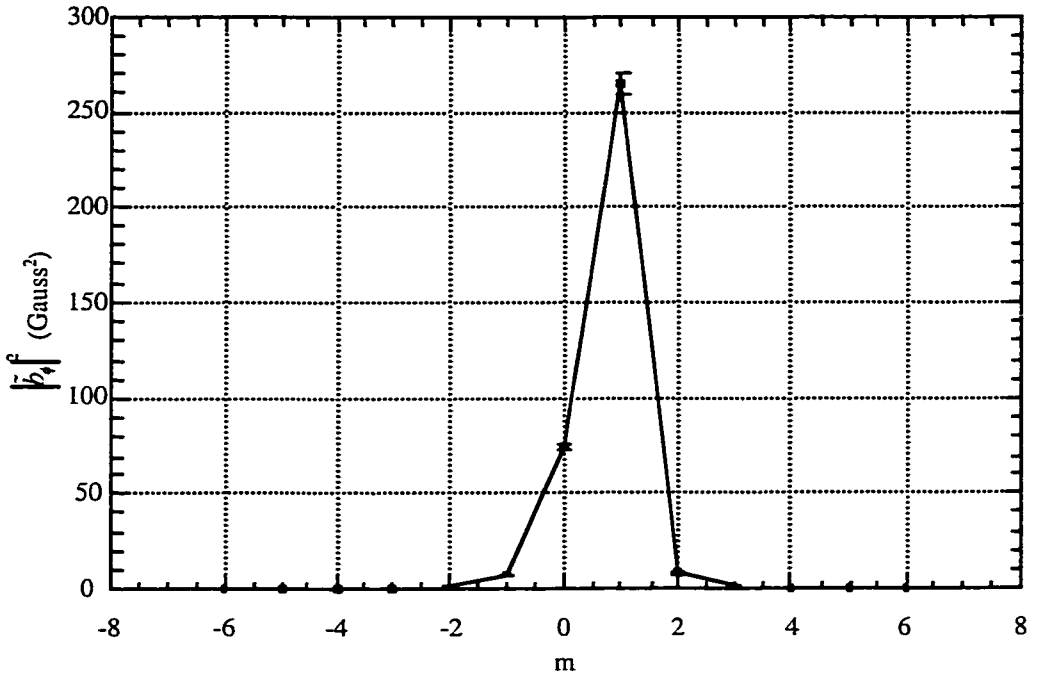

Figure 20: Two-point poloidal spectrum of toroidal magnetic field fluctuations measured during sawtooth crashes at reversal surface. Probes are at 75° P, 120° T and 105° P, 120° T.

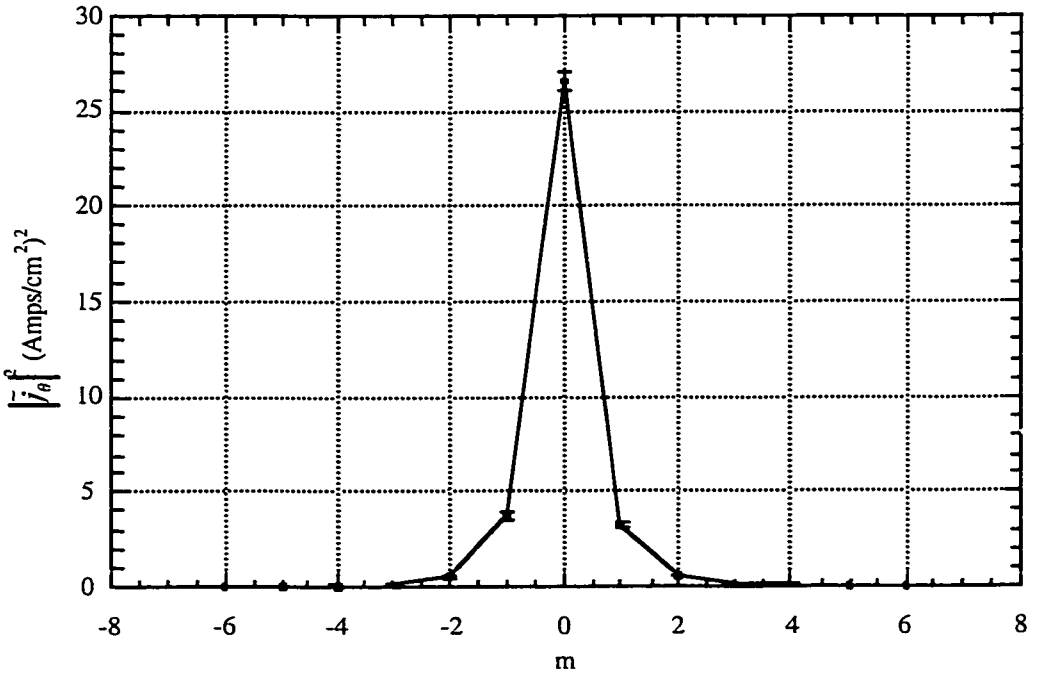

Figure 21: Two-point poloidal spectrum of poloidal current density fluctuations measured during sawtooth crashes at reversal surface. Probes are at 75° P, 120° T and 105° P, 120° T.

4.5 - Comparison of Tearing Mode Structure in MST Edge with Observations in DEBS

The pseudospectral measurements reported in Section 4.2 provide radial profiles of the magnetic and poloidal current density fluctuations in the edge of MST ($r/a > 0.8$), that are believed to the result of tearing mode activity. These measurements may be directly compared to theoretical predictions for the structure of resistive tearing modes in RFPs as obtained from the DEBS code. DEB is a cylindrical geometry, initial value code which performs resistive MHD simulations of various types of plasma configurations, including, in particular, the RFP. (See, for instance, discussion by Schnack, et al..[1])

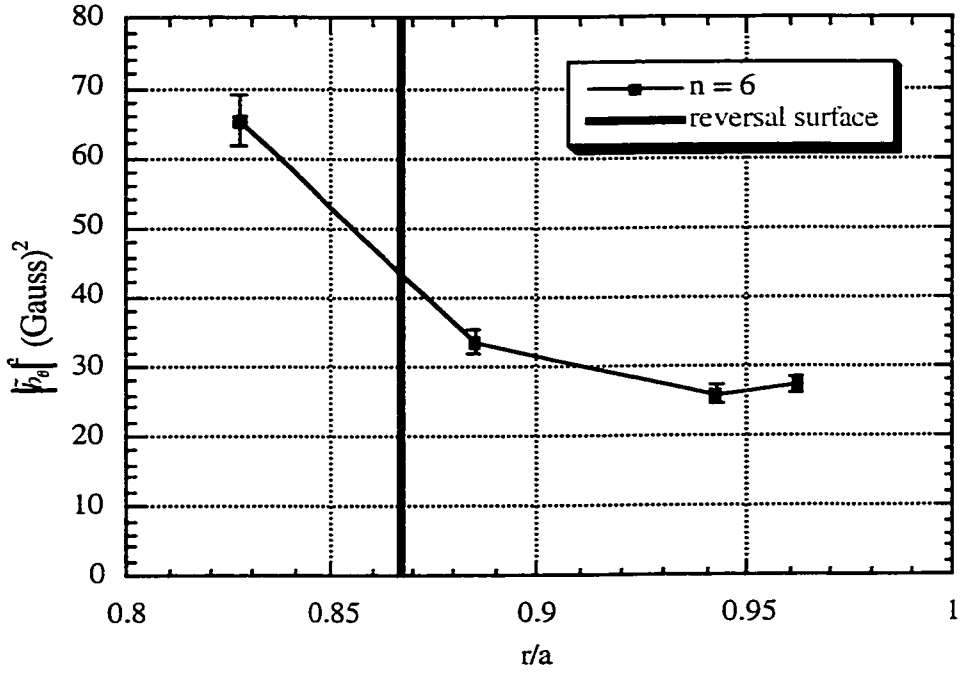

Figure 22: Radial profile of squared toroidal pseudospectral amplitude of poloidal magnetic field fluctuations for the core resonant, n = 6 toroidal mode during sawtooth crashes at -15° P, 330° T. Measured with reference to toroidal magnetic field fluctuations at the wall.

The DEBS code can simulate self-consistently evolved magnetic field equilibria that have several characteristics which render them suitable for comparison in some ways to MST plasmas. (Similarities and differences to MST plasmas will be discussed in more detail later in this

section.) Such simulated plasmas show intermittent bursts of fluctuation activity that are similar in some respects to the sawtooth crashes in MST. The radial structures of the magnetic and poloidal current density fluctuations for the $n = 6$ and $n = -1$ toroidal modes in the edge MST during sawtooth crashes at -15° P and 75° P can be compared with the radial structures of the same quantities for the $n = 6$, $m = 1$ and $n = -1$, $m = 0$ helical modes during a burst of fluctuation activity in a DEBS plasma (DEBS simulation data, courtesy of John Wright). A set of figures showing this complete collection of MST and DEBS profiles, organized for ease of reference, is presented in Appendix A of this dissertation. Here we compare the MST profiles and the DEBS profiles. In particular, we note some qualitative similarities. We also discuss some of the issues in interpreting this comparison.

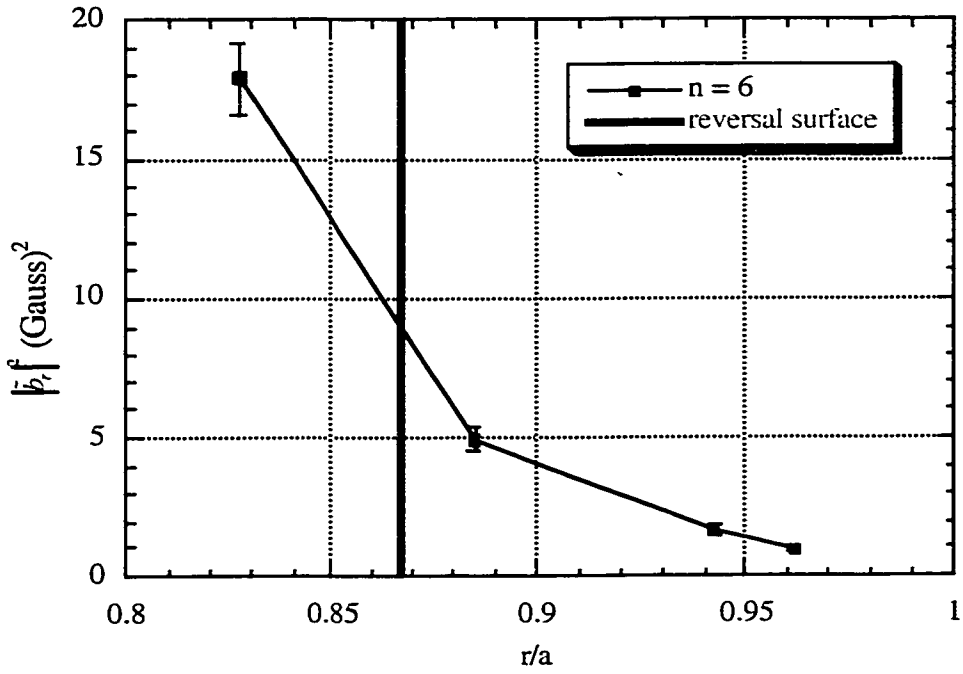

Figure 23: Radial profile of squared toroidal pseudospectral amplitude of radial magnetic field fluctuations for the core resonant, n = 6 toroidal mode during sawtooth crashes at -15° P, 330° T. Measured with reference to toroidal magnetic field fluctuations at the wall.

Pseudospectral analysis of magnetic and poloidal current density fluctuations in the edge of MST, during the crash phase of the sawtooth cycle, shows that for the $n = 6$ toroidal mode the radial and poloidal magnetic field fluctuations, $\tilde{b}_r$ and $\tilde{b}_\theta$, as well the poloidal current density fluctuations, $\tilde{j}_\theta$, increase in amplitude with decreasing minor radius. This is illustrated by, for example, the radial profiles of $\tilde{b}_\theta$ (Fig. 22), $\tilde{b}_r$ (Fig. 23) and $\tilde{j}_\theta$ (Fig. 24) at -15° P. The structure of $\tilde{b}_\phi$ for this toroidal mode is more complicated. At -15° P (Fig. 25), its amplitude decreases with decreasing minor radius, while at 75° P (Fig. 26), its amplitude appears to be relatively independent of minor radius. This difference might possibly be due to a significant contribution to the $n = 6$ toroidal magnetic field fluctuation from poloidal modes that are not core resonant (*i.e.*, not $m = 1$). This possibility is discussed in more detail in Section 4.2 above.

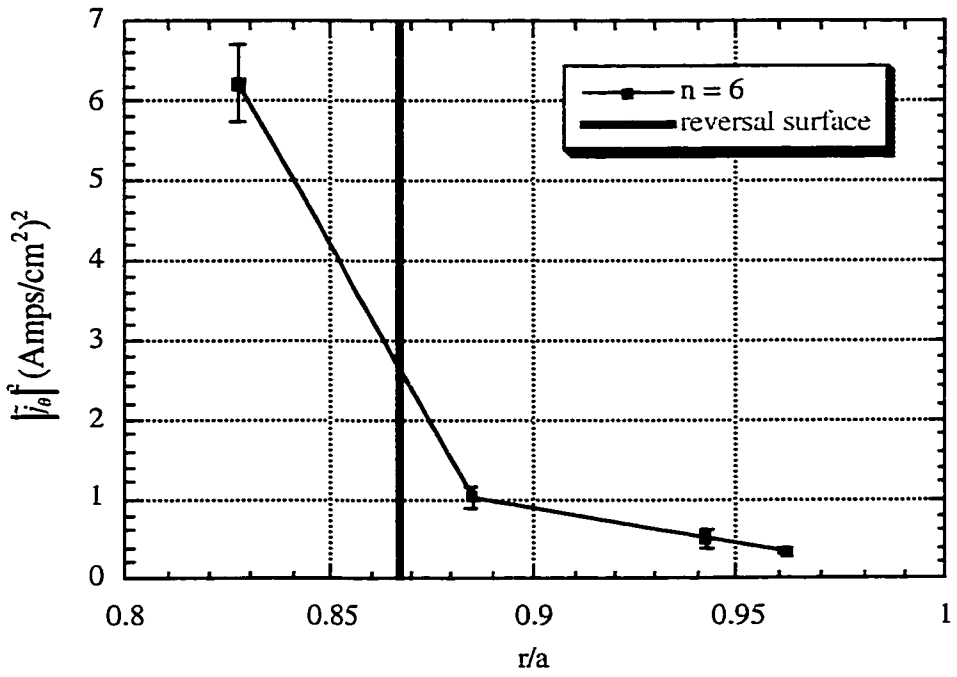

Figure 24: Radial profile of squared toroidal pseudospectral amplitude of poloidal current density fluctuations for the core resonant, n = 6 toroidal mode during sawtooth crashes at -15° P, 330° T. Measured with reference to toroidal magnetic field fluctuations at the wall.

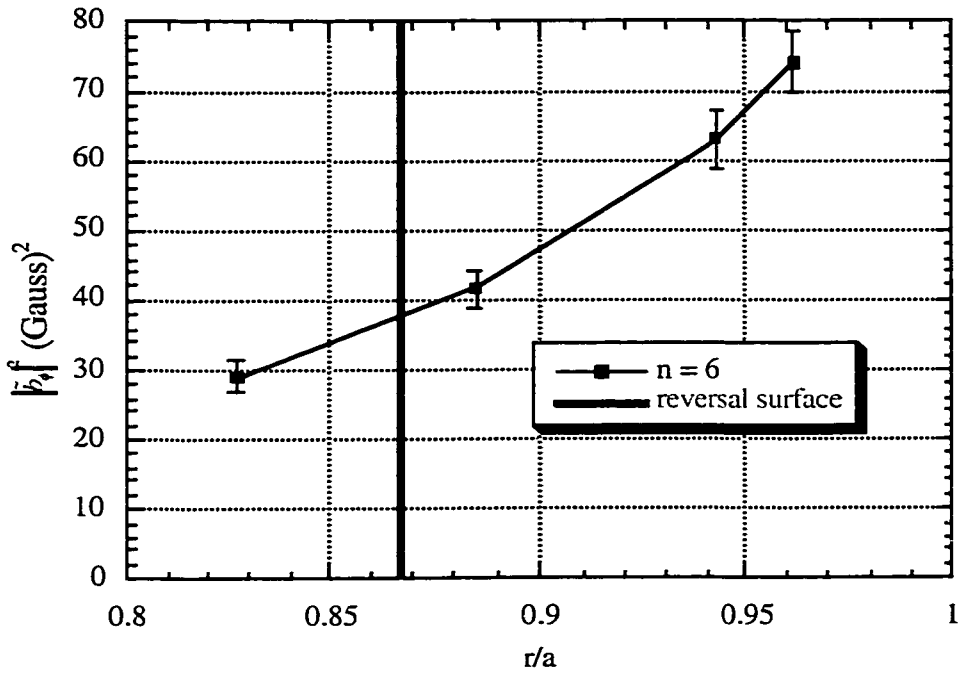

Figure 25: Radial profile of squared toroidal pseudospectral amplitude of toroidal magnetic field fluctuations for the core resonant, n = 6 toroidal mode during sawtooth crashes at -15° P, 330° T. Measured with reference to toroidal magnetic field fluctuations at the wall.

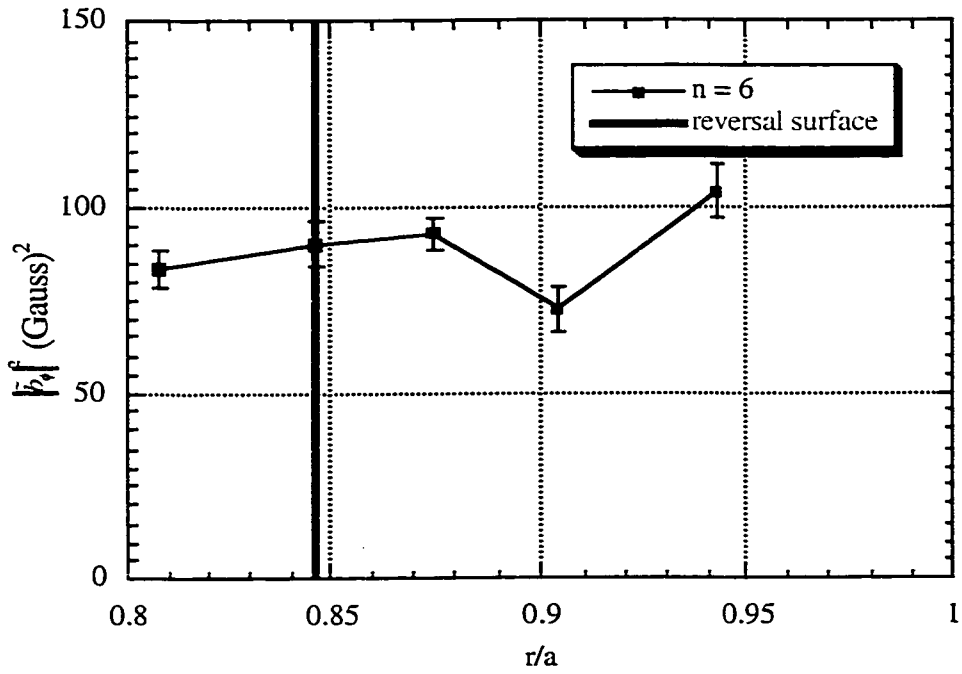

Figure 26: Radial profile of squared toroidal pseudospectral amplitude of toroidal magnetic field fluctuations for the core resonant, n = 6 toroidal mode during sawtooth crashes at 75° P, 120° T. Measured with reference to toroidal magnetic field fluctuations at the wall.

During a burst of fluctuation activity, a DEBS plasma shows radial structures in its edge region for the $m = 1, n = 6$ $\tilde{b}_\theta$ (Fig. 27) and $\tilde{b}_r$ (Fig. 28) that are qualitatively similar to those in MST during crashes (Figs. 22 and 23, respectively). The $m = 1, n = 6$ $\tilde{j}_\theta$ (Fig. 29) and $\tilde{b}_\phi$ (Fig. 30) in the DEBS plasma show a great deal of radial structure in the edge at scales of $(\Delta r)/a \sim 0.1$, which makes detailed comparison with the amplitudes of the $n = 6$ toroidal magnetic field and poloidal current density fluctuations difficult. The measurements of these quantities in MST are averaged over a radial extent of $(\Delta r)/a \sim 0.04$ (by virtue of the probe structure). However, in spite of this difficultly, some qualitative agreement between the DEBS data and the MST data may be seen. Both the edge $m = 1, n = 6$ toroidal magnetic field and poloidal current density fluctuation amplitudes decreases with decreasing minor radius.

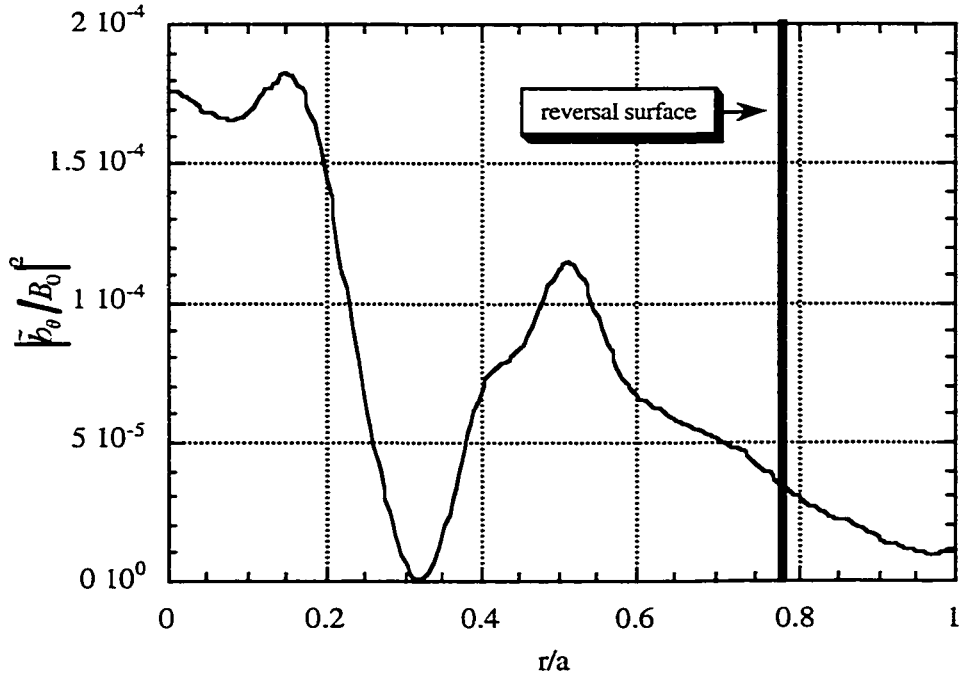

Figure 27: DEBS simulation data obtained during fluctuation burst. Radial profile of squared poloidal magnetic field fluctuation amplitude for core resonant, m = 1, n = 6 helical mode.

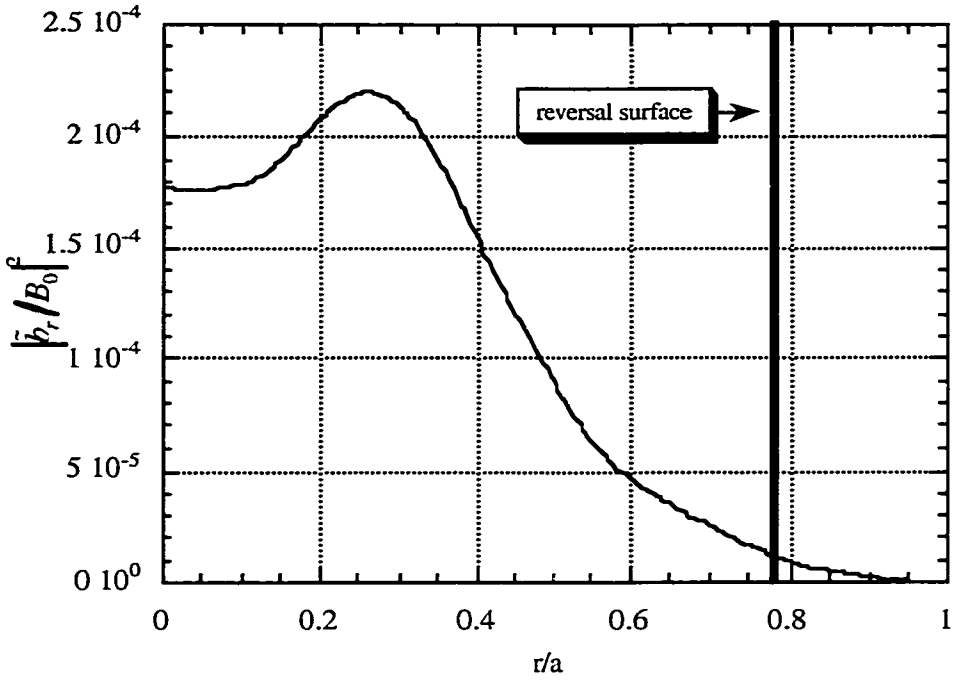

Figure 28: DEBS simulation data obtained during fluctuation burst. Radial profile of squared radial magnetic field fluctuation amplitude for core resonant, m = 1, n = 6 helical mode.

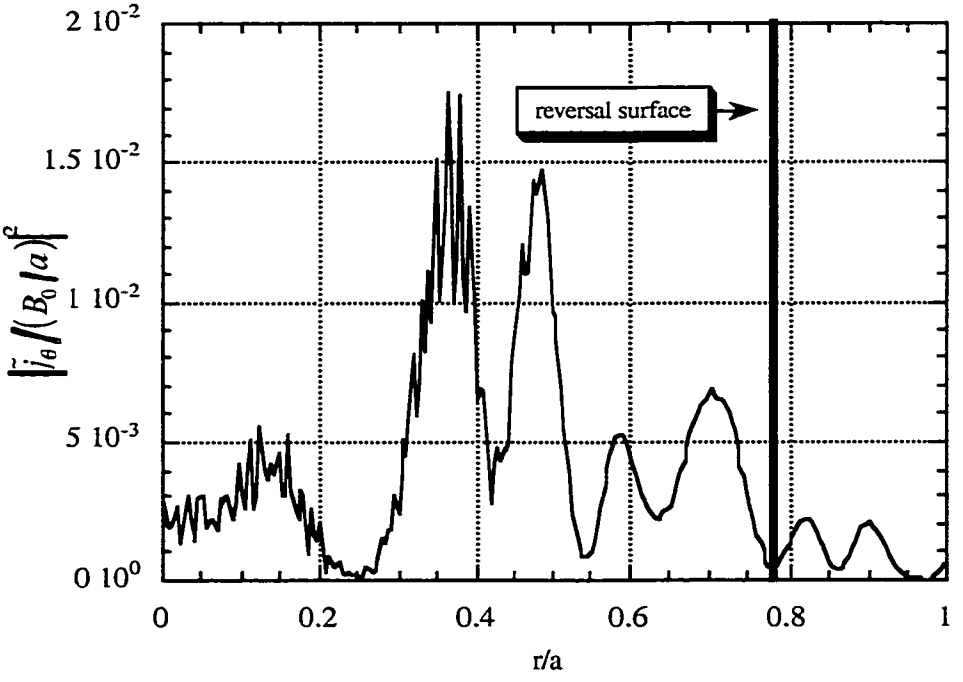

Figure 29: DEBS simulation data obtained during fluctuation burst. Radial profile of squared poloidal current density fluctuation amplitude for core resonant, m = 1, n = 6 helical mode.

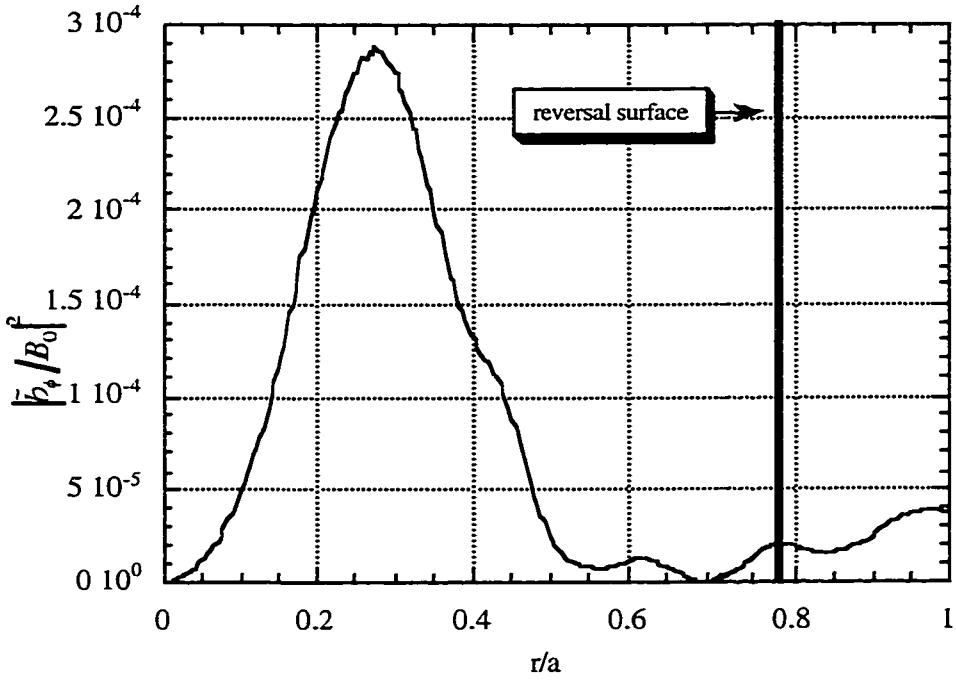

Figure 30: DEBS simulation data obtained during fluctuation burst. Radial profile of squared toroidal magnetic field fluctuation amplitude for core resonant, m = 1, n = 6 helical mode.

During sawtooth crashes, the amplitudes of the $n = -1$ $\tilde{b}_\theta$, $\tilde{b}_r$ and $\tilde{j}_\theta$ increase from the plasma boundary, reaching a maximum near the reversal surface, and then decrease toward the center of the plasma. This is illustrated by, for example, the radial profiles of $\tilde{b}_\theta$ at 75° P (Fig. 31) and $\tilde{b}_r$ (Fig. 32) and $\tilde{j}_\theta$ (Fig. 33) at -15° P. The measurement of amplitude of the $n = -1$ $\tilde{b}_\theta$ at -15° P (Fig. 34), however, is exceptional in that it does not go in deep enough to see a maximum and subsequent downward trend. The amplitude of the $n = -1$ $\tilde{b}_\phi$, on the other hand, decreases from the wall to the reversal surface and increases inside the reversal surface. This is illustrated by, for example, the radial profiles of $\tilde{b}_\phi$ at -15° P in Figure 35. All of these structures are qualitatively reproduced by the radial structures of amplitudes of the DEBS $m = 0, n = -1$ magnetic and poloidal current density fluctuations. Figures 36, 37, 38 and 39 show the DEBS $m = 0, n = -1$ $\tilde{b}_\theta$, $\tilde{b}_r$, $\tilde{j}_\theta$ and $\tilde{b}_\phi$ profiles, respectively.

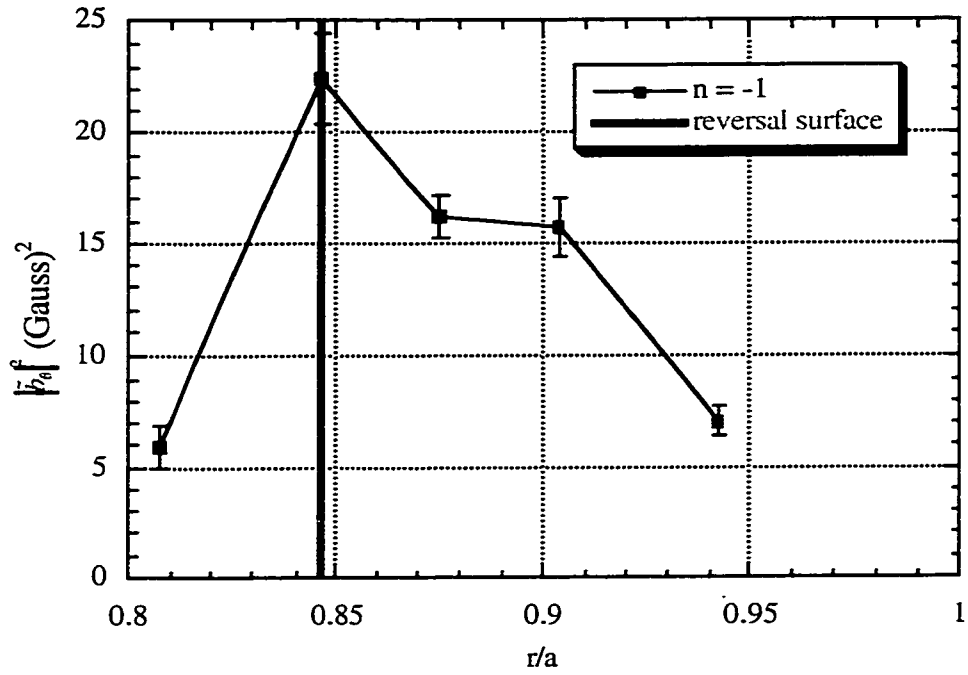

Figure 31: Radial profile of squared toroidal pseudospectral amplitude of poloidal magnetic field fluctuations for the reversal surface resonant, n = -1 toroidal mode during sawtooth crashes at 75° P, 120° T. Measured with reference to toroidal magnetic field fluctuations at the wall.

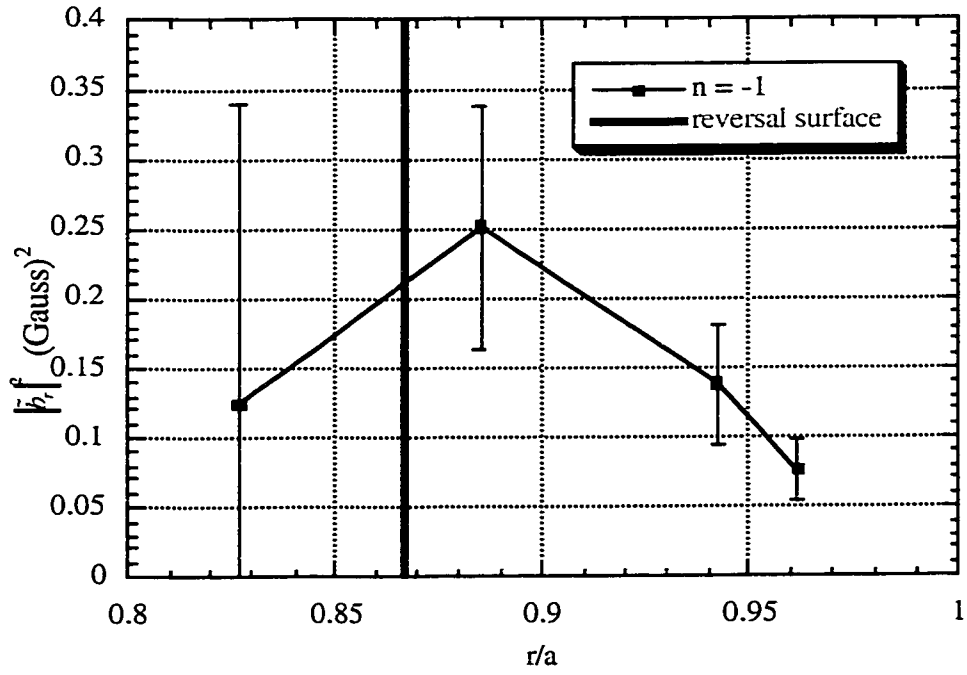

Figure 32: Radial profile of squared toroidal pseudospectral amplitude of radial magnetic field fluctuations for the reversal surface resonant, n = -1 toroidal mode during sawtooth crashes at -15° P, 330° T. Measured with reference to toroidal magnetic field fluctuations at the wall.

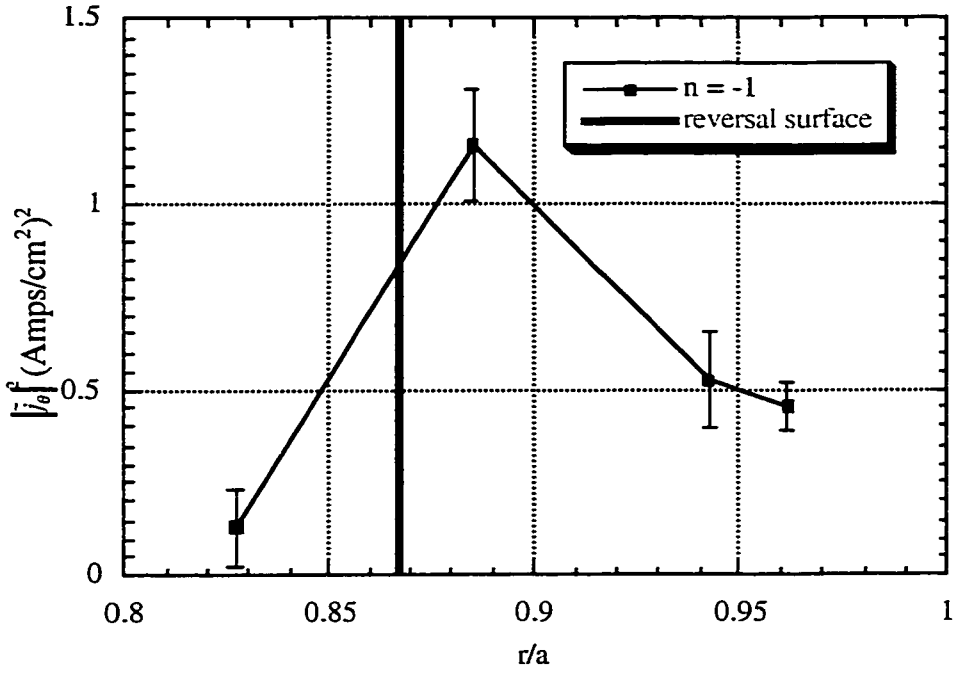

Figure 33: Radial profile of squared toroidal pseudospectral amplitude of poloidal current density fluctuations for the reversal surface resonant, n = -1 toroidal mode during sawtooth crashes at -15° P, 330° T. Measured with reference to toroidal magnetic field fluctuations at the wall.

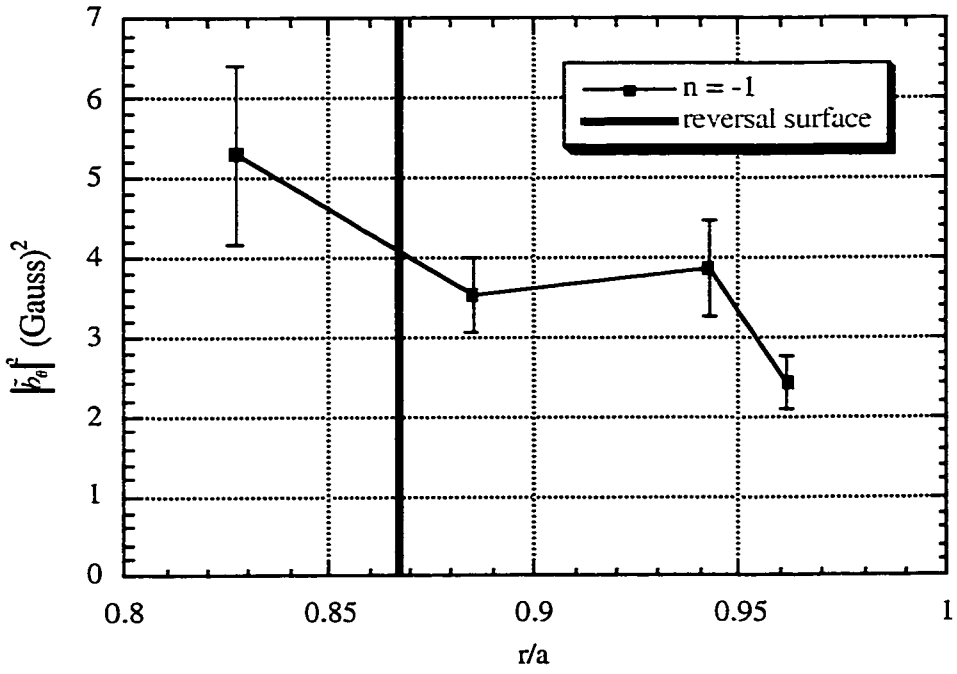

Figure 34: Radial profile of squared toroidal pseudospectral amplitude of poloidal magnetic field fluctuations for the reversal surface resonant, n = -1 toroidal mode during sawtooth crashes at -15° P, 330° T. Measured with reference to toroidal magnetic field fluctuations at the wall.

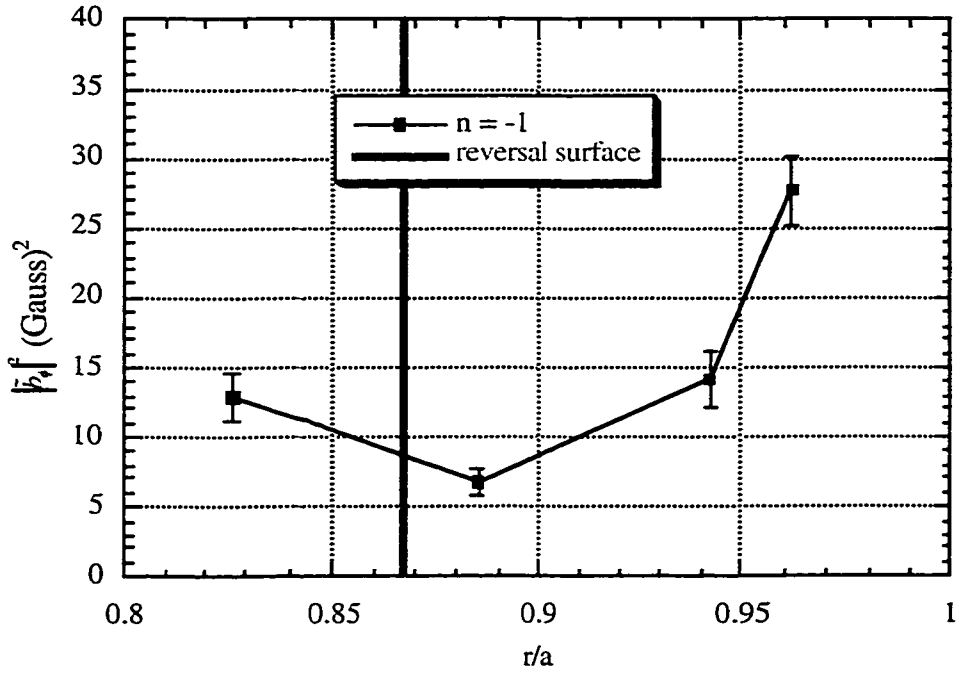

Figure 35: Radial profile of squared toroidal pseudospectral amplitude of toroidal magnetic field fluctuations for the reversal surface resonant, n = -1 toroidal mode during sawtooth crashes at -15° P, 330° T. Measured with reference to toroidal magnetic field fluctuations at the wall.

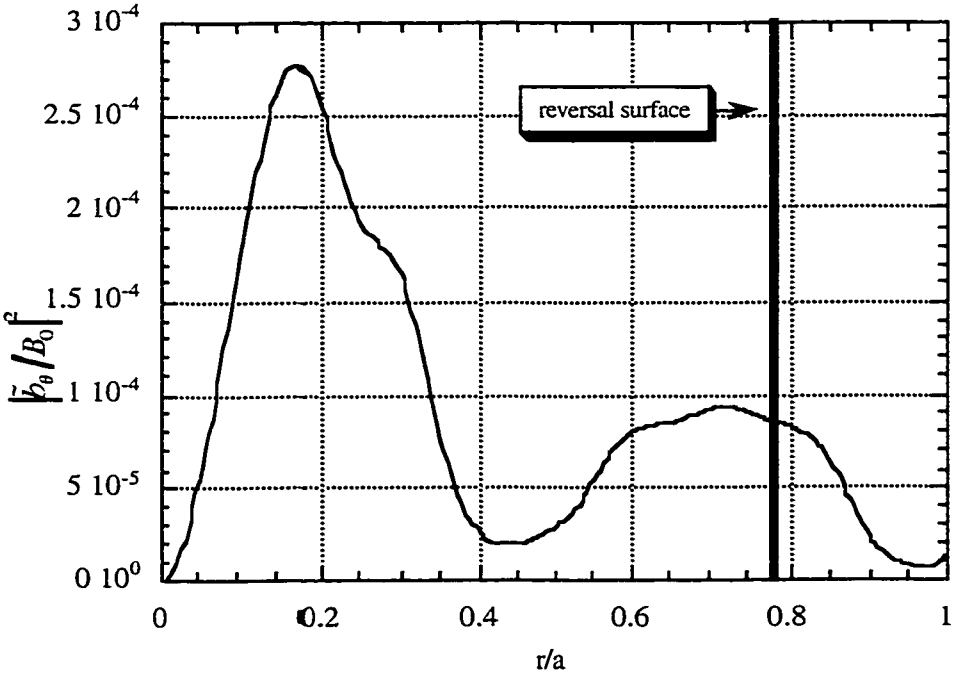

Figure 36: DEBS simulation data obtained during fluctuation burst. Radial profile of squared poloidal magnetic field fluctuation amplitude for reversal surface resonant, m = 0, n = -1 helical mode.

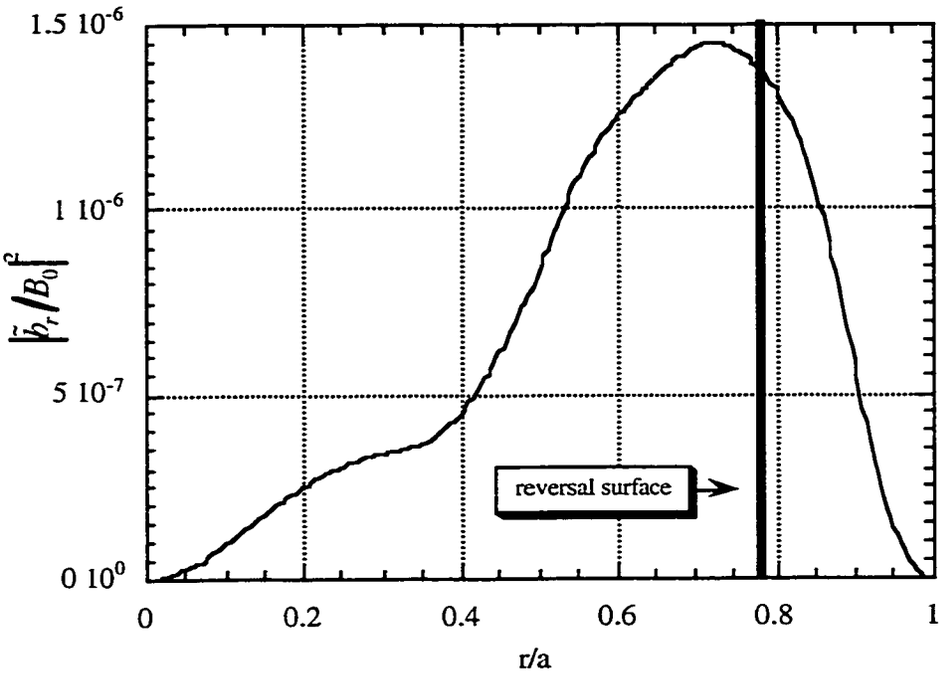

Figure 37: DEBS simulation data obtained during fluctuation burst. Radial profile of squared radial magnetic field fluctuation amplitude for reversal surface resonant, m = 0, n = -1 helical mode.

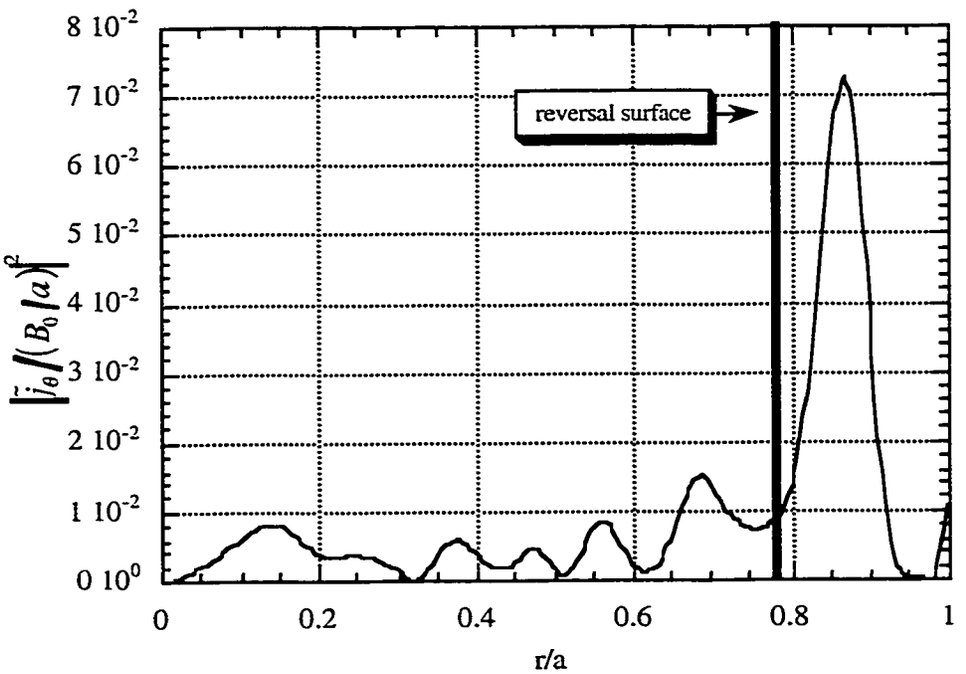

Figure 38: DEBS simulation data obtained during fluctuation burst. Radial profile of squared poloidal current density fluctuation amplitude for reversal surface resonant, m = 0, n = -1 helical mode.

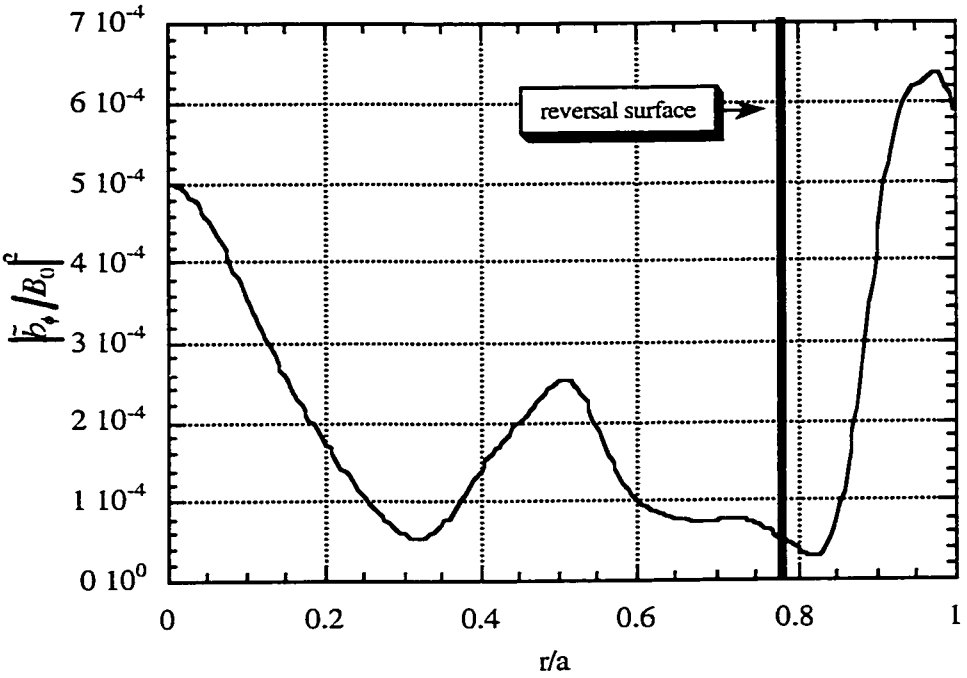

Figure 39: DEBS simulation data obtained during fluctuation burst. Radial profile of squared toroidal magnetic field fluctuation amplitude for reversal surface resonant, m = 0, n = -1 helical mode.

Several other features of the magnetic and poloidal current density fluctuations in MST are qualitatively reproduced by the DEBS code. In particular, several features of the reversal surface resonant $n = -1$ mode are reproduced in the plasma edge. First, in both MST and DEBS plasmas, the relative magnetic fluctuation amplitudes of the different components of the magnetic field, $\tilde{b}/B_0$, are small. In DEBS, they are roughly in the range $0.1\% - 2\%$, where B_0 is the equilibrium magnetic field on axis, while in MST, they are roughly in the range $0.03\% - 0.5\%$ Second, both MST and DEBS plasmas exhibit relative poloidal current density fluctuations fluctuation amplitudes, $\tilde{j}/(B_0/a)$, that are larger than the relative magnetic fluctuation amplitudes. In DEBS, $\tilde{j}/(B_0/a) \gtrsim 10\%$. In MST, $\tilde{j}/(B_0/a) \gtrsim 3\%$. Third, the relative ordering (in magnitude) of the fluctuation amplitudes for the three components of the magnetic field in the vicinity of reversal surface, $\left|\tilde{b}_r\right|^2 < \left|\tilde{b}_\theta\right|^2 < \left|\tilde{b}_\phi\right|^2$, is reproduced.

It also worth noting that the radial structures of the DEBS $m = 0$, $n = -1$ and MST $n = -1$ $\tilde{j}_\theta$ in vicinity of the reversal surface show identifiable current sheets associated with

reconnection at the reversal surface. Sec. 4.7 of this chapter discusses the current sheet in MST in the context of the theory of magnetic reconnection, including, in particular, the results of the DEBS simulation results presented here.

In making such direct comparisons between MST data and DEBS simulation data, several similarities and differences between MST plasmas and DEBS plasmas must be considered. DEBS simulates cylindrical plasmas bounded by a conducting shell which, as is the case for the simulations presented here, may be pressureless. Such plasmas resemble MST plasmas in many respects. One respect in which MST plasmas resemble DEBS simulations is that MST is bounded by a close-fitting conducting shell. Such a conducting shell imposes a significant boundary condition on tearing modes in both DEBS and MST.

A second respect in which MST plasmas resemble DEBS simulations is that MST has an inverse aspect ratio (*i.e.,* ratio of minor radius to major radius) of 1/3. This is significant in two respects. First, this value is significantly smaller than 1, so the cylindrical geometry plasma such as simulated by DEBS is, in some respects, a good geometrical approximation to the toroidal geometry plasmas of MST. Second, the aspect ratio of an RFP determines which rational surfaces will exist in the equilibrium magnetic field (regardless of whether its geometry is cylindrical or toroidal), and, thus, which helical periodicities are possible for tearing modes. The DEBS simulations discussed here have an inverse aspect ratio comparable to that of MST. Thus the tearing modes in these simulations exhibit a range of helical periodicities to similar to the range for those in MST.

A third respect in which MST plasmas resemble the DEBS simulations discussed here is that the radial gradient in the parallel, or magnetic field aligned, component of the equilibrium current density plays a significant, destabilizing role in the evolution of tearing modes in MST. Although DEBS simulations can include a self-consistently evolved pressure profile, the specific simulations discussed here are pressureless. In such pressureless RFP plasmas, a radial gradient in parallel current density is the only destabilizing agent for tearing modes (assuming no

externally imposed perturbation).

One major distinction between DEBS simulations and MST plasmas is that DEBS plasmas have a much larger resistivity than MST plasmas. Specifically DEBS simulations typically use a Lundquist number which is at least one to two orders of magnitude less than those of MST. The Lundquist number of an RFP plasma is given by $S = \tau_{Resistive} v_{Alfvén}/a = \left(a^2\mu_0/\eta\right)\left(B_0/\left(\mu_0 m_i n_i\right)^{1/2}\right)/a$, where a is the minor radius of the plasma, m_i is mass of the ion species and n_i is the ion density. MST plasmas typically have an $S \sim 10^5$ in the edge and an $S \sim 10^6$ in core, while the DEBS data discussed here was obtained from simulations with an $S \sim 10^4$. As discussed in Sec. 2.3 of Ch. 2, the spatial scale of the reconnection process that permits tearing modes to evolve is sensitive to S. More importantly, the relative significance of resistivity to reconnection depends on S. The spatial scale of resistive reconnection becomes smaller as S becomes larger, although its sensitivity to S is weak ($\delta \sim a/S^{2/5}$ for resistive tearing modes). At higher values of S, other non-ideal terms in Ohm's law might have larger associated spatial scales, and thus may become more significant than resistivity. Because of this difference in Lundquist number, resistivity would probably play a more significant role in reconnection in DEBS-like physical plasmas than in MST plasmas. (Of course, in DEBS simulation plasmas, other non-ideal terms in Ohm's law are explicitly neglected, so it plays a very significant role). In spite of the relatively low S in DEBS simulations, however, it is high enough in the simulations discussed here so that they are similar to MST plasmas in one important respect: in DEBS plasmas, just as in MST plasmas, this resistive spatial scale is much smaller than the plasma's minor radius.

Another consideration in comparing the data from MST plasmas with the DEBS simulations discussed here is that the equilibrium magnetic field of the MST plasmas have a moderately different equilibrium magnetic field structure from that of the DEBS simulation. Figure 40 shows the q profile for the specific DEBS simulation whose data is discussed here and a q profile averaged over a sawtooth crash typical of the MST data discussed here. (The MST q

profile from MST equilibrium fitting code MSTFIT[2] is courtesy of Jay Anderson). Note that the $q = 0$ surface of the DEBS simulation is roughly 10% (of the plasma minor radius) deeper than it is in the MST plasma. This means that the radial structure of perturbations in the DEBS simulation will be subtly distorted compared to those measured in MST, even neglecting other differences between the two kinds of plasmas.

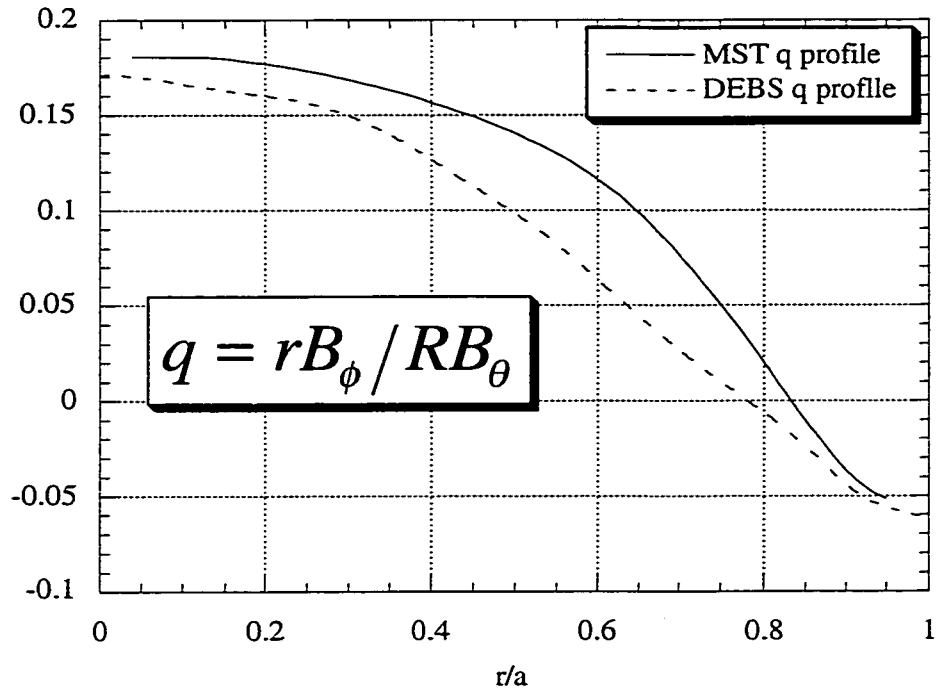

Figure 40: q profiles of MST plasmas during sawtooth crashes (calculated with MSTFIT, by Jay Anderson) and DEBS plasmas during fluctuation burst. Uncertainty of MST reversal surface position is $\delta r/a \sim 0.004$.

Two more considerations in comparing measurements of toroidal mode profiles made in MST with helical mode profiles obtained from DEBS derive from the difference in the statistical characters of the measured profiles discussed here. First, the MST profiles are the product of pseudospectral analysis, and are derived from average products of pairs of fluctuating quantities (see the discussion of pseudospectral analysis in Sec. 3.11 of Ch. 3). Thus, the MST profiles represent, in some sense, average radial profiles for toroidal modes. The DEBS profiles, on the other hand, are obtained from near-instantaneous snapshots of helical modes. Thus, the DEBS profiles potentially have statistically random features that would be washed out by the averaging

process applied in obtaining the MST profiles. Second, because the DEBS profiles represent the radial structure of the amplitudes of helical modes, they are independent of poloidal angle. The MST profiles, on the other hand, represent the radial structure of the amplitudes of toroidal modes. These amplitudes have a poloidal as well as radial structure. Consequently, the MST profiles may vary with the poloidal angle at which they are measured. It is expected, however, that both of these differences may be accounted for, at least qualitatively, in assessing the similarities and differences to the DEBS and MST measurements. First, visual inspection of DEBS profiles at multiple times, as well as certain limited attempts at time averaging, suggest that the major features of the radial structures of resonant magnetic and poloidal current density helical modes are relatively statistically invariant. In particular, these profiles appear to vary in overall magnitude much more than they do in shape. Second, as discussed in Section 4.2, the poloidal angle dependence of the MST profiles is dealt with by comparing the phases of the toroidal modes measured at different poloidal angles relative to a reference fluctuation quantity to determine the poloidal mode content of the measured toroidal modes. Corroboration for the results obtained from this technique is provided by the poloidal two-point spectra reported in Section 4.4, above.

4.6 - Reconnection at the Reversal Surface in MST

Historically, a strong case has been made, based on a combination of tearing mode theory and observations of magnetic fluctuation activity, that magnetic reconnection occurs in RFPs at the reversal surface. This argument has two key components. First, magnetic fluctuations in RFPs are partially composed of helical modes that are resonant with the equilibrium magnetic field at the reversal surface (as discussed in Sec 2.6 of Ch. 2). Second, a strong theoretical case exists that tearing modes capable of producing such fluctuations should be unstable in RFPs, while, at the same time, RFPs are stable against any ideal MHD instability.[3]

In spite of the strong circumstantial case that reconnection occurs at the reversal surface

in RFPs, there have been no measurements that have definitively demonstrated its occurrence. The measurement of the $n = -1$ radial magnetic field fluctuation discussed in Sections 4.2 and 4.5, however, does just that. Figures 32 and 41 show the radial profile of the pseudospectral amplitude of the $n = -1$ $\tilde{b}_r$ during sawtooth crashes, when reconnection is most active, at -15° P and 75° P, respectively. This measurement represents the direct observation of a magnetic perturbation that reconnects magnetic field lines in the vicinity of the reversal surface, thus establishing that magnetic reconnection occurs.

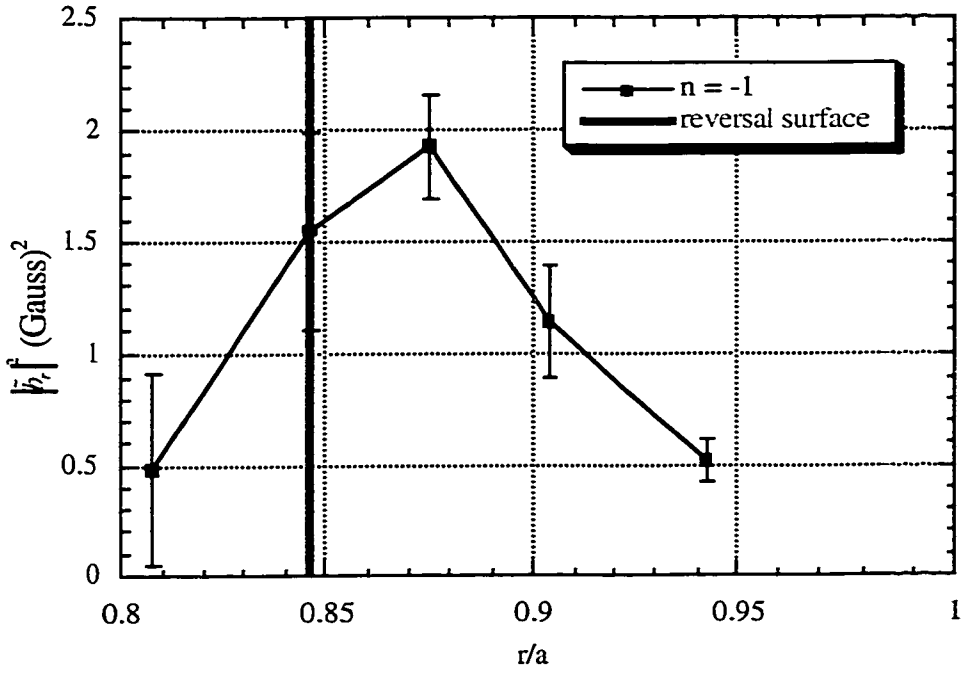

Figure 41: Radial profile of squared toroidal pseudospectral amplitude of radial magnetic field fluctuations for the reversal surface resonant, n = -1 toroidal mode during sawtooth crashes at 75° P, 120° T. Measured with reference to toroidal magnetic field fluctuations at the wall.

As discussed in Sec. 2.4 of Ch 2, a resonant radial magnetic field fluctuation that is non-vanishing at the reversal surface changes the topology of the magnetic field lines in its vicinity. The $n = -1$ $\tilde{b}_r$ has been determined to be non-vanishing at the reversal surface. In addition, this fluctuation is dominantly composed of the $m = 0$ poloidal mode, indicating that it is resonant at the reversal surface.

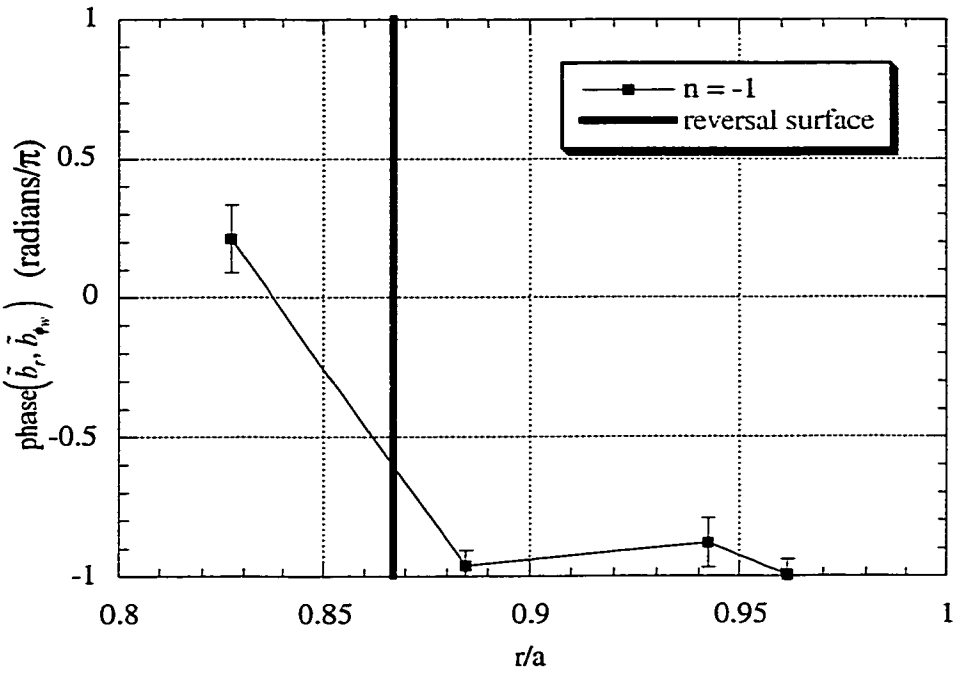

Figure 42: Relative phase between radial magnetic field fluctuation at -15° P and toroidal magnetic field fluctuation at wall at 241° P for the reversal surface resonant, n = -1 toroidal mode measured during sawtooth crashes.

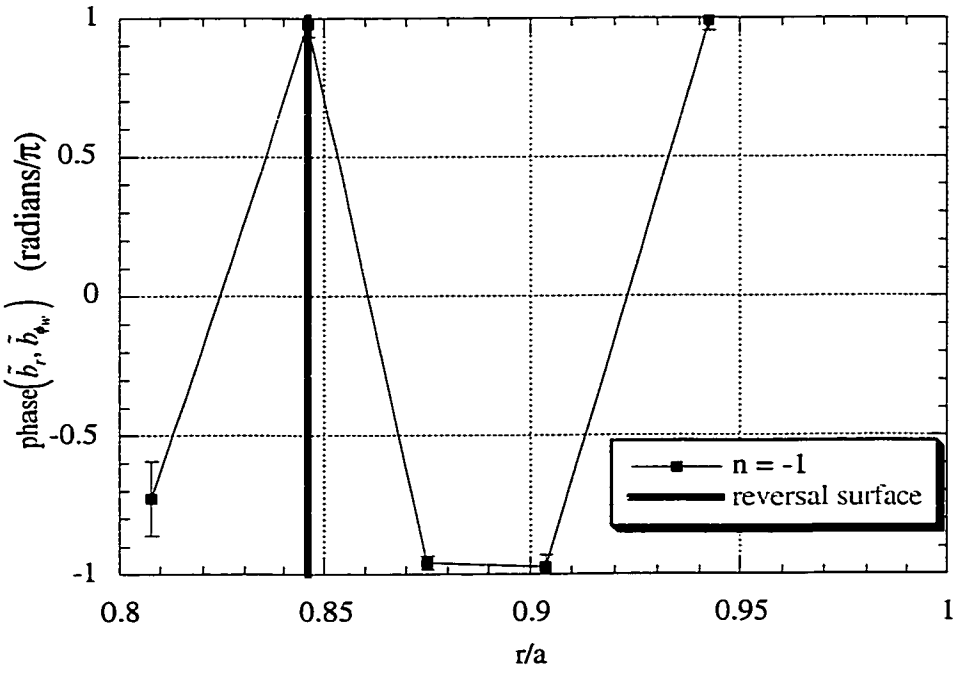

Figure 43: Relative phase between radial magnetic field fluctuation at 75° P and toroidal magnetic field fluctuation at wall at 241° P for the reversal surface resonant, n = -1 toroidal mode measured during sawtooth crashes.

Figures 42 and 43 show the poloidal phase of the $n = -1$ $\tilde{b}_r$ for measurements of $\tilde{b}_r$ during sawtooth crashes at -15° P and 75° P, respectively. This phase, phase$\left(\tilde{b}_r, \tilde{b}_{\phi_w}\right)$, which is measured relative to the toroidal magnetic field fluctuations at the wall at 241° P, $\tilde{b}_{\phi_w}$, is expected to be independent of the poloidal angle at which the $n = -1$ $\tilde{b}_r$ is measured if the $n = -1$ $\tilde{b}_r$ is $m = 0$ in character. At the reversal surface and outwards, this is clearly the case. Inwards of the reversal surface, the value of phase$\left(\tilde{b}_r, \tilde{b}_{\phi_w}\right)$ differs by π between the measurements at -15° P and 75° P. This difference might be due to an $m = 2$ contribution to $n = -1$ $\tilde{b}_r$. However, since the $n = -1$ $\tilde{b}_r$ is near zero at minor radii just inwards of the reversal, the phase difference of π is more probably the result of a node or zero-crossing in the radial profile of the $n = -1$ $\tilde{b}_r$ perturbation whose radial position varies with poloidal angle. Near such a node, a toroidal mode which is $m = 0$ in character would be expected to exhibit a phase difference of either zero or π between pairs of poloidal phase measurements depending on the poloidal positions of the measurements. In fact, this type of node is apparent in the radial profile of the $n = -1$ $\tilde{b}_\phi$ just on the outwards of the reversal surface. Figures 10 and 11 show the radial profiles of phase$\left(\tilde{b}_\phi, \tilde{b}_{\phi_w}\right)$ measured during sawtooth crashes at -15° P and 75° P, respectively.

4.7 - The Reversal Surface Reconnection Current Sheet

In addition to directly verifying that magnetic reconnection occurs at the $q = 0$ surface in MST, as is discussed in Sec. 4.6, the radial structure of the current sheet associated with reconnection at this surface has been probed. The measurement of the $n = -1$ poloidal current density fluctuation discussed in Secs. 4.2 and 4.5 above indicates that it is at least ~ 7 cm wide in the minor radial direction during sawtooth crashes when reconnection is most active. Figures 33 and 44 show the radial profile of the pseudospectral amplitude of the $n = -1$ $\tilde{j}_\theta$ at -15° P and 75° P, respectively. Many of the possible widths of the reconnection current sheet (discussed in Sec. 2.3 of Ch. 2), such as resistive layer width, ion and electron skin depths, island width and ion acoustic gyroradius, are separable in an MST, allowing measurements of this width to

potentially distinguish which non-ideal effects play a role in the reconnection process at the reversal surface.

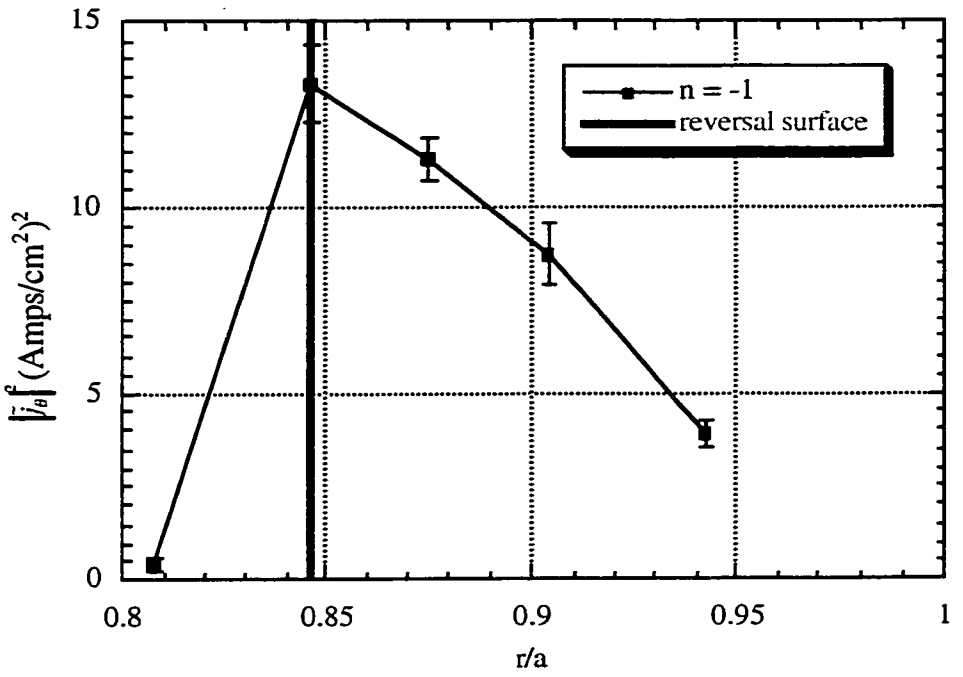

Figure 44: Radial profile of squared toroidal pseudospectral amplitude of poloidal current density fluctuations for the reversal surface resonant, n = -1 toroidal mode during sawtooth crashes at 75° P, 120° T. Measured with reference to toroidal magnetic field fluctuations at the wall.

The width of the current sheet, ~ 7 cm, is much greater than the electron skin depth (c/ω_{pe}) of $\lesssim$ 0.5 cm (calculated assuming $n_o \gtrsim 1 \times 10^{12}$ cm^{-3}). Thus the electron inertial effect cannot, by itself, account for the measured width. On the other hand, the width of the current sheet is, at most, a factor of a few times the ion acoustic gyroradius (ρ_s) of ~ 1.5 cm (calculated assuming T_e ~ 100 eV and B ~ 0.1 T). Thus, electron pressure effects could play a role in reconnection in the edge of MST. We note, also, that the layer width is comparable to the ion skin depth (c/ω_{pi}) which is at least 16 cm (calculated assuming $n_o \lesssim 2 \times 10^{12}$ cm^{-3}); however, the ion skin depth may be a current layer width only in high β, or weakly magnetized, plasmas (*i.e.*, when the magnetic field perpendicular to the plane of plasma inflow and outflow is small compared to the plasma pressure).

The resistive layer width in an RFP whose minor radius is a and whose Lundquist number is S is given by $a/S^{2/5}$. The width of the current sheet, ~ 7 cm, is much greater than this width, which is $\lesssim$ 0.5 cm (calculated assuming $S \sim 10^5$) in the edge of MST. This may not, however, indicate that resistivity cannot explain the observed current sheet width. As discussed in Sec. 2.3 of Ch. 2, the resistive layer width appears as a spatial scale in the linear phase of unstable resistive tearing mode evolution. Resistive tearing mode theory indicates that when a mode grows large enough, as is likely in MST, it reaches a stage of growth where the width of the current sheet is given by the width of the associated magnetic island. Since the observed width of the current sheet is comparable to the $m = 0$ island width of ~ 10 cm calculated for conditions in MST, this suggests that resistivity is, in fact, sufficient to explain the width of the current sheet. (The width of an island at the reversal surface for a tearing mode with toroidal mode number n is calculated using $W = 4\left(\left|R\tilde{b}_{r,n}/B_\phi' n\right|\right)^{1/2} = 4\left(\left|r_{rev}\tilde{b}_{r,n}/B_\theta n q'\right|\right)^{1/2}$, where all quantities are evaluated at r_{rev}, the minor radius of the reversal surface. The indicated island width of ~ 10 cm is calculated for $n = -1$. The value of $\tilde{b}_{r,n}$ is taken from the pseudospectral measurements of the $n = -1$ $\tilde{b}_r$ discussed in Sec. 4.6, above. The values of q' and r_{rev} (~ 1 m^{-1}) are taken from the MSTFIT q profile discussed in Sec. 4.5, above, and shown in Fig. 40. The value for B_θ ~ 700 G.)

It is interesting to note that the DEBS simulation results discussed in Sec. 4.5 of this chapter show a current sheet width that is intermediate between the calculated island width and the resistive layer width. As can be seen in Figure 38, the current sheet associated with reconnection at the reversal surface in these simulations has a radial width of ~ $0.1a$. The resistive layer width for these simulations is ~ $0.025a$, while the calculated island width is ~ $0.4a$. (The DEBS $m = 0$, $n = -1$ island width is obtained using the same procedure, as described above, for calculating the MST reversal surface island width. The DEBS q profile shown in Fig. 40 is used to obtain q' and r_{rev}. The profile of $\tilde{b}_{r,n}$ for the DEBS $m = 0$, $n = -1$ tearing mode is shown in Fig. 37, but it is normalized to the equilibrium magnetic field at $r = 0$.

The value of B_θ at the reversal surface is estimated to be ~ 3 times smaller than the equilibrium magnetic field at $r = 0$, which gives $\tilde{b}_{r,n}/B_\theta$.) Thus, the width of the current sheet in these simulations is a factor of ~ 4 times larger than the resistive layer width, and a factor of ~ 4 times smaller than the magnetic island width. Since these simulations explicitly include resistivity as the only non-ideal effect, resistivity, in one way or another, controls the width of current sheet. Since DEBS simulates the evolution of tearing modes well beyond the linear phase of their development, it might be expected that the current sheet width would be given by the island width. However, the radial magnetic field perturbations in DEBS simulations are generally large enough that the resultant magnetic islands would overlap. This results in the stochasticization of magnetic field lines in DEBS simulations and absence of islands. It is not clear what the expected current layer width is for well developed tearing modes in the absence of magnetic islands. The radial magnetic field perturbations in MST are significantly smaller than those in DEBS, and it is an open question whether the $m = 0$, $n = -1$ island in MST would overlap with other islands and consequently be destroyed.

As noted, the observed current sheet width in MST is comparable to the estimated $m = 0$, $n = -1$ island width. While this current sheet width may simply be the product of resistivity for the case of a well developed tearing mode, it is interesting to note that it might also result from the broadening of some smaller scale current sheet by a process of current transport across the island (by charge carrier motion along the magnetic field lines of the island). If such a current broadening mechanism is active, the actual current sheet might have a distinct multiscale structure (*i.e.*, a large amplitude, narrow current sheet superimposed on a small amplitude, island-sized current sheet). The measurement technique used to observe the current sheet reported here affords us a certain limited ability to detect such a multiscale structure. The profile of the $n = -1$ poloidal current density fluctuation shown in Figure 41 consists of measurements which average over 2 cm of minor radius each and which are spaced 1.5 cm to 2 cm apart. Consequently, if the current sheet had a multiscale structure composed of a small amplitude,

broad current sheet with the observed radial width (~ 7 cm) and a superimposed, large amplitude current sheet with a small radial scale such as ρ_s or c/ω_{pe}, the small scale current sheet would be detected, although it would appear as a having a radial scale of 2 cm and a lesser amplitude. The radial structure of the current sheet shown in Figure 41 does not appear to be qualitatively consistent with such a distinct multiscale structure. This does not exclude the possibility that the observed current sheet results from the broadening of a smaller scale current sheet by current transport due to parallel streaming, but it does place a constraint any theory proposed to explain the radial structure of observed current sheet using that mechanism.

Another possible explanation for the observed current sheet arises from the observation that the reversal surface is positioned close (compared to the island width) to a conducting wall on one side. It is possible that as the magnetic island at the reversal surface grows, its magnetic flux becomes compressed between the reversal surface and the conducting wall. This compression of flux might manifest as an enhanced radial gradient in the toroidal component of the magnetic field between the reversal surface and the edge of the plasma, as compared to the radial gradient in the toroidal magnetic field on the other side of the reversal surface. This would, in turn, give rise to a radial asymmetry in the current sheet, with a relatively greater poloidal current density between the reversal surface and the edge of the plasma. Such an asymmetry is, in fact, apparent in the radial structure of the current sheet in MST. It is interesting to note that such an asymmetry is apparent in the radial structure of the DEBS current sheet (Fig. 38), as well.

4.8 - Conclusions

In conclusion, the spatial structures of the poloidal current density and magnetic field fluctuations associated with tearing mode activity has been probed in the edge region of MST using two-point spectral analysis and pseudospectral analysis. Magnetic fluctuations in the edge of MST are dominantly composed of toroidal modes with mode numbers in the range $n = 5 - 10$

while poloidal current density fluctuations are composed of toroidal modes with mode numbers in the range $n = -1 - -3$. Although the helical Fourier mode amplitudes of the magnetic and poloidal current density fluctuations are not directly measured, there are several indications that the $n = 5 - 10$ toroidal modes of the magnetic fluctuations are, in fact, dominantly composed of $m = 1$, $n = 5 - 10$ helical modes, while the $n = -1 - -3$ toroidal modes of the poloidal current density fluctuations are dominantly composed of $m = 0$, $n = -1 - -3$ helical modes. Such indications arise from two-point poloidal spectral analysis of the magnetic and poloidal current density fluctuations as well as measurements of the poloidal dependence of the poloidal phase of the toroidal modes which compose these fluctuations.

The observed radial structure for the core resonant $n = 6$ toroidal mode and reversal surface resonant $n = -1$ toroidal mode of the magnetic and poloidal current density fluctuations in the edge of MST are compared with predictions of tearing mode structure obtained from the DEBS code. It is observed that, for these fluctuations, the edge radial structures of both the $n = 6$ and $n = -1$ toroidal modes are qualitatively similar to those of the $m = 1$, $n = 6$ and $m = 0$, $n = -1$ helical modes, respectively, in DEBS plasmas. Of particular interest, it is observed that the $n = -1$ poloidal current density perturbation in MST shows a current sheet associated with reconnection at the reversal surface, just as does the $m = 0$, $n = -1$ poloidal current density perturbation in DEBS simulations.

For the first time in the study of reconnection in RFPs, direct evidence is obtained that reconnection occurs at the reversal surface. The measured radial structure of the dominant reversal surface resonant radial magnetic field fluctuation ($m = 0$, $n = -1$) is measured around the reversal surface. It is observed to be non-vanishing at the reversal surface, implying the occurrence of reconnection.

The radial width of the $m = 0$, $n = -1$ poloidal current density perturbation, or current sheet, associated with reconnection at the reversal surface has been compared to the widths that are theoretically and computationally expected from models of reconnection which include,

variously, resistivity, electron inertial effects, electron pressure gradient effects, and the Hall term (*i.e.*, ion inertia). It is determined that the electron inertial effect in Ohm's law cannot, by itself, explain the width of the observed current sheet, since the associated scale length is much smaller than this width. It is noted that the current sheet width is, however, only a few times larger than the width obtained by inclusion of the electron pressure gradient effect in Ohm's Law. The width of the current sheet is much larger than the resistive MHD scale, which might be construed to indicate that resistivity cannot explain the observed current sheet. However width of the observed current sheet is comparable to the calculated width for the associated magnetic island (the $n = -1$, $m = 0$ island). It is noted that, theoretically, the current sheet width for the saturated tearing modes in MST should not be determined by the resistive MHD scale if resistivity is the dominant non-ideal effect, but, rather, the width of the associated magnetic island. Since the width of the current sheet is comparable to the associated magnetic island width, it is alternatively possible that a current sheet with some smaller radial scale, produced by a reconnection mechanism other than resistivity, is distributed radially over the associated magnetic island by streaming of charge carriers along magnetic field lines.

References

[1] D. D. Schnack, et al., J. of Computational Physics **70,** 330 (1987).

[2] C. B. Forest, et al., poster, Annual Meeting of the Division of Plasma Physics of the American Physical Society, 17 – 21 November 1997, Pittsburgh, PA.

[3] H. P. Furth, J. Killeen, and M. N. Rosenbluth, Phys. Fluids **6,** 459 (1963).

Chapter 5 - Charge, Particle and Momentum Transport

5.1 - Introduction

This chapter reports measurements of the flux surface average product of fluctuations in the radial magnetic field and the component of the current density parallel to the equilibrium magnetic field, $\left\langle \tilde{j}_{\parallel}\tilde{b}_r \right\rangle_{F.S.}$, in the edge of MST. The product $\left\langle \tilde{j}_{\parallel}\tilde{b}_r \right\rangle_{F.S.}$ plays a role in the charge, particle and momentum balances of MST. Specifically, it represents a radial charge flux, or radial current density, in the form of $\Gamma_q = \left\langle \tilde{j}_{\parallel}\tilde{b}_r \right\rangle_{F.S.} / B_0$, which, in turn has implications for radial particle transport, and it represents a force density in the form of $\left\langle \tilde{j}_{\parallel}\tilde{b}_r \right\rangle_{F.S.} \hat{b}_0 \times \hat{r}$. The measured $\left\langle \tilde{j}_{\parallel}\tilde{b}_r \right\rangle_{F.S.}$ is non-vanishing but much smaller in magnitude than the maximum possible value permitted by $\tilde{j}_{\parallel}$ and $\tilde{b}_r$, which is given by $\left\langle \left|\tilde{j}_{\parallel}\right|^2 \right\rangle_{F.S.}^{1/2} \left\langle \left|\tilde{b}_r\right|^2 \right\rangle_{F.S.}^{1/2}$. This chapter also reports measurements of the relative phase, coherence and crossspectral amplitude of $\tilde{j}_{\parallel}$ and $\tilde{b}_r$, obtained using crossspectral analysis (discussed in Sec. 3.8 of Ch 3). These measurements are used to probe the physical causes underlying the measured value of $\left\langle \tilde{j}_{\parallel}\tilde{b}_r \right\rangle_{F.S.}$. In particular, they are used to explore why $\left\langle \tilde{j}_{\parallel}\tilde{b}_r \right\rangle_{F.S.}$ is much smaller in magnitude than $\left\langle \left|\tilde{j}_{\parallel}\right|^2 \right\rangle_{F.S.}^{1/2} \left\langle \left|\tilde{b}_r\right|^2 \right\rangle_{F.S.}^{1/2}$ and why it is non-vanishing.

This chapter also reports measurements of the spatial decomposition of $\left\langle \tilde{j}_{\parallel}\tilde{b}_r \right\rangle_{F.S.}$ in terms of toroidal modes. This decomposition is performed using pseudospectral analysis, which is discussed in Sec. 3.11 of Ch 3. In particular, it is used to distinguish the contributions to $\left\langle \tilde{j}_{\parallel}\tilde{b}_r \right\rangle_{F.S.}$ from core and reversal surface resonant tearing modes. The accuracy of the pseudospectral technique in decomposing $\left\langle \tilde{j}_{\parallel}\tilde{b}_r \right\rangle_{F.S.}$ is also discussed.

As discussed in Sec. 2.7 of Ch. 2, it has traditionally been expected that $\left\langle \tilde{j}_{\parallel}\tilde{b}_r \right\rangle_{F.S.}$ would be zero because in an RFP tearing mode theory for an isolated tearing mode predicts that the associated $\tilde{j}_{\parallel}$ and $\tilde{b}_r$ will be spatially out of phase. There are, however, as least two considerations that invalidate this expectation. First, experimental evidence is mounting that, as predicted by the theory for interacting tearing modes, tearing modes may interact to exert $\bar{J} \times \bar{B}$ forces on the plasma of the form $\left\langle \tilde{j}_{\parallel}\tilde{b}_r \right\rangle_{F.S.} \hat{b}_0 \times \hat{r}$ which redistribute its momentum. Second, since

tearing modes alter the magnetic field lines of the plasma to cross the surfaces of the equilibrium magnetic field, the possibility exists for a charge flux, or charge transport, across the equilibrium surfaces due to parallel streaming of charge carriers (given by $\Gamma_q = \left\langle \tilde{j}_\parallel \tilde{b}_r \right\rangle_{F.S.} / B_0$). Traditionally, of course, the theory for isolated tearing modes presupposes that no mechanism other than parallel streaming exists for charge transport across the equilibrium surfaces of a plasma, which constrains charge transport by parallel streaming and, thus, $\left\langle \tilde{j}_\parallel \tilde{b}_r \right\rangle_{F.S.}$ to be zero (so that charge neutrality is maintained). In light of these considerations, a non-vanishing $\left\langle \tilde{j}_\parallel \tilde{b}_r \right\rangle_{F.S.}$ has implications for the understanding of tearing mode interactions in MST, as well as implications the charge, particle and momentum balances in MST. This chapter discusses the significance of the measured $\left\langle \tilde{j}_\parallel \tilde{b}_r \right\rangle_{F.S.}$ in each of these contexts.

The structure of this chapter is as follows:

In Section 5.2, we present measurements of $\left\langle \tilde{j}_\parallel \tilde{b}_r \right\rangle_{F.S.}$ in the edge of MST. In particular, we discuss measurements made during and between sawtooth crashes and at two different poloidal and toroidal locations: -15° P, 330° T and 75° P, 120° T, where, as noted in Sec. 3.7 of Ch. 3, "° P" denotes "degrees poloidal" and "° T" denotes "degrees toroidal." Additionally, for comparison purposes, we present the maximum possible value that $\left\langle \tilde{j}_\parallel \tilde{b}_r \right\rangle_{F.S.}$ permitted to have by the measured $\tilde{j}_\parallel$ and $\tilde{b}_r$, which is given by $\left\langle \left|\tilde{j}_\parallel\right|^2 \right\rangle_{F.S.}^{1/2} \left\langle \left|\tilde{b}_r\right|^2 \right\rangle_{F.S.}^{1/2}$.

In Section 5.3, we present the measurements of the crossspectral phase, coherence and crossspectral amplitude of $\tilde{j}_\parallel$ and $\tilde{b}_r$. Additionally, we discuss the implications of these measurements. Specifically, we note that, while $\left\langle \tilde{j}_\parallel \tilde{b}_r \right\rangle_{F.S.}$ is much smaller than $\left\langle \left|\tilde{j}_\parallel\right|^2 \right\rangle_{F.S.}^{1/2} \left\langle \left|\tilde{b}_r\right|^2 \right\rangle_{F.S.}^{1/2}$ at all the minor radii where it is measured, the degree to which this may be attributed to the relative phase and coherence of $\tilde{j}_\parallel$ and $\tilde{b}_r$ depends on minor radius.

In Section 5.4, we present the decomposition of $\left\langle \tilde{j}_\parallel \tilde{b}_r \right\rangle_{F.S.}$ into contributions from different toroidal modes as estimated using the pseudospectral analysis technique. Additionally, we discuss the implications of this decomposition. In particular, we consider the relative contribution of core and reversal surface resonant tearing modes to $\left\langle \tilde{j}_\parallel \tilde{b}_r \right\rangle_{F.S.}$, which varies with

minor radius. Finally, in order check the accuracy of the pseudospectral decomposition, we use it to construct estimates of the crossspectral phase and amplitude of $\tilde{j}_{\parallel}$ and $\tilde{b}_r$ which we compare to the direct measurements of these quantities. We note that, while the pseudospectral estimates differ significantly from the direct measurements in a statistical sense, they exhibit strong qualitative similarity. This suggests that pseudospectral decomposition of $\left\langle \tilde{j}_{\parallel}\tilde{b}_r \right\rangle_{F.S.}$ is useful in understanding the contributions of core and reversal surface resonant tearing modes to $\left\langle \tilde{j}_{\parallel}\tilde{b}_r \right\rangle_{F.S.}$.

In Section 5.5, we discuss some of the implications of the measured $\left\langle \tilde{j}_{\parallel}\tilde{b}_r \right\rangle_{F.S.}$ for radial charge and particle transport in MST. We note that, while the radial charge flux due to parallel streaming, interpreted as a difference between the radial ion and electron fluxes due to parallel streaming, is small compared to the total particle flux, it is large enough to have a significant impact on the charge balance of the plasma. Consequently, the existence of other charge transport mechanisms is implied.

In Section 5.6, we discuss some of the implications for the measured $\left\langle \tilde{j}_{\parallel}\tilde{b}_r \right\rangle_{F.S.}$ to the momentum balance in MST. In particular, we note that $\left\langle \tilde{j}_{\parallel}\tilde{b}_r \right\rangle_{F.S.}$ amounts to a toroidal force density that is large enough to play a significant role in the momentum balance of MST, and, in fact, is large enough compared to the net force density on the plasma to imply the existence of other significant forces on the plasma. We consider, also, some of the implications of the radial structure of $\left\langle \tilde{j}_{\parallel}\tilde{b}_r \right\rangle_{F.S.}$, and implications for the understanding of tearing mode interactions in MST

Finally, in Section 5.6, we summarize the chapter, outlining the major conclusions.

5.2 - Measurement of $\left\langle \tilde{j}_{\parallel}\tilde{b}_r \right\rangle_{F.S.}$

Using simultaneous measurements of $\tilde{j}_{\parallel}$ and $\tilde{b}_r$ and the crossspectral analysis technique discussed in Sec. 3.9 of Ch. 3, estimates of the flux surface average product of $\tilde{j}_{\parallel}$ and $\tilde{b}_r$, $\left\langle \tilde{j}_{\parallel}\tilde{b}_r \right\rangle_{F.S.}$, have been obtained in the edge of MST. In particular, estimates of $\left\langle \tilde{j}_{\parallel}\tilde{b}_r \right\rangle_{F.S.}$, which include fluctuations in the range of frequencies 1 – 25 kHz, have been obtained both during and

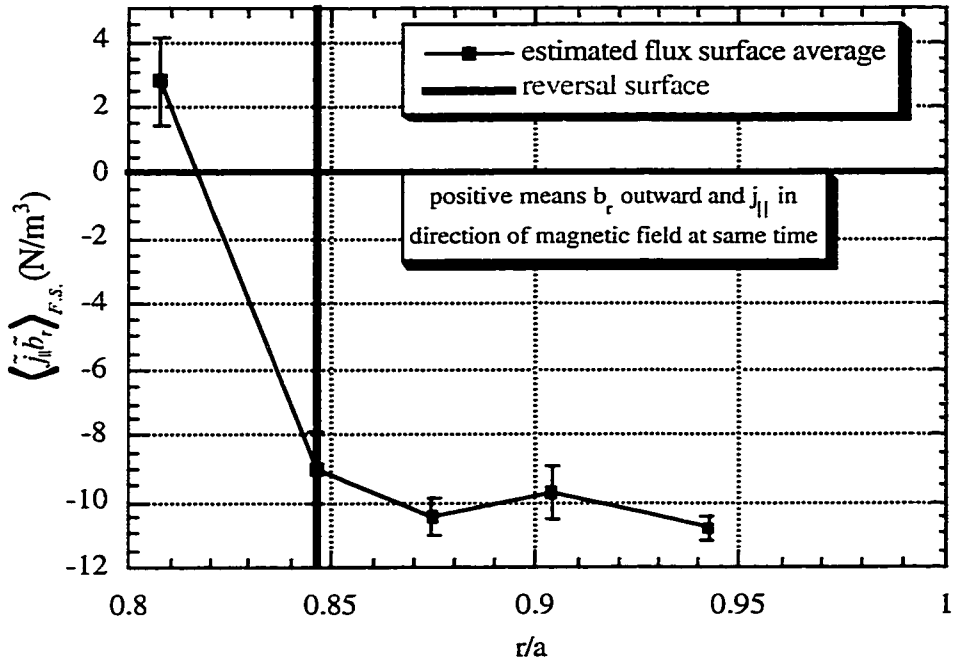

Figure 1: Flux surface average product of $\tilde{j}_{||}$ and $\tilde{b}_r$ during sawtooth crashes at 75° P, 120° T.

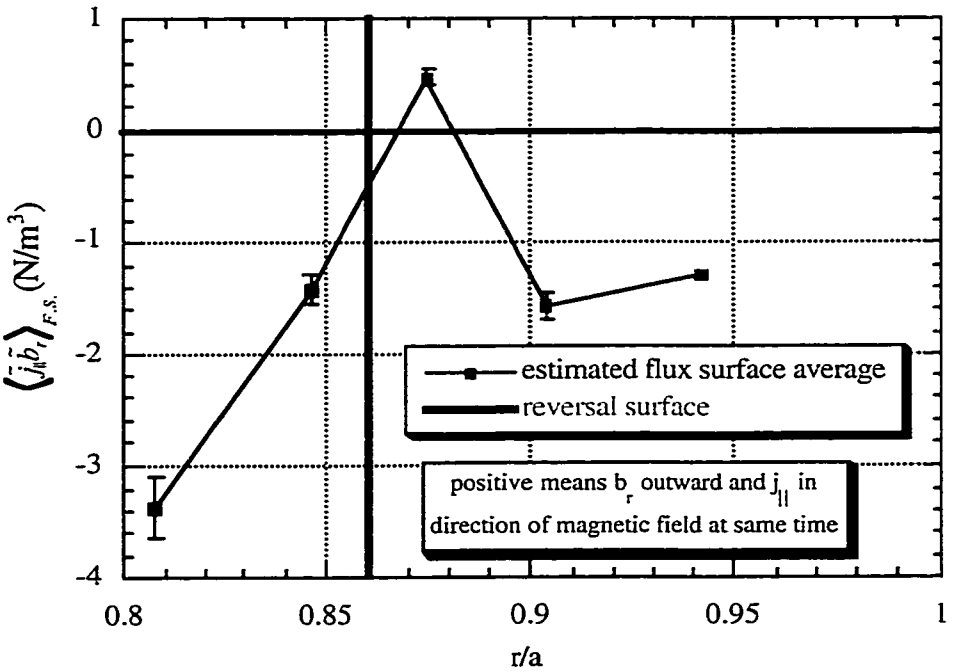

Figure 2: Flux surface average product of $\tilde{j}_{||}$ and $\tilde{b}_r$ between sawtooth crashes at 75° P, 120° T.

between sawtooth crashes, using measurements at each of two different poloidal and toroidal locations (-15° P, 330° T and 75° P, 120° T). Figures showing radial profiles of the measured $\left\langle \tilde{j}_{\|}\tilde{b}_r \right\rangle_{F.S.}$ for each of the four cases are included for reference in Appendix B of this dissertation. Here, we discuss several important features of these measurements. Figures 1 and 2, which show $\left\langle \tilde{j}_{\|}\tilde{b}_r \right\rangle_{F.S.}$ measured at 75° P, 120° T during and between sawtooth crashes, respectively, illustrate several common features of these of these measurements. The product $\left\langle \tilde{j}_{\|}\tilde{b}_r \right\rangle_{F.S.}$ is non-vanishing, to within statistical uncertainty. It ranges between 0 and ~ 10 N/m^{-3} in magnitude, overall, although its exact range is different in each of the four cases. It is negative outwards of the reversal surface. During sawtooth crashes, it is positive inwards of the reversal surface, while between sawtooth crashes, it is positive near the reversal surface and negative inwards of the reversal surface. The sign convention used in Figures 1 and 2 is consistent with $\tilde{b}_r = \tilde{\vec{b}} \cdot \hat{r}$ and $\tilde{j}_{\|} = \tilde{\vec{j}} \cdot \hat{b}_0$, where $\hat{r}$ is the minor radial unit vector, $\tilde{\vec{b}}$ is the magnetic field fluctuation vector, $\hat{b}_0$ is the equilibrium magnetic field unit vector and $\tilde{\vec{j}}$ is the current density fluctuation vector.

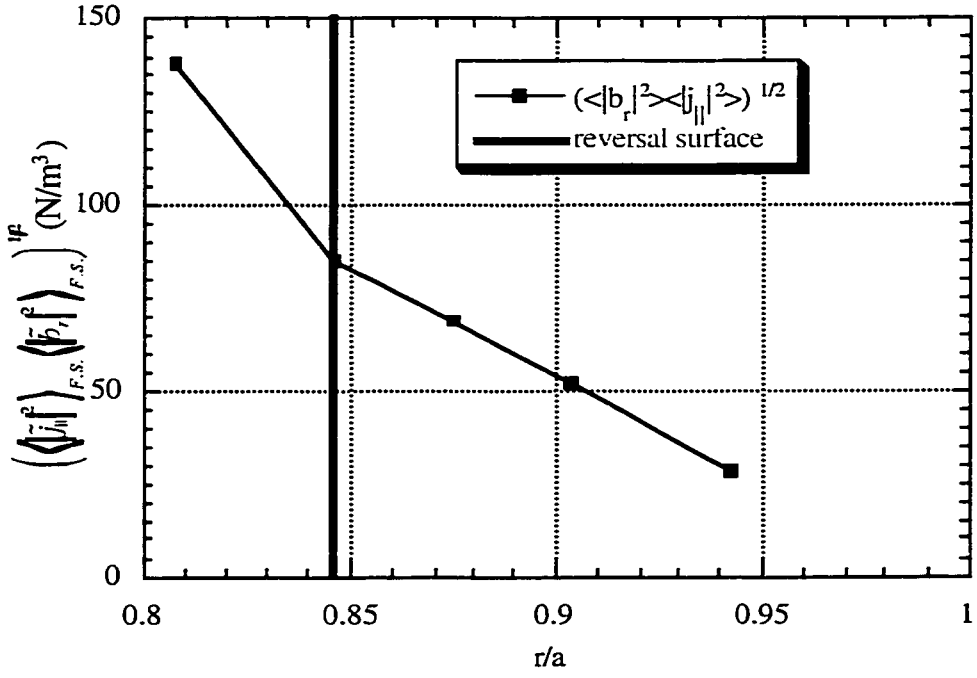

Figure 3: Maximum possible transport (given by product of flux surface r. m. s. values of $\tilde{j}_{\|}$ and $\tilde{b}_r$) during sawtooth crashes at 75° P, 120° T.

The product $\langle \tilde{j}_{\parallel}\tilde{b}_r \rangle_{F.S.}$ may be compared to the maximum possible value it is permitted to have by the measured $\tilde{j}_{\parallel}$ and $\tilde{b}_r$. This upper bound is given by the product of the flux surface root mean square values of $\tilde{j}_{\parallel}$ and $\tilde{b}_r$, which ranges in magnitude between ~ 3 N/m^{-3} and ~ 140 N/m^{-3} depending on position of measurement. The product $\langle \tilde{j}_{\parallel}\tilde{b}_r \rangle_{F.S.}$ is much smaller than this upper bound, as is illustrated by comparing, for example, comparing $\langle \tilde{j}_{\parallel}\tilde{b}_r \rangle_{F.S.}$ measured at 75° P, 120° T during sawtooth crashes (Fig. 1) to $\langle |\tilde{j}_{\parallel}|^2 \rangle_{F.S.}^{1/2} \langle |\tilde{b}_r|^2 \rangle_{F.S.}^{1/2}$ measured simultaneously at the same location (Fig. 3). Figures showing radial profiles of the measured estimates of $\langle |\tilde{j}_{\parallel}|^2 \rangle_{F.S.}^{1/2} \langle |\tilde{b}_r|^2 \rangle_{F.S.}^{1/2}$ corresponding to the four cases in which $\langle \tilde{j}_{\parallel}\tilde{b}_r \rangle_{F.S.}$ is measured are included for reference in Appendix B of this dissertation.

An important consideration arises in interpreting the measurements of $\langle \tilde{j}_{\parallel}\tilde{b}_r \rangle_{F.S.}$ reported here. As an estimate of a flux surface average, the measured $\langle \tilde{j}_{\parallel}\tilde{b}_r \rangle_{F.S.}$ should be independent of the poloidal angle at which $\tilde{j}_{\parallel}$ and $\tilde{b}_r$ are measured. It is clear, however, that this is not the case. This is illustrated by, for example, comparing $\langle \tilde{j}_{\parallel}\tilde{b}_r \rangle_{F.S.}$ during sawtooth crashes at -15° P (Fig. 4) and 75° P (Fig. 1). It is worth noting, however, that, while there appears to be some

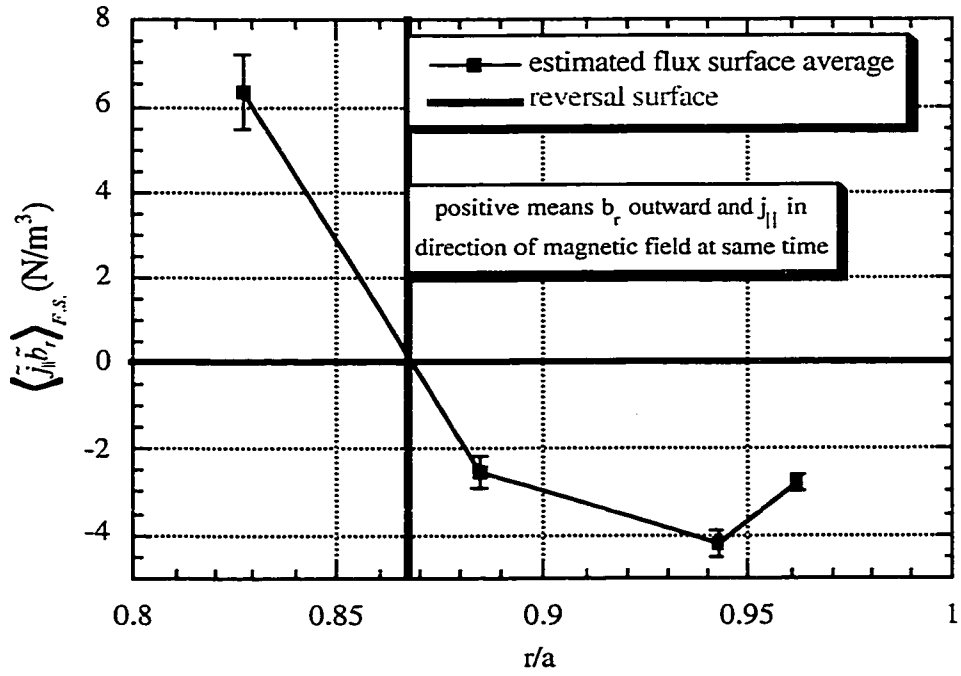

Figure 4: Flux surface average product of $\tilde{j}_{\parallel}$ and $\tilde{b}_r$ during sawtooth crashes at -15° P, 330° T.

variation in its magnitude, the radial structure of $\langle \tilde{j}_{\parallel} \tilde{b}_r \rangle_{F.S.}$ appears to be roughly independent of poloidal angle. As discussed in Sec. 3.9 of Ch. 3, this dependence on poloidal angle results from imperfect poloidal symmetry in MST's equilibrium. Because of MST's poloidal asymmetry, the estimated flux surface averages reported here may, perhaps, be more accurately viewed as estimated toroidal averages. Ultimately, the poloidal dependence of the measured estimate of $\langle \tilde{j}_{\parallel} \tilde{b}_r \rangle_{F.S.}$ is not expected to qualitatively change any of the conclusions presented here.

5.3 - Coherence and Phase Relationship of $\tilde{j}_{\parallel}$ and $\tilde{b}_r$

In addition to providing estimates of the flux surface average of $\tilde{j}_{\parallel}$ and $\tilde{b}_r$, crossspectral analysis also provides a tool for probing the physics underlying its value. In particular, it allows us to determine to what extent the value of $\langle \tilde{j}_{\parallel} \tilde{b}_r \rangle_{F.S.}$ is influenced by one of three possible factors: the phase relation between $\tilde{j}_{\parallel}$ and $\tilde{b}_r$, the degree of coherence of $\tilde{j}_{\parallel}$ and $\tilde{b}_r$ or the amplitudes of $\tilde{j}_{\parallel}$ and $\tilde{b}_r$. Using this tool, we determine that the cause of the small magnitude of

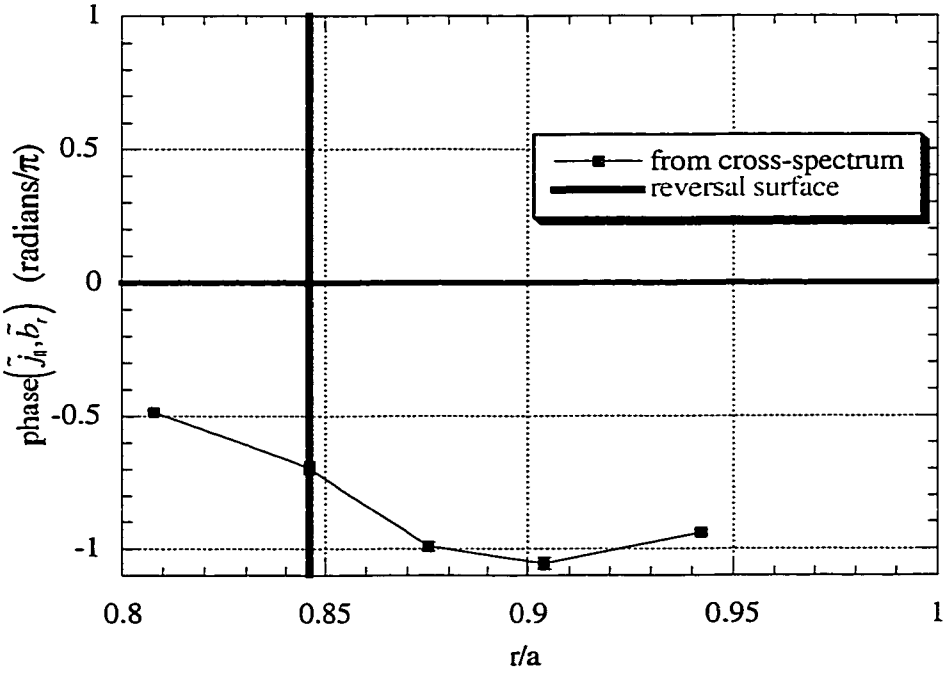

Figure 5: Crossspectral phase between $\tilde{j}_{\parallel}$ and $\tilde{b}_r$ during sawtooth crashes at 75° P, 120° T.

$\left\langle \tilde{j}_{\|}\tilde{b}_r \right\rangle_{F.S.}$ relative to $\left\langle \left|\tilde{j}_{\|}\right|^2 \right\rangle_{F.S.}^{1/2} \left\langle \left|\tilde{b}_r\right|^2 \right\rangle_{F.S.}^{1/2}$, varies with minor radius. In Appendix B of this dissertation, for reference purposes, we include figures showing edge radial profiles of the relative phase, coherence and crossspectral amplitude, or coherent part, of $\tilde{j}_{\|}$ and $\tilde{b}_r$ corresponding to each of the four cases in which we have obtained estimates of $\left\langle \tilde{j}_{\|}\tilde{b}_r \right\rangle_{F.S.}$: between and during sawtooth crashes, at two different poloidal and toroidal locations each (-15° P, 330° T and 75° P, 120° T). Here, we discuss the causes underlying the value $\left\langle \tilde{j}_{\|}\tilde{b}_r \right\rangle_{F.S.}$.

Measurements of the phase of $\tilde{j}_{\|}$ and $\tilde{b}_r$ indicate that, between and during sawtooth crashes, they are roughly 180° out of phase at minor radii outwards of the reversal surface ($r/a > \sim 0.85$). This is illustrated by, for instance, the edge radial profile of the phase of $\tilde{j}_{\|}$ and $\tilde{b}_r$, phase$\left(\tilde{j}_{\|},\tilde{b}_r\right)$, at 75° P, 120° T during sawtooth crashes, which is shown in Figure 5. Since the magnitude of $\left\langle \tilde{j}_{\|}\tilde{b}_r \right\rangle_{F.S.}$ is proportional to $\left|\cos\left(\text{phase}\left(\tilde{j}_{\|},\tilde{b}_r\right)\right)\right|$, the small magnitude of $\left\langle \tilde{j}_{\|}\tilde{b}_r \right\rangle_{F.S.}$ compared to $\left\langle \left|\tilde{j}_{\|}\right|^2 \right\rangle_{F.S.}^{1/2} \left\langle \left|\tilde{b}_r\right|^2 \right\rangle_{F.S.}^{1/2}$ in this range of minor radii is due to the imperfect coherence between $\tilde{j}_{\|}$ and $\tilde{b}_r$ rather than their relative phase. On the other hand, near the reversal surface and inwards of it, $\tilde{j}_{\|}$ and $\tilde{b}_r$ are roughly 90° degrees out of phase (Fig. 5). Thus, their relative

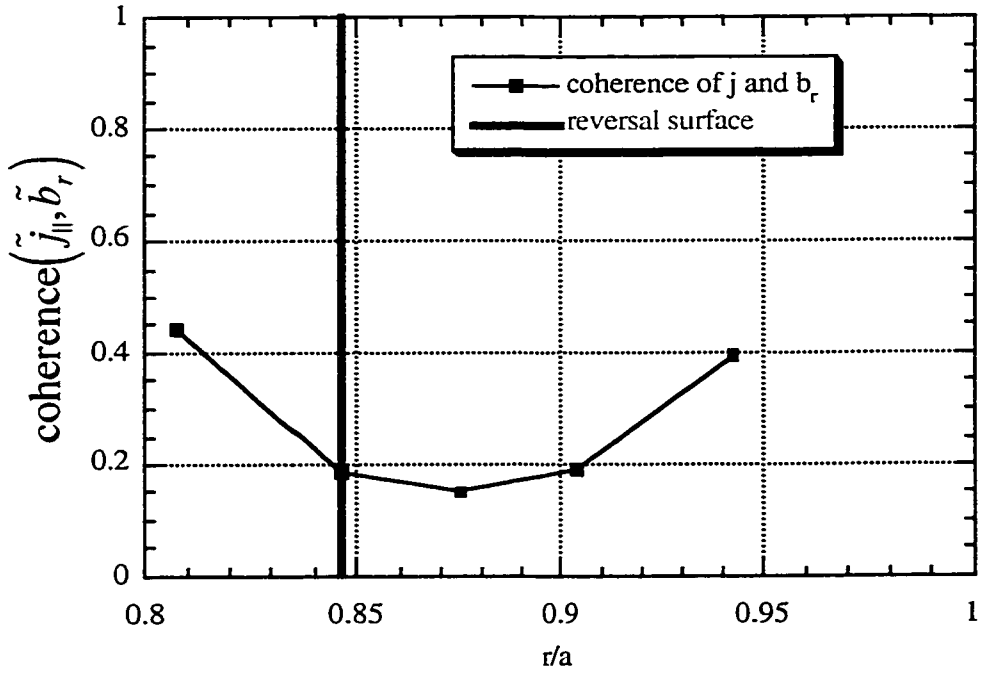

Figure 6: Crossspectral coherence of $\tilde{j}_{\|}$ and $\tilde{b}_r$ during sawtooth crashes at 75° P, 120° T.

phase contributes to the small magnitude of $\langle \tilde{j}_{\parallel}\tilde{b}_r \rangle_{F.S.}$ compared to $\langle |\tilde{j}_{\parallel}|^2 \rangle_{F.S.}^{1/2} \langle |\tilde{b}_r|^2 \rangle_{F.S.}^{1/2}$. Imperfect coherence between $\tilde{j}_{\parallel}$ and $\tilde{b}_r$ also contributes in this region of minor radius. This is illustrated by, for instance, the edge radial profile of the coherence of $\tilde{j}_{\parallel}$ and $\tilde{b}_r$, coherence$\left(\tilde{j}_{\parallel},\tilde{b}_r\right)$, at 75° P, 120° T during sawtooth crashes, which is shown in Figure 6. Measurements of coherence$\left(\tilde{j}_{\parallel},\tilde{b}_r\right)$ corresponding to each of the four cases in which $\langle \tilde{j}_{\parallel}\tilde{b}_r \rangle_{F.S.}$ is measured, which include those shown in Figure 6, indicate that in both regions of minor radius, the coherent part of $\tilde{j}_{\parallel}$ and $\tilde{b}_r$ is always at least a factor of 2 smaller than $\langle |\tilde{j}_{\parallel}|^2 \rangle_{F.S.}^{1/2} \langle |\tilde{b}_r|^2 \rangle_{F.S.}^{1/2}$, and often much smaller.

5.4 - Decomposition of $\langle \tilde{j}_{\parallel}\tilde{b}_r \rangle_{F.S.}$ in Terms of Toroidal Modes

Another tool that provides insight into the physical factors which determine $\langle \tilde{j}_{\parallel}\tilde{b}_r \rangle_{F.S.}$ is pseudospectral analysis (discussed in Sec. 3.11 of Ch. 3). Both $\tilde{j}_{\parallel}$ and $\tilde{b}_r$ are composed of toroidal Fourier modes. The toroidal modes of $\tilde{j}_{\parallel}$ and $\tilde{b}_r$ with mode number n, $\tilde{j}_{\parallel,n}$ and $\tilde{b}_{r,n}$, contribute an amount to $\langle \tilde{j}_{\parallel}\tilde{b}_r \rangle_{F.S.}$ given by the their flux surface average product, $\langle \tilde{j}_{\parallel,n}\tilde{b}_{r,n} \rangle_{F.S.}$.

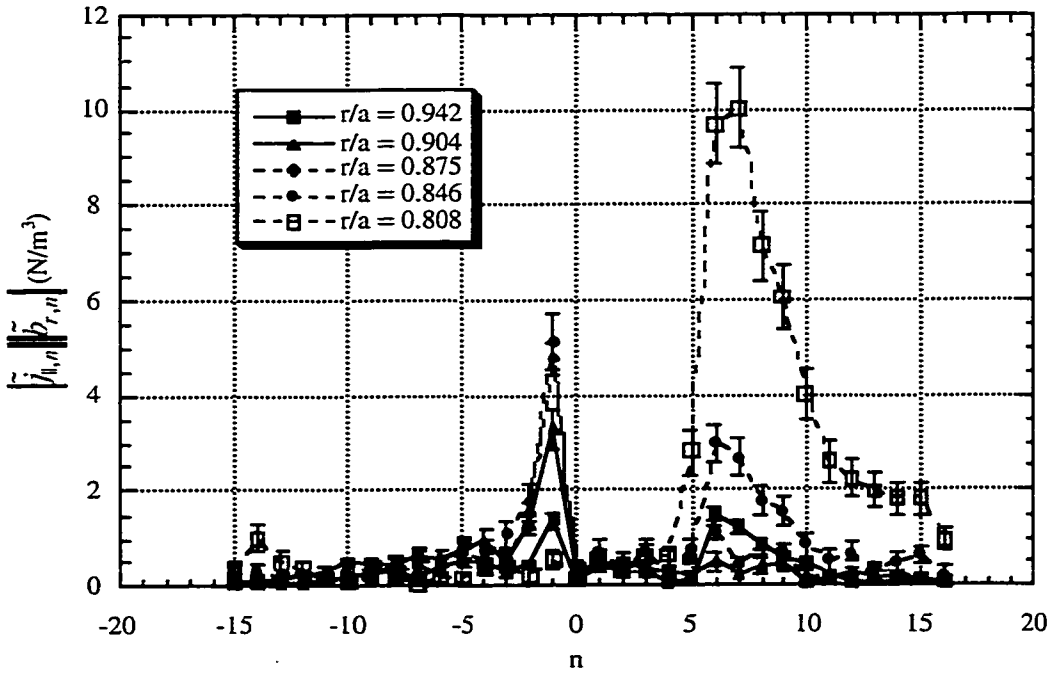

Figure 7: Combined magnitude of $\tilde{j}_{\parallel}$ and $\tilde{b}_r$ for each toroidal mode. Measured during sawtooth crashes at 75° P, 120° T. Measured with pseudospectral technique using toroidal magnetic field fluctuations at the wall as the reference fluctuation.

Pseudospectral analysis provides estimates of these products. Additionally, pseudospectral analysis provides estimates of the spatial phase between $\tilde{j}_{\parallel,n}$ and $\tilde{b}_{r,n}$, phase$\left(\tilde{j}_{\parallel,n},\tilde{b}_{r,n}\right)$. Thus, it allows us to determine the degree to which $\left\langle \tilde{j}_{\parallel,n}\tilde{b}_{r,n}\right\rangle_{F.S.}$ is influenced by phase$\left(\tilde{j}_{\parallel,n},\tilde{b}_{r,n}\right)$ and the magnitudes of $\tilde{j}_{\parallel,n}$ and $\tilde{b}_{r,n}$, $\left|\tilde{j}_{\parallel,n}\right|$ and $\left|\tilde{b}_{r,n}\right|$, since $\left\langle \tilde{j}_{\parallel,n}\tilde{b}_{r,n}\right\rangle_{F.S.} = \left|\tilde{j}_{\parallel,n}\right|\left|\tilde{b}_{r,n}\right|\cos\left(\text{phase}\left(\tilde{j}_{\parallel,n},\tilde{b}_{r,n}\right)\right)$. Pseudospectral decomposition of $\left\langle \tilde{j}_{\parallel}\tilde{b}_{r}\right\rangle_{F.S.}$ has been performed using toroidal magnetic field fluctuations at the wall as the reference quantity for each of the four cases in which $\left\langle \tilde{j}_{\parallel}\tilde{b}_{r}\right\rangle_{F.S.}$ has been measured: between and during sawtooth crashes, at two different poloidal and toroidal locations each (-15° P, 330° T and 75° P, 120° T). Appendix B of this dissertation contains, for reference purposes, an exhaustive set of figures showing the results of this decomposition. In particular, it contains figures showing the measurements of the combined magnitude $\left|\tilde{j}_{\parallel,n}\right|\left|\tilde{b}_{r,n}\right|$, as well as figures showing phase$\left(\tilde{j}_{\parallel,n},\tilde{b}_{r,n}\right)$, for a broad range of toroidal modes obtained at several probe insertion depths in the plasma for each of the four cases. In addition, it contains edge radial profiles of $\left|\tilde{j}_{\parallel,n}\right|\left|\tilde{b}_{r,n}\right|$ and phase$\left(\tilde{j}_{\parallel,n},\tilde{b}_{r,n}\right)$ for selected core resonant ($n = 5 - 10$) and reversal

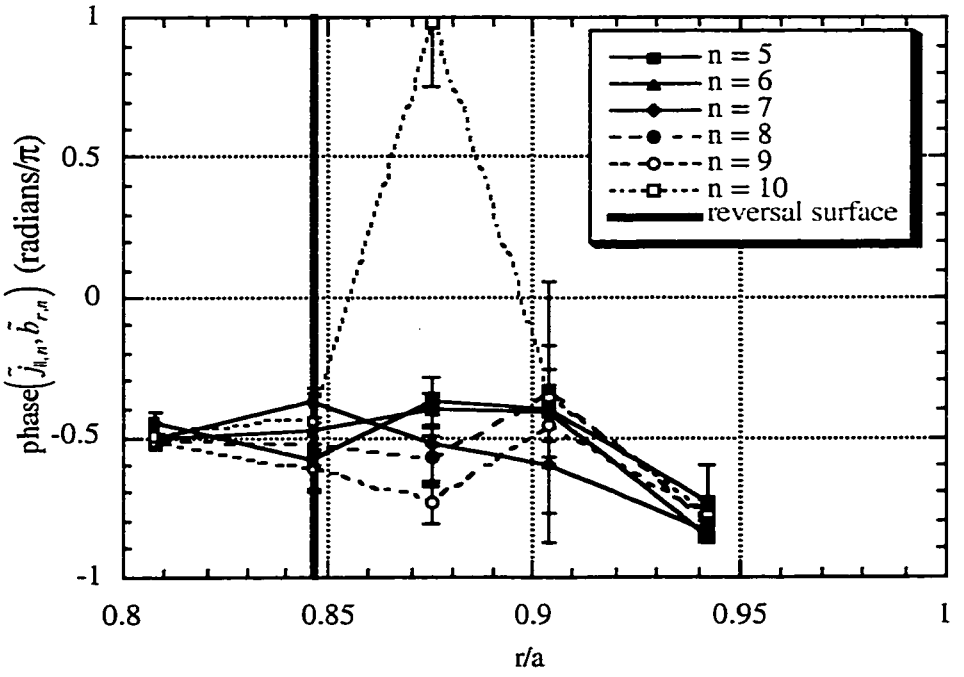

Figure 8: Radial profiles of the phase between $\tilde{j}_{\parallel}$ and $\tilde{b}_{r}$ for selected core resonant toroidal modes. Measured during sawtooth crashes at 75° P, 120° T. Measured with pseudospectral technique using toroidal magnetic field fluctuations at the wall as the reference fluctuation.

surface resonant ($n = -3 - -1$) modes for each of the four cases. Here, we discuss several key results of this decomposition. Additionally, we consider its accuracy.

During and between sawtooth crashes, at minor radii inwards of the reversal surface, the crossspectral amplitude, or coherent part, of $\tilde{j}_{\|}$ and $\tilde{b}_r$, is dominated by core resonant modes with toroidal mode numbers approximately in the range $n = 5 - 10$. On the other hand, at minor radii outwards of the reversal surface, it exhibits a strong contribution from the $n = -1$ reversal surface resonant mode and, to some extent, other reversal surface resonant toroidal modes with modes numbers $n \leq -2$. This is illustrated by, for example, measurements of $\left|\tilde{j}_{\|,n}\right|\left|\tilde{b}_{r,n}\right|$, which is an indication of the contribution of the toroidal mode n to the coherent part of of $\tilde{j}_{\|}$ and $\tilde{b}_r$, at 75° P, 120° T during sawtooth crashes (Fig. 7). For this case, the reversal surface is at $r/a = 0.846$.

For core resonant modes, both during and between sawtooth crashes, $\text{phase}\left(\tilde{j}_{\|,n}, \tilde{b}_{r,n}\right)$ is roughly $-\pi/2$, for the most part. This is illustrated by, for example, measurements of $\text{phase}\left(\tilde{j}_{\|,n}, \tilde{b}_{r,n}\right)$ for modes $n = 5 - 10$ at 75° P, 120° T during sawtooth crashes (Fig. 8). Since

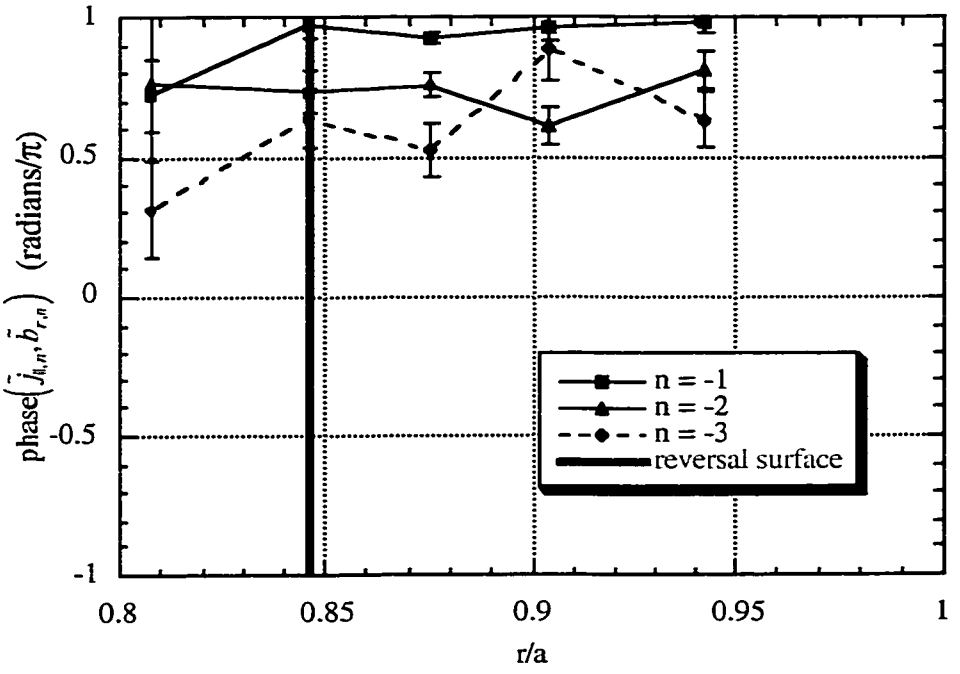

Figure 9: Radial profiles of the phase between $\tilde{j}_{\|}$ and $\tilde{b}_r$ for selected reversal surface resonant toroidal modes. Measured during sawtooth crashes at 75° P, 120° T. Measured with pseudospectral technique using toroidal magnetic field fluctuations at the wall as the reference fluctuation.

the coherent part of $\tilde{j}_{\|}$ and $\tilde{b}_r$ is dominated by such modes at minor radii inwards of the reversal surface, this is consistent with the measured value of roughly -π/2 for the overall crossspectral phase between $\tilde{j}_{\|}$ and $\tilde{b}_r$ in this region (Fig. 5).

On the other hand, both during and between sawtooth crashes, measured values of $\text{phase}\left(\tilde{j}_{\|,n}, \tilde{b}_{r,n}\right)$ for reversal surface resonant modes range between -π to π and are usually very different from the value of -π/2 seen for core resonant modes. For instance, measurements of $\text{phase}\left(\tilde{j}_{\|,n}, \tilde{b}_{r,n}\right)$ for modes $n = -3 - -1$ at 75° P, 120° T during sawtooth crashes (Fig. 9) show values roughly in the range π/2 to π. Since the reversal surface resonant modes contribute strongly to the coherent part of $\tilde{j}_{\|}$ and $\tilde{b}_r$ at minor radii outwards of the reversal surface, the value of the overall crossspectral phase between $\tilde{j}_{\|}$ and $\tilde{b}_r$ should be different from -π/2 in this region, as, in fact, it is (Fig. 5).

Because the pseudospectral analysis technique only estimates true spectral analysis, it is important to assess its accuracy in some way. Unfortunately, since direct measurements of the

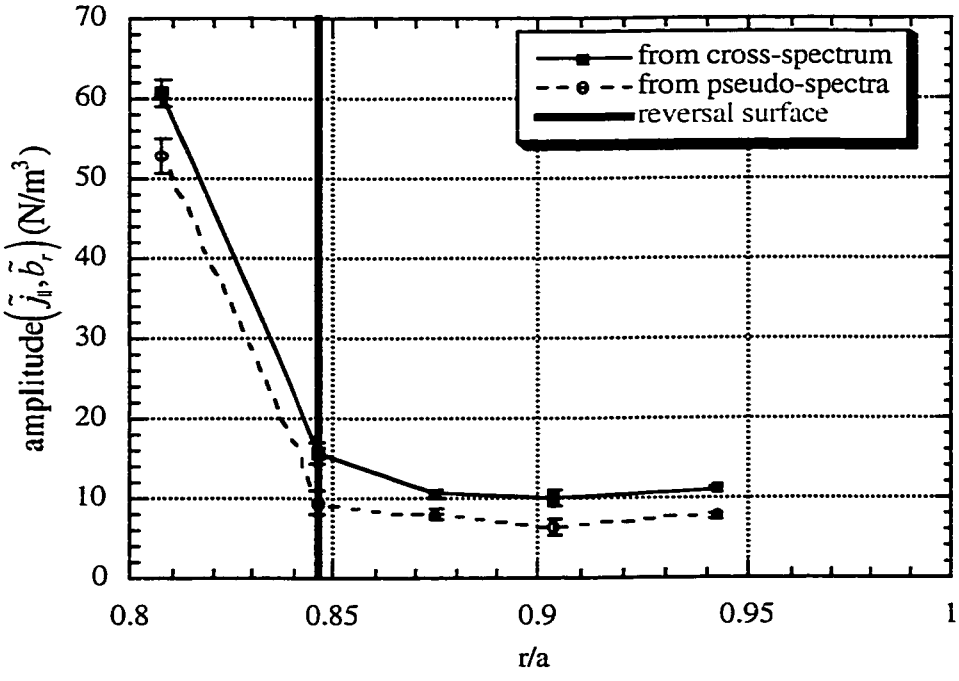

Figure 10: Comparison of direct measurement with pseudospectral estimate of crossspectral magnitude of $\tilde{j}_{\|}$ and $\tilde{b}_r$ during sawtooth crashes at 75° P, 120° T.

toroidal spectra of $\tilde{j}_{\|}$ and $\tilde{b}_r$ are not available for comparison, indirect indicators of its accuracy must be relied upon. One such indicator, which is of particular relevance to the use of pseudospectral analysis to decompose $\langle \tilde{j}_{\|}\tilde{b}_r \rangle_{F.S.}$, is to construct estimates of the crossspectral amplitude of $\tilde{j}_{\|}$ and $\tilde{b}_r$, as well as the crossspectral phase between them, which may be compared to the direct measurements which were discussed in Sec 5.3 above.

The measurements of $\langle \tilde{j}_{\|,n}\tilde{b}_{r,n} \rangle_{F.S.}$ obtained from pseudospectral analysis can be summed over toroidal mode number, n, while taking into account the measured phase, $\text{phase}\left(\tilde{j}_{\|,n}, \tilde{b}_{r,n}\right)$, to produce estimates of the crossspectral amplitude of $\tilde{j}_{\|}$ and $\tilde{b}_r$ and the crossspectral phase between them. Appendix B of this dissertation includes, for reference purposes, figures comparing the pseudospectral estimates of the crossspectral amplitude of $\tilde{j}_{\|}$ and $\tilde{b}_r$with the direct measurements for four cases in which $\langle \tilde{j}_{\|}\tilde{b}_r \rangle_{F.S.}$ is measured: both between and during sawtooth crashes, at two different poloidal and toroidal locations each (-15° P, 330° T and 75° P, 120° T). Additionally, it include figures comparing the pseudospectral estimates of $\text{phase}\left(\tilde{j}_{\|}, \tilde{b}_r\right)$ with the

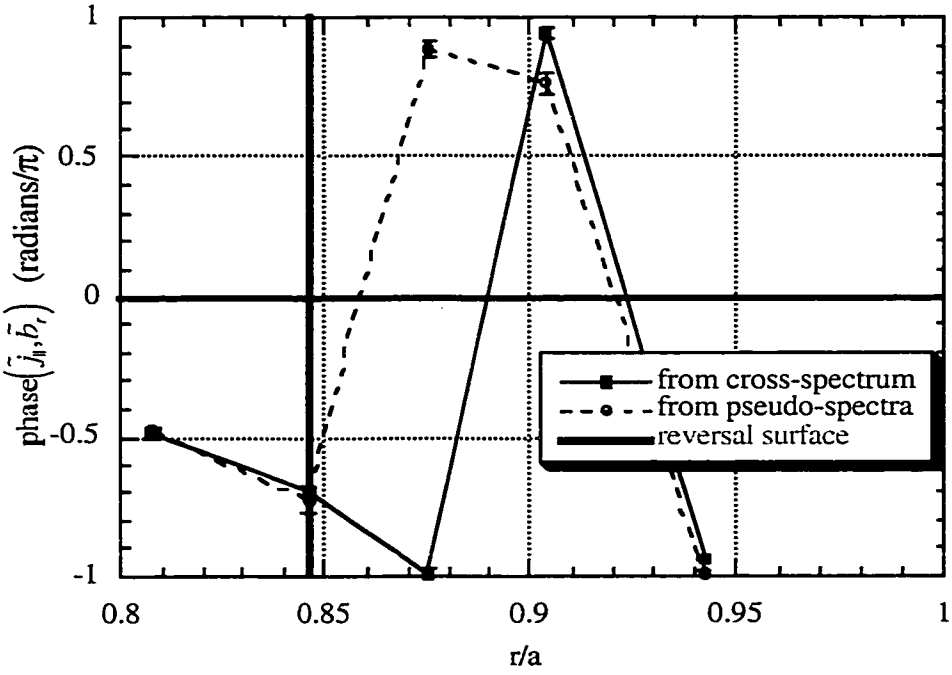

Figure 11: Comparison of direct measurement with pseudospectral estimate of crossspectral phase between $\tilde{j}_{\|}$ and $\tilde{b}_r$ during sawtooth crashes at 75° P, 120° T.

direct measurements for the same four cases. Here, we note several key results of this comparison.

Figure 10 compares the pseudospectral estimate with the direct measurement of the crossspectral amplitude of $\tilde{j}_{\parallel}$ and $\tilde{b}_r$ for the case in which $\langle \tilde{j}_{\parallel}\tilde{b}_r \rangle_{F.S.}$ is measured during sawtooth crashes at 75° P, 120° T. Figure 11 compares the pseudospectral estimate and the direct measurement for phase$\left(\tilde{j}_{\parallel},\tilde{b}_r\right)$ for same case. Taking into account the statistical uncertainties of the direct measurements and the pseudospectral estimates, it can be seen that they frequently differ significantly in a statistical sense. On the other hand, the pseudospectral estimate are qualitatively very similar to the direct measurement. Such comparison for the other three cases in which $\langle \tilde{j}_{\parallel}\tilde{b}_r \rangle_{F.S.}$ is measured yield the same results. This suggests that pseudospectral decomposition of $\langle \tilde{j}_{\parallel}\tilde{b}_r \rangle_{F.S.}$ may, in fact, be useful in understanding the contributions of core and reversal surface resonant tearing modes to $\langle \tilde{j}_{\parallel}\tilde{b}_r \rangle_{F.S.}$, as has been assumed in the discussion above.

5.5 - Charge and Particle Transport due to Parallel Streaming of Particles

The measurements of $\langle \tilde{j}_{\parallel}\tilde{b}_r \rangle_{F.S.}$ discussed in Section 5.2 above can be used to obtain estimates of the radial charge transport, or radial current density, due to streaming of charge carriers along magnetic field lines. As discussed in Sec. 2.7 of Ch. 2, the radial charge transport, or radial charge flux, due to parallel streaming is given by $\langle \tilde{j}_{\parallel}\tilde{b}_r \rangle_{F.S.}/B_0$, where B_0 is the equilibrium magnetic field at the magnetic flux surface at which $\langle \tilde{j}_{\parallel}\tilde{b}_r \rangle_{F.S.}$ is measured. In addition the measurements of $\langle \tilde{j}_{\parallel}\tilde{b}_r \rangle_{F.S.}$ can be used to obtain estimates of the difference between the radial ion and electron particle radial particle fluxes due to parallel particle streaming. In MST plasmas, $\tilde{j}_{\parallel} = e(\tilde{\Gamma}_{\parallel,i} - \tilde{\Gamma}_{\parallel,e})$, where $\tilde{\Gamma}_{\parallel,i}$ and $\tilde{\Gamma}_{\parallel,e}$ are the parallel ion and electron particle fluxes, respectively. Consequently, the difference in the radial particle fluxes due to parallel streaming is given by $\langle \tilde{j}_{\parallel}\tilde{b}_r \rangle_{F.S.}/eB_0$. Appendix B of this dissertation includes, for reference purposes, figures showing radial profiles of both $\langle \tilde{j}_{\parallel}\tilde{b}_r \rangle_{F.S.}/B_0$ and $\langle \tilde{j}_{\parallel}\tilde{b}_r \rangle_{F.S.}/eB_0$ in the plasma

edge for the four cases in which $\left\langle \tilde{j}_{\parallel}\tilde{b}_r \right\rangle_{F.S.}$ is measured: between and during sawtooth crashes at two different poloidal and toroidal locations each: -15° P, 330° T and 75° P, 120° T. Here, we discuss several important results of these measurements, as well as discussing some of their implications for the charge and particle balances in MST.

During sawtooth crashes, $\left\langle \tilde{j}_{\parallel}\tilde{b}_r \right\rangle_{F.S.}/B_0$ ranges from ~ +50 Amps/m^2 to ~ -150 Amps/m^2 and its magnitude depends on radial position and the poloidal angle at which it is measured. In terms of a difference in particle fluxes, this range is from ~ +3 x 10^{20} particles m^{-2} sec^{-1} to ~ -10 x 10^{20} particles m^{-2} sec^{-1}. At both -15° P and 75° P, it is positive inwards of the reversal surface and negative outwards of the reversal surface. This is illustrated by, for example, $\left\langle \tilde{j}_{\parallel}\tilde{b}_r \right\rangle_{F.S.}/B_0$ measured during sawtooth crashes at 75° P, 120° T (Fig. 12). Given the sign convention used (see Sec. 5.2, above), this indicates that positive charge pinches, or flows, towards the reversal surface on average during sawtooth crashes.

The radial structure of $\left\langle \tilde{j}_{\parallel}\tilde{b}_r \right\rangle_{F.S.}/B_0$ between sawtooth crashes is slightly more

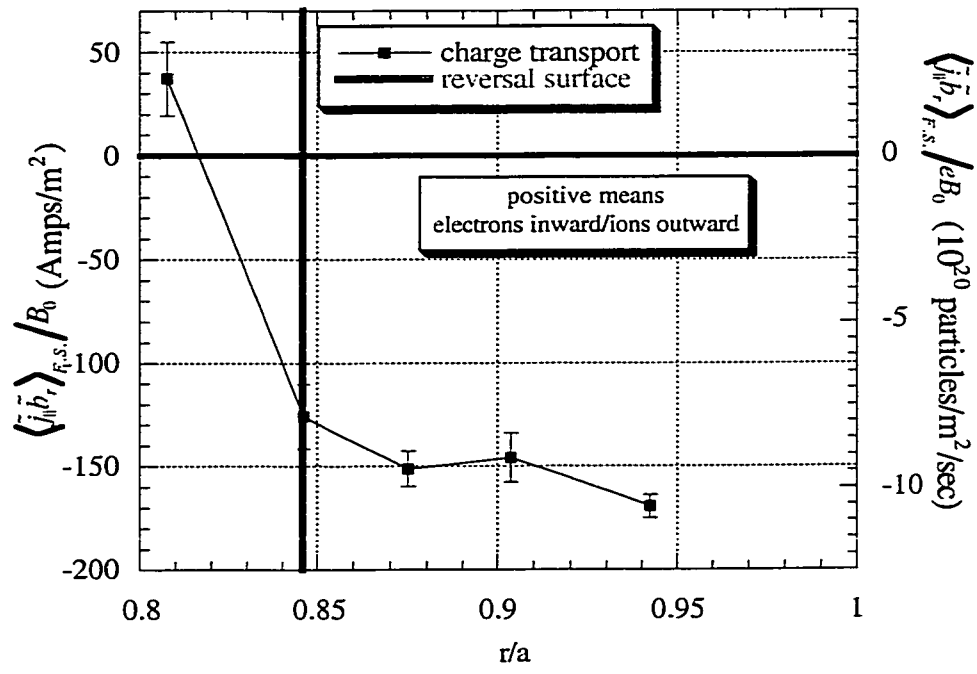

Figure 12: Radial charge flux (and difference between ion and electron particle fluxes) implied by flux surface average product of $\tilde{j}_{\parallel}$ and $\tilde{b}_r$. Measured during sawtooth crashes at 75° P, 120° T.

complicated. Its value ranges from ~ +10 Amps/m^2 to ~ -120 Amps/m^2 and depends on radial position and poloidal angle of measurement. In terms of a difference in particle fluxes, this range is from ~ +1 x 10^{20} particles m^{-2} sec^{-1} to ~ -3 x 10^{20} particles m^{-2} sec^{-1}. At both -15° P and 75° P, the radial charge flux is positive near the reversal surface and negative farther from the reversal surface. This is illustrated by, for example, $\left\langle \tilde{j}_{\|}\tilde{b}_r \right\rangle_{F.S.}/B_0$ measured between sawtooth crashes at 75° P, 120° T (Fig. 13). Such a radial structure indicates that positive charge pinches, or flows, toward a position just outwards of the reversal surface while negative charge pinches, or flows, toward a position just inwards of the reversal surface.

Interpreted as a difference between ion and electron radial particle fluxes, the radial charge transport, which can have a magnitude as large as 10 x 10^{20} particles m^{-2} sec^{-1}, is small on the scale of total particle transport. Making use of line-averaged ionization rates and electron density (obtained from line-averaged H_α emission and a $C0_2$ interferometer, respectively) and making some reasonable assumptions about the ionization and density profiles, the total particle flux is estimated to be ~ 25 x 10^{20} particles m^{-2} sec^{-1} between sawtooth crashes and

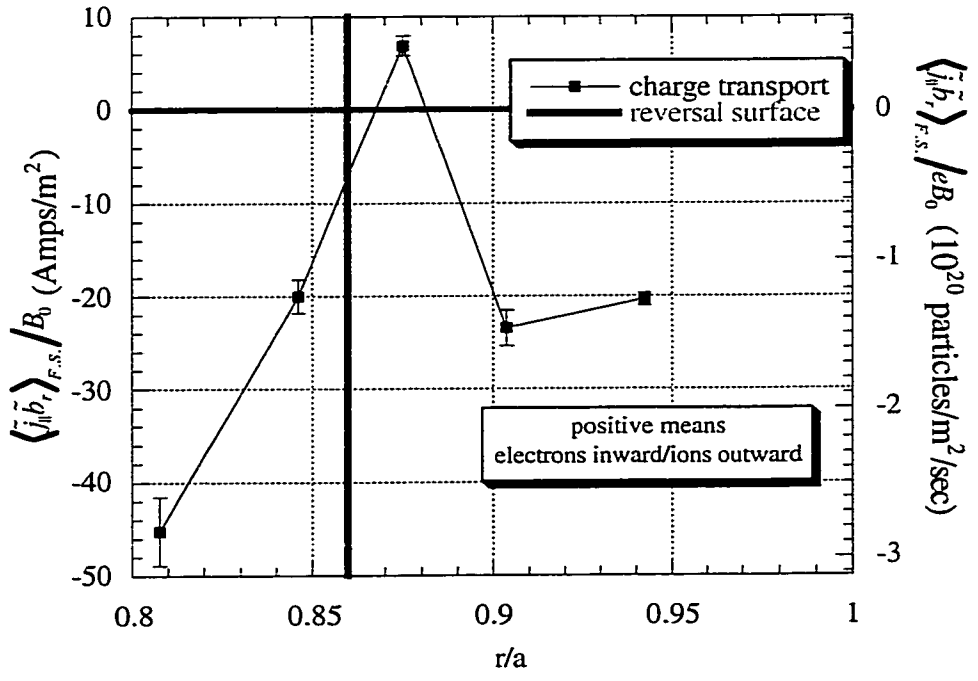

Figure 13: Radial charge flux (and difference between ion and electron particle fluxes) implied by flux surface average product of $\tilde{j}_{\|}$ and $\tilde{b}_r$. Measured between sawtooth crashes at 75° P, 120° T.

~ 40 x 10^{20} particles m^{-2} sec^{-1} during crashes. (The profiles assumptions here are based on a much more precise treatment of the particle balance in MST given by Lanier.[1,2] Also, these estimates are similar to much more precise measurements made by Lanier for similar plasmas.)

Although the radial charge flux measurements discussed here represent a small difference between ion and electron radial particle flux when compared to the total particle flux, they are very significant in terms of the charge balance in MST. The measured radial charge flux due to parallel streaming, $\left\langle \tilde{j}_{\parallel} \tilde{b}_r \right\rangle_{F.S.} / B_0$, can range as high as ~ 150 Amps m^{-2} in magnitude in edge of MST. Such a charge flux must be balanced by other charge transport mechanisms. If a charge flux of this magnitude existed across the entire minor radius, it would violate the quasi-neutrality constraint on very short time scales if not very precisely balanced by other charge transport mechanisms. In other words, an unbalanced global radial charge flux of 150 Amps m^{-2} would very rapidly produce a radial electric field which was physically significant on a global scale. For instance, using Gauss' law, it can be seen that such a radial charge flux would produce a globally significant flux surface average $E_r \sim (T_e/e)/a$, in $\varepsilon_0((T_e/e)/a)/(150 \text{ Amps } m^{-2}) = 6 \times 10^{-11}$ sec (using a core electron temperature of $T_e \sim 500$ eV). Even if the charge flux existed, unbalanced, only over the region of measurement, which extends ~ 10 cm and where $T_e \sim 100$ eV, a locally significant flux surface average electric field would be produced on same time scale.

It must be noted that charge transport due parallel streaming of charge carriers has been previously measured on MST by Shen, et al.,[3,4] with results that are consistent with those presented here. In particular, although Shen's measurements differ from ours in significant ways, we argue that these differences do not, in fact, represent an inconsistency, but, rather, may be explained by differences in the character of the plasmas used, which, in turn, result in differences in what is actually measured.

Shen's measurements made use of the same technique as that used here, although there were minor differences in signal processing, as well as in the diagnostics used to make the

measurements of the parallel current density and radial magnetic field. He saw a vanishing charge transport to within experimental uncertainty for all $r/a < 0.8$ and was able to place an upper bound on its magnitude (cast in terms of a difference of particle transports) of $\sim 0.5 \times 10^{20}$ particles m^{-2} sec^{-1}. This upper bound is significantly smaller (by a factor of ~ 10) than the extremes of magnitude for charge transport reported here. Additionally, he saw a relative phase between $\tilde{j}_{\parallel}$ and $\tilde{b}_r$ of $\pi/2$ to within experimental uncertainty which was constant throughout the region of measurement, while we see a relative phase which varies between $-\pi/2$ and $-\pi$ depending on minor radius. This variation in phase with minor radius represents a significant difference from the constant phase reported by Shen.

The differences between Shen's measurements and those reported here may be attributed to a combination of differences in the plasmas used and a weakness in the flux surface average estimation technique used in both cases. Specifically, the plasmas in which Shen's measurements were made very probably exhibited wall-locked (*i.e.*, non-rotating) reversal surface resonant $m = 0$ modes. First, they have significantly higher plasma currents than the plasmas used here (> 200 kAmps vs. 160 kAmps), which makes wall-locking of such modes a virtual certainty. Second, toroidal magnetic fluctuation spectra reported by Shen for these plasmas[5] do not show significant fluctuation power for such modes, which it to be expected if such modes are wall-locked, because they do not cause magnetic field fluctuations at "fluctuation" frequencies. Since tearing modes that do not rotate toroidally do not contribute to fluctuations measured by magnetic sensing coils or Rogowskii coils, they do not contribute to estimated flux surface averages of fluctuation products. As discussed in Sec. 5.4, above, pseudospectral analysis indicates that at the minor radii where the relative phase of $\tilde{j}_{\parallel}$ and $\tilde{b}_r$ differs significantly from $-\pi/2$, it is due to contributions from $\tilde{j}_{\parallel}$ and $\tilde{b}_r$ reversal surface resonant $m = 0$ modes. This would explain why Shen sees a constant $\pi/2$ phase between $\tilde{j}_{\parallel}$ and $\tilde{b}_r$ at all minor radii while we see a phase between them that varies with minor radius. The variation of phase away from $-\pi/2$, of course, explains why we, unlike Shen, see a non-vanishing charge

transport.

5.6 - $\left\langle \tilde{j}_{\parallel}\tilde{b}_r \right\rangle_{F.S.}$ as a $\bar{J}\times\bar{B}$ Force

The measurements of $\left\langle \tilde{j}_{\parallel}\tilde{b}_r \right\rangle_{F.S.}$ in the edge of MST discussed in Sec. 5.2 above represent a $\bar{J}\times\bar{B}$ force density on the plasma of the form $\left\langle \tilde{j}_{\parallel}\tilde{b}_r \right\rangle_{F.S.}\hat{b}_0\times\hat{r}$, where $\hat{b}_0$ is the direction of the equilibrium magnetic field. Since the equilibrium magnetic field is oriented approximately in the positive poloidal direction in the edge of MST, the $\hat{b}_0\times\hat{r}$ vector is in the positive toroidal direction. (See Sec. 3.7, Ch. 3 for discussion of MST coordinate system.) Thus, given the sign convention used here (see Sec. 5.2, above),. a positive $\left\langle \tilde{j}_{\parallel}\tilde{b}_r \right\rangle_{F.S.}$ represents a force density in the positive toroidal direction. The measured $\left\langle \tilde{j}_{\parallel}\tilde{b}_r \right\rangle_{F.S.}$ during sawtooth crashes corresponds to a force density that ranges between ~ +7 N/m^3 and ~ -11 N/m^3 and depends on radial position and the poloidal angle of measurement. As can be seen in Figure 1, $\left\langle \tilde{j}_{\parallel}\tilde{b}_r \right\rangle_{F.S.}$ measured during sawtooth crashes is positive inwards of the reversal surface, indicating a force density in the positive toroidal direction, and negative outwards of the reversal surface, indicating a force density in the negative toroidal direction. Between crashes, the measured $\left\langle \tilde{j}_{\parallel}\tilde{b}_r \right\rangle_{F.S.}$ corresponds to a force density that ranges between ~ +0.5 N/m^3 and ~ -9 N/m^3 and depends on radial position and the poloidal angle of measurement. As can be seen in Figure 2, it is positive near the reversal surface and negative farther from the reversal surface. This indicates that $\tilde{j}_{\parallel}$ and $\tilde{b}_r$ together exert a net force density in the positive toroidal direction near the reversal surface and a net force density in the negative toroidal direction farther away.

Several interesting observations can be made regarding the $\bar{J}\times\bar{B}$ force density exerted by $\tilde{j}_{\parallel}$ and $\tilde{b}_r$. First, it is of sufficient magnitude to play a significant role in the momentum balance of MST. In fact, it is large enough that there must be other forces which play a significant role in the momentum balance of MST. During a sawtooth crash, MST typically exhibits a change of toroidal fluid velocity $\Delta V_\phi \sim 5 \times 10^3$ m sec^{-1} over a time period $\Delta t \sim 10^{-4}$ sec. (See, for instance, Figure 14.) The plasmas in which the measurements reported here were made

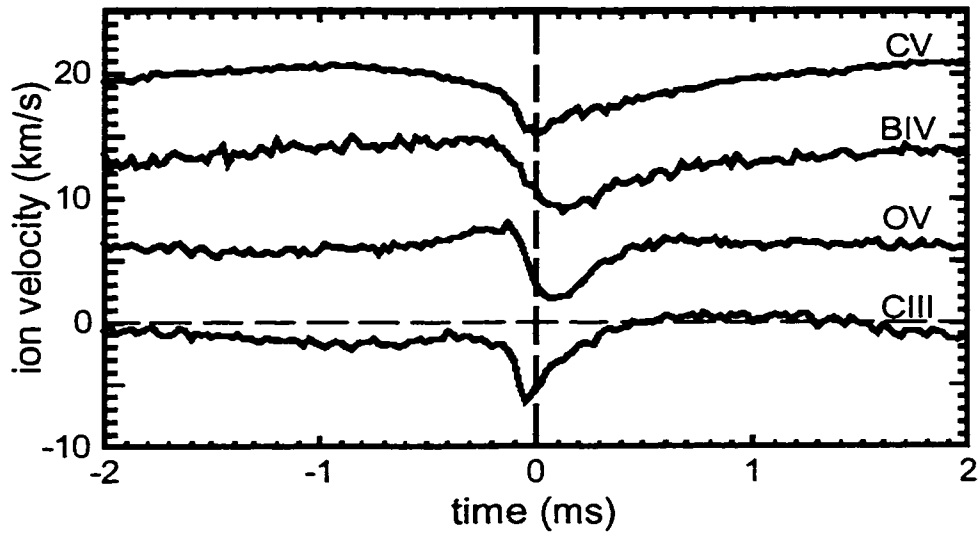

Figure 14: Toroidal flow velocity of multiple impurity ion species averaged over ensemble of sawtooth crashes. Sign convention is such that positive velocity is in negative toroidal direction. Time t = 0 is time of peak toroidal gap voltage (i.e. during sawtooth crash). Note that ordering of species velocity corresponds to ordering of minor radial position where species exhibits dominant emission. Also, CIII dominantly emits in edge, while CV dominantly emits in core. This indicates that cores species have fastest flow. (Courtesy J. Chapman. Measurements were made with Doppler Spectrometer.)

typically have a line average density of $n \sim 5 \times 10^{18}\ m^{-3}$. This combination of plasma density and change in toroidal velocity of sawtooth requires a net toroidal force density on the plasma of $m_p n \Delta V_\phi / \Delta t \sim 1/2\ N\ m^{-3}$.

One possible source for a force density that may offset $\left\langle \tilde{j}_\parallel \tilde{b}_r \right\rangle_{F.S.} \hat{b}_0 \times \hat{r}$ is a $\bar{J} \times \bar{B}$ force density $\tilde{j}_r$ and $\tilde{b}_\parallel$ of the form $-\left\langle \tilde{j}_r \tilde{b}_\parallel \right\rangle_{F.S.} \hat{b}_0 \times \hat{r}$. Unfortunately, no direct measurement of $-\left\langle \tilde{j}_r \tilde{b}_\parallel \right\rangle_{F.S.} \hat{b}_0 \times \hat{r}$ exists, and, in fact, such a measurement would be technically challenging to make. However, there is reason to expect that $-\left\langle \tilde{j}_r \tilde{b}_\parallel \right\rangle_{F.S.} \hat{b}_0 \times \hat{r}$ cannot be large enough to completely offset $\left\langle \tilde{j}_\parallel \tilde{b}_r \right\rangle_{F.S.} \hat{b}_0 \times \hat{r}$. In particular, although the measurements of $\tilde{b}_\parallel$ and $\tilde{b}_r$ discussed in Ch. 4 of this dissertation indicate that they are comparable in magnitude, $\tilde{j}_r$ is expected to be almost two orders of magnitude smaller than $\tilde{j}_\parallel$. This is because $\tilde{j}_\parallel$ ($\tilde{j}_\theta$ in region of discussion) is produced by a radial gradient in $\tilde{b}_\phi$, which has a radial scale length of < 10 cm, while $\tilde{j}_r$ is produced by poloidal and toroidal gradients in $\tilde{b}_\phi$ and $\tilde{b}_\theta$, whose associated scale

lengths are ~ 1 m and ~ 10 m. Of course, it might be argued that since $\tilde{j}_{\parallel}$ and $\tilde{b}_r$ are nearly -π/2 out of phase at minor radii inwards of the reversal surface, $\left\langle \tilde{j}_r \tilde{b}_{\parallel} \right\rangle_{F.S.}$ could be of significant magnitude compared to $\left\langle \tilde{j}_{\parallel} \tilde{b}_r \right\rangle_{F.S.}$, even if $\tilde{j}_r$ is much smaller than $\tilde{j}_{\parallel}$, as long as the relative phase between $\tilde{j}_r$ and $\tilde{b}_{\parallel}$ is 0 or π,. This possibility cannot be discounted. However, this argument does not apply at minor radii outwards of the reversal surface, where the relative phase between $\tilde{j}_{\parallel}$ and $\tilde{b}_r$ is near π.

A second observation can be made regarding the $\tilde{J} \times \tilde{B}$ force density exerted by $\tilde{j}_{\parallel}$ and $\tilde{b}_r$. Specifically, in the edge of MST plasmas it has a radial structure such that, during sawtooth crashes, it tends to flatten MST's equilibrium velocity profile. For the plasmas in which these measurements were made, the equilibrium toroidal component of the plasma velocity in the core of the plasma is in the negative toroidal direction, while the toroidal component of the edge plasma velocity *relative to the core plasma velocity* is positive. Consequently, MST's equilibrium has a positive toroidal velocity shear ($\partial V_\phi / \partial r$). This is illustrated in Figure 14, which shows flow velocities for a series of ion impurities that dominantly emit from different regions of minor radius in MST plasmas.[6] The sign convention in Figure 14 is such that a positive velocity corresponds to a velocity in the negative toroidal direction.

Finally, a third observation can be made regarding the $\tilde{J} \times \tilde{B}$ force density exerted by $\tilde{j}_{\parallel}$ and $\tilde{b}_r$. Specifically, the pattern of contributions to it from different toroidal modes in the edge of MST plasmas is consistent with the current theoretical and experimental understanding of interactions between core and reversal surface resonant tearing modes during sawtooth crashes. As discussed in Sec. 2.9 of Ch. 2, such interactions are believed to transfer momentum from the plasma core to the edge in such way as to flatten MST's equilibrium velocity profile. In particular, this momentum transfer is expected to be mediated by $\tilde{J} \times \tilde{B}$ forces exerted by the parallel current density and radial magnetic field fluctuations associated with the interacting tearing modes. As discussed in Sec. 5.4 above, during sawtooth crashes, at minor radii inwards of the reversal surface, $\left\langle \tilde{j}_{\parallel} \tilde{b}_r \right\rangle_{F.S.}$ is dominated by contributions from core resonant toroidal

modes, while outwards of the reversal surface, reversal surface resonant modes contribute strongly to it. As can be seen from the radial structure of $\left\langle \tilde{j}_{\parallel}\tilde{b}_r \right\rangle_{F.S.}$, both core and reversal surface resonant tearing modes contribute to $\left\langle \tilde{j}_{\parallel}\tilde{b}_r \right\rangle_{F.S.}$ in such way as to flatten the velocity profile.

5.7 - Conclusions

In conclusion, the measured estimates of $\left\langle \tilde{j}_{\parallel}\tilde{b}_r \right\rangle_{F.S.}$, which ranges from $\sim +7$ N/m^3 to ~ -11 N/m^3, depending on minor radius, has implications for the particle, charge and momentum balances in MST. Treated as a difference between radial ion and electron particl fluxes due to parallel streaming, the measured $\left\langle \tilde{j}_{\parallel}\tilde{b}_r \right\rangle_{F.S.}$ is small compared to the total radial particle flux. Yet it is large enough, treated as a radial current density, to have a very significant impact on the charge balance of the plasma and to imply the existence of other radial charge transport mechanisms (to maintain charge neutrality). Treated as a force density, the measured $\left\langle \tilde{j}_{\parallel}\tilde{b}_r \right\rangle_{F.S.}$ can be as much as an order of magnitude larger than the net force density experienced by MST plasmas during a sawtooth crash. Consequently, there must be other significant forces operating on MST plasmas. Also, $\left\langle \tilde{j}_{\parallel}\tilde{b}_r \right\rangle_{F.S.}$ has a radial structure during sawtooth crashes which indicates that, as a force density, it tends to flatten the toroidal velocity profile in MST. It is worth noting that the measured $\left\langle \tilde{j}_{\parallel}\tilde{b}_r \right\rangle_{F.S.}$, treated both as a charge transport and a force density, is large enough to imply the existence of something which competes with it.

The measured $\left\langle \tilde{j}_{\parallel}\tilde{b}_r \right\rangle_{F.S.}$ also has implications for the understanding of tearing mode interactions in MST. It clearly fails to meet the expectation for isolated tearing modes in RFPs. This theory predicts that the associated $\tilde{j}_{\parallel}$ and $\tilde{b}_r$ would be spatially out of phase and, consequently, that $\left\langle \tilde{j}_{\parallel}\tilde{b}_r \right\rangle_{F.S.}$ would be zero. On the other hand, the measured $\left\langle \tilde{j}_{\parallel}\tilde{b}_r \right\rangle_{F.S.}$ is consistent with the current theoretical and experimental understanding of the interaction of core and reversal surface resonant tearing modes in MST during sawtooth crashes. Such interactions are believed to affect the phase relationship between the $\tilde{j}_{\parallel}$ and $\tilde{b}_r$ associated with each tearing

mode. This, in turn, is expected to result in a non-vanishing $\left\langle \tilde{j}_{\parallel}\tilde{b}_{r}\right\rangle_{F.S.}$ and a $\bar{J}\times\bar{B}$ force on MST plasmas that would tend to flatten the equilibrium toroidal velocity profile, as is, in fact, observed.

It must be noted that measured estimates of $\left\langle \tilde{j}_{\parallel}\tilde{b}_{r}\right\rangle_{F.S.}$ have some dependence on poloidal position (although the radial structure of $\left\langle \tilde{j}_{\parallel}\tilde{b}_{r}\right\rangle_{F.S.}$ doesn't) which is not consistent with the interpretation of these estimates as a flux surface average. However, such dependence, which is believed to result from the imperfect poloidal symmetry of MST's equilibrium, is not expected to qualitatively change any of the conclusions presented in this chapter.

References

[1] N. E. Lanier, *Electron Density Fluctuations and Fluctuation-Induced Transport in the Reversed Field Pinch*, (Ph. D. dissertation, University of Wisconsin – Madison, 1999) p. 96.

[2] N. E. Lanier, et al., Phys. Rev. Lett. **85,** 2120 (2000)

[3] W. Shen, R. N. Dexter, and S. C. Prager, Phys. Rev. Lett. **68,** 1319 (1992).

[4] W. Shen, *Measurement of Current Density Fluctuations and Ambipolar Particle Flux Due to Magnetic Fluctuations in MST*, (Ph. D. dissertation, University of Wisconsin – Madison, 1992) p. 96.

[5] W. Shen, *Measurement of Current Density Fluctuations and Ambipolar Particle Flux Due to Magnetic Fluctuations in MST*, (Ph. D. dissertation, University of Wisconsin – Madison, 1992) p. 76.

[6] J. T. Chapman, *Spectroscopic Measurement of the MHD Dynamo in the MST Reversed Field Pinch*,(Ph. D. dissertation, University of Wisconsin – Madison, 1992) p. 52.

Chapter 6 - Conclusions and Future Work

6.1 - Conclusions

In conclusion, the spatial structures of the poloidal current density and magnetic field fluctuations associated with tearing mode activity have been probed in the edge region of MST using two-point spectral analysis and pseudospectral analysis. Magnetic fluctuations in the edge of MST are dominantly composed of toroidal modes with mode numbers in the range $n = 5 - 10$ while poloidal current density fluctuations are composed of toroidal modes with mode numbers in the range $n = -3 - -1$. Although these measurements do not resolve the contributions of specific poloidal modes to each toroidal mode, there are several indications that the $n = 5 - 10$ toroidal modes of the magnetic fluctuations are, in fact, dominantly composed of $m = 1$ poloidal modes, while the $n = -1 - -3$ toroidal modes of the poloidal current density fluctuations are dominantly composed of $m = 0$ poloidal modes. In particular, these conclusion are based on two sets of measurements: two-point poloidal spectral analysis of the magnetic and poloidal current density fluctuations and measurements of the poloidal dependence of the poloidal phase of the toroidal modes which compose these fluctuations.

Measurements of magnetic and poloidal current density fluctuation in the edge of MST have been compared with analogous measurements in resistive MHD simulations produced by the DEBS code. In particular, the observed radial structure for the core resonant $n = 6$ toroidal mode and reversal surface resonant $n = -1$ toroidal modes of the magnetic and poloidal current density fluctuations in the edge of MST are compared with measurements of the corresponding helical modes in DEBS simulations. It is observed that the edge radial structures of both the $n = 6$ and $n = -1$ toroidal modes are qualitatively similar to those of the $m = 1, n = 6$ and $m = 0$, $n = -1$ helical modes, respectively, in DEBS simulations. Of particular interest, the $n = -1$ poloidal current density perturbation in MST shows a current sheet associated with reconnection at the reversal surface, just as does the $m = 0$, $n = -1$ poloidal current density perturbation in DEBS simulations.

The measured radial structure of the dominant reversal surface resonant radial magnetic field fluctuation ($m = 0$, $n = -1$) is measured around the reversal surface. It is observed to be non-vanishing at the reversal surface, implying the occurrence of reconnection. This is the first direct observation of reconnection at the reversal surface in an RFP.

As previously noted, the radial structure of the $m = 0$, $n = -1$ poloidal current density perturbation, or current sheet, which is associated with reconnection at the reversal surface, is observed. The radial width of this current sheet is compared to the widths that are theoretically and computationally expected from models of reconnection which include, variously, resistivity, electron inertial effects, electron pressure gradient effects, and the Hall term (*i.e.*, ion inertia). It is determined that the electron inertial effect in Ohm's law cannot, by itself, explain the observed width of the current sheet, since the associated scale length is much smaller than this width. It is noted that the current sheet width is, however, only a few times larger than the width obtained by inclusion of the electron pressure gradient effect in Ohm's Law. The observed width of the current sheet is much larger than the resistive MHD scale, which might be construed to indicate that resistivity cannot account for the observed width. However, the observed width is comparable to the calculated width of the associated magnetic island. It is noted that theoretically, the current sheet width for the saturated tearing modes in MST should not be determined by the resistive MHD scale if resistivity is the dominant non-ideal effect, but, rather, the width of the associated magnetic island. Since the width of the observed current sheet is comparable to the associated magnetic island width, the alternative possibility exists that a current sheet with some smaller radial scale, produced by some reconnection mechanism other than resistivity, is distributed radially over the associated magnetic island by streaming of charge carriers along magnetic field lines.

The roles of tearing modes in the charge, particle and momentum balances of MST have been probed. In particular, estimates of $\left\langle \tilde{j}_{\parallel} \tilde{b}_r \right\rangle_{F.S.}$, the flux surface average product of the associated $\tilde{j}_{\parallel}$ and $\tilde{b}_r$, have been obtained, indicating that it ranges from ~ +7 N/m^3 to ~ -11 N/m^3,

depending on minor radius. Treated as the difference between radial ion and electron fluxes due to parallel streaming, it is small compared to the total radial particle flux. However, treated as a radial current density, it is large enough to have a very significant impact on the charge balance of the plasma, thus implying the existence of other radial charge transport mechanisms. Treated as a force density, it is as much as an order of magnitude larger than the net force toroidal density observed for MST plasmas during a sawtooth crash (as determined from measurements of toroidal velocity changes), thus implying the existence of other significant forces operating on MST plasmas. Also, it has a radial structure during sawtooth crashes which indicates that, as a force density, it tends to flatten the toroidal velocity profile in MST. It is worth noting that the measured $\left\langle \tilde{j}_{\parallel}\tilde{b}_r \right\rangle_{F.S.}$ represents both a charge transport and a force density which are large enough to imply the existence of something which competes with them.

The measured $\left\langle \tilde{j}_{\parallel}\tilde{b}_r \right\rangle_{F.S.}$ also has implications for the understanding of tearing mode interactions in MST. It clearly fails to meet the expectation for isolated tearing modes in RFPs, which predicts that the associated $\tilde{j}_{\parallel}$ and $\tilde{b}_r$ would be spatially out of phase and, consequently, that $\left\langle \tilde{j}_{\parallel}\tilde{b}_r \right\rangle_{F.S.}$ would be zero. On the other hand, it is consistent with the current theoretical and experimental understanding of the interaction of core and reversal surface resonant tearing modes in MST during sawtooth crashes. Such interactions are believed to affect the phase relationship between the $\tilde{j}_{\parallel}$ and $\tilde{b}_r$ associated with each tearing mode. This, in turn, is expected to result in a non-vanishing $\left\langle \tilde{j}_{\parallel}\tilde{b}_r \right\rangle_{F.S.}$ and a $\bar{J}\times\bar{B}$ force on MST plasmas that would tend to flatten the equilibrium toroidal velocity profile, as is, in fact, observed.

It must be noted that the measured $\left\langle \tilde{j}_{\parallel}\tilde{b}_r \right\rangle_{F.S.}$ actually depends on the poloidal position at which the measurement is made (although the radial structure of $\left\langle \tilde{j}_{\parallel}\tilde{b}_r \right\rangle_{F.S.}$ does not). This dependence on poloidal position is not consistent with the interpretation of these estimates as flux surface averages. However, such dependence, which is believed to result from the imperfect poloidal symmetry of MST's equilibrium, is not expected to qualitatively change any of the conclusions presented here.

6.2 - Future Work

There are several areas in which the work described in this dissertation might be extended or built upon to further the understanding of magnetic reconnection in general and magnetic reconnection in RFPs in particular. For instance, there are at least two obvious, modest extensions of the experiments described here that would be fairly easily implemented in the near term on MST. First, detailed and accurate diagnosis of a variety of plasma quantities, such as temperature, density and impurity flow velocity can be obtained in the plasma edge. In particular, the spatial structure of fluctuations in such parameters could be measured using the pseudospectral technique. The equilibrium radial structure of such parameters may also be measured. Such measurements, in conjunction with simultaneous measurements of the spatial structure of magnetic field and current density fluctuations of the type described here, would allow for a more rigorous comparison with present and future theoretical work on reconnection in RFPs than is possible with the measurements presented here.

A second modest extension of the experiments described here would be to obtain more accurate measurements of the spatial structure of magnetic field and current density fluctuations. The are two simple methods for achieving this. The first method, which makes use of existing resources, is to simply extend the measurements described here to a greater variety of poloidal locations than those used (75°P and -15° P). This could be achieved by inserting Rogowskii probes at other poloidal positions. Such an extension would be extremely useful in characterizing the significance of MST's poloidal asymmetry to the measurements described here, including, in particular, the measurements of $\left\langle \tilde{j}_{\parallel}\tilde{b}_r \right\rangle_{F.S.}$. Additionally, MST has poloidally distributed arrays of wall mounted magnetic sensing coils similar to those composing the toroidal arrays. Each of the coils in these poloidal arrays could be subjected to toroidal pseudospectral analysis, providing, in particular, highly poloidally resolved measurements of the relative poloidal phases of each toroidal mode. This would provide a much more accurate characterization of the poloidal mode content of each toroidal mode than was possible from the

measurements presented here. The second method for obtaining more accurate measurements of the spatial structure of magnetic field and current density fluctuations would be to construct and make use of a probe consisting of two extensive radial arrays of triplets of radial, poloidal and toroidal magnetic sensing coils. The two arrays would be separated by ~ 1 – 2 cm and would be positioned within the plasma so that they are separated in the toroidal direction. Such a probe, unlike the existing Rogowskii probes, would allow for instantaneous measurements of edge radial profiles of parallel current density and all three components of the magnetic field. Such instantaneous measurements of radial profiles would potentially allow for a stronger comparison to theoretical predictions for reconnection in an RFP. [Note: A probe similar to the one proposed already exists within MST's inventory of diagnostics (the so-called *forked probe*, so named, perhaps, because of its resemblance to a tuning fork), but the two radial arrays composing the probe are of radial limited extent, allowing measurement of the parallel current density at only one radial location.]

In addition to such simple extensions of the experiments described in this dissertation, there are other ways in which the understanding of reconnection in RFPs could be advanced. For instance, time resolved measurements of the spatial structures of the parallel current density and magnetic field fluctuations in MST could be compared to theoretical predictions for the time scales associated with reconnection. Perhaps most importantly, time resolved measurements of the radial magnetic field perturbation which causes reconnection might be compared with theoretical predictions for reconnection rates. Although such measurements represent a technical challenge, measurements of the spatial structure of fluctuations in current density, magnetic field and other plasma quantities in the region of reconnection for core resonant modes would also advance the understanding of reconnection in RFPs. Collisionless reconnection theory and computation specific to RFPs is in its infancy right now. However, as it develops it will advance the understanding of reconnection in RFPs by permitting more rigorous comparison of reconnection measurements in an RFP to theoretical predictions for reconnection.

Appendix A - Supplemental Figures and Description of Data Sets for Chapter 4

A.1 - Introduction

As discussed in Ch. 4, fluctuations in the poloidal current density and magnetic field associated with tearing mode activity have been measured in the edge of MST and their spatial structure has been probed making use of two different spectral analysis techniques. Additionally, the radial structure of selected toroidal modes MST is compared to the radial structure of those modes as seen in the resistive MHD code DEBS. The results of these measurements, analyses and comparison, each of which is obtained for several cases, represents a rather large collection of figures. All discussion of these measurements is confined to Ch. 4. This appendix serves to organize and present these figures, many of which were not presented in Ch. 4 for sake of clarity, for reference purposes. Additionally, this appendix describes the data sets used to produce these figures, including, in particular, the information necessary to access this data from the MST database.

Section A.2 presents toroidal pseudospectra and poloidal phases for each toroidal mode measured relative to the toroidal magnetic fluctuations at the wall (obtained with the toroidal array at 241° P).

Section A.3 presents toroidal two-point spectra.

Section A.4 presents poloidal two-point spectra

Section A.5 present comparisons of selected toroidal modes as seen in DEBS and MST.

A.2 - Pseudospectra of Poloidal Current Density and Magnetic Field Fluctuations in MST Edge

The toroidal pseudospectra for fluctuations in the poloidal current density and all three components of the magnetic field are shown in Figures 1 – 16. Figures 1 – 8 show measurements at -15° P, 330° T, while Figures 9 – 16 show measurements at 75° P, 120°. Each

of these sets of figures shows pseudospectra measured both between and during crash phase of the sawtooth cycle. Figures 17 – 48 show radial profiles of squared pseudospectral amplitudes for selected modes. All of these pseudospectral measurements were made using toroidal magnetic field fluctuations at the wall of MST (measured with the toroidal array at 241 °P) as the reference fluctuation.

The relative phases between the toroidal modes of the toroidal magnetic field at the wall and the toroidal modes of the poloidal current density as well as all three components of the magnetic field in the plasma are shown in Figures 49 – 64. These relative phases are measured with the probe at each of two different poloidal positions. Figures 49 – 56 show relative phases measured with the probe at -15° P, while Figures 57 – 64 show relative phases with the probe at 75° P. For each of these cases, the probe was at different toroidal positions, but the measured phases have been adjusted to eliminate any dependence on the toroidal position of measurement. Figures 65 – 96 show radial profiles of these relative phase for selected modes.

For the figures showing pseudospectral and relative phase measurements presented in this section, the list of MST shots used is described in Tables A.1 and A.2.

Table A.1 – Data sets for pseudospectral analysis using probe at 75° P, 120° T (Rogowskii #8, as discussed in Secs. 3.3 – 3.5 of Ch 3.). Data taken on May 21, 1999.

probe depth (cm)	*r/a*	Shot numbers
3	0.942	488, 490 – 494, 497, 499, 501 – 504, 506, 507
5	0.904	510, 513, 515 – 517, 519, 520, 522
6.5	0.875	524, 525, 527, 529, 530 – 533, 536, 537 – 539, 543 – 546, 548, 550 – 558, 560 – 562
8	0.846	563 – 567, 569 – 573, 575, 576
10	0.808	578, 581 – 584, 587 – 589, 592, 594 – 596, 599 – 601, 604

The poloidal current density and magnetic field measurements taken during the shots

listed in Tables A.1 and A.2 are stored in the MST database under signal names indicated in Table A.3. Table A.3 also indicates the gain applied to each coil signal(by an integrator circuit, as described in Sec. 3.3 of Ch. 3) prior storage in the MST database. These signals were processed as described in Ch. 3 to produces the figure presented in this Section.

Table A.2 – Data sets for toroidal two-point spectral analysis using probes at -15° P, 320° T and -15° P, 330° T (Rogowskiis #7 and #8, respectively, as discussed in Secs. 3.3 – 3.5 of Ch 3.) and simultaneous pseudospectral analysis using probe at -15° P, 330° T (Rogowskii #8). Data taken on May 29, 1999.

probe depth (cm)	r/a	Shot numbers
2	0.962	145, 146, 149 – 152, 262 – 273, 275, 277, 290 – 295, 297
3	0.942	230 – 250
6	0.885	157 – 164, 166 – 170, 172, 175, 178, 180, 184 – 188, 251 – 256
9	0.827	201 – 220, 222, 225 – 228, 257, 258, 260, 261

Table A.3 - List of signals, applied amplifications and MST database signal names

Measured Quantity	Probe used	Applied Gain	Database Signal name
J_θ	Rog. #8	50	JROG_8
B_θ	Rog. #8	10	BPARA_8
B_ϕ	Rog. #8	50	BPERP_8
B_r	Rog. #8	100	BPERPR_8
J_θ	Rog. #7	50	JROG_7
B_θ	Rog. #7	10	BPARA_7
B_ϕ	Rog. #7	50	BPERP_7

A.3 - Two-Point Toroidal Spectra of Poloidal Current Density and Magnetic Field Fluctuations in MST Edge

The toroidal two-point spectra for fluctuations in the poloidal current density and poloidal and toroidal components of the magnetic field are shown in Figures 97 – 102. These spectra are measured with probes at -15° P, 320° T and -15° P, 330° T, both between and during crash phase of the sawtooth cycle. Figures 103 – 114 show radial profiles of squared two point spectral amplitudes for selected modes.

For the figures showing toroidal two-point spectral measurements presented in this section, the list of MST shots used is described in Table A.2. The poloidal current density and magnetic field measurements taken during the shots listed in Tables A.1 and A.2 are, as noted in Section A.3 of this appendix, stored in the MST database under signal names indicated in Table A.3.

A.4 - Two-Point Poloidal Spectra of Poloidal Current Density and Magnetic Field Fluctuations in MST Edge

The poloidal two-point spectra for fluctuations in the poloidal current density and poloidal and toroidal components of the magnetic field are shown in Figures 115 – 120. These spectra are measured at the reversal surface with probes at 75° P, 120° T and 105° P, 120° T, both between and during the crash phase of the sawtooth cycle.

For the figures showing poloidal two-point spectral measurements presented in this section, the MST shots used were Shots 437 – 485 on May 21, 1999. The poloidal current density and magnetic field measurements taken during the shots listed in Tables A.1 and A.2 are, as noted in Section A.3 of this appendix, stored in the MST database under signal names indicated in Table A.3. For these poloidal two-point spectra, both probes were positioned at near the reversal surface: 8 cm depth (r/a = 0.846) for Rogowskii #7 and 6.5 cm depth (r/a = 0.875) for Rogowskii #8.

A.5 - Comparison of Tearing Mode Structure in MST Edge with Observations in DEBS

Measurements of the radial structure of the magnetic and poloidal current density fluctuations for the $n = 6$ toroidal modes in the edge MST during sawtooth crashes are shown in Figures 121 – 128. The radial structures of the same quantities for the $n = 6$, $m = 1$ helical mode during a burst of fluctuation activity in a DEBS plasma are shown in Figures 129 – 132. Measurements of the radial structure magnetic and poloidal current density fluctuations for the $n = -1$ toroidal mode are shown in Figure 133 – 140. The radial structures of the same quantities for the $n = -1$, $m = 0$ helical mode during a burst of fluctuation activity in a DEBS plasma are shown in Figures 141 – 144.

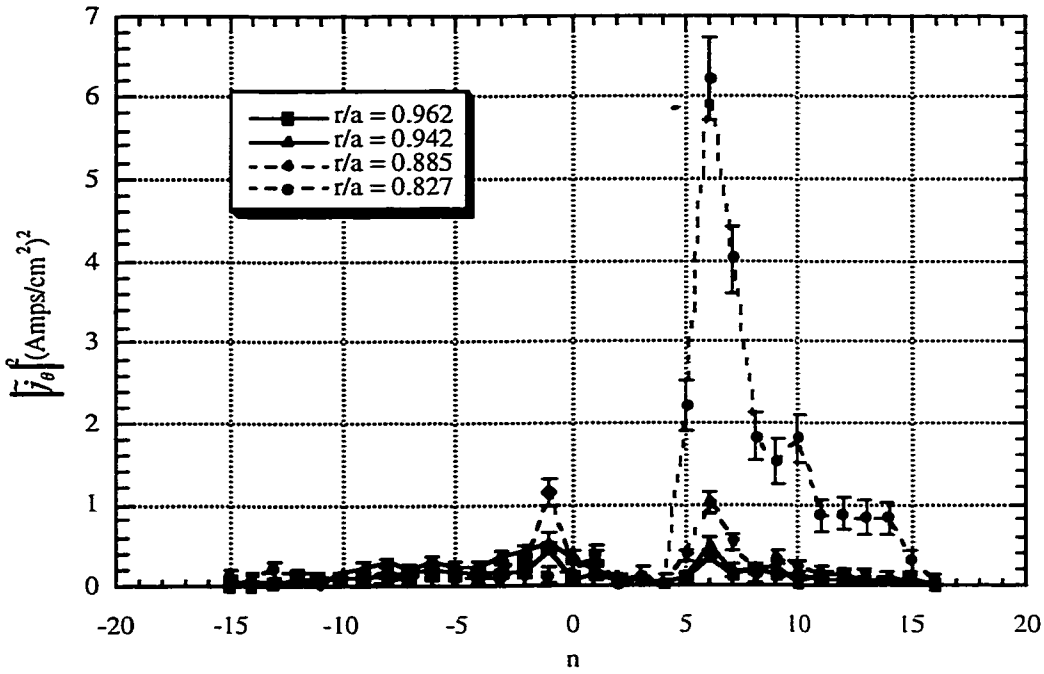

Figure 1: Toroidal pseudospectrum of poloidal current density fluctuations during sawtooth crashes at -15° P, 330° T. Measured with reference to toroidal magnetic field fluctuations at the wall.

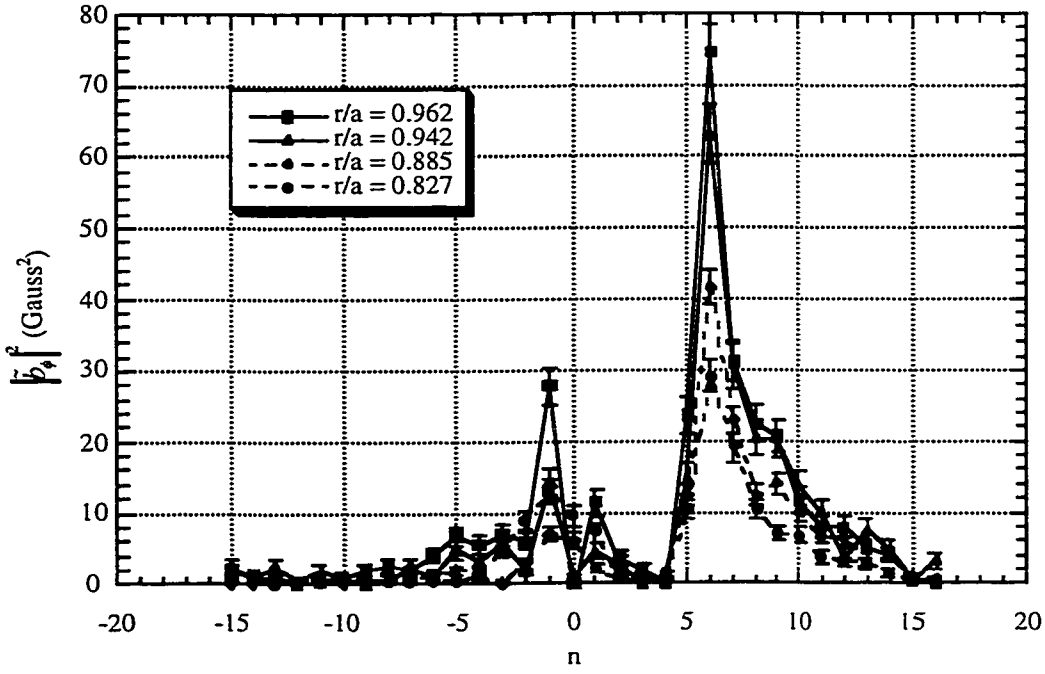

Figure 2: Toroidal pseudospectrum of toroidal magnetic field fluctuations during sawtooth crashes at -15° P, 330° T. Measured with reference to toroidal magnetic field fluctuations at the wall.

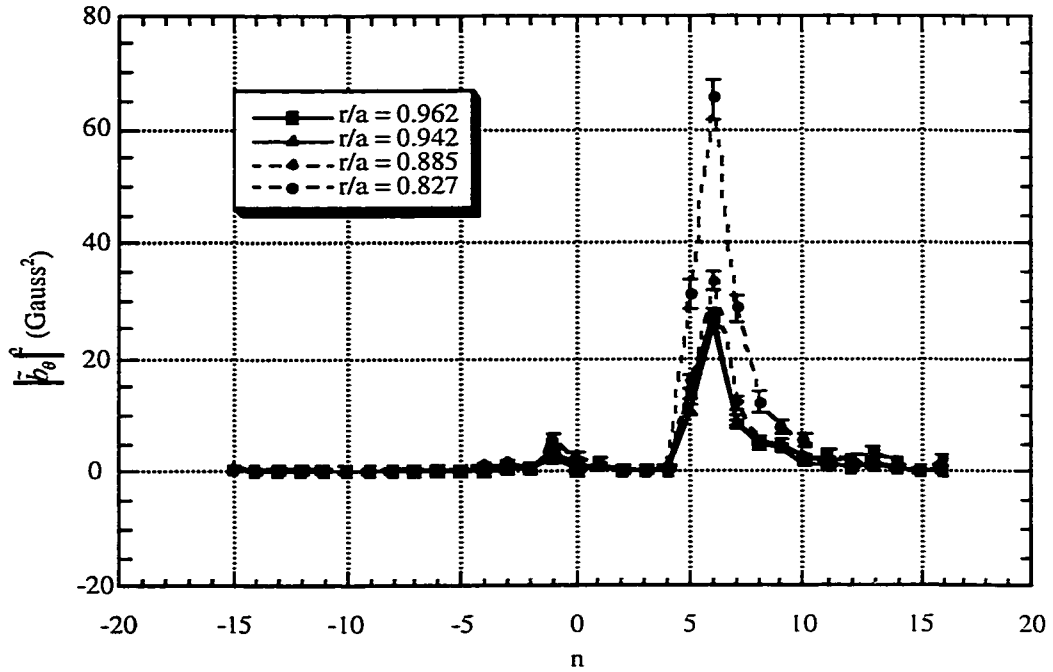

Figure 3: Toroidal pseudospectrum of poloidal magnetic field fluctuations during sawtooth crashes at -15° P, 330° T. Measured with reference to toroidal magnetic field fluctuations at the wall.

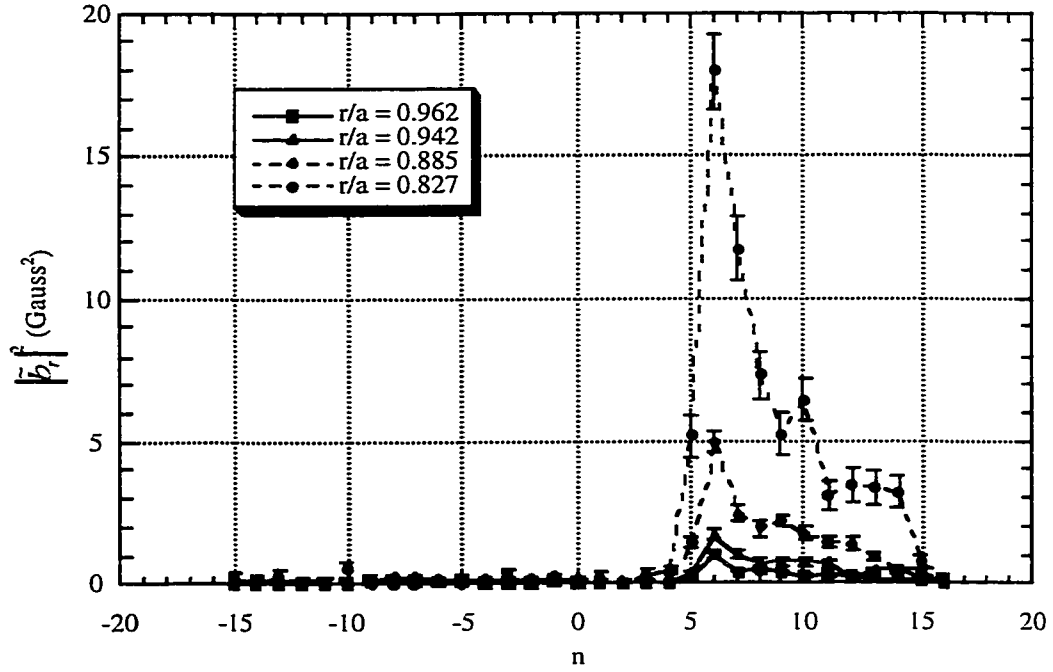

Figure 4: Toroidal pseudospectrum of radial magnetic field fluctuations during sawtooth crashes at -15° P, 330° T. Measured with reference to toroidal magnetic field fluctuations at the wall.

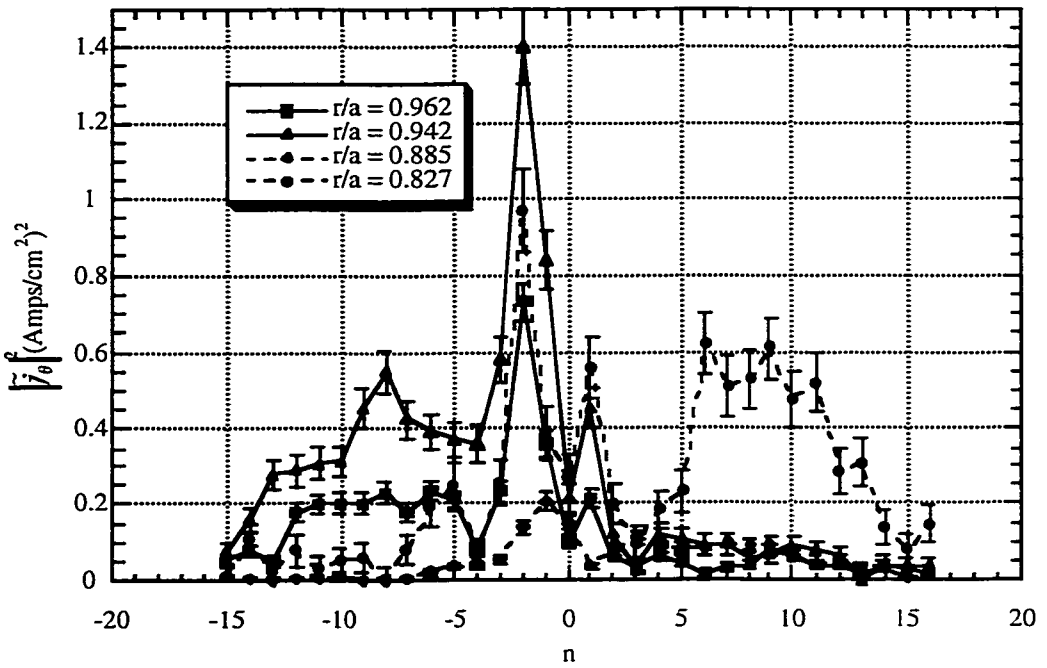

Figure 5: Toroidal pseudospectrum of poloidal current density fluctuations between sawtooth crashes at -15° P, 330° T. Measured with reference to toroidal magnetic field fluctuations at the wall.

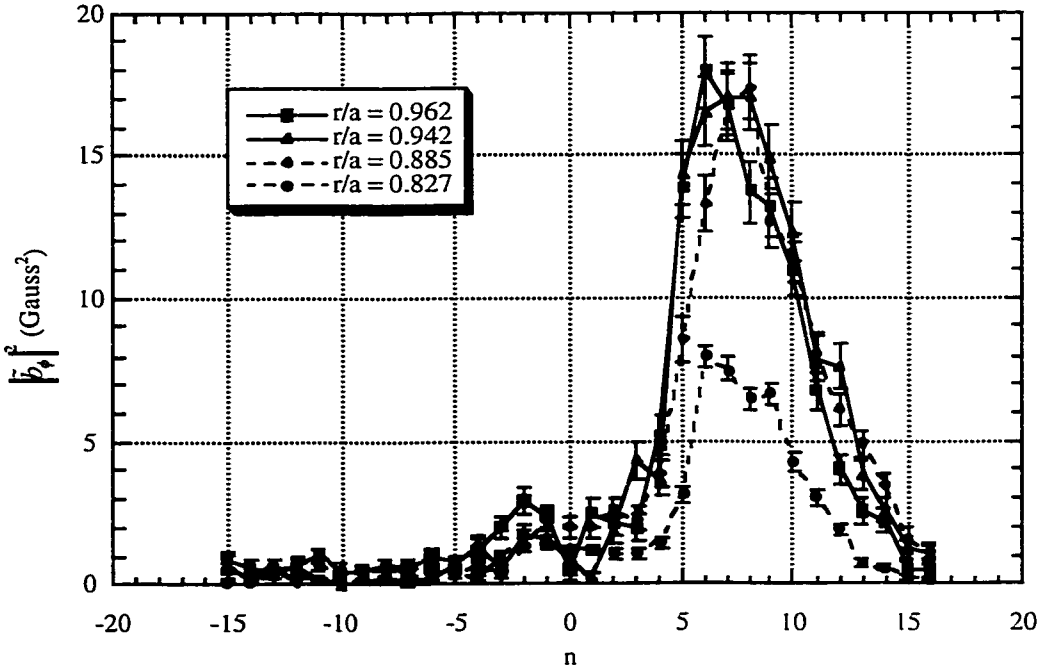

Figure 6: Toroidal pseudospectrum of toroidal magnetic field fluctuations between sawtooth crashes at -15° P, 330° T. Measured with reference to toroidal magnetic field fluctuations at the wall.

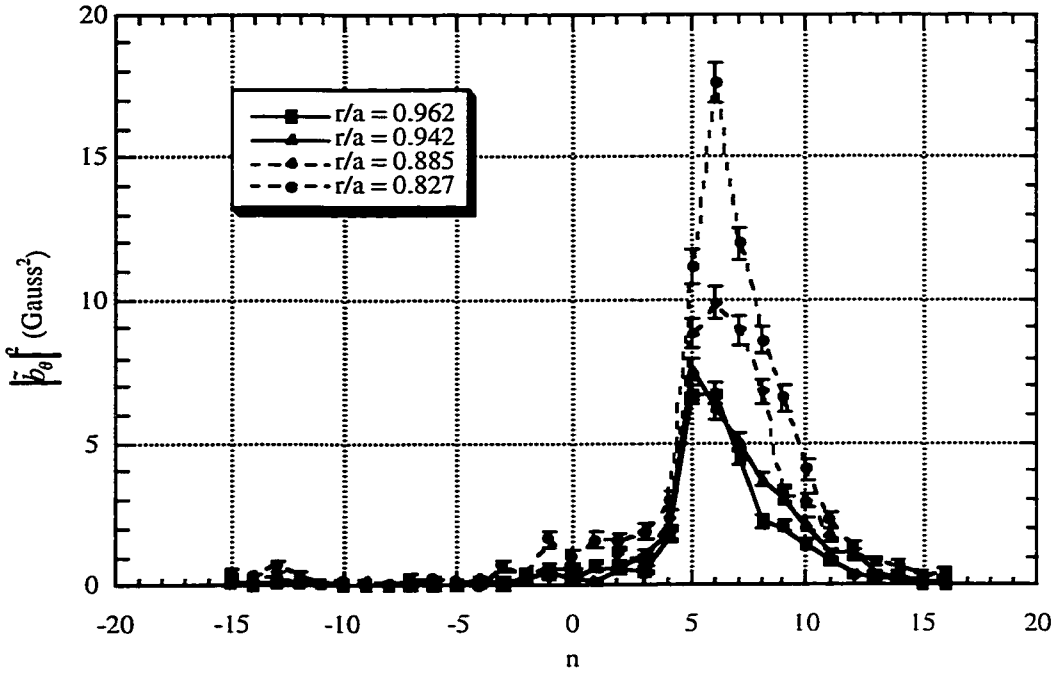

Figure 7: Toroidal pseudospectrum of poloidal magnetic field fluctuations between sawtooth crashes at -15° P, 330° T. Measured with reference to toroidal magnetic field fluctuations at the wall.

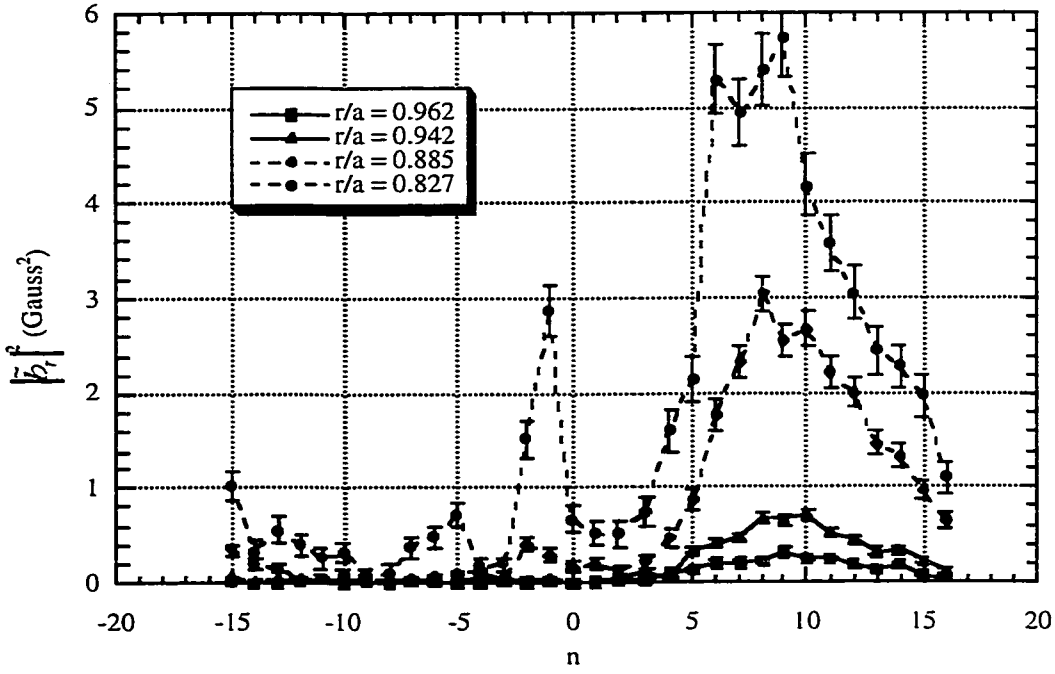

Figure 8: Toroidal pseudospectrum of radial magnetic field fluctuations between sawtooth crashes at -15° P, 330° T. Measured with reference to toroidal magnetic field fluctuations at the wall.

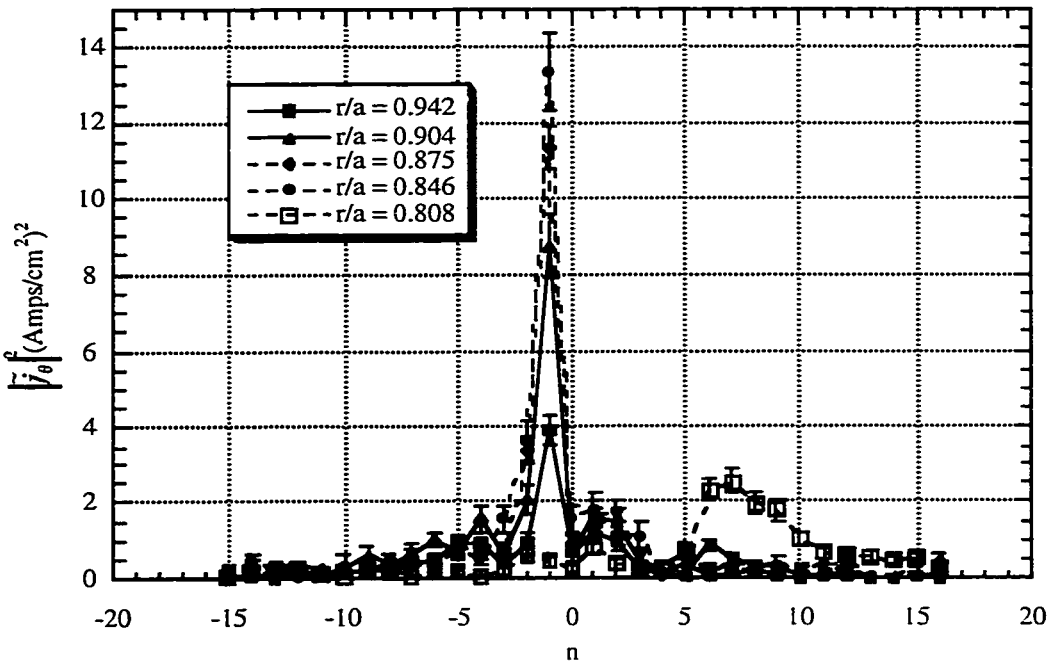

Figure 9: Toroidal pseudospectrum of poloidal current density fluctuations during sawtooth crashes at 75° P, 120° T. Measured with reference to toroidal magnetic field fluctuations at the wall.

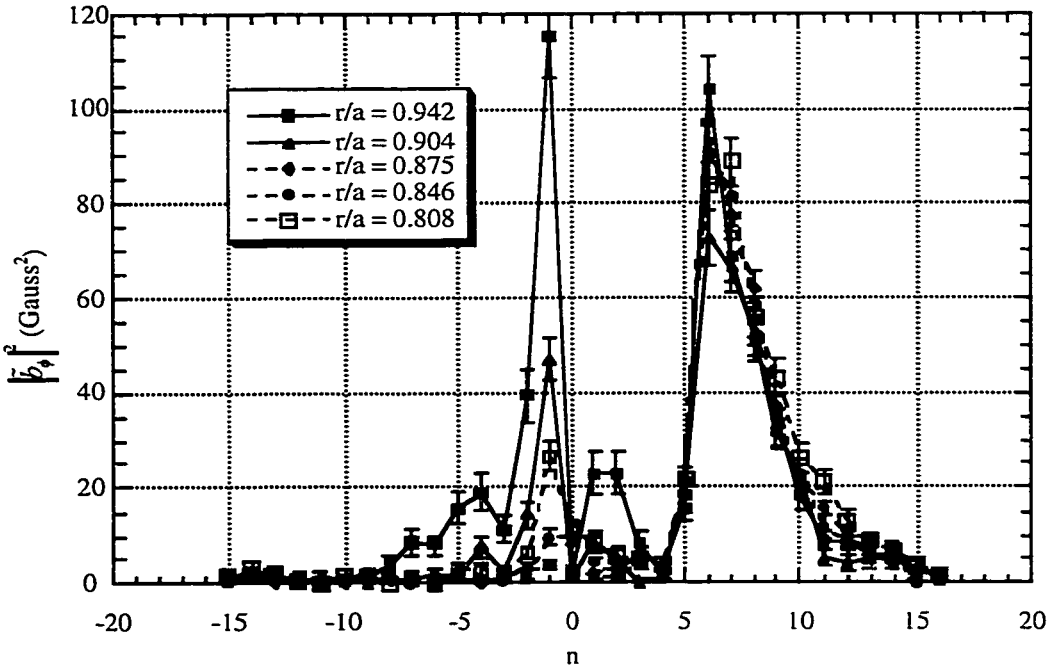

Figure 10: Toroidal pseudospectrum of toroidal magnetic field fluctuations during sawtooth crashes at 75° P, 120° T. Measured with reference to toroidal magnetic field fluctuations at the wall.

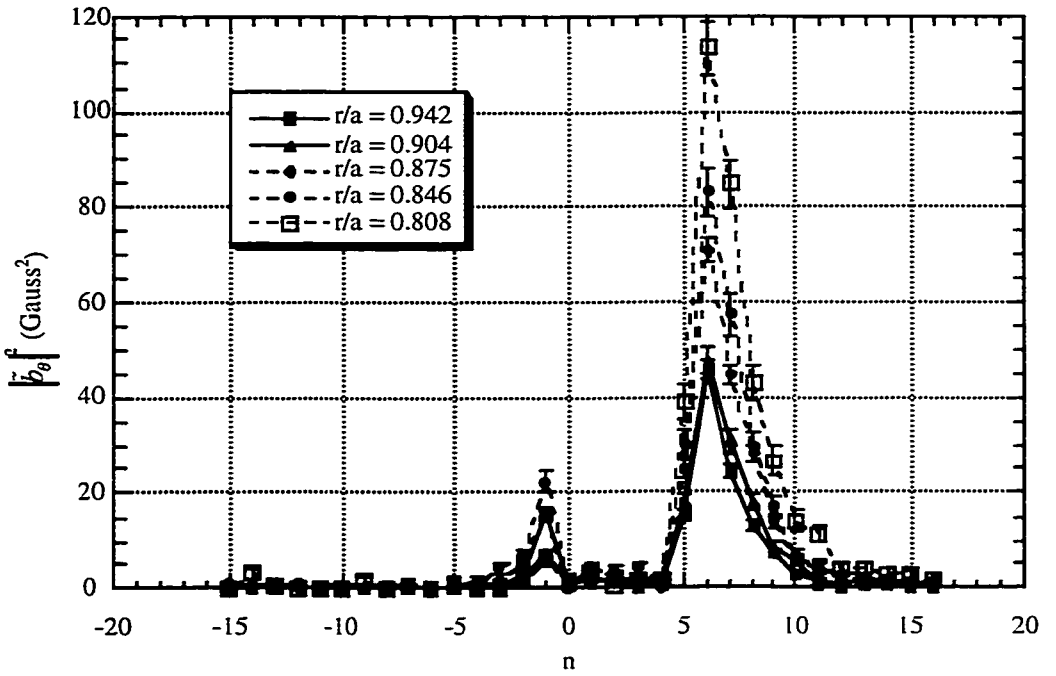

Figure 11: Toroidal pseudospectrum of poloidal magnetic field fluctuations during sawtooth crashes at 75° P, 120° T. Measured with reference to toroidal magnetic field fluctuations at the wall.

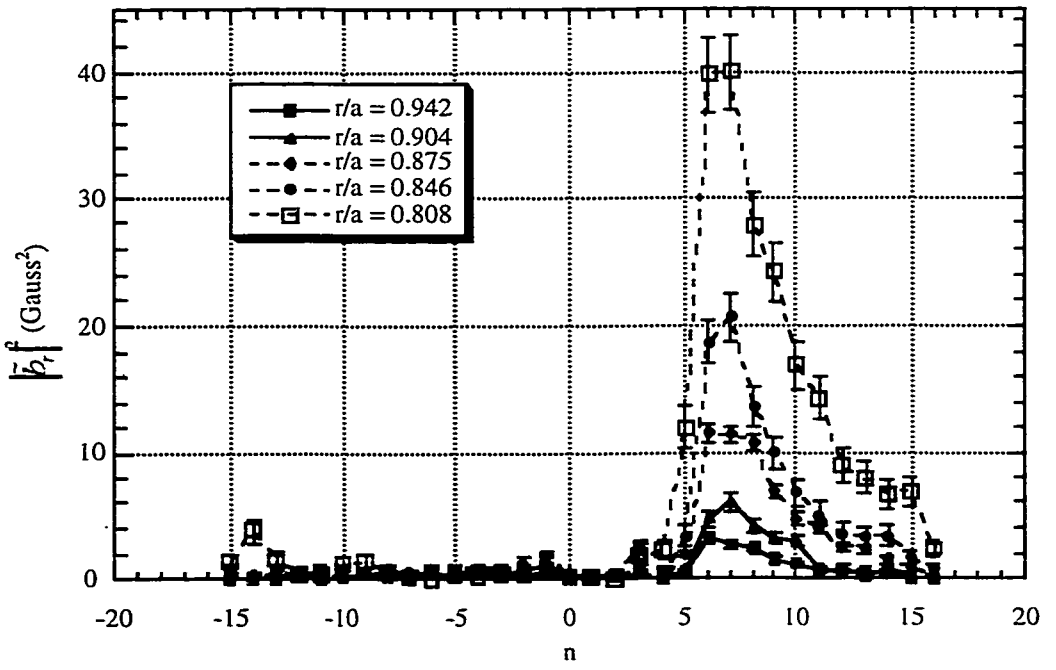

Figure 12: Toroidal pseudospectrum of radial magnetic field fluctuations during sawtooth crashes at 75° P, 120° T. Measured with reference to toroidal magnetic field fluctuations at the wall.

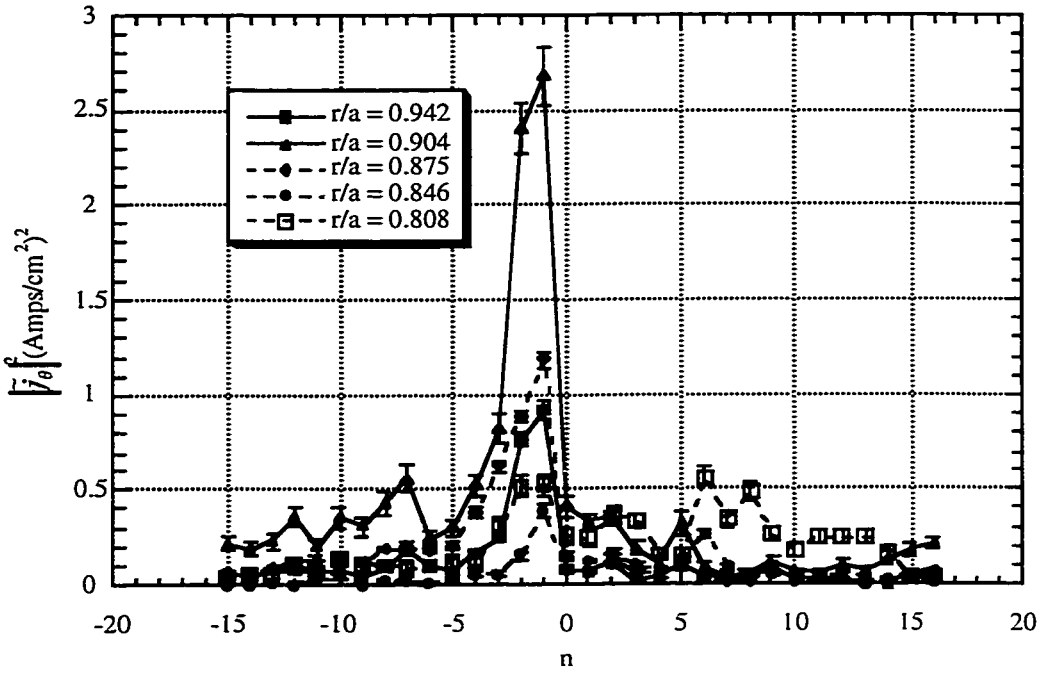

Figure 13: Toroidal pseudospectrum of poloidal current density fluctuations between sawtooth crashes at 75° P, 120° T. Measured with reference to toroidal magnetic field fluctuations at the wall.

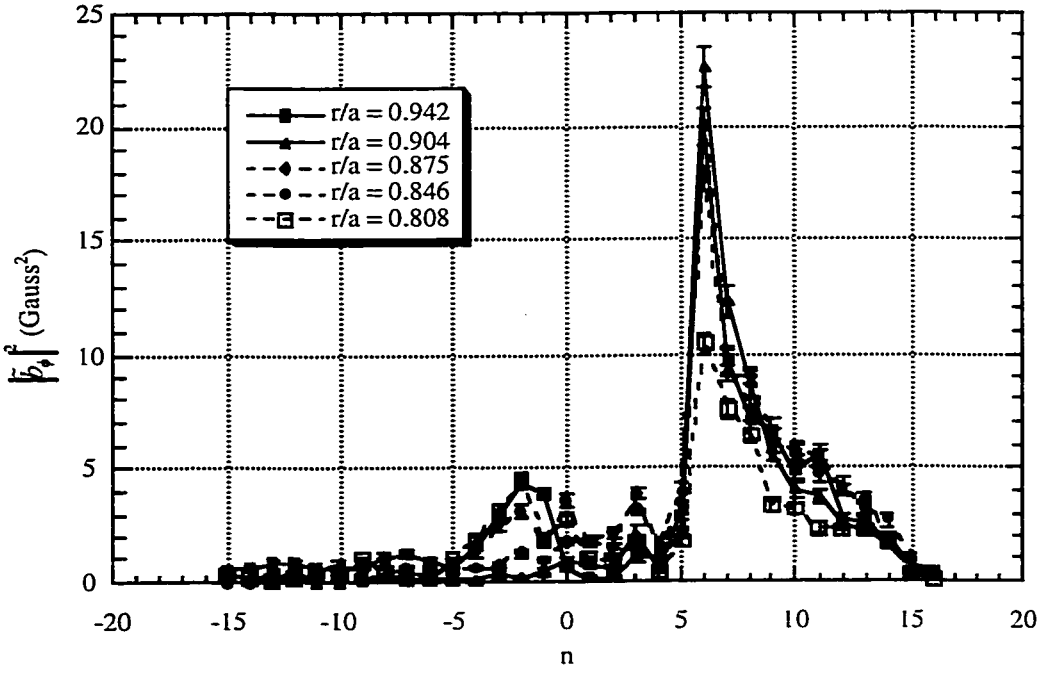

Figure 14: Toroidal pseudospectrum of toroidal magnetic field fluctuations between sawtooth crashes at 75° P, 120° T. Measured with reference to toroidal magnetic field fluctuations at the wall.

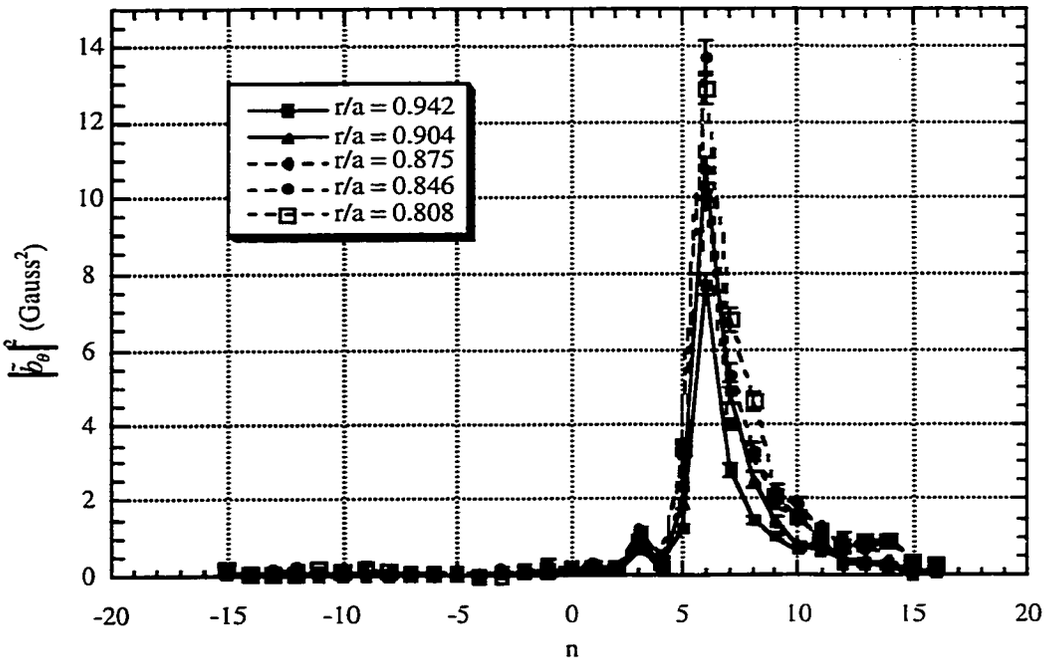

Figure 15: Toroidal pseudospectrum of poloidal magnetic field fluctuations between sawtooth crashes at 75° P, 120° T. Measured with reference to toroidal magnetic field fluctuations at the wall.

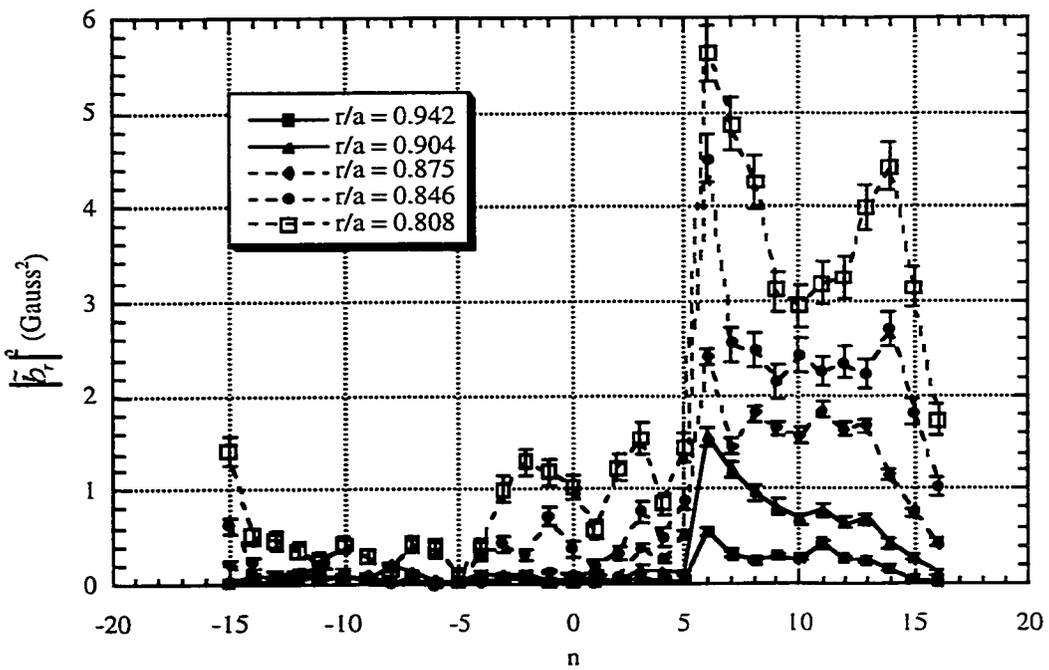

Figure 16: Toroidal pseudospectrum of radial magnetic field fluctuations between sawtooth crashes at 75° P, 120° T. Measured with reference to toroidal magnetic field fluctuations at the wall.

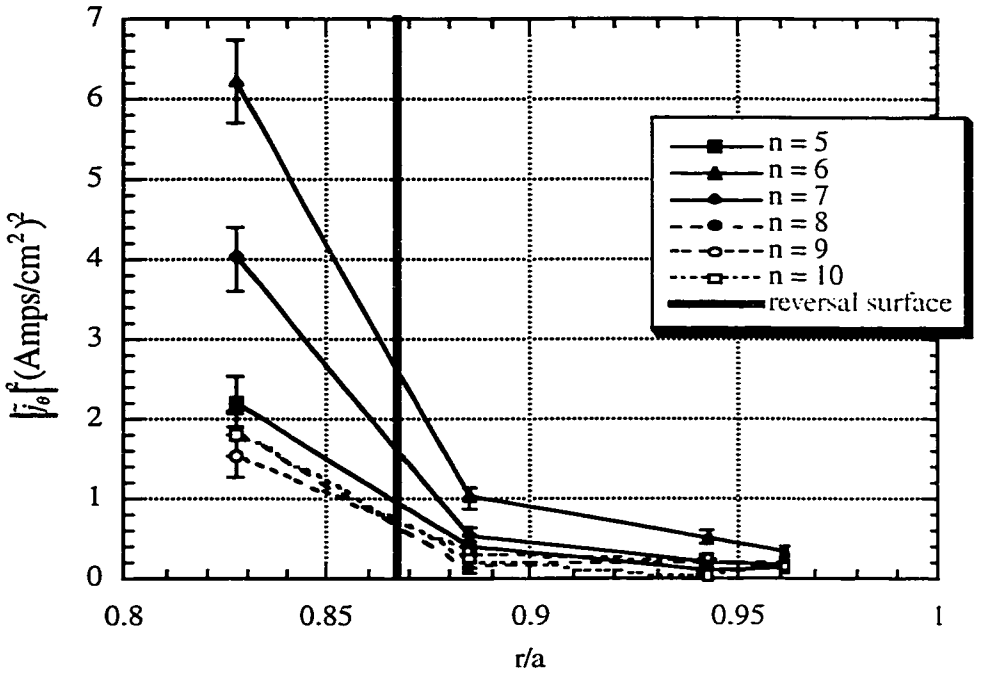

Figure 17: Radial profile of squared toroidal pseudospectrum amplitude of poloidal current density fluctuations for core resonant toroidal modes during sawtooth crashes at -15° P, 330° T. Measured with reference to toroidal magnetic field fluctuations at the wall.

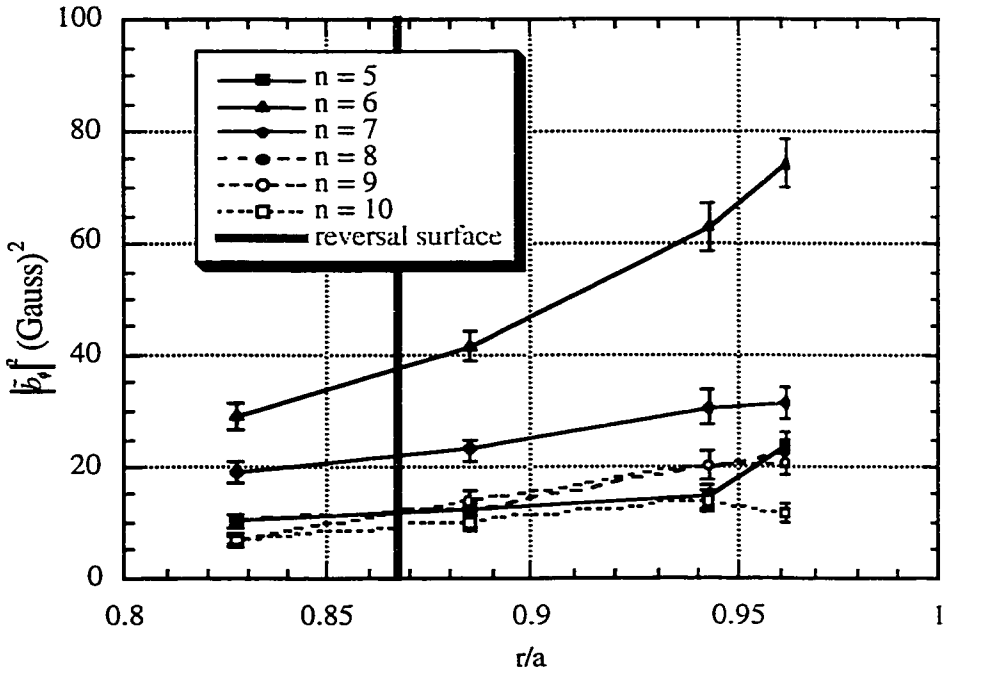

Figure 18: Radial profile of squared toroidal pseudospectrum amplitude of toroidal magnetic field fluctuations for core resonant toroidal modes during sawtooth crashes at -15° P, 330° T. Measured with reference to toroidal magnetic field fluctuations at the wall.

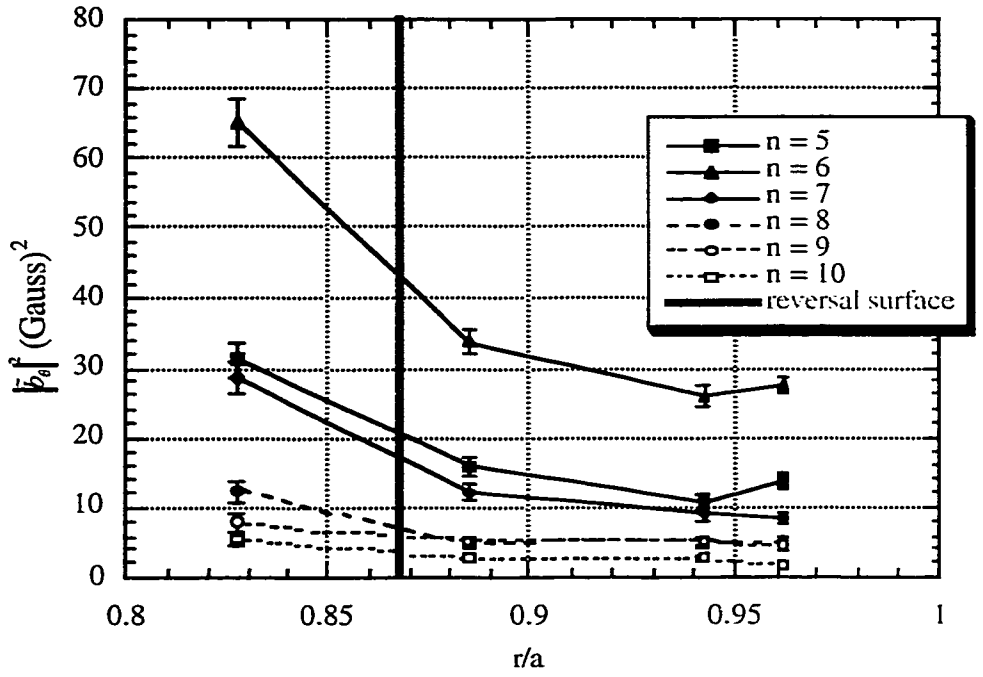

Figure 19: Radial profile of squared toroidal pseudospectrum amplitude of poloidal magnetic field fluctuations for core resonant toroidal modes during sawtooth crashes at -15° P, 330° T. Measured with reference to toroidal magnetic field fluctuations at the wall.

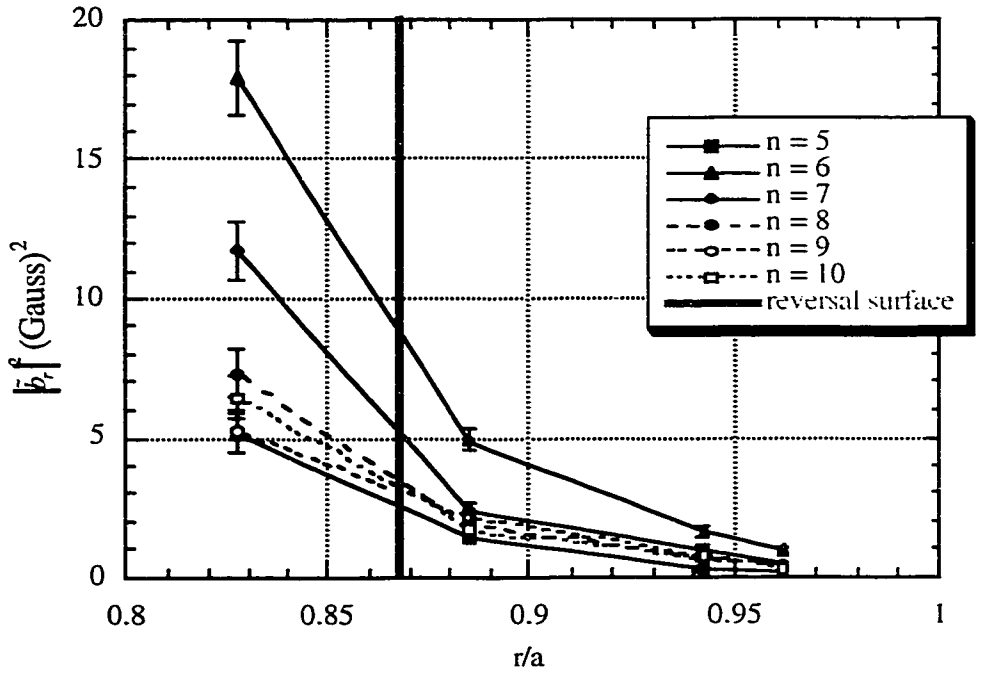

Figure 20: Radial profile of squared toroidal pseudospectrum amplitude of radial magnetic field fluctuations for core resonant toroidal modes during sawtooth crashes at -15° P, 330° T. Measured with reference to toroidal magnetic field fluctuations at the wall.

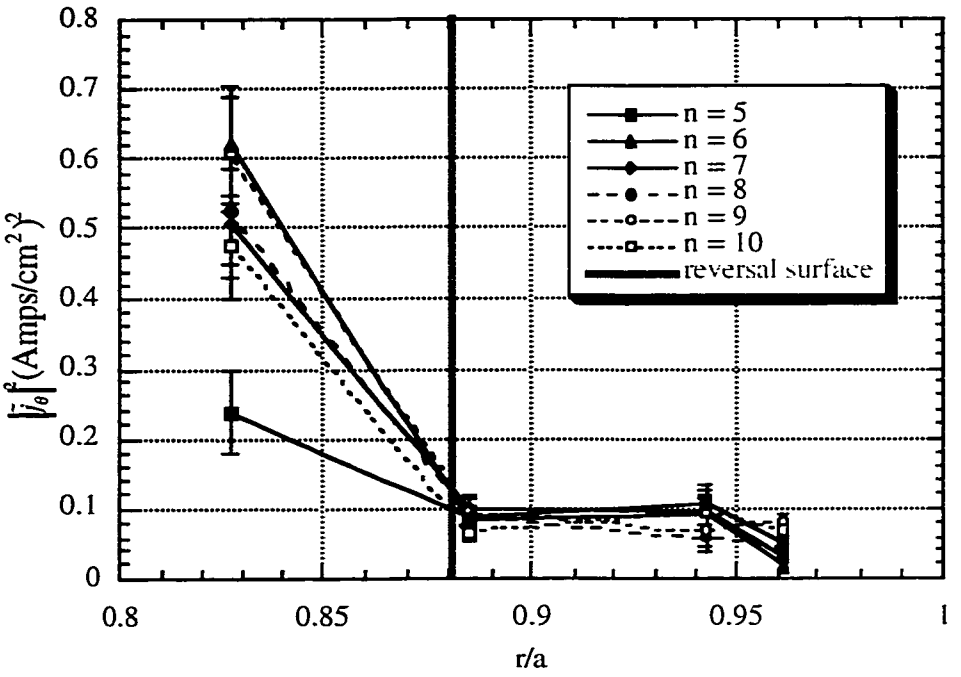

Figure 21: Radial profile of squared toroidal pseudospectrum amplitude of poloidal current density fluctuations for core resonant toroidal modes between sawtooth crashes at -15° P, 330° T. Measured with reference to toroidal magnetic field fluctuations at the wall.

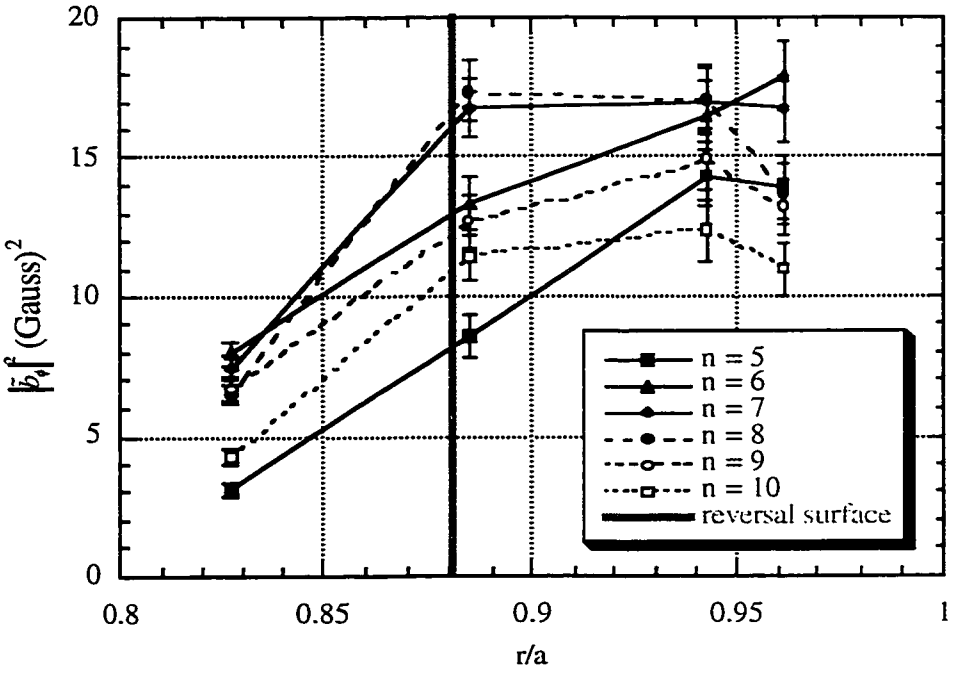

Figure 22: Radial profile of squared toroidal pseudospectrum amplitude of toroidal magnetic field fluctuations for core resonant toroidal modes between sawtooth crashes at -15° P, 330° T. Measured with reference to toroidal magnetic field fluctuations at the wall.

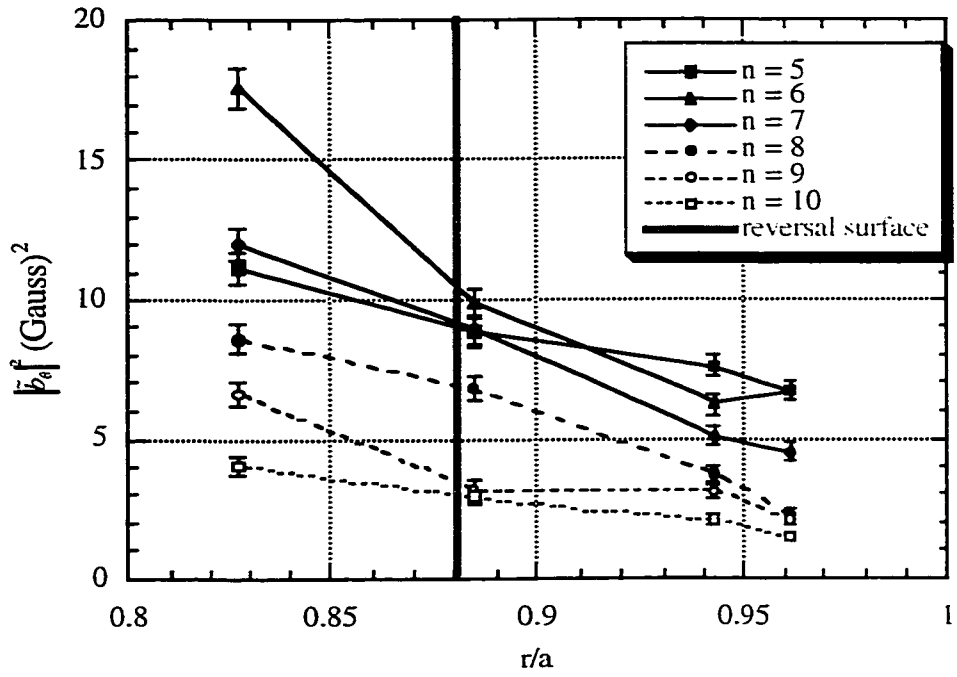

Figure 23: Radial profile of squared toroidal pseudospectrum amplitude of poloidal magnetic field fluctuations for core resonant toroidal modes between sawtooth crashes at -15° P, 330° T. Measured with reference to toroidal magnetic field fluctuations at the wall.

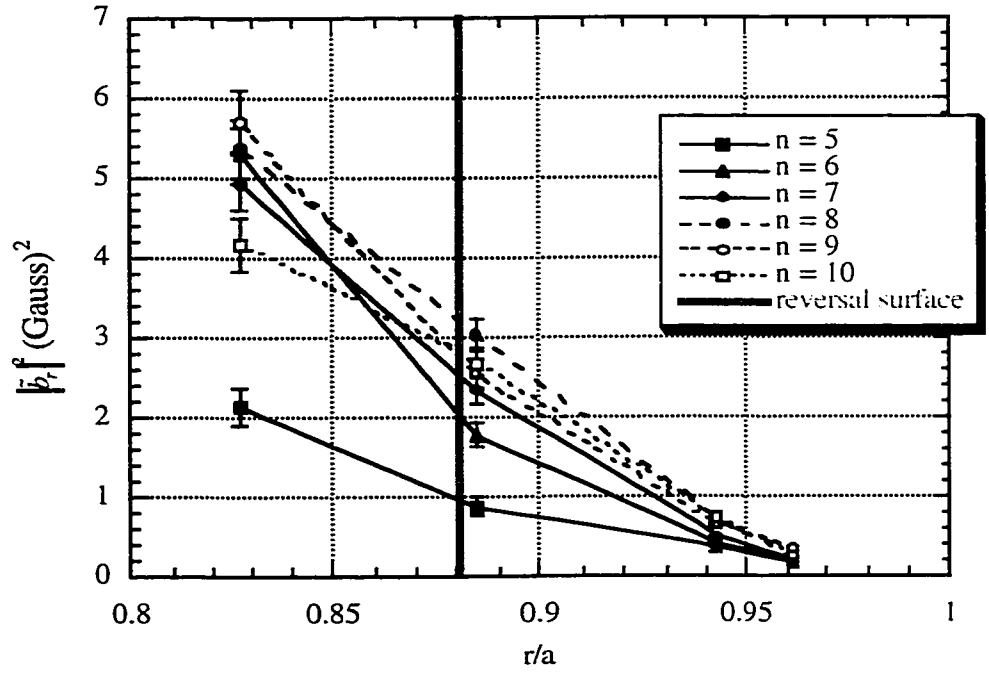

Figure 24: Radial profile of squared toroidal pseudospectrum amplitude of radial magnetic field fluctuations for core resonant toroidal modes between sawtooth crashes at -15° P, 330° T. Measured with reference to toroidal magnetic field fluctuations at the wall.

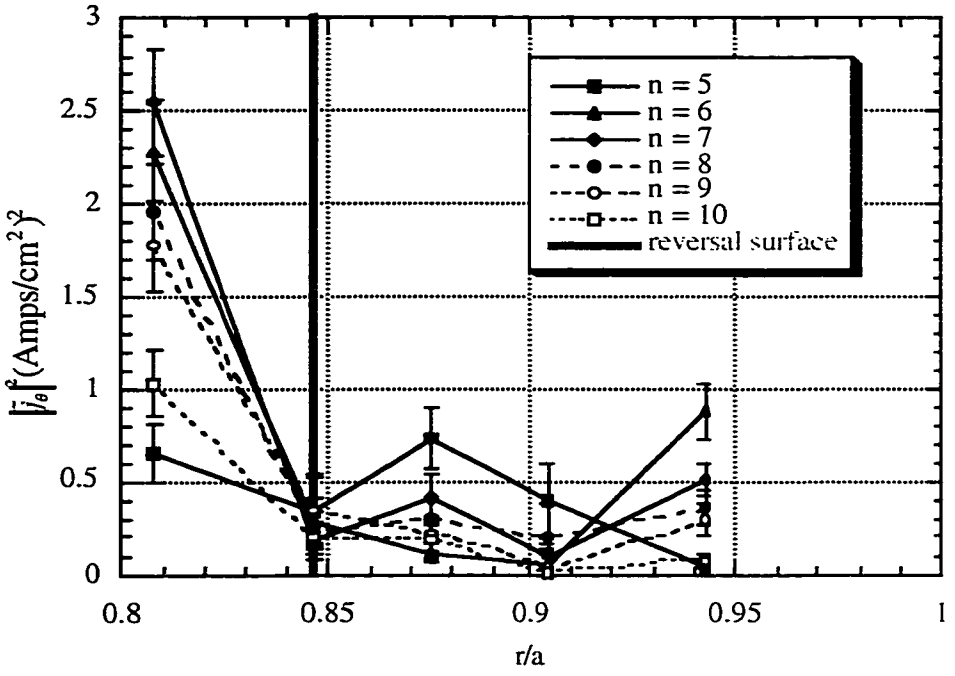

Figure 25: Radial profile of squared toroidal pseudospectrum amplitude of poloidal current density fluctuations for core resonant toroidal modes during sawtooth crashes at 75° P, 120° T. Measured with reference to toroidal magnetic field fluctuations at the wall.

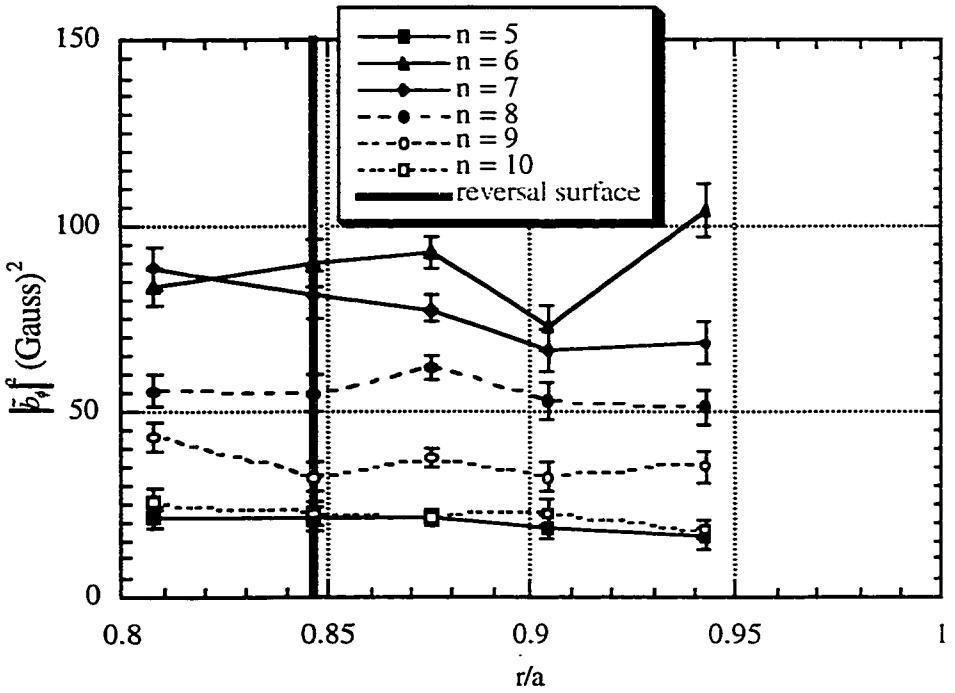

Figure 26: Radial profile of squared toroidal pseudospectrum amplitude of toroidal magnetic field fluctuations for core resonant toroidal modes during sawtooth crashes at 75° P, 120° T. Measured with reference to toroidal magnetic field fluctuations at the wall.

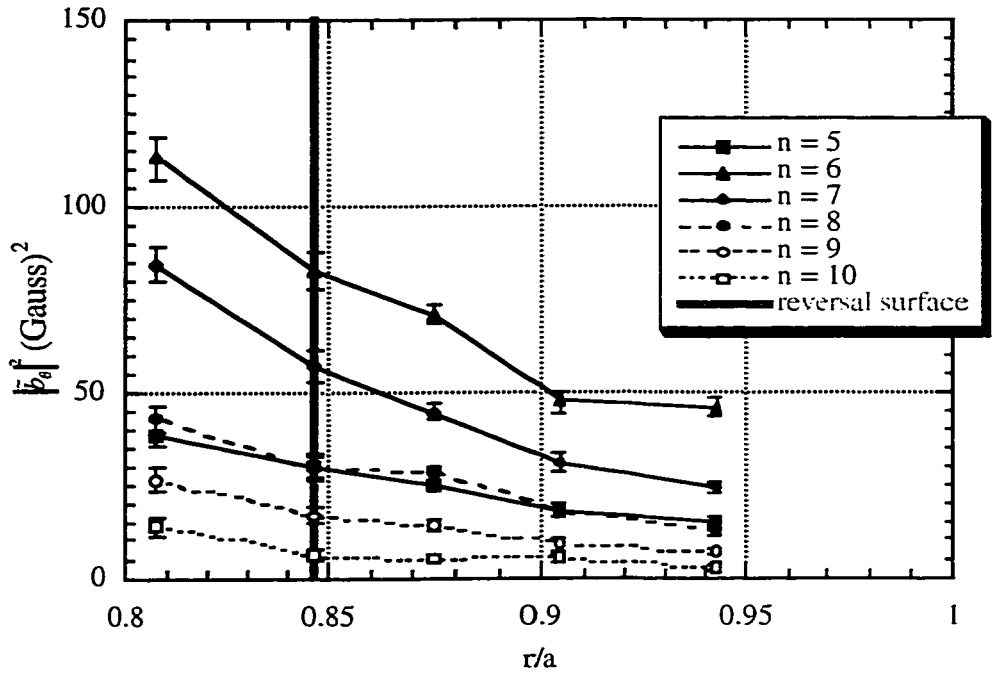

Figure 27: Radial profile of squared toroidal pseudospectrum amplitude of poloidal magnetic field fluctuations for core resonant toroidal modes during sawtooth crashes at 75° P, 120° T. Measured with reference to toroidal magnetic field fluctuations at the wall.

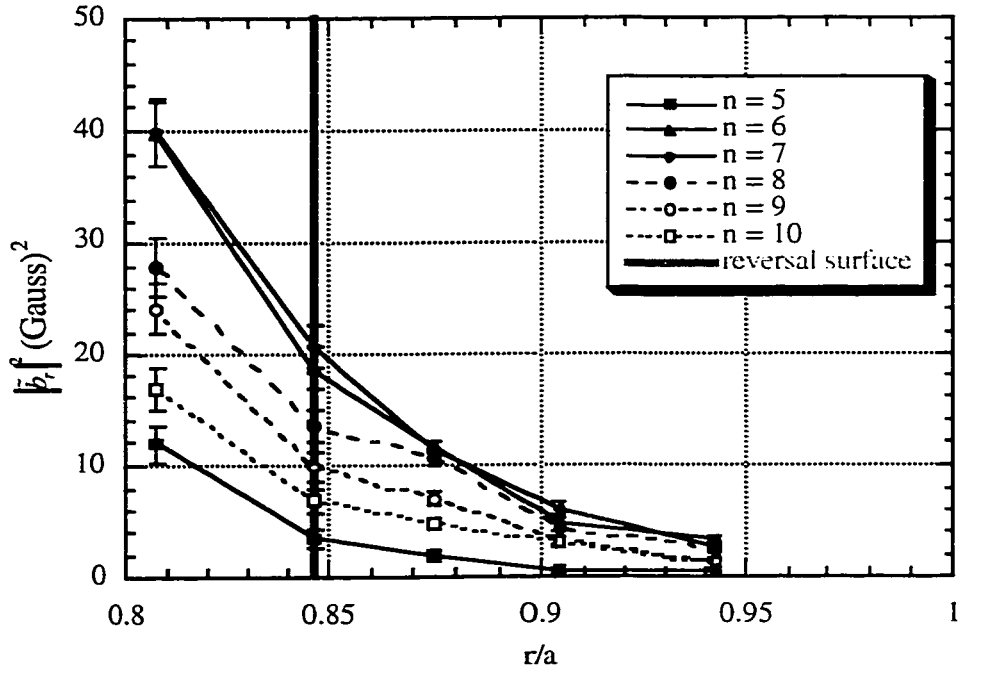

Figure 28: Radial profile of squared toroidal pseudospectrum amplitude of radial magnetic field fluctuations for core resonant toroidal modes during sawtooth crashes at 75° P, 120° T. Measured with reference to toroidal magnetic field fluctuations at the wall.

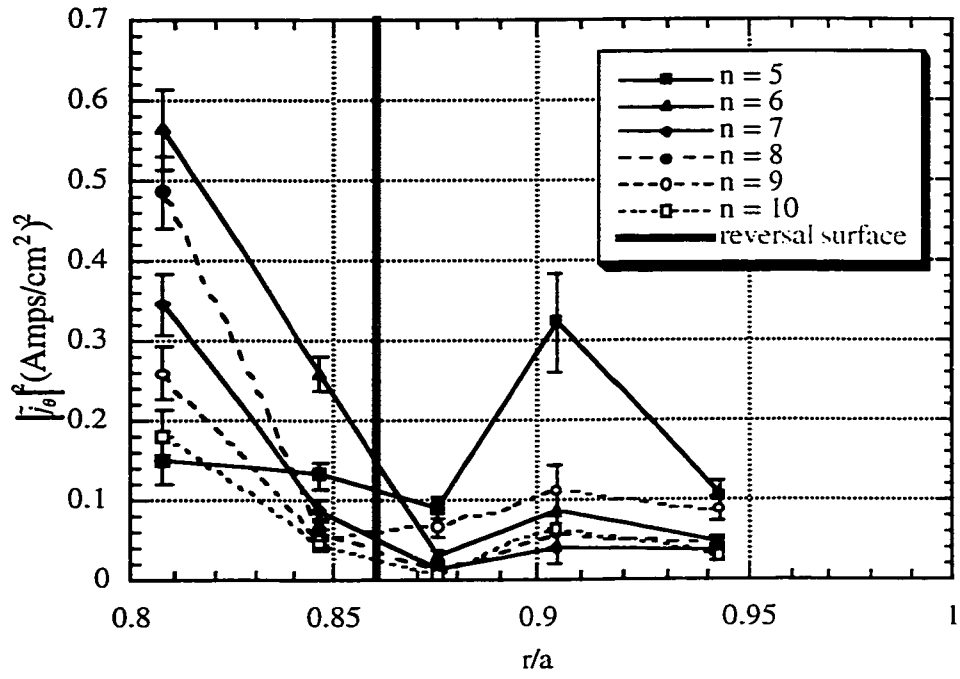

Figure 29: Radial profile of squared toroidal pseudospectrum amplitude of poloidal current density fluctuations for core resonant toroidal modes between sawtooth crashes at 75° P, 120° T. Measured with reference to toroidal magnetic field fluctuations at the wall.

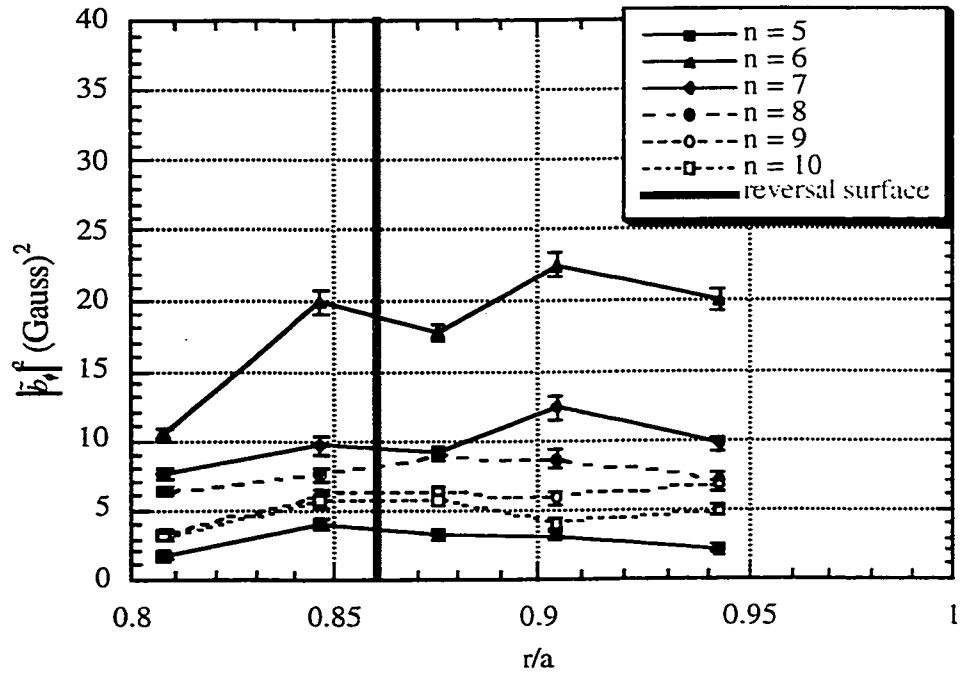

Figure 30: Radial profile of squared toroidal pseudospectrum amplitude of toroidal magnetic field fluctuations for core resonant toroidal modes between sawtooth crashes at 75° P, 120° T. Measured with reference to toroidal magnetic field fluctuations at the wall.

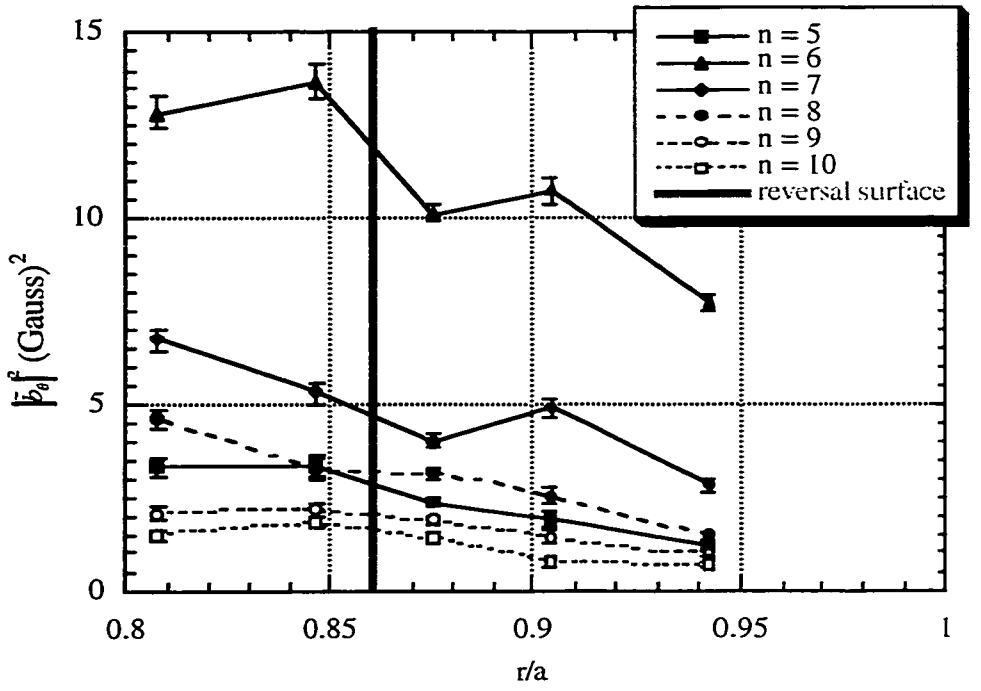

Figure 31: Radial profile of squared toroidal pseudospectrum amplitude of poloidal magnetic field fluctuations for core resonant toroidal modes between sawtooth crashes at 75° P, 120° T. Measured with reference to toroidal magnetic field fluctuations at the wall.

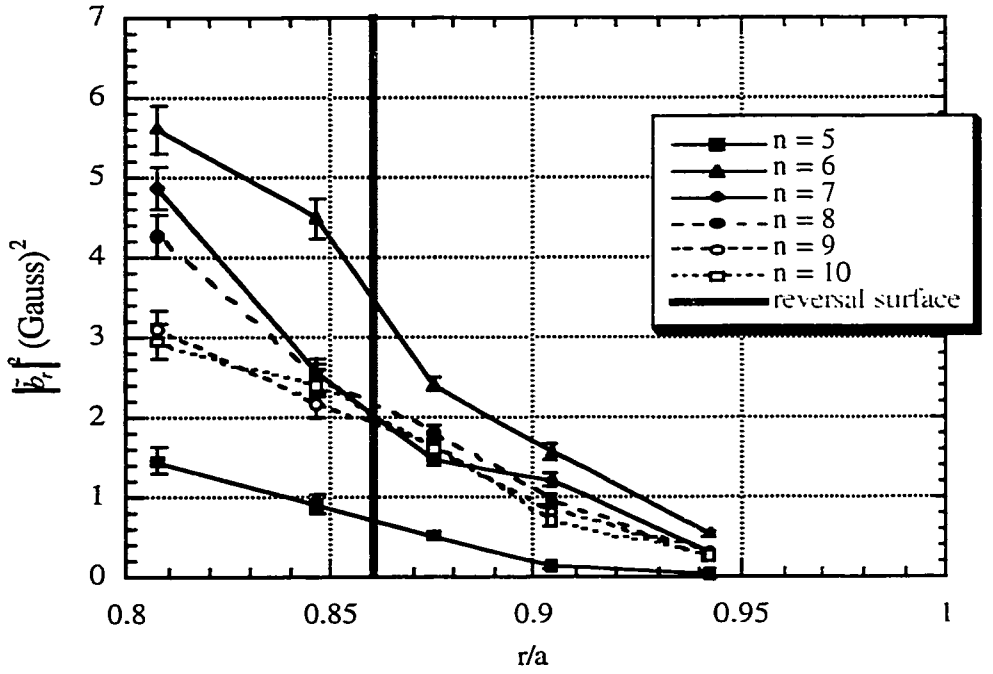

Figure 32: Radial profile of squared toroidal pseudospectrum amplitude of radial magnetic field fluctuations for core resonant toroidal modes between sawtooth crashes at 75° P, 120° T. Measured with reference to toroidal magnetic field fluctuations at the wall.

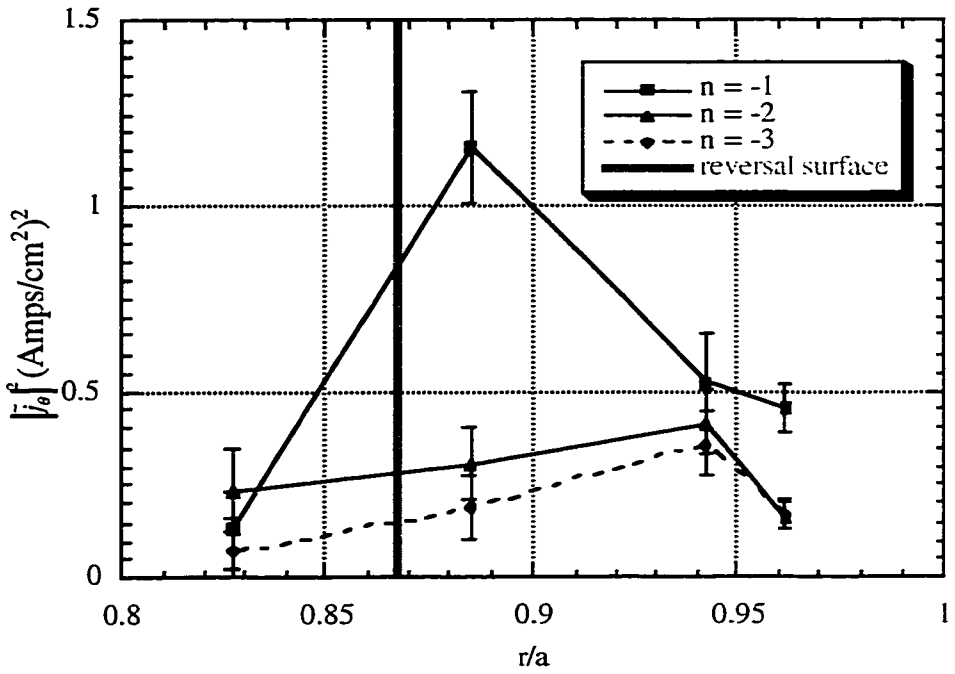

Figure 33: Radial profile of squared toroidal pseudospectrum amplitude of poloidal current density fluctuations for reversal surface resonant toroidal modes during sawtooth crashes at -15° P, 330° T. Measured with reference to toroidal magnetic field fluctuations at the wall.

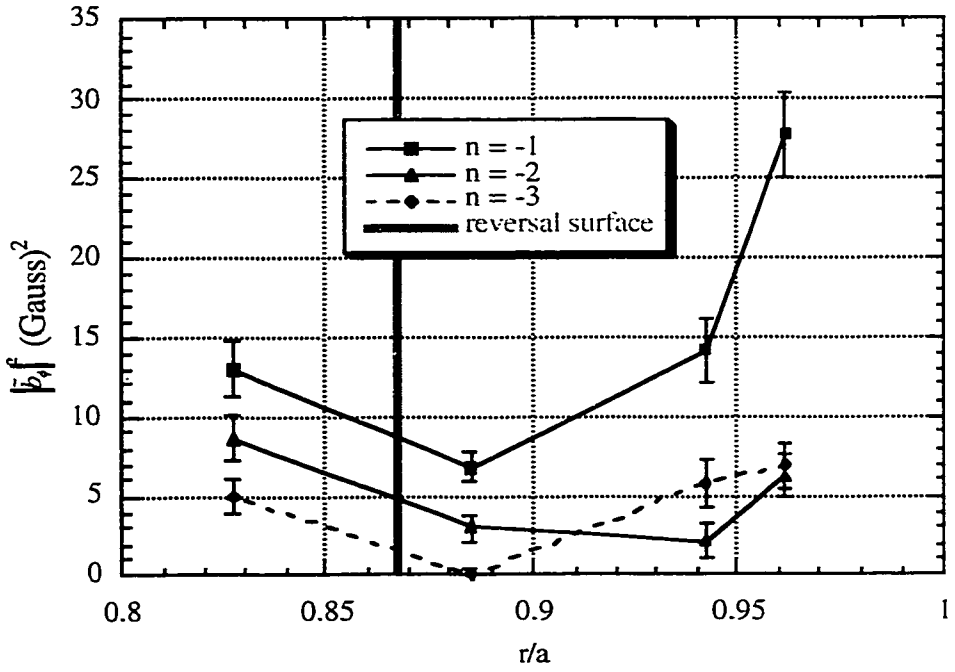

Figure 34: Radial profile of squared toroidal pseudospectrum amplitude of toroidal magnetic field fluctuations for reversal surface resonant toroidal modes during sawtooth crashes at -15° P, 330° T. Measured with reference to toroidal magnetic field fluctuations at the wall.

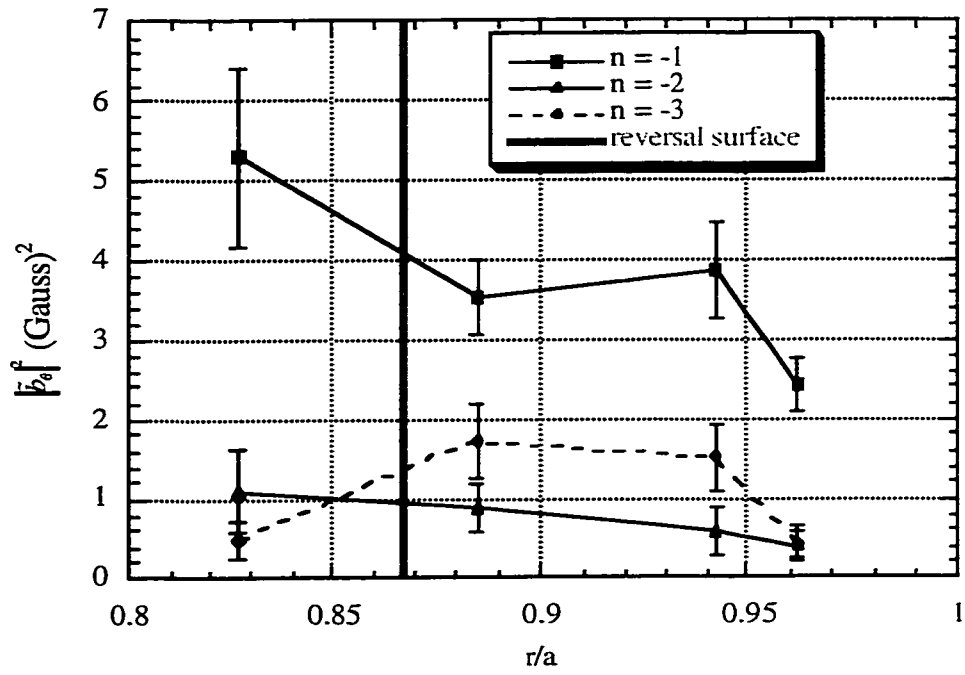

Figure 35: Radial profile of squared toroidal pseudospectrum amplitude of poloidal magnetic field fluctuations for reversal surface resonant toroidal modes during sawtooth crashes at -15° P, 330° T. Measured with reference to toroidal magnetic field fluctuations at the wall.

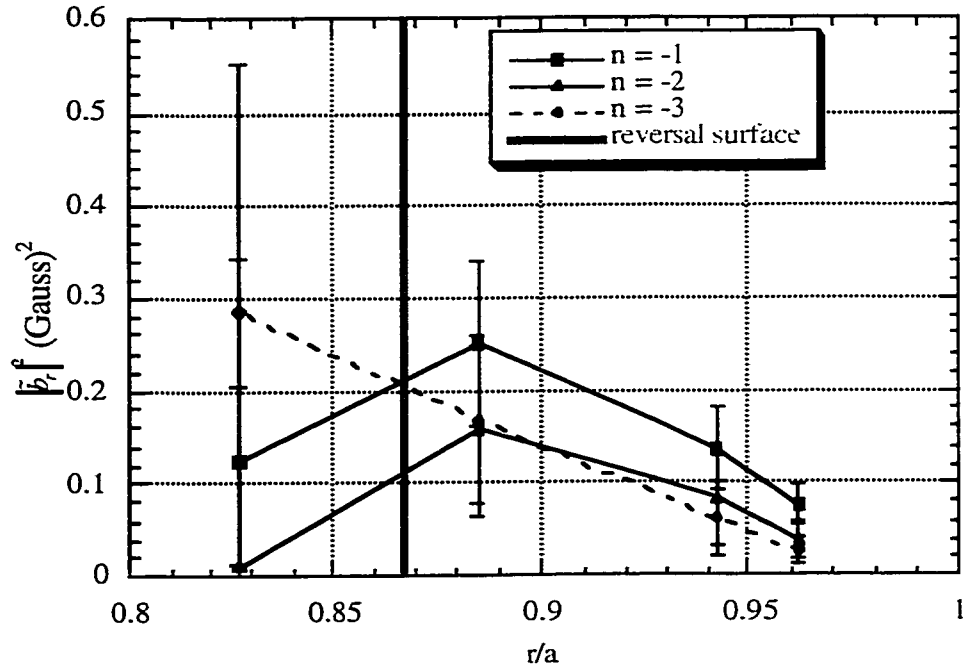

Figure 36: Radial profile of squared toroidal pseudospectrum amplitude of radial magnetic field fluctuations for reversal surface resonant toroidal modes during sawtooth crashes at -15° P, 330° T. Measured with reference to toroidal magnetic field fluctuations at the wall.

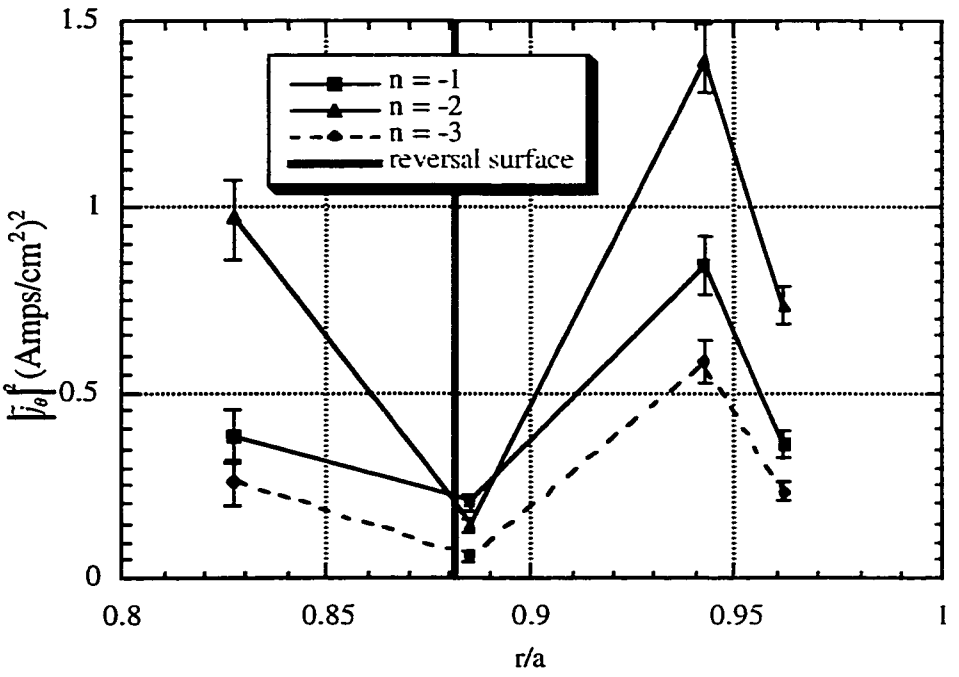

Figure 37: Radial profile of squared toroidal pseudospectrum amplitude of poloidal current density fluctuations for reversal surface resonant toroidal modes between sawtooth crashes at -15° P, 330° T. Measured with reference to toroidal magnetic field fluctuations at the wall.

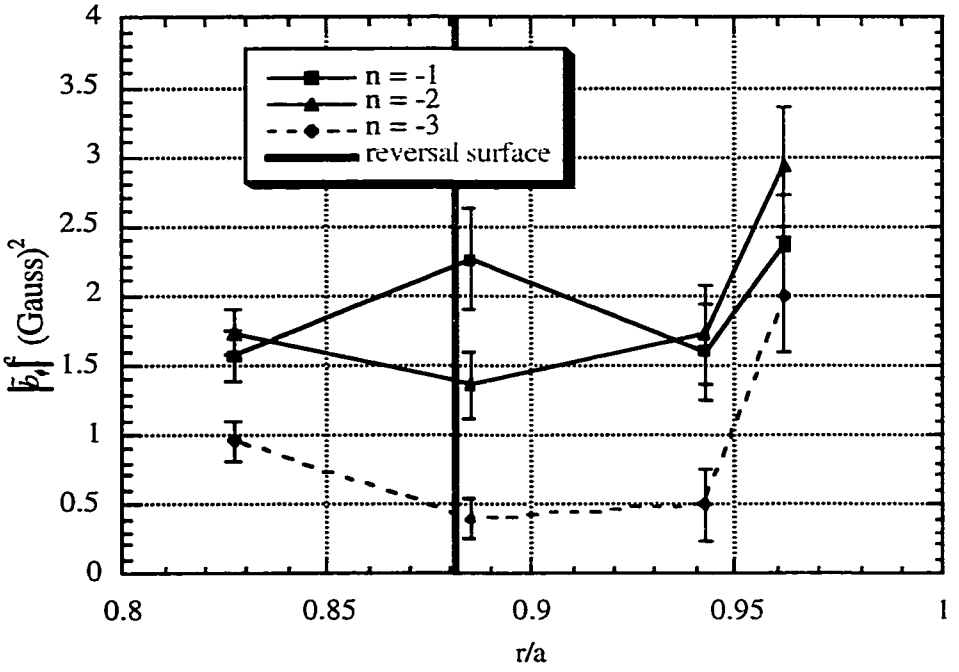

Figure 38: Radial profile of squared toroidal pseudospectrum amplitude of toroidal magnetic field fluctuations for reversal surface resonant toroidal modes between sawtooth crashes at -15° P, 330° T. Measured with reference to toroidal magnetic field fluctuations at the wall.

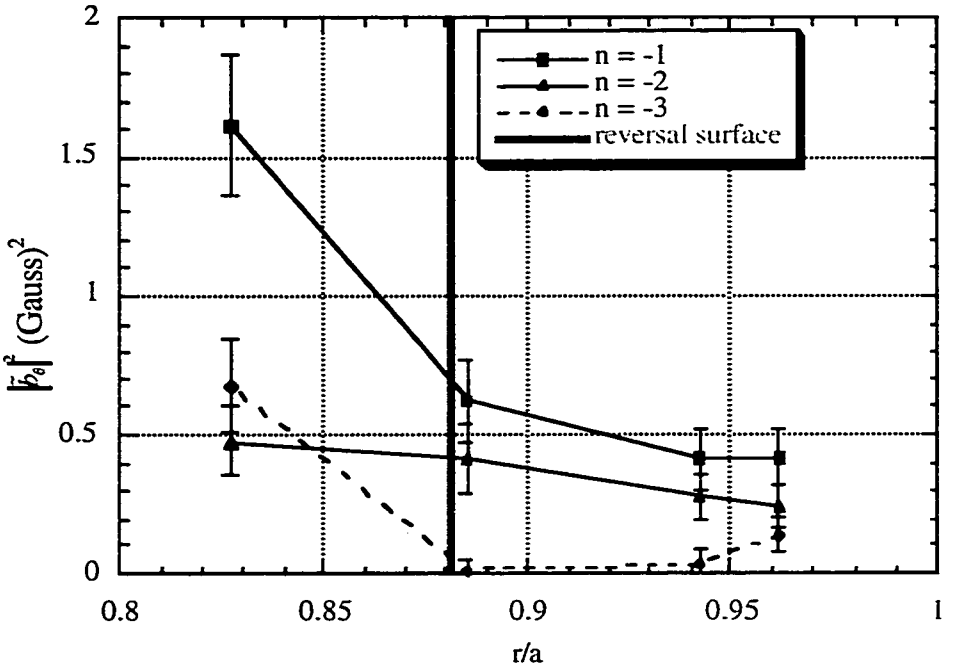

Figure 39: Radial profile of squared toroidal pseudospectrum amplitude of poloidal magnetic field fluctuations for reversal surface resonant toroidal modes between sawtooth crashes at -15° P, 330° T. Measured with reference to toroidal magnetic field fluctuations at the wall.

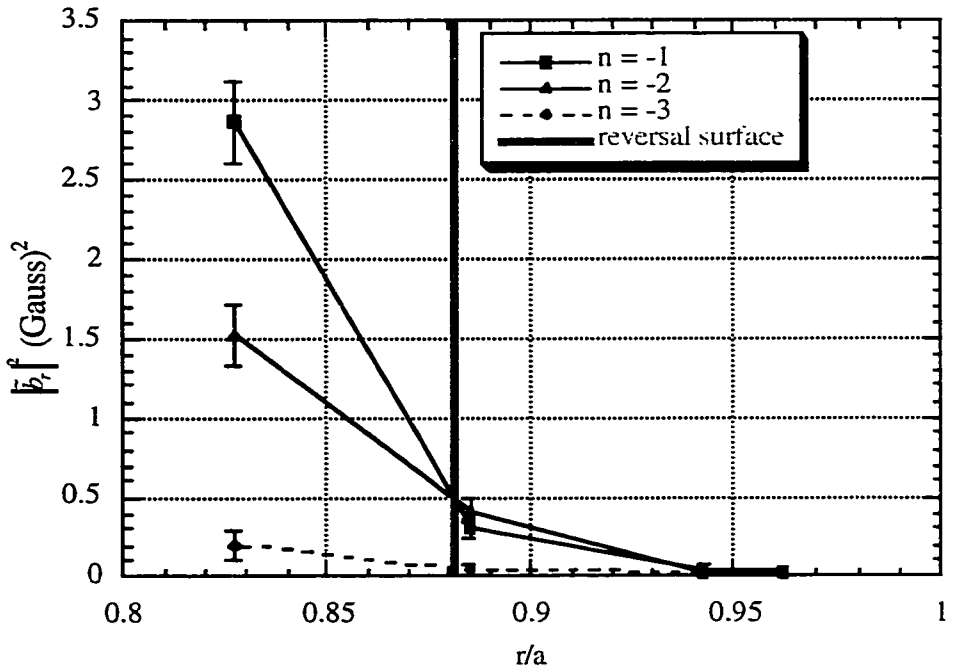

Figure 40: Radial profile of squared toroidal pseudospectrum amplitude of radial magnetic field fluctuations for reversal surface resonant toroidal modes between sawtooth crashes at -15° P, 330° T. Measured with reference to toroidal magnetic field fluctuations at the wall.

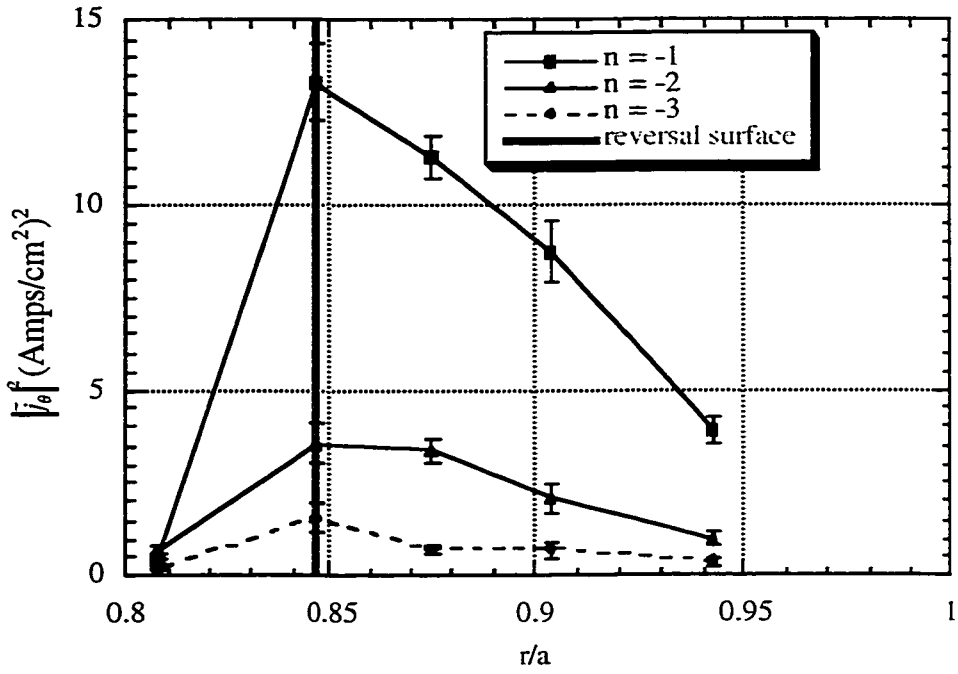

Figure 41: Radial profile of squared toroidal pseudospectrum amplitude of poloidal current density fluctuations for reversal surface resonant toroidal modes during sawtooth crashes at 75° P, 120° T. Measured with reference to toroidal magnetic field fluctuations at the wall.

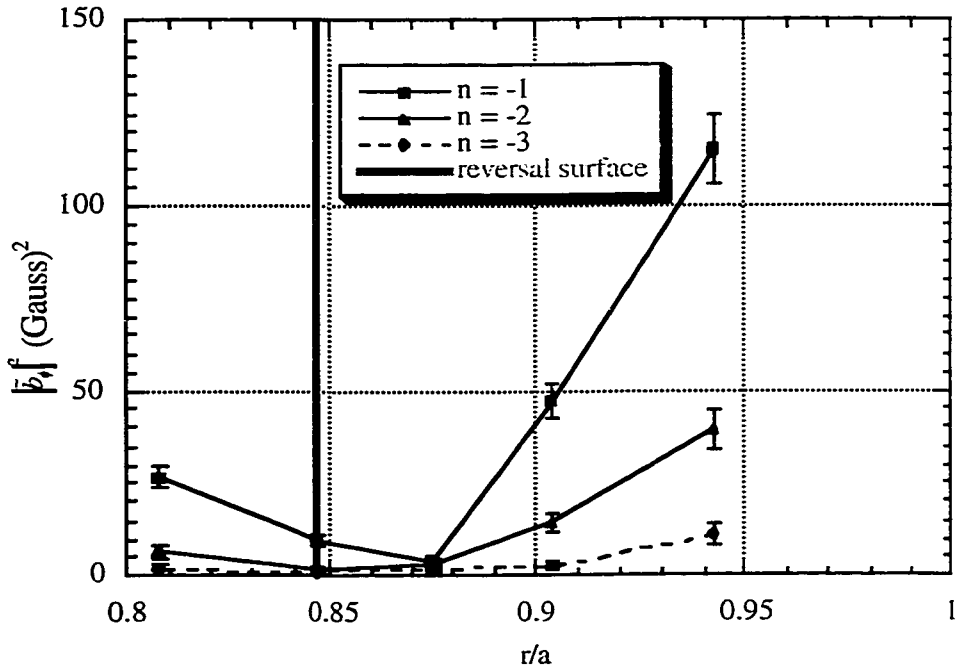

Figure 42: Radial profile of squared toroidal pseudospectrum amplitude of toroidal magnetic field fluctuations for reversal surface resonant toroidal modes during sawtooth crashes at 75° P, 120° T. Measured with reference to toroidal magnetic field fluctuations at the wall.

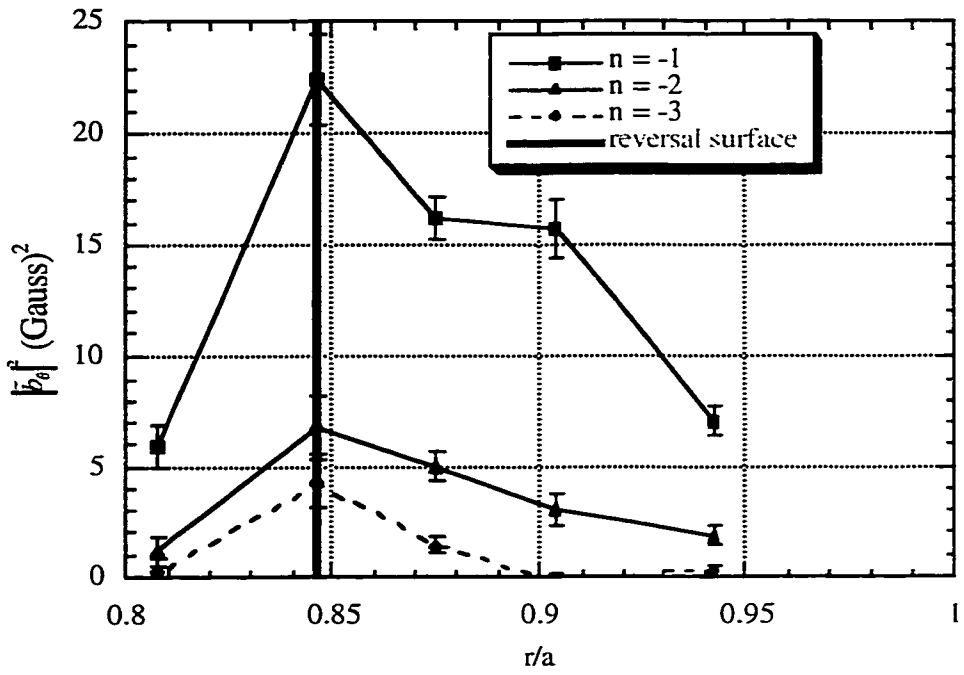

Figure 43: Radial profile of squared toroidal pseudospectrum amplitude of poloidal magnetic field fluctuations for reversal surface resonant toroidal modes during sawtooth crashes at 75° P, 120° T. Measured with reference to toroidal magnetic field fluctuations at the wall.

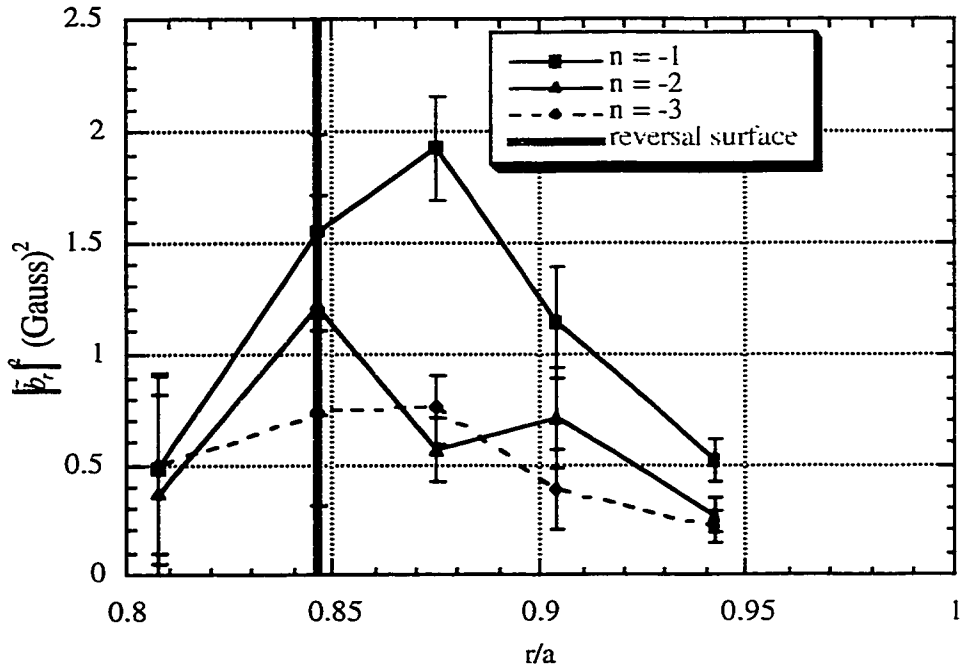

Figure 44: Radial profile of squared toroidal pseudospectrum amplitude of radial magnetic field fluctuations for reversal surface resonant toroidal modes during sawtooth crashes at 75° P, 120° T. Measured with reference to toroidal magnetic field fluctuations at the wall.

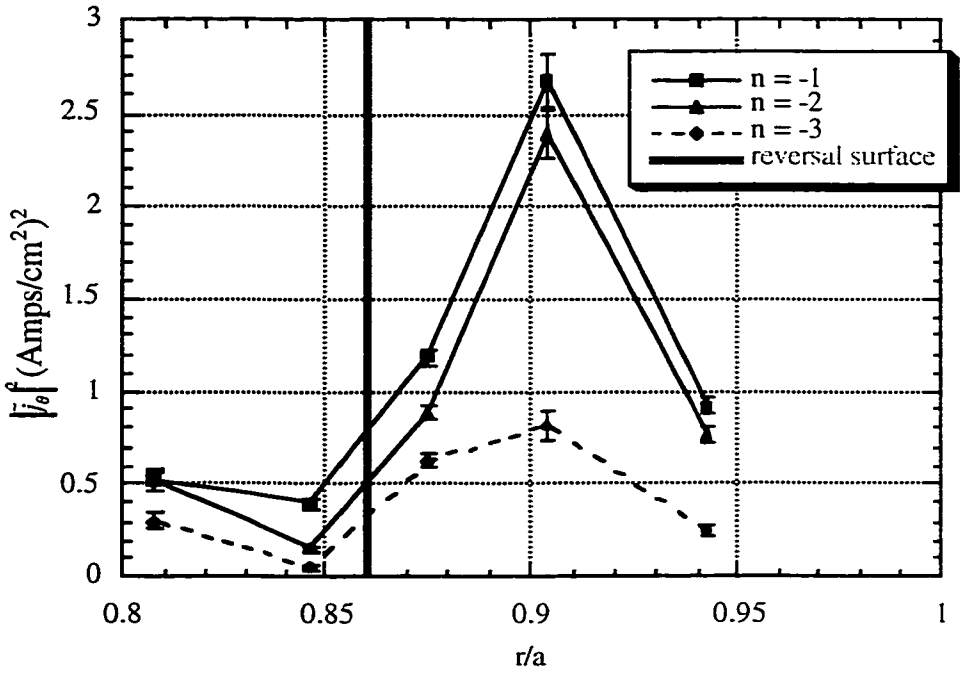

Figure 45: Radial profile of squared toroidal pseudospectrum amplitude of poloidal current density fluctuations for reversal surface resonant toroidal modes between sawtooth crashes at 75° P, 120° T. Measured with reference to toroidal magnetic field fluctuations at the wall.

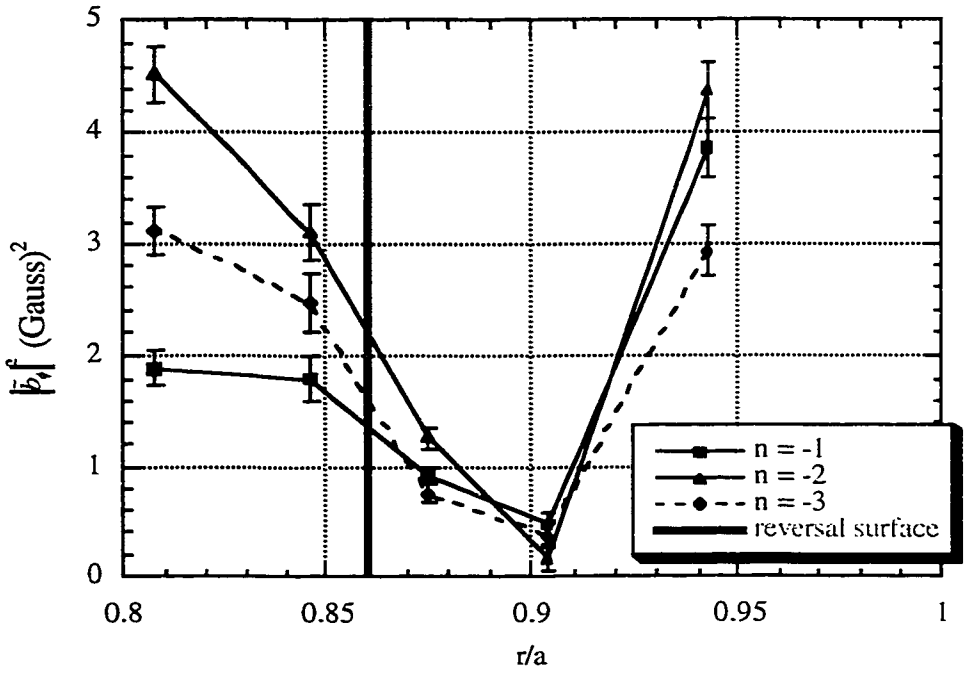

Figure 46: Radial profile of squared toroidal pseudospectrum amplitude of toroidal magnetic field fluctuations for reversal surface resonant toroidal modes between sawtooth crashes at 75° P, 120° T. Measured with reference to toroidal magnetic field fluctuations at the wall.

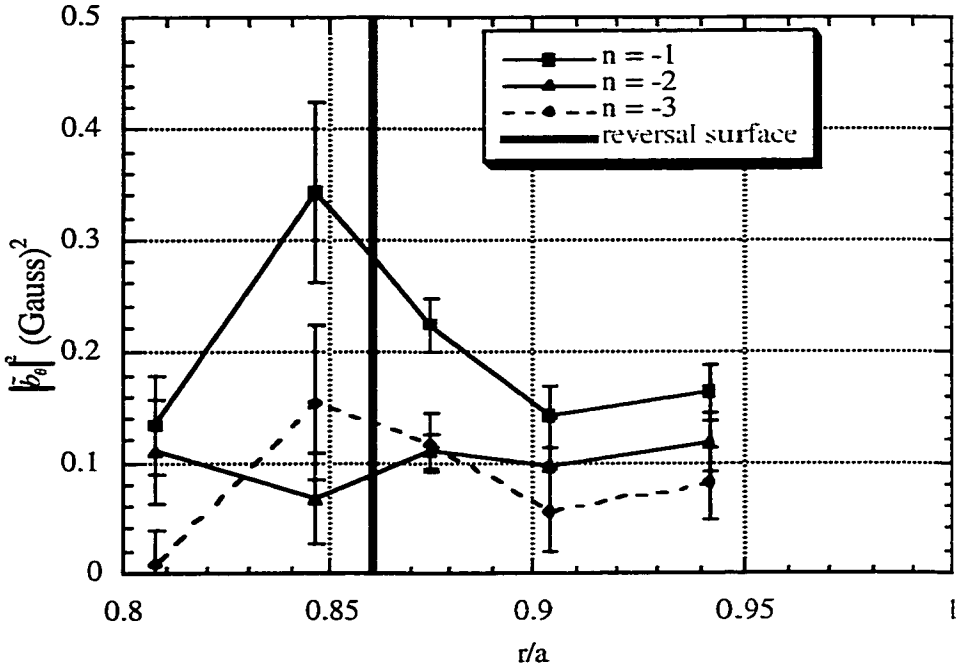

Figure 47: Radial profile of squared toroidal pseudospectrum amplitude of poloidal magnetic field fluctuations for reversal surface resonant toroidal modes between sawtooth crashes at 75° P, 120° T. Measured with reference to toroidal magnetic field fluctuations at the wall.

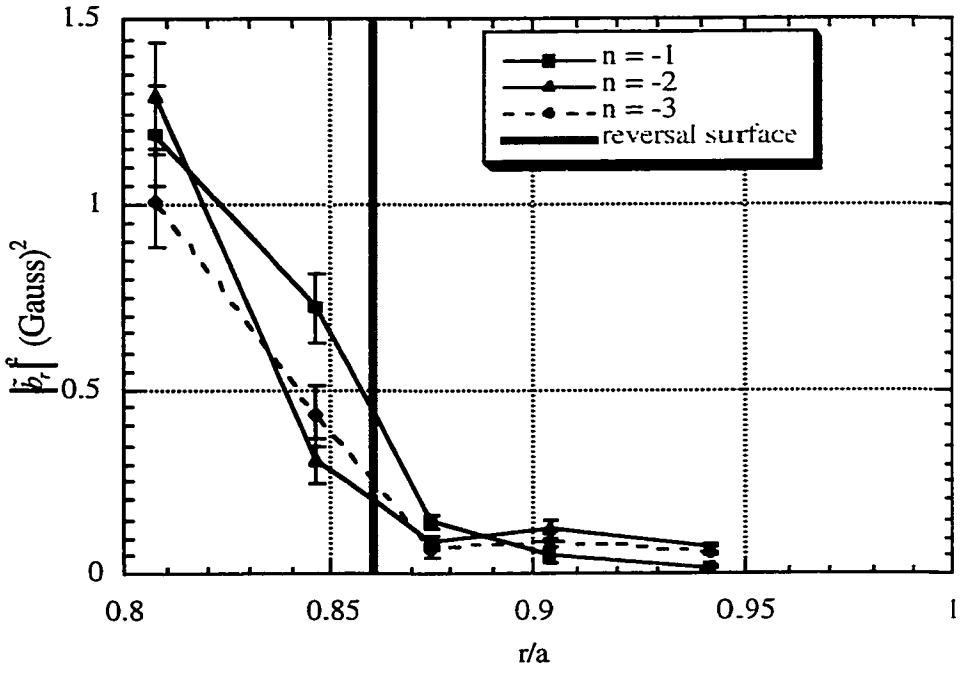

Figure 48: Radial profile of squared toroidal pseudospectrum amplitude of radial magnetic field fluctuations for reversal surface resonant toroidal modes between sawtooth crashes at 75° P, 120° T. Measured with reference to toroidal magnetic field fluctuations at the wall.

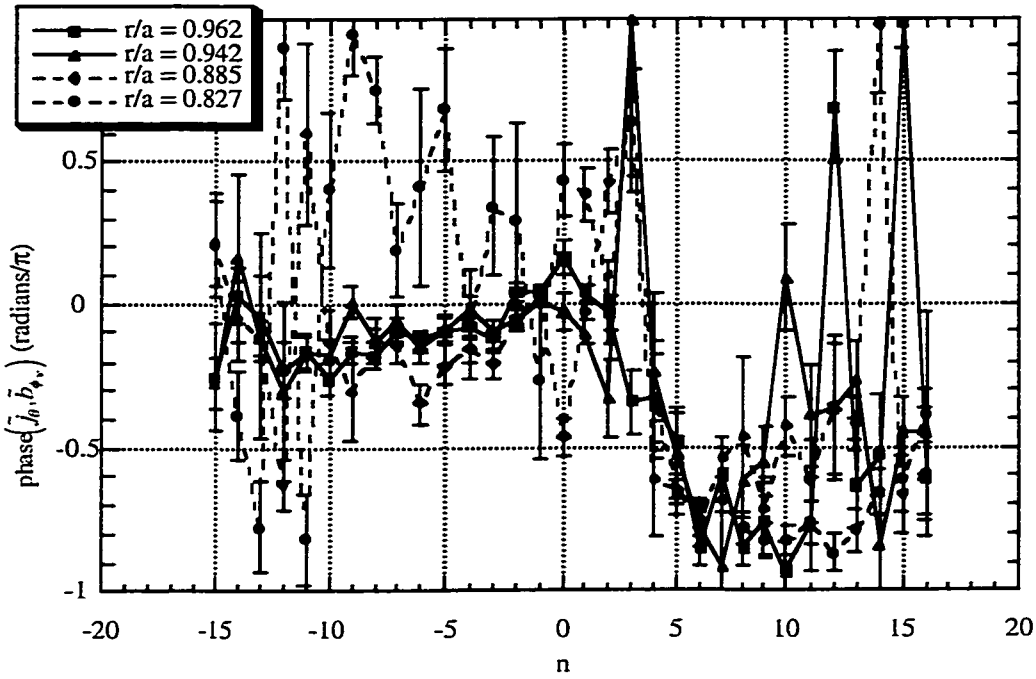

Figure 49: For each toroidal mode, relative phase between poloidal current density fluctuation at -15° P and toroidal magnetic field fluctuation at wall at 241° P measured during sawtooth crashes.

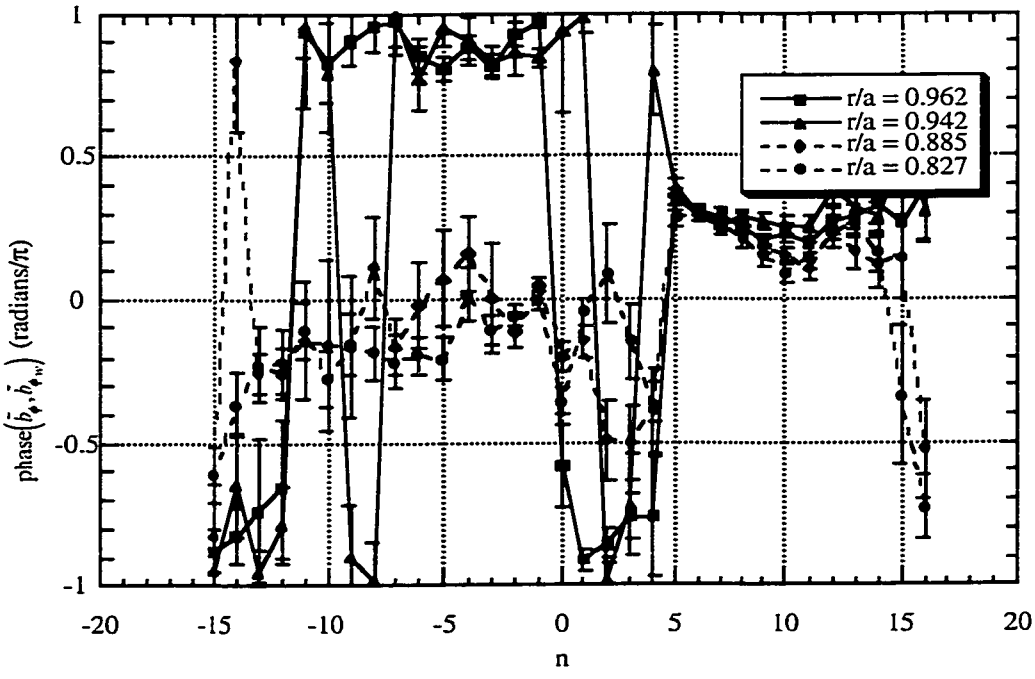

Figure 50: For each toroidal mode, relative phase between toroidal magnetic field fluctuation at -15° P and toroidal magnetic field fluctuation at wall at 241° P measured during sawtooth crashes.

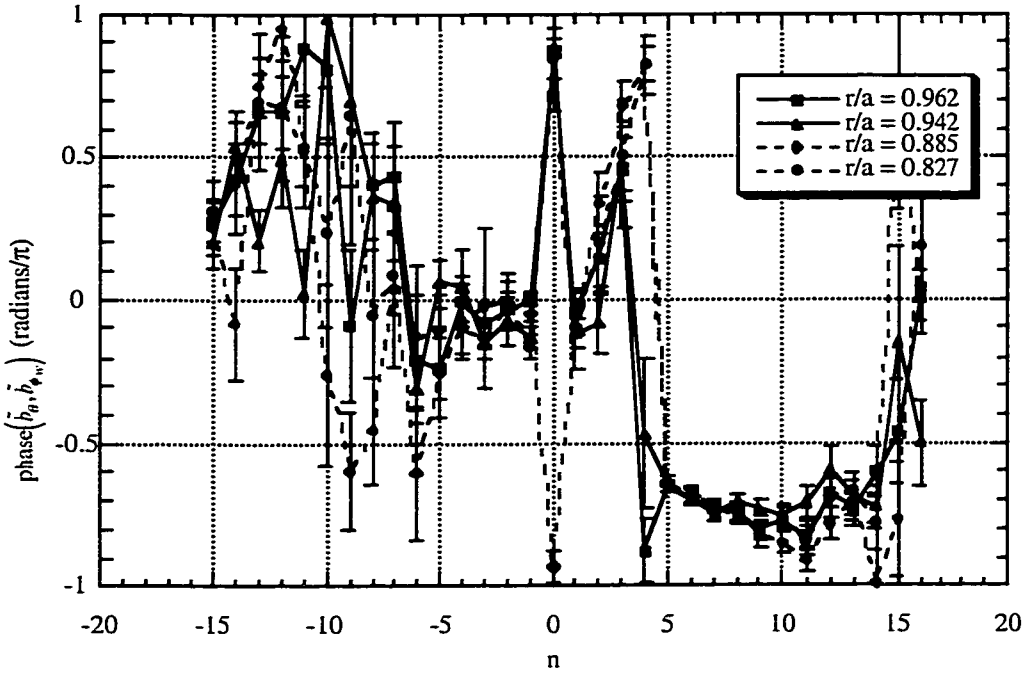

Figure 51: For each toroidal mode, relative phase between poloidal magnetic field fluctuation at -15° P and toroidal magnetic field fluctuation at wall at 241° P measured during sawtooth crashes.

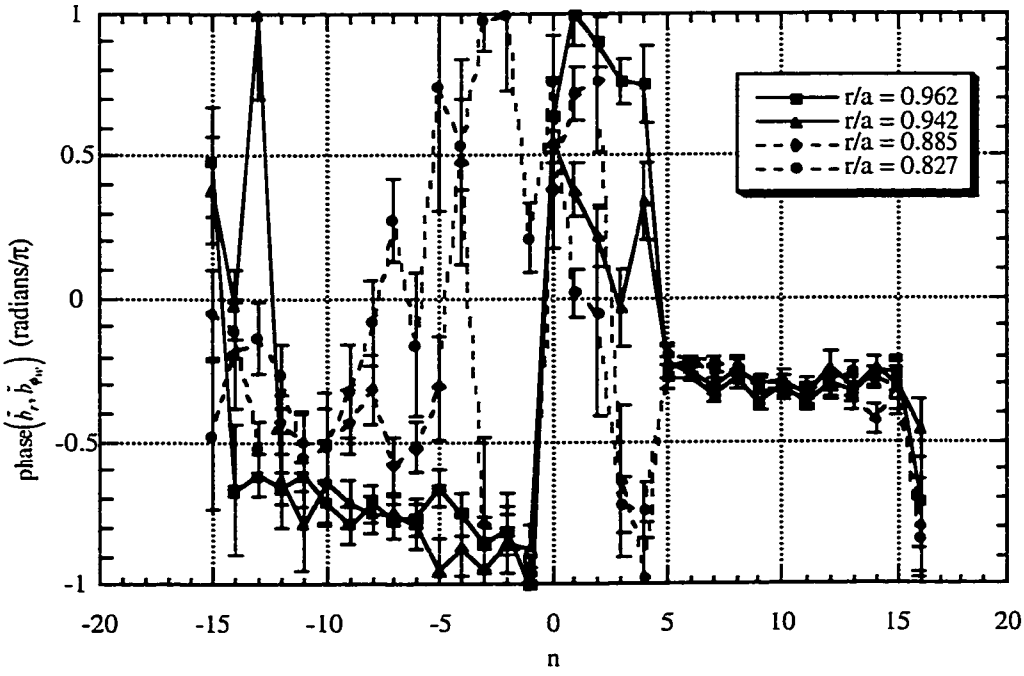

Figure 52: For each toroidal mode, relative phase between radial magnetic field fluctuation at -15° P and toroidal magnetic field fluctuation at wall at 241° P measured during sawtooth crashes.

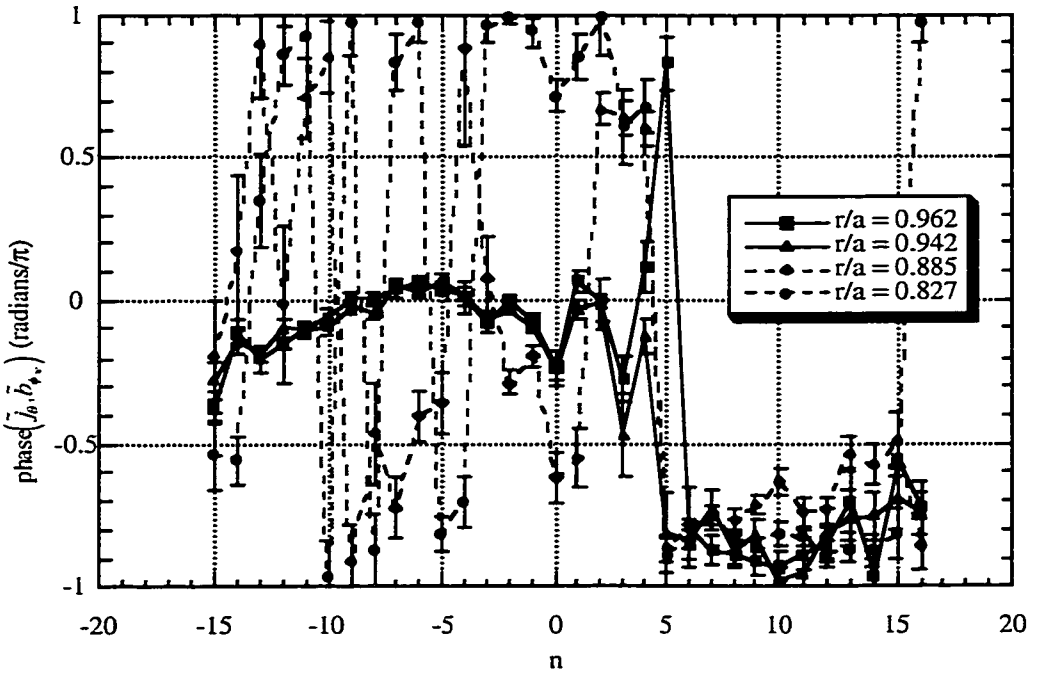

Figure 53: For each toroidal mode, relative phase between poloidal current density fluctuation at -15° P and toroidal magnetic field fluctuation at wall at 241° P measured between sawtooth crashes.

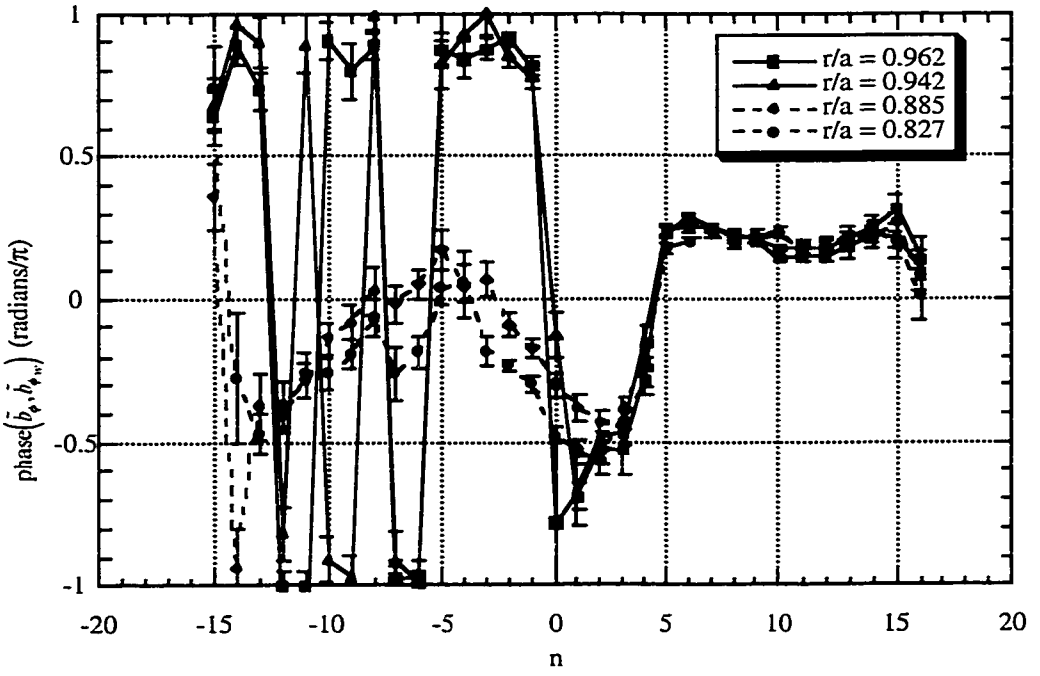

Figure 54: For each toroidal mode, relative phase between toroidal magnetic field fluctuation at -15° P and toroidal magnetic field fluctuation at wall at 241° P measured between sawtooth crashes.

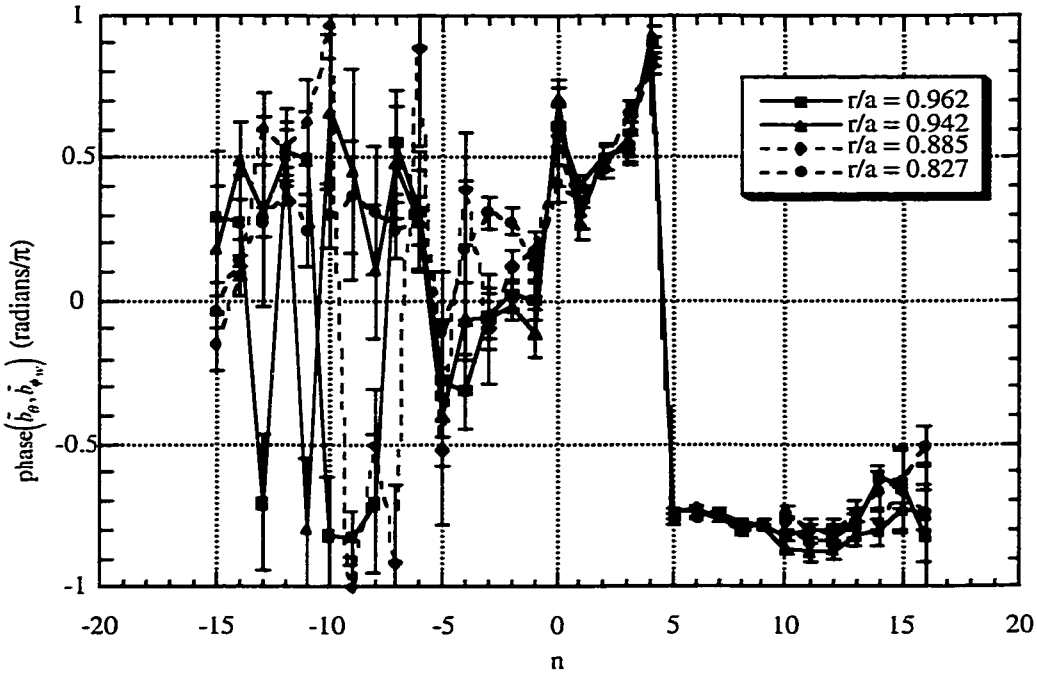

Figure 55: For each toroidal mode, relative phase between poloidal magnetic field fluctuation at -15° P and toroidal magnetic field fluctuation at wall at 241° P measured between sawtooth crashes.

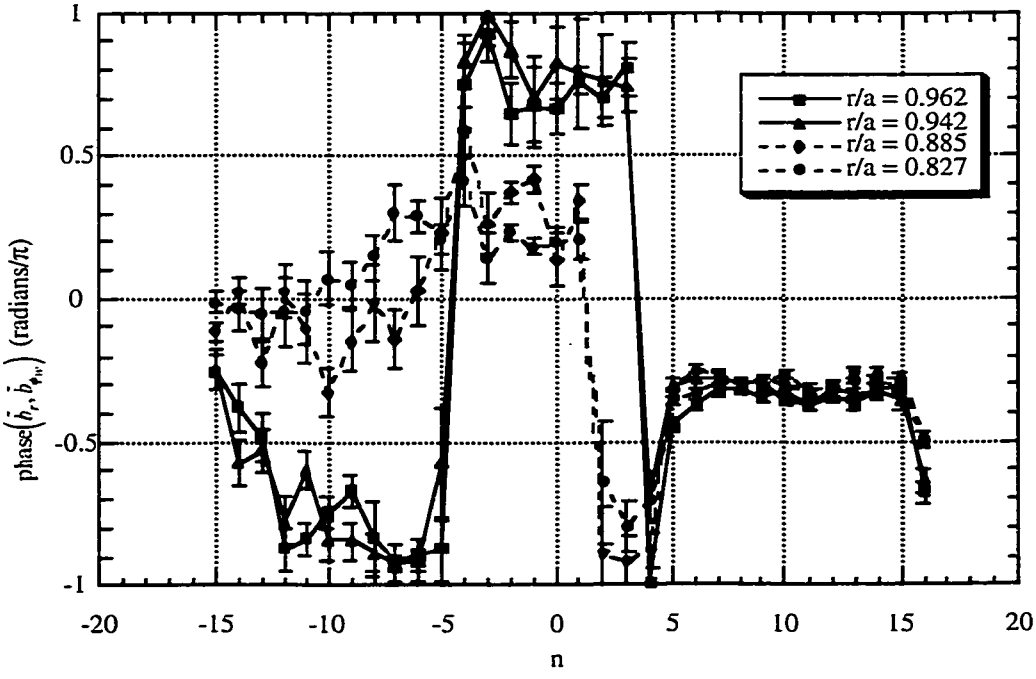

Figure 56: For each toroidal mode, relative phase between radial magnetic field fluctuation at -15° P and toroidal magnetic field fluctuation at wall at 241° P measured between sawtooth crashes.

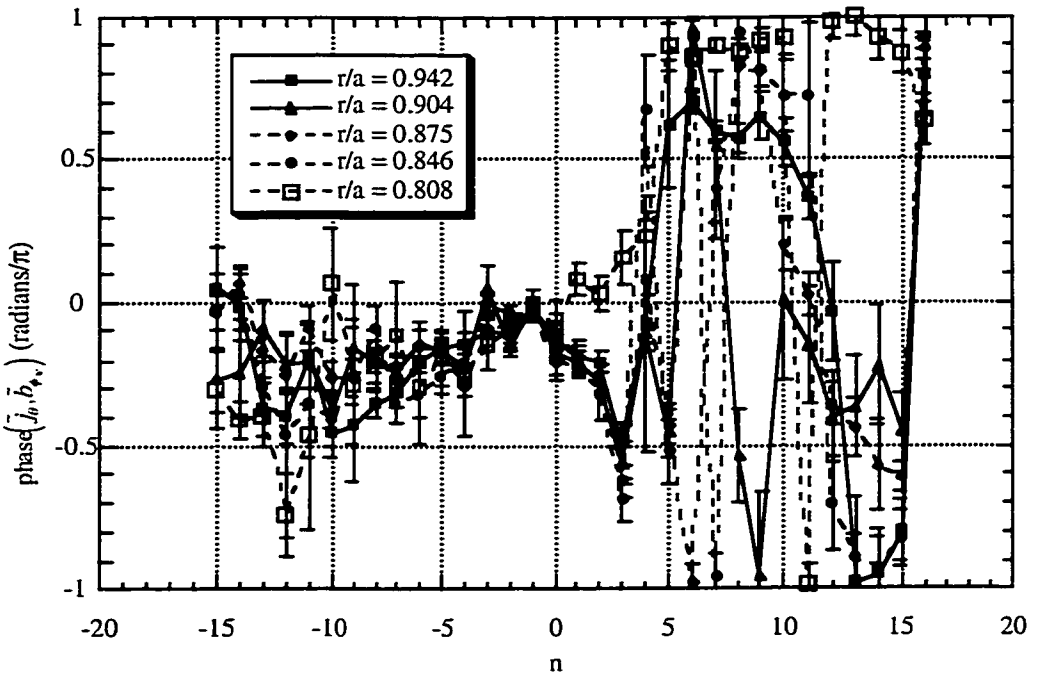

Figure 57: For each toroidal mode, relative phase between poloidal current density fluctuation at 75° P and toroidal magnetic field fluctuation at wall at 241° P measured during sawtooth crashes.

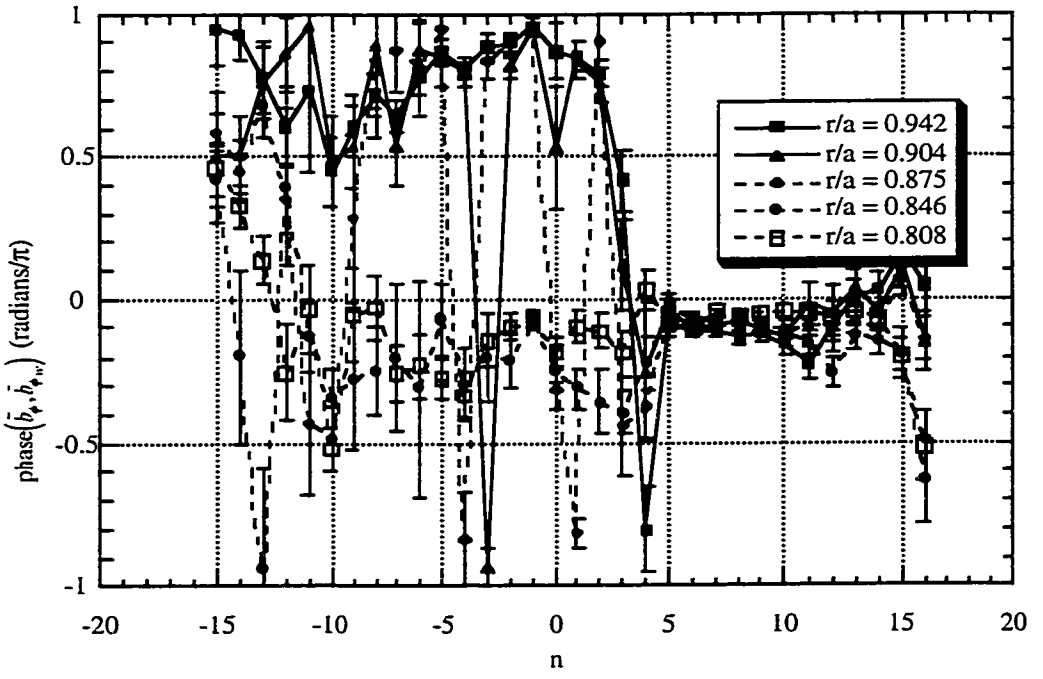

Figure 58: For each toroidal mode, relative phase between toroidal magnetic field fluctuation at 75° P and toroidal magnetic field fluctuation at wall at 241° P measured during sawtooth crashes.

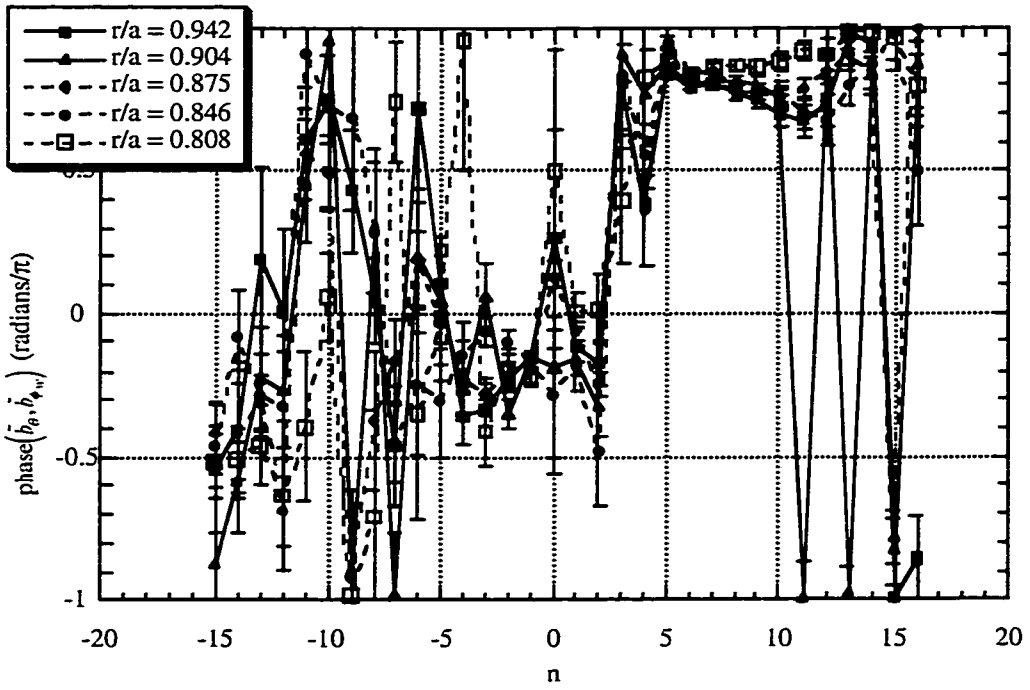

Figure 59: For each toroidal mode, relative phase between poloidal magnetic field fluctuation at 75° P and toroidal magnetic field fluctuation at wall at 241° P measured during sawtooth crashes.

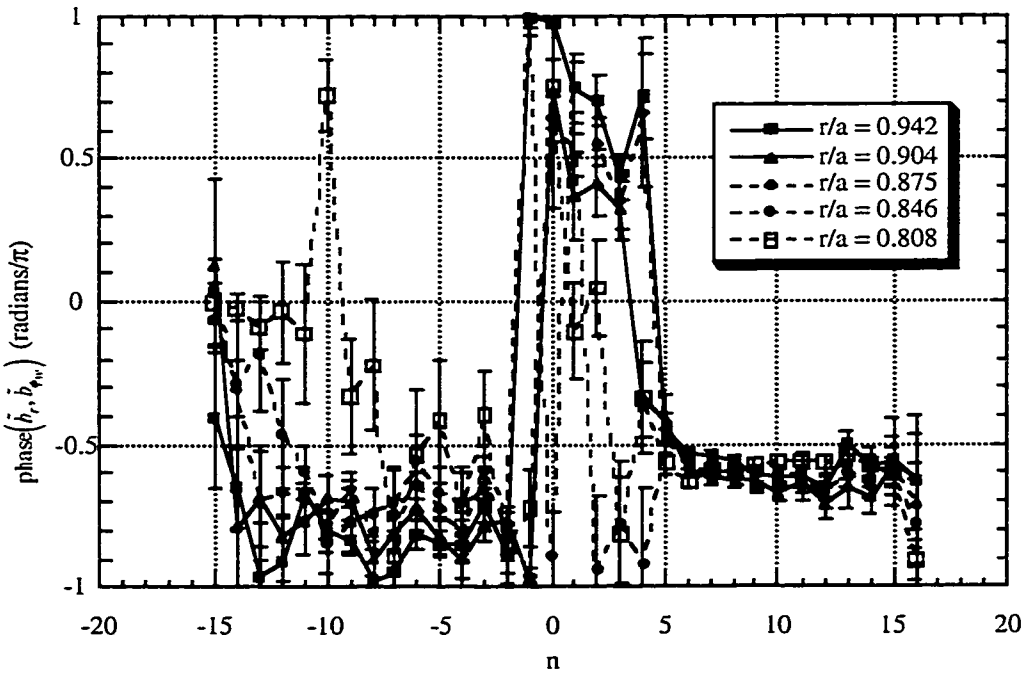

Figure 60: For each toroidal mode, relative phase between radial magnetic field fluctuation at 75° P and toroidal magnetic field fluctuation at wall at 241° P measured during sawtooth crashes.

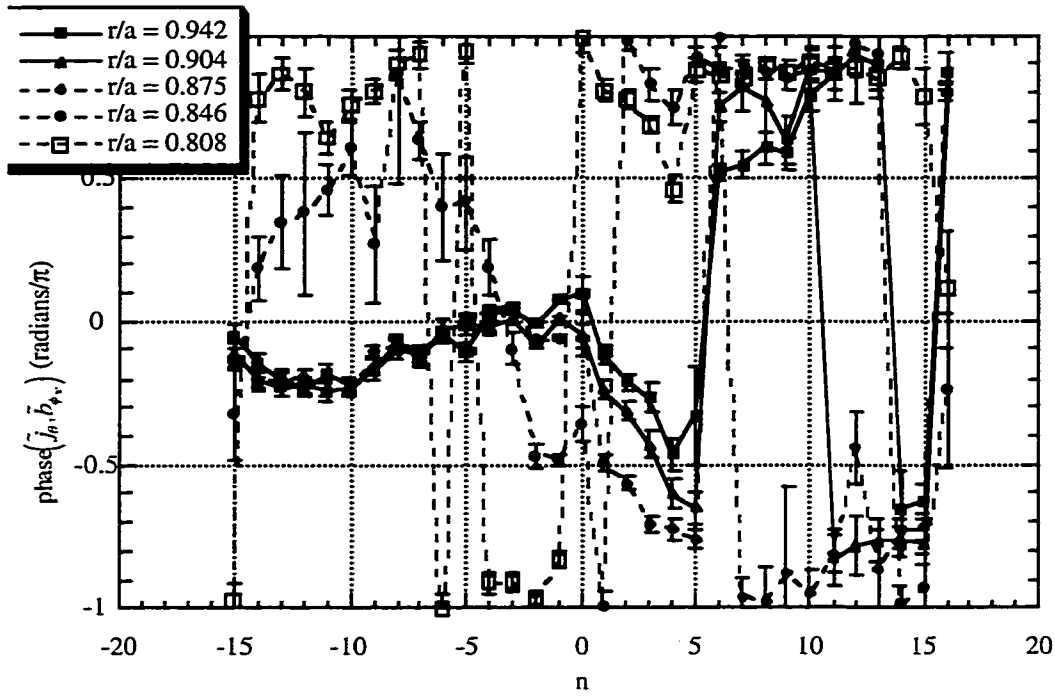

Figure 61: For each toroidal mode, relative phase between poloidal current density fluctuation at 75° P and toroidal magnetic field fluctuation at wall at 241° P measured between sawtooth crashes.

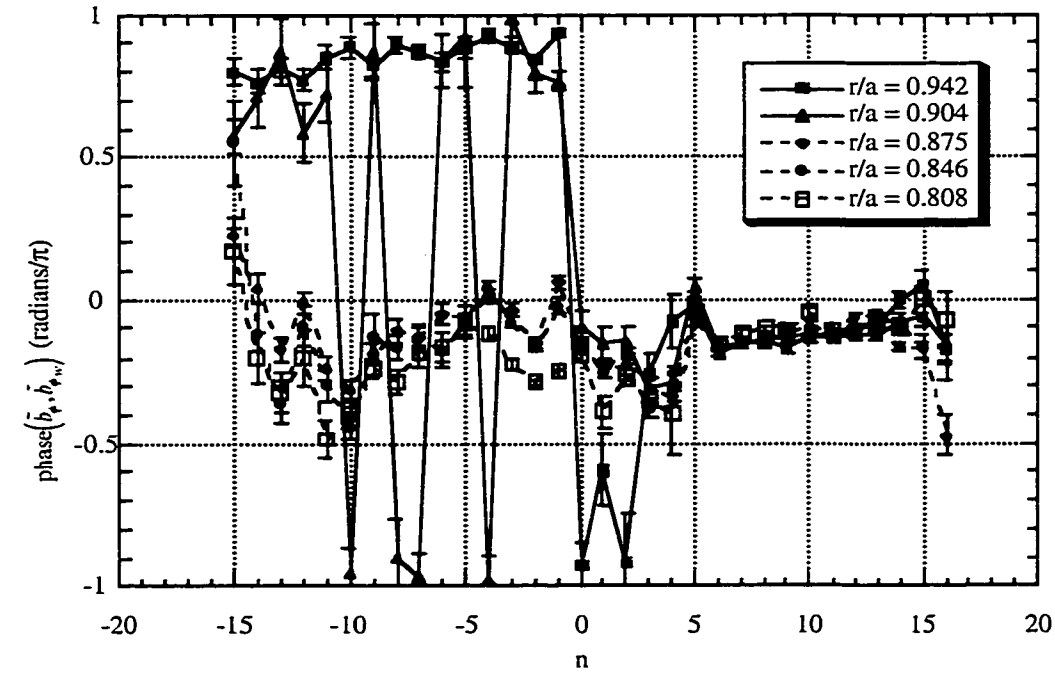

Figure 62: For each toroidal mode, relative phase between toroidal magnetic field fluctuation at 75° P and toroidal magnetic field fluctuation at wall at 241° P measured between sawtooth crashes.

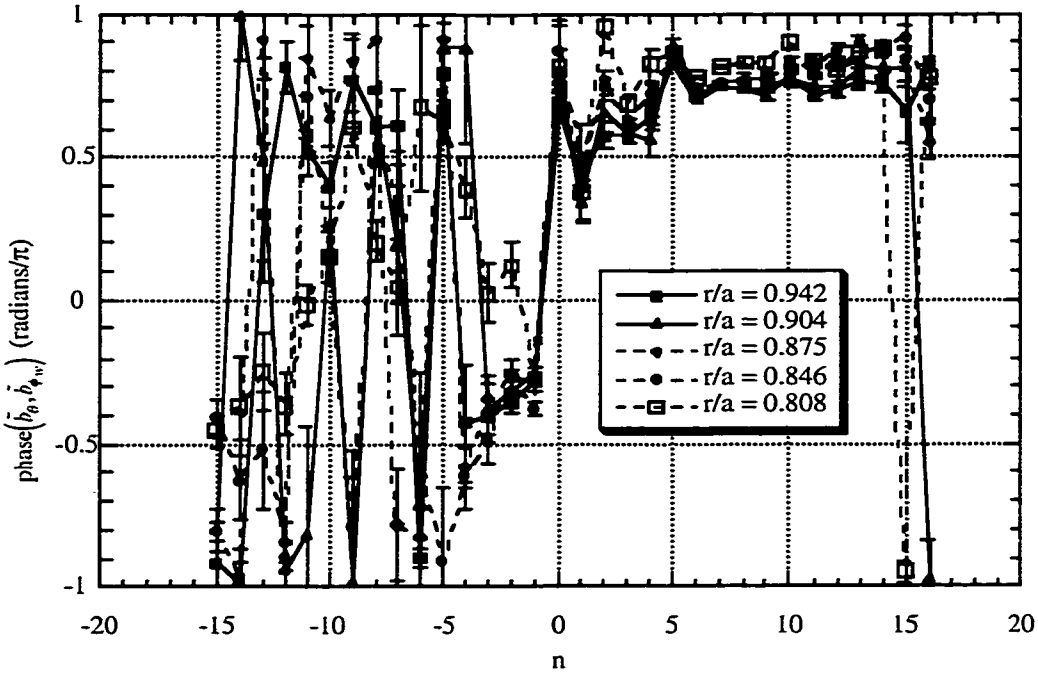

Figure 63: For each toroidal mode, relative phase between poloidal magnetic field fluctuation at 75° P and toroidal magnetic field fluctuation at wall at 241° P measured between sawtooth crashes.

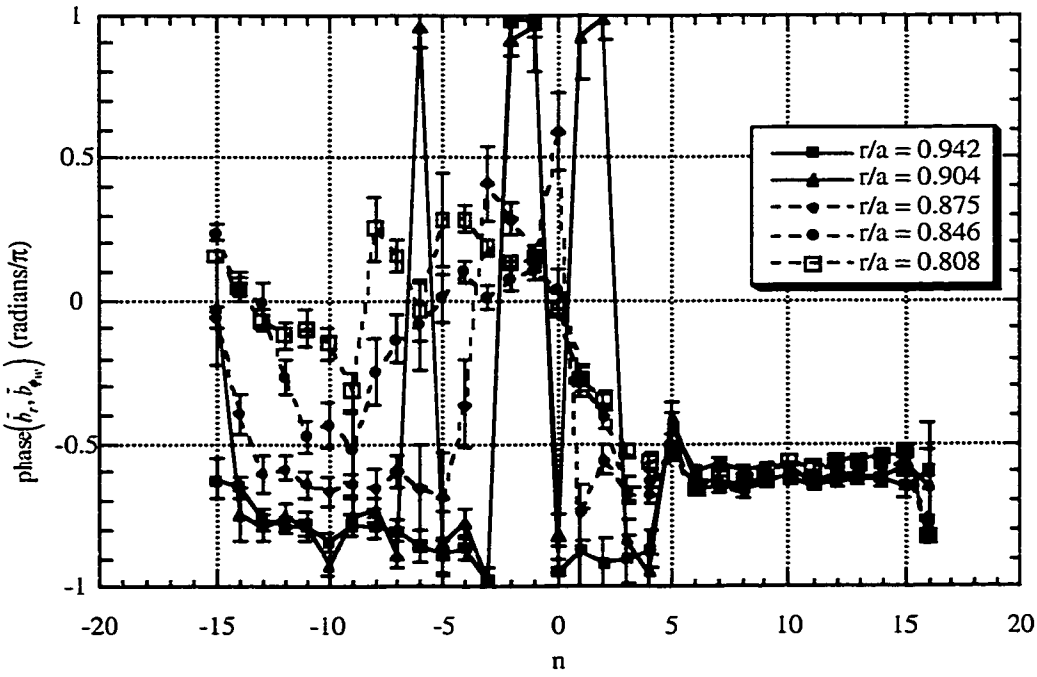

Figure 64: For each toroidal mode, relative phase between radial magnetic field fluctuation at 75° P and toroidal magnetic field fluctuation at wall at 241° P measured between sawtooth crashes.

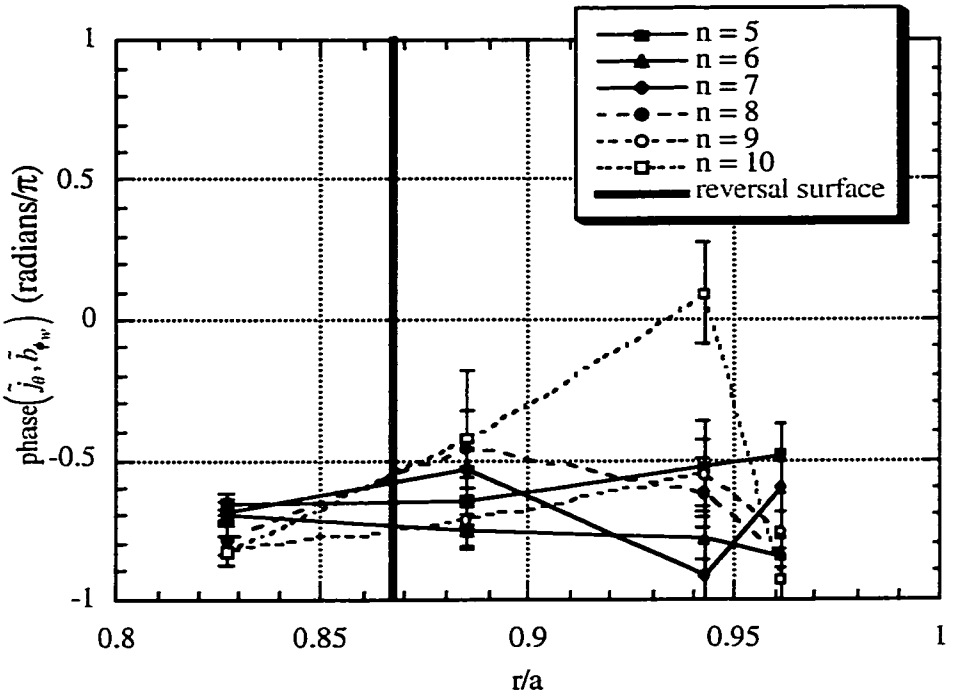

Figure 65: Relative phase between poloidal current density fluctuation at -15° P and toroidal magnetic field fluctuation at wall at 241° P for core resonant toroidal modes measured during sawtooth crashes.

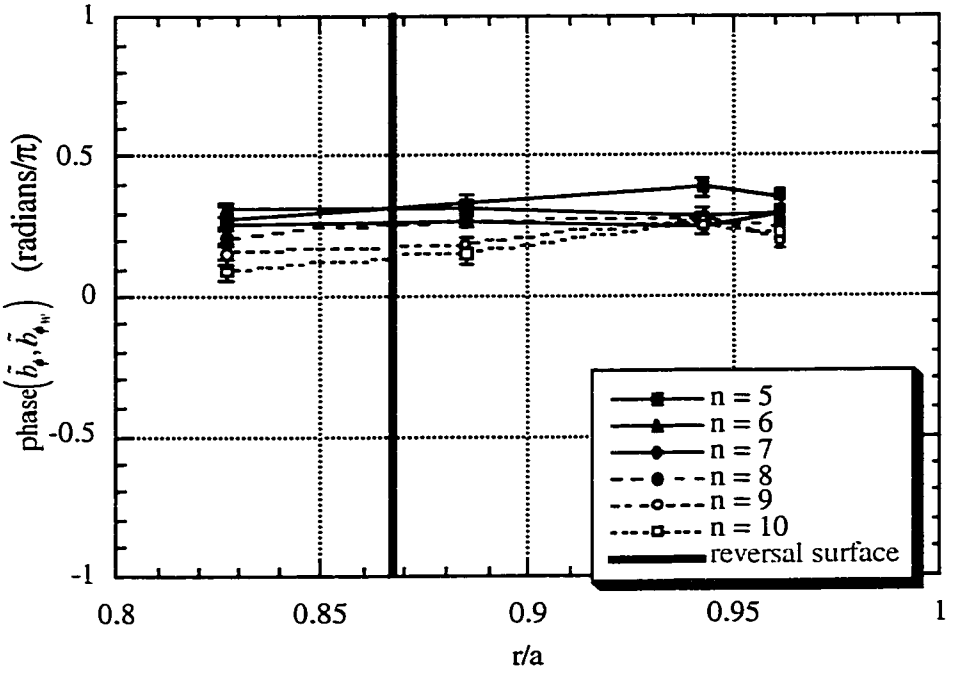

Figure 66: Relative phase between toroidal magnetic field fluctuation at -15° P and toroidal magnetic field fluctuation at wall at 241° P for core resonant toroidal modes measured during sawtooth crashes.

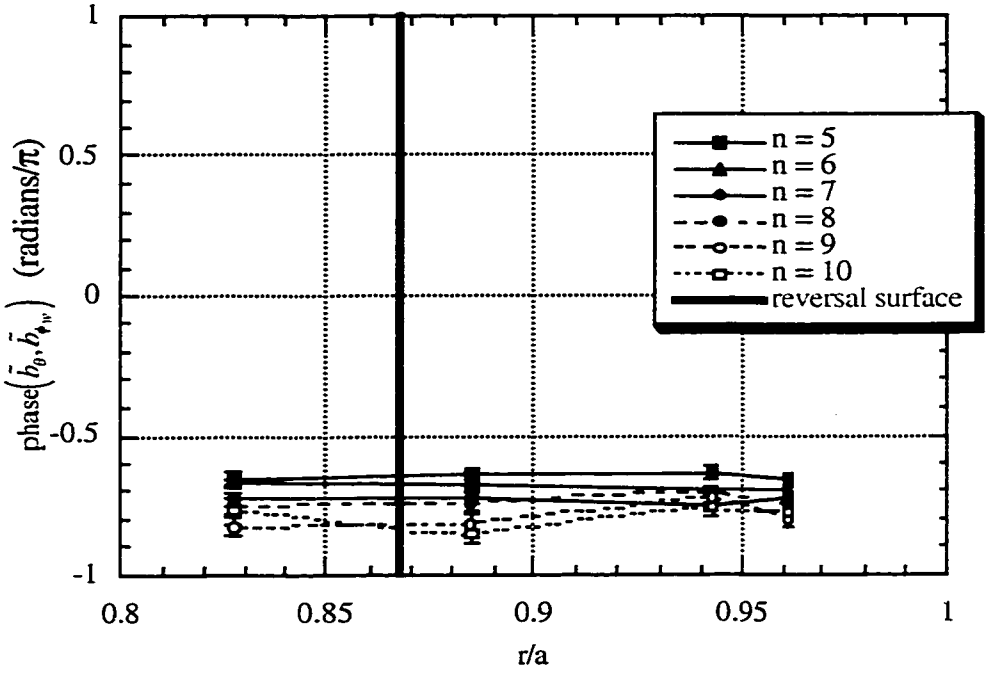

Figure 67: Relative phase between poloidal magnetic field fluctuation at -15° P and toroidal magnetic field fluctuation at wall at 241° P for core resonant toroidal modes measured during sawtooth crashes.

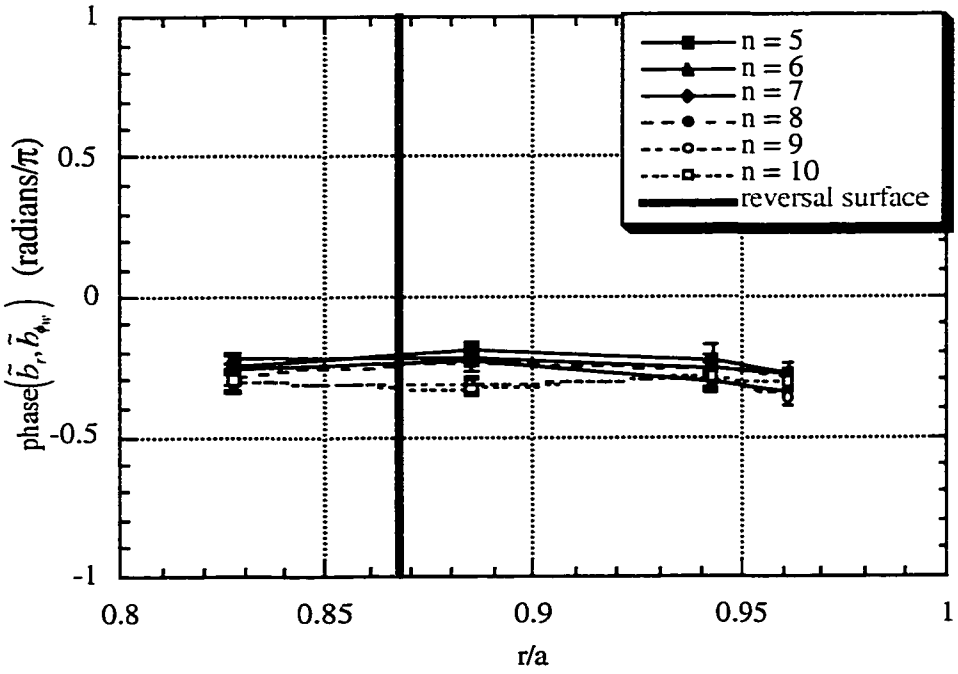

Figure 68: Relative phase between radial magnetic field fluctuation at -15° P and toroidal magnetic field fluctuation at wall at 241° P for core resonant toroidal modes measured during sawtooth crashes.

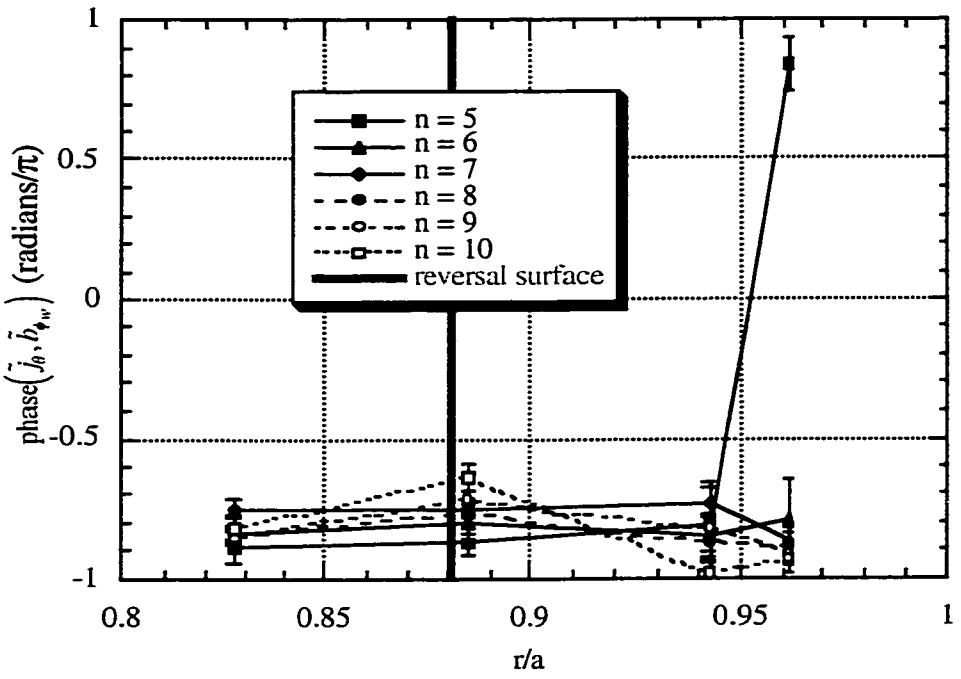

Figure 69: Relative phase between poloidal current density fluctuation at -15° P and toroidal magnetic field fluctuation at wall at 241° P for core resonant toroidal modes measured between sawtooth crashes.

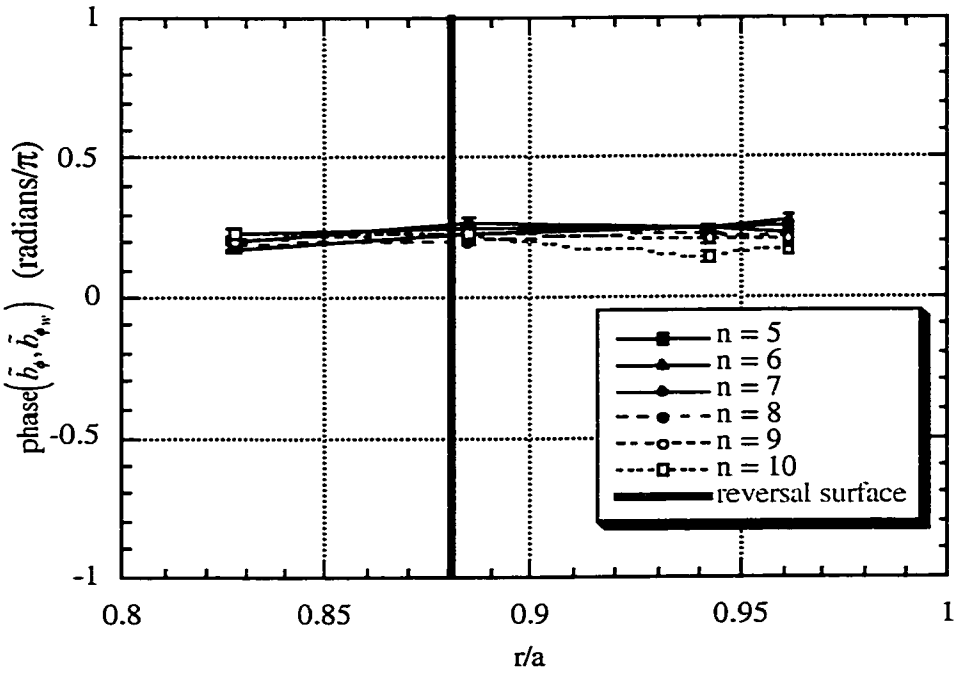

Figure 70: Relative phase between toroidal magnetic field fluctuation at -15° P and toroidal magnetic field fluctuation at wall at 241° P for core resonant toroidal modes measured between sawtooth crashes.

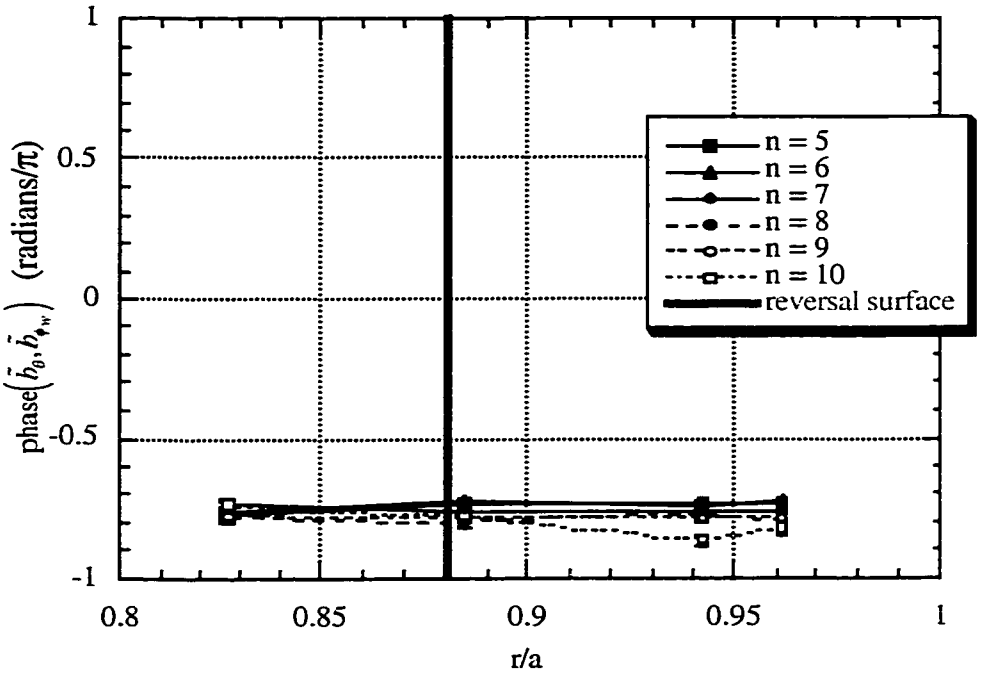

Figure 71: Relative phase between poloidal magnetic field fluctuation at -15° P and toroidal magnetic field fluctuation at wall at 241° P for core resonant toroidal modes measured between sawtooth crashes.

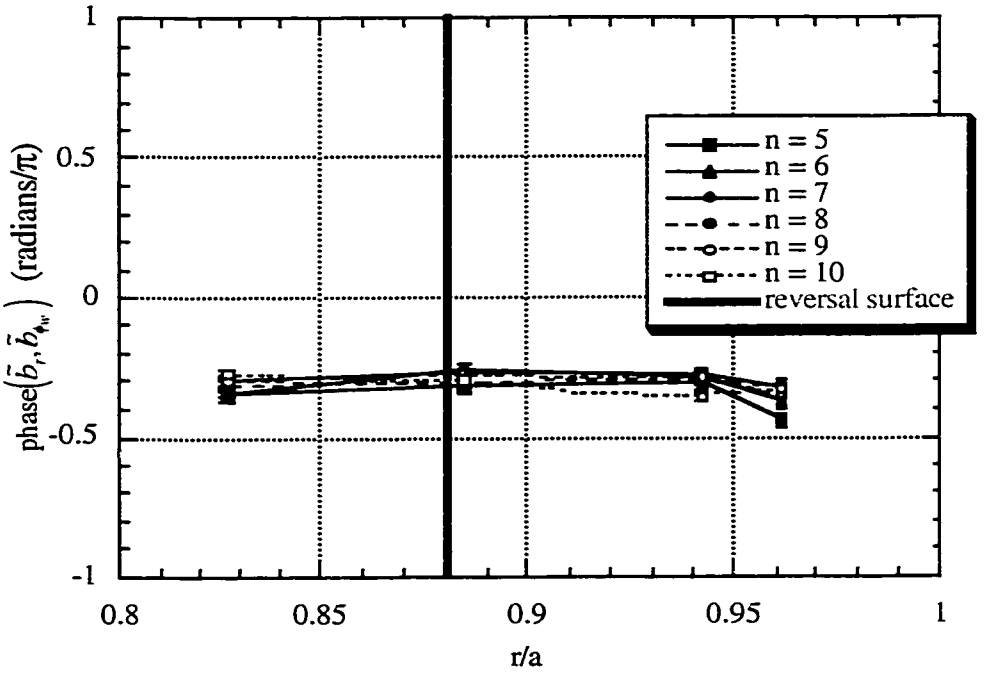

Figure 72: Relative phase between radial magnetic field fluctuation at -15° P and toroidal magnetic field fluctuation at wall at 241° P for core resonant toroidal modes measured between sawtooth crashes.

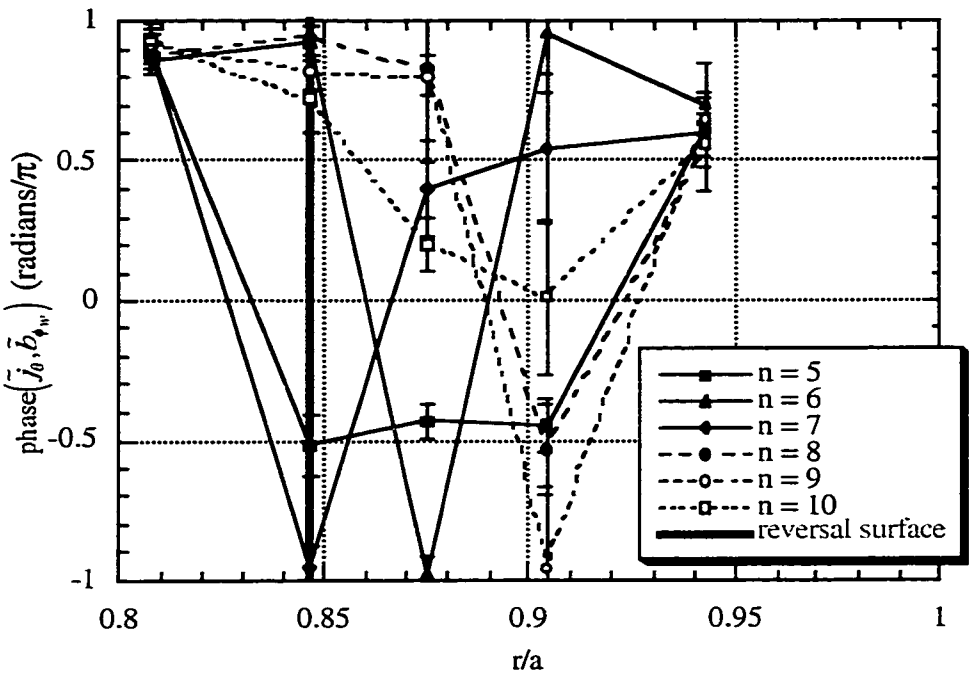

Figure 73: Relative phase between poloidal current density fluctuation at 75° P and toroidal magnetic field fluctuation at wall at 241° P for core resonant toroidal modes measured during sawtooth crashes.

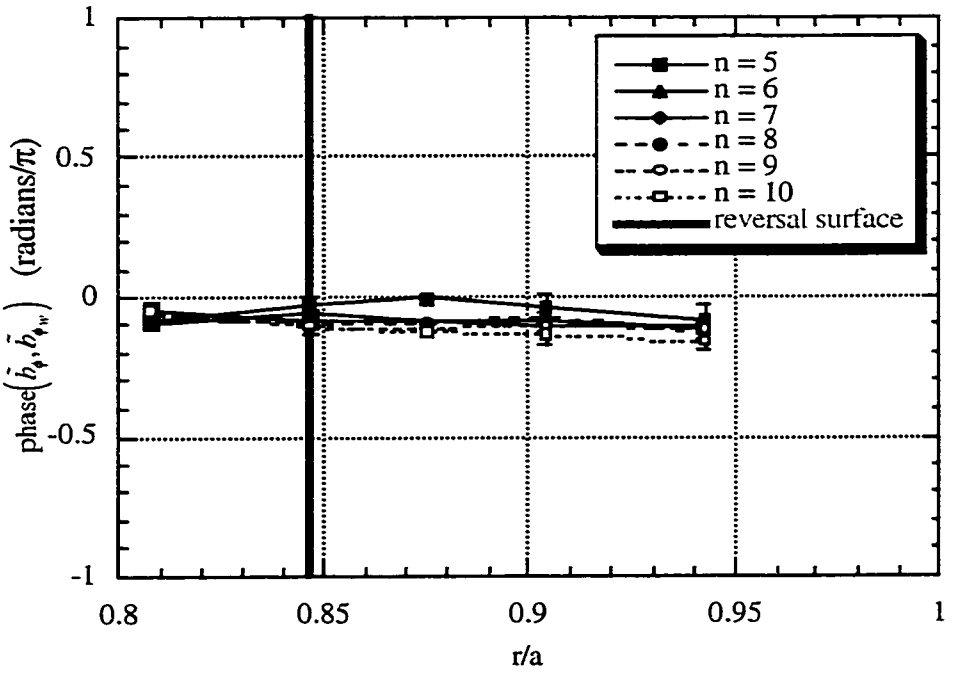

Figure 74: Relative phase between toroidal magnetic field fluctuation at 75° P and toroidal magnetic field fluctuation at wall at 241° P for core resonant toroidal modes measured during sawtooth crashes.

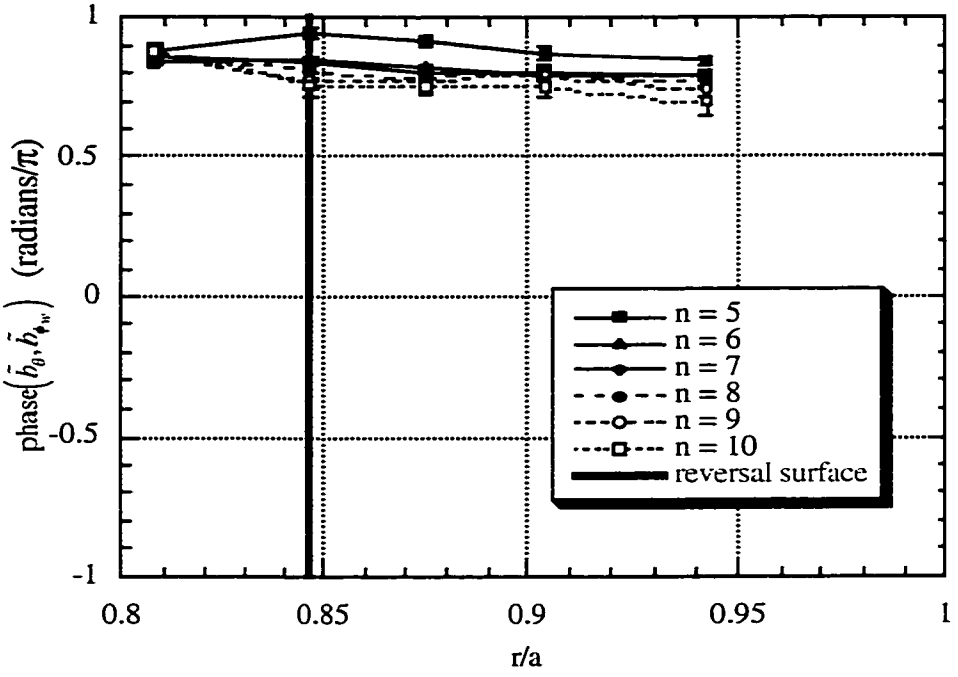

Figure 75: Relative phase between poloidal magnetic field fluctuation at 75° P and toroidal magnetic field fluctuation at wall at 241° P for core resonant toroidal modes measured during sawtooth crashes.

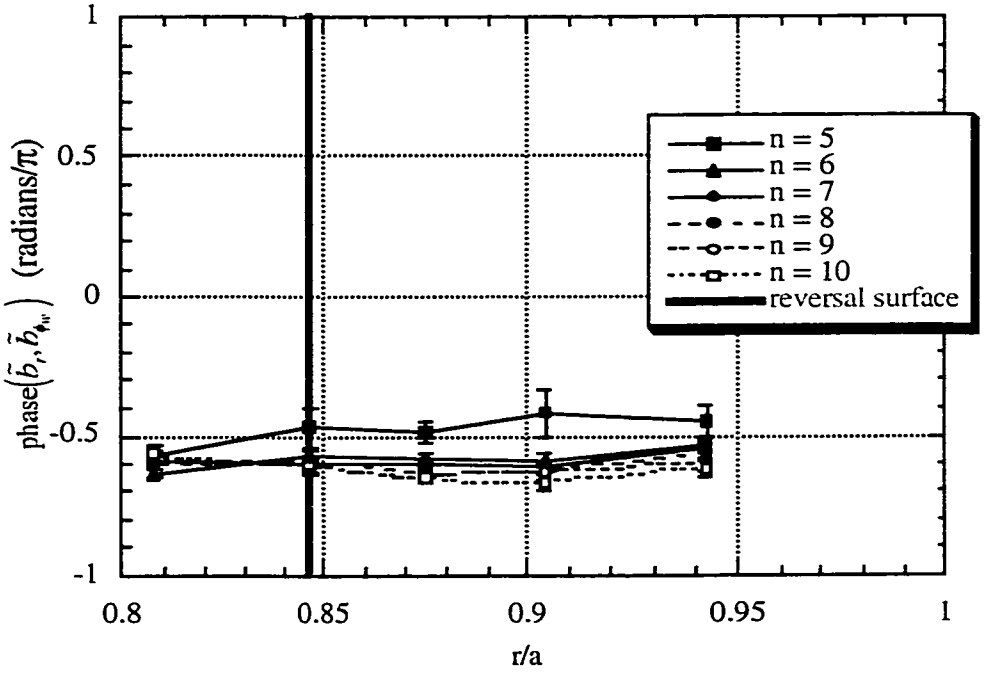

Figure 76: Relative phase between radial magnetic field fluctuation at 75° P and toroidal magnetic field fluctuation at wall at 241° P for core resonant toroidal modes measured during sawtooth crashes.

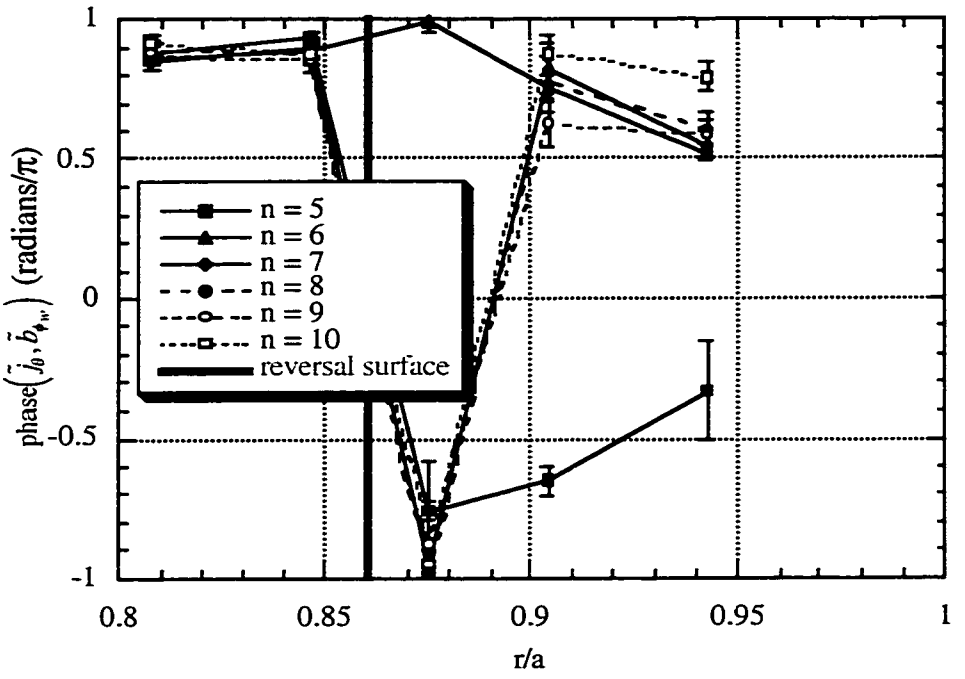

Figure 77: Relative phase between poloidal current density fluctuation at 75° P and toroidal magnetic field fluctuation at wall at 241° P for core resonant toroidal modes measured between sawtooth crashes.

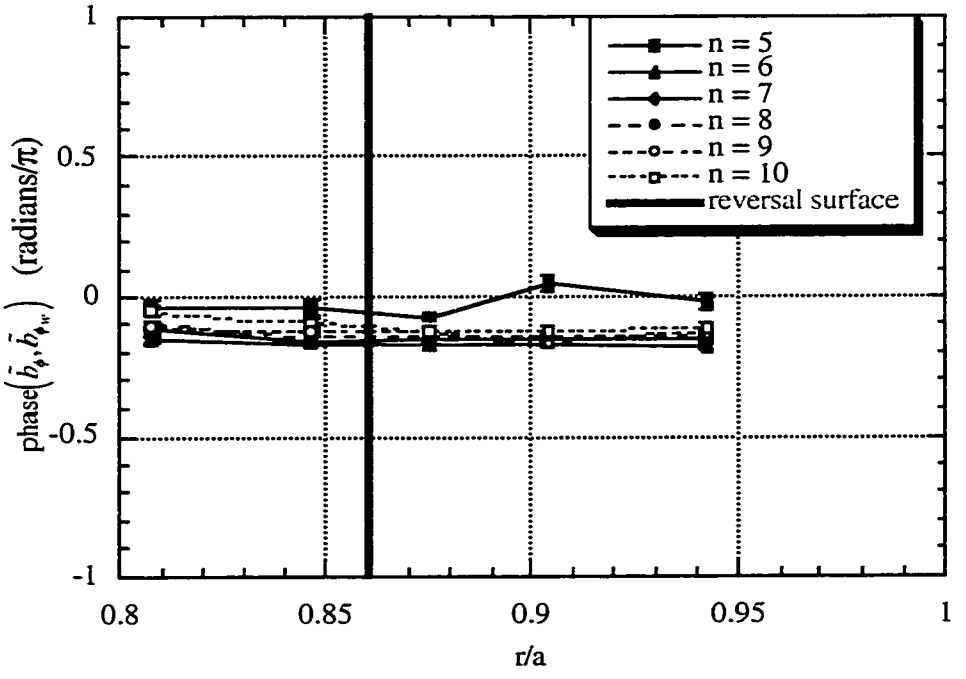

Figure 78: Relative phase between toroidal magnetic field fluctuation at 75° P and toroidal magnetic field fluctuation at wall at 241° P for core resonant toroidal modes measured between sawtooth crashes.

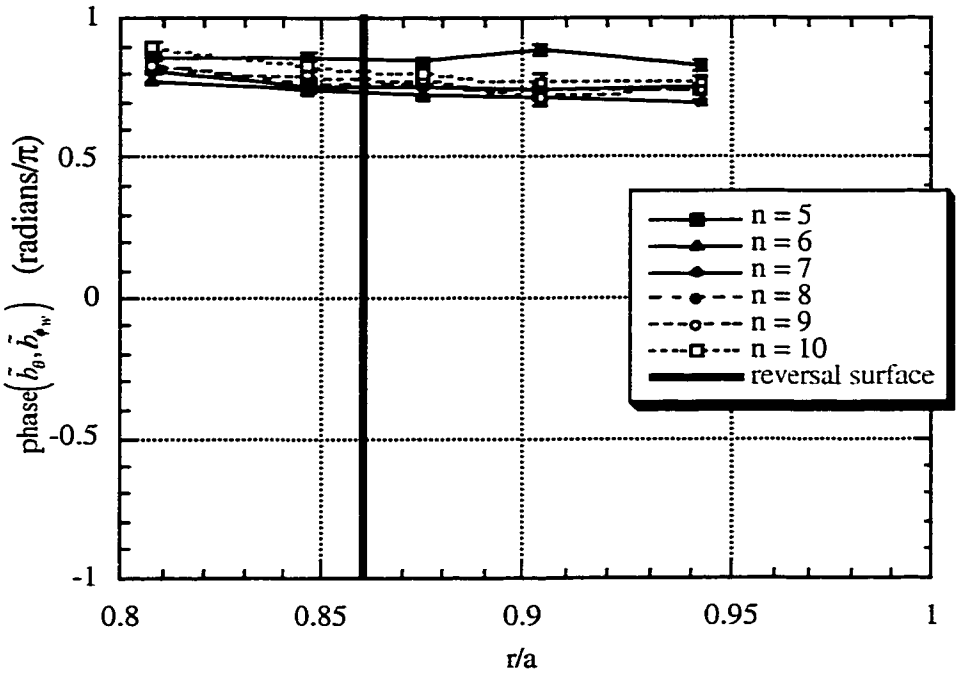

Figure 79: Relative phase between poloidal magnetic field fluctuation at 75° P and toroidal magnetic field fluctuation at wall at 241° P for core resonant toroidal modes measured between sawtooth crashes.

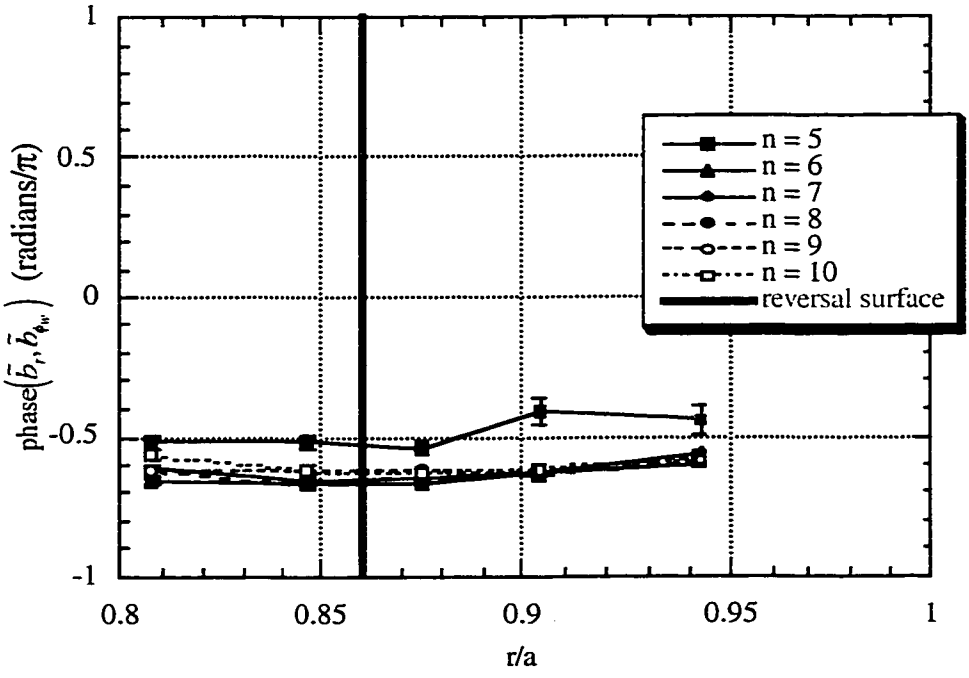

Figure 80: Relative phase between radial magnetic field fluctuation at 75° P and toroidal magnetic field fluctuation at wall at 241° P for core resonant toroidal modes measured between sawtooth crashes.

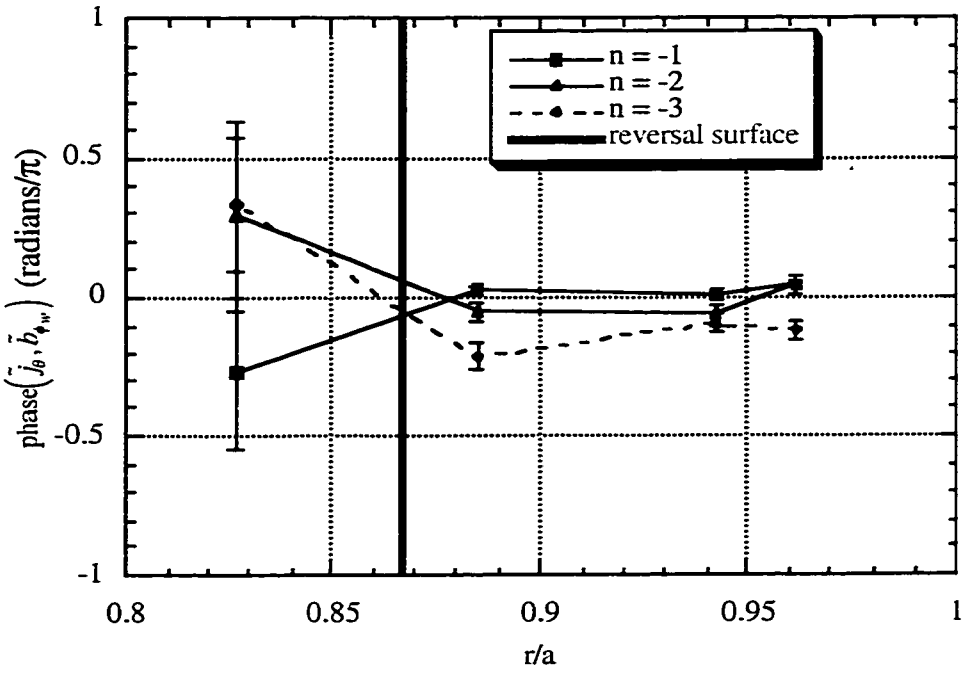

Figure 81: Relative phase between poloidal current density fluctuation at -15° P and toroidal magnetic field fluctuation at wall at 241° P for reversal surface resonant toroidal modes measured during sawtooth crashes.

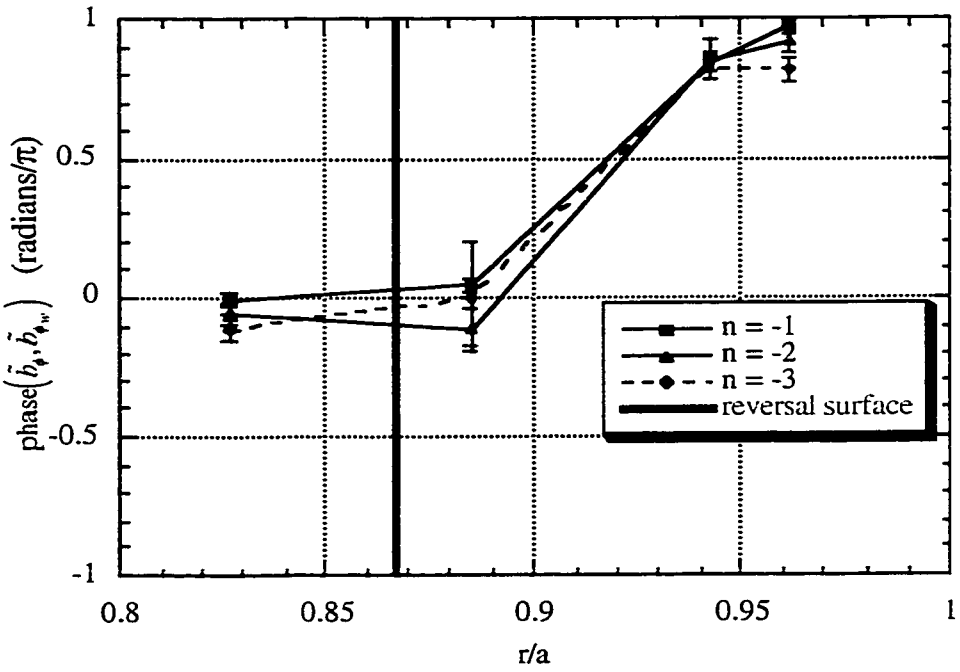

Figure 82: Relative phase between toroidal magnetic field fluctuation at -15° P and toroidal magnetic field fluctuation at wall at 241° P for reversal surface resonant toroidal modes measured during sawtooth crashes.

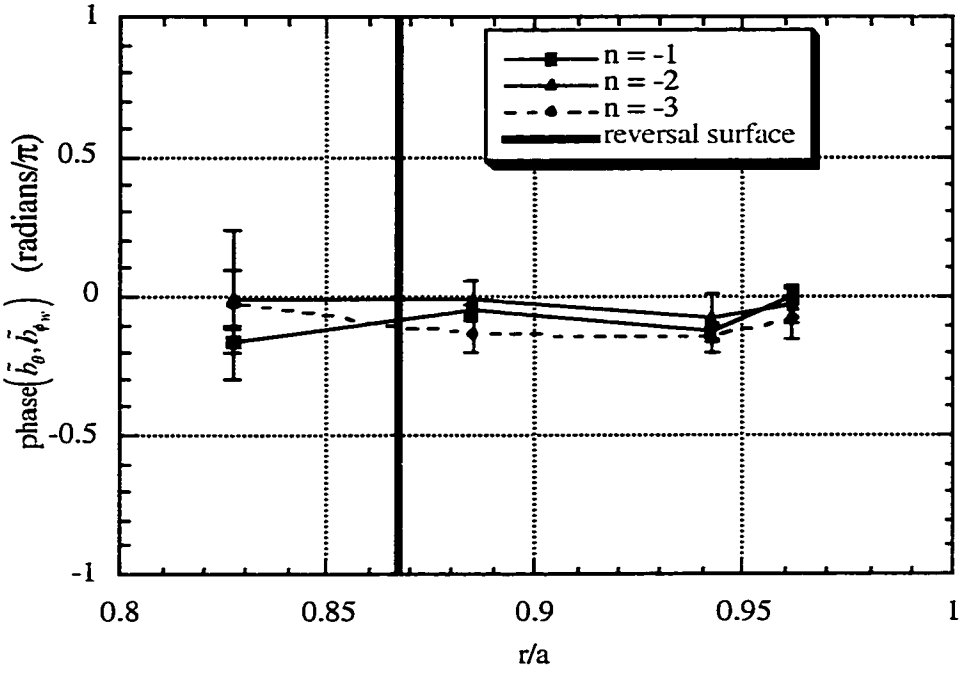

Figure 83: Relative phase between poloidal magnetic field fluctuation at -15° P and toroidal magnetic field fluctuation at wall at 241° P for reversal surface resonant toroidal modes measured during sawtooth crashes.

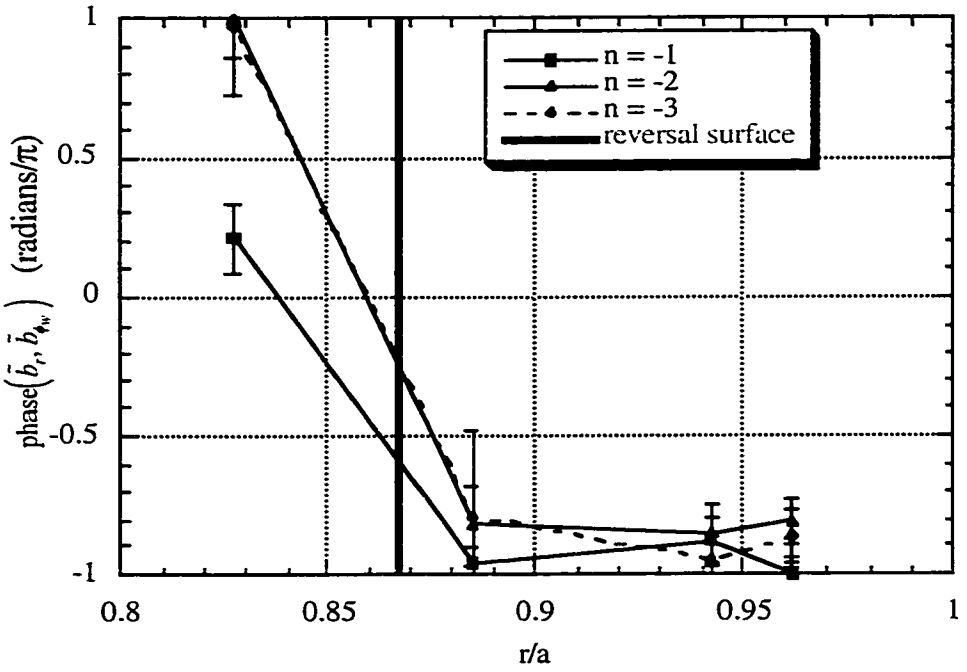

Figure 84: Relative phase between radial magnetic field fluctuation at -15° P and toroidal magnetic field fluctuation at wall at 241° P for reversal surface resonant toroidal modes measured during sawtooth crashes.

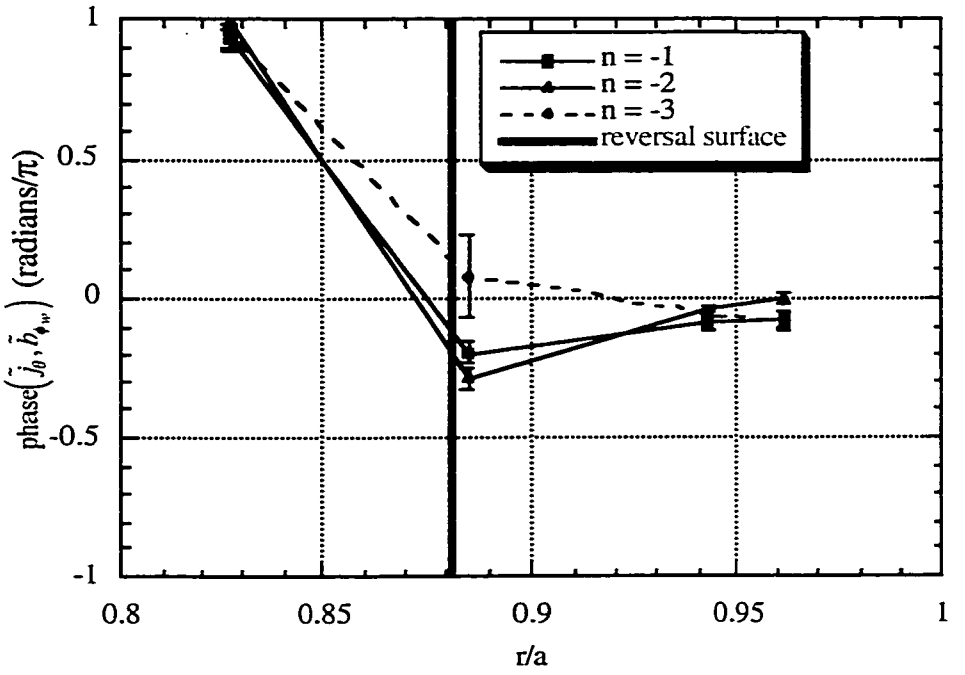

Figure 85: Relative phase between poloidal current density fluctuation at -15° P and toroidal magnetic field fluctuation at wall at 241° P for reversal surface resonant toroidal modes measured between sawtooth crashes.

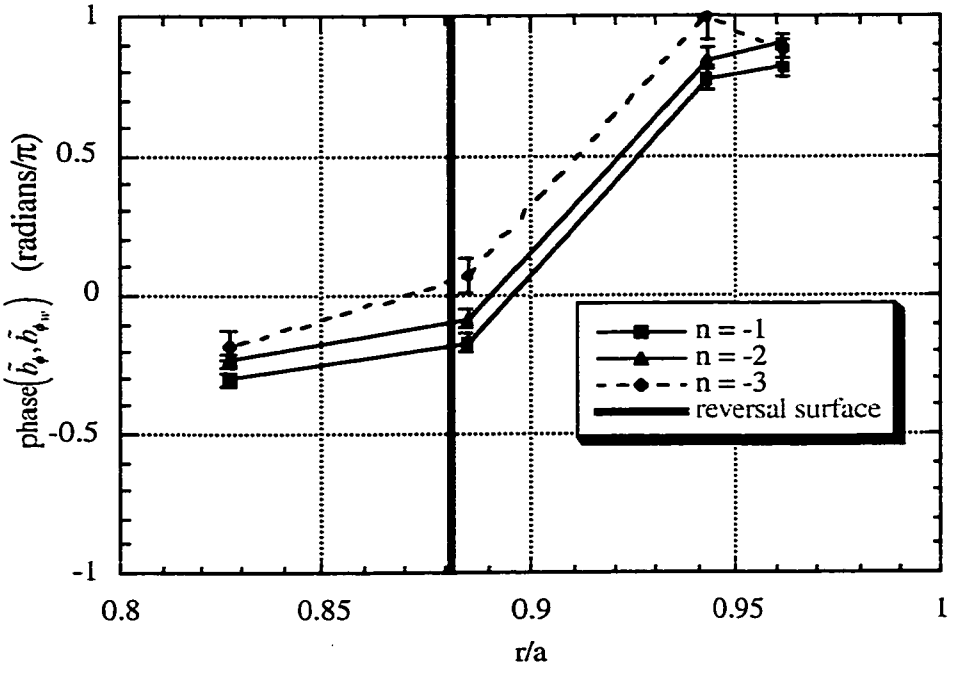

Figure 86: Relative phase between toroidal magnetic field fluctuation at -15° P and toroidal magnetic field fluctuation at wall at 241° P for reversal surface resonant toroidal modes measured between sawtooth crashes.

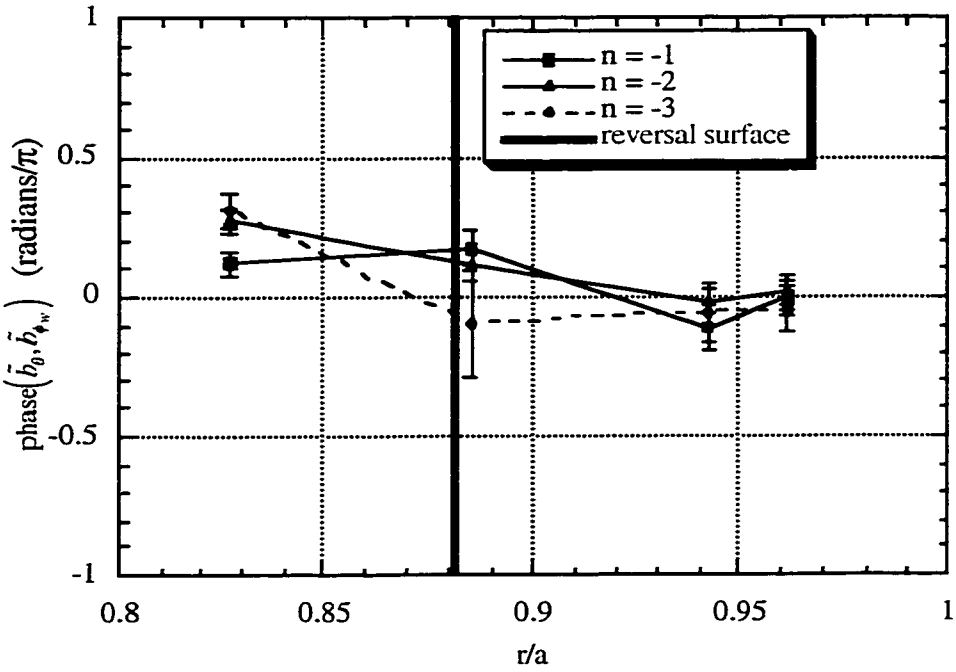

Figure 87: Relative phase between poloidal magnetic field fluctuation at -15° P and toroidal magnetic field fluctuation at wall at 241° P for reversal surface resonant toroidal modes measured between sawtooth crashes.

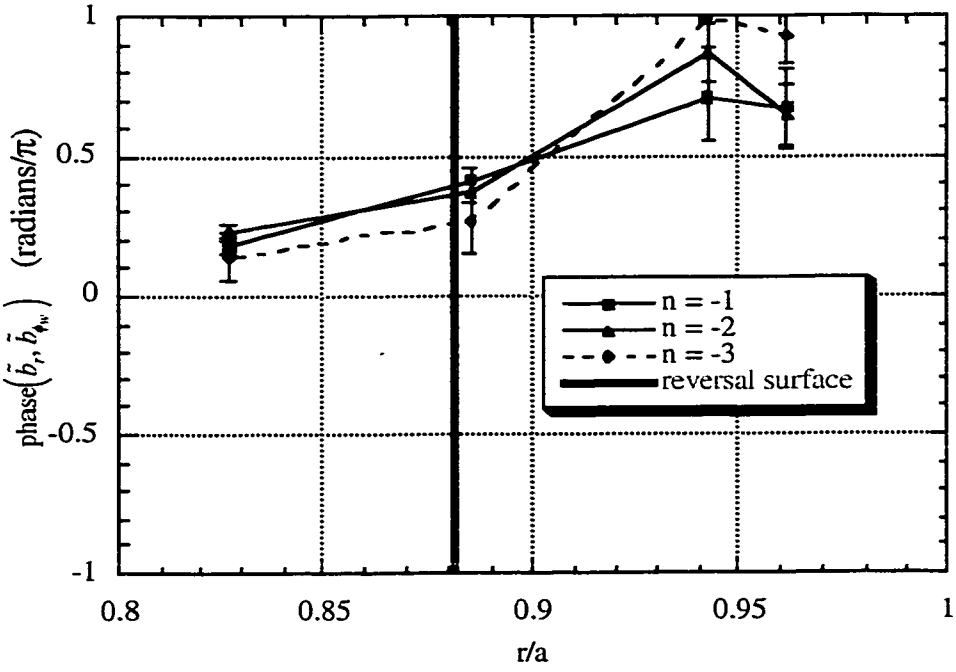

Figure 88: Relative phase between radial magnetic field fluctuation at -15° P and toroidal magnetic field fluctuation at wall at 241° P for reversal surface resonant toroidal modes measured between sawtooth crashes.

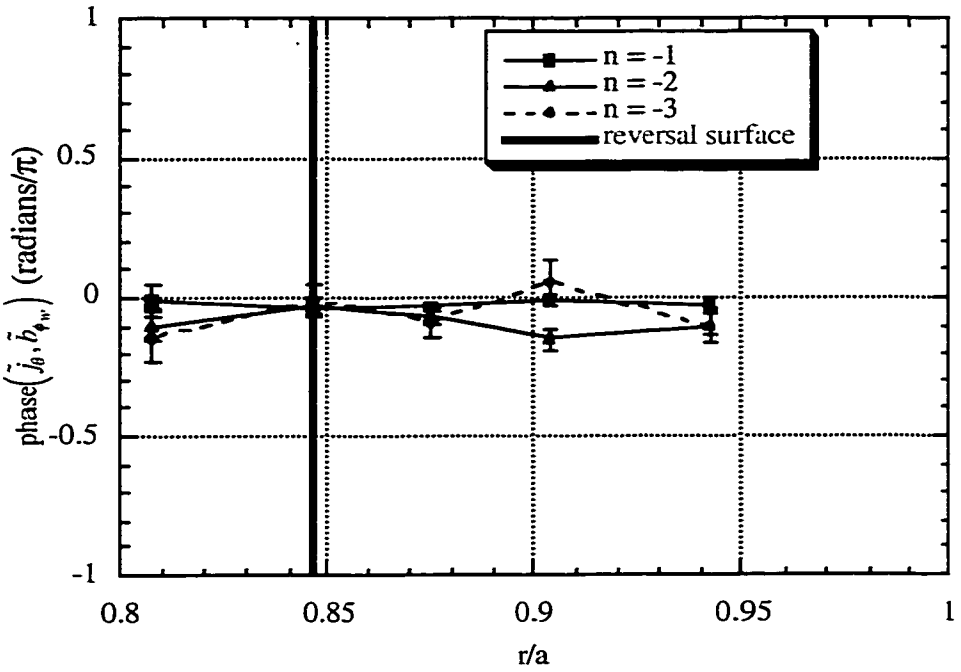

Figure 89: Relative phase between poloidal current density fluctuation at 75° P and toroidal magnetic field fluctuation at wall at 241° P for reversal surface resonant toroidal modes measured during sawtooth crashes.

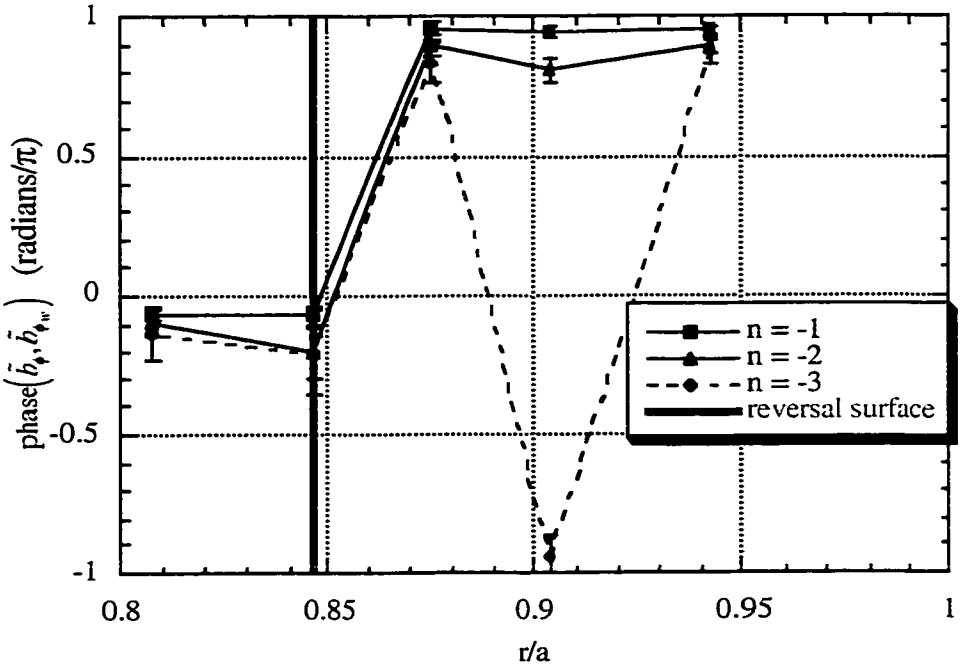

Figure 90: Relative phase between toroidal magnetic field fluctuation at 75° P and toroidal magnetic field fluctuation at wall at 241° P for reversal surface resonant toroidal modes measured during sawtooth crashes.

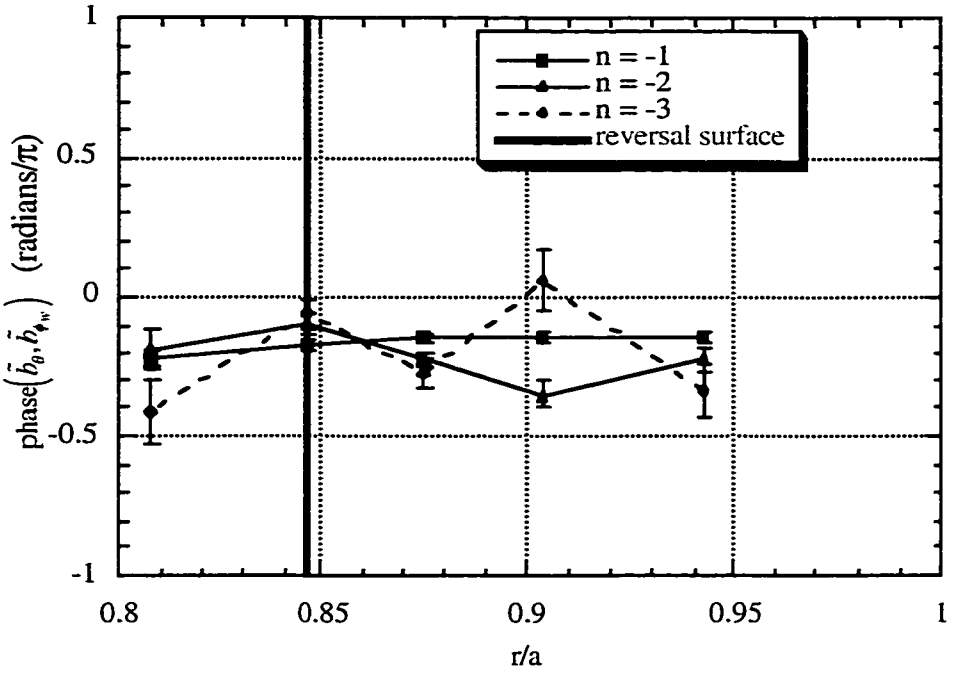

Figure 91: Relative phase between poloidal magnetic field fluctuation at 75° P and toroidal magnetic field fluctuation at wall at 241° P for reversal surface resonant toroidal modes measured during sawtooth crashes.

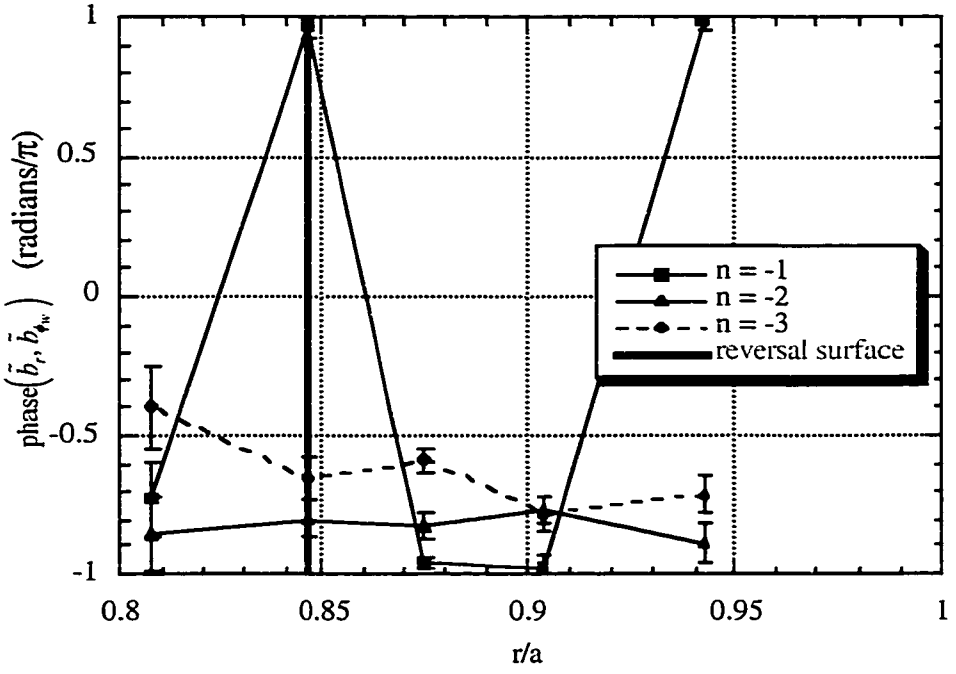

Figure 92: Relative phase between radial magnetic field fluctuation at 75° P and toroidal magnetic field fluctuation at wall at 241° P for reversal surface resonant toroidal modes measured during sawtooth crashes.

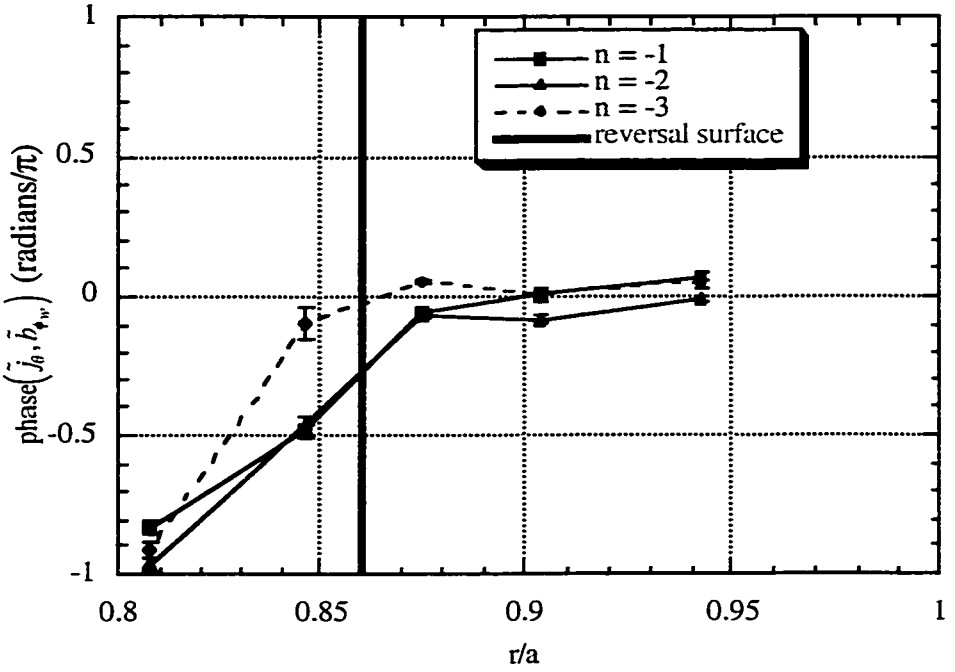

Figure 93: Relative phase between poloidal current density fluctuation at 75° P and toroidal magnetic field fluctuation at wall at 241° P for reversal surface resonant toroidal modes measured between sawtooth crashes.

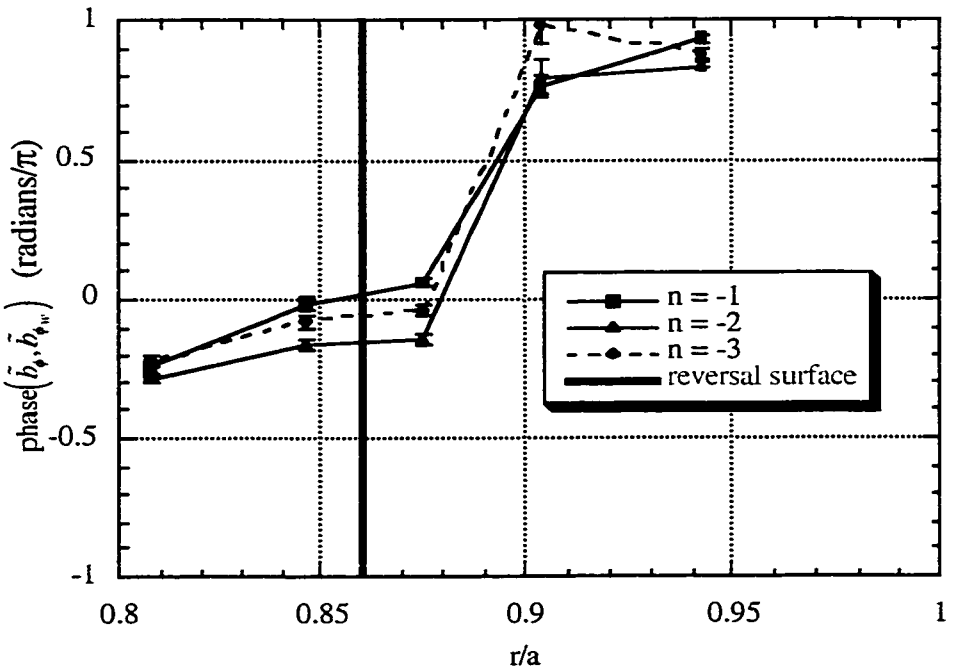

Figure 94: Relative phase between toroidal magnetic field fluctuation at 75° P and toroidal magnetic field fluctuation at wall at 241° P for reversal surface resonant toroidal modes measured between sawtooth crashes.

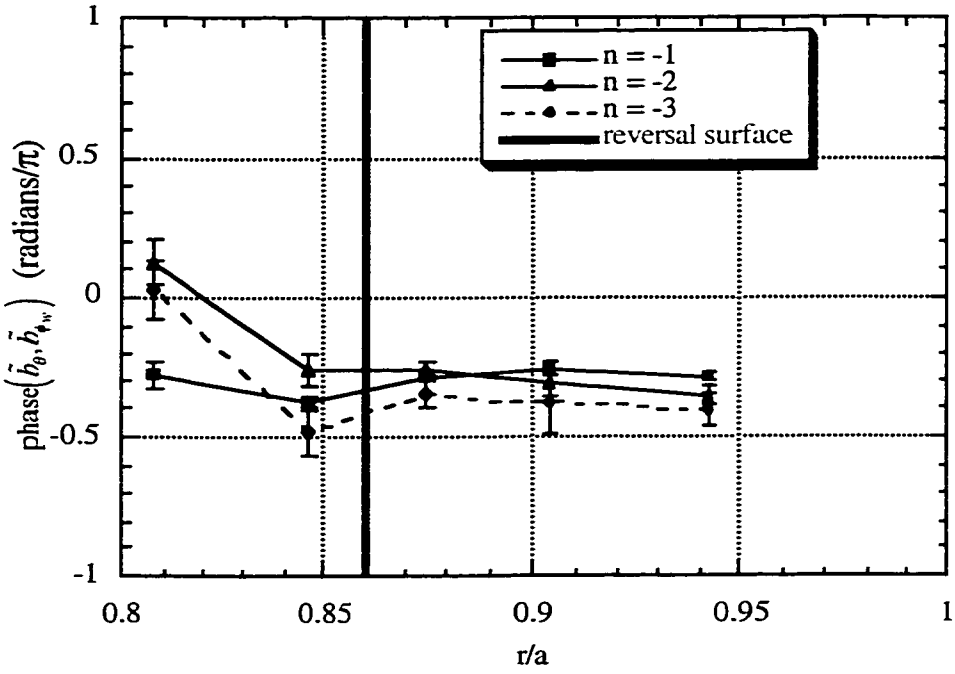

Figure 95: Relative phase between poloidal magnetic field fluctuation at 75° P and toroidal magnetic field fluctuation at wall at 241° P for reversal surface resonant toroidal modes measured between sawtooth crashes.

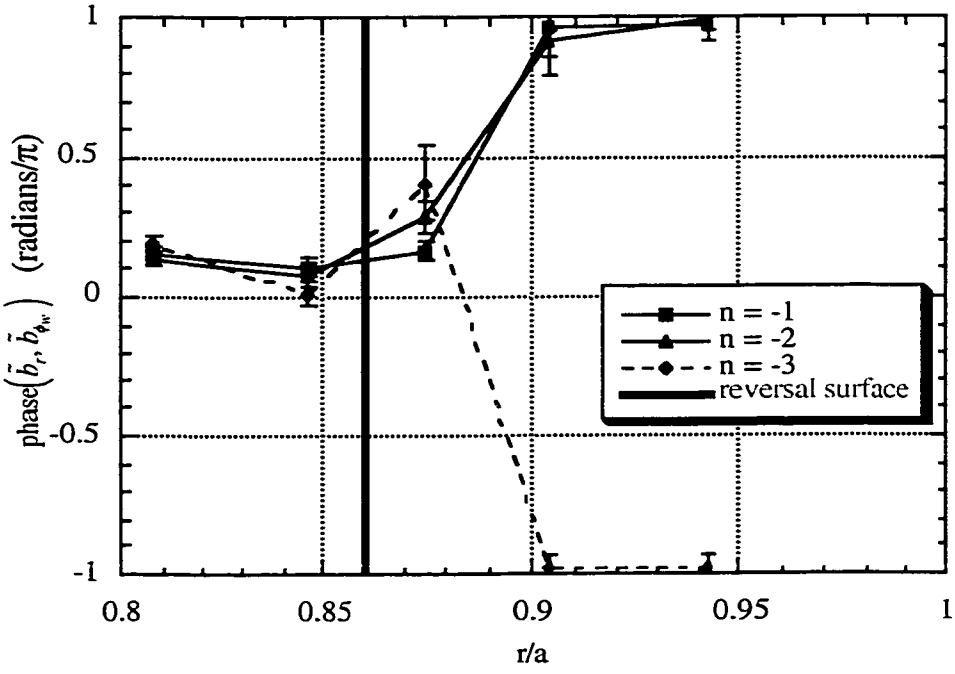

Figure 96: Relative phase between radial magnetic field fluctuation at 75° P and toroidal magnetic field fluctuation at wall at 241° P for reversal surface resonant toroidal modes measured between sawtooth crashes.

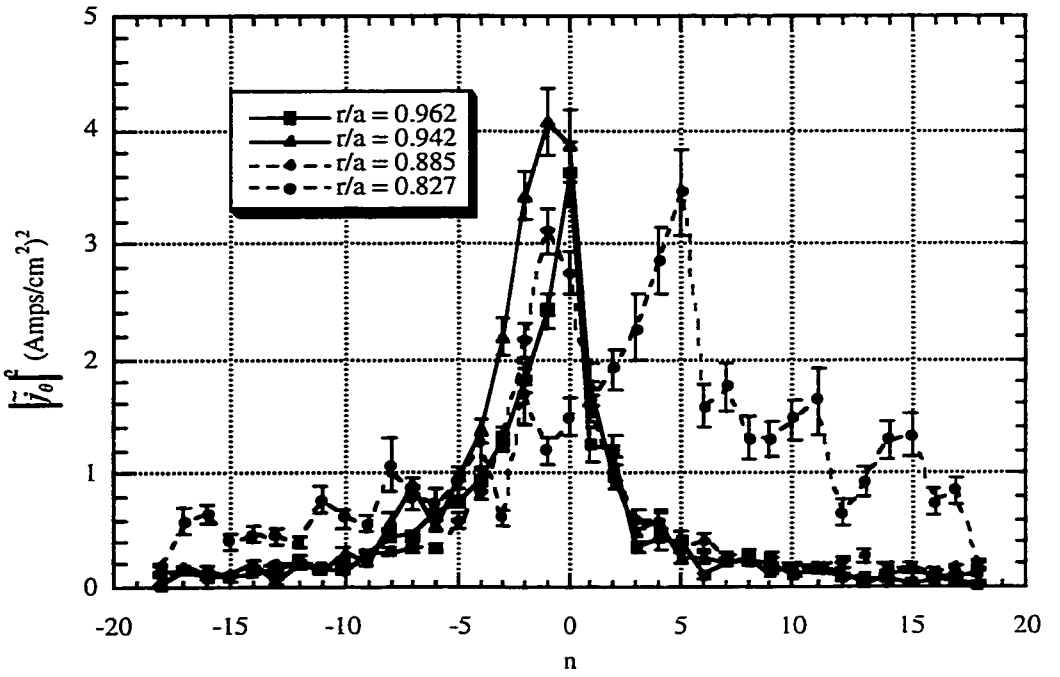

Figure 97: Two-point toroidal spectrum of poloidal current density fluctuations measured during sawtooth crashes with probes at -15° P, 320° T and -15° P, 330° T.

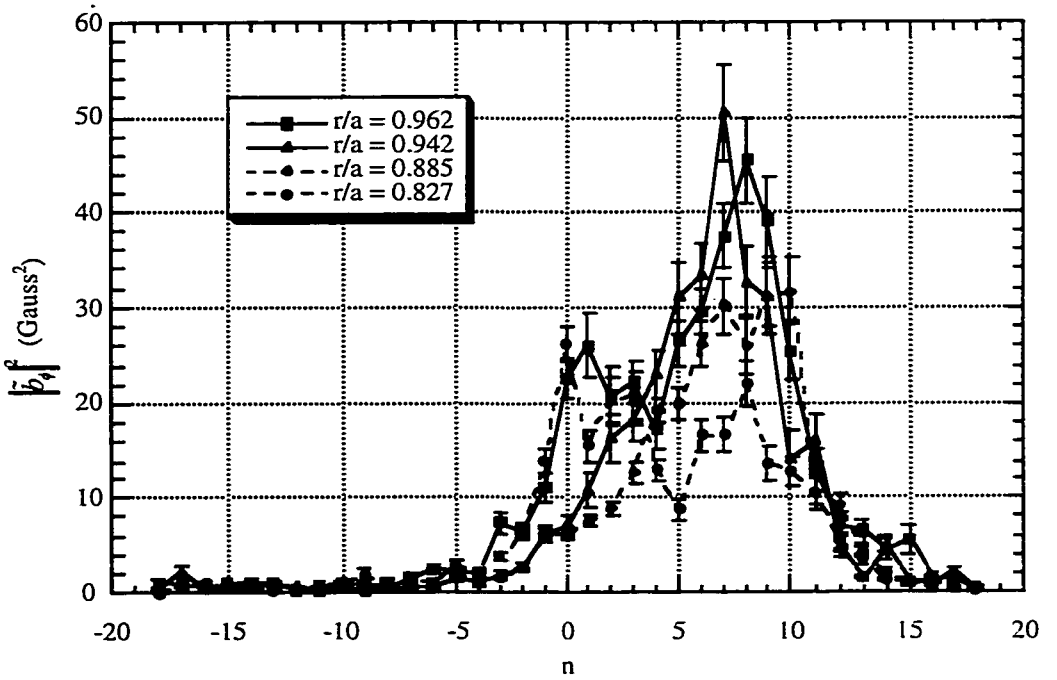

Figure 98: Two-point toroidal spectrum of toroidal magnetic field fluctuations measured during sawtooth crashes with probes at -15° P, 320° T and -15° P, 330° T.

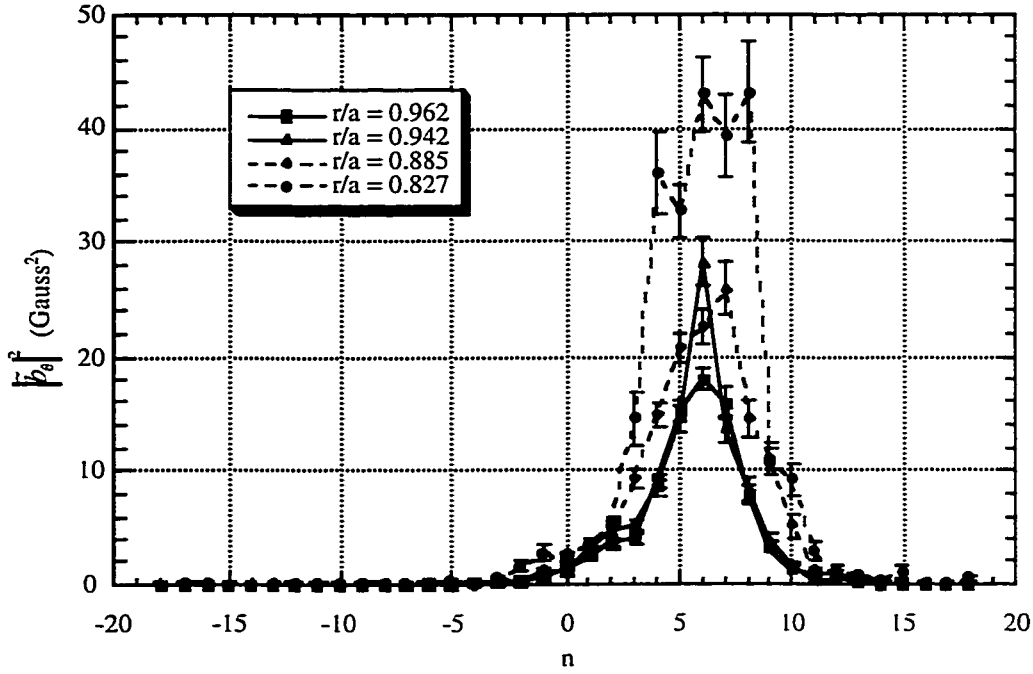

Figure 99: Two-point toroidal spectrum of poloidal magnetic field fluctuations measured during sawtooth crashes with probes at -15° P, 320° T and -15° P, 330° T.

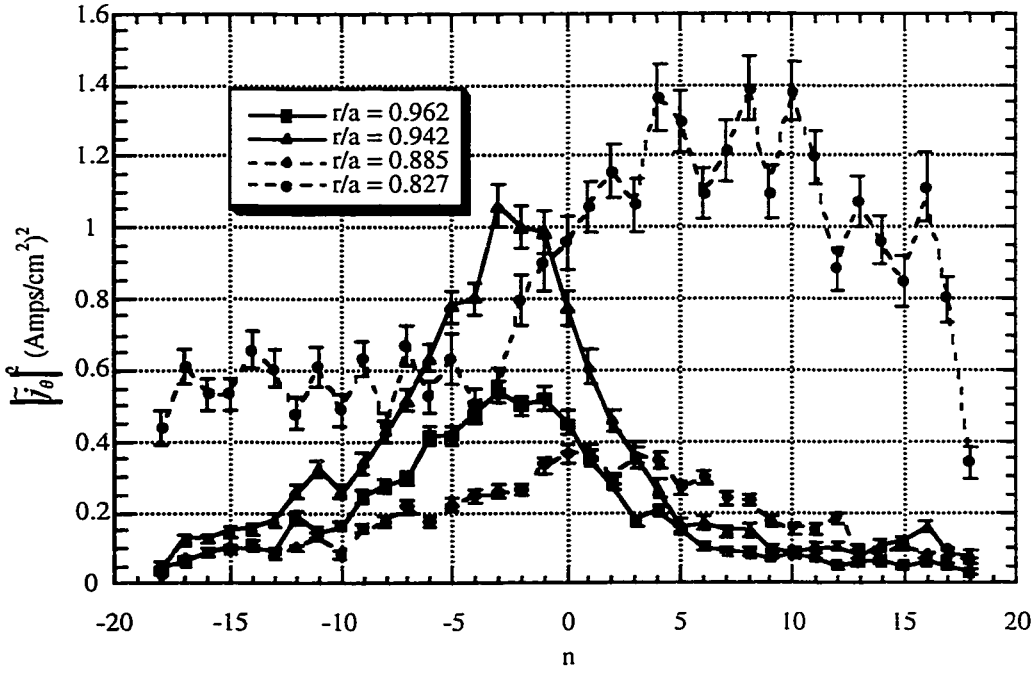

Figure 100: Two-point toroidal spectrum of poloidal current density fluctuations measured between sawtooth crashes with probes at -15° P, 320° T and -15° P, 330° T.

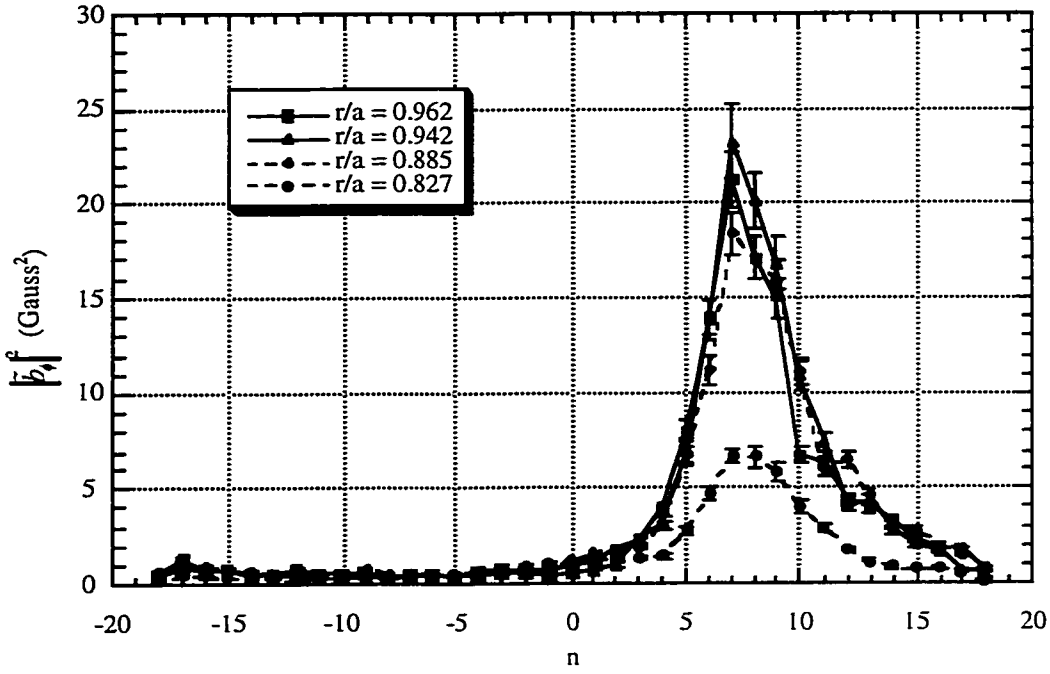

Figure 101: Two-point toroidal spectrum of toroidal magnetic field fluctuations measured between sawtooth crashes with probes at -15° P, 320° T and -15° P, 330° T.

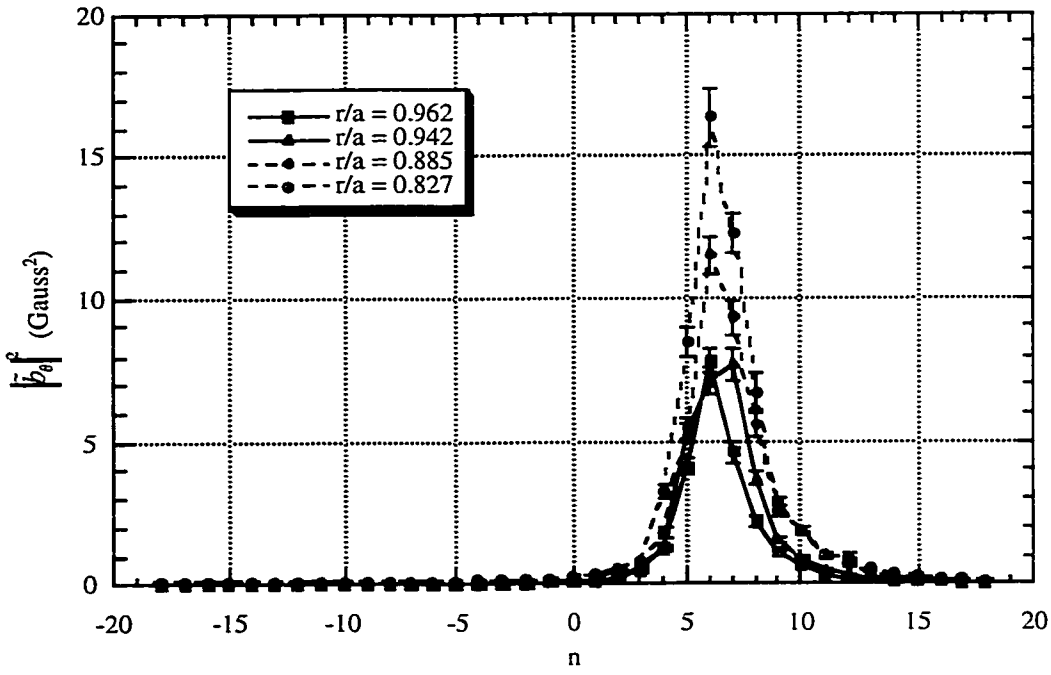

Figure 102: Two-point toroidal spectrum of poloidal magnetic field fluctuations measured between sawtooth crashes with probes at -15° P, 320° T and -15° P, 330° T.

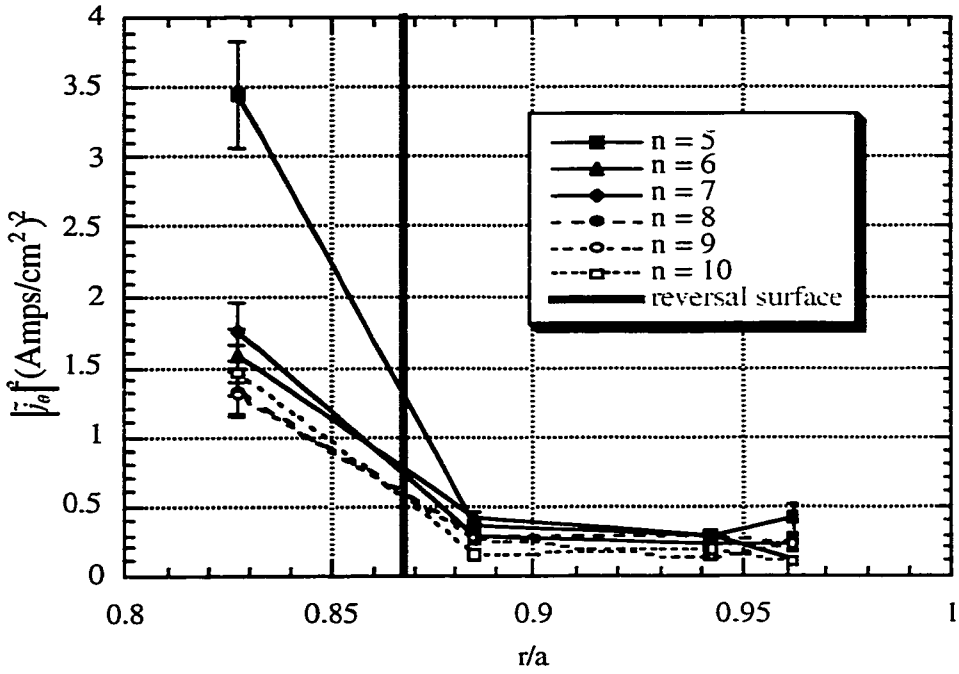

Figure 103: Radial profile of squared two-point toroidal spectral amplitude of poloidal current density fluctuations for core resonant toroidal modes measured during sawtooth crashes with probes at -15° P, 320° T and -15° P, 330° T.

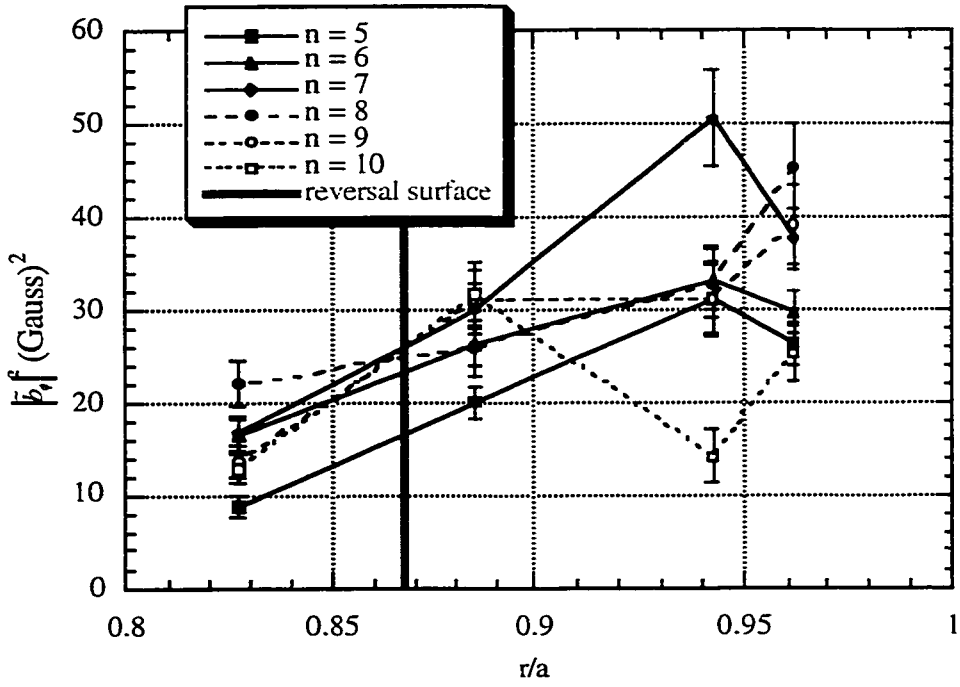

Figure 104: Radial profile of squared two-point toroidal spectral amplitude of toroidal magnetic field fluctuations for core resonant toroidal modes measured during sawtooth crashes with probes at -15° P, 320° T and -15° P, 330° T.

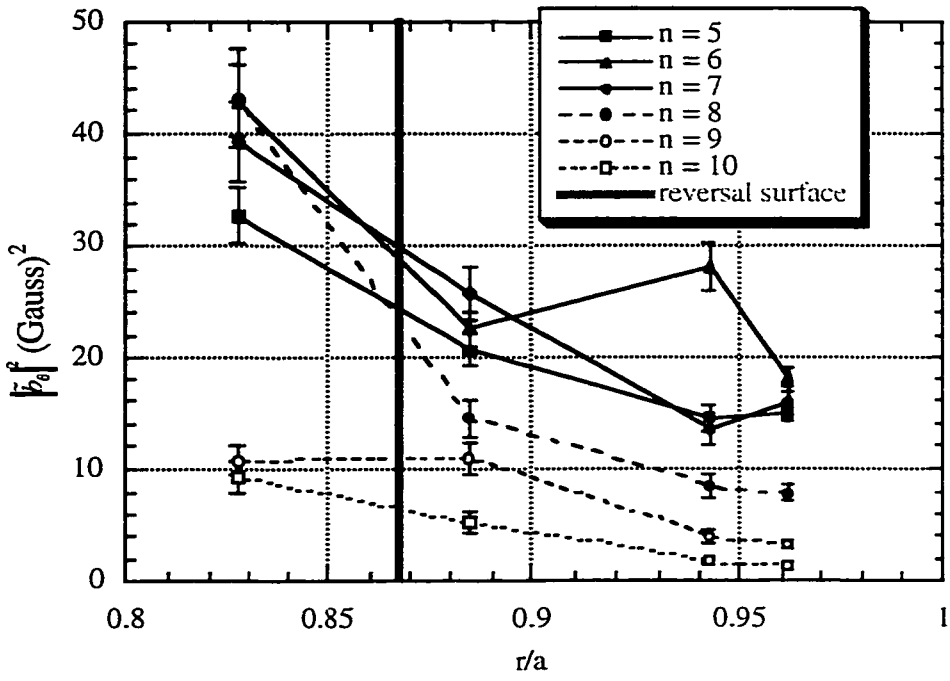

Figure 105: Radial profile of squared two-point toroidal spectral amplitude of poloidal magnetic field fluctuations for core resonant toroidal modes measured during sawtooth crashes with probes at -15° P, 320° T and -15° P, 330° T.

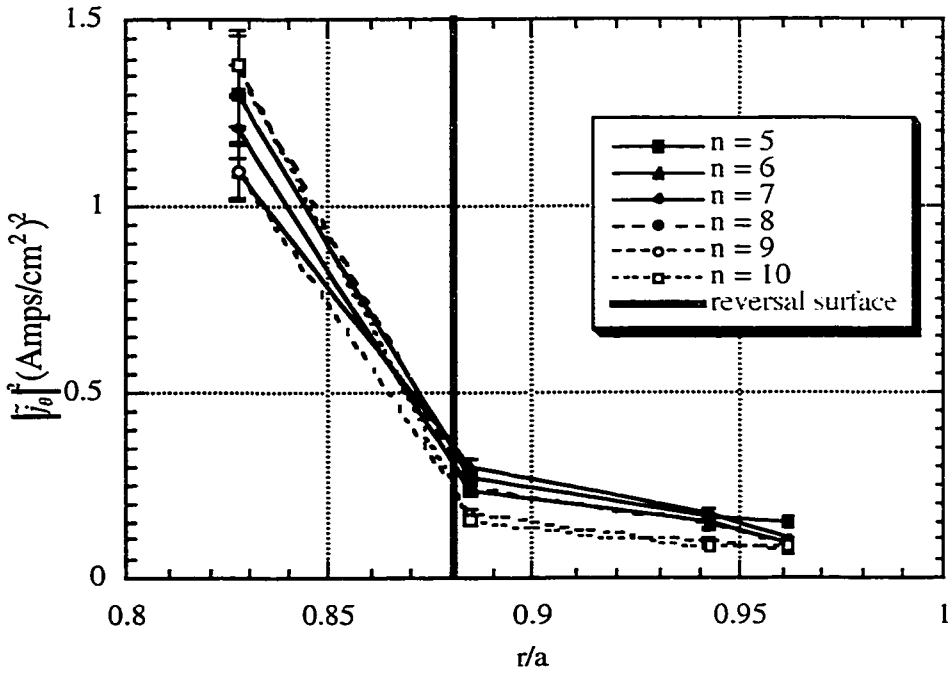

Figure 106: Radial profile of squared two-point toroidal spectral amplitude of poloidal current density fluctuations for core resonant toroidal modes measured between sawtooth crashes with probes at -15° P, 320° T and -15° P, 330° T.

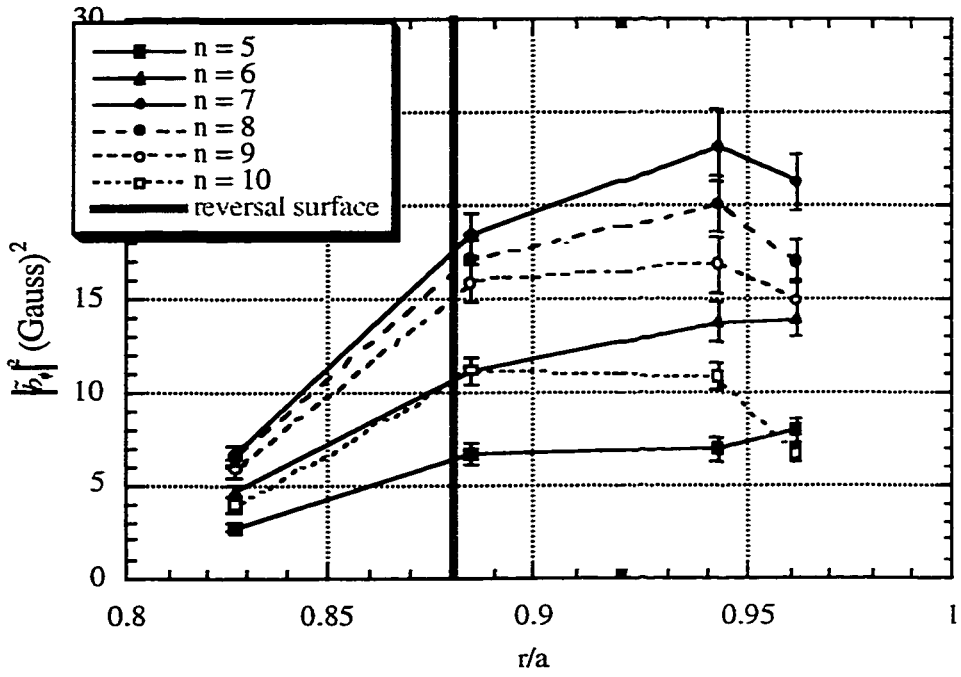

Figure 107: Radial profile of squared two-point toroidal spectral amplitude of toroidal magnetic field fluctuations for core resonant toroidal modes measured between sawtooth crashes with probes at -15° P, 320° T and -15° P, 330° T.

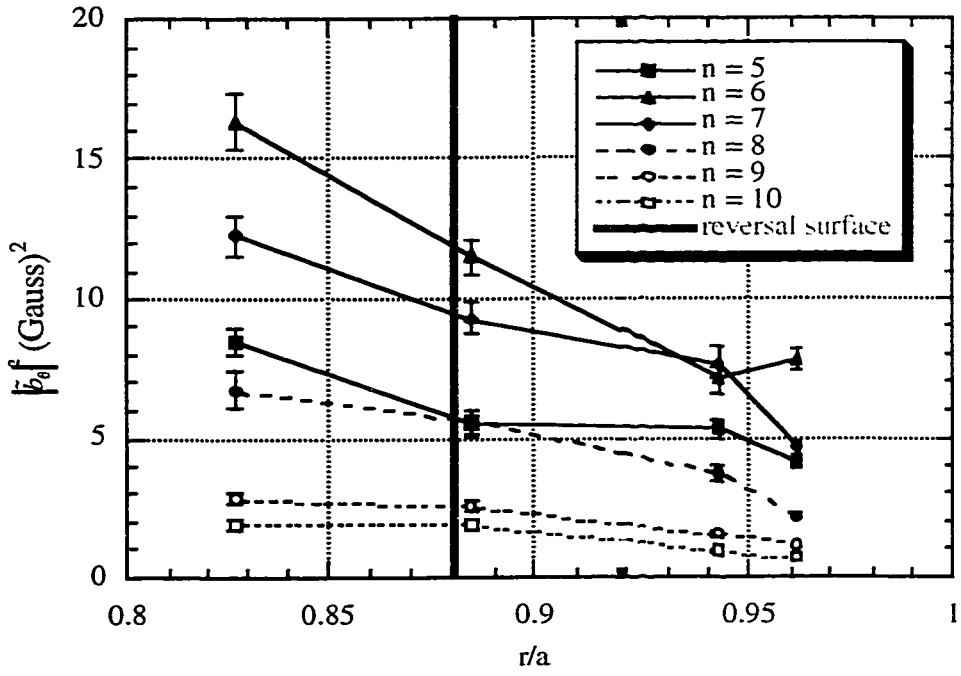

Figure 108: Radial profile of squared two-point toroi-dal spectral amplitude of poloidal magnetic field fluctuations for core resonant toroidal modes measured between sawtooth crashes with probes at -15° P, 320° T and -15° P, 330° T.

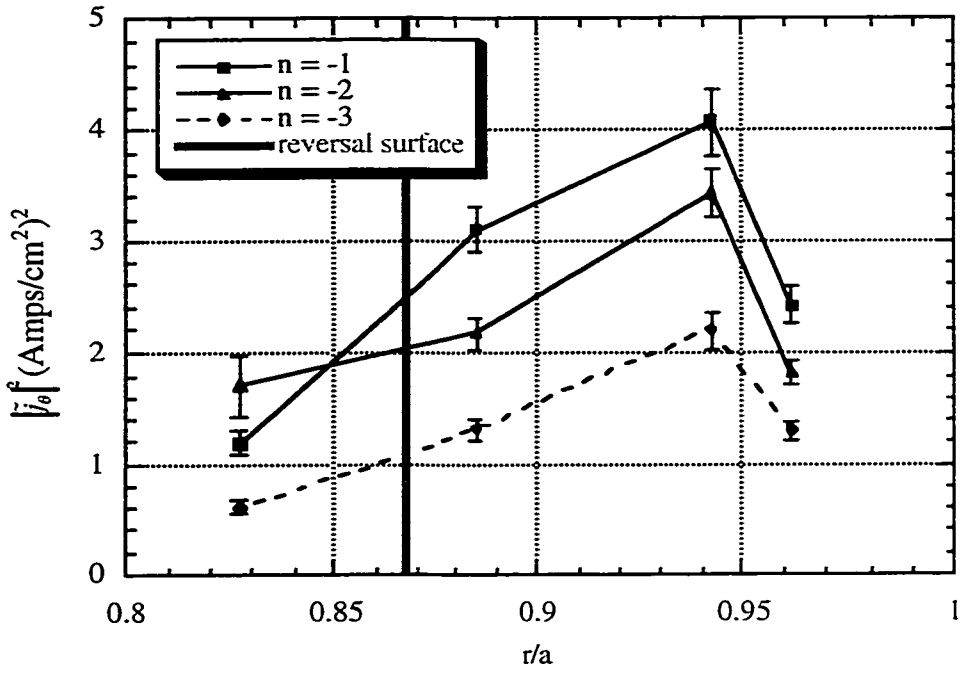

Figure 109: Radial profile of squared two-point toroidal spectral amplitude of poloidal current density fluctuations for reversal surface resonant toroidal modes measured during sawtooth crashes with probes at -15° P, 320° T and -15° P, 330° T.

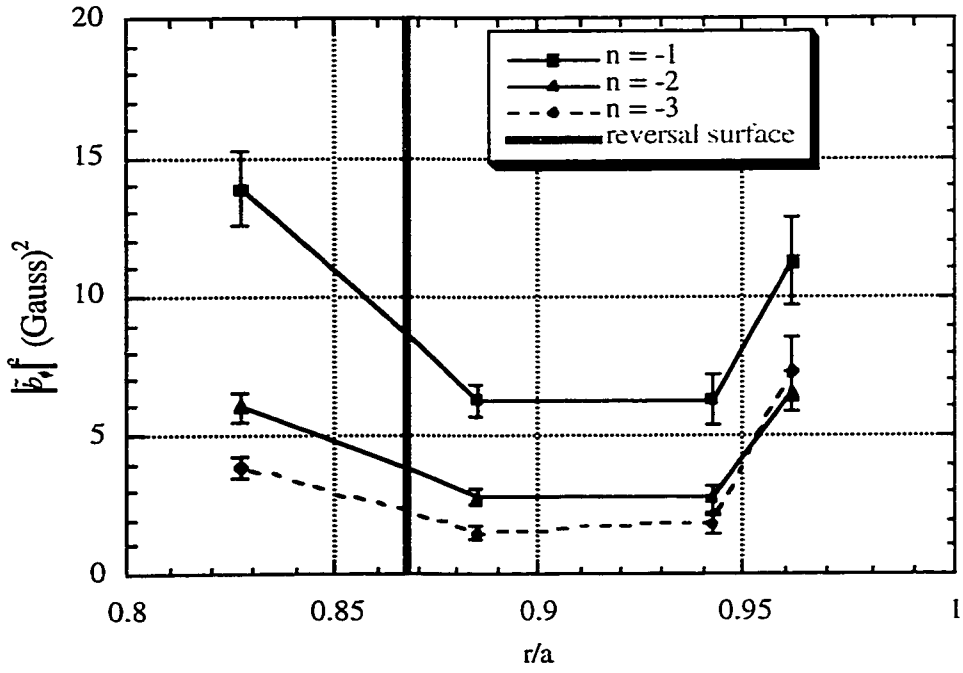

Figure 110: Radial profile of squared two-point toroidal spectral amplitude of toroidal magnetic field fluctuations for reversal surface resonant toroidal modes measured during sawtooth crashes with probes at -15° P, 320° T and -15° P, 330° T.

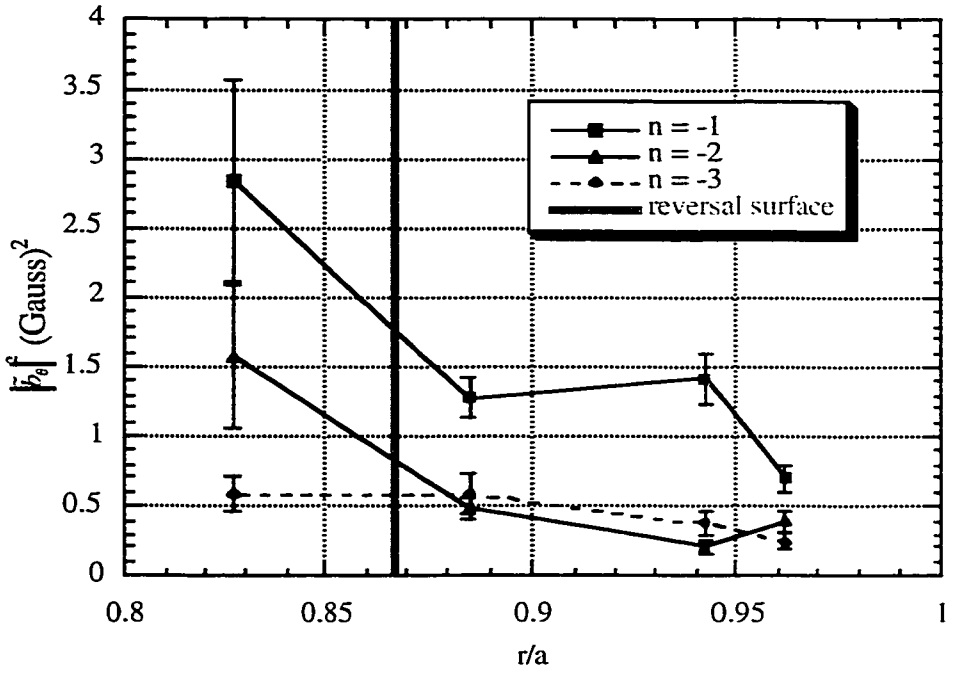

Figure 111: Radial profile of squared two-point toroidal spectral amplitude of poloidal magnetic field fluctuations for reversal surface resonant toroidal modes measured during sawtooth crashes with probes at -15° P, 320° T and -15° P, 330° T.

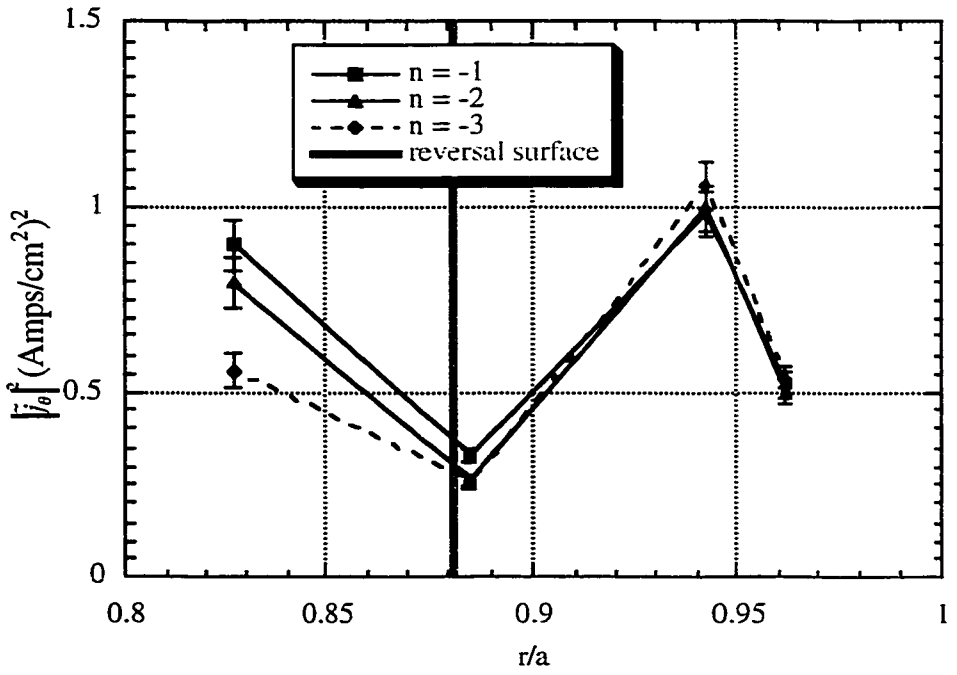

Figure 112: Radial profile of squared two-point toroidal spectral amplitude of poloidal current density fluctuations for reversal surface resonant toroidal modes measured between sawtooth crashes with probes at -15° P, 320° T and -15° P, 330° T.

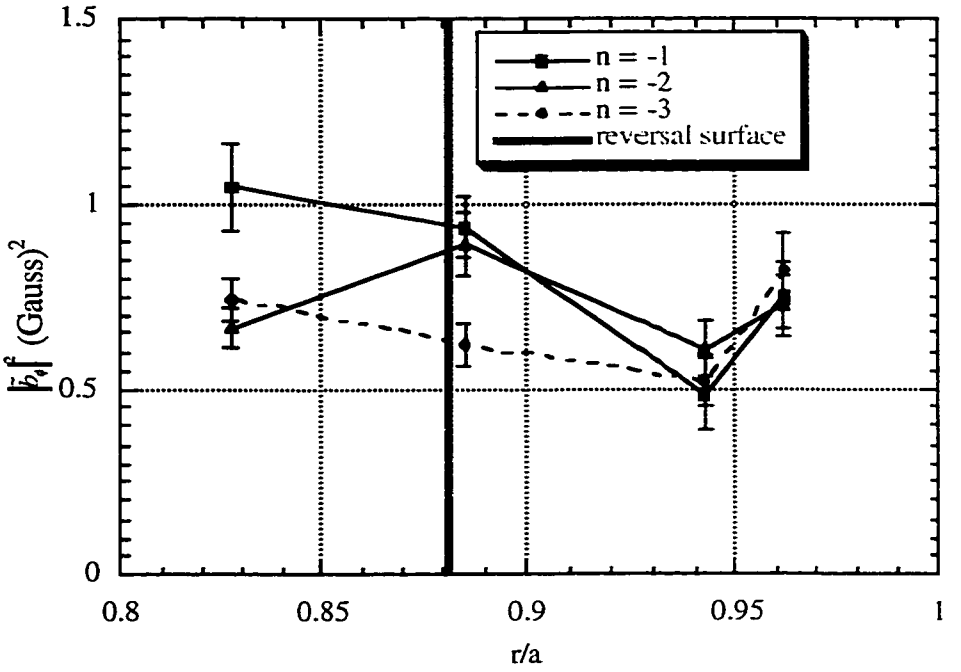

Figure 113: Radial profile of squared two-point toroidal spectral amplitude of toroidal magnetic field fluctuations for reversal surface resonant toroidal modes measured between sawtooth crashes with probes at -15° P, 320° T and -15° P, 330° T.

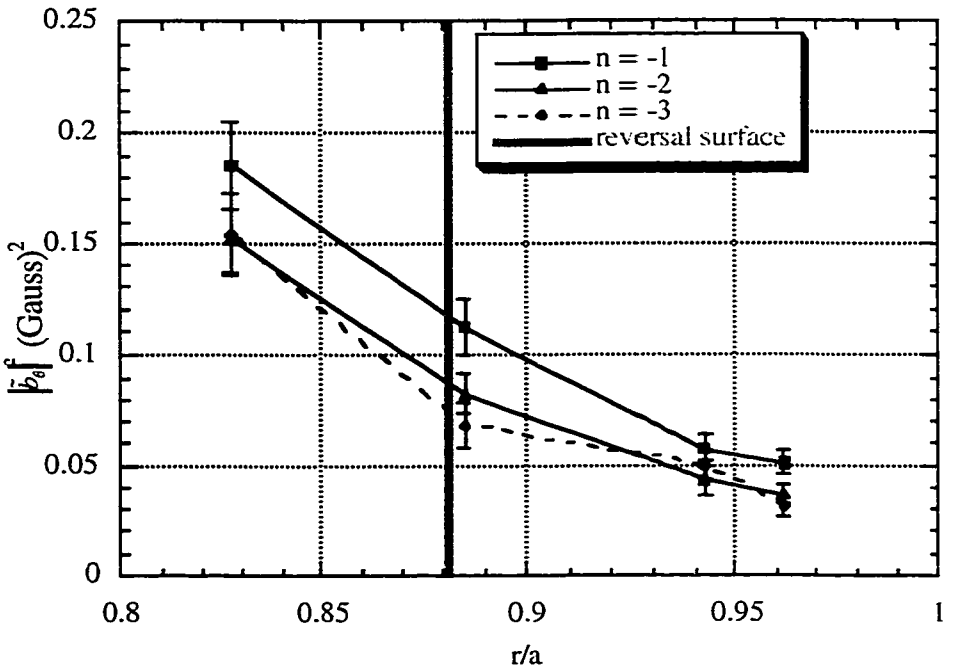

Figure 114: Radial profile of squared two-point toroidal spectral amplitude of poloidal magnetic field fluctuations for reversal surface resonant toroidal modes measured between sawtooth crashes with probes at -15° P, 320° T and -15° P, 330° T.

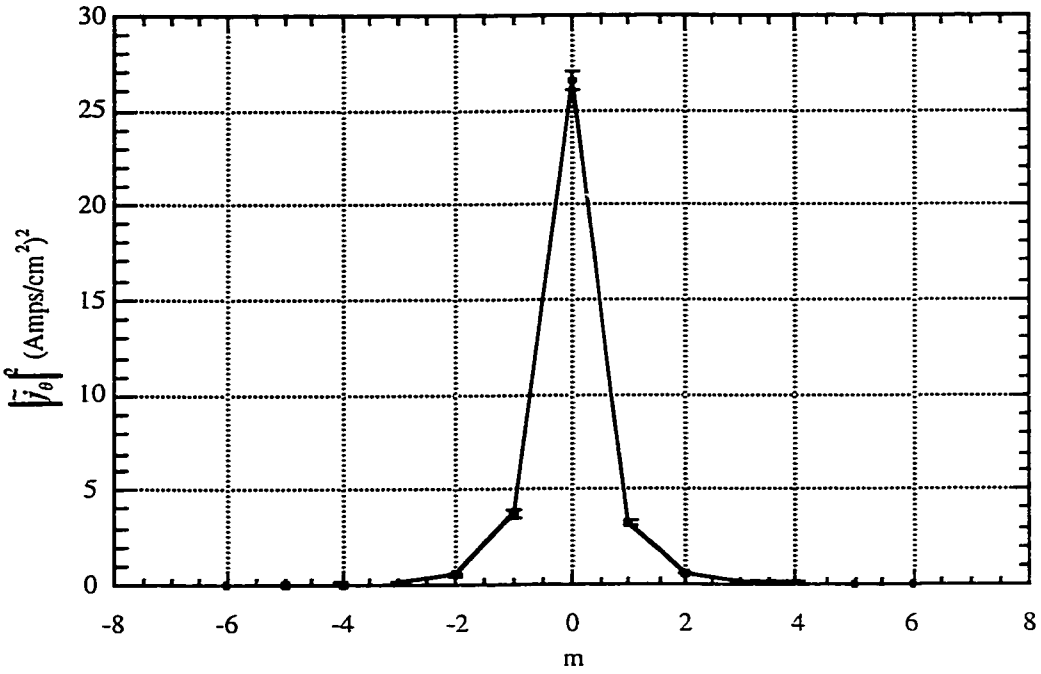

Figure 115: Two-point poloidal spectrum of poloidal current density fluctuations measured during sawtooth crashes at reversal surface. Probes are at 75° P, 120° T and 105° P, 120° T.

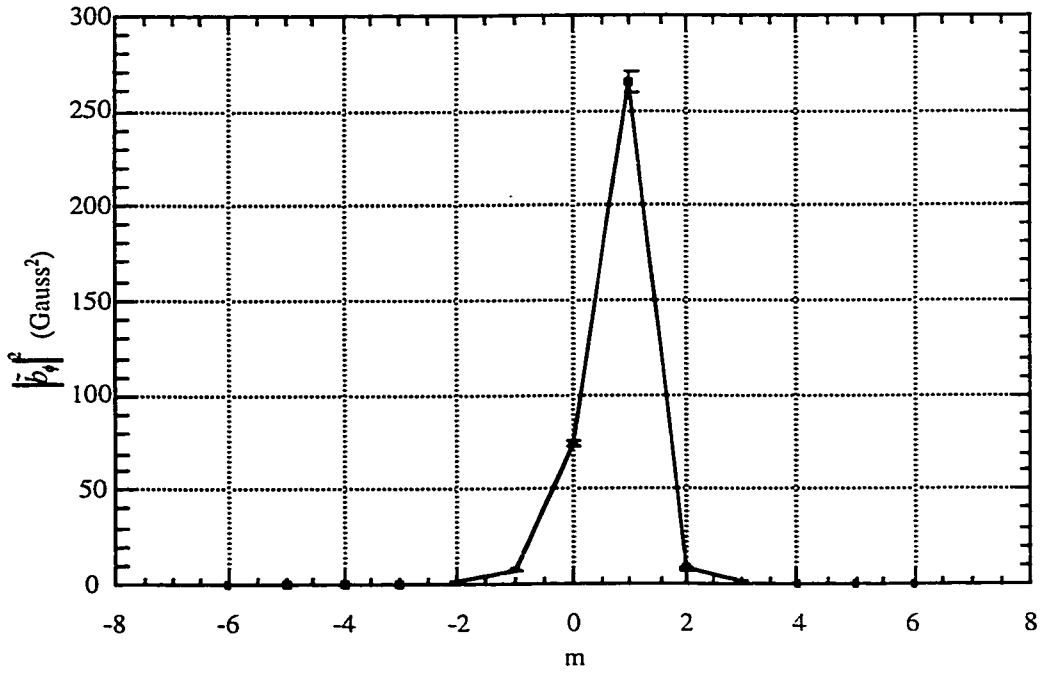

Figure 116: Two-point poloidal spectrum of toroidal magnetic field fluctuations measured during sawtooth crashes at reversal surface. Probes are at 75° P, 120° T and 105° P, 120° T.

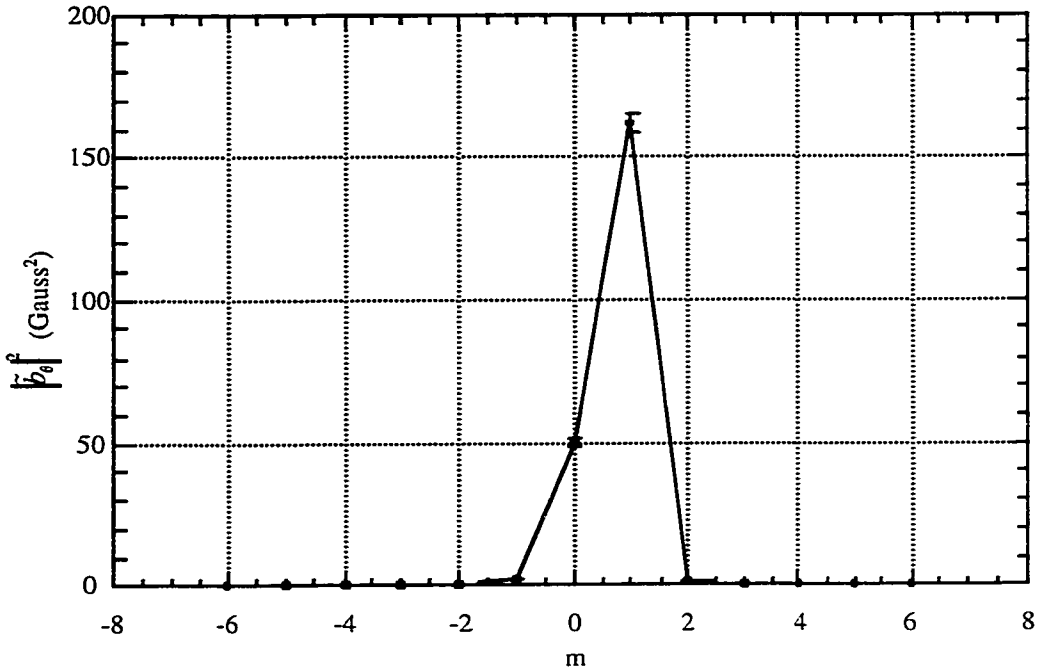

Figure 117: Two-point poloidal spectrum of poloidal magnetic field fluctuations measured during sawtooth crashes at reversal surface. Probes are at 75° P, 120° T and 105° P, 120° T.

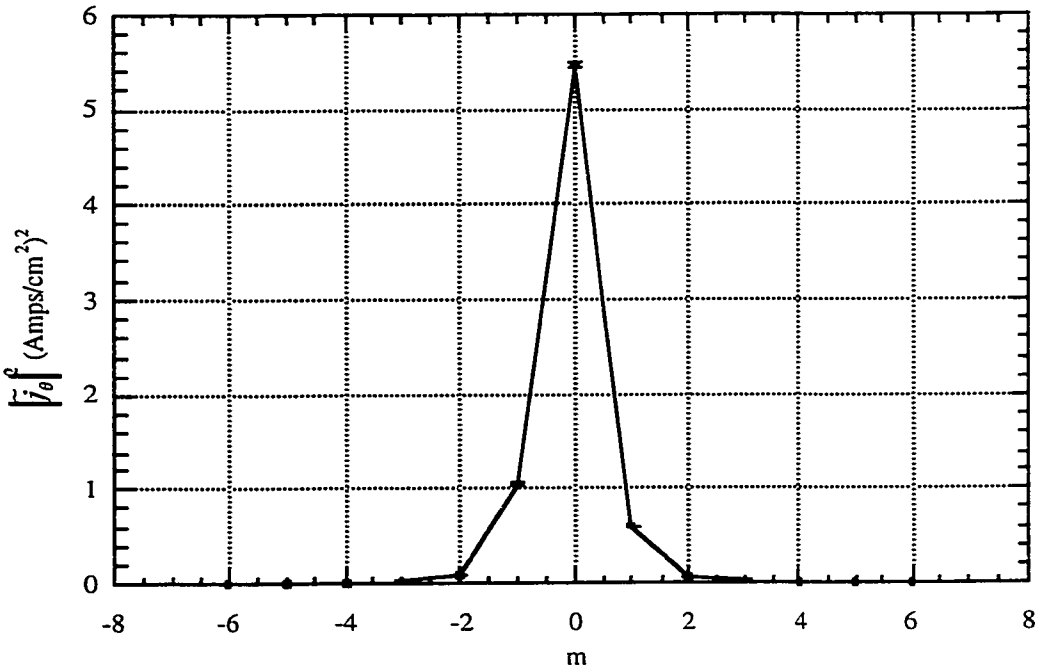

Figure 118: Two-point poloidal spectrum of poloidal current density fluctuations measured between sawtooth crashes at reversal surface. Probes are at 75° P, 120° T and 105° P, 120° T.

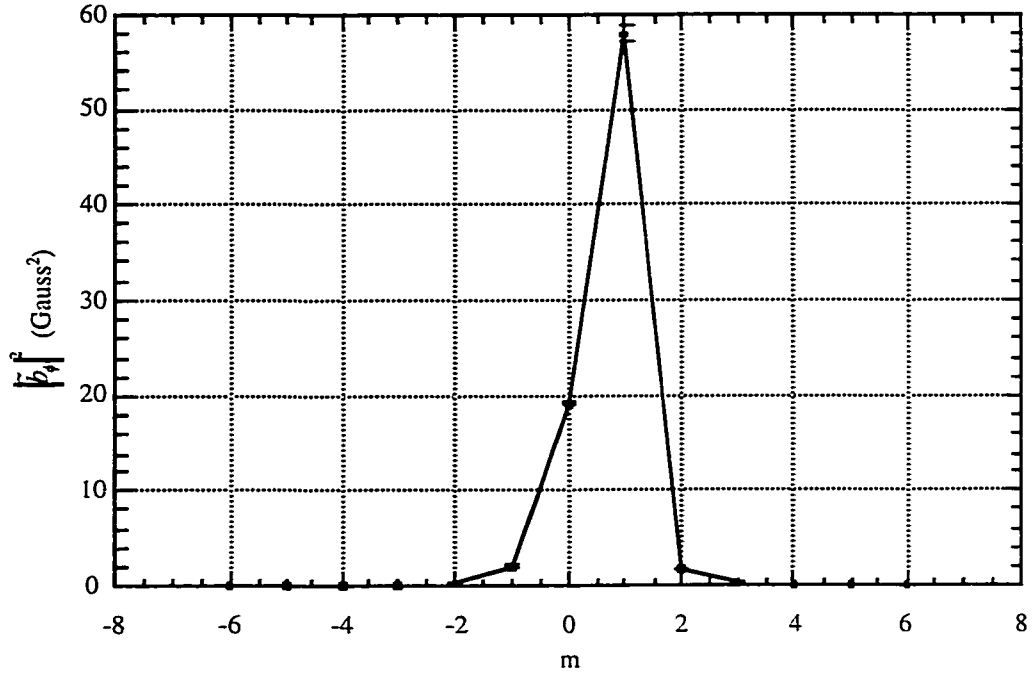

Figure 119: Two-point poloidal spectrum of toroidal magnetic field fluctuations measured between sawtooth crashes at reversal surface. Probes are at 75° P, 120° T and 105° P, 120° T.

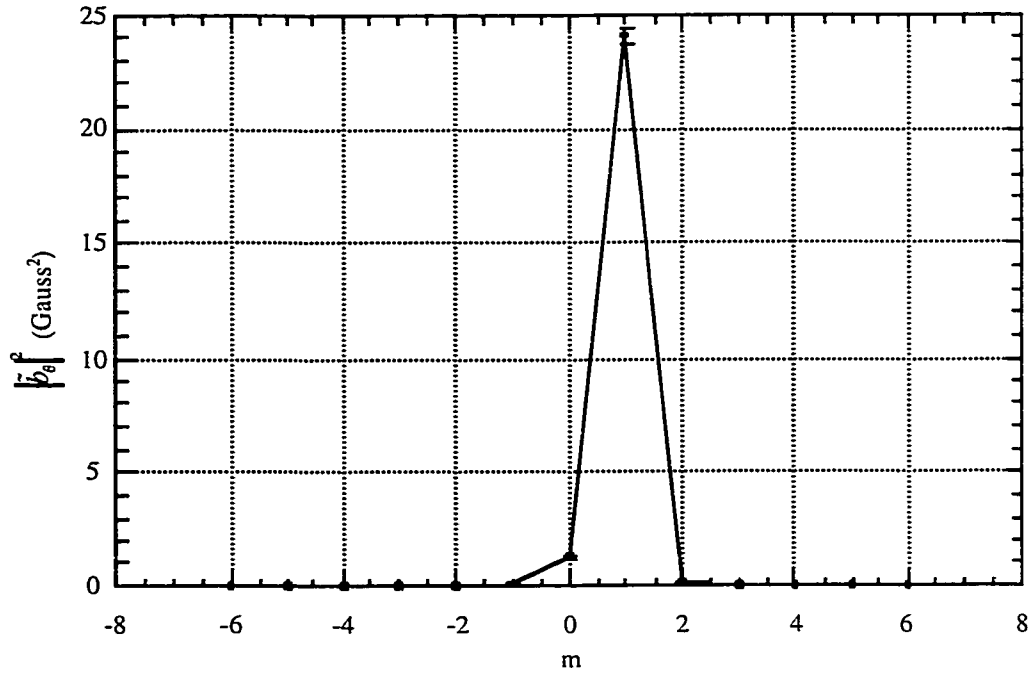

Figure 120: Two-point poloidal spectrum of poloidal magnetic field fluctuations measured between sawtooth crashes at reversal surface. Probes are at 75° P, 120° T and 105° P, 120° T.

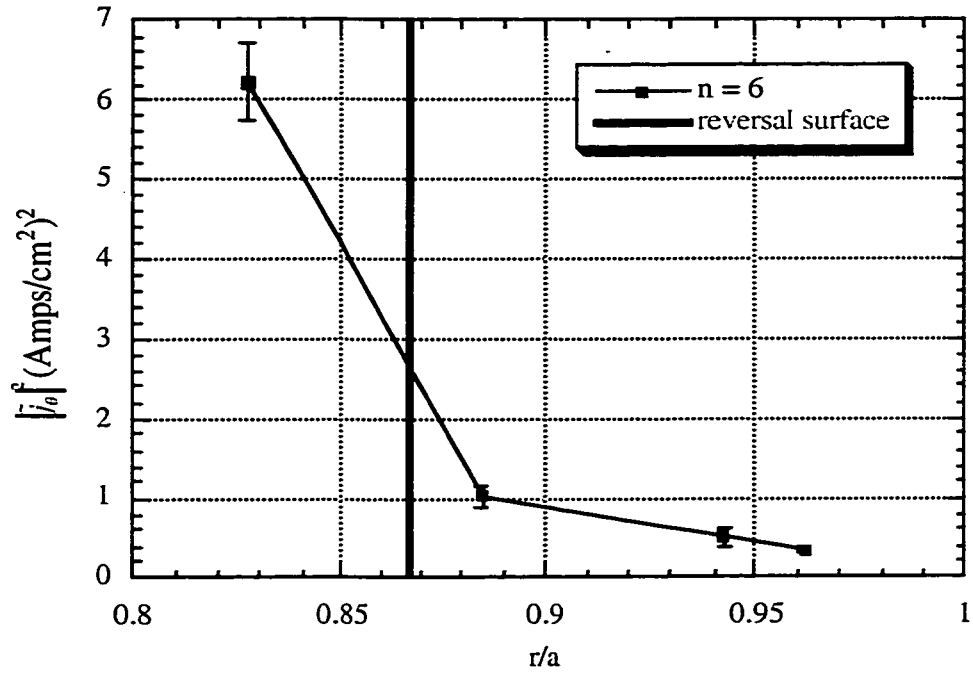

Figure 121: Radial profile of squared toroidal pseudospectrum amplitude of poloidal current density fluctuations for the core resonant, n = 6 toroidal mode during sawtooth crashes at -15° P, 330° T. Measured with reference to toroidal magnetic field flucuations at the wall.

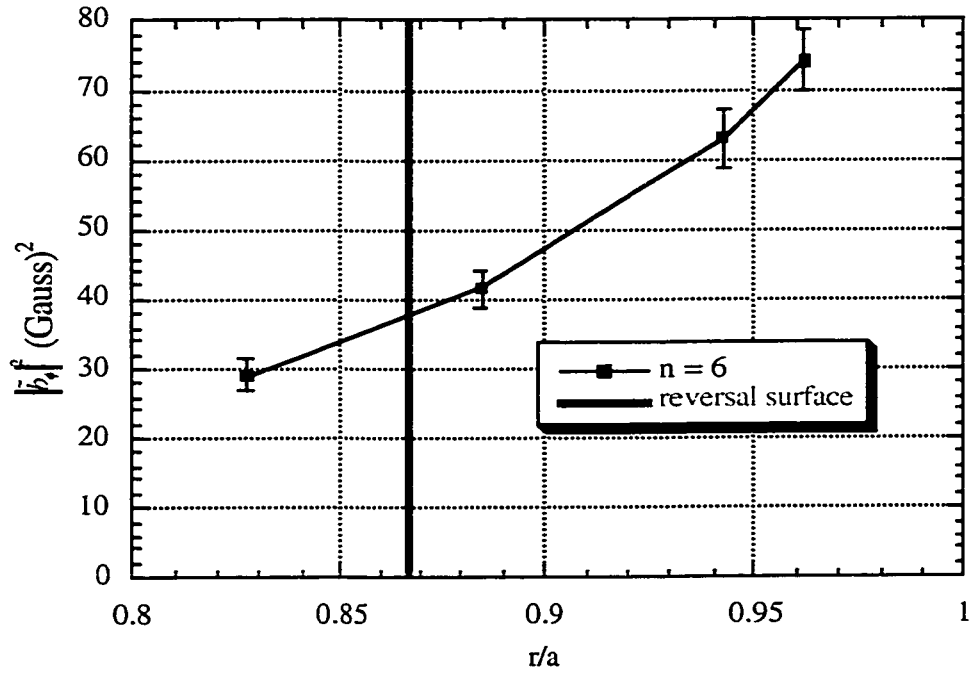

Figure 122: Radial profile of squared toroidal pseudospectrum amplitude of toroidal magnetic field fluctuations for the core resonant, n = 6 toroidal mode during sawtooth crashes at -15° P, 330° T. Measured with reference to toroidal magnetic field flucuations at the wall.

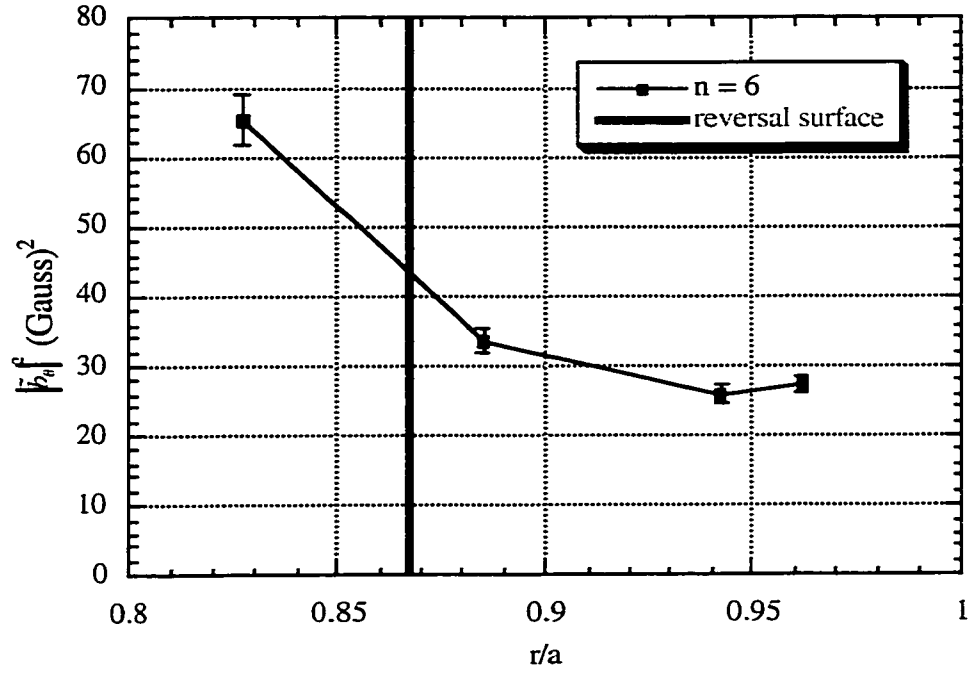

Figure 123: Radial profile of squared toroidal pseudospectrum amplitude of poloidal magnetic field fluctuations for the core resonant, n = 6 toroidal mode during sawtooth crashes at -15° P, 330° T. Measured with reference to toroidal magnetic field flucuations at the wall.

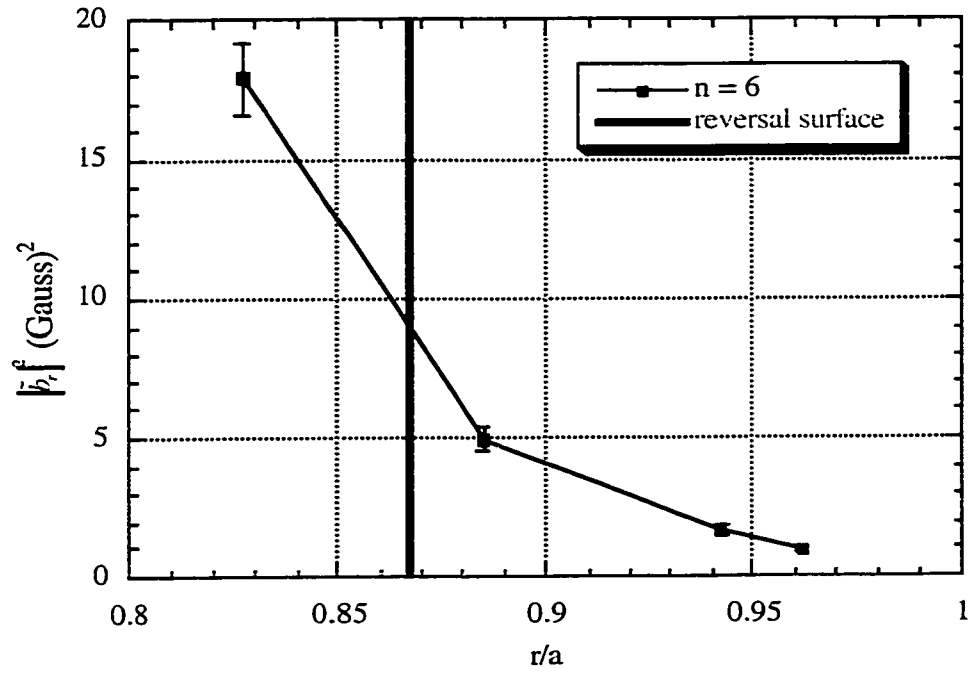

Figure 124: Radial profile of squared toroidal pseudospectrum amplitude of radial magnetic field fluctuations for the core resonant, n = 6 toroidal mode during sawtooth crashes at -15° P, 330° T. Measured with reference to toroidal magnetic field flucuations at the wall.

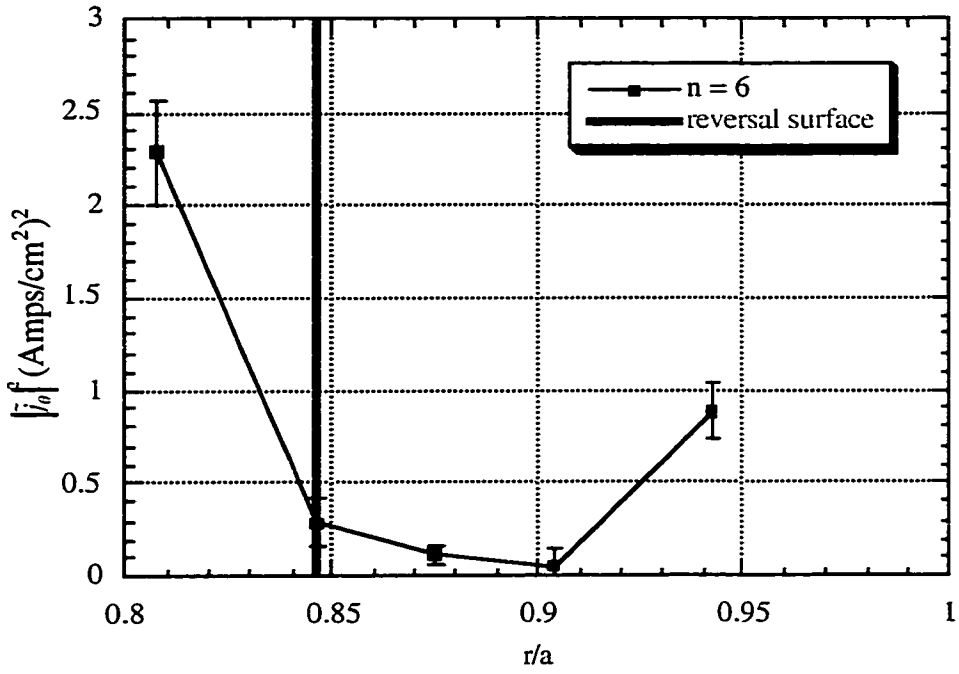

Figure 125: Radial profile of squared toroidal pseudospectrum amplitude of poloidal current density fluctuations for the core resonant, n = 6 toroidal mode during sawtooth crashes at 75° P, 120° T. Measured with reference to toroidal magnetic field flucuations at the wall.

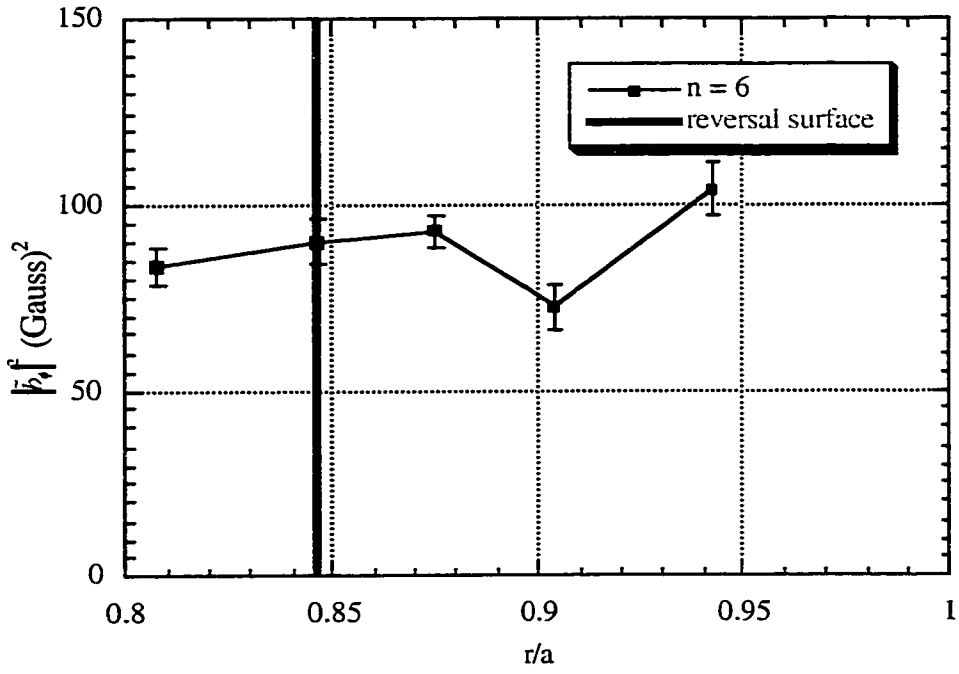

Figure 126: Radial profile of squared toroidal pseudospectrum amplitude of toroidal magnetic field fluctuations for the core resonant, n = 6 toroidal mode during sawtooth crashes at 75° P, 120° T. Measured with reference to toroidal magnetic field flucuations at the wall.

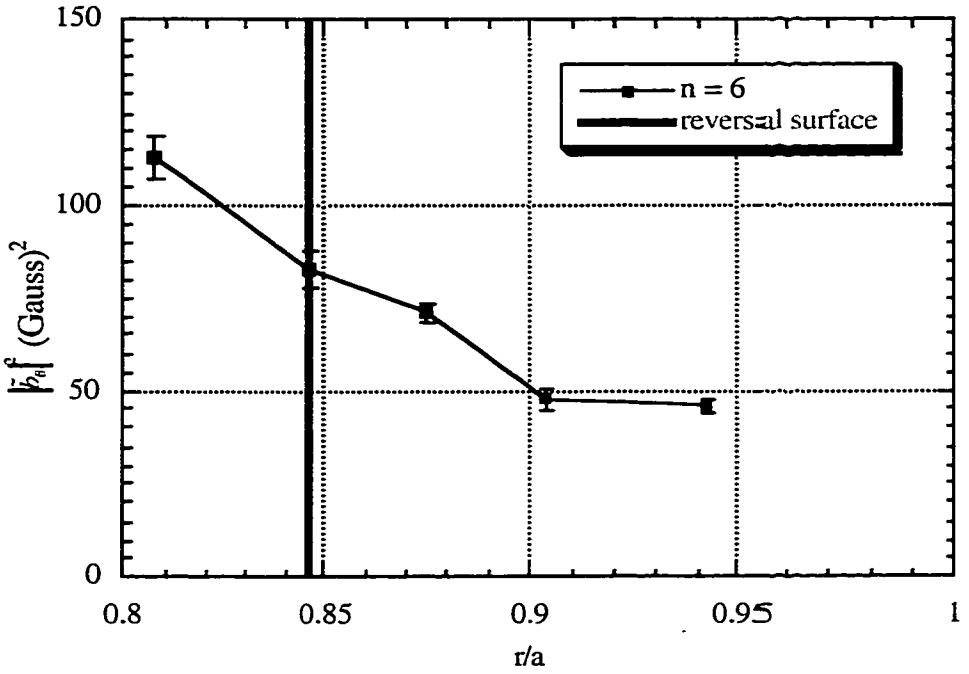

Figure 127: Radial profile of squared toroidal pseudospectrum amplitude of poloidal magnetic field fluctuations for the core resonant, n = 6 toroidal mode during sawtooth crashes at 75° P, 120° T. Measured with reference to toroidal magnetic field flucuations at the wall.

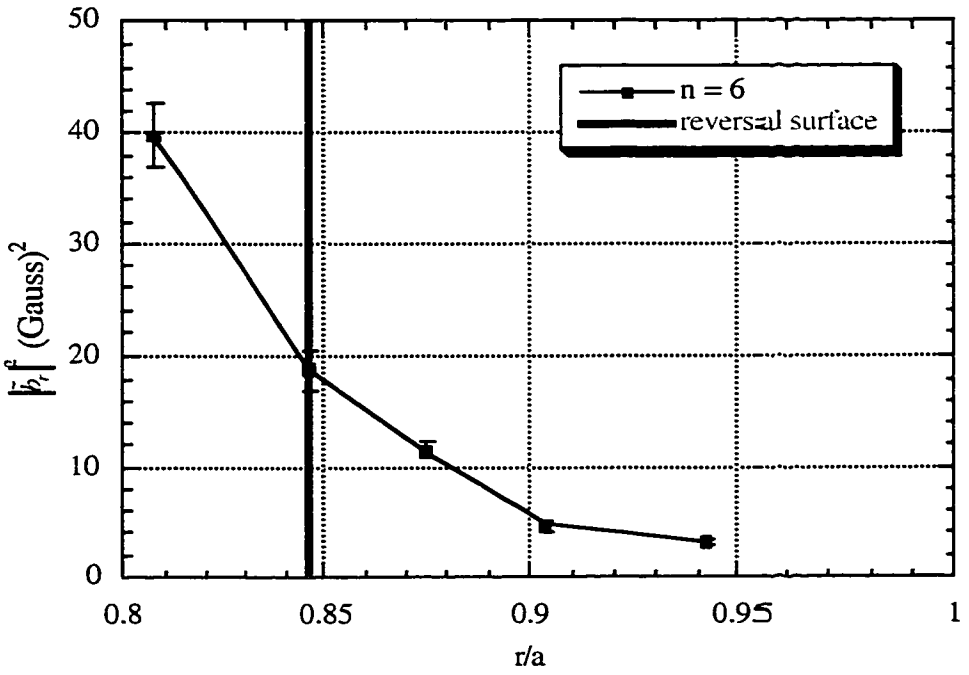

Figure 128: Radial profile of squared toroidal pseudospectrum amplitude of radial magnetic field fluctuations for the core resonant, n = 6 toroidal mode during sawtooth crashes at 75° P, 120° T. Measured with reference to toroidal magnetic field flucuations at the wall.

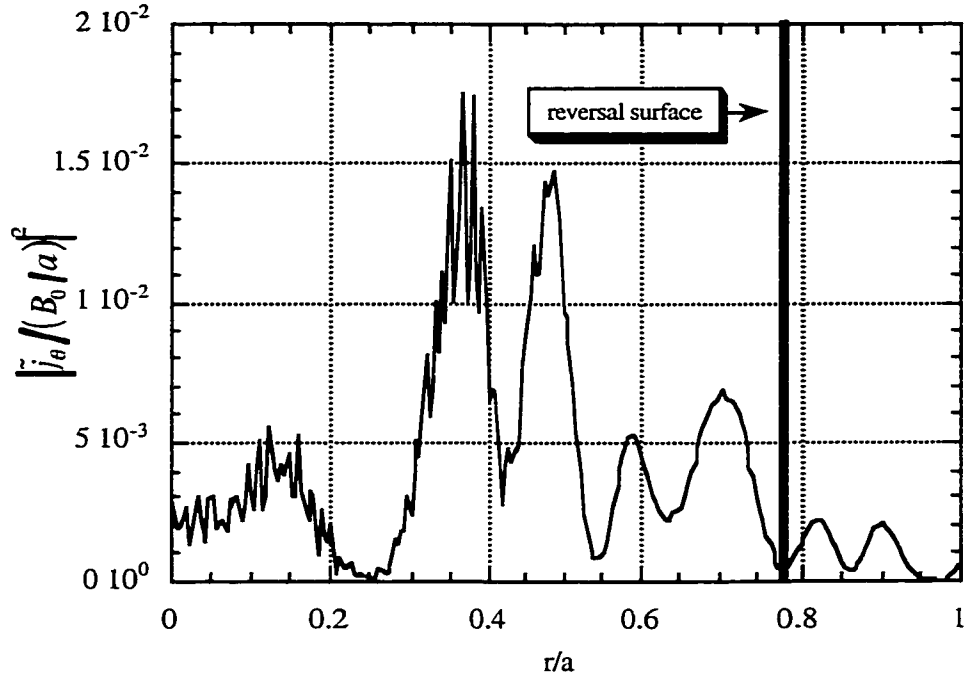

Figure 129: DEBS simulation data obtained during fluctuation burst. Radial profile of squared poloidal current density fluctuation amplitude for core resonant, m = 1, n = 6 helical mode.

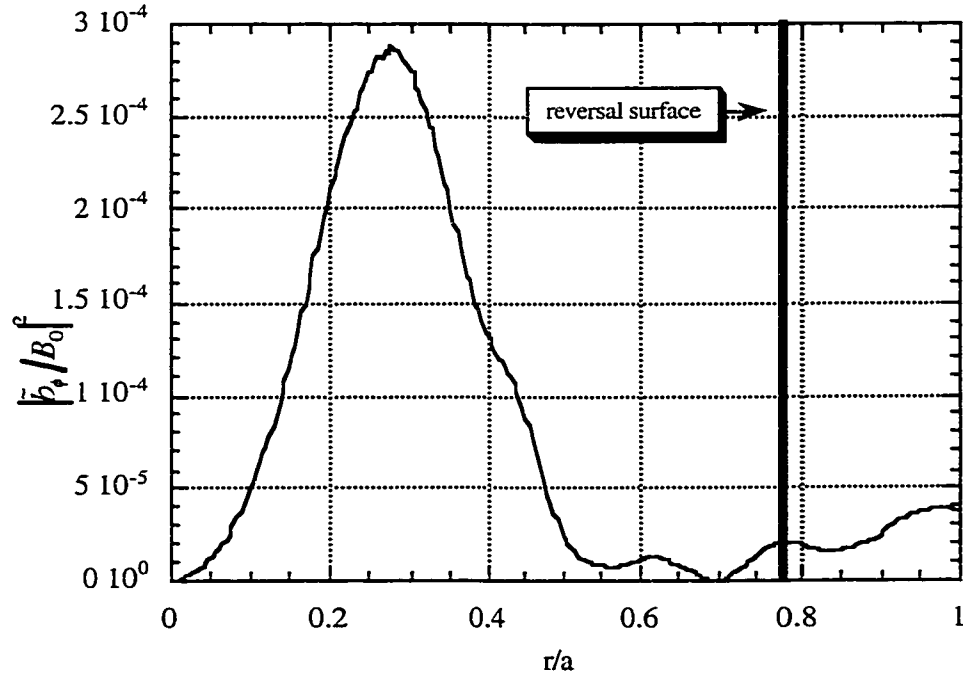

Figure 130: DEBS simulation data obtained during fluctuation burst. Radial profile of squared toroidal magnetic field fluctuation amplitude for core resonant, m = 1, n = 6 helical mode.

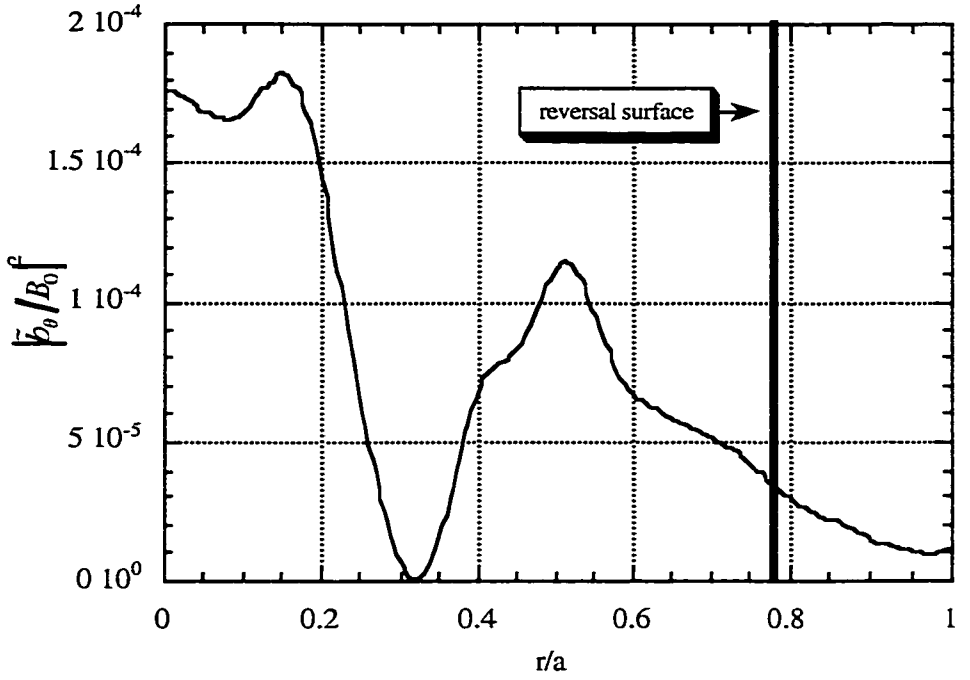

Figure 131: DEBS simulation data obtained during fluctuation burst. Radial profile of squared poloidal magnetic field fluctuation amplitude for core resonant, m = 1, n = 6 helical mode.

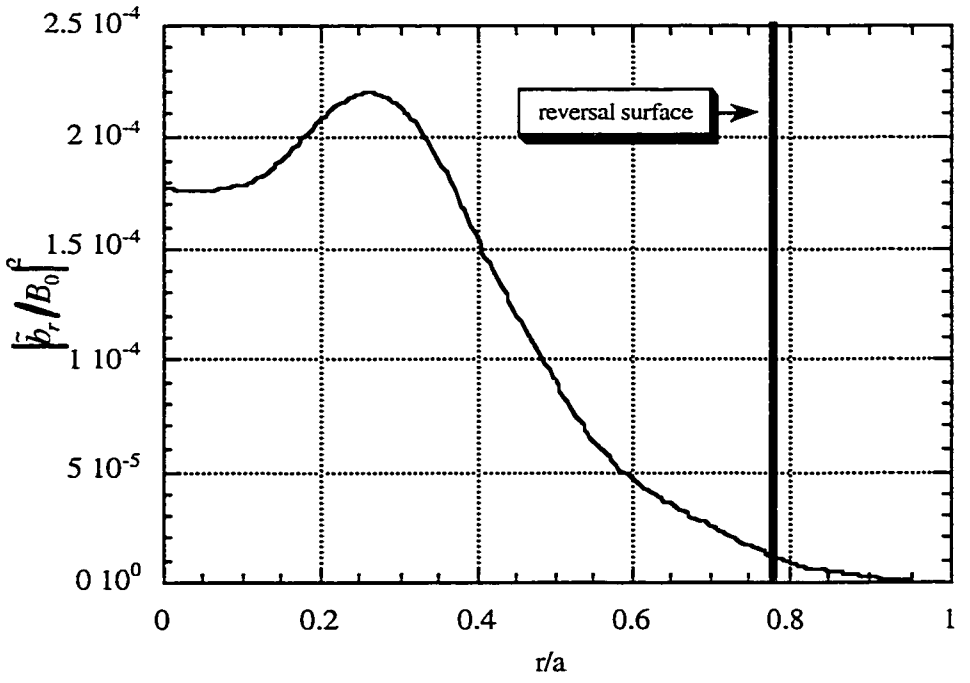

Figure 132: DEBS simulation data obtained during fluctuation burst. Radial profile of squared radial magnetic field fluctuation amplitude for core resonant, m = 1, n = 6 helical mode.

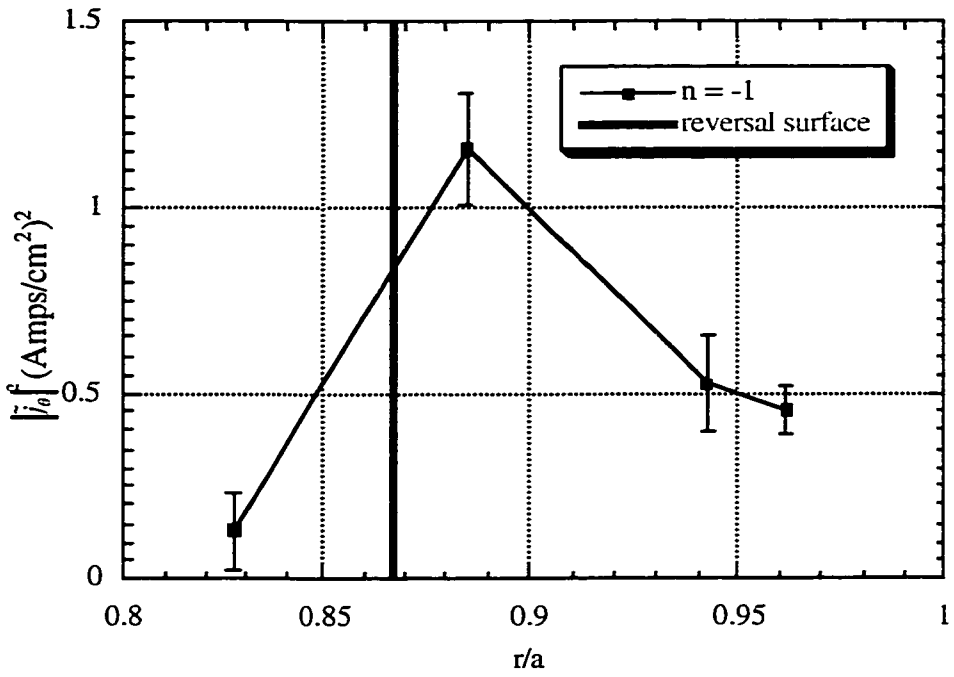

Figure 133: Radial profile of squared toroidal pseudospectrum amplitude of poloidal current density fluctuations for the reversal surface resonant, n = -1 toroidal mode during sawtooth crashes at -15° P, 330° T. Measured with reference to toroidal magnetic field flucuations at the wall.

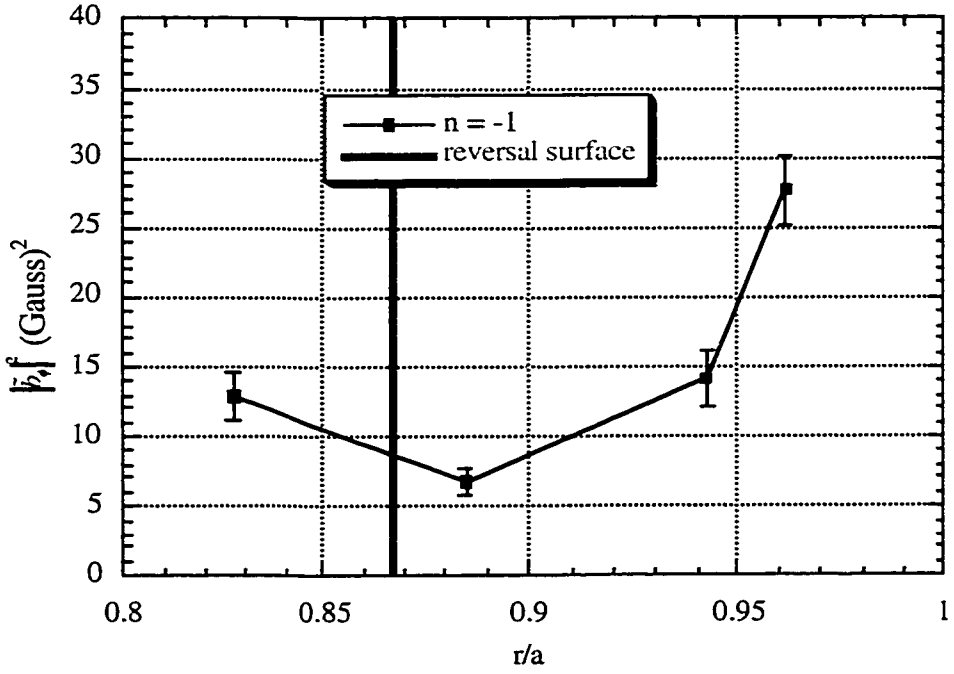

Figure 134: Radial profile of squared toroidal pseudospectrum amplitude of toroidal magnetic field fluctuations for the reversal surface resonant, n = -1 toroidal mode during sawtooth crashes at -15° P, 330° T. Measured with reference to toroidal magnetic field flucuations at the wall.

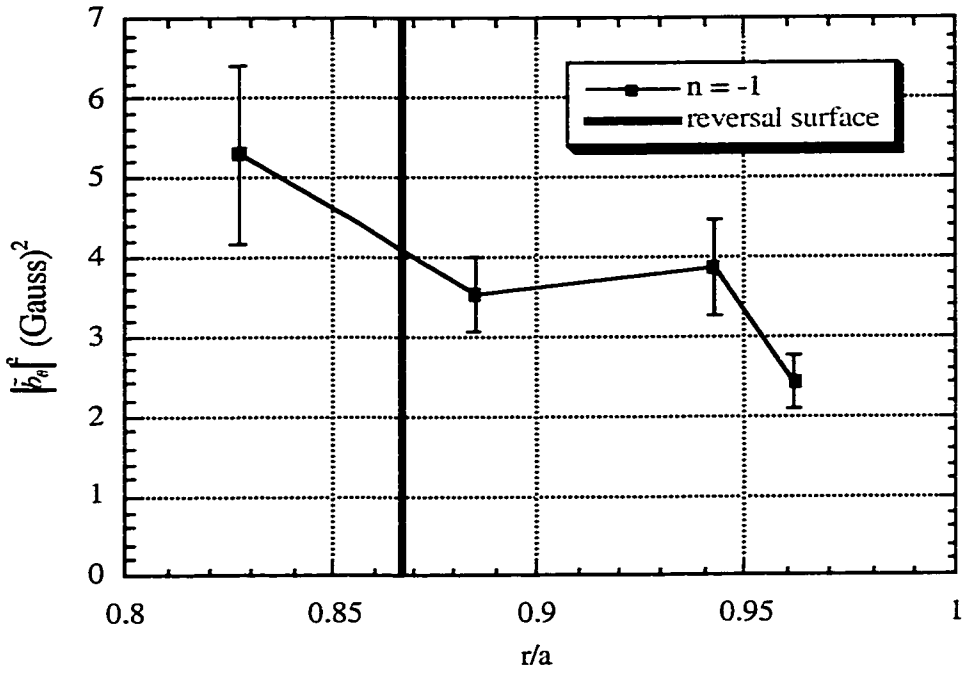

Figure 135: Radial profile of squared toroidal pseudospectrum amplitude of poloidal magnetic field fluctuations for the reversal surface resonant, n = -1 toroidal mode during sawtooth crashes at -15° P, 330° T. Measured with reference to toroidal magnetic field flucuations at the wall.

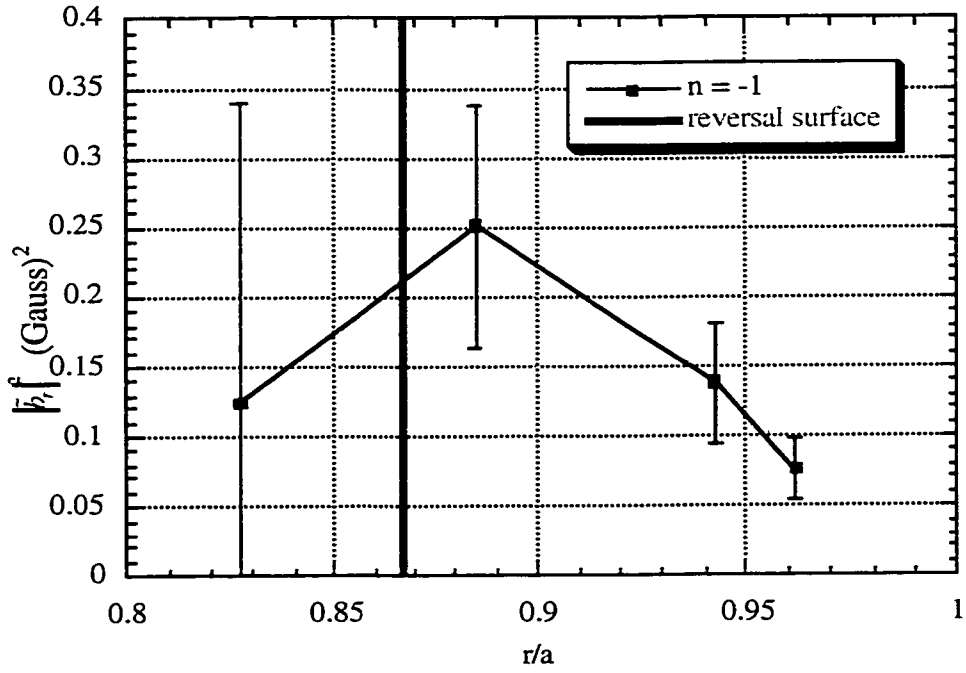

Figure 136: Radial profile of squared toroidal pseudospectrum amplitude of radial magnetic field fluctuations for the reversal surface resonant, n = -1 toroidal mode during sawtooth crashes at -15° P, 330° T. Measured with reference to toroidal magnetic field flucuations at the wall.

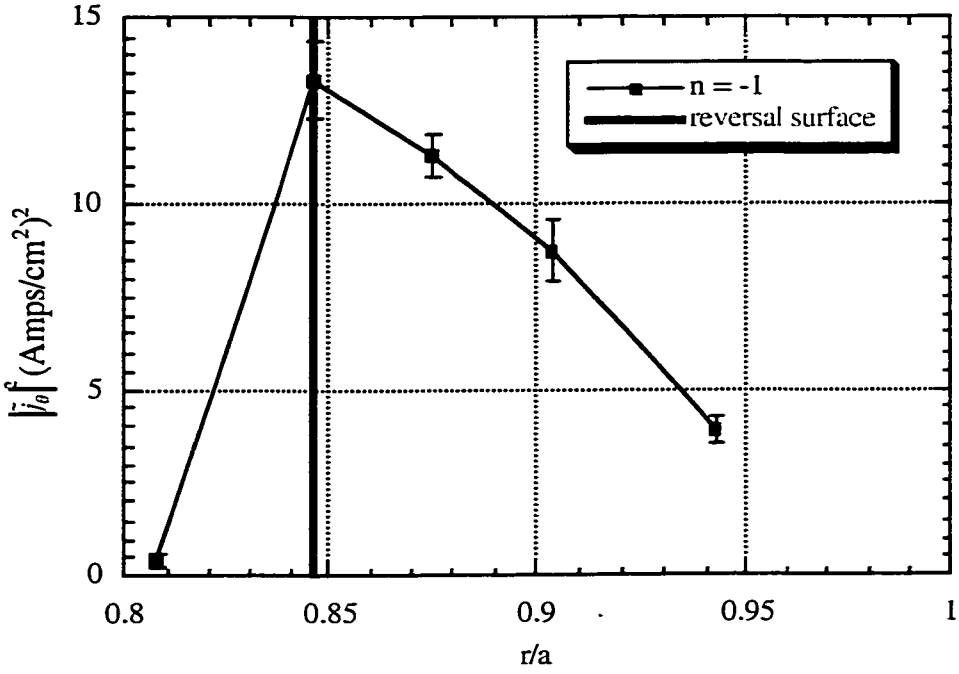

Figure 137: Radial profile of squared toroidal pseudospectrum amplitude of poloidal current density fluctuations for the reversal surface resonant, n = -1 toroidal mode during sawtooth crashes at 75° P, 120° T. Measured with reference to toroidal magnetic field flucuations at the wall.

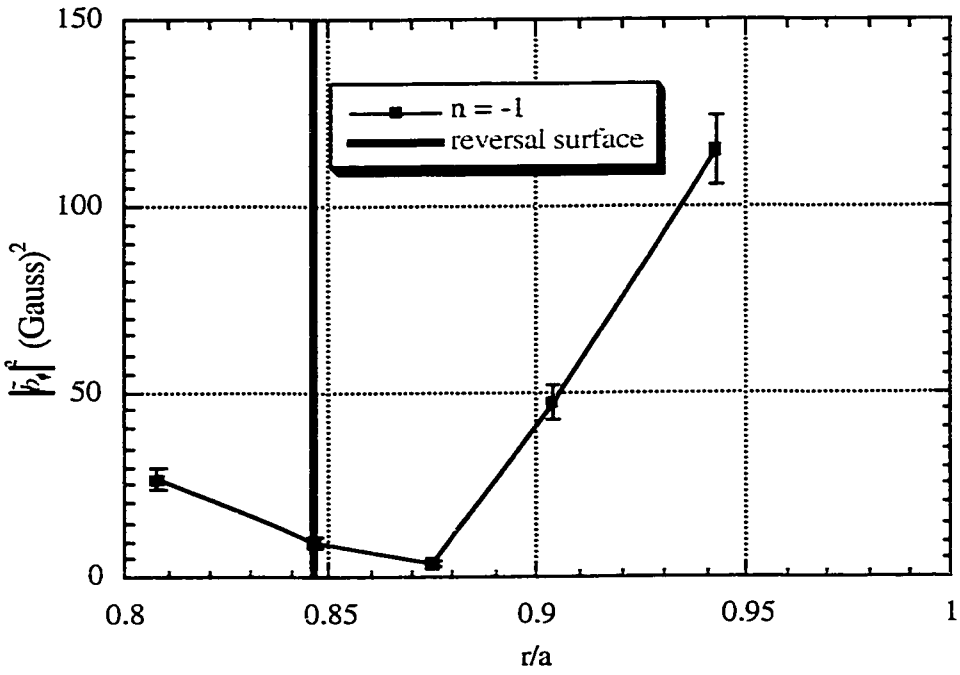

Figure 138: Radial profile of squared toroidal pseudospectrum amplitude of toroidal magnetic field fluctuations for the reversal surface resonant, n = -1 toroidal mode during sawtooth crashes at 75° P, 120° T. Measured with reference to toroidal magnetic field flucuations at the wall.

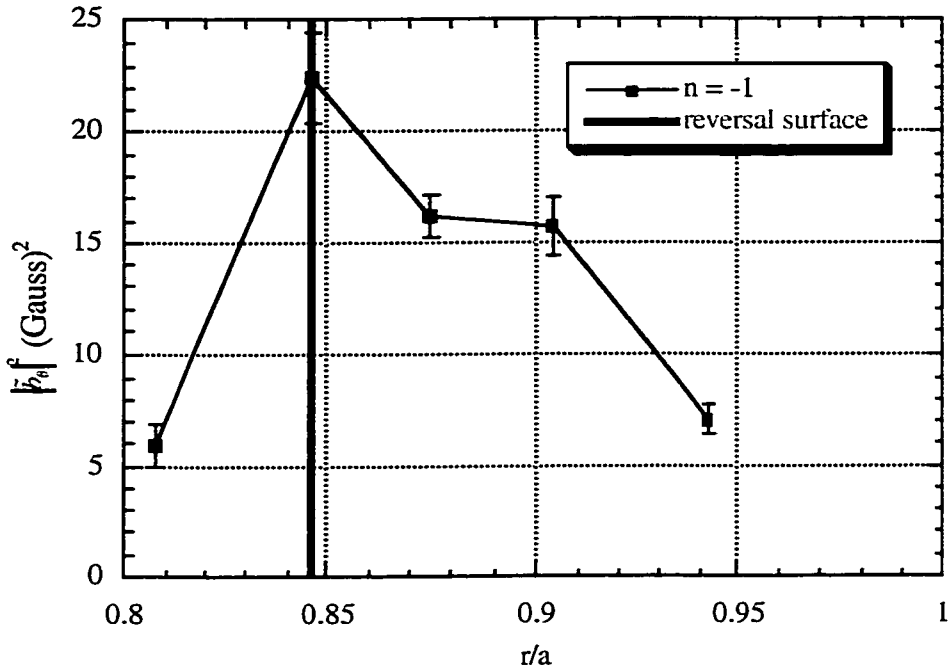

Figure 139: Radial profile of squared toroidal pseudospectrum amplitude of poloidal magnetic field fluctuations for the reversal surface resonant, n = -1 toroidal mode during sawtooth crashes at 75° P, 120° T. Measured with reference to toroidal magnetic field flucuations at the wall.

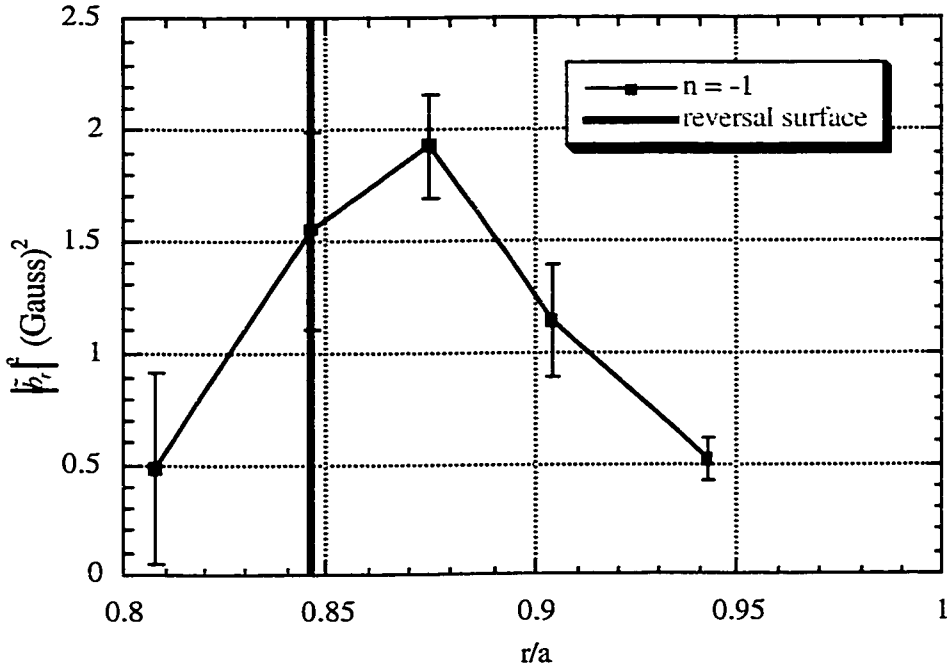

Figure 140: Radial profile of squared toroidal pseudospectrum amplitude of radial magnetic field fluctuations for the reversal surface resonant, n = -1 toroidal mode during sawtooth crashes at 75° P, 120° T. Measured with reference to toroidal magnetic field flucuations at the wall.

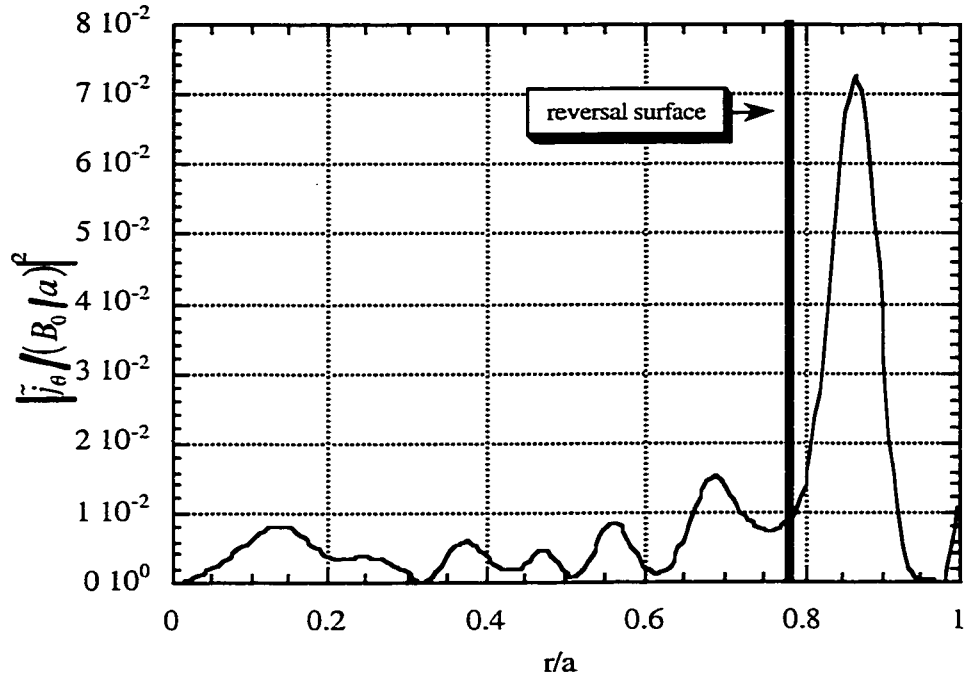

Figure 141: DEBS simulation data obtained during fluctuation burst. Radial profile of squared poloidal current density fluctuation amplitude for reversal surface resonant, m = 0, n = -1 helical mode.

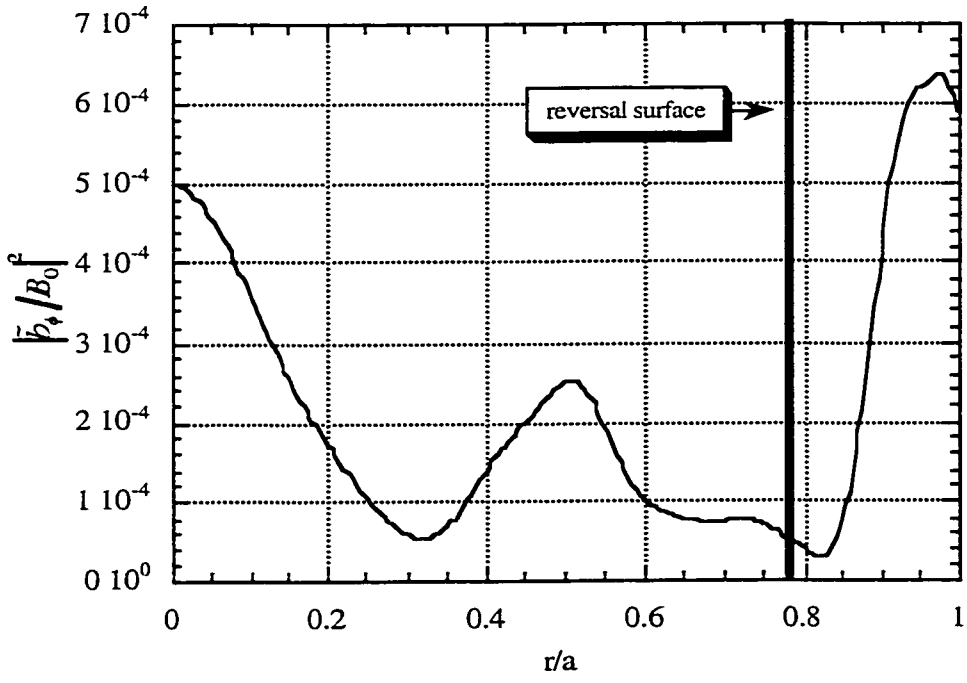

Figure 142: DEBS simulation data obtained during fluctuation burst. Radial profile of squared toroidal magnetic field fluctuation amplitude for reversal surface resonant, m = 0, n = -1 helical mode.

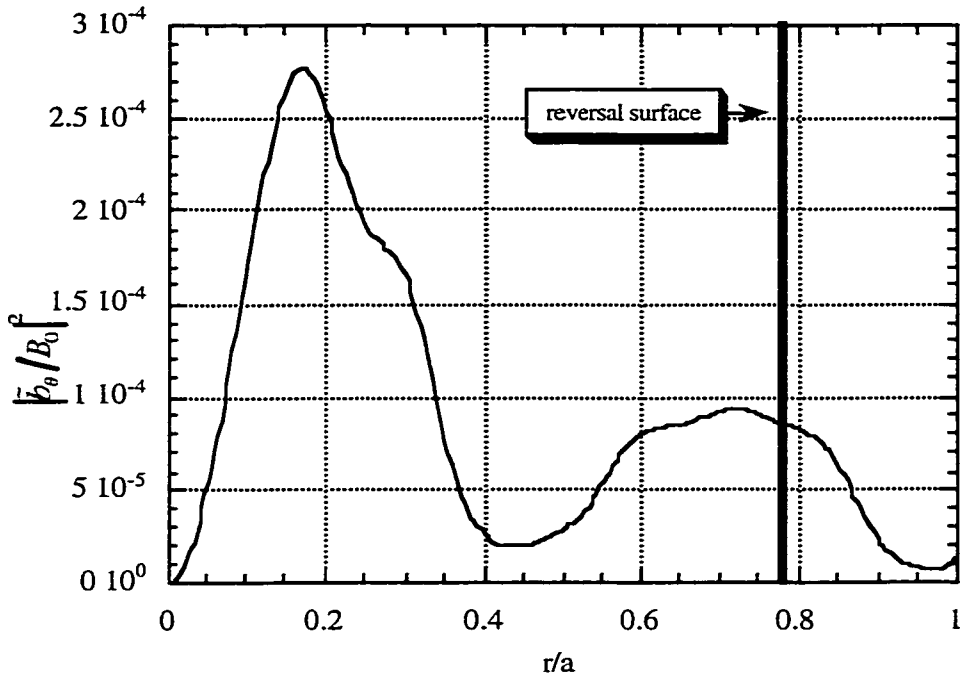

Figure 143: DEBS simulation data obtained during fluctuation burst. Radial profile of squared poloidal magnetic field fluctuation amplitude for reversal surface resonant, m = 0, n = -1 helical mode.

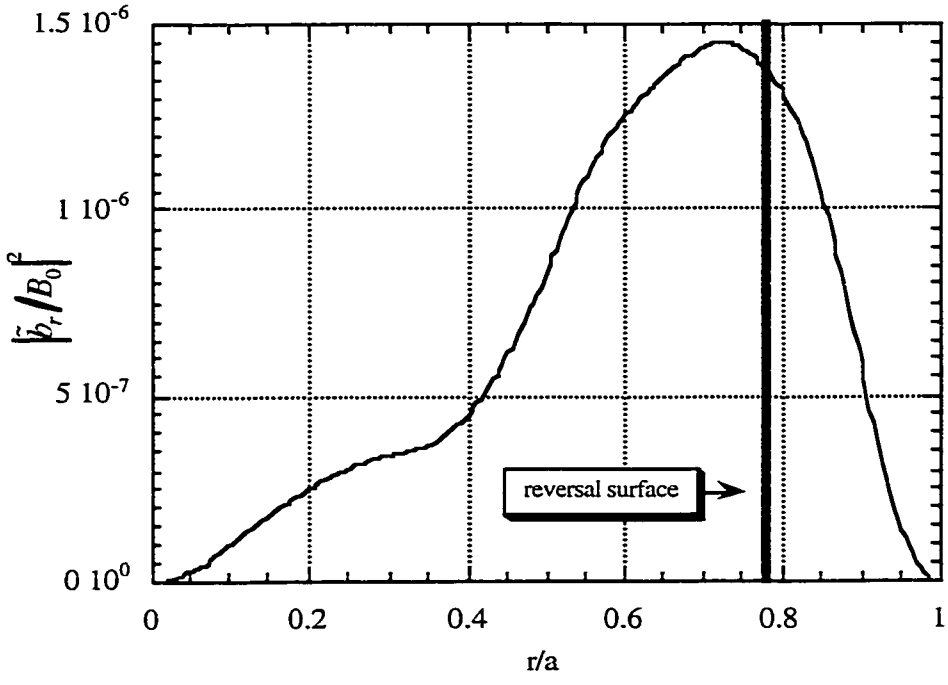

Figure 144: DEBS simulation data obtained during fluctuation burst. Radial profile of squared radial magnetic field fluctuation amplitude for reversal surface resonant, m = 0, n = -1 helical mode.

Appendix B - Supplemental Figures and Description of Data Sets for Chapter 5

B.1 - Introduction

As discussed in Ch. 5 of this dissertation, estimates of the flux surface average product of $\tilde{j}_{\parallel}$ and $\tilde{b}_r$ have been obtained in the edge of MST. Additionally, crossspectral analysis and pseudospectral analysis were used to explore the dynamics underlying this flux surface average product. The results of these measurements and analyses, each of which is obtained for several cases, represents a rather large collection of figures. All discussion of these measurements is confined to Ch. 5. This appendix serves to organize and present these figures, many of which were not presented in Ch. 5 for sake of clarity, for reference purposes.

Section B.2 presents measurements of $\left\langle \tilde{j}_{\parallel}\tilde{b}_r \right\rangle_{F.S.}$.

Section B.3 presents crossspectral phase, coherence and amplitude measurement for $\tilde{j}_{\parallel}$ and $\tilde{b}_r$.

Section B.4 presents the results of a pseudospectral decomposition of $\left\langle \tilde{j}_{\parallel}\tilde{b}_r \right\rangle_{F.S.}$ into contributions from different toroidal modes. It includes measurements of the combined amplitude of $\tilde{j}_{\parallel}$ and $\tilde{b}_r$ for each toroidal mode, as well as the phase between $\tilde{j}_{\parallel}$ and $\tilde{b}_r$ for each mode. Additionally, it includes a comparison of the the crossspectral phase and amplitude of $\tilde{j}_{\parallel}$ and $\tilde{b}_r$ with estimates of these quantities obtained using pseudospectral analysis.

Finally, Section B.5 presents the measurements of $\left\langle \tilde{j}_{\parallel}\tilde{b}_r \right\rangle_{F.S.}$ in the form of a radial charge flux (*i.e.*, radial current density) and in the form a difference in radial ion and electron particle fluxes.

For the figures shown in this appendix, the list of MST shots in which the measurements were made is described in Tables A.1 and A.2 of Appendix A. The parallel (poloidal) current density and radial magnetic field measurements taken during the shots listed in Tables A.1 and A.2 are, as noted in Section A.3 of Appendix A, stored in the MST database under signal names indicated in Table A.3. Note that Rogowskii #8 was used for the measurements presented in this

appendix.

B.2 - Measurements of $\left\langle \tilde{j}_{\parallel}\tilde{b}_r \right\rangle_{F.S.}$ and $\left\langle \left|\tilde{j}_{\parallel}\right|^2 \right\rangle_{F.S.}^{1/2} \left\langle \left|\tilde{b}_r\right|^2 \right\rangle_{F.S.}^{1/2}$

Figures 1 – 4 show edge radial profiles of the estimated flux surface average product of $\tilde{j}_{\parallel}$ and $\tilde{b}_r$, $\left\langle \tilde{j}_{\parallel}\tilde{b}_r \right\rangle_{F.S.}$. The four figures represent four cases: both between and during sawtooth crashes, at two different poloidal and toroidal locations each (-15° P, 330° T and 75° P, 120° T). The sign convention used in these figures is consistent with $\tilde{b}_r = \tilde{\vec{b}} \cdot \hat{r}$ and $\tilde{j}_{\parallel} = \tilde{\vec{j}} \cdot \hat{b}_0$, where $\hat{r}$ is the minor radial unit vector, $\tilde{\vec{b}}$ is the magnetic field fluctuation vector, $\hat{b}_0$ is the equilibrium magnetic field unit vector and $\tilde{\vec{j}}$ is the current density fluctuation vector. The product of the flux surface r. m. s. values of $\tilde{j}_{\parallel}$ and $\tilde{b}_r$, $\left\langle \left|\tilde{j}_{\parallel}\right|^2 \right\rangle_{F.S.}^{1/2} \left\langle \left|\tilde{b}_r\right|^2 \right\rangle_{F.S.}^{1/2}$ is shown for each the four cases in Figures 5 – 8.

B.3 - Crossspectral Coherence and Phase and Amplitude of $\tilde{j}_{\parallel}$ and $\tilde{b}_r$

Figures 9 – 12 show edge radial profiles of the crossspectral amplitude of $\tilde{j}_{\parallel}$ and $\tilde{b}_r$. The four figures represent four cases: both between and during sawtooth crashes, at two different poloidal and toroidal locations each (-15° P, 330° T and 75° P, 120° T). Figures 13 – 16 show edge radial profiles of the relative phase between $\tilde{j}_{\parallel}$ and $\tilde{b}_r$. Figures 17 – 20 show edge radial profiles of the crossspectral coherence of $\tilde{j}_{\parallel}$ and $\tilde{b}_r$.

B.4 - Pseudospectral Decomposition of $\left\langle \tilde{j}_{\parallel}\tilde{b}_r \right\rangle_{F.S.}$

For the pseudospectral results reported below, the reference fluctuating quantity is the toroidal magnetic field at the wall.

Figures 21 – 24 show the combined amplitude of $\tilde{j}_{\parallel}$ and $\tilde{b}_r$ for each toroidal mode, at several depths (*i.e.*, probe insertions) in the plasma each. The four figures represent four cases: both between and during sawtooth crashes, at two different poloidal and toroidal locations each (-15° P, 330° T and 75° P, 120° T). Figures 25 – 28 show the phase between $\tilde{j}_{\parallel}$ and $\tilde{b}_r$ for each

toroidal mode, for the same cases. Figures 29 – 32 show radial profiles of the combined amplitude of $\tilde{j}_{\parallel}$ and $\tilde{b}_r$ for selected core resonant modes ($n = 5 - 10$), for each of the four cases. Figures 33 – 36 show edge radial profiles of the phase between $\tilde{j}_{\parallel}$ and $\tilde{b}_r$ for the same modes. Figures 37 – 40 show edge radial profiles of the combined amplitude of $\tilde{j}_{\parallel}$ and $\tilde{b}_r$ for selected reversal surface resonant modes ($n = -3 - -1$), for each of the four cases. Figures 41 – 44 show edge radial profiles of the phase between $\tilde{j}_{\parallel}$ and $\tilde{b}_r$ for the same modes.

In Figures 45 – 48, the crossspectral amplitude of $\tilde{j}_{\parallel}$ and $\tilde{b}_r$ is compared with the pseudospectral estimate thereof for four cases: both between and during sawtooth crashes, at two different poloidal and toroidal locations each (-15° P, 330° T and 75° P, 120° T). In Figures 49 – 52, the crossspectral phase between $\tilde{j}_{\parallel}$ and $\tilde{b}_r$ is compared with the pseudospectral estimates thereof for the same cases.

B.5 - Magnetic Fluctuation Driven Charge and Particle Transport

Radial profiles of both $\left\langle \tilde{j}_{\parallel}\tilde{b}_r \right\rangle_{F.S.} / B_0$ (radial charge flux) and $\left\langle \tilde{j}_{\parallel}\tilde{b}_r \right\rangle_{F.S.} / eB_0$ (difference in radial ion and electron particle fluxes) in the plasma edge are shown in Figures 53 – 56. These figures show measurements made between and during sawtooth crashes at two different poloidal and toroidal locations: -15° P, 330° T and 75° P, 120° T.

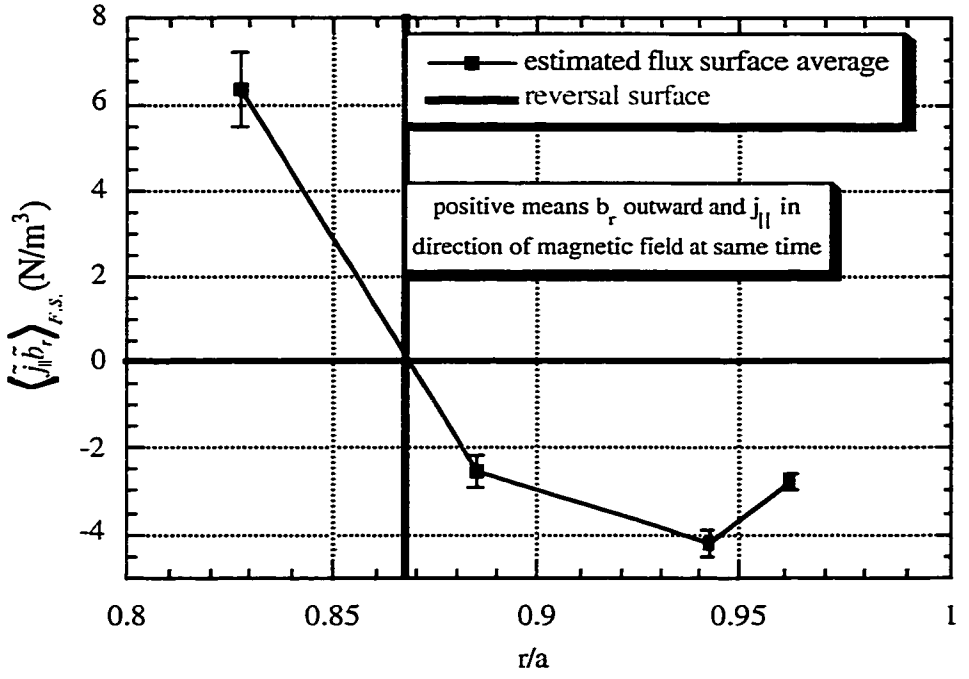

Figure 1: Flux surface average product of $\tilde{j}_{||}$ and $\tilde{b}_r$ during sawtooth crashes at -15° P, 330° T.

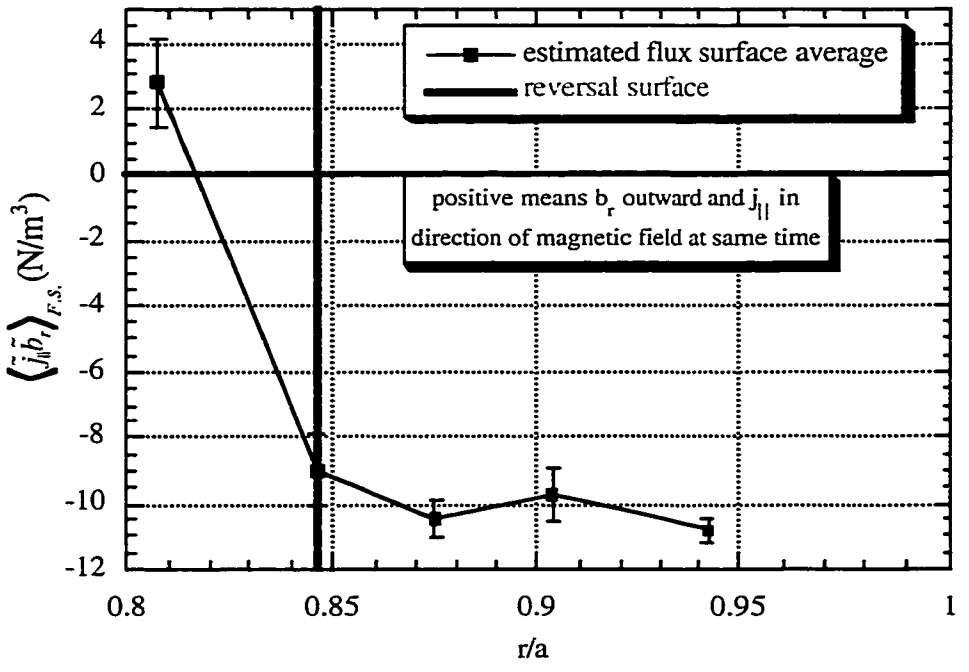

Figure 2: Flux surface average product of $\tilde{j}_{||}$ and $\tilde{b}_r$ during sawtooth crashes at 75° P, 120° T.

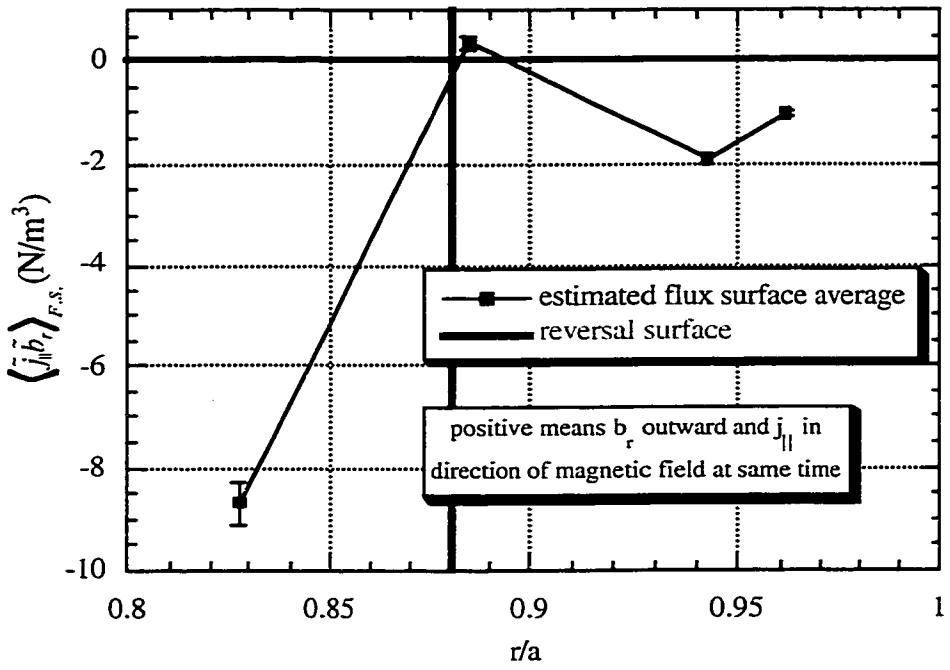

Figure 3: Flux surface average product of $\tilde{j}_{\parallel}$ and $\tilde{b}_r$ between sawtooth crashes at -15° P, 330° T.

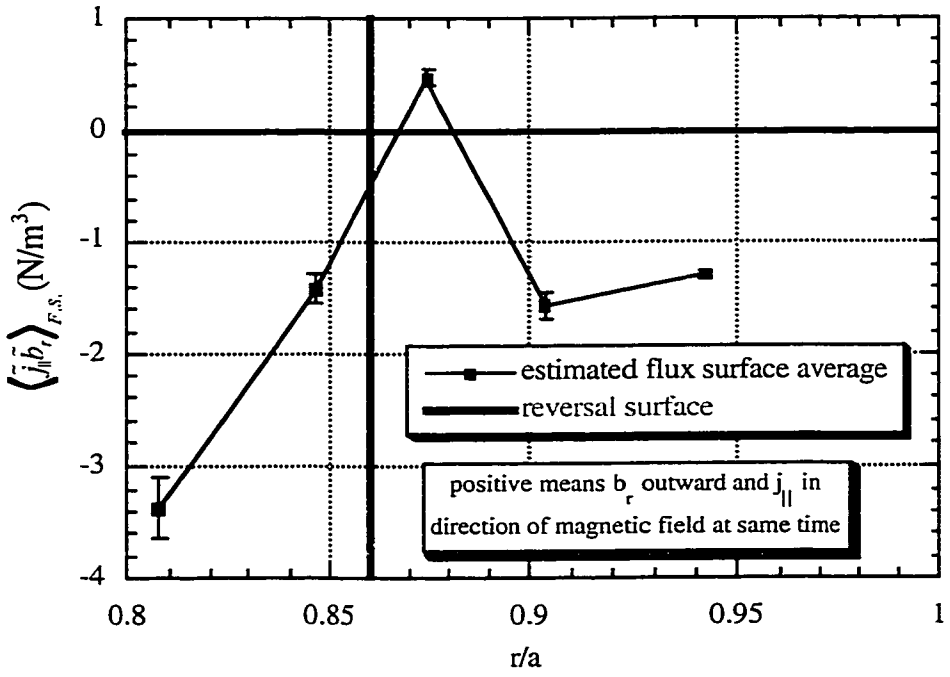

Figure 4: Flux surface average product of $\tilde{j}_{\parallel}$ and $\tilde{b}_r$ between sawtooth crashes at 75° P, 120° T.

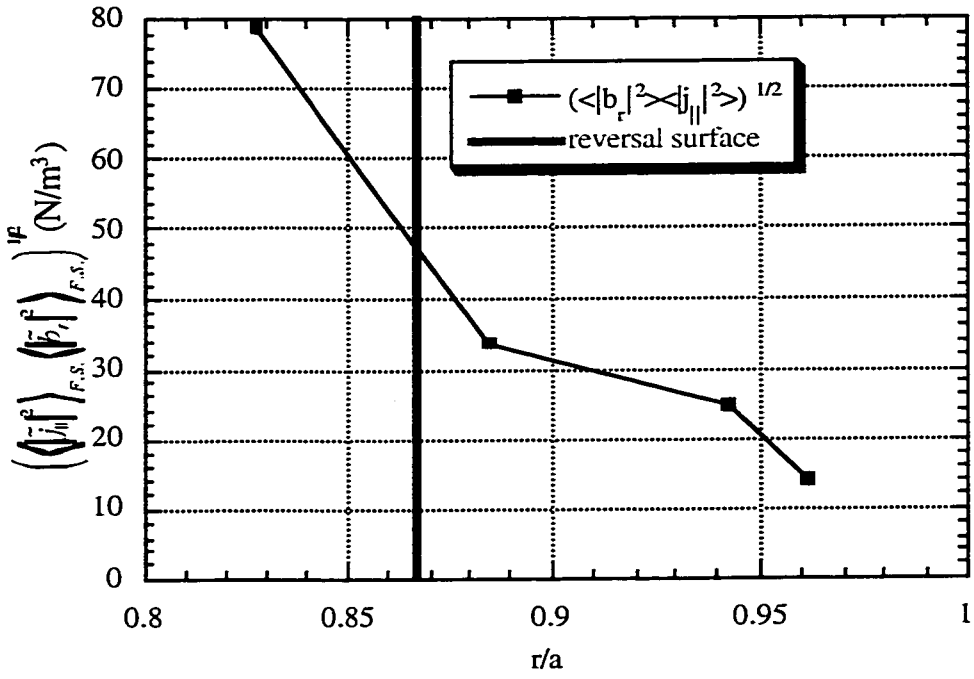

Figure 5: Maximum possible transport (given by product of flux surface r.m.s. values of $\tilde{j}_{\parallel}$ and $\tilde{b}_r$) during sawtooth crashes at -15° P, 330° T.

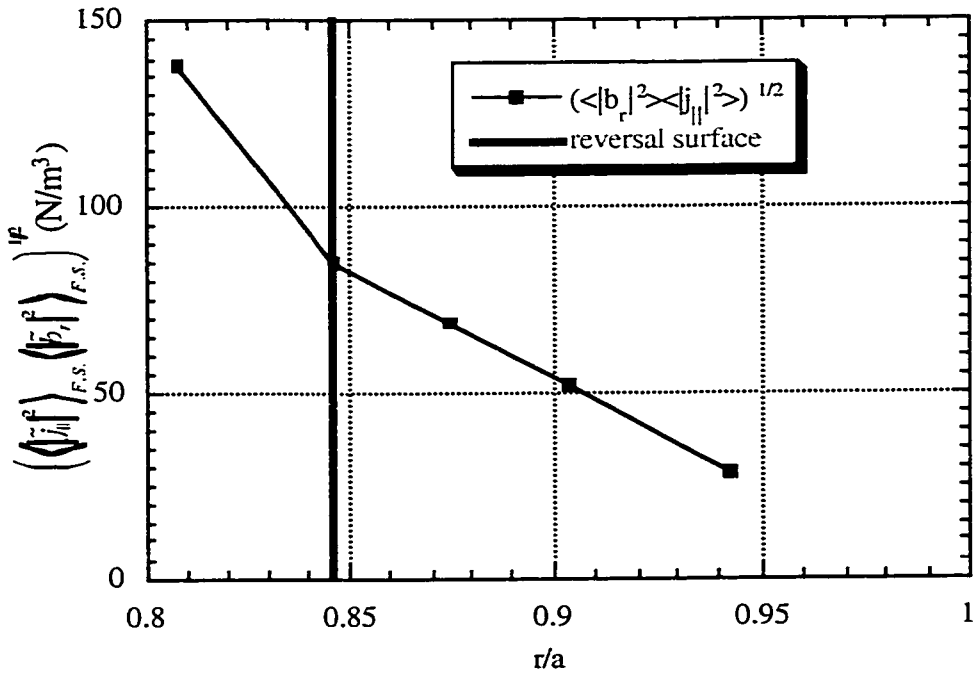

Figure 6: Maximum possible transport (given by product of flux surface r.m.s. values of $\tilde{j}_{\parallel}$ and $\tilde{b}_r$) during sawtooth crashes at 75° P, 120° T.

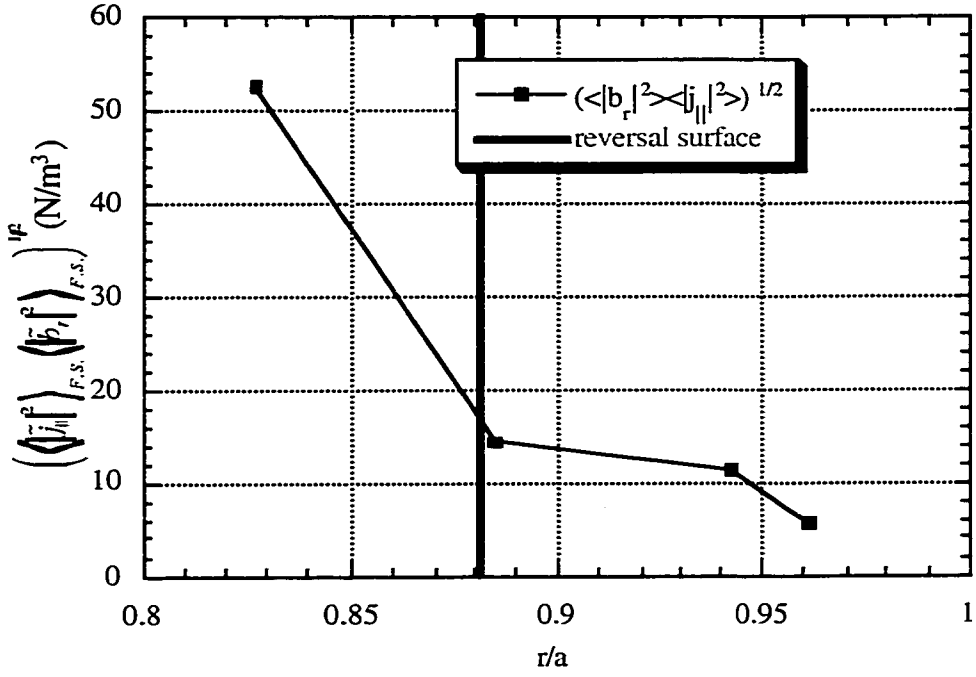

Figure 7: Maximum possible transport (given by product of flux surface r.m.s. values of $\tilde{j}_{\|}$ and $\tilde{b}_r$) between sawtooth crashes at -15° P, 330° T.

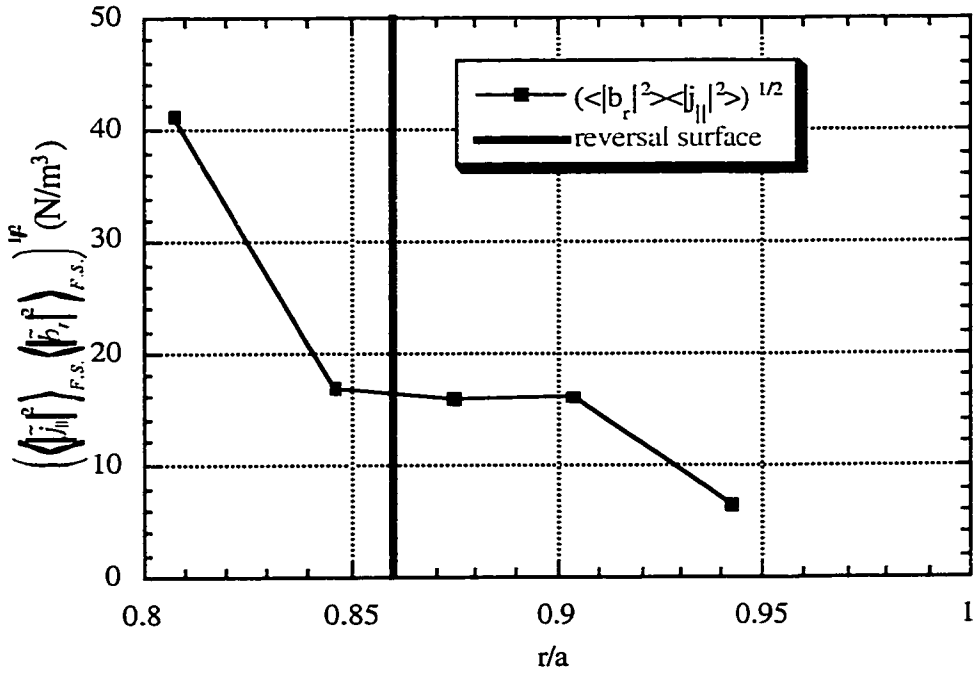

Figure 8: Maximum possible transport (given by product of flux surface r.m.s. values of $\tilde{j}_{\|}$ and $\tilde{b}_r$) between sawtooth crashes at 75° P, 120° T.

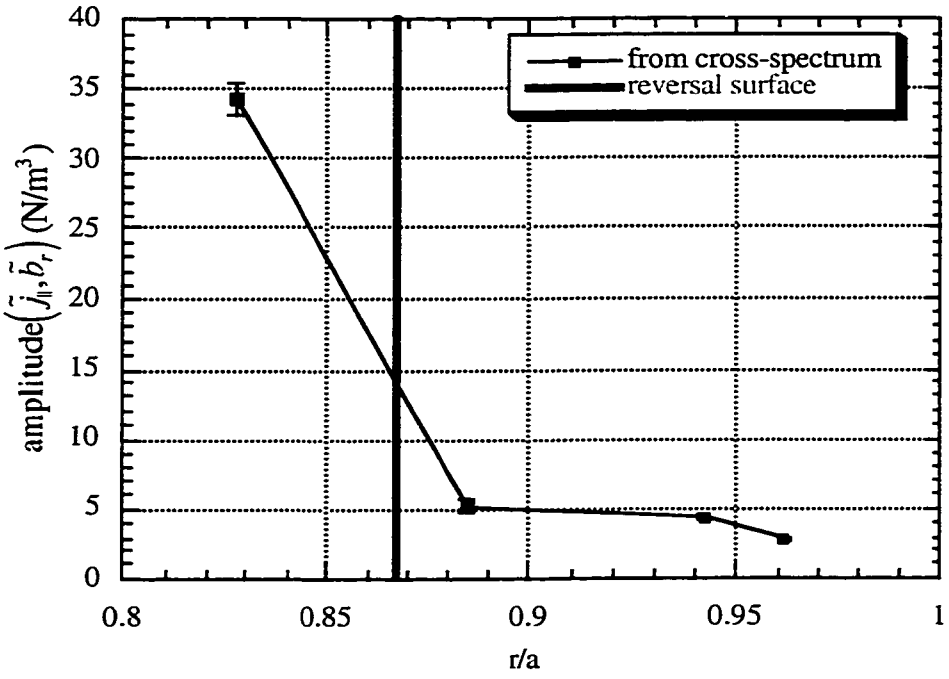

Figure 9: Coherent part (e.g. crossspectral magnitude) of $\tilde{j}_{\|}$ and $\tilde{b}_r$ during sawtooth crashes at -15° P, 330° T.

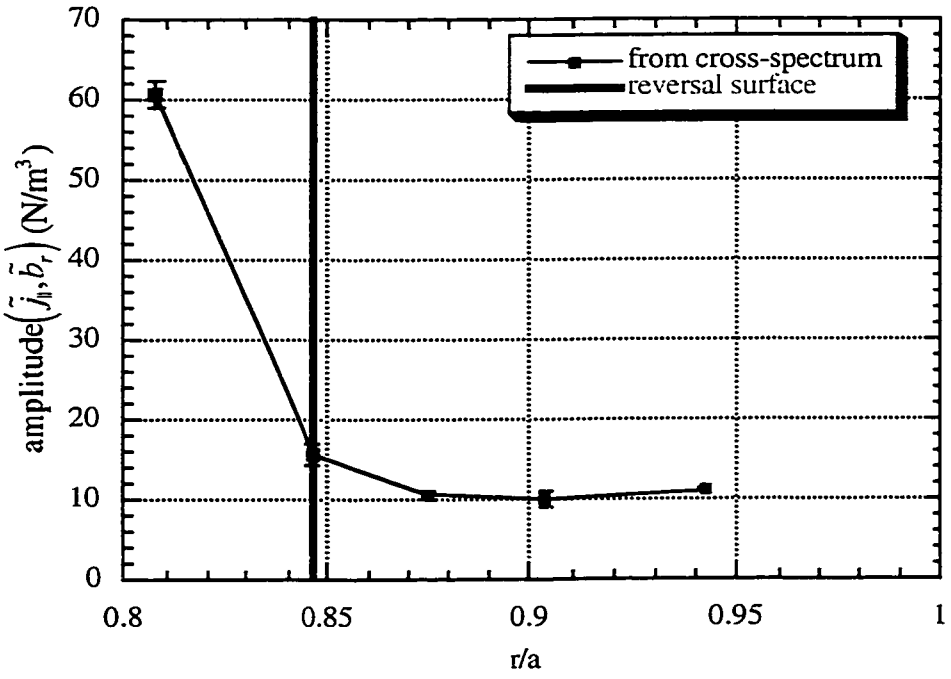

Figure 10: Coherent part (e.g. crossspectral magnitude) of $\tilde{j}_{\|}$ and $\tilde{b}_r$ during sawtooth crashes at 75° P, 120° T.

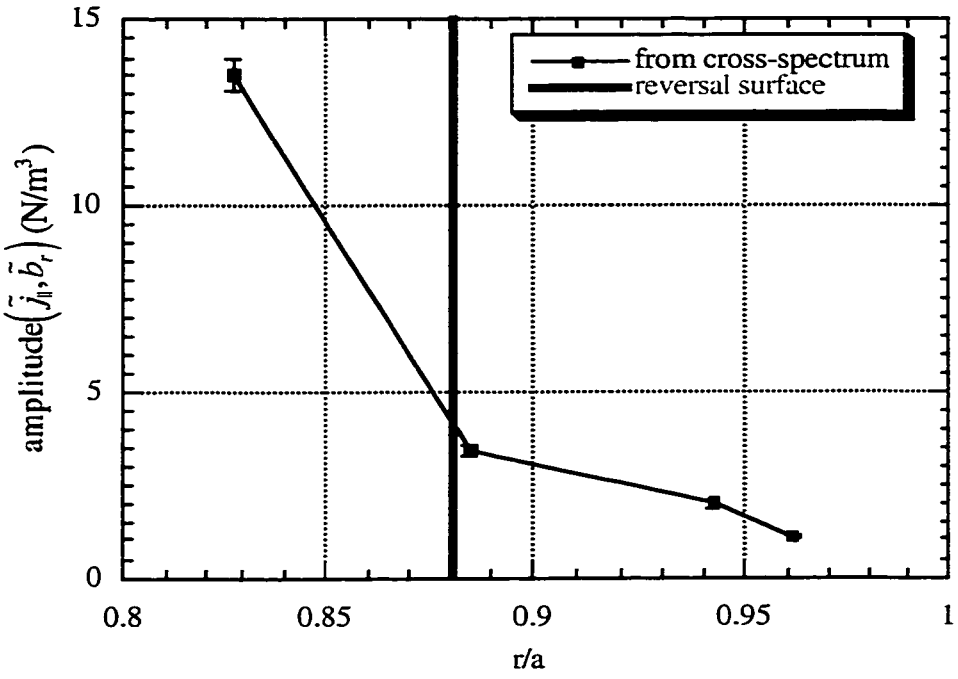

Figure 11: Coherent part (e.g. crossspectral magnitude) of $\tilde{j}_{\|}$ and $\tilde{b}_r$ between sawtooth crashes at -15° P, 330° T.

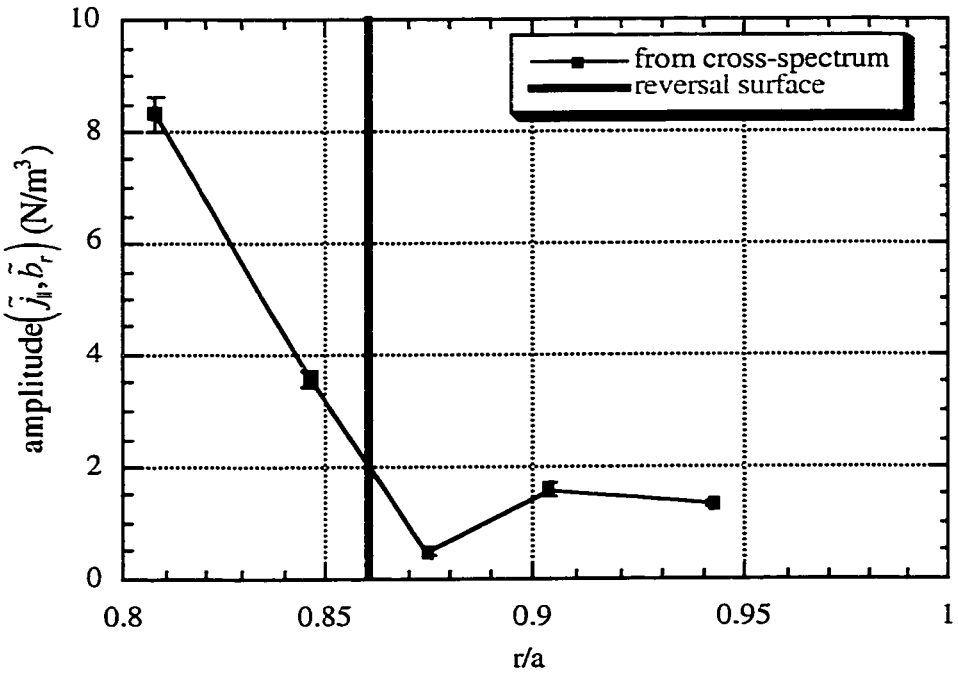

Figure 12: Coherent part (e.g. crossspectral magnitude) of $\tilde{j}_{\|}$ and $\tilde{b}_r$ between sawtooth crashes at 75° P, 120° T.

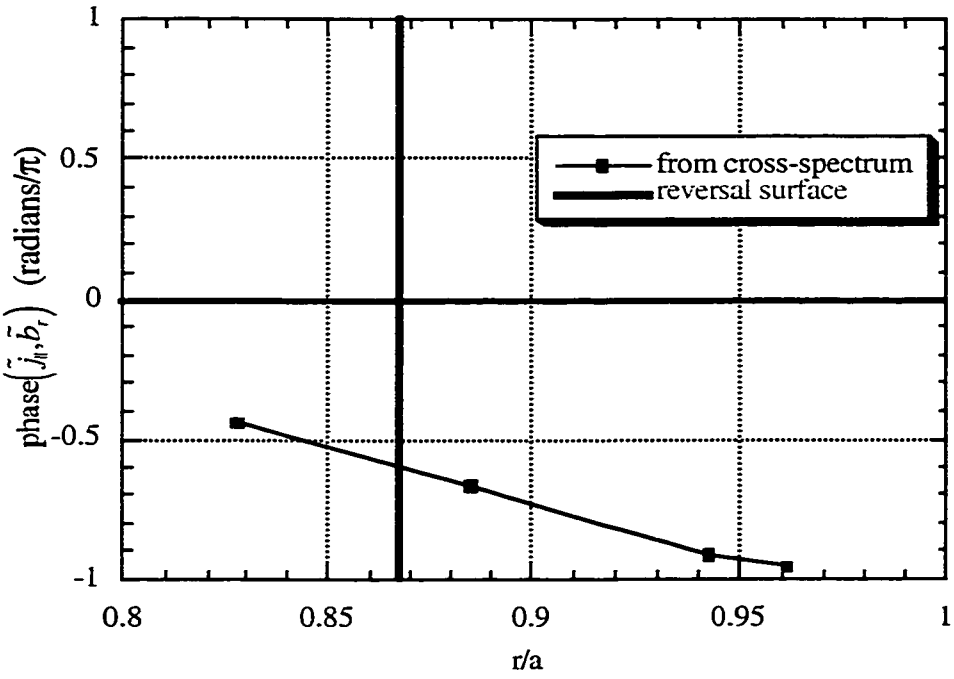

Figure 13: Crossspectral phase between $\tilde{j}_{\|}$ and $\tilde{b}_r$ during sawtooth crashes at -15° P, 330° T.

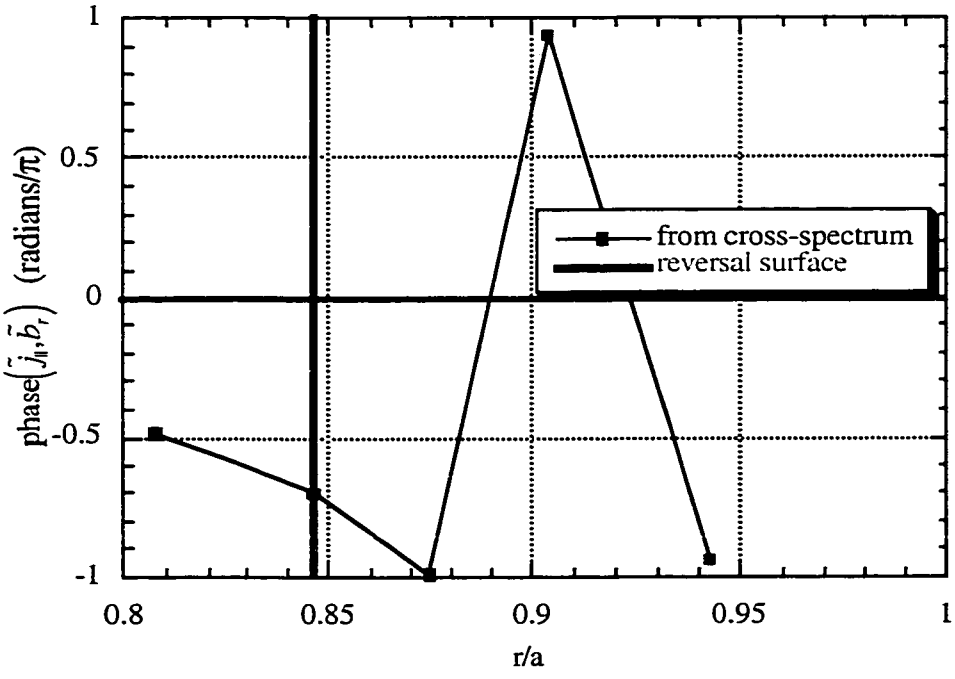

Figure 14: Crossspectral phase between $\tilde{j}_{\|}$ and $\tilde{b}_r$ during sawtooth crashes at 75° P, 120° T.

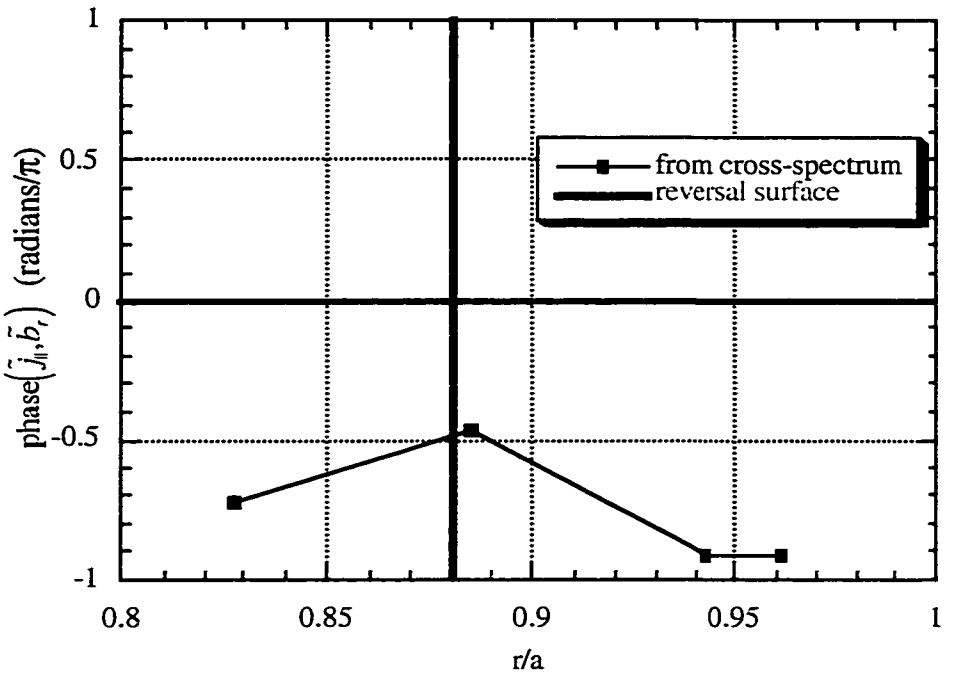

Figure 15: Crossspectral phase between $\tilde{j}_{\|}$ and $\tilde{b}_r$ between sawtooth crashes at -15° P, 330° T.

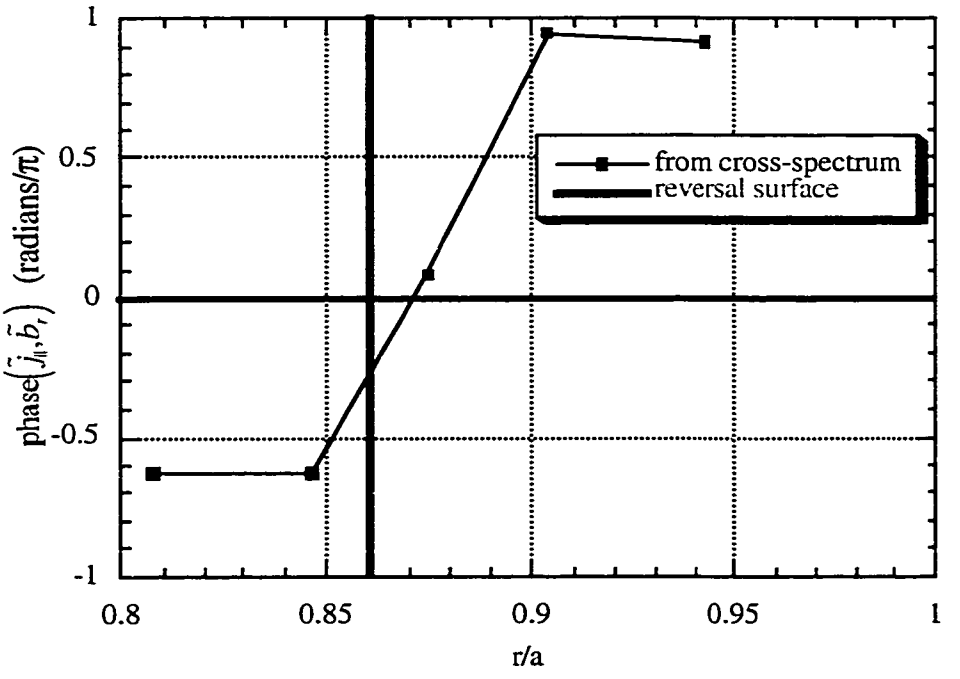

Figure 16: Crossspectral phase between $\tilde{j}_{\|}$ and $\tilde{b}_r$ between sawtooth crashes at 75° P, 120° T.

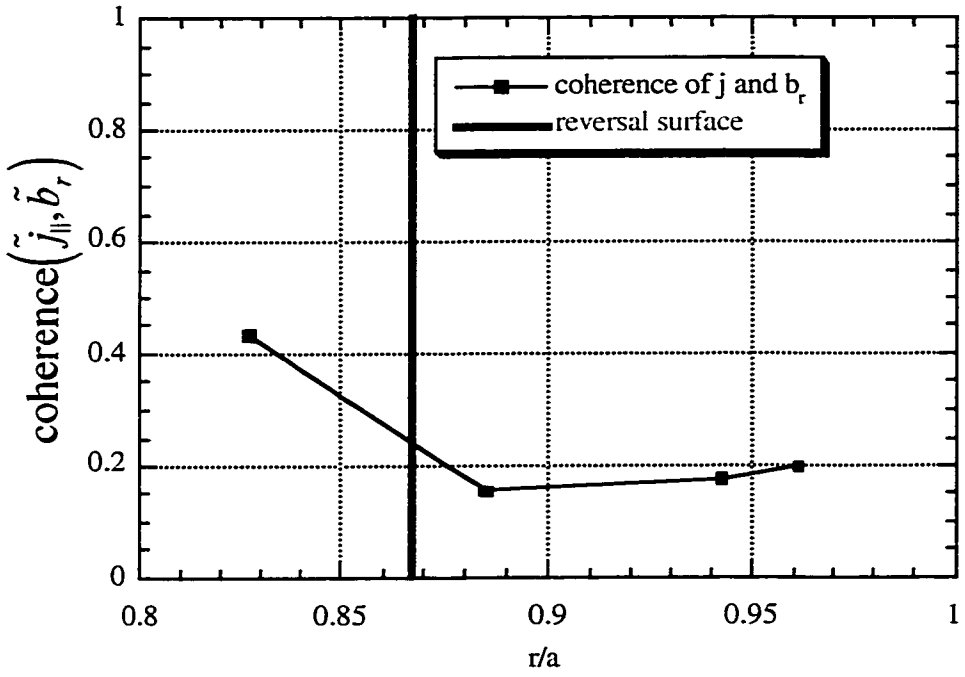

Figure 17: Crossspectral coherence of $\tilde{j}_{\|}$ and $\tilde{b}_r$ during sawtooth crashes at -15° P, 330° T.

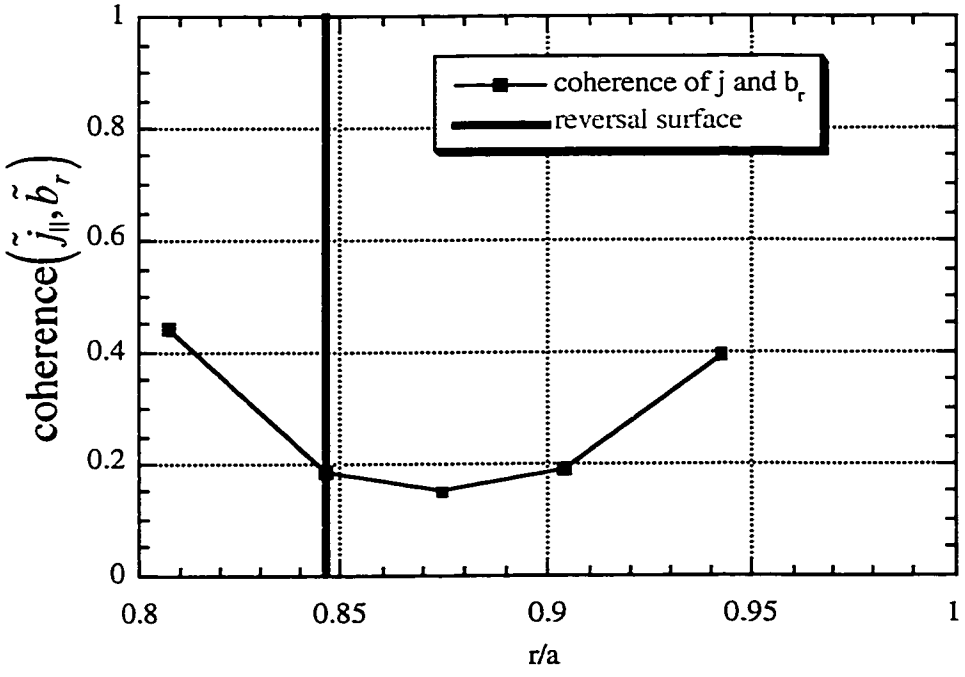

Figure 18: Crossspectral coherence of $\tilde{j}_{\|}$ and $\tilde{b}_r$ during sawtooth crashes at 75° P, 120° T.

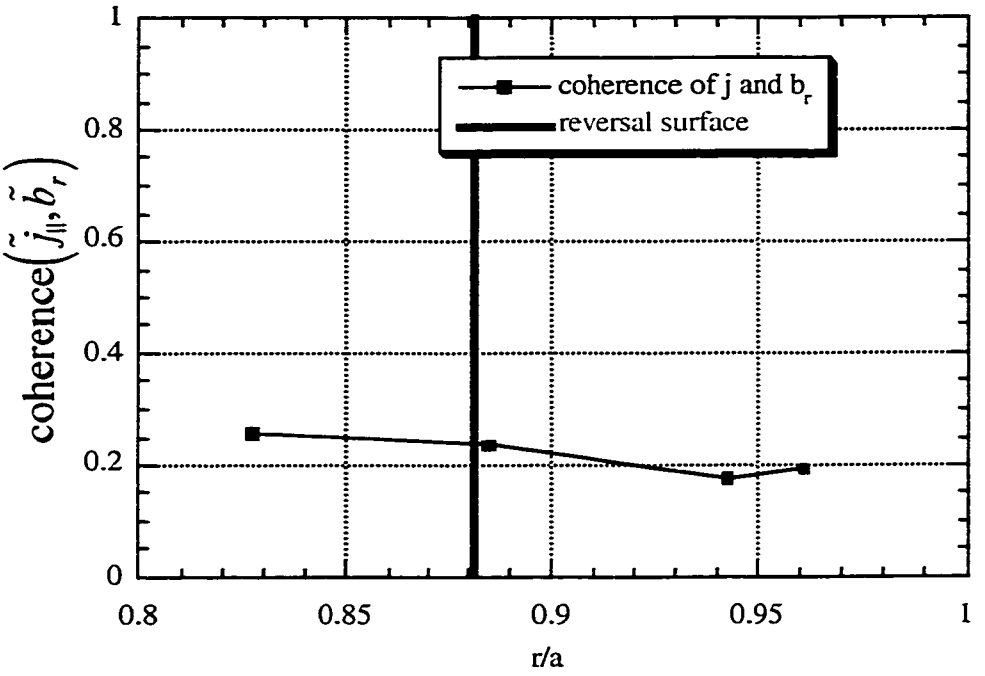

Figure 19: Crossspectral coherence of $\tilde{j}_{\|}$ and $\tilde{b}_r$ between sawtooth crashes at -15° P, 330° T.

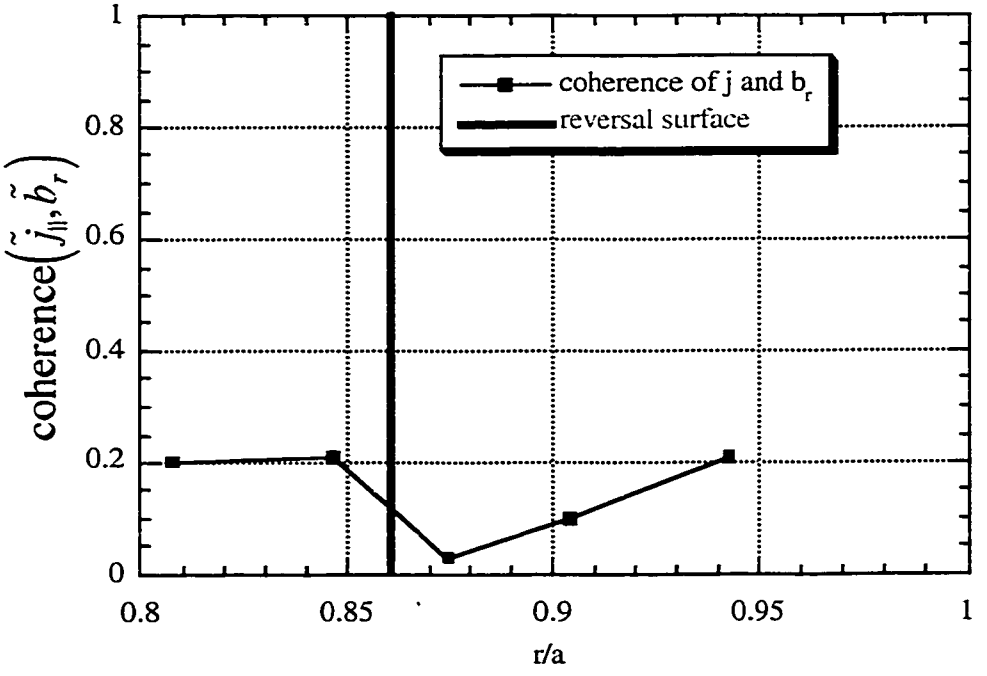

Figure 20: Crossspectral coherence of $\tilde{j}_{\|}$ and $\tilde{b}_r$ between sawtooth crashes at 75° P, 120° T.

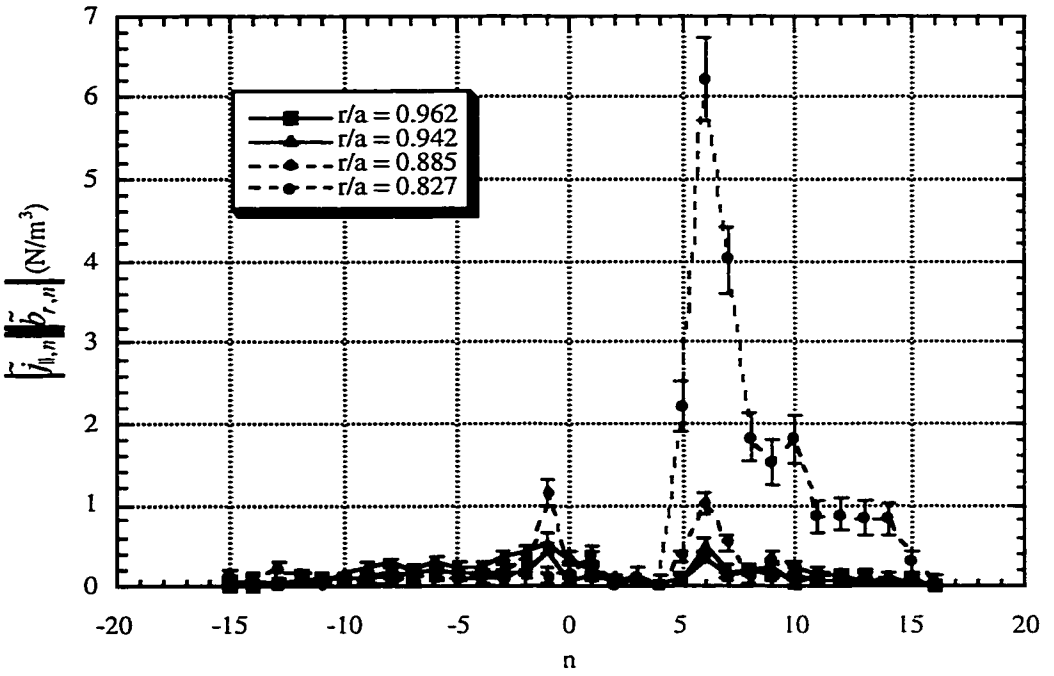

Figure 21: Combined magnitude of $\tilde{j}_{\parallel}$ and $\tilde{b}_r$ for each toroidal mode. Measured during sawtooth crashes at -15° P, 330° T. Measured with pseudo-spectral technique using toroidal magnetic field flucuations at the wall as the reference fluctuation.

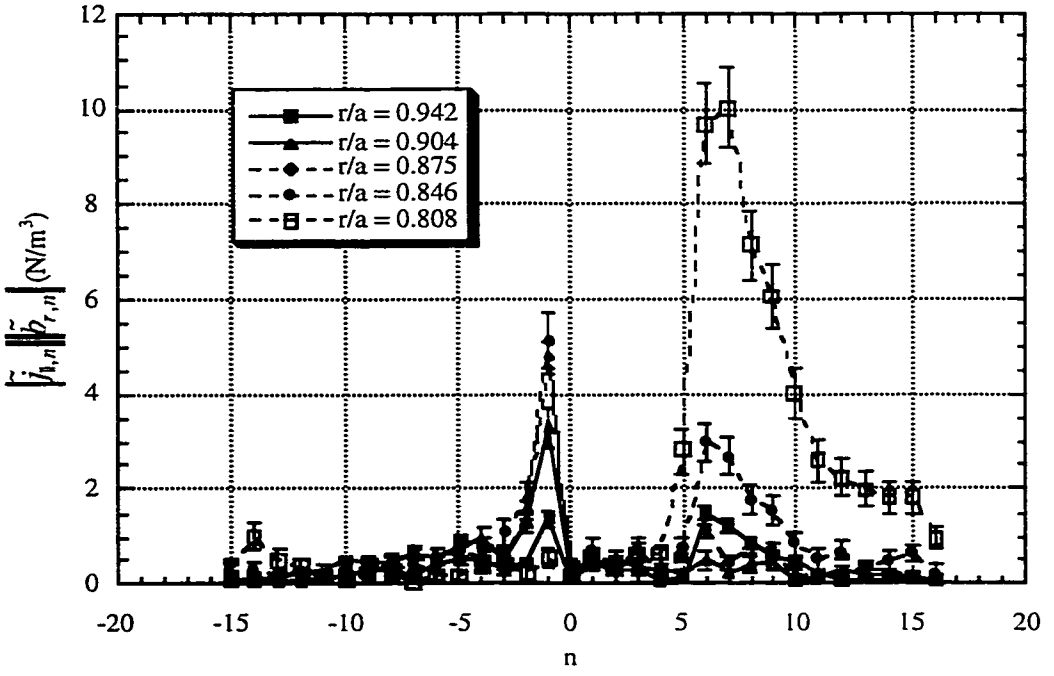

Figure 22: Combined magnitude of $\tilde{j}_{\parallel}$ and $\tilde{b}_r$ for each toroidal mode. Measured during sawtooth crashes at 75° P, 120° T. Measured with pseudo-spectral technique using toroidal magnetic field flucuations at the wall as the reference fluctuation.

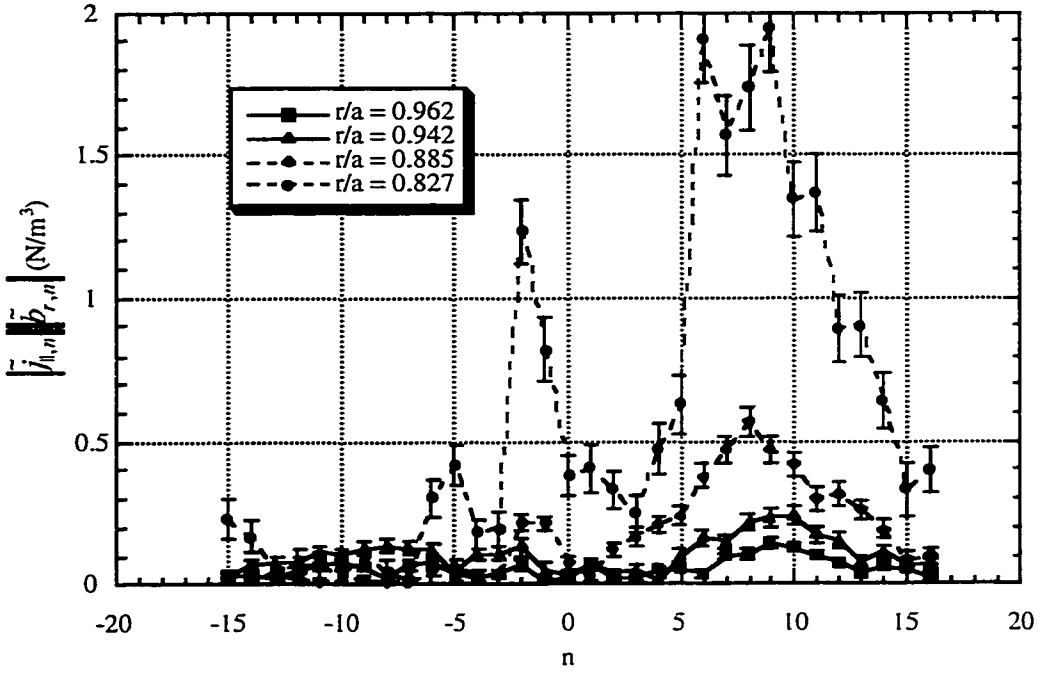

Figure 23: Combined magnitude of $\tilde{j}_{\parallel}$ and $\tilde{b}_r$ for each toroidal mode. Measured between sawtooth crashes at -15° P, 330° T. Measured with pseudo-spectral technique using toroidal magnetic field flucuations at the wall as the reference fluctuation.

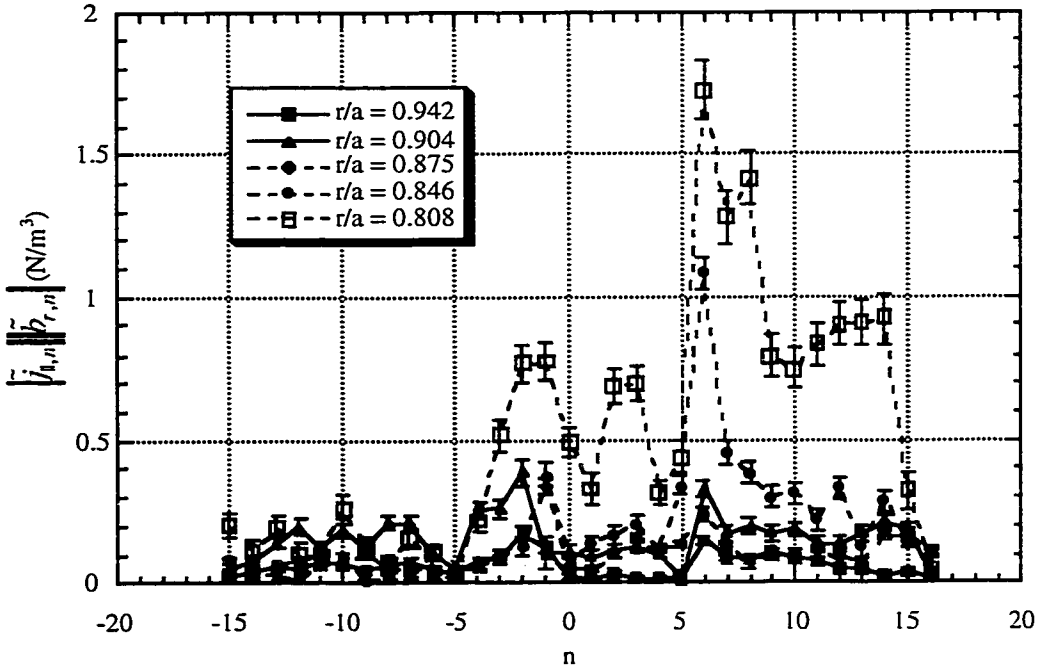

Figure 24: Combined magnitude of $\tilde{j}_{\parallel}$ and $\tilde{b}_r$ for each toroidal mode. Measured between sawtooth crashes at 75° P, 120° T. Measured with pseudo-spectral technique using toroidal magnetic field flucuations at the wall as the reference fluctuation.

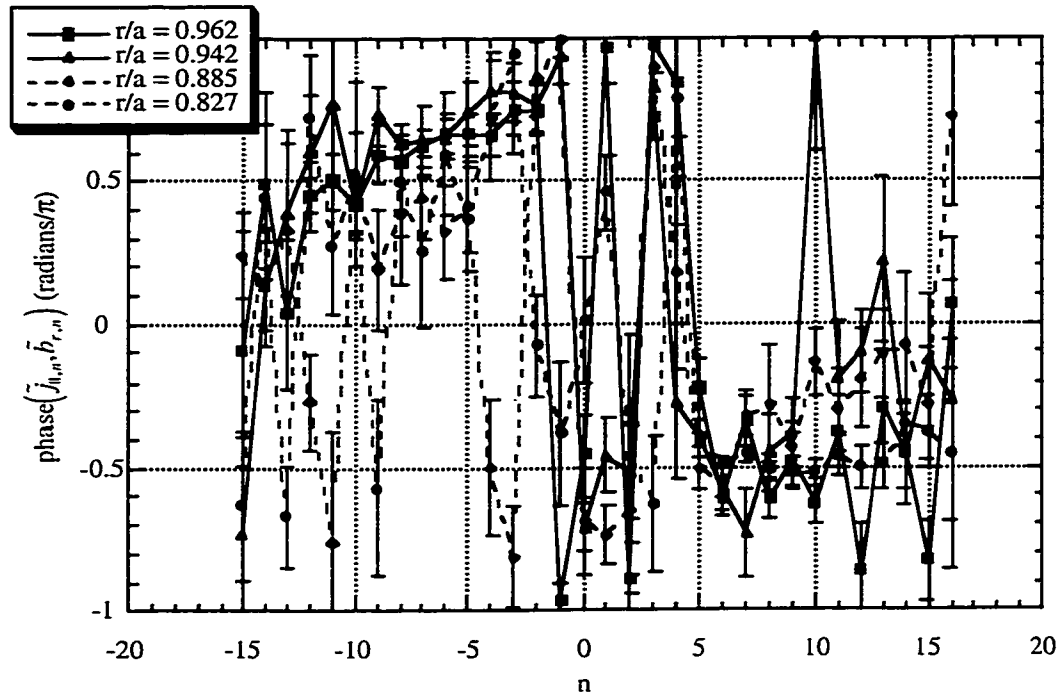

Figure 25: Phase between $\tilde{j}_{\|}$ and $\tilde{b}_r$ for each toroidal mode. Measured during sawtooth crashes at -15° P, 330° T. Measured with pseudo-spectral technique using toroidal magnetic field flucuations at the wall as the reference fluctuation.

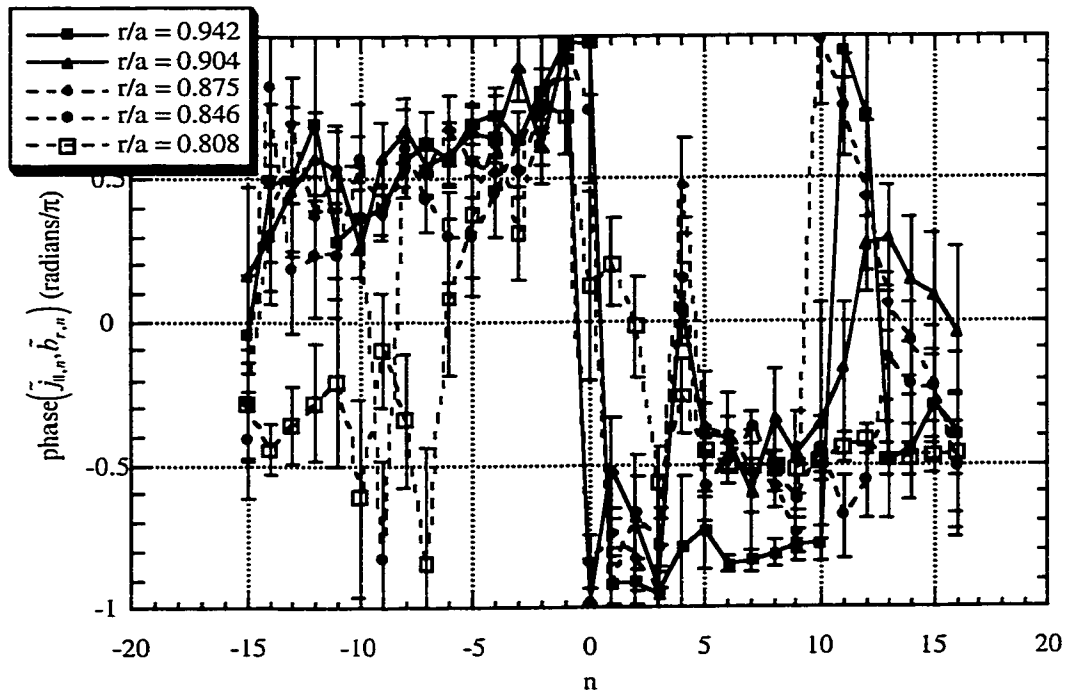

Figure 26: Phase between $\tilde{j}_{\|}$ and $\tilde{b}_r$ for each toroidal mode. Measured during sawtooth crashes at 75° P, 120° T. Measured with pseudo-spectral technique using toroidal magnetic field flucuations at the wall as the reference fluctuation.

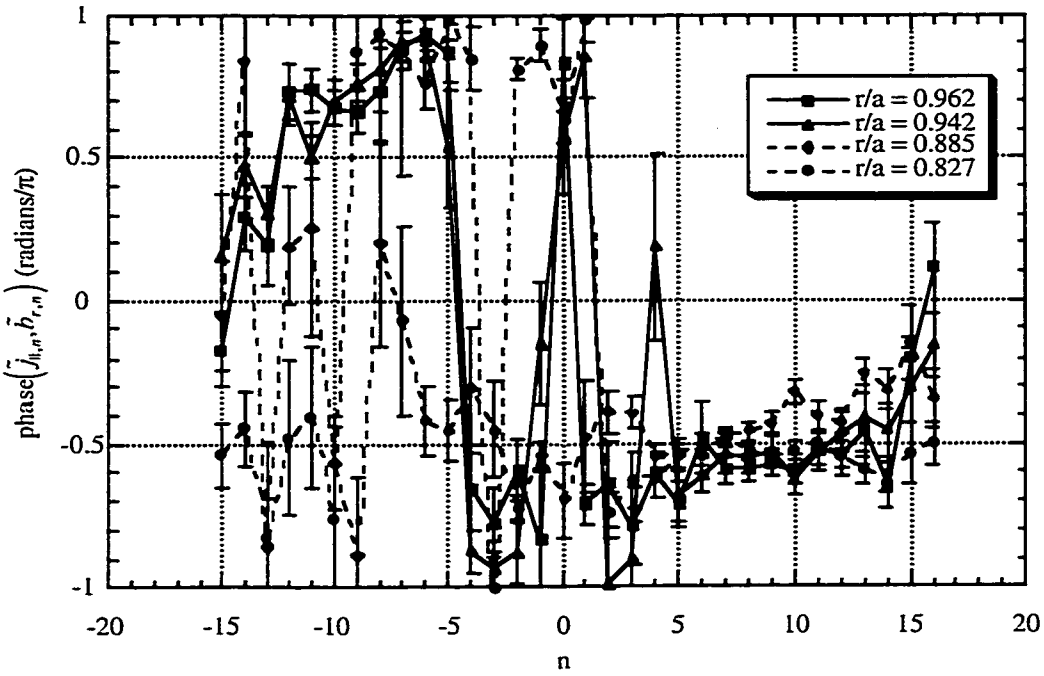

Figure 27: Phase between $\tilde{j}_{\|}$ and $\tilde{b}_r$ for each toroidal mode. Measured between sawtooth crashes at -15° P, 330° T. Measured with pseudo-spectral technique using toroidal magnetic field flucuations at the wall as the reference fluctuation.

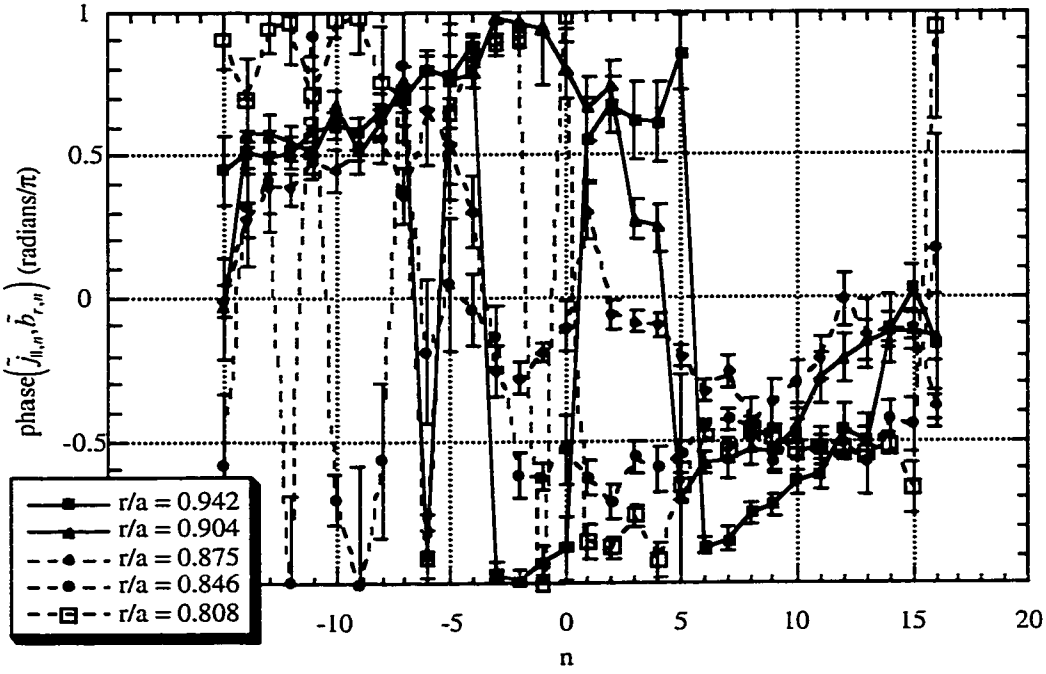

Figure 28: Phase between $\tilde{j}_{\|}$ and $\tilde{b}_r$ for each toroidal mode. Measured between sawtooth crashes at 75° P, 120° T. Measured with pseudo-spectral technique using toroidal magnetic field flucuations at the wall as the reference fluctuation.

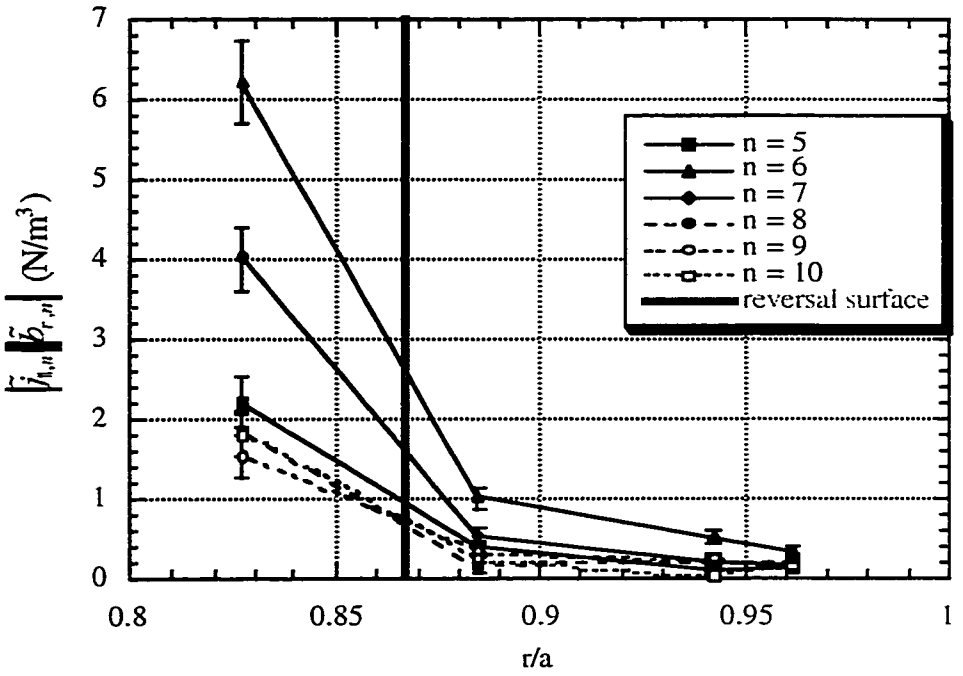

Figure 29: Radial profiles of the combined magnitude of $\tilde{j}_{\parallel}$ and $\tilde{b}_r$ for selected core resonant toroidal modes. Measured during sawtooth crashes at -15° P, 330° T. Measured with pseudo-spectral technique using toroidal magnetic field flucuations at the wall as the reference fluctuation.

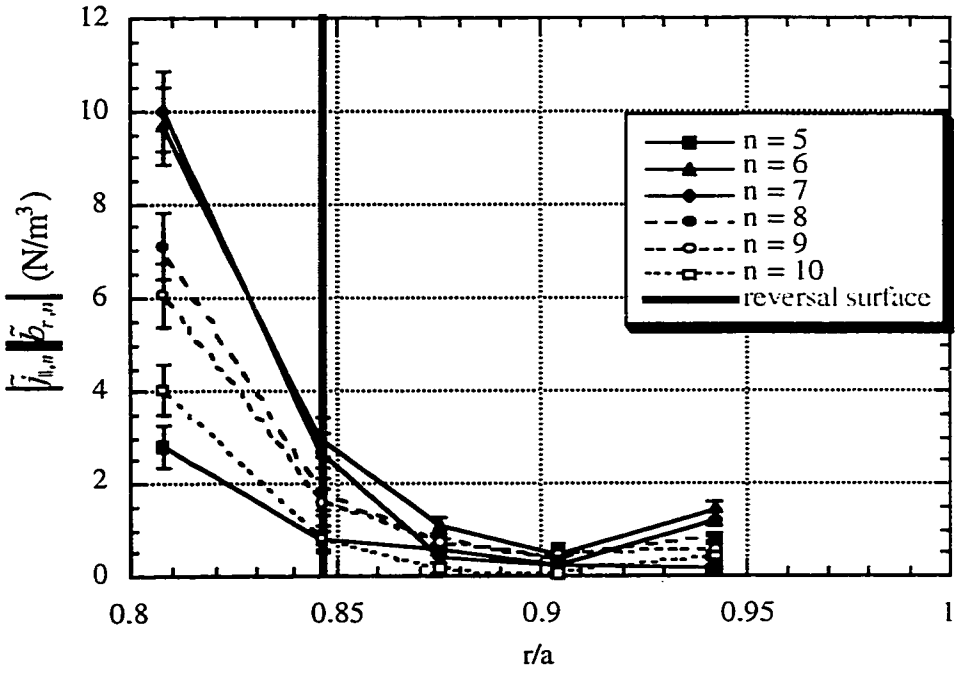

Figure 30: Radial profiles of the combined magnitude of $\tilde{j}_{\parallel}$ and $\tilde{b}_r$ for selected core resonant toroidal modes. Measured during sawtooth crashes at 75° P, 120° T. Measured with pseudo-spectral technique using toroidal magnetic field flucuations at the wall as the reference fluctuation.

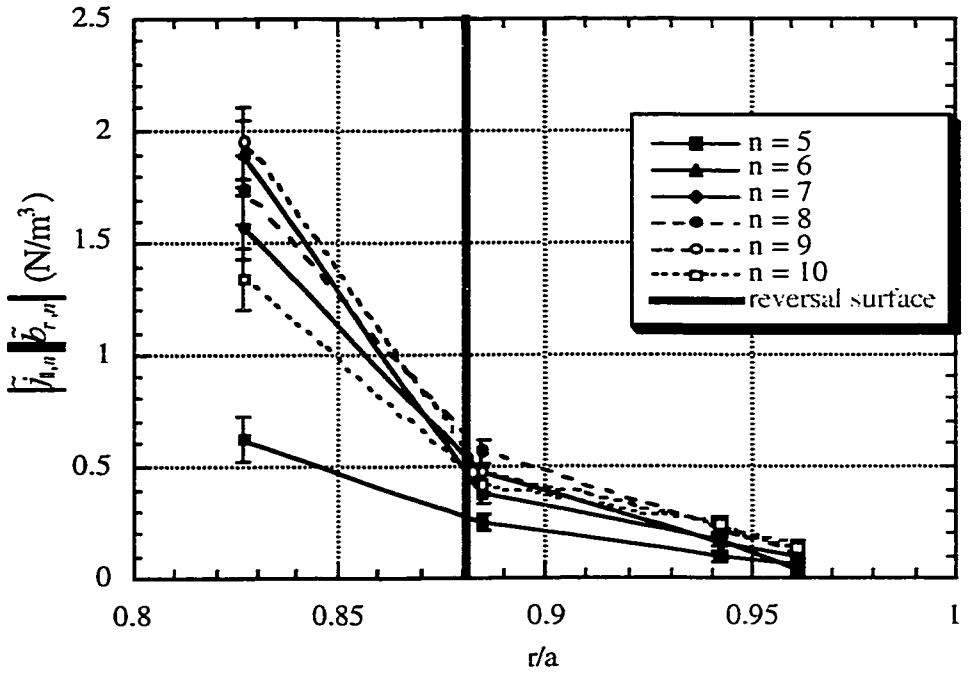

Figure 31: Radial profiles of the combined magnitude of $\tilde{j}_{\parallel}$ and $\tilde{b}_r$ for selected core resonant toroidal modes. Measured between sawtooth crashes at -15° P, 330° T. Measured with pseudo-spectral technique using toroidal magnetic field flucuations at the wall as the reference fluctuation.

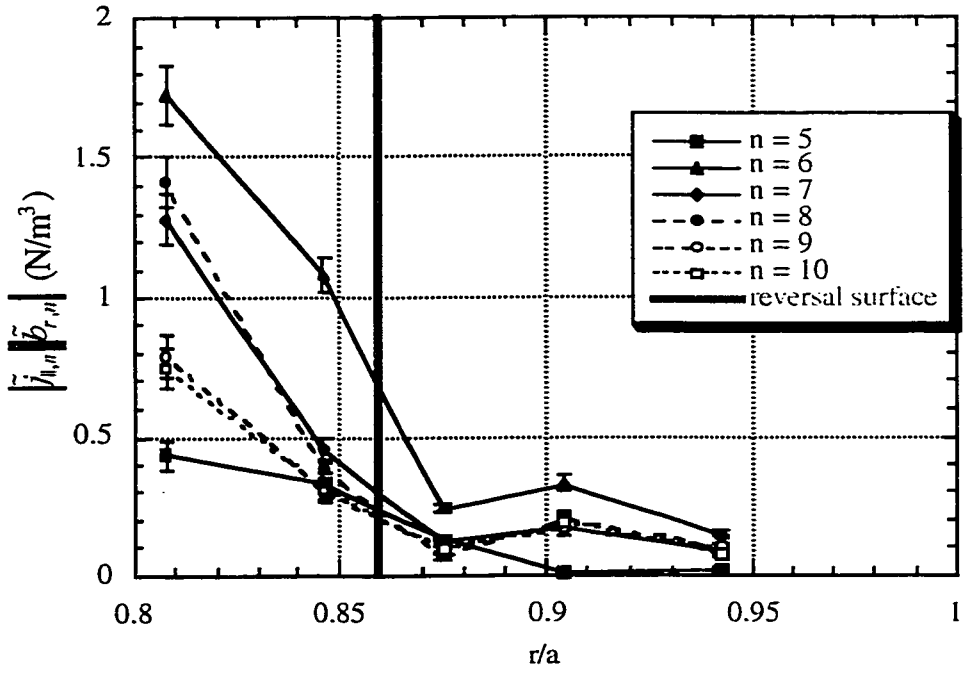

Figure 32: Radial profiles of the combined magnitude of $\tilde{j}_{\parallel}$ and $\tilde{b}_r$ for selected core resonant toroidal modes. Measured between sawtooth crashes at 75° P, 120° T. Measured with pseudo-spectral technique using toroidal magnetic field flucuations at the wall as the reference fluctuation.

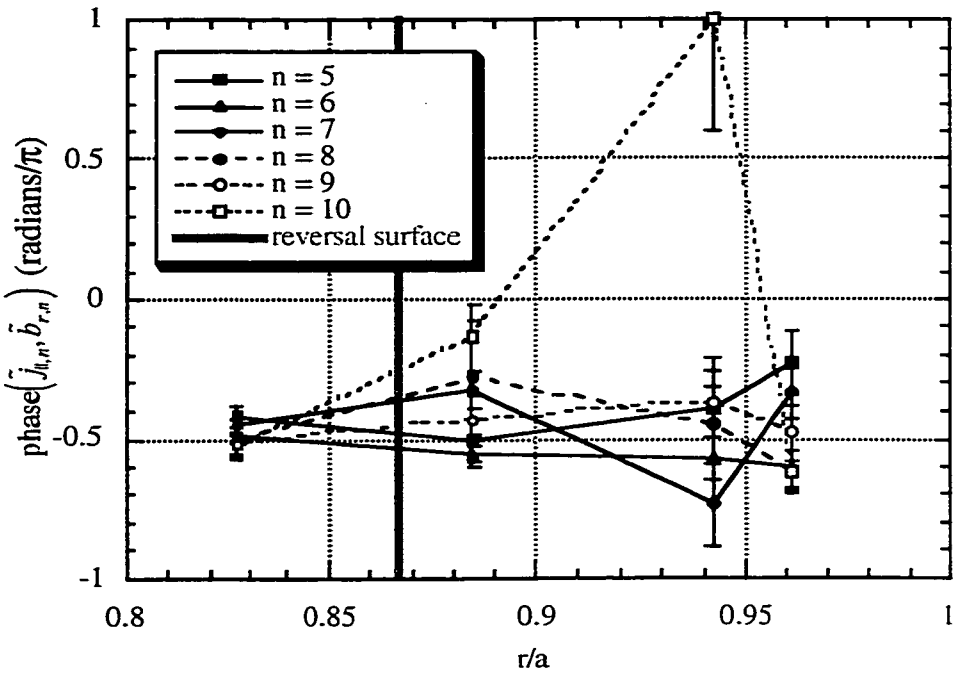

Figure 33: Radial profiles of phase between $\tilde{j}_{\parallel}$ and $\tilde{b}_r$ for selected core resonant toroidal modes. Measured during sawtooth crashes at -15° P, 330° T. Measured with pseudo-spectral technique using toroidal magnetic field flucuations at the wall as the reference fluctuation.

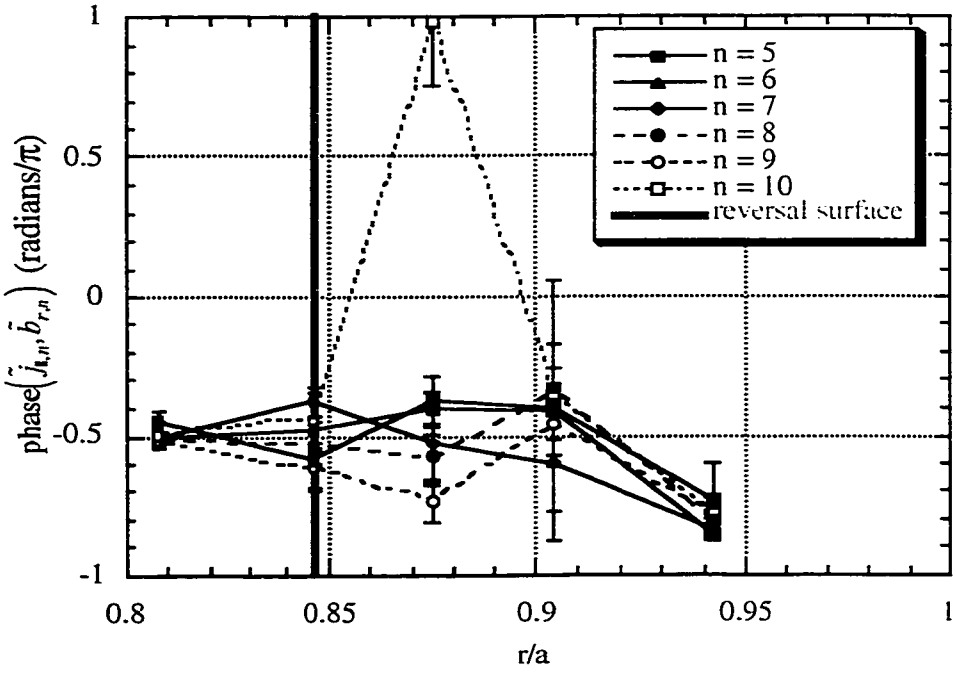

Figure 34: Radial profiles of the phase between $\tilde{j}_{\parallel}$ and $\tilde{b}_r$ for selected core resonant toroidal modes. Measured during sawtooth crashes at 75° P, 120° T. Measured with pseudo-spectral technique using toroidal magnetic field flucuations at the wall as the reference fluctuation.

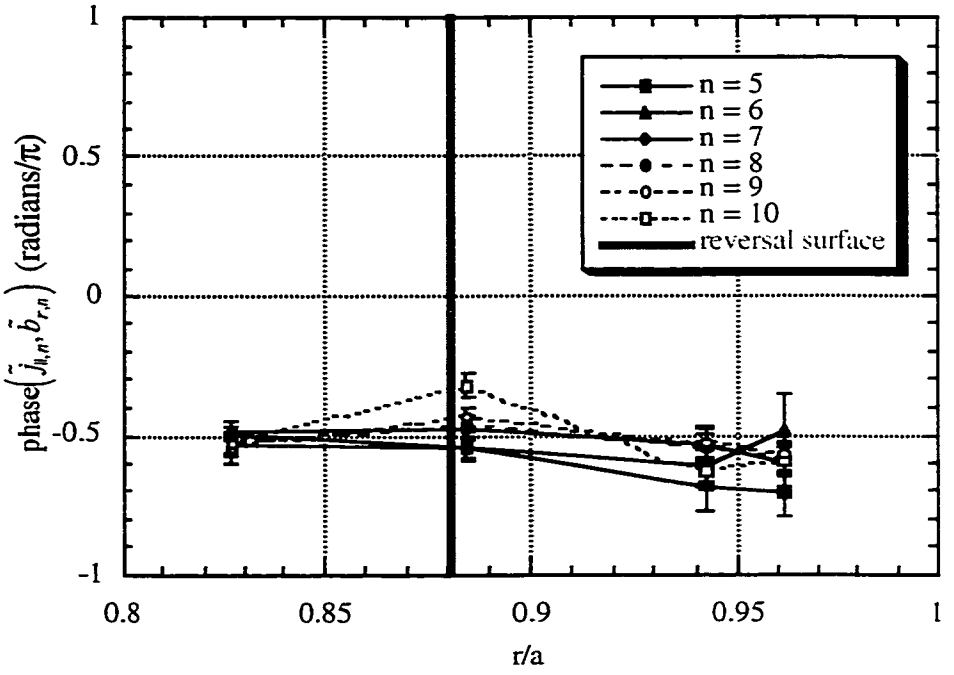

Figure 35: Radial profiles of the phase between $\tilde{j}_{\parallel}$ and $\tilde{b}_r$ for selected core resonant toroidal modes. Measured between sawtooth crashes at -15° P, 330° T. Measured with pseudo-spectral technique using toroidal magnetic field flucuations at the wall as the reference fluctuation.

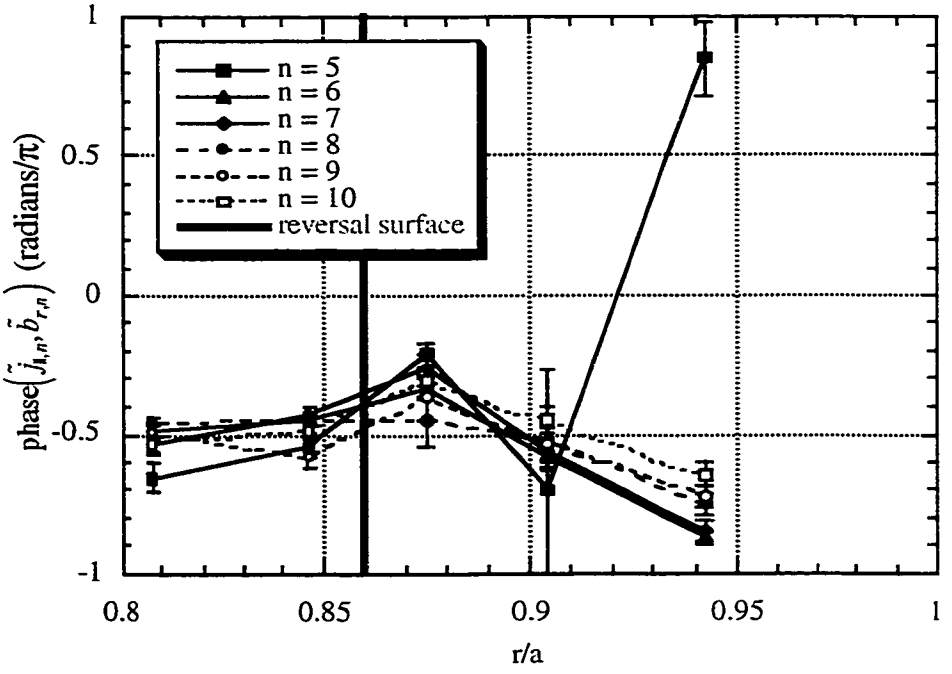

Figure 36: Radial profiles of the phase between $\tilde{j}_{\parallel}$ and $\tilde{b}_r$ for selected core resonant toroidal modes. Measured between sawtooth crashes at 75° P, 120° T. Measured with pseudo-spectral technique using toroidal magnetic field flucuations at the wall as the reference fluctuation.

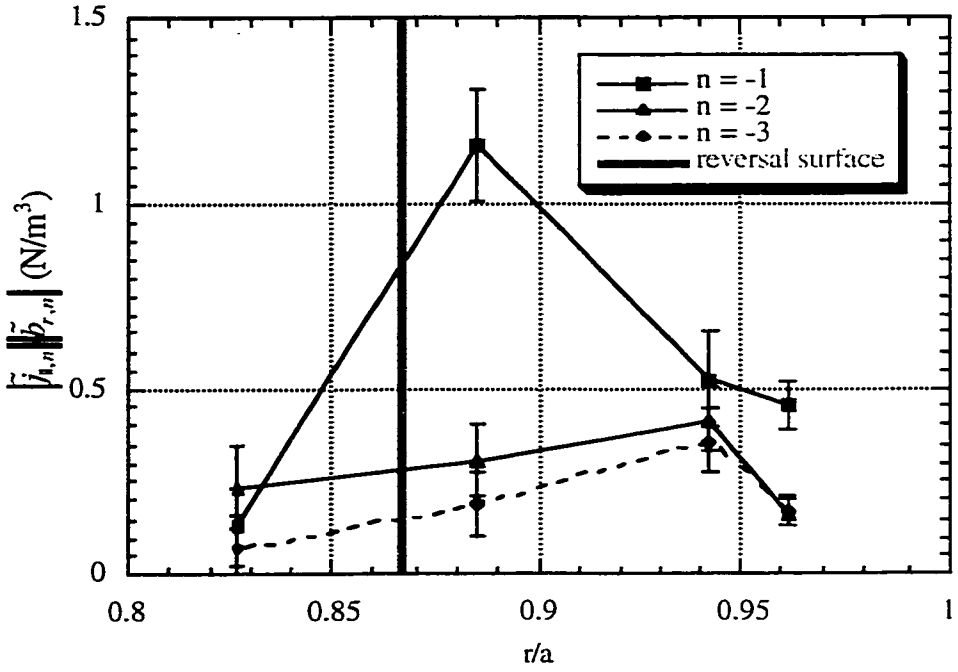

Figure 37: Radial profiles of the combined magnitude of $\tilde{j}_{\parallel}$ and $\tilde{b}_r$ for selected reversal surface resonant toroidal modes. Measured during sawtooth crashes at -15° P, 330° T. Measured with pseudo-spectral technique using toroidal magnetic field flucuations at the wall as the reference fluctuation.

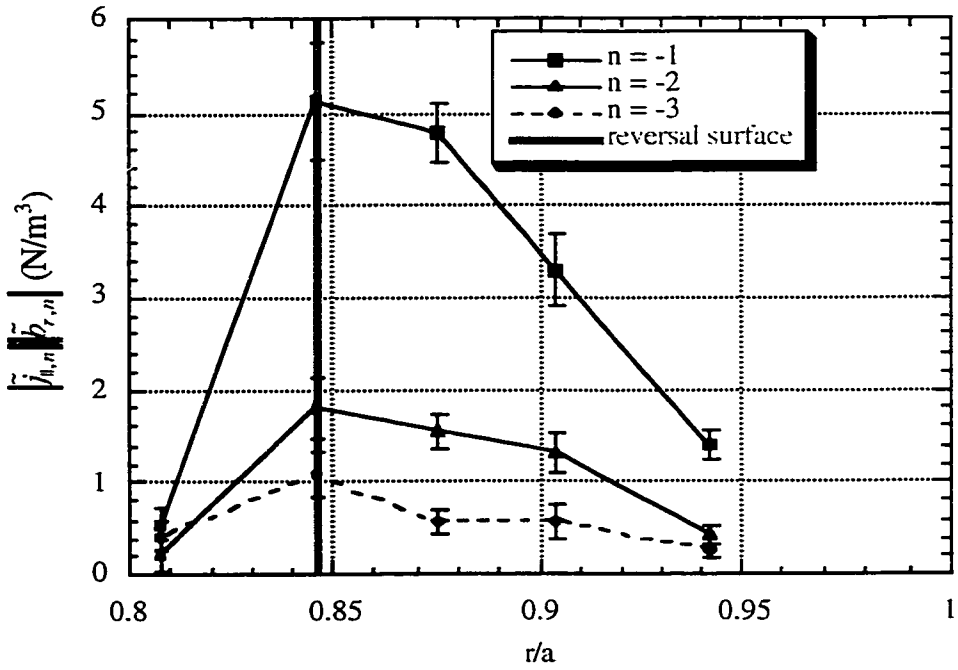

Figure 38: Radial profiles of the combined magnitude of $\tilde{j}_{\parallel}$ and $\tilde{b}_r$ for selected reversal surface resonant toroidal modes. Measured during sawtooth crashes at 75° P, 120° T. Measured with pseudo-spectral technique using toroidal magnetic field flucuations at the wall as the reference fluctuation.

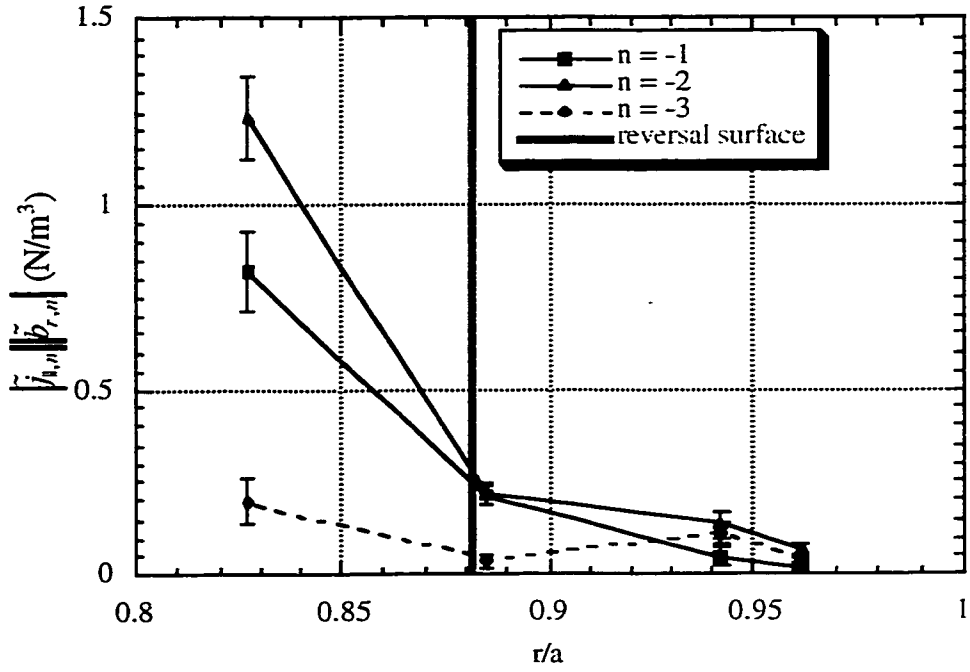

Figure 39: Radial profiles of the combined magnitude of $\tilde{j}_{\parallel}$ and $\tilde{b}_r$ for selected reversal surface resonant toroidal modes. Measured between sawtooth crashes at -15° P, 330° T. Measured with pseudo-spectral technique using toroidal magnetic field flucuations at the wall as the reference fluctuation.

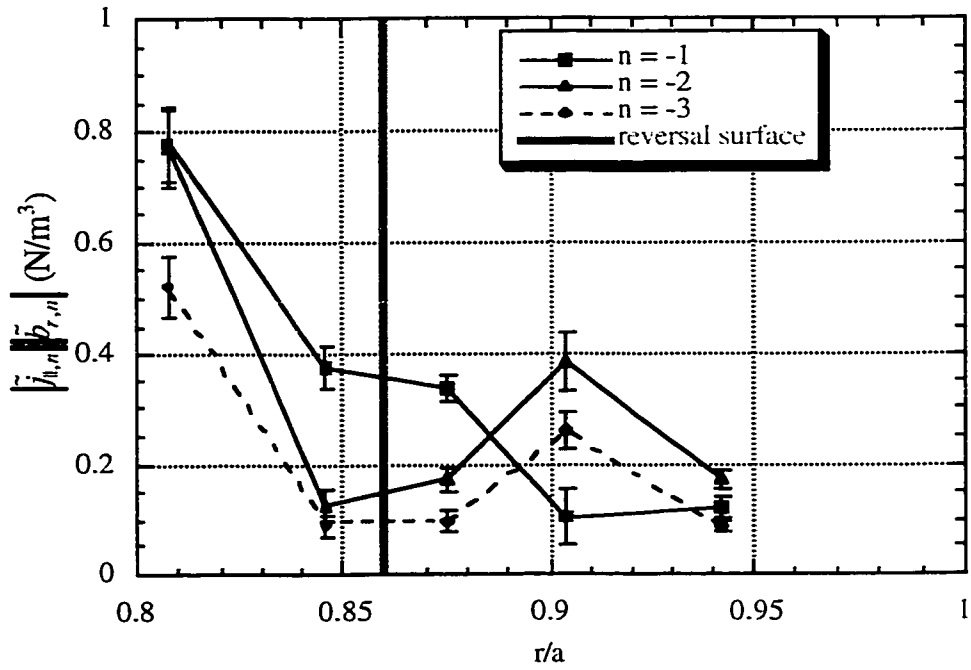

Figure 40: Radial profiles of the combined magnitude of $\tilde{j}_{\parallel}$ and $\tilde{b}_r$ for selected reversal surface resonant toroidal modes. Measured between sawtooth crashes at 75° P, 120° T. Measured with pseudo-spectral technique using toroidal magnetic field flucuations at the wall as the reference fluctuation.

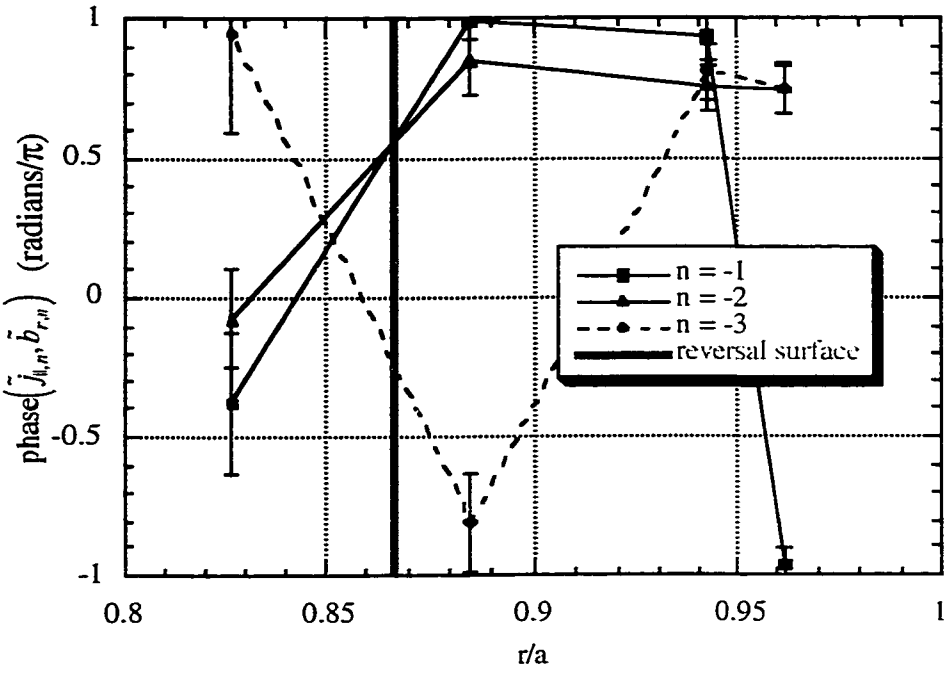

Figure 41: Radial profiles of the phase between $\tilde{j}_{\parallel}$ and $\tilde{b}_r$ for selected reversal surface resonant toroidal modes. Measured during sawtooth crashes at -15° P, 330° T. Measured with pseudo-spectral technique using toroidal magnetic field flucuations at the wall as the reference fluctuation.

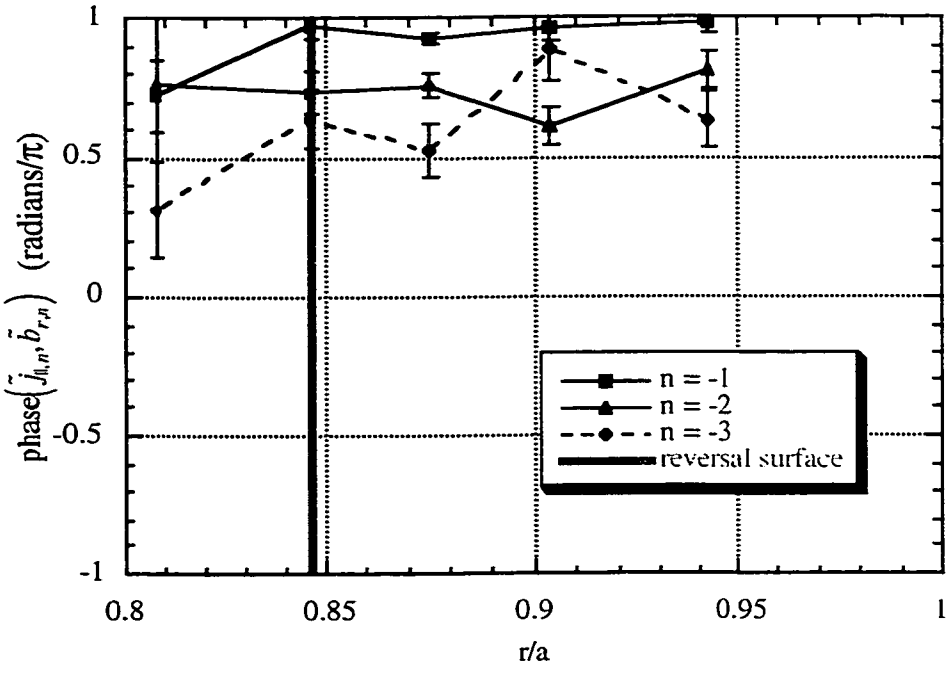

Figure 42: Radial profiles of the phase between $\tilde{j}_{\parallel}$ and $\tilde{b}_r$ for selected reversal surface resonant toroidal modes. Measured during sawtooth crashes at 75° P, 120° T. Measured with pseudo-spectral technique using toroidal magnetic field flucuations at the wall as the reference fluctuation.

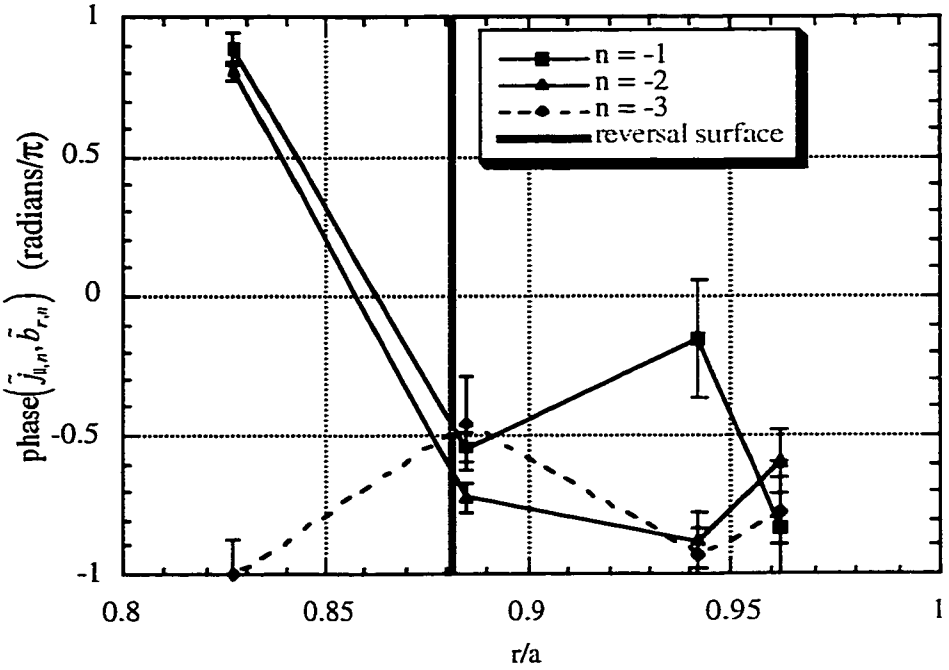

Figure 43: Radial profiles of the phase between $\tilde{j}_{\parallel}$ and $\tilde{b}_r$ for selected reversal surface resonant toroidal modes. Measured between sawtooth crashes at -15° P, 330° T. Measured with pseudo-spectral technique using toroidal magnetic field flucuations at the wall as the reference fluctuation.

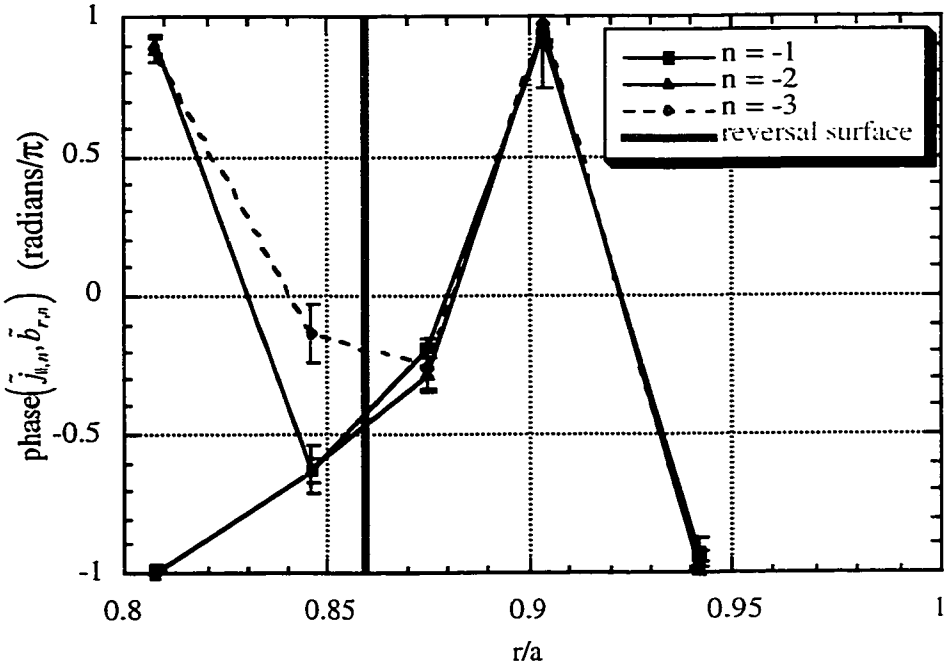

Figure 44: Radial profiles of the phase between $\tilde{j}_{\parallel}$ and $\tilde{b}_r$ for selected reversal surface resonant toroidal modes. Measured between sawtooth crashes at 75° P, 120° T. Measured with pseudo-spectral technique using toroidal magnetic field flucuations at the wall as the reference fluctuation.

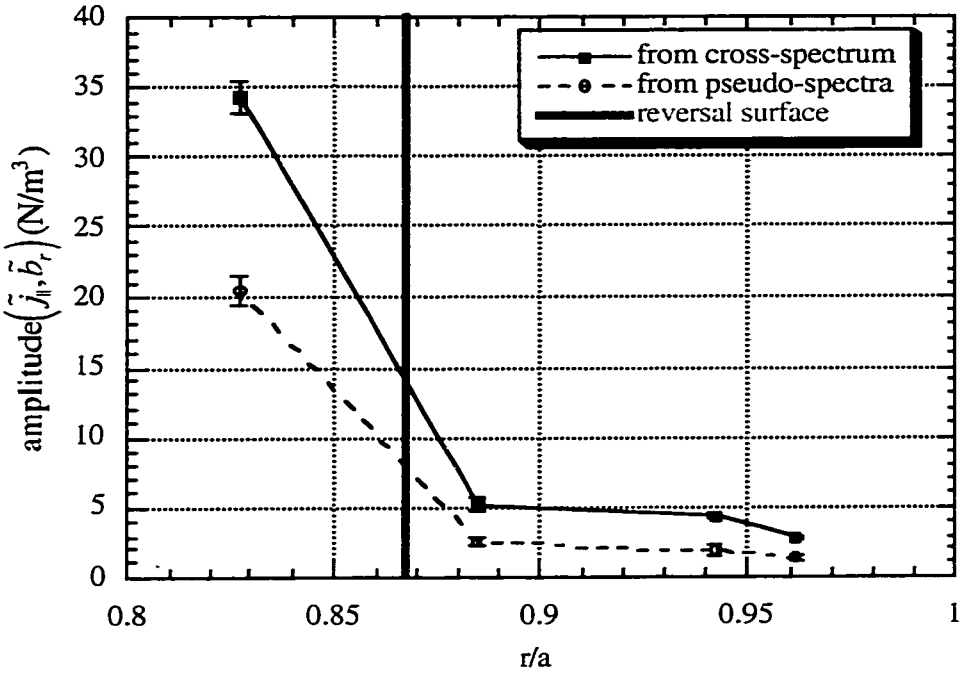

Figure 45: Comparison of direct measurement with pseudo-spectral esitmate of cross-spectral magnitude of $\tilde{j}_{\|}$ and $\tilde{b}_r$ during sawtooth crashes at -15° P, 330° T

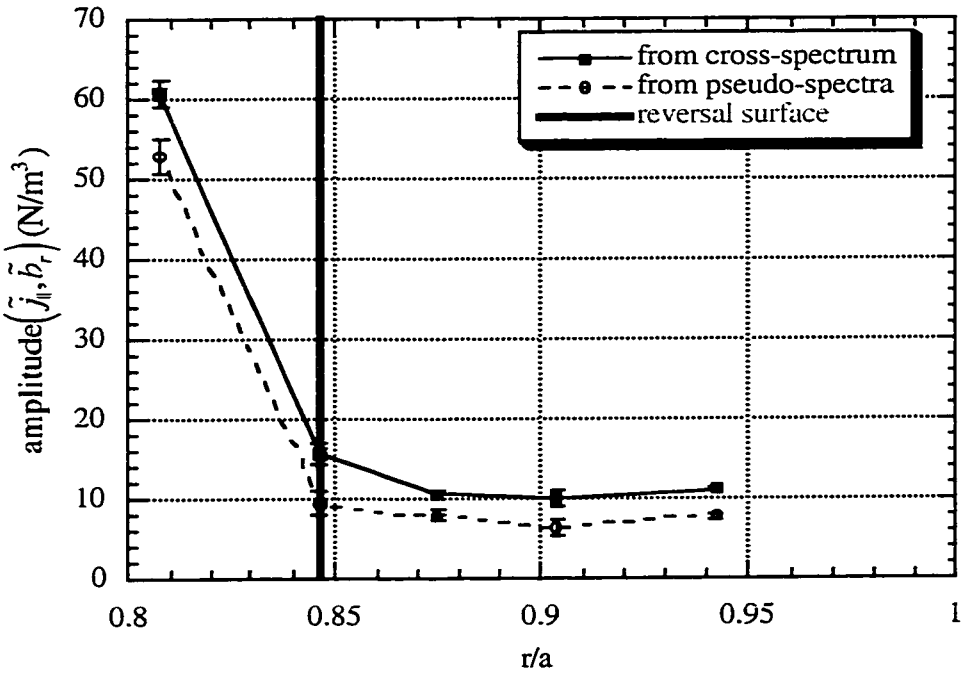

Figure 46: Comparison of direct measurement with pseudo-spectral esitmate of cross-spectral magnitude of $\tilde{j}_{\|}$ and $\tilde{b}_r$ during sawtooth crashes at 75° P, 120° T.

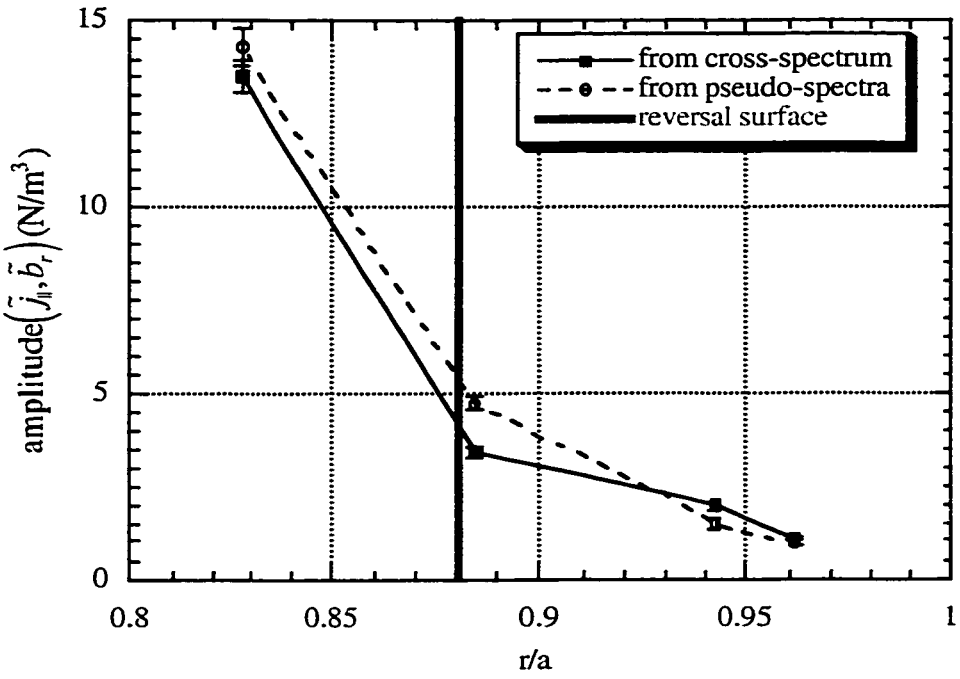

Figure 47: Comparison of direct measurement with pseudo-spectral esitmate of cross-spectral magnitude of $\tilde{j}_{\parallel}$ and $\tilde{b}_r$ between sawtooth crashes at -15° P, 330° T.

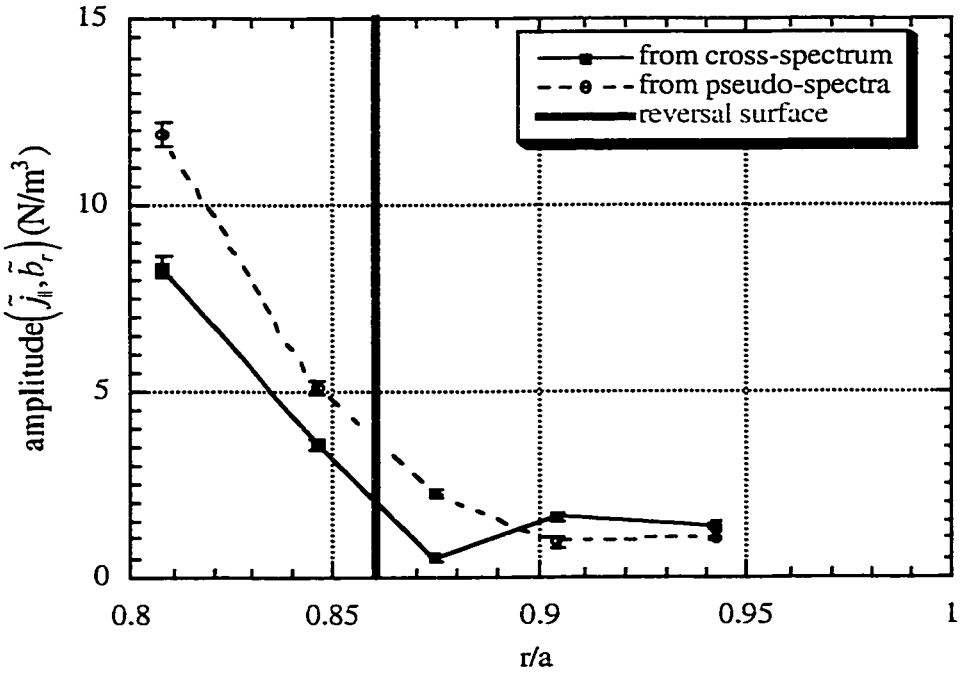

Figure 48: Comparison of direct measurement with pseudo-spectral esitmate of cross-spectral magnitude of $\tilde{j}_{\parallel}$ and $\tilde{b}_r$ between sawtooth crashes at 75° P, 120° T.

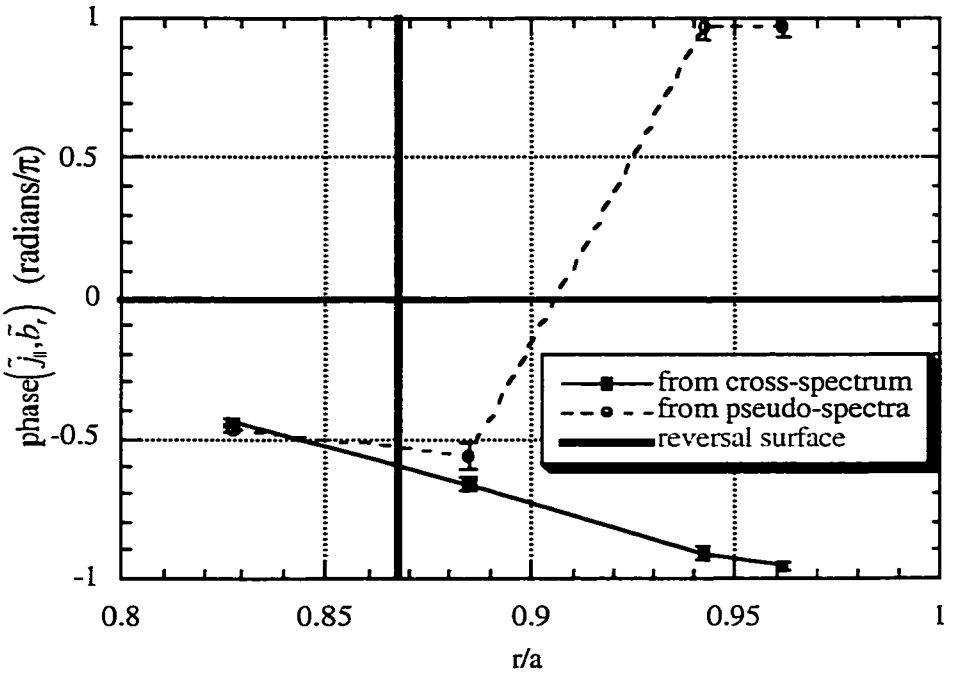

Figure 49: Comparison of direct measurement with pseudo-spectral esitmate of cross-spectral phase between $\tilde{j}_{\|}$ and $\tilde{b}_r$ during sawtooth crashes at -15° P, 330° T.

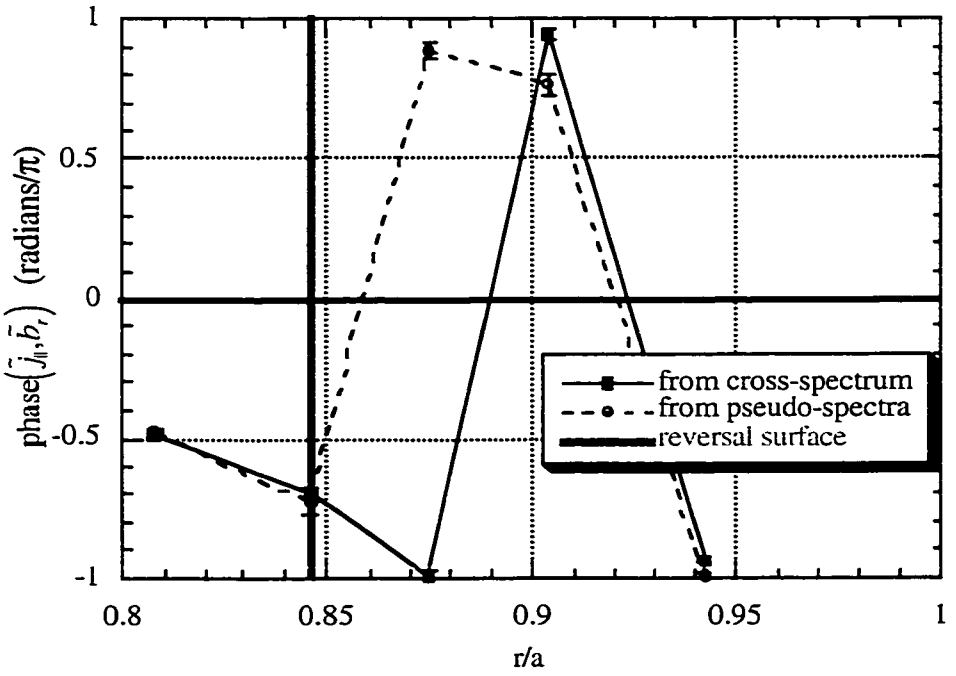

Figure 50: Comparison of direct measurement with pseudo-spectral esitmate of cross-spectral phase between $\tilde{j}_{\|}$ and $\tilde{b}_r$ during sawtooth crashes at 75° P, 120° T.

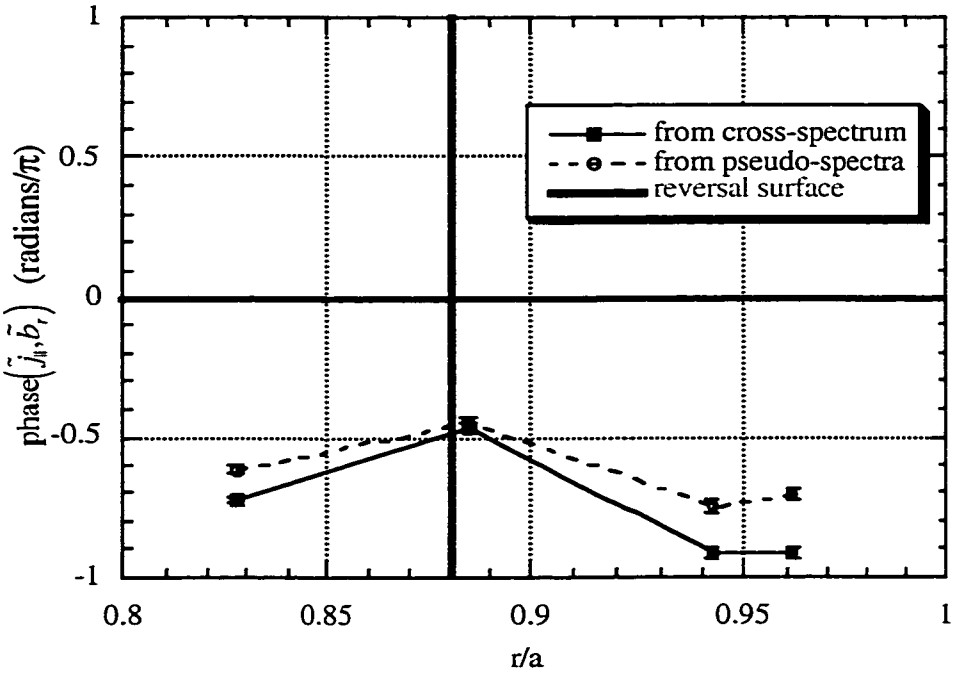

Figure 51: Comparison of direct measurement with pseudo-spectral esitmate of cross-spectral phase between $\tilde{j}_{\|}$ and $\tilde{b}_r$ between sawtooth crashes at -15° P, 330° T.

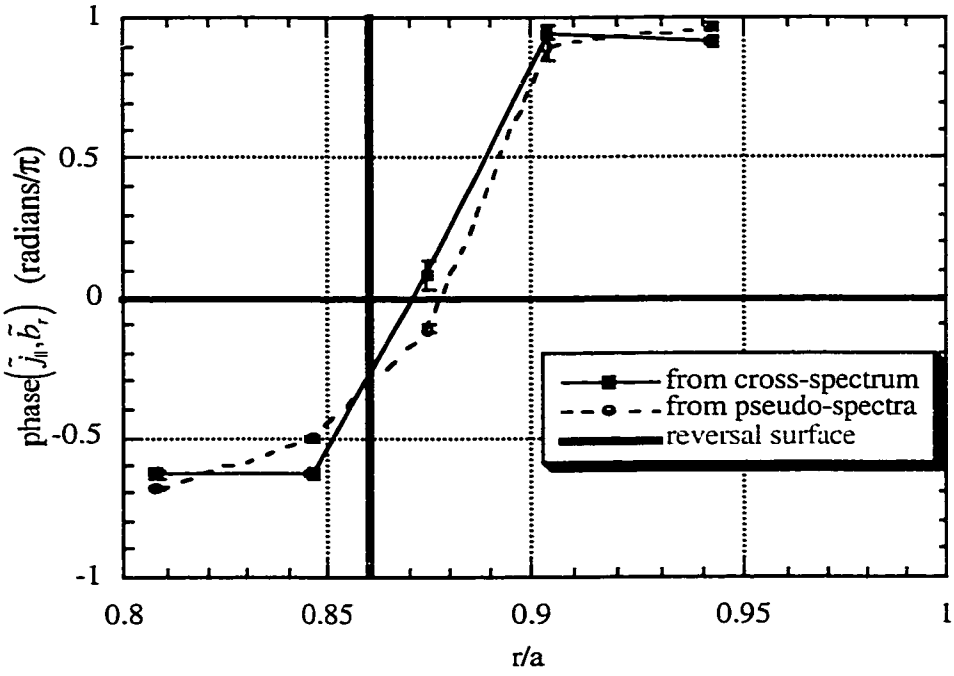

Figure 52: Comparison of direct measurement with pseudo-spectral esitmate of cross-spectral phase between $\tilde{j}_{\|}$ and $\tilde{b}_r$ between sawtooth crashes at 75° P, 120° T.

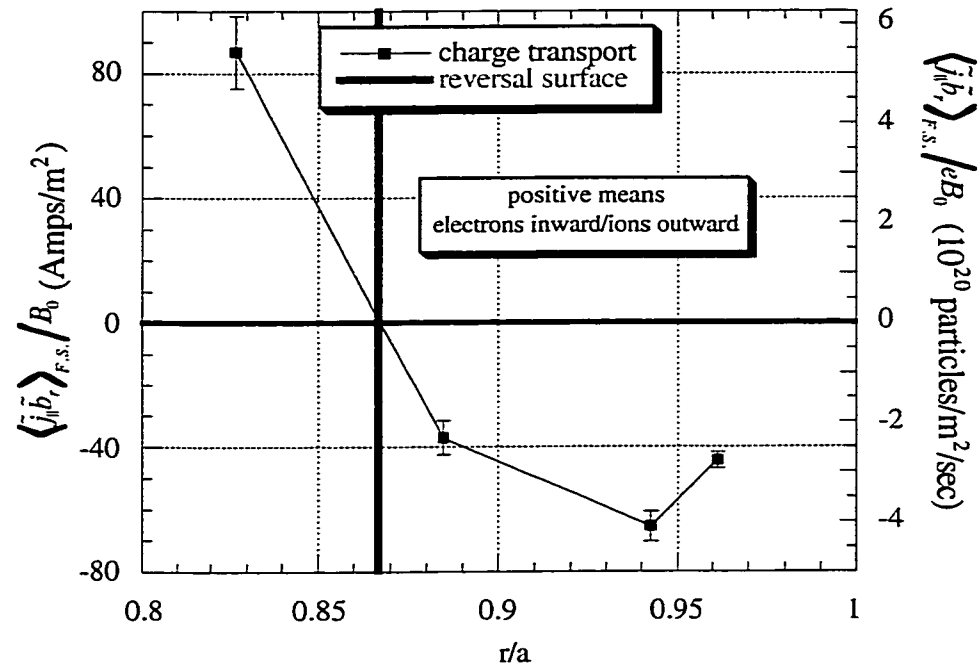

Figure 53: Radial charge flux (and difference between ion and electron particle fluxes) implied by flux surface average product of $\tilde{j}_\parallel$ and $\tilde{b}_r$. Measured during sawtooth crashes at -15° P, 330° T.

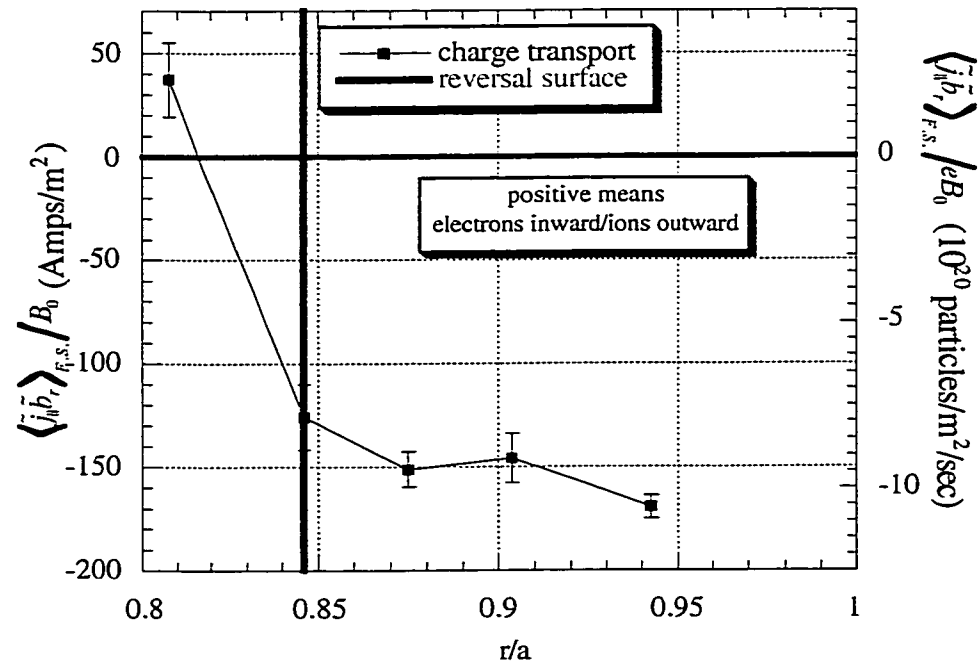

Figure 54: Radial charge flux (and difference between ion and electron particle fluxes) implied by flux surface average product of $\tilde{j}_\parallel$ and $\tilde{b}_r$. Measured during sawtooth crashes at 75° P, 120° T.

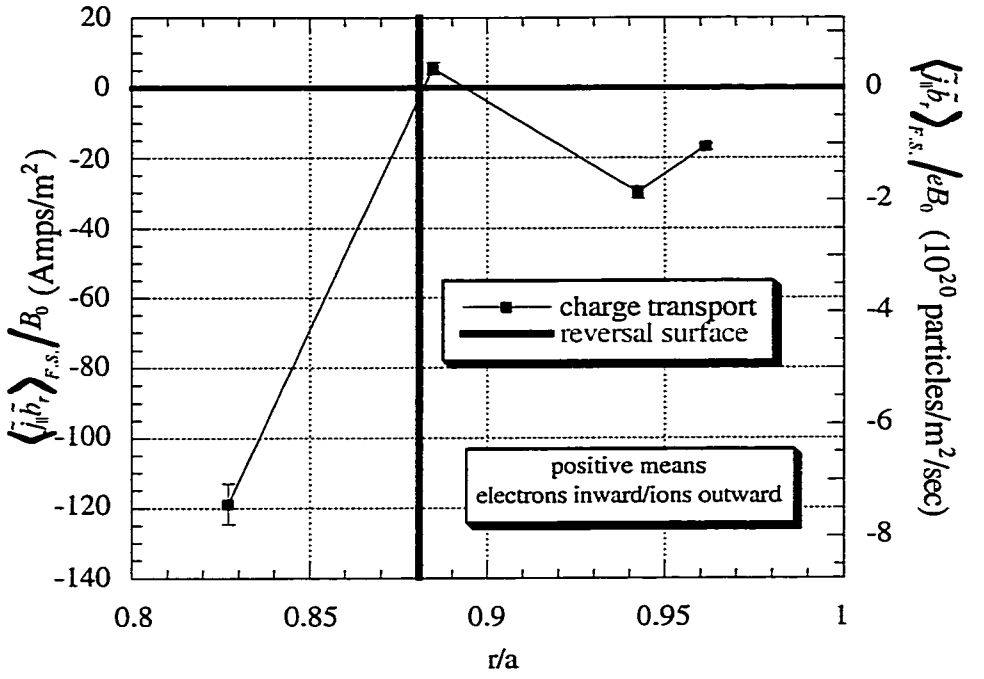

Figure 55: Radial charge flux (and difference between ion and electron particle fluxes) implied by flux surface average product of $\tilde{j}_{\parallel}$ and $\tilde{b}_r$. Measured between sawtooth crashes at -15° P, 330° T.

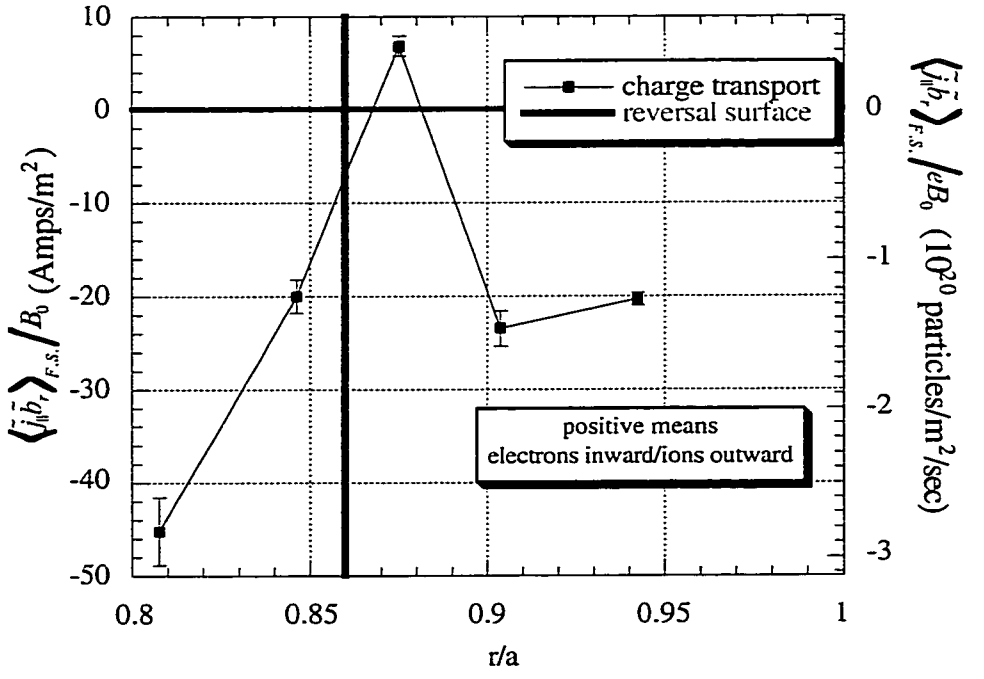

Figure 56: Radial charge flux (and difference between ion and electron particle fluxes) implied by flux surface average product of $\tilde{j}_{\parallel}$ and $\tilde{b}_r$. Measured between sawtooth crashes at 75° P, 120° T.